

AGARD-CP-346

AGARD-CP-346

# AGARD

ADVISORY GROUP FOR AEROSPACE RESEARCH & DEVELOPMENT

7 RUE ANCELLE 92200 NEUILLY SUR SEINE FRANCE

AD-A145 046

AGARD CONFERENCE PROCEEDINGS No. 346

## Characteristics of the Lower Atmosphere Influencing Radio Wave Propagation

This document has been approved  
for public release and sale; its  
distribution is unlimited.

DTIC  
S E L E C T E D  
MAY 24 1984

DTIC FILE COPY

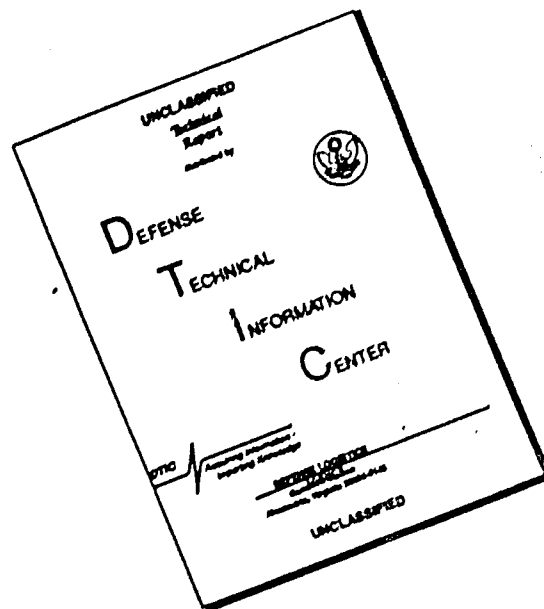
NORTH ATLANTIC TREATY ORGANIZATION



DISTRIBUTION AND AVAILABILITY  
ON BACK COVER

84 05 23 045

# DISCLAIMER NOTICE



THIS DOCUMENT IS BEST QUALITY AVAILABLE. THE COPY FURNISHED TO DTIC CONTAINED A SIGNIFICANT NUMBER OF PAGES WHICH DO NOT REPRODUCE LEGIBLY.

DTIC

SEP 10 1984

## COMPONENT PART NOTICE

THIS PAPER IS A COMPONENT PART OF THE FOLLOWING COMPILATION REPORT:

A

(TITLE): Characteristics of the Lower Atmosphere Influencing Radio Wave Propagation:  
Conference Proceedings of the Symposium of the Electromagnetic Wave  
Propagation Panel (33rd) Held at Spatind, Norway on 4-7 October 1983.

(SOURCE): Advisory Group for Aerospace Research and Development, Neuilly-sur-Seine  
(France).

TO ORDER THE COMPLETE COMPILATION REPORT USE AD-A145 046.

THE COMPONENT PART IS PROVIDED HERE TO ALLOW USERS ACCESS TO INDIVIDUALLY AUTHORED SECTIONS OF PROCEEDINGS, ANNALS, SYMPOSIA, ETC. HOWEVER, THE COMPONENT SHOULD BE CONSIDERED WITHIN THE CONTEXT OF THE OVERALL COMPILATION REPORT AND NOT AS A STAND-ALONE TECHNICAL REPORT.

THE FOLLOWING COMPONENT PART NUMBERS COMPRISE THE COMPILATION REPORT:

AD#:	TITLE:
AD-P003 885	Ice Depolarization on Low-Angle 11 GHz Satellite Downlinks.
AD-P003 886	The Effects of a Low-Altitude Nuclear Burst on Millimeter Wave Propagation.
AD-P003 887	Measurements of Atmospheric Effects on Satellite Links at Very Low Elevation Angle.
AD-P003 888	The Effects of Meteorology on Marine Aerosol and Optical and IR Propagation.
AD-P003 889	A System to Measure LOS (Line-of-Sight) Atmospheric Transmittance at 19 GHz.
AD-P003 890	A GaAs FET Microwave Refractometer for Tropospheric Studies.
AD-P003 891	Prediction of Multipath Fading on Terrestrial Microwave Links at Frequencies of 11 GHz and Greater.
AD-P003 892	Multipath Outage Performance of Digital Radio Receivers Using Finite-Tap Adaptive Equalizers.
AD-P003 893	Spherical Propagation Models for Multipath-Propagation Predictions.
AD-P003 894	Correcting Radio Astronomy Interferometry Observations for Ionospheric Refraction.
AD-P003 895	The Estimation and Correction of Refractive Bending in the AR3-D Tactical Radar Systems.
AD-P003 896	Effect of Multiple Scattering on the Propagation of Light Beams in Dense Nonhomogeneous Media.
AD-P003 897	Adaptive Compensation for Atmospheric Turbulence Effects on Optical Propagation.
AD-P003 898	Effects of Atmospheric Turbulence on Optical Propagation.
AD-P003 899	A Radio Interference Model for Western Europe.
AD-P003 900	Transhorizon Microwave Propagation Measurements related to Surface Meteorological Parameters.
AD-P003 901	Tropospheric Propagation Assessment.

This document has been approved  
for public release and sale; its  
distribution is unlimited.

# COMPONENT PART NOTICE (CON'T)

AD#:

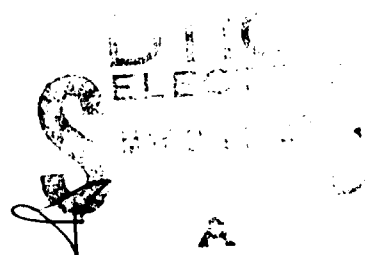
TITLE:

AD-P003 902	Distortion of a Narrow Radio Beam in a Convective Medium.
AD-P003 903	Anomalous Propagation and Radar Coverage through Inhomogeneous Atmospheres.
AD-P003 904	The Prediction of Field Strength in the Frequency Range 30 - 1000 MHz.
AD-P003 905	VHF and UHF Propagation in the Canadian High Arctic.
AD-P003 906	Considerations Pertinent to Propagation Prediction Methods Applied to Airborne Microwave Equipments.

Accession For	
NTIS GRA&I	<input checked="" type="checkbox"/>
DTIC TAB	<input type="checkbox"/>
Unannounced	<input type="checkbox"/>
Justification	
By	
Distribution/	
Availability Codes	
Dist	Avail and/or Special
A-1	

NORTH ATLANTIC TREATY ORGANIZATION  
ADVISORY GROUP FOR AEROSPACE RESEARCH AND DEVELOPMENT  
(ORGANISATION DU TRAITE DE L'ATLANTIQUE NORD)

AGARD Conference Proceedings No.346  
CHARACTERISTICS OF THE LOWER ATMOSPHERE INFLUENCING  
RADIO WAVE PROPAGATION



Papers presented at the 33rd Symposium of the Electromagnetic Wave Propagation Panel  
held in Spåtind, Norway 4-7 October 1983.

## THE MISSION OF AGARD

The mission of AGARD is to bring together the leading personalities of the NATO nations in the fields of science and technology relating to aerospace for the following purposes:

- *Exchanging of scientific and technical information;*
- Continuously stimulating advances in the aerospace sciences relevant to strengthening the common defence posture;
- Improving the co-operation among member nations in aerospace research and development;
- Providing scientific and technical advice and assistance to the North Atlantic Military Committee in the field of aerospace research and development;
- Rendering scientific and technical assistance, as requested, to other NATO bodies and to member nations in connection with research and development problems in the aerospace field;
- Providing assistance to member nations for the purpose of increasing their scientific and technical potential;
- Recommending effective ways for the member nations to use their research and development capabilities for the common benefit of the NATO community.

The highest authority within AGARD is the National Delegates Board consisting of officially appointed senior representatives from each member nation. The mission of AGARD is carried out through the Panels which are composed of experts appointed by the National Delegates, the Consultant and Exchange Programme and the Aerospace Applications Studies Programme. The results of AGARD work are reported to the member nations and the NATO Authorities through the AGARD series of publications of which this is one.

Participation in AGARD activities is by invitation only and is normally limited to citizens of the NATO nations.

The content of this publication has been reproduced directly from material supplied by AGARD or the authors.

Published February, 1984

Copyright © AGARD 1984  
All Rights Reserved

ISBN 92-835-0347-3



*Printed by Specialised Printing Services Limited  
40 Chigwell Lane, Loughton, Essex IG10 3TZ*

## THEME

Radio waves must necessarily travel through the lower atmosphere for any ground or space link where at least one end is near the ground. Consequently, the influence of the lower atmosphere on wave propagation act on the whole radio spectrum and the influence becomes much greater above 30 MHz. Optical propagation is also affected by the lower atmosphere. Though all the possible physical phenomena which can influence wave propagation are clearly identified, difficulties occur when predicting the effects of these phenomena, mainly due to insufficient knowledge of radio and optical meteorological parameters. Therefore, the objectives of this symposium were:

- (a) To discuss the present knowledge of the meteorological and radiometeorological parameters which may have an influence on terrestrial or earth-space radio links,
- (b) To discuss the various models and the various methods of predicting the effects of these parameters on radio wave propagation,
- (c) To discuss the effects of turbulence and particle scattering on optical propagation,
- (d) To investigate possible methods to overcome the perturbations due to these propagation effects.

Toute liaison terrestre ou spatiale dont une extrémité au moins est située à proximité du sol exige que les ondes radios se propagent à travers la basse atmosphère. Par conséquent, l'influence de la basse atmosphère sur la propagation des ondes affecte la totalité du spectre radio et devient beaucoup plus marquée au-dessus de 30 MHz. La basse atmosphère affecte également la propagation optique. Bien que tous les phénomènes physiques susceptibles d'influencer la propagation des ondes soient clairement identifiés, des difficultés surgissent lorsqu'il s'agit de prédire les effets de ces phénomènes, du fait, essentiellement, de l'insuffisance de nos connaissances concernant les paramètres météorologiques radio et optiques. Le symposium poursuivait donc les objectifs suivants:

- (a) Passer en revue les connaissances actuelles concernant les paramètres météorologiques et radiométéorologiques susceptibles d'influer sur les liaisons radio soit terrestres soit entre la Terre et l'espace.
- (b) Examiner les divers modèles et les diverses méthodes permettant de prédire les effets de ce paramètres sur la propagation des ondes radio.
- (c) Etudier les effets de la turbulence et la dispersion des particules sur la propagation optiques.
- (d) Rechercher des méthodes permettant de maîtriser les perturbations créés par ces effets de la propagation.



Application For	
Radio	<input checked="" type="checkbox"/>
Optical	<input type="checkbox"/>
Both	<input type="checkbox"/>
Availability Codes	
Avail and/or	Special
1st	2nd
3rd	4th

## **ELECTROMAGNETIC WAVE PROPAGATION PANEL**

**CHAIRMAN:** Dr J. Belrose  
Communications Research Center  
Department of Communications  
P.O. Box 11490, Station H  
Ottawa, K2H 8S2, Canada

**DEPUTY CHAIRMAN:** Dr J.H. Blythe  
Marconi Research Centre  
West Hanningfield Road  
Great Baddow  
Chelmsford, CM2 8HN, UK

## **TECHNICAL PROGRAM COMMITTEE**

**Chairman:**  
Ing. en Chef L. Boithias  
C.N.E.T.  
38-40, rue du Général Leclerc  
92131 Issy-les-Moulineaux, France

## **COMMITTEE**

Dr E. Altshuler, US  
Dr H.T. Dougherty, US  
Dr F. Fedi, IT  
Mr M.P.M. Hall, UK  
Dr -Ing. E.W. Lampert, GE  
Dr K.S. McCormick, CA  
Ir. J.T.A. Neessen, NE  
Dr M.B. White, US

## **EDITOR**

Dr A.W. Biggs

## **LOCAL COORDINATOR**

Mr R. Skaug  
N.D.R.E.  
P.O. Box No. 25  
N-2007 Kjeller  
Norway

## **PANEL EXECUTIVE**

Lt. Colonel Timothy B. Russell  
AGARD/OTAN  
7, rue Ancelle  
92200 Neuilly-sur-Seine  
France

From US  
and Canada  
AGARD/NATO  
APO New York 09777

# CONTENTS

	Page
THEME	iii
MEETING AND PANEL OFFICIALS	iv
TECHNICAL EVALUATION REPORT by A.W.Biggs	ix
EXECUTIVE SUMMARY	xiv
Reference	
<u>SESSION I – INFLUENCE OF RAIN AND OTHER PARTICLES</u>	
MODELE STATISTIQUE DE LA PROPAGATION PAR TRAJETS MULTIPLES TROPOSPHERIQUES par L.Boithias	1 <i>X</i>
DEUX TYPES D'ERREURS FAITES DANS LA PREVISION DES ATTENUATIONS DES ONDES PAR LA PLUIE par L.Boithias	2 <i>X</i>
ICE DEPOLARIZATION ON LOW-ANGLE 11 GHz SATELLITE DOWNLINKS by W.L.Stutzman, C.W.Bostian, A.Tsolaskis and T.Pratt	3
THE EFFECTS OF A LOW-ALTITUDE NUCLEAR BURST ON MILLIMETER WAVE PROPAGATION by E.E.Altshuler	4
MEASUREMENTS OF ATMOSPHERIC EFFECTS ON SATELLITE LINKS AT VERY LOW ELEVATION ANGLE by O.Gutteberg	5
BLUE-GREEN PROPAGATION THROUGH CLOUDS† by G.Mooradian	6
THE EFFECTS OF METEOROLOGY ON MARINE AEROSOL AND OPTICAL AND IR PROPAGATION by S.G.Gathman	7
<u>SESSION II – REFRACTION EFFECTS INCLUDING MULTIPATH AND LOS PATH</u>	
A SYSTEM TO MEASURE LOS ATMOSPHERIC TRANSMITTANCE AT 19 GHz by E.Vilar, T.J.Moulsley, J.Austin, A.Hewitt, J.N.Norbury and S.K.Barton	8
A GaAs FET MICROWAVE REFRACTOMETER FOR TROPOSPHERIC STUDIES by U.M.Yilmaz, G.R.Kennedy and M.P.M.Hall	9
PREDICTION OF MULTIPATH FADING ON TERRESTRIAL MICROWAVE LINKS AT FREQUENCIES OF 11 GHz AND GREATER by D.D.Crombie	10
EFFET DE LA LONGUEUR DU BOND SUR LA QUALITE DES LIAISONS NUMERIQUES A GRANDE CAPACITE par J.Battesti	11 <i>L</i>
Paper 12 withdrawn	
MULTIPATH OUTAGE PERFORMANCE OF DIGITAL RADIO RECEIVERS USING FINITE-TAP ADAPTIVE EQUALIZERS by N.Amitay and L.J.Greenstein	13

† Abstract only

	Reference
SPHERICAL PROPAGATION MODELS FOR MULTIPATH-PROPAGATION PREDICTIONS by L.P.Ligthart	14
CORRECTING RADIO ASTRONOMY INTERFEROMETRY OBSERVATIONS FOR IONOSPHERIC REFRACTION by T.A.Th. Spoelstra	15
THE ESTIMATION AND CORRECTION OF REFRACTIVE BENDING IN THE AR3-D TACTICAL RADAR SYSTEMS by F.Barker	16
EFFECT OF MULTIPLE SCATTERING ON THE PROPAGATION OF LIGHT BEAMS IN DENSE NONHOMOGENEOUS MEDIA by P.Bruscaglioni, A.Ismaeli, L. Lo Porto and G.Zaccanti	17
ADAPTIVE COMPENSATION FOR ATMOSPHERIC TURBULENCE EFFECTS ON OPTICAL PROPAGATION by D.P.Greenwood	18
EFFECTS OF ATMOSPHERIC TURBULENCE ON OPTICAL PROPAGATION by R.S.Lawrence	19
 <u>SESSION III – LONG RANGE PROPAGATION INCLUDING DUCTING AND COVERAGE PROBLEMS</u> 	
EVALUATION DE LA HAUTEUR DU CONDUIT TROPOSPHERIQUE D'EVAPORATION par B.Strauss	20
A RADIO INTERFERENCE MODEL FOR WESTERN EUROPE by S. Rotheram	21
TRANSHORIZON MICROWAVE PROPAGATION MEASUREMENTS RELATED TO SURFACE METEOROLOGICAL PARAMETERS by R.Ambrosini, M.Caporaloni and G.Tomassetti	22
TROPOSPHERIC PROPAGATION ASSESSMENT by K.A.Anderson	23
DISTORTION OF A NARROW RADIO BEAM IN A CONVECTIVE MEDIUM by W.G.Burrows	24
ANOMALOUS PROPAGATION AND RADAR COVERAGE THROUGH INHOMOGENEOUS ATMOSPHERES by H.W.Ko, J.W.Sari, M.E.Thomas, P.J.Herchenroeder and P.J.Martone	25
THE PREDICTION OF FIELD STRENGTH IN THE FREQUENCY RANGE 30–1000 MHz by R.S.Sandell and D.W.Taplin	26
VHF AND UHF PROPAGATION IN THE CANADIAN HIGH ARCTIC by R.S.Butler, J.I.Strickland and C.Bilodeau	27
CONSIDERATIONS PERTINENT TO PROPAGATION PREDICTION METHODS APPLIED TO AIRBORNE MICROWAVE EQUIPMENTS by T.Almond	28

**SOME OF THE PAPERS PRESENTED AT THE 1983 IEEE INTERNATIONAL SYMPOSIUM  
ON ANTENNAS AND PROPAGATION AND USNC/URSI MEETING**  
by A.W.Biggs

29

**REVIEW OF SOME PAPERS PRESENTED AT THE 1983 URSI COMMISSION F SYMPOSIUM**  
by A.W.Biggs

30

**ROUND TABLE DISCUSSION**

RTD

**LIST OF PARTICIPANTS**

P

## TECHNICAL EVALUATION REPORT

BY

ALBERT W. BIGGS

REMOTE SENSING LABORATORY, UNIVERSITY OF KANSAS, LAWRENCE, KANSAS 66045 USA

### 1. INTRODUCTION

The 33rd symposium of the Electromagnetic Wave Propagation Panel on "Characteristics of the Lower Atmosphere Influencing Radio Wave Propagation" was held in Spatind, Norway, 4-7 October 1983. The Program Committee consisted of Mr. L. Boithias (France), Chairman, Dr. E. Altshuler (U.S.), Dr. H.T. Dougherty (U.S.), Dr. F. Fedi (Italy), Mr. M.P.M. Hall (U.K.), Dr.-Ing. E.W. Lampert (Germany), Dr. K.S. McCormick (Canada), Ir. J.T.A. Neessen (The Netherlands), and Dr. M.B. White (U.S.).

The technical evaluation for Sessions I and III were performed by the session chairmen, while that for Session II was performed by Dr.A.W. Biggs (U.S.).

This report represents an attempt to provide a summary of the entire symposium and to draw conclusions and derive recommendations which were received from authors and participants of the symposium.

### 2. THEME

Radio waves must necessarily travel through the lower atmosphere for any ground or space link where at least one end is near the ground. Consequently, the influence of the lower atmosphere on wave propagation act on the whole radio spectrum and the influence becomes much greater above 30 MHz. Optical propagation is also affected by the lower atmosphere. Though all the possible physical phenomena which can influence wave propagation are clearly identified, difficulties occur when predicting the effects of these phenomena, mainly due to insufficient knowledge of radio and optical meteorological parameters. Therefore, the objectives of this symposium were:

- o To discuss the present knowledge of the meteorological and radio-meteorological parameters which may have an influence on terrestrial or earth-space radio links.
- o To discuss the various models and the various methods of predicting the effects of these parameters on radio wave propagation.
- o To discuss the effects of turbulence and particle scattering on optical propagation.
- o To investigate possible methods to overcome the perturbations due to these propagation effects.

The symposium was organized in three sessions in which 26 formal papers were presented covering

I Influence of Rain and Other Particles

II Refraction Effects Including Multipath and LOS Path

III Long Range Propagation Including Ducting and Coverage Problems

Papers (29) and (30) in the symposium Proceedings were reviews of "Some of the Papers Presented at the 1983 International Symposium on Antennas and Propagation and USNC/URSI Meeting", in Houston, Texas, USA, 23-26 May 1983, and "Review of Some Papers Presented at the 1983 URSI Commission F Symposium", in Louvain-la-Neuve, Belgium, 9-15 June 1983. Papers relevant to each of the three sessions were briefly described by Dr. A.W. Biggs (U.S.).

Brief summaries of the Final Round Table Discussion and the Closing Ceremony follow the technical evaluation of the three session.

PREVIOUS PAGE  
IS BLANK

### 3. TECHNICAL EVALUATION

#### 3.1. SESSION I - INFLUENCE OF RAIN AND OTHER PARTICLES

CHAIRMAN: Mr. M.P.M. Hall, Rutherford Appleton Laboratory, Chilton, Oxfordshire, UK

##### Introduction

This session examined particles in the form of rain, ice, and dust and sand from nuclear explosions in the microwave spectrum. Unfortunately an interesting paper (1) by E. Raschke was cancelled. Therefore only six papers were presented. They represented samples from a broad field, but the subsequent discussions drew a wider range of applicability.

##### Technical Evaluation

Paper No. 1 was cancelled. Based on discussions a new paper (1) is included in the Proceedings.

The first paper, by Mr. L. Boithias (2), was "Deux Types d'Erreurs Faites dans la Prévision de l'Atténuation des Ondes par la Pluie", considered several aspects of the prediction due to rain on an earth-space path. Attention was given to the correct modelling of rainfall rate distribution at a point, to the structure modelling of its horizontal structure, and to its vertical extent. The discussion emphasized the first of these, particularly for the high rainfall rates, but also mentioned the need for modelling low rainfall rates for prediction of interference due to scatter from rain at frequencies above 10 GHz.

Dr. C.W. Bostian (3) presented a very interesting paper, "Ice Depolarization on Low-Angle 11 GHz Satellite Downlinks," which was concerned with effects on low-angle paths. It concentrated on the effect of ice events on the cross-polar discrimination (XPD) statistics on two 10.9° elevation paths operating in the state of Virginia in the U.S., and also on the joint statistics with attenuation. Ice effects were found to be only minor, relative to those of rain, but they were more significant on the lower elevation paths than in the case of higher elevations.

The paper by Dr. E.E. Altshuler (4), "The Effect of a Low-Altitude Nuclear Burst on Millimeter Wave Propagation", described a study of effects on millimeter wave propagation of very high densities of particles, e.g., 100 grams per cubic meter, extending up to very large sizes, e.g., 100 mm radii, but the results were presented in a form which naturally occurring sand and dust storms could be modelled. As long as the sizes do not exceed about 0.3 mm radius (as likely to be the case in natural events), the attenuation due to clouds of clay or sand particles is quite small. Immediately after a nuclear explosion, the effects would be severe, especially within the fireball.

Mr. A.O. Gutteberg's paper (5) "Measurements of Atmospheric Effects on Satellite Links at Very Low Elevation Angles", was similar to Dr. Bostian's paper in its interest in low-angle paths, but in rather different climatic conditions. It described various measurements made at only 3.2° elevation from a site in the Arctic Islands of Spitzbergen at a frequency of 11.8 GHz. They comprised scintillation, XPD, and site diversity improvement obtained with a 1.1 km spacing. Rainfall is not significant in this Arctic region, compared with snow and sleet.

Paper N° 6, "Blue Green Propagation through Clouds", was read by Dr. H. Hodara. It was a study of a space to underwater link with the adverse presence of clouds. A blue-green pulse was selected for minimum cloud and sea water absorption.

The final paper by Dr. S.G. Gathman (7), "Effects of Meteorology on Marine Aerosols and Optical and IR Propagation", described the formation, dispersion, and nature of aerosols in the marine boundary layer. Their effects on the extinction and absorption of optical and infra-red (IR) energy can be predicted from a knowledge of the sea surface meteorology, so that meteorological forecasting can be the basis for optical and IR forecasting.

#### 3.2. Session II - REFRACTION EFFECTS INCLUDING MULTIPATH AND LOS PATH Chairman: Mr. L. Boithias, C.N.E.T., Issy-les-Moulineaux, France

##### Introduction

One paper (12) on atmospheric refractive structure, multipath, and digital radio performance was cancelled. These subjects were extremely well described in the other 11 papers presented in this session. The first 8

papers described radio wave propagation, while the last 3 papers covered optical propagation in a somewhat tutorial sense.

#### Technical Evaluation

"A System to Measure LOS Atmospheric Transmittance at 19 GHz" was presented by Dr. T.J. Mousley (8). It described a wideband test system for evaluating a LOS microwave link, subject to both fading and multipath. The technique, using cross correlation between pseudo-binary random sequences, is equivalent to a direct-sequence spread-spectrum modulation. Computer simulations and preliminary experimental results were presented.

M.P.M. Hall (9) described a very interesting refractometer in "A GaAs FET Microwave Refractometer for Tropospheric Studies". The refractometer has been successfully tested in a light airplane with on-board processing. In one of the experimental studies, a large refractivity gradient was observed without a corresponding change in the temperature profile.

"Prediction of Multipath Fading on Terrestrial Microwave Paths at Frequencies of 11 GHz or Higher", was presented by Dr. D.D. Crombie (10). He made an analysis of multipath fading on 18 different paths with lengths up to 58 km, frequencies from 10.92 to 36.3 GHz, in the U.K., Japan, and the US. His results would indicate that multipath fading probabilities can be estimated without detailed knowledge of climate of terrain, but with knowledge of path clearance and/or antenna beamwidth.

Mr. J. Battesti (11) presented "Effet de la Longueur du Bond sur la Qualité des Liaisons Numériques à Grande Capacité". His results allow calculations of fading depths for digital links.

Paper N° 12 was cancelled.

Dr. N. Amitay (13) presented "Multipath-Outage Performance of Digital Radio Receivers Using Finite-Tap Adaptive Equalizers". This paper shows that a practical fractionally spaced tapped delay line equalizer can provide digital radio outage performance like an ideal tap equalizer. The tapped delay line may be viewed as a weighted Fourier series for making an adaptive filter to minimize mean square distortion.

Paper N° 14 on "Spherical Propagation Models for Multipath Propagation Models", by Mr. L.P. Ligthart, introduced a spherical model for path delay computations in multipath fading conditions. An example was presented for a refractive index profile of a duct above water. Experimental verification of the model is still to be done.

In his paper, Dr. A.T.A.Th. Spoelstra (15) spoke about "Correcting Radio Astronomy Interferometry Observations for Ionospheric Refraction". He reviewed a correction procedure for ionospheric refraction for radio astronomy interferometry. Applications were made for observations with the Westerbork Synthesis Radio Telescope.

"The Estimation and Correction of Refractive Bending in the AR3-D Tactical Radar Systems", read by Dr. A. Morley (16), is the development of techniques for estimating and correcting refractive bending in a family of radar systems. An algorithm was presented for an exact solution, but requiring pressure, humidity, and temperature profiles.

Mr. G. Zaccanti (17) described "Effects of Multiple Scattering on the Propagation of Light Beams in Dense Nonhomogeneous Media". Calculations were made with the Monte Carlo method for a laser beam in a medium with strong inhomogeneities. Experimental verifications were made later in a dense homogeneous fog in a one meter laboratory chamber, and still later in an actual fog in field conditions.

"Adaptive Compensation for Atmospheric Turbulence Effects on Optical Propagation" presented by Dr. D. Greenwood (18), was a very interesting tutorial review of research of optical waves in atmospheric turbulence, followed by an equally good review of the adaptive optics field. The latter area represents excellent opportunities for research studies.

The last paper in this session was "The Effects of Atmospheric Turbulence on Optical Propagation", presented by Dr. R.S. Lawrence (19). Like the previous paper, this paper was also a good review paper about the refractive index of the atmosphere, and how it depends on temperature, humidity, and pressure.

#### 3.3. SESSION III - LONG RANGE PROPAGATION INCLUDING DUCTING AND COVERAGE PROBLEMS

Chairman: Dr. E.E. Altshuler, R.A.D.C., Hanscom AFB, MA, USA

## Introduction

The papers presented in the final session of this meeting were concerned primarily with tropospheric ducting and tropo-scatter propagation. Experimental results were reviewed, and tropospheric models to explain these phenomena were formulated. Finally, several prediction models were discussed. Based on the papers and the subsequent discussions, it can be concluded that progress is being made in the understanding and in the prediction of tropospheric ducting. Yet improved models are still needed in order to provide the user with the confidence he desires.

## Technical Evaluation

Mr. B. Strauss (20), in "Evaluation de la Hauteur du Conduit Troposphérique d'Evaporation", discussed the relationship of the height of tropospheric ducts with meteorological parameters for locations in the North Atlantic and Indian Oceans. Comparisons were made between results obtained from a model and those that were measured.

"A Radio Interference Model for Western Europe", presented by Dr. S. Rotherham (21), used field strength measurements from land, sea, and mixed paths to obtain a statistical model of field strength variations as a function of distance. He showed that propagation over land-sea paths was influenced more by the land section of the path. He also showed the frequency dependence to be very weak.

"Transhorizon Microwave Propagation Measurements Related to Surface Meteorological Parameters", related by Dr. R. Ambrosini (22), reviewed tropo-scatter measurements made at a wavelength of 3 cm over both land and sea paths. They found that the strong daily dependence that occurred over land was essentially non-existent over sea. They attribute this to the fact that meteorological day/night differences are much greater over land than over sea.

Dr. K.D. Anderson (23) outlined a technique that is currently being used by the U.S. Navy to forecast tropospheric refractivity conditions that adversely affect the performance of EM systems in "Tropospheric Propagation Assessment". The method uses a shipboard computing capability which generates displays of system performance based on inputs of refractivity data and equipment parameters.

Dr. W.G. Burrows (24) modelled the troposphere as an array of Benard cells in "Distortion of a Narrow Beam in a Convective Medium". He explained that the refractive index distribution in such a cell structure may be equivalent to a concave lens and thus produce some of the tropospheric propagation phenomena that have been observed.

Dr. H.W. Ko (25), in "Anomalous Propagation and Radar Coverage through Inhomogeneous Atmospheres", described a computer program that has been developed to obtain radar coverage predictions under conditions of anomalous propagation. The program has the capability of handling refractive index changes in both horizontal and vertical directions. Results obtained from this code have been compared with measured data and the agreement has been very favorable.

In the paper delivered by Mr. D.W. Taplin (26), "The Prediction of Field Strengths in the Frequency Range 30-1000 MHz", a large set of VHF and UHF propagation data was reviewed in an effort to obtain a more accurate prediction method. He hopes to incorporate these results into a revision of CCIR Recommendation 370 (propagation from broadcast services).

"VHF and UHF Propagation in the Canadian High Arctic", read by Dr. S. McCormick (27), portrayed results from VHF and UHF line-of-sight measurements in the Canadian Arctic. For most of the VHF paths, the fading was minimal. However, for two VHF paths, severe fading occurred which was believed to be caused by ducting. Unfortunately there were no meteorological data available to verify this. Future propagation measurements, to be supported with meteorological data, are planned.

The last paper of this discussion provoked a long and stimulating discussion. Flight Lieutenant T. Almond (28), in "Considerations Pertinent to Propagation Prediction Methods Applied to Airborne Microwave Equipments", summarized the needs of the typical user regarding tropospheric ducts and coverage diagrams. He emphasized that the assumption of horizontally stratified layers of refractivity is often not valid, particularly in regions of constantly changing air masses such as those over the North Sea. He further emphasized the need for improved sounding techniques that would lead to more accurate predictions.

#### 4. FINAL ROUND TABLE DISCUSSION AND CLOSING CEREMONY

The following summarizes the comments made by the participants in the Final Round Table Discussion and the Closing Ceremony.

Given the complexity of the propagation medium and sophisticated systems, limited research funding, and the multitude of problems caused by propagation limitations on systems, the discussions centered on two questions. The first question was: What modelling approach provides the best results? The second question was: How should the most relevant emerging problems be identified and prioritized?

The resulting debate treated the advantages and disadvantages of: site specific models versus large, almost global models; complex versus simple models; and empirical models using long term statistics like those favored by CCIR Commission 5 (because they are required for system planning) versus the physical models favored by URSI that include a knowledge of the physical processes in the propagation medium. The difficult task of selecting the most appropriate model is constrained by the problem faced by the system designer and/or system user, funding available, ability to collect and use the pertinent data, and the limits to which empirical models can be improved without the additional knowledge that could be provided by physical models.

Propagation experts, systems engineers, and systems users all find problems caused by propagation limitations on systems. The timeliness of the resolution of these problems by propagation experts was discussed. Systems engineers would like propagation problems to be identified and resolved before new systems are designed. Propagation studies are somewhat cyclic in nature. When sufficient knowledge of a particular phenomenon for the current usage and technology is available, propagation studies then examine other phenomena of topical interest. As usage increases and technology advances new problems emerge requiring resolution. New propagation studies that refine past propagation studies are then initiated.

From the whole universe of propagation problems, a means to prioritize the most relevant emerging problems should be established. Some governments have recently established formal procedures. AGARD and other symposia and conferences enable propagation experts, systems engineers, and systems users to meet and interchange ideas. A benefit from these resident meetings is the opportunity for participants to talk with each other during coffee breaks, during dinner and other social activities.

The topics covered at this meeting were of timely interest. There was an USRI meeting a few months previous to this meeting and a CCIR meeting a few months after this meeting that have and will cover related topics. The Panel perspective concerning propagation problems is different from that of CCIR and URSI, but it was generally agreed that the innovation at this meeting to highlight the topics presented at other recent symposia and conferences with similar themes was beneficial.

## EXECUTIVE SUMMARY

The following summarizes the significant conclusions and recommendations from the Technical Evaluation.

### Conclusions:

- o New concepts in the modelling of ice and rain depolarization indicate the continuing interest in this area. New models are needed for prediction of interference due to scatter from rain at frequencies greater than 10 GHz.
- o Optical and IR propagation phenomena are continuing to be better understood in terms of absorption, attenuation, and forecasting. This leads to better system design.
- o Propagation models for multipath propagation allow for improved prediction techniques. Finite-tap adaptive equalizers offer a good systems approach to overcome multipath outage problems.
- o Adaptive compensation for atmospheric turbulence effects indicates interesting applications in the optical propagation field.
- o Based on the papers presented, and subsequent discussion, progress is being made in the understanding and prediction of tropospheric ducting. Improved models are still needed by military and civilian users.
- o Reviews of related URSI, CCIR, and IEEE meeting presentations, given by an AGARD participant who went to one or more of these meetings, were of interest and value to the AGARD participants.
- o Meetings such as this AGARD meeting provide valuable opportunities for mixing systems engineers and pure scientific people together.

### Recommendations:

- o AGARD should continue to have meetings with a balance of scientific and applied presentations with a corresponding balance of participants.
- o Review of other related meetings should continue at AGARD meetings.

# MODELE STATISTIQUE DE LA PROPAGATION PAR TRAJETS MULTIPLES TROPOSPHERIQUES

par

L.Boithias

Centre National d'Etudes des Télécommunications

92131 Issy les Moulineaux

France

Dans la discussion de certaines contributions on a mentionné un certain modèle statistique de propagation par trajets multiples. Comme ce modèle a été présenté dans plusieurs publications [1] [2], on se limitera à un bref résumé.

On sait que la distribution des niveaux reçus sur une liaison en visibilité, qui ne comporte pas de réflexions stables sur le sol, peut être représentée en général par une loi de Rice-Nakagami, car cette loi donne la distribution statistique de la somme d'un vecteur déterministe et d'un vecteur aléatoire. Lorsque le vecteur déterministe a une amplitude nulle ou négligeable on obtient une loi de Rayleigh. Le problème essentiel est de trouver les relations qui existent entre les paramètres de la distribution et les paramètres de la liaison (distance, fréquence, climat, etc...). Dans le présent modèle ces relations découlent des propositions suivantes :

1) La somme de la puissance transportée par le vecteur déterministe et de celle transportée par le vecteur aléatoire est une variable aléatoire dont la moyenne est égale à la puissance reçue en espace libre et l'écart-type est proportionnel à la distance. Pour les distances inférieures à environ 50 km l'écart type peut être considéré comme nul, c'est-à-dire que la somme des puissances est une grandeur non aléatoire.

2) La puissance transportée par le vecteur déterministe décroît de façon exponentielle avec la distance.

En se plaçant dans le cas des distances assez courtes, en désignant par  $P_d$  et  $P_a$  les puissances respectives du vecteur déterministe et du vecteur aléatoire, et en prenant comme référence la puissance reçue en espace libre, les propositions ci-dessus s'écrivent :

$$P_d + P_a = 1 \quad \text{et} \quad P_d = e^{-\frac{\Delta}{\Delta_0}}$$

$\Delta$  étant une longueur qui dépend de la fréquence et du climat. Si on pose en outre

$$e^{-\frac{\Delta}{\Delta_0}} = \cos^2 \varphi$$

la probabilité d'un niveau inférieur à  $x$  s'écrit :

$$P_r(x < x) = 2 e^{-\frac{1}{2} \frac{x^2}{\Delta_0^2}} \int_0^{\frac{x}{\Delta_0}} e^{-\frac{1}{2} v^2} I_0\left(\frac{xv}{\Delta_0^2}\right) dv$$

La figure 1 donne les distributions ainsi calculées pour un certain nombre de distances, en choisissant une valeur de 265 km pour  $\Delta_0$ , car cette valeur permet le meilleur ajustement avec les résultats expérimentaux à 4 GHz en climat tempéré. Pour des fréquences différentes on peut admettre que  $\Delta$  est inversement proportionnel à la racine quatrième de la fréquence, c'est-à-dire :

$$\Delta_f = \Delta_4 \left(\frac{4}{f}\right)^{1/4}$$

On doit noter qu'il revient au même de multiplier la valeur de  $\Delta$  par un facteur ou de diviser la valeur de la distance par ce même facteur. En d'autres termes les courbes de la figure 1 sont des courbes universelles à condition de considérer les distances indiquées comme des "distances équivalentes" et de les multiplier par un facteur convenable pour la fréquence et le climat considérés. Par exemple on a constaté que sur une liaison de 43 km aux Etats-Unis, on a obtenu pratiquement la même distribution que sur une liaison de 75 km en Europe.

Si on considère seulement des niveaux reçus très faibles (c'est-à-dire des atténuations élevées) et des distances assez grandes, on voit sur la figure 1 que les courbes sont pratiquement des droites parallèles et on constate en outre que l'influence de la distance peut être représentée approximativement par une loi en  $d^{1/4}$ . Cette remarque justifie certaines formules approchées souvent utilisées, mais on voit que ces formules approchées ont un domaine de validité limité et ne sont pas utilisables pour des distances courtes.

De même dans le cas des niveaux reçus très faibles la pente de la distribution est la même que pour une distribution de Rayleigh, c'est-à-dire 10 dB par décade de probabilité. Mais pour des niveaux reçus plus élevés, c'est-à-dire pour de faibles atténuations, la pente est nettement plus faible que celle d'une distribution de Rayleigh.

Si on considère des niveaux reçus voisins de l'espace libre, on peut montrer que la distribution est pratiquement équivalente à une distribution gaussienne, ce qui correspond au phénomène de scintillation.

## REFERENCES

- L. BOITHIAS - Multipath propagation in line of sight links - Electronics letters-Vol.15 n°7 1979.
- L. BOITHIAS - Distribution statistique des niveaux reçus en propagation par trajets multiples troposphériques- Annales des Télécommunications - Mai-Juin 1981.

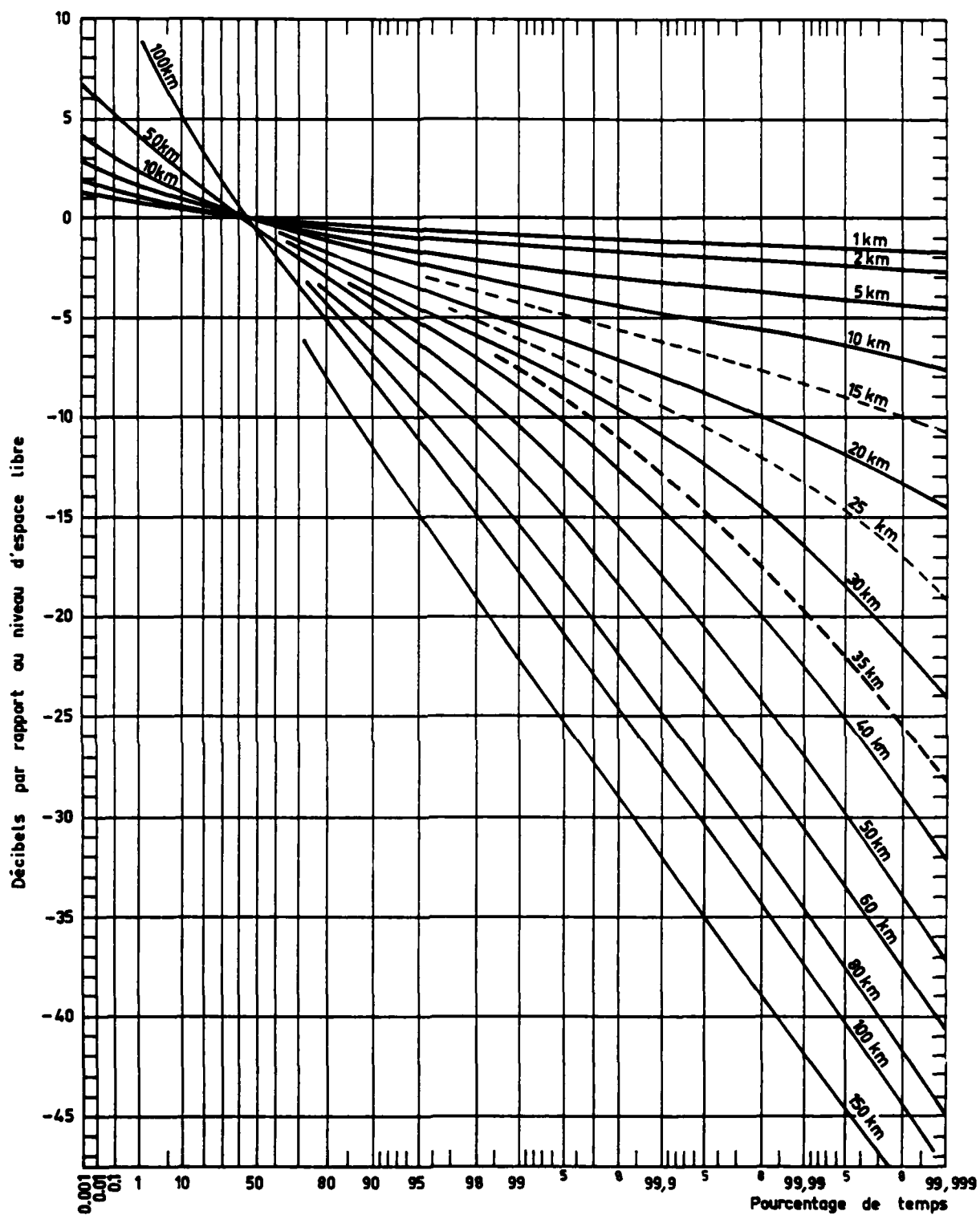


Fig. 1 - Evanouissements dus aux trajets multiples atmosphériques  
 $F = 4 \text{ GHz}$  - Climat tempéré

DEUX TYPES D'ERREURS FAITES DANS LA PREVISION  
DE L'ATTENUATION DES ONDES PAR LA PLUIE  
Par L. BOITHIAS.

Centre National d'Etudes des Télécommunications  
92131 ISSY LES MOULINEAUX

Abstract : For the prediction of wave attenuation due to rain a number of methods have been proposed. Most of them take as aim to derive the statistical distribution of attenuation on a path from the statistical distribution of rain rate at a point of the path. For that, these methods require the choice of a space model of rainy area or rainy volume.

It appears that, in these models, two erroneous assumptions have been often made.

1. In the horizontal rain model there has been a confusion in the general concept of rain cell, between the rainy area of 15 to 20 kilometres in diameter which has to be considered for rain attenuation and the "core" of a few kilometres in diameter which has to be considered for rain scatter.

2. In the vertical rain model there has been a confusion between the vertical extent of rain fall and the height of 0° isotherm. In fact these quantities may be significantly different especially for low latitudes.

These two erroneous assumptions have somewhat delayed the elaboration of a simple and reliable rain model for the prediction of rain attenuation.

Sommaire : Pour la prévision de l'atténuation des ondes par la pluie, un certain nombre de méthodes de calcul ont été proposées. La plupart d'entre elles ont comme objectif de déterminer la distribution statistique des atténuations sur un trajet à partir de la distribution statistique des intensités de pluie en un point. Elles doivent donc utiliser une modélisation spatiale de la zone pluvieuse. On constate que pour une modélisation, deux hypothèses erronées ont été souvent faites :

1. Pour la modélisation horizontale de la pluie, on a confondu sous le concept général de cellule de pluie d'une part la zone pluvieuse, ayant 15 à 20 kilomètres de diamètre, qui intervient pour l'atténuation et d'autre part, le "noyau" ayant quelques kilomètres de diamètre, qui intervient principalement pour la diffusion.

2. Pour la modélisation verticale de la pluie, on a confondu l'étendue verticale d'une précipitation avec la hauteur de l'isotherme 0°, alors que ces deux quantités peuvent être très différentes surtout aux basses latitudes.

Ces deux hypothèses erronées ont sensiblement retardé la mise au point d'une méthode simple et fiable pour le calcul de l'atténuation des ondes par la pluie.

## 1 - INTRODUCTION

Lorsque l'utilisation des fréquences supérieures à environ 10 GHz a commencé à être envisagée par les services de télécommunication, et qu'il a donc fallu s'intéresser à l'atténuation des ondes radio-électriques par la pluie on s'est aperçu que les renseignements pluviométriques que l'on pouvait obtenir des services de Météorologie, étaient extrêmement limités et très insuffisants pour les besoins des services de Télécommunications. Cette situation a une double cause :

a) la structure de la pluie est extrêmement compliquée et très difficile à modéliser dans le temps et dans l'espace, surtout si on doit tenir compte de la structure verticale.

b) les "clients" habituels des services météorologiques, c'est-à-dire principalement l'agriculture, le transport aérien et les travaux publics, n'ont pas besoin de connaître avec précision la structure fine de la pluie, ni ses variations rapides.

La conséquence de cette situation a été que les services de télécommunications ont dû faire eux-mêmes des mesures de pluie, parfois même en développant des pluviomètres capables de donner des mesures plus fines que celles obtenues avec les appareils courants utilisés par les services météorologiques.

Une autre conséquence de cette mauvaise connaissance de la pluie a été l'élaboration de modèles trop simplifiés qui se sont avérés par la suite dangereux à utiliser sans précaution pour certains calculs. On va donner quelques exemples de cette situation.

## 2 - CLASSIFICATION DES PRECIPITATIONS

A titre d'information, on rappelle la façon habituelle de classer les précipitations.

Dans les régions tempérées, on classe généralement les précipitations en deux types : stratiformes et convectives. Dans les régions tropicales ou équatoriales il s'y ajoute deux autres types, le cyclone et la pluie de mousson.

Une précipitation stratiforme couvre une vaste région qui peut atteindre plusieurs centaines de kilomètres avec une faible intensité de précipitation, généralement inférieure à 10 mm/h, mais elle peut contenir de petites averses allant jusqu'à 25 mm/h. La précipitation est à stratification horizontale : elle est constituée de pluie jusqu'à une altitude voisine de la couche de fusion (qui peut être au-dessous de 0°C à cause des phénomènes de surfusion), puis de neige jusqu'à l'altitude d'environ 7 km et de cristaux de glace jusqu'à environ 9 km. Une précipitation stratiforme est souvent associée au passage d'un front c'est-à-dire d'une discontinuité de température dans les masses d'air. Elle peut donc avoir une dimension très grande dans la direction perpendiculaire au déplacement du front.

Une zone de précipitations convectives a des dimensions horizontales totales qui ne dépassent guère 15 km, mais une hauteur très élevée pouvant atteindre la tropopause. Cette masse d'air est animée de mouvements verticaux très intenses dus au fait qu'elle se trouve au-dessus d'un sol ayant été fortement chauffé par le Soleil. Elle contient des précipitations extrêmement intenses, accompagnées de foudre et ayant des dimensions horizontales de quelques kilomètres et des durées de quelques dizaines de minutes. Ces précipitations constituent les orages.

Une pluie de mousson est constituée d'une séquence de bandes de précipitations convectives intenses suivies d'intervalles de précipitations stratiformes. Ces bandes peuvent avoir 50 km de largeur et plusieurs centaines de kilomètres de longueur. Elles donnent lieu à des fortes pluies qui peuvent durer plusieurs heures.

Un cyclone est caractérisé par plusieurs bandes de précipitations intenses enroulées en spirale et s'étendant sur des centaines de kilomètres. Au centre de la spirale existe une zone de calme (œil du cyclone).

### 3 - OBSERVATION ET MESURE DES PRECIPITATIONS

La source d'information la plus simple et la plus courante sur les précipitations pluvieuses est constituée par les données fournies par les pluviomètres. On obtient ainsi, au moins en principe, les statistiques d'intensités de pluie et de durée des précipitations en un point. En réalité, les caractéristiques des équipements choisis par la plupart des services météorologiques pour les mesures de routine ne permettent pas d'atteindre les fortes intensités de pluie ni les précipitations de courte durée. Dans la plupart des cas il est impossible de connaître l'intensité de pluie sur des intervalles de temps de 1 minute. De même les valeurs supérieures à environ 50 mm/h sont généralement entachées d'erreurs. C'est d'ailleurs pour cette raison que les services de télécommunications ont été amenés à développer des pluviomètres mieux adaptés à leurs besoins.

La source principale d'information sur la structure spatiale des précipitations est fournie par les radars météorologiques, qui mesurent en réalité la réflectivité des zones contenant des particules d'eau. Or la réflectivité dépend du nombre et du diamètre de ces particules. Comme l'intensité de pluie dépend des mêmes grandeurs, il y a une relation entre la réflectivité et l'intensité de pluie. Cependant la forme de cette relation fait que le radar est un instrument peu précis pour la mesure absolue des intensités de pluie. Il fournit la répartition spatiale des zones de pluie à un instant donné, mais avec une résolution pas toujours suffisante. Grâce à l'utilisation de l'effet Doppler le radar permet aussi de déterminer la vitesse de déplacement des éléments diffusants.

### 4 - STRUCTURE HORIZONTALE DE LA PLUIE

Pour les problèmes relatifs aux liaisons entre deux points à la surface de la Terre, c'est-à-dire les problèmes d'atténuation sur un trajet ou de brouillage dû à la diffusion par la pluie, il suffit de considérer la structure horizontale des précipitations en tenant compte des variations temporelles de cette structure.

D'après ce qui a été dit plus haut on peut considérer que les pluies stratiformes n'interviennent que pour les faibles atténuations, c'est-à-dire les atténuations non dépassées pendant plus de 0,1 % du temps environ. Or, les atténuations qui ont le plus d'importance pour les performances de la liaison sont plutôt celles qui sont dépassées pendant 0,01 % à 0,001 % du temps, et ces précipitations sont à peu près exclusivement d'origine convective c'est-à-dire orageuse.

#### 4.1. Point de vue météorologique

L'observation radar montre que les précipitations sont formées d'éléments d'échelle différente imbriqués, un élément d'échelle donnée renfermant toujours un ou plusieurs éléments d'échelle inférieure [1]. Ces sous structures sont associées à des variations dans l'espace et dans le temps de l'intensité des précipitations.

Pour décrire ces structures imbriquées on utilise couramment le terme de "cellule", et de ce fait une cellule est constituée par d'autres cellules plus petites. Certains auteurs ont étudié la distribution statistique du nombre de cellules d'intensité donnée contenu à l'intérieur d'une cellule d'intensité plus faible [2]. Par exemple à l'intérieur d'une cellule définie par un seuil de 10 mm/h on aurait une probabilité de 10 % de trouver 4 cellules. Cette ambiguïté dans l'emploi du terme cellule n'est pas très grave si on reste à un point de vue descriptif et qualitatif, mais elle devient source de confusion dès qu'on envisage de chiffrer les dimensions de ces cellules. La figure 1 illustre la dispersion des résultats auxquels on aboutit. Il est évident que pour les auteurs de ces diverses courbes, le terme cellule n'a pas la même signification [3]. Pour éviter cela, certains ont proposé de faire une distinction entre les cellules et les noyaux des cellules, mais cette terminologie n'a pas été universellement adoptée.

#### 4.2. Point de vue radioélectrique

Considérons maintenant le point de vue radioélectrique. Les deux principaux effets de la pluie sont d'une part l'atténuation sur un trajet entre deux points, et d'autre part le couplage entre deux trajets qui se croisent, dû à la diffusion par les particules d'eau situées dans le volume commun aux lobes des antennes.

Dans le cas habituel où le couplage par diffusion se fait par l'intermédiaire des lobes principaux des antennes, le volume de l'atmosphère qui intervient dans le couplage est extrêmement petit. Par exemple

le lobe principal d'une antenne de station terrienne de classe A a une section transversale de l'ordre de 300 m à la distance de 100 km. Il est donc clair que dans ce cas ce sont les éléments structuraux relativement réduits constitués par des maximums locaux d'intensité de pluie qui créent le couplage, le reste de la zone pluvieuse ayant plutôt un effet contraire à cause de son atténuation. Si on étudie la diffusion par la pluie on est donc conduit à considérer des dimensions de cellules de 1 à 2 km. (figure 2).

Si par contre on s'intéresse à l'atténuation sur un trajet terrestre, le volume de l'atmosphère qui intervient est beaucoup plus étendu, surtout dans la direction du trajet, et, contrairement au cas précédent, l'effet est cumulatif à travers toute la zone pluvieuse. On est alors amené à considérer soit la présence simultanée de plusieurs des petites cellules mentionnées ci-dessus, soit un modèle comportant une seule cellule, mais de taille beaucoup plus grande (5 à 15 km par exemple). En aucun cas on ne doit considérer une seule petite cellule, contrairement à ce qui est fait dans certaines méthodes.

Cette constatation n'a rien de très nouveau, et il est bien connu que pour modéliser un phénomène physique on est souvent conduit à établir plusieurs modèles différents suivant l'usage envisagé. Cependant la méconnaissance de ce fait a conduit à l'établissement de méthodes de prévision de l'atténuation basées sur des dimensions de cellules adaptées à la prévision de la diffusion et non de l'atténuation. De ce fait, ces méthodes se sont avérées complètement erronées dans certains cas, et donc dangereuses à utiliser.

Pour la prévision des atténuations, si on utilise une méthode "d'équiprobabilité" c'est-à-dire une méthode dans laquelle on associe l'atténuation et l'intensité de pluie qui correspondent au même pourcentage de temps, le problème de la modélisation ne se pose pratiquement pas, puisqu'on fait intervenir une distance équivalente, déterminée en général de façon empirique. Par contre le choix du modèle de pluie est d'une importance capitale dans les méthodes "d'intégration" dans lesquelles on effectue la sommation des contributions de toutes les intensités de pluie, en tenant compte de leurs probabilités respectives. Le résultat obtenu dépend du "produit" de deux facteurs, d'une part la dimension de la cellule de pluie d'autre part l'intensité de pluie associée. Il est donc possible de compenser une sous-estimation de l'un des facteurs par une surestimation de l'autre, mais c'est un procédé très dangereux car en général la compensation n'a lieu que pour un ensemble restreint de valeurs des facteurs.

Pour les statistiques d'intensités de pluie on sait que les modèles les plus courants de distribution sont représentés par la loi log-normale pour les faibles intensités de précipitation et par la loi gamma pour les fortes intensités. Pour les intensités "moyennes" qui jouent un grand rôle dans les problèmes d'atténuation, c'est-à-dire 20 à 80 mm/h environ, les deux modèles donnent des représentations acceptables. Par contre si on doit faire intervenir dans les calculs des fortes intensités de précipitation, le choix du modèle n'est pas indifférent. Pour illustrer ce fait, considérons deux distributions (log-normale et gamma) donnant la même valeur d'intensité de pluie pour  $10^{-2}$  % ainsi que pour  $10^{-3}$  % du temps. On constate que la densité de probabilité au voisinage de 300 mm/h est environ 6 fois plus grande avec la loi log-normale qu'avec la loi gamma. Vers 600 mm/h le rapport est d'environ 1000 (Fig. 3 et 4). En outre une petite variation dans l'ajustement du modèle aux valeurs mesurées pourra se traduire par une variation extrêmement importante pour les intensités supérieures à quelques centaines de mm/h. La modélisation par une loi log-normale pour les très fortes intensités de pluie ne devrait plus être prise en considération.

On peut donc conclure que les méthodes utilisant l'intégration sur toute la gamme possible des intensités de pluie, bien que plus satisfaisantes d'un point de vue théorique, doivent être utilisées avec beaucoup de prudence, car elles nécessitent une modélisation extrêmement précise à la fois des dimensions des cellules et des distributions d'intensité de pluie. Leur succès apparent lorsque les erreurs des modèles se compensent, par exemple pour certains régimes pluvieux, ne doit pas cacher les résultats aberrants que l'on obtient lorsque la compensation ne joue pas, par exemple en climat tropical.

Pour cette raison, il est heureux que le CCIR se soit orienté vers des méthodes d'équiprobabilité.

## 5 - STRUCTURE VERTICALE DE LA PLUIE

Les trajets Terre Satellite traversent toute l'épaisseur de la zone orageuse c'est-à-dire à la fois la région où les gouttes de pluie tombent vers le sol et la région des nuages où les particules, partiellement ou totalement congelées, subissent des mouvements de toutes directions en raison des courants ascendants et des vents.

La première modélisation envisagée a été de supposer que la pluie tombait depuis l'isotherme  $0^{\circ}$  et que la chute de pluie remplissait toute l'épaisseur comprise entre cette isotherme et le sol. Ce modèle a été utilisé pendant un certain temps par le CCIR. Cependant l'expérience a montré qu'il ne convenait pas, ce qui pouvait d'ailleurs être prévu à partir de quelques remarques simples :

1. Il peut exister de l'eau en surfusion bien au dessus de l'isotherme  $0^{\circ}$ . En outre les particules de glace partiellement fondues peuvent aussi provoquer un affaiblissement notable.

2. Les gouttes de pluie tombent avec une vitesse finie qui ne dépasse pas de 10 à 12 m/s pour les gouttes les plus grosses et qui est nettement plus faible pour les gouttes de petite taille. Une goutte de pluie a donc une durée de chute de l'ordre de 10 minutes, ce qui est du même ordre de grandeur que la durée, en un point, d'une averse de forte intensité. En d'autres termes, une colonne d'atmosphère comprise entre le sol et l'altitude d'où tombent les gouttes de pluie n'est pratiquement jamais occupée entièrement par un flux intense de gouttes de pluie. Si on veut modéliser une "cellule de pluie en volume", par une forme géométrique simple, il semble qu'un cylindre ayant 2 à 4 km de hauteur moyenne serait convenable. Les dimensions horizontales du cylindre dépendent de l'application considérée, ainsi qu'on l'a expliqué plus haut. A un instant donné ce cylindre peut se trouver en une position quelconque entre le sol et une altitude d'isotherme négative, par exemple  $-10^{\circ}$  ou  $-15^{\circ}$ . En outre, il peut exister simultanément plusieurs cylindres décalés horizontalement et verticalement (Figure 5).

On peut déduire de ces remarques qu'il n'y a aucune relation directe entre la hauteur de l'isotherme  $0^{\circ}$  et l'épaisseur de la pluie à un instant donné, puisque ces deux grandeurs ne dépendent pas des mêmes paramètres. L'introduction, parfois envisagée, d'un coefficient de réduction pour passer de l'une à l'autre est donc complètement artificielle et n'a aucune justification théorique. En particulier on peut prévoir que l'épaisseur de la pluie doit dépendre assez peu de la latitude sauf éventuellement pour les latitudes très élevées, alors que l'altitude de l'isotherme  $0^{\circ}$  en dépend fortement. Il peut même tomber des gouttes de pluie surfondues alors que la température au sol est négative.

Comme pour les trajets terrestres, le CCIR considère seulement des méthodes d'équiprobabilité, pour la prévision des atténuations sur les trajets Terre-satellite. Cependant, la situation dans ce cas est beaucoup plus complexe et les données expérimentales rassemblées par le CCIR, à partir de mesures sur des balises de satellites ou de mesures radiométriques ne font pas apparaître clairement l'influence de la latitude ou de l'angle d'élévation sur l'atténuation. Il reste donc encore beaucoup de travail à faire dans ce domaine.

#### 6 - CONCLUSION

On a seulement voulu attirer l'attention sur des possibilités d'erreurs dans la modélisation de la pluie et les conséquences de ces erreurs pour la prévision des atténuations. Rappelons à ce sujet que la qualité principale d'une méthode de prévision est la fiabilité. Il est préférable d'avoir une méthode de qualité moyenne mais dont on est sûr qu'elle ne donnera jamais de résultats très erronés plutôt qu'une méthode donnant de façon plus ou moins aléatoire, tantôt des résultats excellents, tantôt des résultats aberrants.

#### Bibliographie

- 1 - H. SAUVAGEOT - Radarmétéorologie - Eyrolles 1982.
- 2 - G. DRUFUCA ; A. PAWLINA - Radar derived - statistics on the structure of precipitation patterns URSI com-F Symposium, La Baule 1977.
- 3 - R.K. CRANE - A review of transhorizon propagation phenomena URSI Com. F Symposium - Lennoxville 1980.
- 4 - CCIR - Volume V UIT 1982 - Rapports 563-2 ; 721-1 ; 338-4 ; 564-2 ; 882 ; 569-2.
- 5 - L. BOITHIAS - Propagation des ondes radioélectriques dans l'environnement terrestre - DUNOD, Paris, 1983.

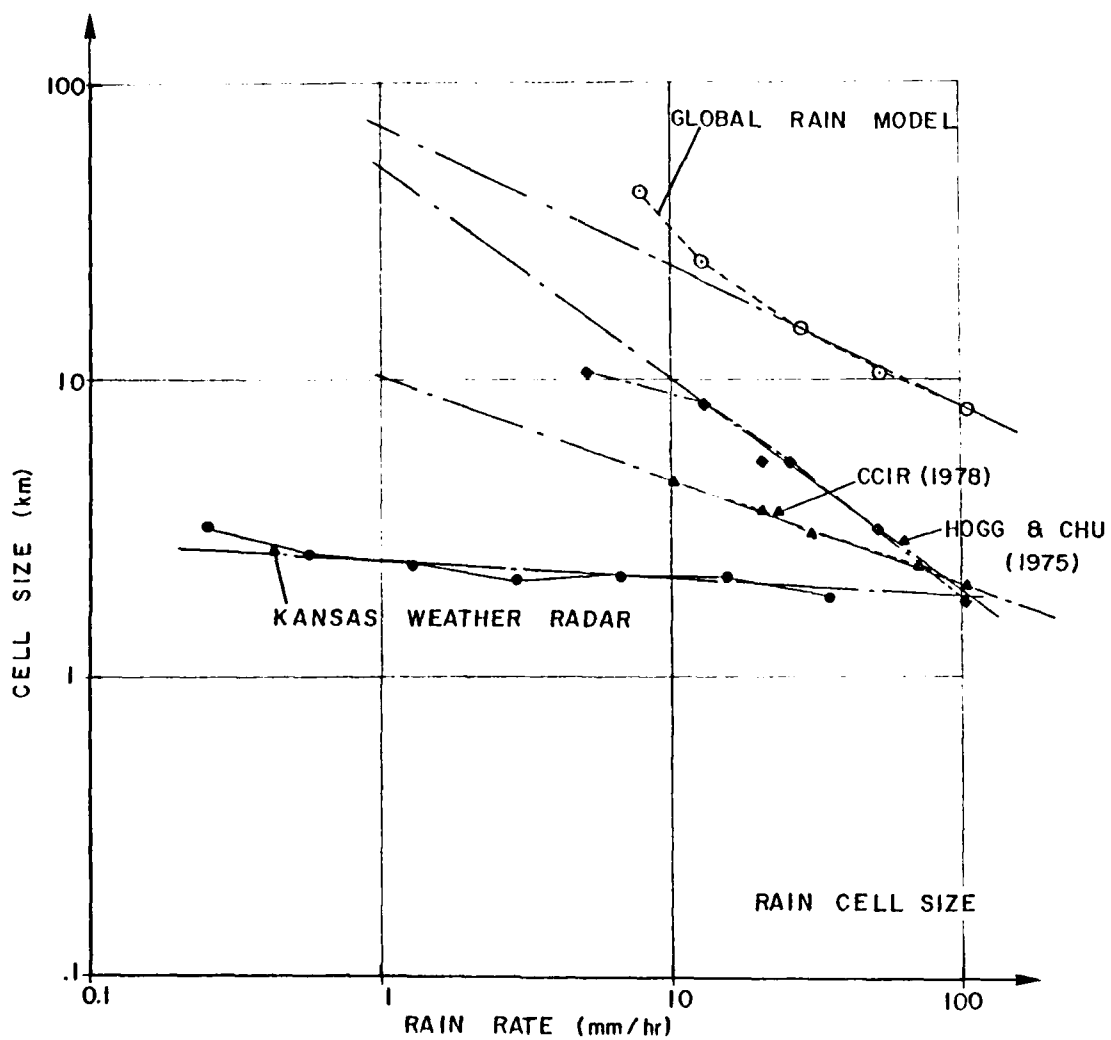


Fig.1: Dimensions des "cellules de pluie". ( d'après R.K CRANE - 1980 - Symposium de Lennoxville )

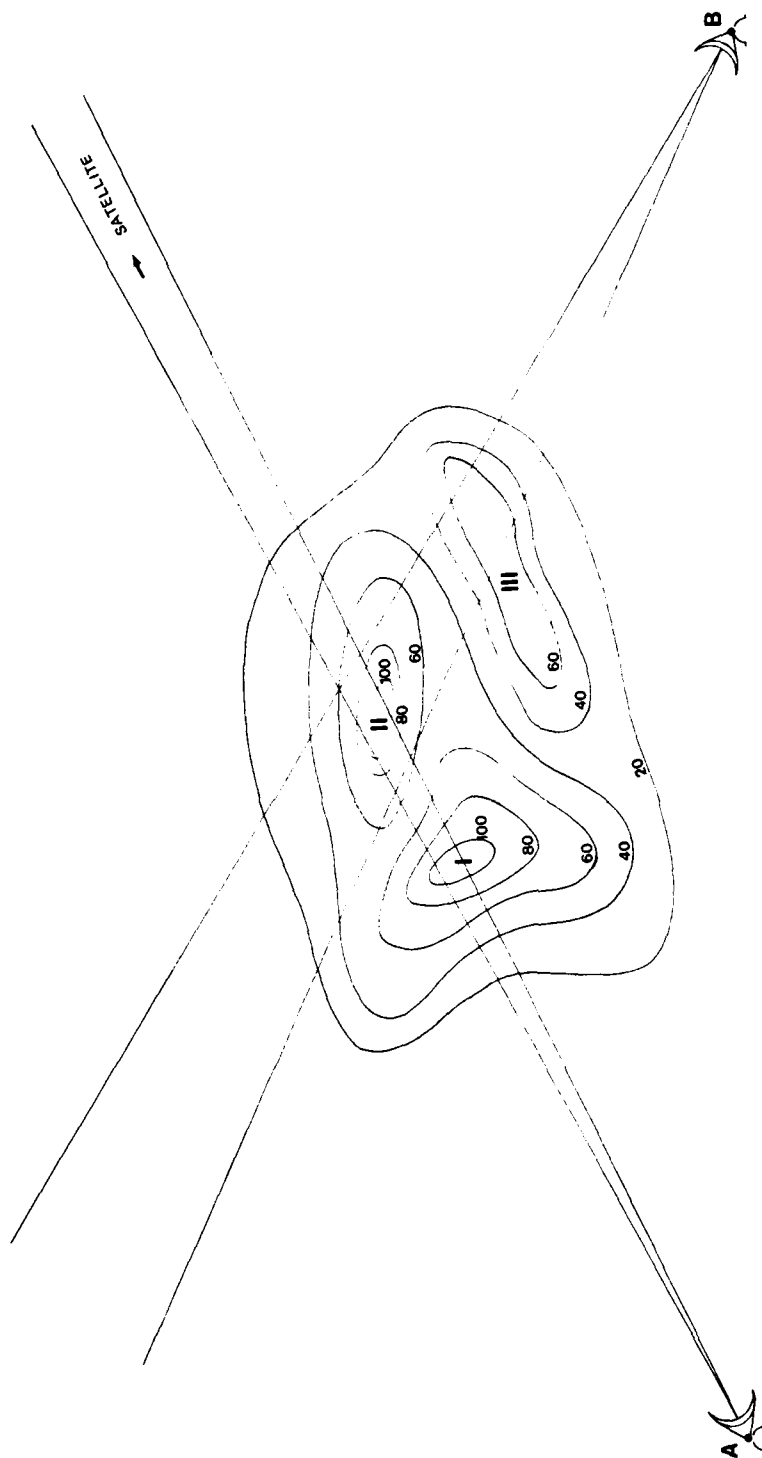


Fig.2: Modélisation d'une chute de pluie à un instant donné (vue en plan).  
 Les nombres représentent les intensités de pluie à un instant donné, dans le plan de la liaison AB (trajet de brouillage).  
 La cellule II crée une atténuation sur les deux trajets et un couplage entre eux.  
 Les cellules I et III créent seulement de l'atténuation.

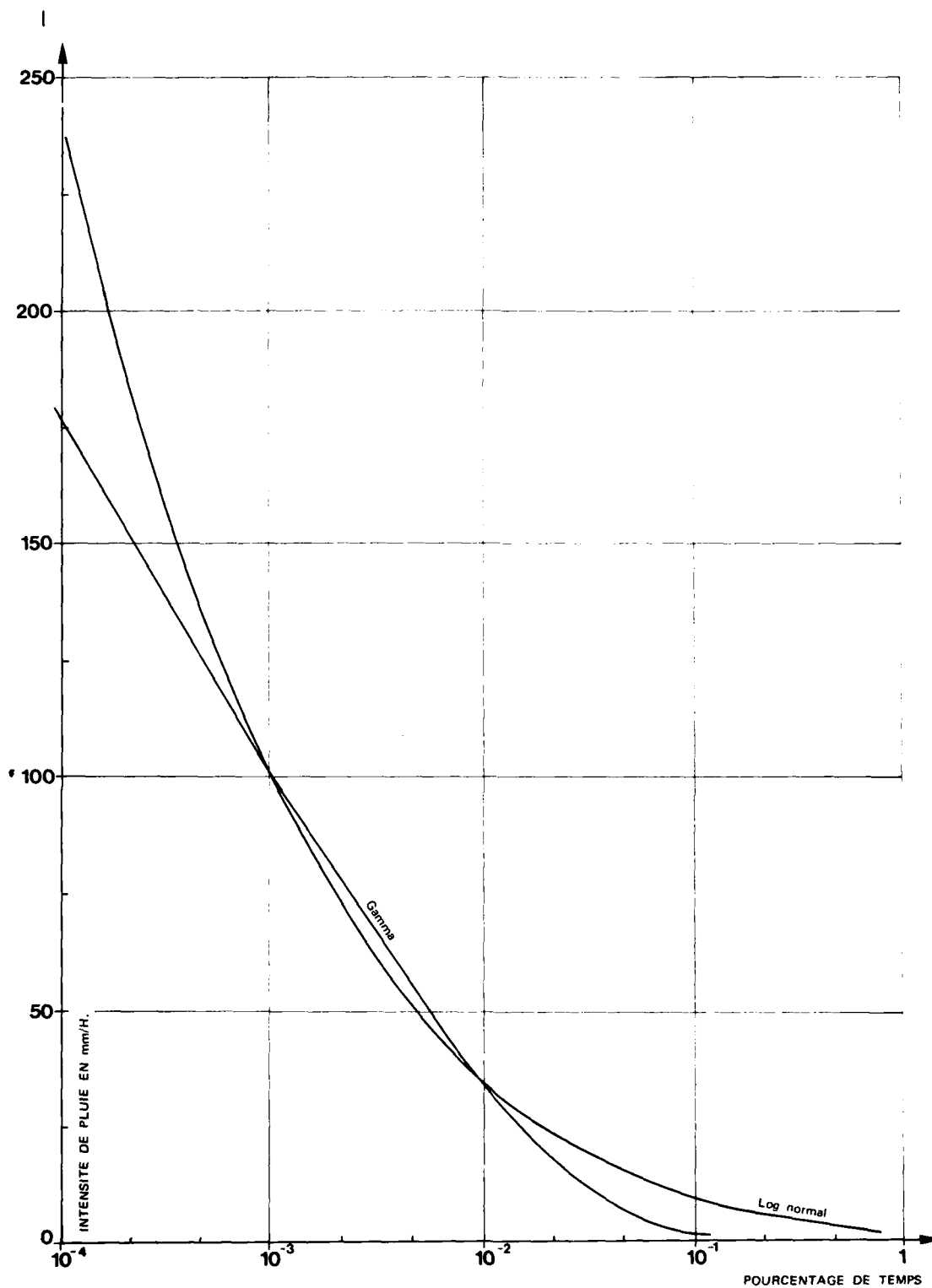


Fig.3: Modélisation statistique des intensités de pluie.

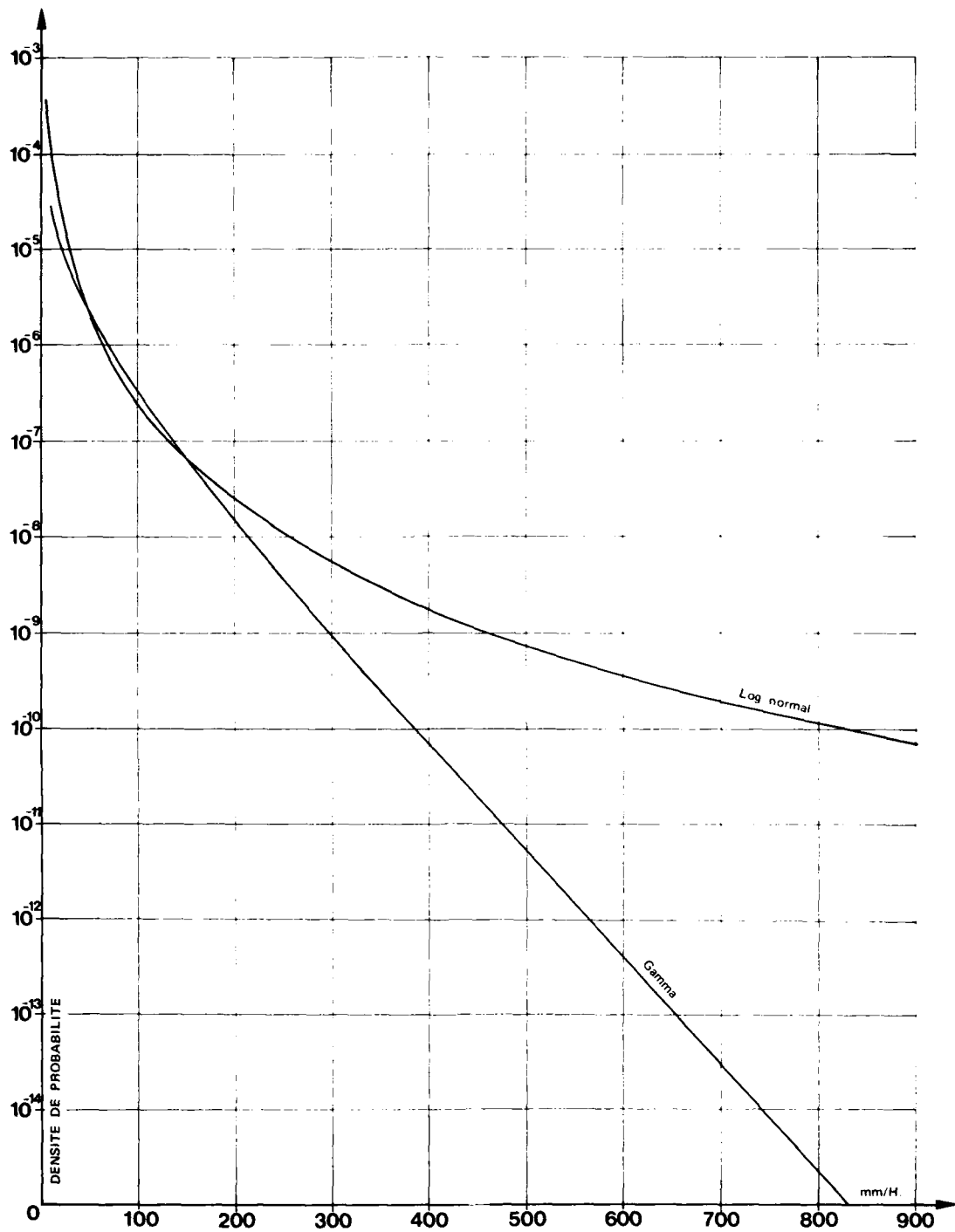


Fig.4: Densité de probabilité pour deux modèles statistiques des intensités de pluie.

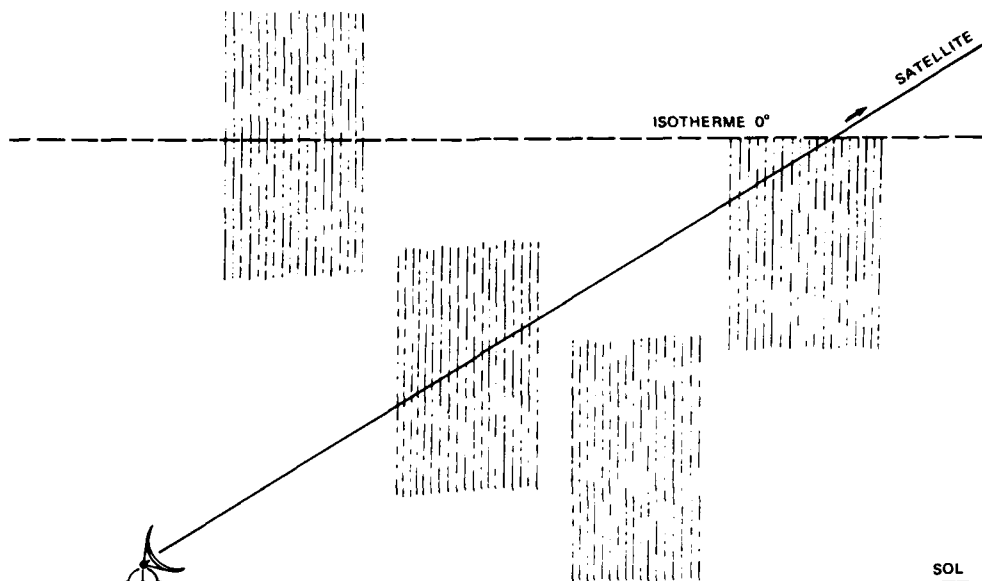


Fig.5: Modélisation verticale de la pluie à un instant donné.

#### DISCUSSION

T. Almond (U.K.): You stated that the log-normal law was not correct for rainfall intensities above 5<sup>th</sup> mm/h. I was not clear how you had established this fact as you stated that it was difficult to obtain actual figures of rainfall intensity of sufficient reliability (i.e., at less than one minute time intervals).

L. Boithias (France): Les mesures faites avec les pluviomètres les plus rapides, et même en appliquant une correction empirique, donnent une rapidité de croissance de l'intensité de pluie, pour des pourcentages de temps décroissants, qui est toujours trop petite être compatible avec une loi log-normale.

E. Vilar (U.K.): 1) We have found in the field of tropospheric scintillations that one has to modify the distribution of the fluctuations (log-normal) so as to fit the long term experimental distribution which includes fractional probabilities down to 0.001 percent. The modification involves considering the distribution of the variance which is no longer constant (stationary process), but random. I wonder whether this is the reason why the log-normal distribution for precipitation rate is unsatisfactory to explain the "tails" of the distribution which are responsible for the small percent of the time considered.

2) Surely what matters in planning a telecommunication line is not only the excess precipitation rate but also the duration of the events, in order to avoid overdesigning the system. This then leads to a conditional probability of excess precipitation rate and of duration of events. Could you comment on the possible need and availability of such information?

L. Boithias (France): 1) Il faut peut être chercher une cause physique à cette réduction de "pente" de la distribution par rapport ou la pente de la distribution log-normale, les très fortes intensités de précipitation étant priorisées par un mécanisme différent de celui des intensités faibles et moyennes.

2) Jusqu'à présent le CCIR n'a pas établi de Recommandations sur la durée cumulée. Ce dernier paramètre est donc le plus important à connaître.

J.T.A. Neesen (The Netherlands): 1) In Figure 3 you have shown some discrepancy between the log-normal and gamma distributions. Can you give the parameters of distributions shown in Figure 3? These parameters may be different for the distinguished rain climate zones.

2) To account for the horizontal structure of rain, some theories use the horizontal reduction coefficient in connection with the equivalent path length concept. The value of the reduction coefficient may be related to the rain rate or time percentage. What is the best choice, the reduction coefficient as a function of the rain rate or the reduction coefficient as a function of the time percentage?

L. Boithias (France): 1) La figure 3 était destinée en particulier à montrer la différence des "pentes" des distributions des très fortes intensités de pluie suivant le modèle choisi, et à justifier le choix par le CCIR d'une méthode d'équiprobabilité pour la prévision des atténuations, car cette méthode est indépendante de cette pente. Au dessous de 20 mm/h environ, dans tous les climats la distribution peut être représentée par une distribution log-normale.

2) La figure 5 concerne une modélisation des "cellules" des fortes intensités de pluie. Elle ne tient pas compte des pluies de faible intensité qui peuvent relier ces cellules entre elles. En outre c'est un modèle "moyen" et il peut y avoir des situations différentes.

3) Instead of the  $0^{\circ}$  isotherm, one may use the concept of effective height to account for the vertical structure of rain. Do you think that this technique is appropriate for the prediction of slant path attenuation?

L. Boithias (France): 1) La figure 3 est seulement destinée à comparer les "pentes," pour les faibles pourcentages de temps, des deux distributions log-normale et gamma qui correspondraient aux mêmes valeurs de l'intensité de pluie pour 0.01 % et pour 0.001 % du temps. La distribution log-normale a une pente qui est extrêmement forte et puis augmente quand l'intensité de pluie augmente, ce qui est en contradiction avec les résultats des mesures, même en appliquant des corrections pour tenir compte du temps d'intégration des pluviomètres. Evidemment dans chaque climat on doit ajuster les paramètres du distributeur.

2) L'affaiblissement spécifique est relié à l'intensité de pluie. Si on choisit un coefficient de réduction (ou une distance équivalente) reliée aussi à l'intensité de pluie, le pourcentage de temps n'est pas suffisamment pris en compte. Par exemple si 50 mm/h correspond à 0.01 % du temps dans un climat et 0.001 % du temps dans un autre, on trouverait le même affaiblissement dans les deux cas, ce qui est peu vraisemblable. En choisissant un coefficient de réduction relié au pourcentage de temps ou à un paramètre d'ajustement supplémentaire, on constate que les prévisions obtenues sont meilleures.

3) Pour utiliser une méthode d'équiprobabilité on doit déterminer une "longueur effective" du trajet à travers la pluie, ou bien (ce qui est équivalent) une hauteur effective. Mais cette hauteur effective n'a pas a priori de relation directe avec la hauteur d'une isotherme quelconque. Elle doit être déterminée expérimentalement.

M.P.M. Hall (U.K.): 1) Your Figure 3 draws attention to the similarity of log-normal and gamma distributions between 0.001 and 0.01 percent of the time if they are made to fit data at these two points, but you emphasize the differences that may occur for very much smaller time percentages (which is probably not of general concern to users) and mention a less severe difference for larger time percentages. Fortunately, the CCIR is able to base its rainfall rate curves on data where these are available, but the lack of data for rainfall rate exceeded for about 1.0 percent of the time is a problem for predicting interference due to rain scatter (as illustrated in your Figure 2), especially for frequencies in excess of about 20 GHz. Attenuation due to light rain on the "arms" of the transmitter-scatter volume-receiver path is then very significant, and the correct choice of a correct model in the absence of data would be very important.

2) In Figure 5, and associated text, you suggest that rain does not have any vertical continuity to the  $0^{\circ}$  isotherm, and you express reservations with conventional meteorological radar which we all share. However, several authors, including ourselves, have used specialized radars in temperate climates and found radar reflectivity statistics to be constant up to the melting layer. Moreover, with our dual-polarization radar, we have been able to demonstrate columns of constant rainfall rate between ground and the melting layers during what are often regarded as "stratiform" conditions, though we sometimes see a depression of this height in convective rain columns. You will of course be aware that the CCIR does not assume these statistics to be constant up to the  $0^{\circ}$  isotherm in low latitudes.

## ICE DEPOLARIZATION ON LOW-ANGLE 11 GHZ SATELLITE DOWNLINKS

by

W. L. Stutzman

C. W. Bostian

A. Tsolakis

T. Pratt

Satellite Communications Group

Electrical Engineering Department

Virginia Polytechnic Institute and State University

Blacksburg, Virginia 24061

## ABSTRACT

Although many observations of ice depolarization have appeared in the literature, little has been reported on the impact of ice depolarization on the statistical performance of satellite downlinks. As part of an experiment with the SIRIO spacecraft's 11.6 GHz beacon, we have analyzed propagation data recorded during 1979 and 1980 to see what impact ice depolarization would have had on link performance. Our measurements were made with first one and then with two dual-circularly-polarized terminals spaced 7.2 km apart; the elevation angle was 10.7 degrees. While periods of intense ice depolarization occurred, the overall effects on the XPD statistics amounted to at most a 2 to 4 dB reduction in the XPD values that rain acting alone would have produced for a given percentage of time. Ice depolarization had no effect on the statistics of XPD values below the 0.01% level.

Most of the severe ice depolarization events which occurred were associated with drops in barometric pressure and the passage of intense cold fronts through our area.

To model the theoretical behavior of ice depolarization, we have defined ice contents as the product of three individually undetermined quantities: ice particle density (number of ice particles per  $m^3$ ), ice cloud thickness (in m), and the average volume (in  $m^3$ ) of the ice crystals. A comparison with our measurements indicates that populations of ice particles with ice contents on the order of  $0.002 m^4/m^3$  are probably responsible for the lower values of measured XPD.

## 1. INTRODUCTION

Intense depolarization in the absence of attenuation was first reported on satellite paths in 1976 during the European phase of the ATS-6 millimeter wave propagation experiments. At first called anomalous depolarization, this phenomenon was soon correctly attributed to scattering by high-altitude ice crystals. Bostian and Allnutt (1979) and Cox (1981) have reviewed research in this area; generally it has concentrated on individual propagation events and the physics of depolarization by ice crystals. In contrast, the effect of ice depolarization on satellite communications system performance has received relatively little attention. In this paper we will present some data measured on a low-angle 11.6 GHz path with SIRIO and investigate the effect which ice depolarization had on the cross polarization discrimination (XPD) statistics and which it would have had on the performance of hypothetical dual-polarized digital communications systems.

## 2. THE VIRGINIA TECH SIRIO EXPERIMENT

The data which we will discuss were collected using the SIRIO 11.6 GHz beacon from 1979 through 1981. The beacon transmitted right-hand circular polarization, and we measured both the co-polarized and the cross-polarized components of the received signal. Initially we operated a single receiving site called the main site; in July 1980 we added a second one called the remote site and collected 30 months of diversity data. The experiment was unique in its first U.S. use of dual-polarized diversity reception and in the low 10.6 degree elevation angle of the propagation path. For more details on this experiment, please consult (Marshall et al., 1979) and (Towner et al., 1982).

The diversity aspect of the experiment produced one surprising result: the main site experienced more ice depolarization than the remote site. Ice depolarization at the remote site was always accompanied by ice depolarization at the main site, and we could usually match features in plots of XPD versus time from the two sites. But the converse was not true; there were occasional events when ice depolarization at the main site was not accompanied by any activity at the remote site. We have no explanation for this.

## 3. ELEVATION ANGLE EFFECTS ON THE FREQUENCY OF OCCURRENCE OF ICE DEPOLARIZATION

With the SIRIO experiment we observed an average of about two ice depolarization events per month. The most severe of these brought the XPD down to values around 10 dB. This contrasted surprisingly with our earlier measurements with CTS (11.7 GHz) and COMSTAR (19.04 GHz), where we saw only four weak events in two years. None of these produced XPD values worse than 20 dB (Bostian et al., 1981). We attribute this difference to the low elevation angle of the SIRIO experiment, since CTS was at 33 degrees and the elevation angles of the COMSTAR spacecraft we used were around 45 degrees. If ice is located in storms above rain, then low-angle paths would have a greater probability of intersecting only ice crystals. Higher angle paths would tend to pass through regions of rain and regions of ice, and depolarization by the rain would mask the effects of the ice. Thus we would expect ice depolarization to occur more often on paths with low elevation angles.

#### 4. SEASONAL EFFECTS

We observed the most severe cases of ice depolarization in October and November. A drop in barometric pressure and the passage of an intense cold front usually accompanied instances of strong ice depolarization.

#### 5. MODELING IMPLICATIONS

One of the practical problems in modeling ice depolarization is the inconveniently large number of parameters which are involved. Products of undetermined quantities appear in the theory, and different combinations of parameters can lead to the same value of XPD. In a forthcoming paper (Tsoulakis and Stutzman, 1983) we have tried to simplify the situation by defining ice content as the product of three individually undetermined quantities: ice particle density (number of ice particles per  $m^3$ ), ice cloud thickness (in m), and the average volume (in  $m^3$ ) of the ice crystals. A comparison with our measurements on an event by event basis indicates that populations of ice particles with ice contents on the order of  $0.002 m^4/m^3$  are probably responsible for the lowest values of XPD (around 12 dB) that we measured.

#### 6. THE EFFECT OF ICE ON THE CUMULATIVE DISTRIBUTION OF XPD

While the joint distribution of attenuation and XPD is of greater interest from a systems viewpoint, percent-of-time data for XPD have been widely published. We will begin with the effect that ice has on statistics of this kind.

The practical question here, we think, is the degree to which the XPD distribution is predictable from the attenuation distribution. This predictability depends on the relative importance of ice depolarization, since ice causes no attenuation and its depolarizing effects cannot be determined from an attenuation distribution.

The results for our main receiving site appear in Figures 1 and 2. The first describes the 1979 calendar year and the second is for 1980. In both cases we present three curves. The first, labeled "all data," shows the measured XPD probability distribution. The second, called "ice events excluded," shows what the XPD would have done if all periods of depolarization by ice acting alone (i.e., ice unaccompanied by rain) had instead been periods of clear weather. We defined clear weather here as propagation conditions for which the attenuation (A) is less than 3 dB and simultaneously the XPD is better than 26 dB. We classified as ice events those periods when propagation conditions caused XPDs poorer than 26 dB accompanied by attenuations less than 3 dB. The third curve, labeled SIM, represents a model calculation of XPD from our measured attenuation distribution. We will discuss its significance below.

Consider first the "all data" and "ice events excluded" curves. These show that for strong depolarization (XPD worse than 20 dB) removing the ice events improves the XPD occurring for a given percent-of-time by 3 dB at most. Ice is this significant only at the upper end of the curves, where its effects are beginning to blend in with those of the antenna residuals. If we restrict our attention to percentages of time at or below 0.1%, we see that the effect of ice is no more than a 2 dB decrease in XPD. For both years it vanishes at the 0.01% point.

The 2 dB value is consistent with an earlier finding on which we based the first abstract for this paper and which will be reported in a forthcoming article (Stutzman et al. 1983). There we looked at 5.5 months (July 15 - December 31, 1980) of data from both diversity sites and carefully removed the antenna residuals and spacecraft diurnal effects prior to computing the XPD distributions. At the percentages of time of interest, the XPD distributions with and without the residuals were so similar to each other that we felt it unnecessary to remove the residuals in subsequent work.

The curves labeled "SIM" are the predicted XPD distribution based on the attenuation distribution measured over the same time periods as the XPD. SIM is a model which we have recently developed for rain depolarization (Runyon, 1983). It excludes the effects of ice and for our SIRIO experiment it predicts a relationship between XPD and attenuation (A, in dB) given by (1) for  $A > 3$ .

$$XPD = 32.15 - 19 \log_{10} (A) \quad (1)$$

For each attenuation we calculated an XPD with SIM and plotted that XPD for the percent-of-time corresponding to the attenuation.

The SIM curve shows the depolarization distribution that theoretically would have resulted from rain acting alone. The difference between it and the "ice events excluded" curve may be attributed to depolarization by a mixture of rain and ice and to possible errors in the model. At most this difference amounts to about 4 dB over the interval of interest. In general the numbers are consistent with the 2 dB difference that Chu (1980) noted between model predictions of XPD and measurements and which he included in his model to account for depolarization by ice accompanying rain.

#### 7. THE EFFECT OF ICE DEPOLARIZATION ON THE JOINT DISTRIBUTION OF XPD AND ATTENUATION

The representation of the joint distribution which we will use was first presented at an earlier AGARD meeting by Thirlwell and Howell (1980). It uses contour lines to

display the percent-of-time that the XPD and attenuation are worse than (i.e., below or to the right of) the XPD and A values shown on the axes. Figures 3 and 4 present our overall calendar year 1979 and 1980 data in this way.

This presentation of XPD and A data is particularly useful in analyzing communication systems because system performance depends on both attenuation and XPD. Contours of constant system performance (i.e. contours of constant worst-channel SNR for analog systems or of error rate for digital systems) may be superimposed on the XPD-A plot. We have done this in Figures 3 and 4 using the symbol error probability for a QPSK link with a clear weather carrier-to-thermal noise ratio (CNR) of 20 dB and a clear weather XPD of 26 dB. This CNR value may be high for practical systems, but it is convenient for this analysis. We made our symbol error probability calculations using Prabhu's equations (Prabhu, 1969).

To determine the effect that ice depolarization has on the joint XPD/A distribution, we computed the joint distributions for our 1979 and 1980 data with ice events excluded. The results appear in Figures 5 and 6. The main effect is a slight straightening of the percent-of-time contours and an improvement in the 14 to 18 dB XPD range.

The straightening of the contours is an effect first noted by Gaines and Bostian (1982). If XPD and attenuation were related by a single valued deterministic equation, the percent-of-time contours would be straight lines making a right angle been at the locus of (XPD, A) values determined by the equation. Ice adds randomness to what is a deterministic and reasonably well-behaved relationship for rain. Removing the ice depolarization removes the randomness and straightens the contours.

#### 8. CONCLUSIONS

From this study we conclude that ice depolarization is more frequent on low elevation angle paths than at higher angles. While quite low values of XPD can result from ice, the overall effect on XPD statistics is only 2 to 4 dB reduction over that which would result from rain acting alone, and this at percentages of time greater than 0.01. Ice depolarization seems to have had no effect on our XPD statistics below the 0.01% level.

#### 9. ACKNOWLEDGEMENTS

This work was performed for Intelsat and for the Jet Propulsion Laboratory, California Institute of Technology, sponsored by the National Aeronautics and Space Administration. Each sponsor supported one SIRIO terminal, and the detailed SIRIO data analysis and study of ice depolarization events was funded by Intelsat. NASA/JPL supported the work on joint XPD/A statistics, propagation modeling, and on communications system performance. The opinions expressed are not necessarily those of either sponsor. We appreciate the comments and assistance of Dr. J. E. Allnutt of Intelsat and Dr. E. K. Smith, Jr., of JPL.

This manuscript was prepared for publication by Linda J. White.

#### 10. REFERENCES

1. C. W. Bostian, T. Pratt, and A. Tsolakis, 1981, "Ice Depolarization at 11.7 and 19 GHz on Slant Paths in Virginia, USA," Ann. Telecommunic., vol. 36, pp. 148-153.
2. C. W. Bostian and J. E. Allnutt, 1979, "Ice Crystal Depolarization on Satellite-Earth Microwave Radio Paths," Proc. IEEE (London), vol. 126, pp. 951-960.
3. T. S. Chu, 1980, "Microwave Depolarization on an Earth-Space Path," Bell Sys. Tech. J. vol. 59, pp. 987-1007.
4. D. C. Cox, 1981, "Depolarization of Radio Waves by Atmospheric Hydrometeors in Earth-Space Paths: A Review," Radio Science, vol. 16, pp. 781-812.
5. J. M. Gaines and C. W. Bostian, 1982, "Modeling the Joint Statistics of Satellite Path XPD and Attenuation," IEEE Trans. Antennas and Propagation, vol. AP-30, pp. 815-817.
6. R. E. Marshall, S. O. Lane, S. M. Babula, P. Santago, and E. G. Ackerman, 1979, "Preliminary Results of Propagation Measurements in the Eastern U.S. Using the SIRIO Satellite," Alta Frequenza, vol. 48, pp. 397-398.
7. V. K. Prabhu, 1969, "Error Rate Considerations for Coherent Phase-Shift Keyed Systems with Co-Channel Interference," Bell Sys. Tech. J. vol. 48, pp. 743-767.
8. D. L. Runyon, Jr., 1983, "A Simple Model for the Depolarizing Effects of Rain and Ice on Earth Satellite Links in the 10 to 30 GHz Frequency Range," M.S. Thesis, Virginia Polytechnic Institute and State University.
9. W. L. Stutzman, C. W. Bostian, A. Tsolakis, and T. Pratt, 1983, "The Impact of Ice Along Satellite-to-Earth Paths on 11 GHz Depolarization Statistics," Radio Science, in press.
10. J. Thirlwell and R. G. Howell, 1980, "20 and 30 GHz Slant Path Propagation Measurements at Martelsham Heath, UK," Proceedings of the 26th AGARD Symposium on EM Wave Propagation, pp. 1-9.

11. G. C. Towner, R. E. Marshall, W. L. Stutzman, C. W. Bostian, T. Pratt, E. A. Manus, and P. H. Wiley, 1982, "Initial Results from the VPI&SU SIRIO Diversity Experiment," Radio Science, vol. 17, pp. 1489-1494.
12. A. Tsolakis and W. L. Stutzman, 1983, "Calculation of Ice Depolarization on Satellite Radio Paths," Radio Science, in press.

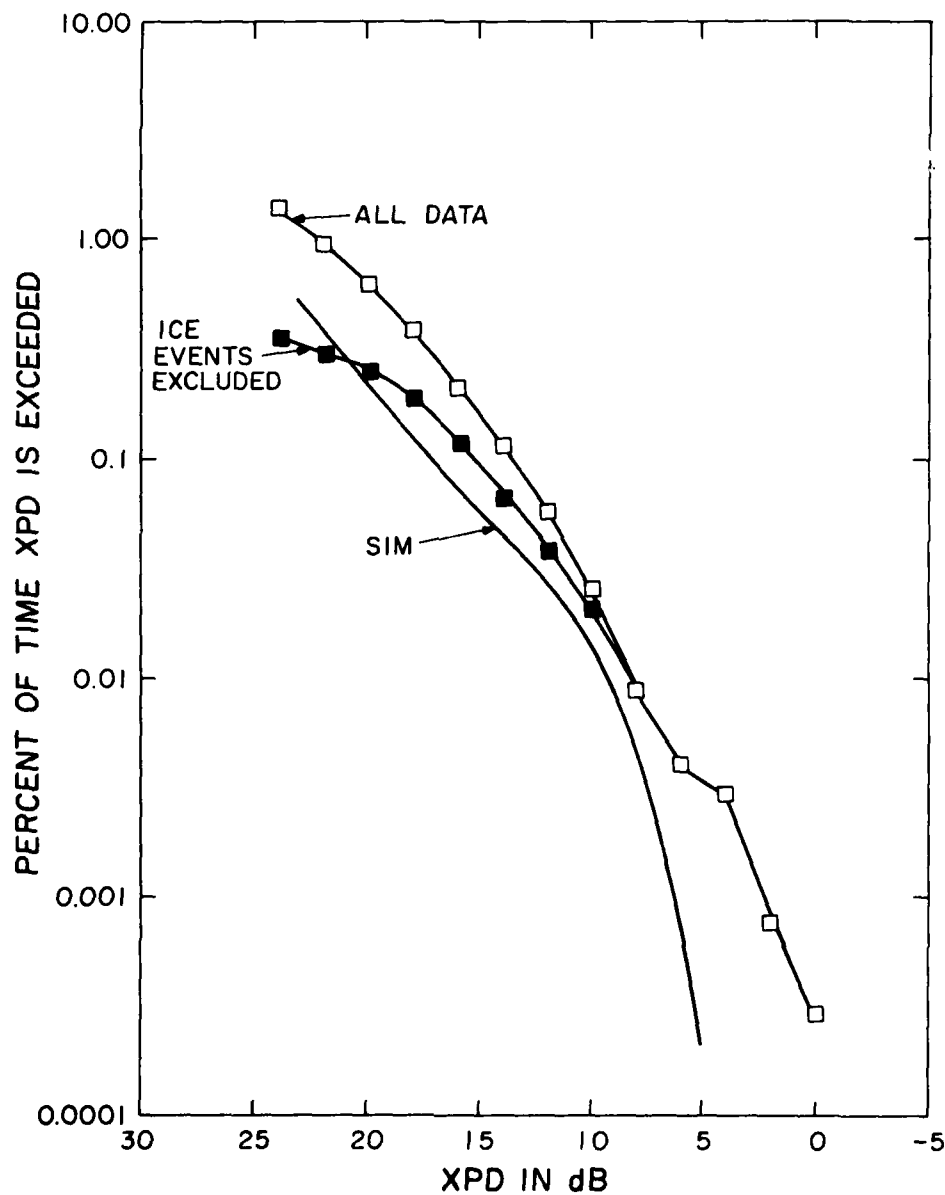


Figure 1. Cumulative XPD distributions on the VPI&SU SIRIO downlink for the 1979 calendar year. Curves shown are for all measured data, for the measured data with ice events artificially reset to clear weather, and for a predictive model called SIM.

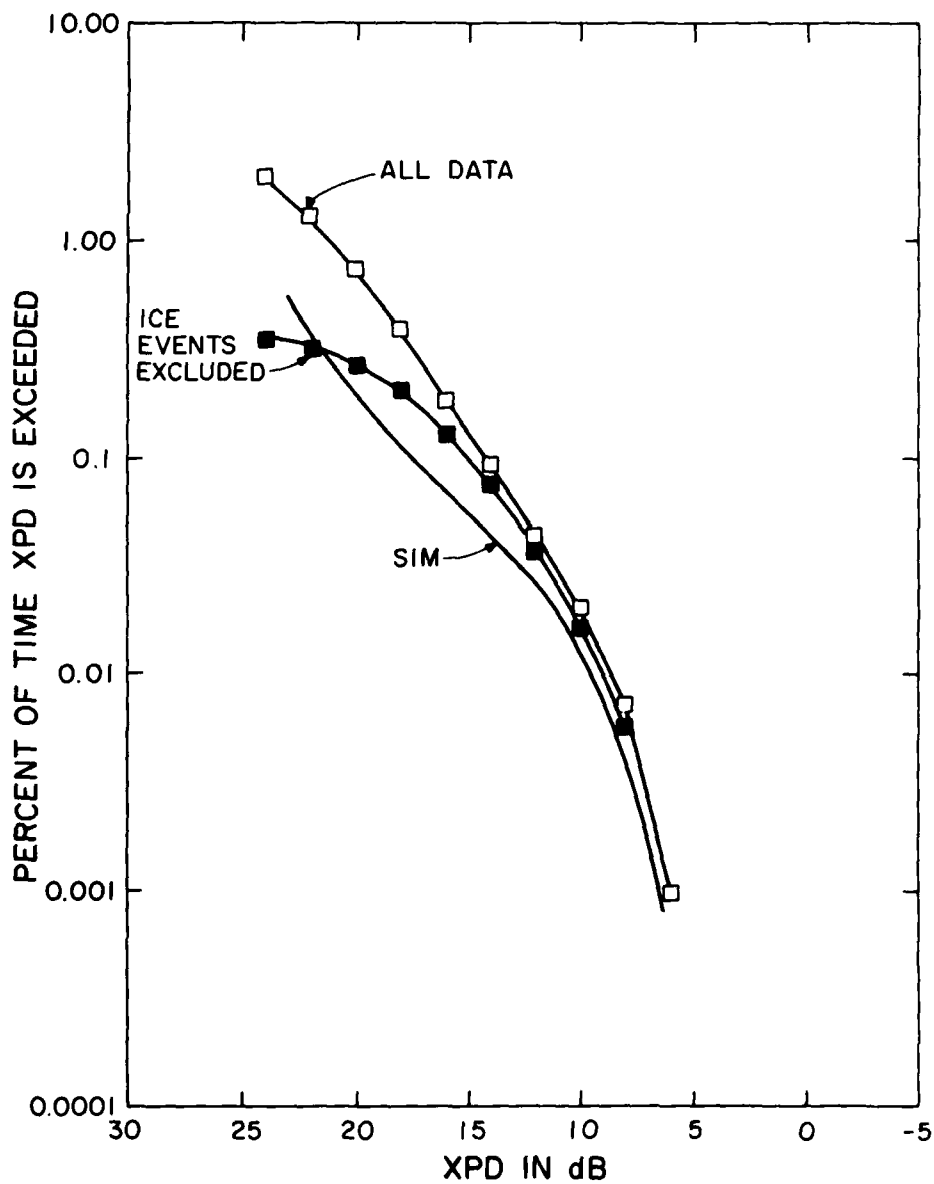


Figure 2. Cumulative XPD distributions on the VPIASU SIRIO downlink for the 1980 calendar year. Curves shown are for all measured data, for the measured data with ice events artificially reset to clear weather, and for a predictive model called SIM.

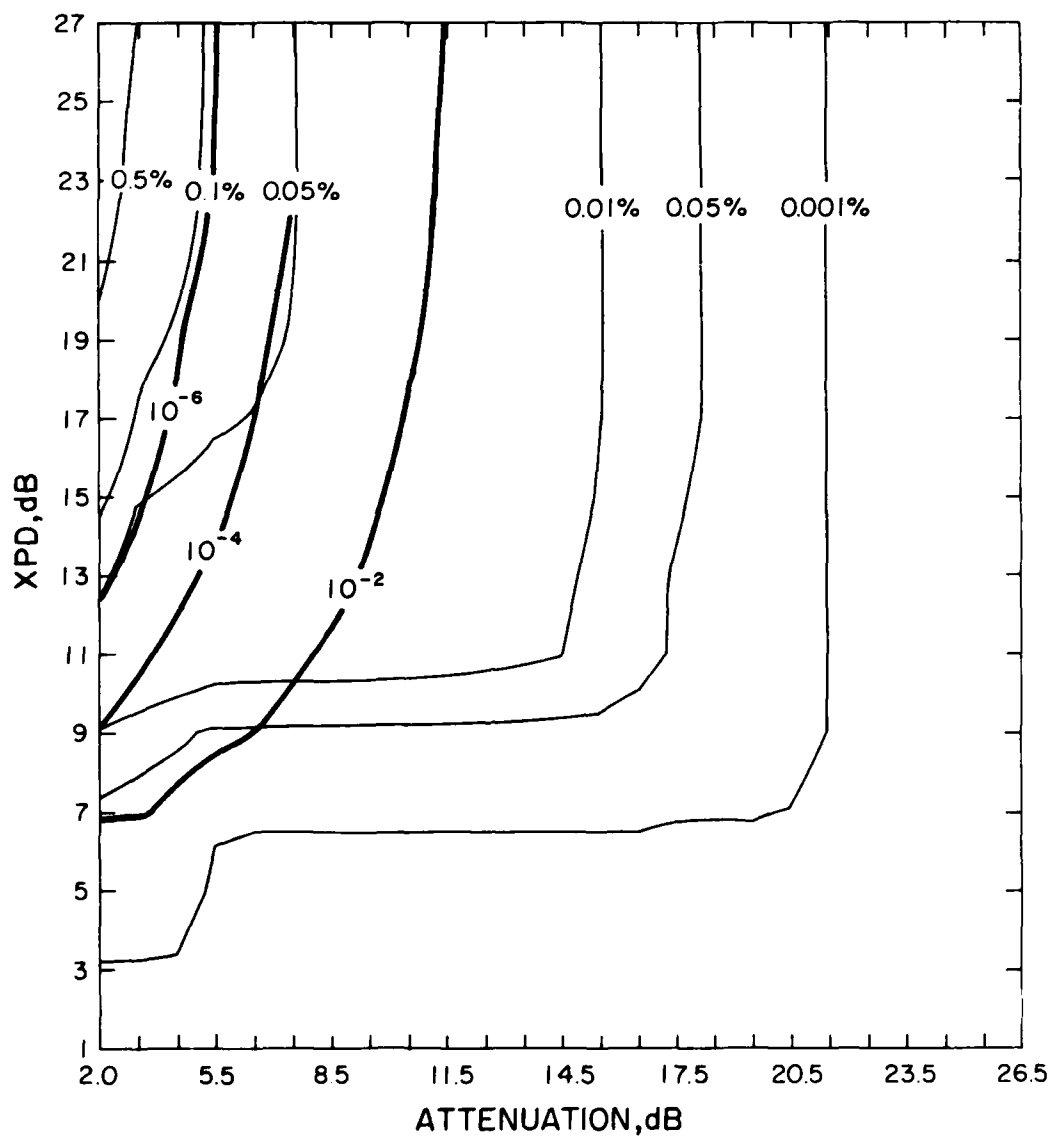


Figure 3. Joint XPD and attenuation distribution for 1979. Thin lines with decimal numbers are percent time contours. Thick lines with exponential numbers are symbol error probabilities for a dual-polarized QPSK system with clear air C/N of 20 dB.

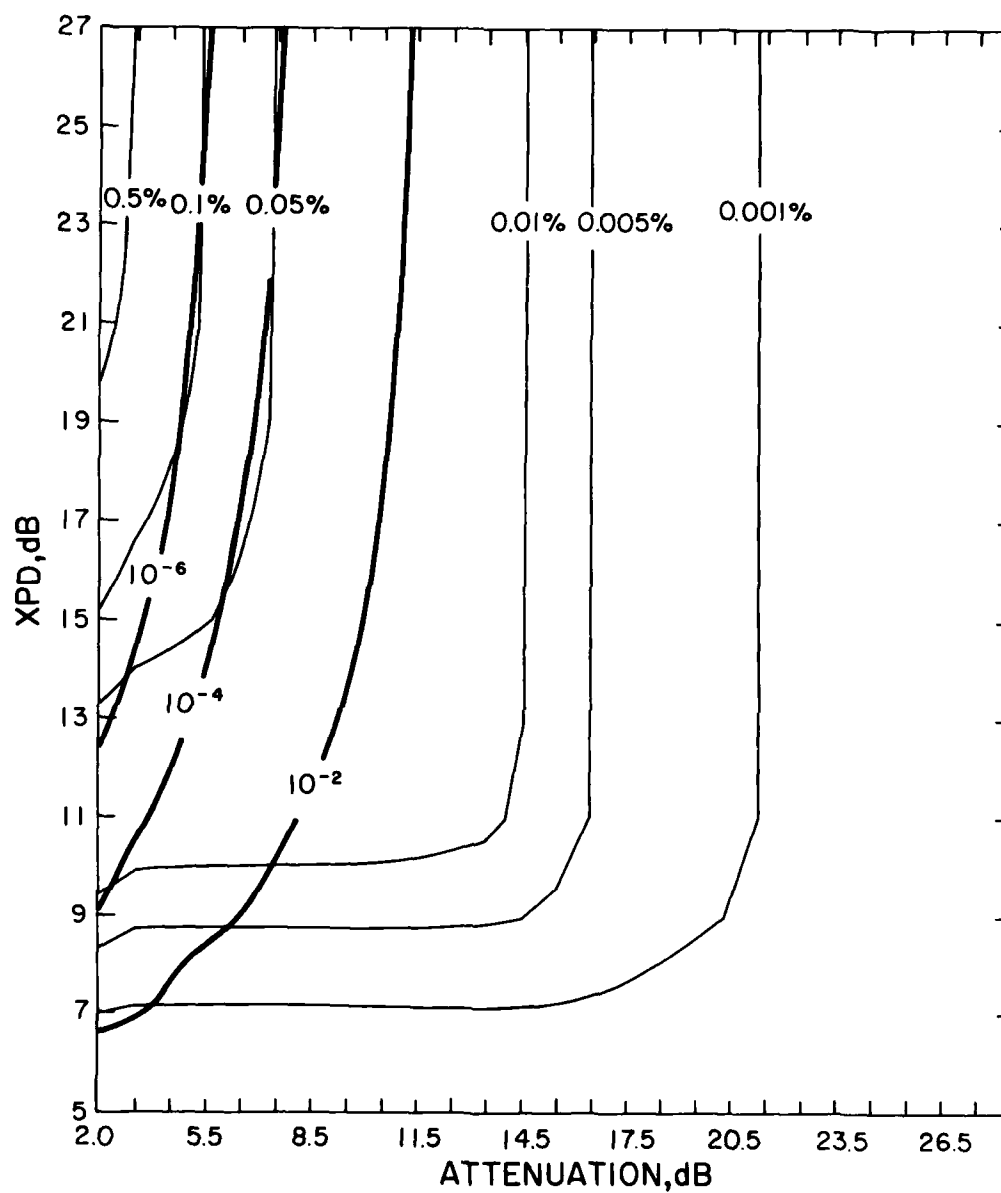


Figure 4. Joint XPD and attenuation distribution for 1980. Thin lines with decimal numbers are percent time contours. Thick lines with exponential numbers are symbol error probabilities for a dual-polarized QPSK system with clear air C/N of 20 dB.

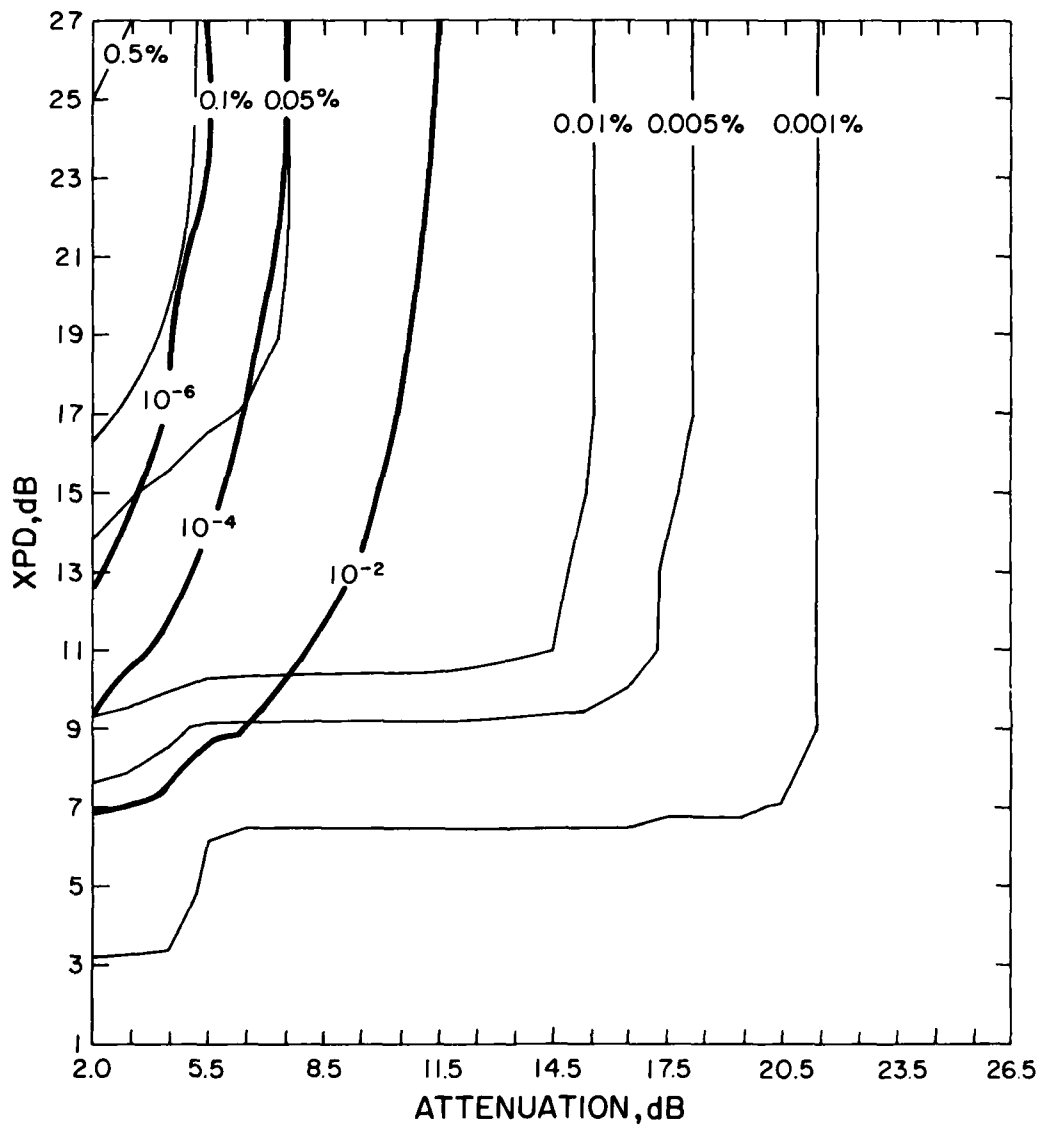


Figure 5. Joint XPD and attenuation distribution for 1979 with ice depolarization periods set to clear weather. Thin lines with decimal numbers are percent time contours. Thick lines with exponential numbers are symbol error probabilities for a dual-polarized QPSK system with clear air  $C/N$  of 20 dB.

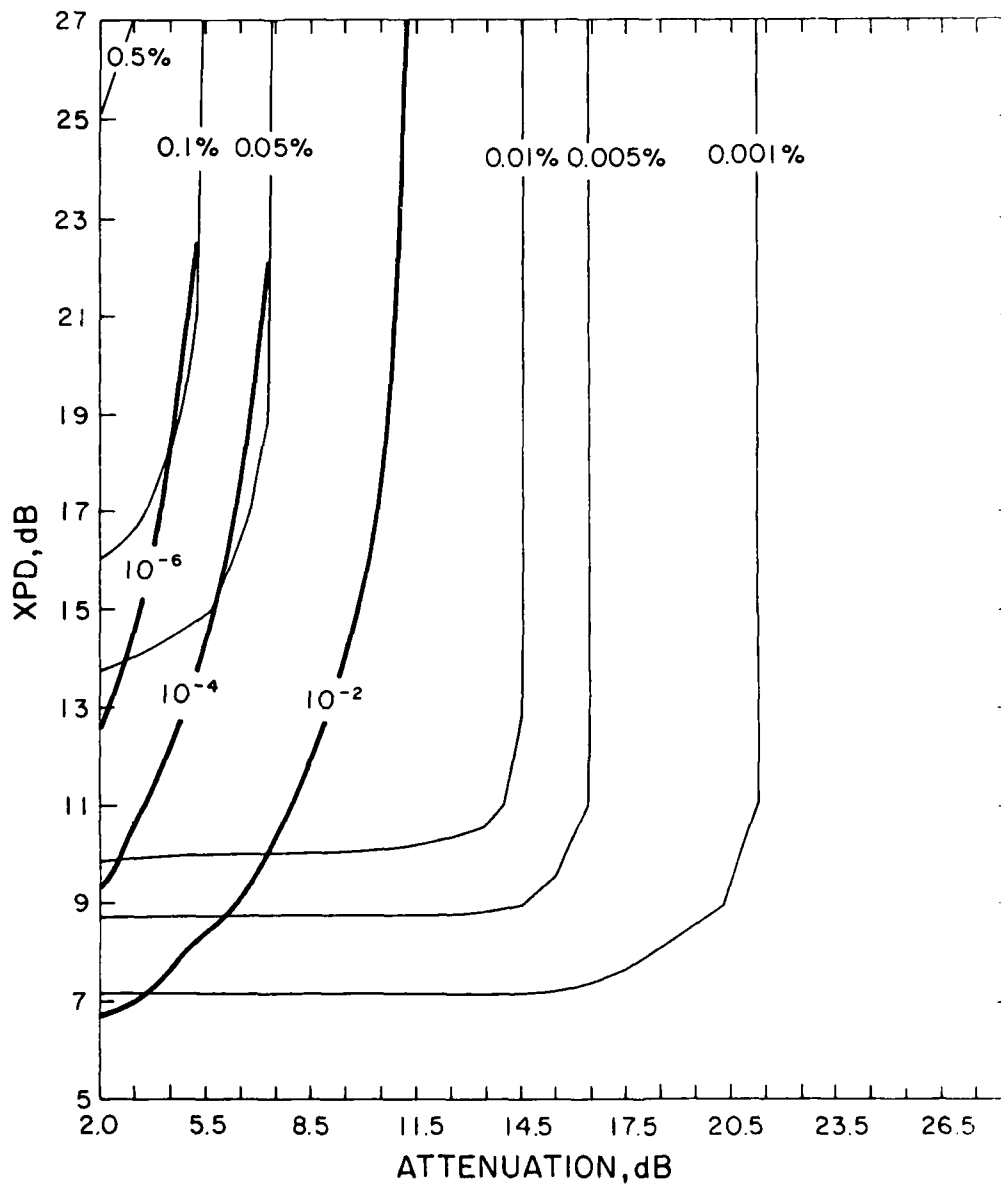


Figure 6. Joint XPD and attenuation distribution for 1980 with ice depolarization periods set to clear weather. Thin lines with decimal numbers are percent time contours. Thick lines with exponential numbers are symbol error probabilities for a dual-polarized QPSK system with clear air C/N of 20 dB.

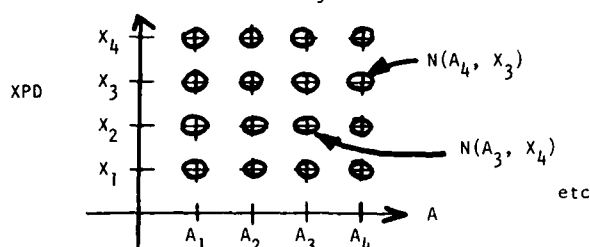
## DISCUSSION

J.R. Larsen (Denmark): 1) When ice depolarization modifies the distribution curve by 3 dB, is it an indication that ice and rain depolarization are of equal magnitude?

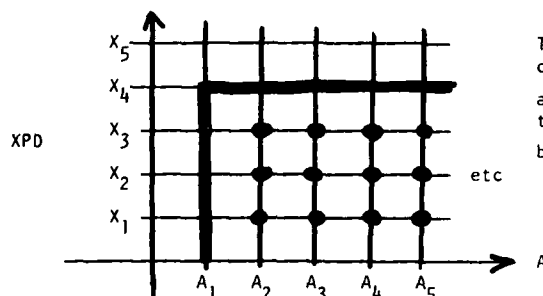
2) Since you define ice depolarization as that associated with attenuation under 3 dB (although it may also occur during heavy rain), should the modifications in Figures 5 and 6, in comparison with Figures 3 and 4, be in the part of the diagram corresponding to attenuation of 2 to 3 dB?


C.W. Bostian (U.S.): 1) In cases where ice modifies the cross polarization discrimination (XPD) percent time contours by 3 dB, this is true. However the 3 dB value is a worst case; consider Figure 2 of my paper. The difference between the "all data" and "ice events excluded" curves is greater or equal to 3 dB only for XPD values greater than 15 dB. There is little difference in these curves below 10-12 dB. We say that ice depolarization is as important as rain for XPD greater than 15 dB. I want to look at a plot for "ice events only" to verify this comment.

2) Yes, these modifications apply in the 2-3 dB region. I believe this after some deliberations. I will explain my beliefs below, and refer to reference [5] in my paper for more details. Assume that we have measured a set of A and XPD pairs at uniform time intervals. Also assume for convenience that they have been integerized so that  $N(A_i, XPD_j)$  is the number of observations for which attenuation =  $A_i$  and the XPD =  $XPD_j$ . Now suppose we write the  $N(A_i, XPD_j)$  values on a grid like the axes of my figures below.



The joint distributions plotted in my paper use contours to show the percent of time A exceeds a value on the x-axis and XPD is less than the value on the y-axis. We compute these for the contour passing through the point  $(A_i, XPD_j)$  by drawing a rectangle with its corner at  $(A_i, XPD_j)$  and containing all  $N(A_i, XPD_j)$  values with  $A_j$  greater than  $A_i$  and  $XPD_j$  less than  $XPD_i$ .



To get the percent time contour value at  $(A_i, XPD_j)$  we count all of the N's for points (●) in the  rectangle and divide those by the total number of observations.

The number of observations at a given point thus influences the contours at all points above or to the left of the given point. When we make a measurement with A between 2 and 3 dB, and replace the observed XPD by an arbitrary clear weather value, we change the percent times of all 2 dB attenuation points in the plot.

M.P.M. Hall (U.K.): 1) You comment in your paper on the effects of ice particle density, ice cloud thickness, and average volume of ice particles. It would seem that ice particle shape is also important, in particular the oblateness. For the last one or two years we have reported studies of the development of oblateness and density of falling ice crystals, deduced from our dual polarization radar data. Typically we see high density (high dielectric constant), small size, highly oblate, and horizontally oriented ice particles at the top of a cloud, large, low density (low dielectric constant for air/ice mixture), and near spherical particles in the middle of a cloud, and large wet (high dielectric constant), highly oblate, and horizontally oriented particles in the melting layer. The intention is to use this information in the United Kingdom to comment on the XPD results on an earth-space path.

2) You comment in your paper that you see more depolarization at low elevation angles than at high elevation angles. Could this occur because there is no very significant change in volume intercepted for low and high angles in vertical raincells, while there is significant increase of volume intercepted at low elevation with the melting layer (of large wet highly oblate horizontally oriented particles) due to its horizontal nature?

C.W. Bostian (U.S.): 1) We are hoping to make similar measurements soon, and are interested in your results. In calculating ice depolarization we write  $[k]$  as

$$[k] = \frac{k_0}{2} pL \langle V \rangle \{ p[F']_{\text{plate}} + (1-p)\langle F' \rangle_{\text{needle}} \}$$

where  $pL < V >$  is ice content,  $[F']_{\text{plate}}$  is scattering matrix for ice plates,  $<[F']_{\text{needle}}>$  is scattering matrix for ice needles over the azimuth angle, and  $p$  is fraction of ice in the form of ice plates. Our ice content value quoted at 0.002 assumed 100 % plates. Obviously the fractions of plates and needles can be varied as described in reference [12] in our paper.

2) That is a possibility. When our radar is operational, we will look at melting layer effects.

I. Anderson (U.K.): What is the time variation of the cross polarized component?

C.W. Bostian (U.S.): Our receiver has a 10 second time constant. We are still analyzing the rate of change of the X component and of the XPD, and hope to publish this soon. Generally the most common changes were  $\pm 1$  to  $\pm 2$  dB in 30 seconds. In a typical event the XPD would drop (i.e., get worse) sharply, remain relatively constant for 5 - 30 minutes, and then quietly return to the original level (reference [9] in our paper).



THE EFFECTS OF A LOW-ALTITUDE  
NUCLEAR BURST ON MILLIMETER  
WAVE PROPAGATION

by  
Edward E. Altshuler  
Rome Air Development Center  
Electromagnetic Sciences Division  
Hanscom AFB, MA 01731  
U.S.A.

# SUMMARY

The main objective of this paper is to examine the limitations imposed on millimeter wave propagation by the dust produced by a low altitude nuclear burst. The closer the burst is to the surface, the larger will be the dust loaded into the nuclear fireball, an extremely hot and highly ionized spherical mass of air and gaseous weapon residues. The fireball absorbs, scatters and refracts the propagated wave and may also produce scintillations. In this study, only losses due to absorption and scattering are calculated.

Since there is a great deal of uncertainty as to how representative the dust model is of the true nuclear environment, a sensitivity analysis of attenuation dependence on the pertinent dust parameters was first conducted. It was found that the dust attenuation is very heavily dependent on the maximum particle radius, the number of large particles in the distribution and the real and imaginary components of the index of refraction over the range from dry sand to clay. The attenuation is also proportional to the fraction of the atmosphere filled with dust. The total attenuation produced by a 1 megaton burst at the surface is then computed using the WESCOM code. The attenuation includes losses due to fireball ionization, dust and atmospheric oxygen and water vapor. Results are obtained as a function of time after burst, distance from burst, elevation angle and frequency up to 95 GHz. It is found that very high attenuations occur within about 20 seconds after the burst if the path intersects the fireball. At later times attenuations of the order of tens of dB are possible due to dust alone. After several minutes the larger dust particles have settled and attenuations of several dB are present. Oxygen and water vapor attenuations are typically less than one dB in the window regions.

## 1. INTRODUCTION

In this paper the limitations imposed on millimeter waves by a low altitude nuclear burst are examined. Associated with the burst is a fireball, an extremely hot and highly ionized spherical mass of air and gaseous weapon residues. The fireball grows rapidly and because of its intense heat some of the soil and other material in the area are vaporized and taken into the fireball; strong afterwinds cause large amounts of dirt and debris to be sucked up as the fireball rises.

In order to estimate the effects of dust on the performance of a millimeter wave system it is necessary to first develop a dust model. Since there is a great deal of uncertainty as to how representative the model is of the true nuclear environment, a sensitivity analysis of the attenuation dependence on pertinent dust parameters is conducted. It is assumed that the dust particle sizes follow a power law distribution. Then the attenuation is computed as a function of minimum particle radius, maximum particle radius, particle size distribution, index of refraction and density. A Mie formulation is used to calculate the absorption and scattering losses produced by dust.

The total attenuation produced by a 1 Megaton surface burst is then computed using the WESCOM code. The attenuation consists of contributions due to fireball ionization, dust and atmospheric oxygen and water vapor. Attenuations are obtained as a function of time after burst, distance from burst, elevation angle and frequency.

## 2. PARTICLE SIZE DISTRIBUTION

The sizes of dust particles are often represented by a power law probability distribution of the form

$$P(r) = kr^{-p} \quad (1)$$

where  $r$  is the particle radius,  $p$  is the exponent and  $k$  is a constant, selected such that  $P(r)$  is a proper probability distribution. For some applications a log-normal distribution of particle sizes is used since it provides a better model of the very small particles. For this study, however, we will show that the actual distribution of the very small dust particles does not significantly affect the attenuation so the power law distribution is suitable.

$$\text{Thus} \quad k \int_{r_{\min}}^{r_{\max}} r^{-p} dr = 1 \quad (2)$$

Solving for  $k$  we have

$$k = \frac{p-1}{r_{\min}^{-(p-1)} - r_{\max}^{-(p-1)}} \quad (3)$$

where  $r_{\min}$  and  $r_{\max}$  are the minimum and maximum particle radii respectively. The total number of particles of radius  $r$  is then

$$N(r) = N_T P(r) \quad (4)$$

where  $N_T$  is the total number of dust particles,

$$N_T = \frac{M_T}{\rho_b \bar{V}} \quad (5)$$

and

$M_T$  = total mass of particulates

$\rho_b$  = bulk density of particulate material

$\bar{V}$  = mean volume of a particulate

Then

$$N(r) = \frac{M_T}{\rho_b (4/3 \pi r^3)} \cdot \frac{r^{p-1}}{r_{\min}^{-(p-1)} - r_{\max}^{-(p-1)}} r^{-p} \quad (6)$$

It can be shown that

$$\frac{1}{r^3} = \frac{p-1}{p-4} \cdot \frac{r^{-(p-4)}}{r_{\min}^{-(p-1)} - r_{\max}^{-(p-1)}} \cdot \frac{-r^{-(p-4)}}{-r_{\min}^{-(p-1)} - r_{\max}^{-(p-1)}} \quad (7)$$

Finally

$$N(r) = \frac{M_T (p-4) r^{-p}}{4/3 \pi \rho_b \left[ r_{\min}^{-(p-4)} - r_{\max}^{-(p-4)} \right]} \quad (8)$$

### 3. ATTENUATION OF DUST PARTICLES

Millimeter waves incident on atmospheric particulates undergo absorption and scattering, the degree of each being dependent on the size, shape and complex dielectric constant of the particle and the wavelength and polarization of the wave. An expression for calculating the absorption and scattering from a dielectric sphere was first derived by Mie (1908). It has the form

$$Q_t = -\frac{\lambda^2}{2\pi} \operatorname{Re} \sum_{n=1}^{\infty} (2n+1) (a_n^s + b_n^s) \quad (9)$$

where  $Q_t$ , the extinction cross section, represents losses due to both absorption  $Q_a$ , and scattering  $Q_s$ , and  $a_n^s$  and  $b_n^s$  are very complicated functions of the spherical Bessel terms that correspond to the magnetic and electric modes of the particle respectively.  $Q_t$  has the dimension of area and is usually expressed as  $\text{cm}^2$ . Physically, if a wave having a flux density of  $S$  watts/ $\text{cm}^2$  is incident on the particle, then  $S \times Q_t$  is the power absorbed and scattered.

When the size of a dust particle is very small with respect to wavelength, then the Rayleigh approximation is valid. For this case

$$Q_a = \frac{8\pi^2 r^3}{\lambda} \operatorname{Im} \left( -\frac{n^2-1}{n^2+2} \right) \quad (10)$$

$$Q_s = \frac{128\pi^5 r^6}{3\lambda^4} \left| \frac{n^2-1}{n^2+2} \right|^2 \quad (11)$$

It is seen that the absorption is inversely proportional to the wavelength while the scattering loss is inversely proportional to the fourth power of the wavelength; thus when the wavelength is large compared to the particle size, the absorption dominates and scattering losses are often assumed negligible. Furthermore, since the absorption is proportional to the particle volume, the total attenuation is proportional to the total volume of dust.

As the dust particles become larger, then the Rayleigh approximation is no longer valid and the Mie formulation must be used. Both absorption and scattering cross sections continue to increase with particle size. Finally, after reaching a peak the total cross section begins to level off and would eventually approach a value of twice the geometric cross section of the particle when it is very large with respect to wavelength (Van de Hulst, 1957). Thus we note that as the particle becomes larger the extinction cross section which was initially proportional to the particle volume becomes proportional to the particle cross sectional area.

The attenuation coefficient is equal to

$$\alpha = \int_0^{\infty} N(r) Q_t dr \quad (12)$$

This expression is in nepers/cm, if  $r$  and  $Q_t$  have units of cm and  $N(r)$  is in  $\text{cm}^{-3}$ . In order to convert to dB/km a multiplicative factor of  $4.343 \times 10^5$  must be introduced.

Attenuation and albedo, the ratio of scattered loss to total loss  $\frac{Q_s}{Q_t}$ , for a particle size power law distribution are plotted in Fig. 1 for sand and clay for frequencies from 10 to 95 GHz. It is assumed that the minimum and maximum particle radii are .005 and 5 mm respectively, that the power law exponent is -3.5, and that the densities of the dust material and average mass are  $2.6 \text{ gm/cm}^3$  and  $100 \text{ gm/m}^3$  respectively. It is seen that the attenuation increases very rapidly with increasing frequency. It should be pointed out that attenuation is plotted on a logarithmic scale so the apparent linear increase in attenuation at the higher frequencies actually corresponds to an exponential increase, in reality. Since clay has a higher index refraction than sand, the attenuations are significantly higher.

The ratio of the scattering losses to the total losses, often referred to as the albedo, is also plotted in Fig. 1. It is interesting to note that the albedo for sand is approximately .7, even for a wavelength as long as 30 mm when the average particle radius is only .02675 mm, less than .001 wavelength. This indicates that even though the average dust particles are very small with respect to wavelength the scattering losses are certainly not negligible as compared to the absorption because of the limited number of large particles that are present. This issue is discussed later when the results of the albedo dependence on maximum particle radius are presented.

### 3A. Dependence of Dust Attenuation on Minimum Particle Radius

In Figs. 2(a) and 2(b) the attenuations are plotted for sand and clay respectively as a function of minimum particle radius for a set of frequencies from 10 to 95 GHz. It is seen that the attenuation rises only very slightly as the minimum particle radius is increased. It is interesting to note that it passes through a very broad peak at 95 GHz and would probably behave similarly at the lower frequencies for larger minimum particle radii. On the basis of these results it can be concluded that the attenuation is not very sensitive to the minimum particle radius.

### 3B. Dependence of Dust Attenuation and Albedo on Maximum Particle Radius.

In Figs. 3(a) and 3(b) the attenuations and albedos are plotted for sand and clay respectively as a function of maximum particle radius for the same set of frequencies from 10 to 95 GHz. It is seen that the attenuation and albedo both rise very abruptly as the maximum particle radius is increased. The attenuation reaches a peak and the albedo begins to level off when the maximum particle diameter is approximately equal to the wavelength. As mentioned previously it is seen that the scattering losses are comparable and in some instances even larger than the absorption losses. This is due to the fact that the imaginary component of the index of refraction is very small, thus resulting in a small absorption.

### 3C. Dependence of Dust Attenuation on the Power Law Exponent

In Figs. 4(a) and 4(b) attenuation is plotted as a function of power law exponent for sand and clay respectively for the set of frequencies from 10 to 95 GHz. When the exponent  $p$ , is small the probability of having large particles in the distribution is relatively high. As  $p$  becomes larger fewer large particles are present. Thus the attenuation passes through a very broad peak for low values of  $p$  and then drops off very rapidly when  $p$  becomes larger. Thus the power law exponent can significantly affect the attenuation.

### 3D. Dependence of Dust Attenuation and Albedo on the Index of Refraction

In Fig. 5 the attenuation and albedo are plotted as a function of index of refraction  $n=n_1-jn_2$ , for the set of frequencies from 10 to 95 GHz. Both the real and imaginary components of the index of refraction are increased linearly so that the particulates have an index of refraction that corresponds to dry sand for the lowest values and water for the highest values. It is seen that the attenuation increases and the albedo decreases sharply as the particulates change from dry sand to clay and then both essentially level off as the real and imaginary components are increased further. The attenuation and albedo are examined more closely in Fig. 6. In Fig. 6(a) the imaginary component is fixed at  $n_2=.2$  and the real component is varied from 1.6 to 3.4; in Fig. 6(b) the real component is fixed at  $n_1=2.5$ , and the imaginary component is varied from zero to .6. For both cases the attenuation increases gradually as either of the components of index of refraction is increased. Based on the curves for the albedo it is seen that increasing the imaginary component, increases the absorptive losses while increasing the real component results in an increase in the scattering losses. Thus it can be concluded that the attenuation is very dependent on both the real and imaginary components of the index of refraction over the ranges from about  $2 < n_1 < 4$  and  $0 < n_2 < .8$ .

### 3E. Dependence of Dust Attenuation on Density of Particles

In Eq. (5) it is seen that the total number of dust particles is directly proportional to the total mass of the particles  $M_T$ , divided by the bulk density  $\rho_b$  of the individual particles. In this formulation a single scattering model is used so the attenuation is directly proportional to the number of particles as seen in Eq. (12) and therefore directly proportional to  $M_T/\rho_b$ . Thus any uncertainty in either the total mass or particle density will produce a corresponding error in the attenuation.

#### 4. ATTENUATION PRODUCED BY A NUCLEAR BURST

As mentioned previously associated with the nuclear burst is a fireball. The initial electron density within the fireball is extremely high and for a period of about 20 seconds blacks out the propagated wave. After that time, beta radiation from the radioactive debris within the fireball may sustain sufficiently high ionization levels to absorb millimeter wave signals for several minutes. Thus the two principal sources that attenuate the propagated wave are fireball ionization and dust.

The nuclear explosion dust model is often divided into five distinct regions which are modeled somewhat crudely in Fig. 7. The ejecta region consists of relatively large particles of dust and debris thrown out of the crater; settling occurs quickly and its importance diminishes in about a minute or so. The blast wave produces a low level dust region often referred to as the pedestal or sweep-up layer. This region has high dust densities for about a minute also; lower densities exist for many minutes later. The cylindrical stem region forms after the establishment of the fireball vortex and lasts for several minutes. The mushroom shaped cloud or main cloud is the major dust region and exists for many minutes. Finally, the main cloud transcends into the fallout region which exists for a long period of time.

In this study the Weapons Effects on Satellite Communications code (WESCOM) is used. It utilizes environment, propagation and signal processing models developed by the Defense Nuclear Agency (DNA) and attempts to provide a best estimate of the quantities being modeled. Included along with ionization and dust losses are the oxygen and water vapor losses of the ambient troposphere.

The WESCOM dust model is a somewhat simplified model in that it assumes that all the dust is initially contained within the fireball and then forms a main cloud which eventually becomes the fallout region (Thompson, 1978). The stem and pedestal are not included in the WESCOM dust model. Dust particulates within the fireball are divided into the 8 particle size ranges shown in Table 1. Each group of particle sizes are initially assumed to be uniformly distributed throughout a disc-like cylinder.

TABLE 1. Particle Size Distribution

DUST GROUP	MINIMUM PARTICLE DIAMETER	FRACTION OF PARTICLES
1	.01 mm	$1-1.372 \times 10^{-6}$
2	.9	$1.356 \times 10^{-6}$
3	4.0	$1.463 \times 10^{-8}$
4	10.0	$8.750 \times 10^{-10}$
5	20.0	$9.587 \times 10^{-11}$
6	32.5	$2.222 \times 10^{-11}$
7	52.5	$4.540 \times 10^{-12}$
8	75	$1.370 \times 10^{-12}$

These discs are stacked within the fireball as shown in Fig. 8(a) with the largest particles contained within the lowest disc and with decreasingly smaller particles in the upper discs. Each particle size group rises to a maximum altitude at which point the particles start to fall with their respective terminal velocities. A simplified model of the size and height of the rising fireball as a function of time is shown in Fig. 8(b). The terminal velocities are plotted in Fig. 9. Thus we have a model for which the largest particles remain aloft for a relatively short period of time while the smaller particles may remain suspended for many minutes.

A set of attenuations were computed, using the WESCOM code, as a function of frequency, elevation angle, distance from the burst and time after burst for a megaton surface burst. In Fig. 10 the attenuation is plotted as a function of time for a slant path  $30^\circ$  above the horizon, distance from burst of 10 km and frequencies of 10, 20, 45 and 95 GHz. It is seen that the attenuation has essentially two peaks; the first peak occurs about 35 seconds after the burst and is caused by the dust rising through the antenna beam, the broader and lower attenuation second peak is due to the settling dust passing through the beam again. As expected, dust attenuation increases significantly with frequency.

In Fig. 11 the angle dependence of the attenuation is examined for the same conditions at a frequency of 45 GHz. As expected the first peak occurs earliest and the attenuation is highest for the lowest elevation angle. Also the separation in time of the peaks decreases with increasing elevation angle.

In Fig. 12 the distance dependence of the attenuation is plotted for the same conditions for a fixed elevation angle of  $30^\circ$ . It is seen that the highest attenuations occur earliest for distances closest to the burst and then decrease and occur at later times as the distance from the burst is increased.

In general it is seen that high attenuations occur at all frequencies as the rising dust cloud passes through the antenna beam. For low elevation angles and distances close to the burst these attenuations may exceed 100 dB. Attenuations produced by the falling dust are significantly lower and do not generally exceed 5 dB.

## 5. CONCLUSIONS

Upon examining the effects of dust on slant path propagation at millimeter wavelengths it has been shown that the attenuation is heavily dependent on the maximum particle radius, the number of large particles in the distribution and the real and imaginary components of the index of refraction in the range from dry sand to clay. The attenuation is also directly proportional to the fraction of the atmosphere filled with dust. Dust attenuations, while low at frequencies below 10 GHz increase significantly at millimeter wavelengths.

For the WESCOM code, the computed attenuations behave as would be expected. Very large attenuations occur immediately after the burst due to fireball ionization and dust when the antenna beam is close to the fireball. At later times the attenuation is caused mostly by dust. The attenuation due to oxygen and water vapor is typically less than 1 dB in the window regions.

On the basis of these results it appears that if the antenna beam intersects the fireball within the first 20 seconds after the burst, then attenuations greater than 100 dB are likely, and the lower frequencies are attenuated more than the higher frequencies because the losses are due predominantly to fireball ionization. For this reason it would seem that the very early dust model is not too critical since the attenuations are always prohibitive. At times from about 20 seconds to several minutes, the period after ionization losses have essentially disappeared, but during which dust losses can be tens of dBs, the accuracy of the dust model parameters discussed above can significantly influence the results. Finally, when the dust settles, although attenuations of the order of several dB are likely, it would seem that it should be possible to model these more accurately than those at earlier times since the terminal velocities of the dust particles are known. Since only the very small particles remain suspended the size distribution is less critical and only the density and index of refraction of the dust are important.

## REFERENCES

1. Mie, G., Contribution to the Optics of Suspended Media Specifically Colloidal Metal Suspensions (In German), Ann. Physik, 25, (1908) 377-445.
2. Thompson, Dust Clouds - Models and Propagation Effects, Proceedings of Submillimeter Atmospheric Propagation Applicable to Radar and Missile Systems, Redstone Arsenal, AL. TR 80-3, (1980) pp. 114-117.
3. Van De Hulst, H.C., Light Scattering by Small Particles, Wiley, NY, (1957).

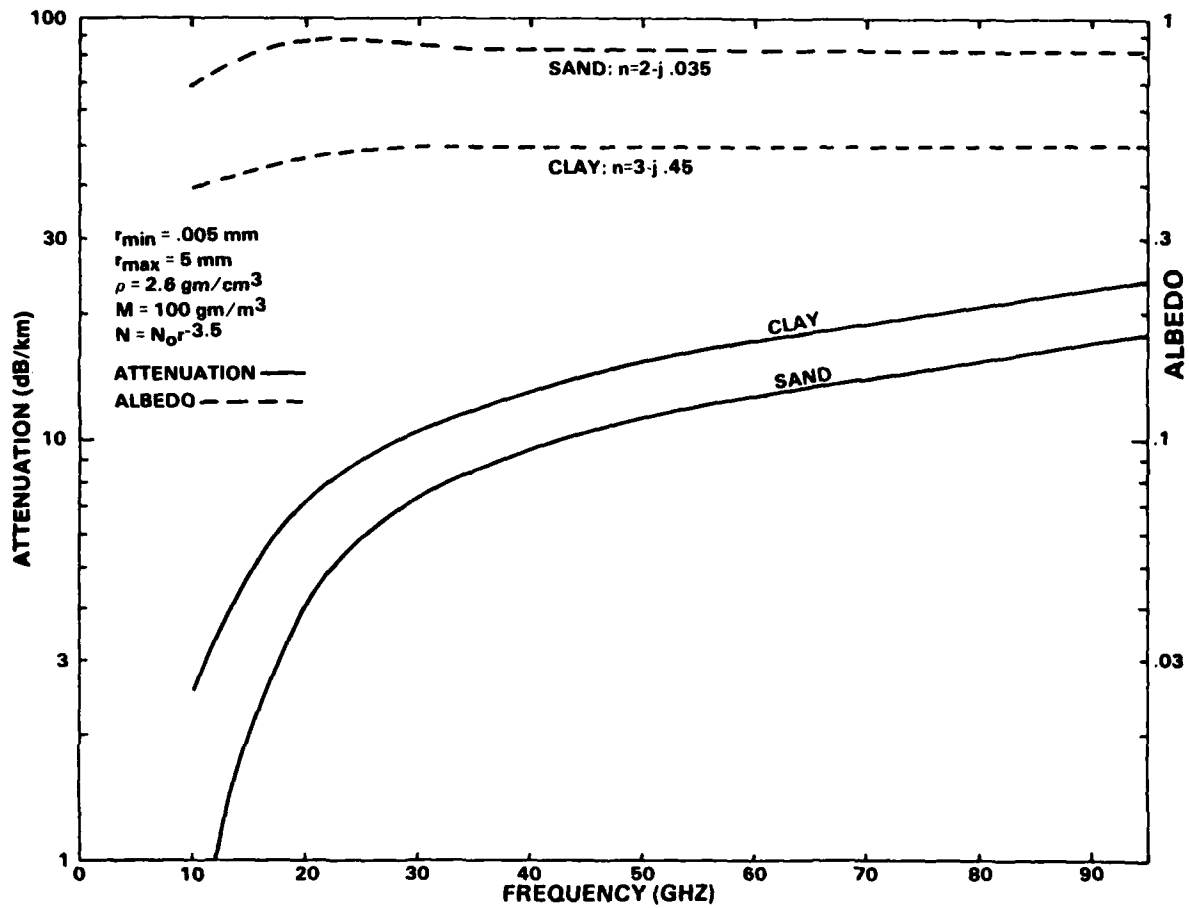


Fig. 1 Attenuation and albedo of sand and clay particles at millimeter wavelengths.

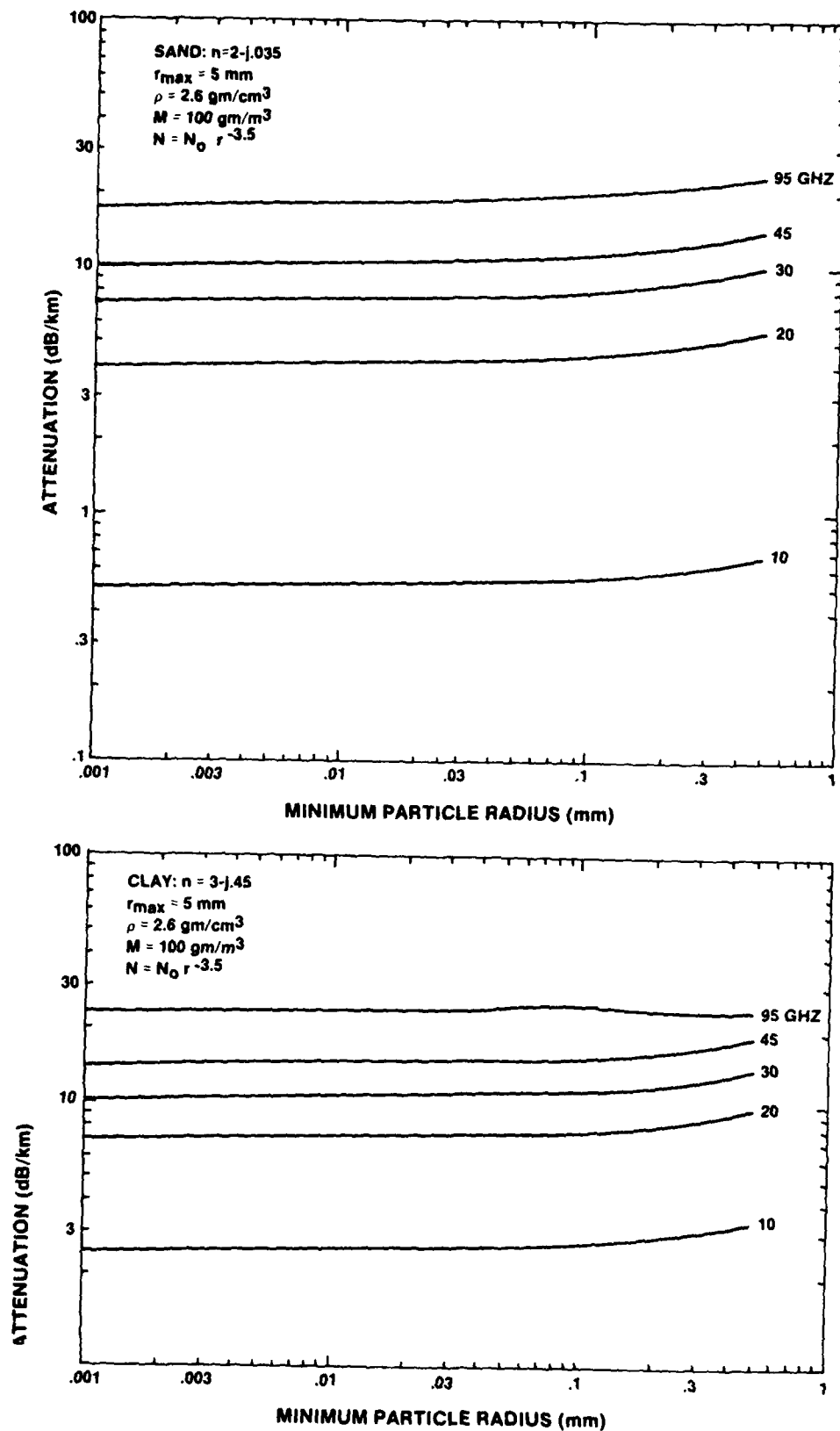


Fig. 2 Attenuation at millimeter wavelengths as a function of minimum particle radius

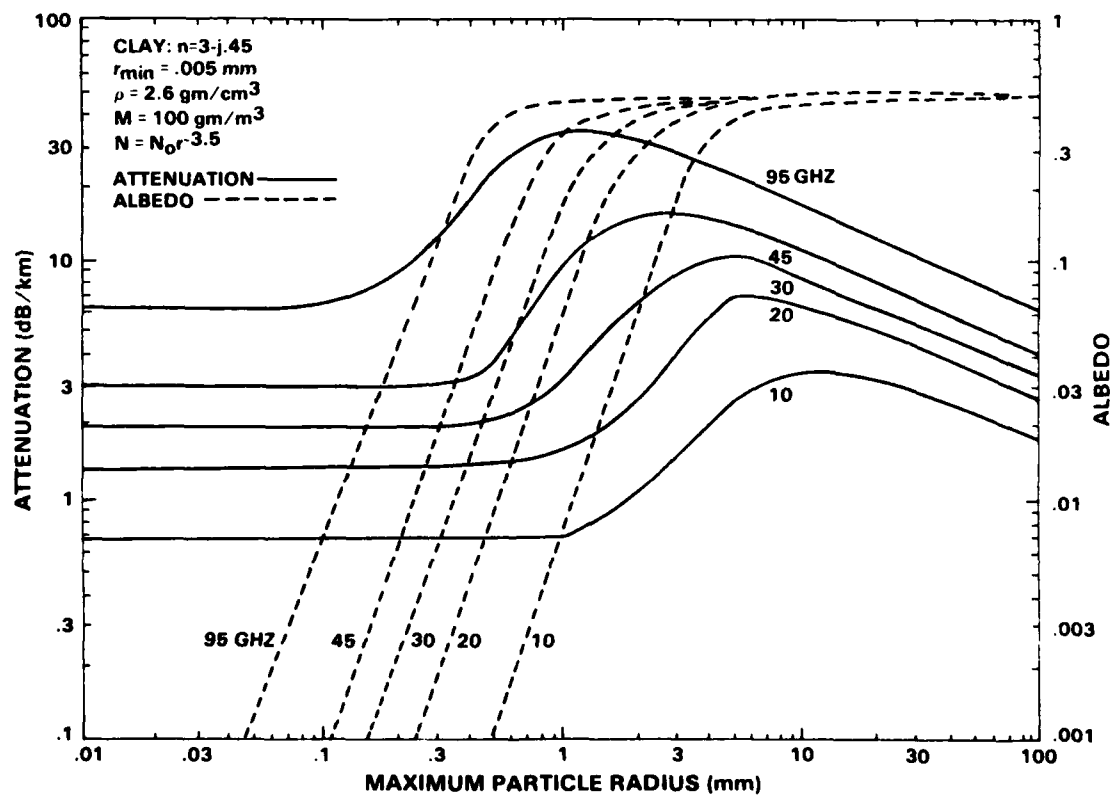
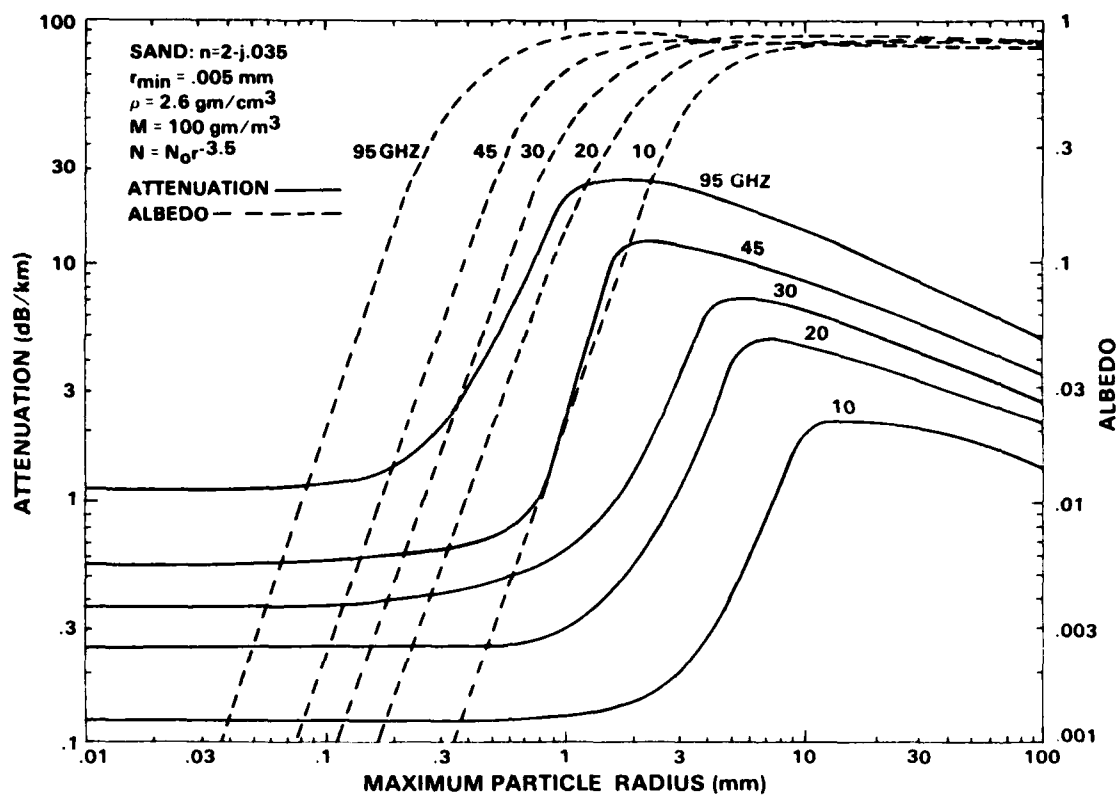


Fig. 3 Attenuation and albedo at millimeter wavelengths as a function of maximum particle radius

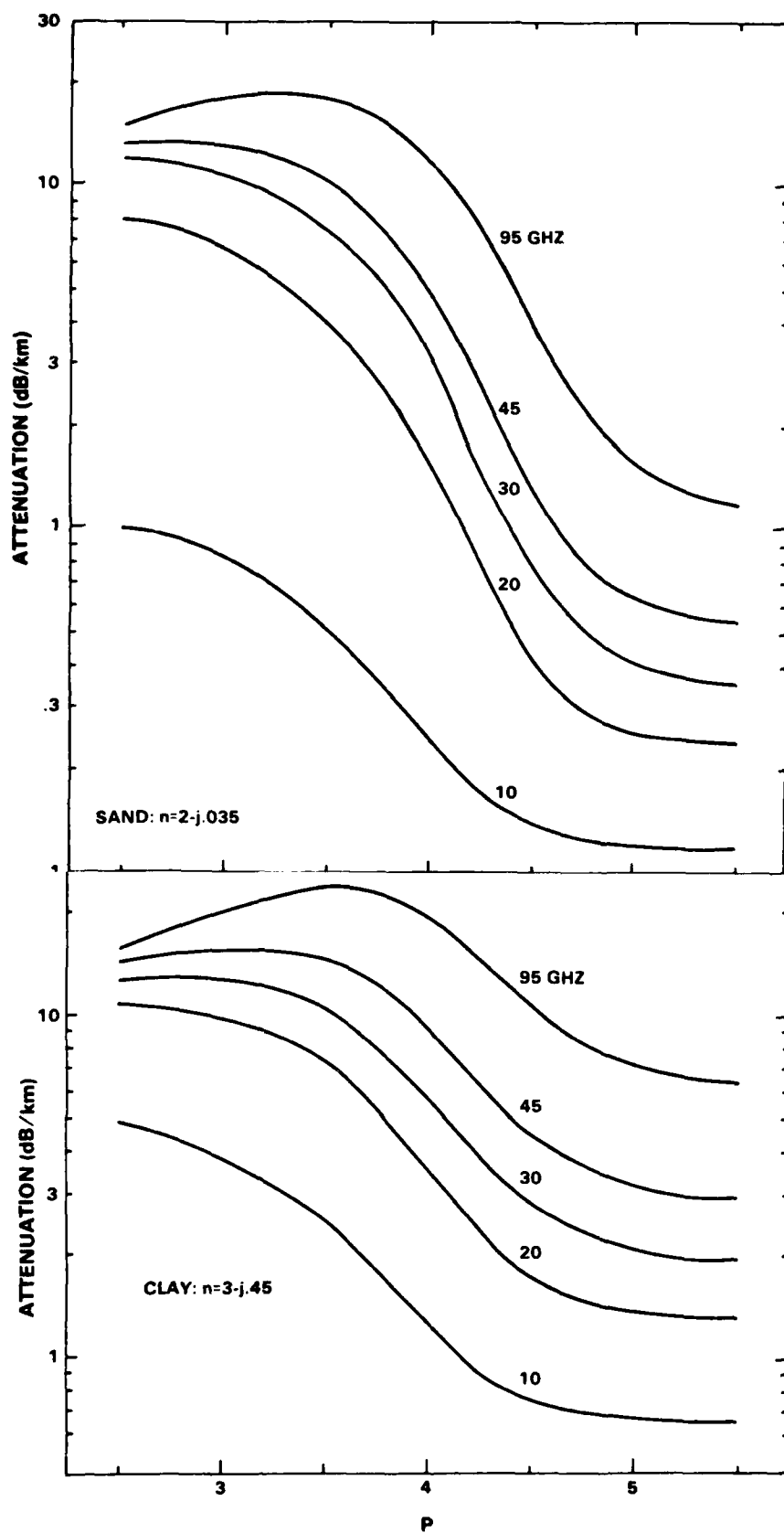


Fig. 4 Attenuation at millimeter wavelengths as a function of power law exponent

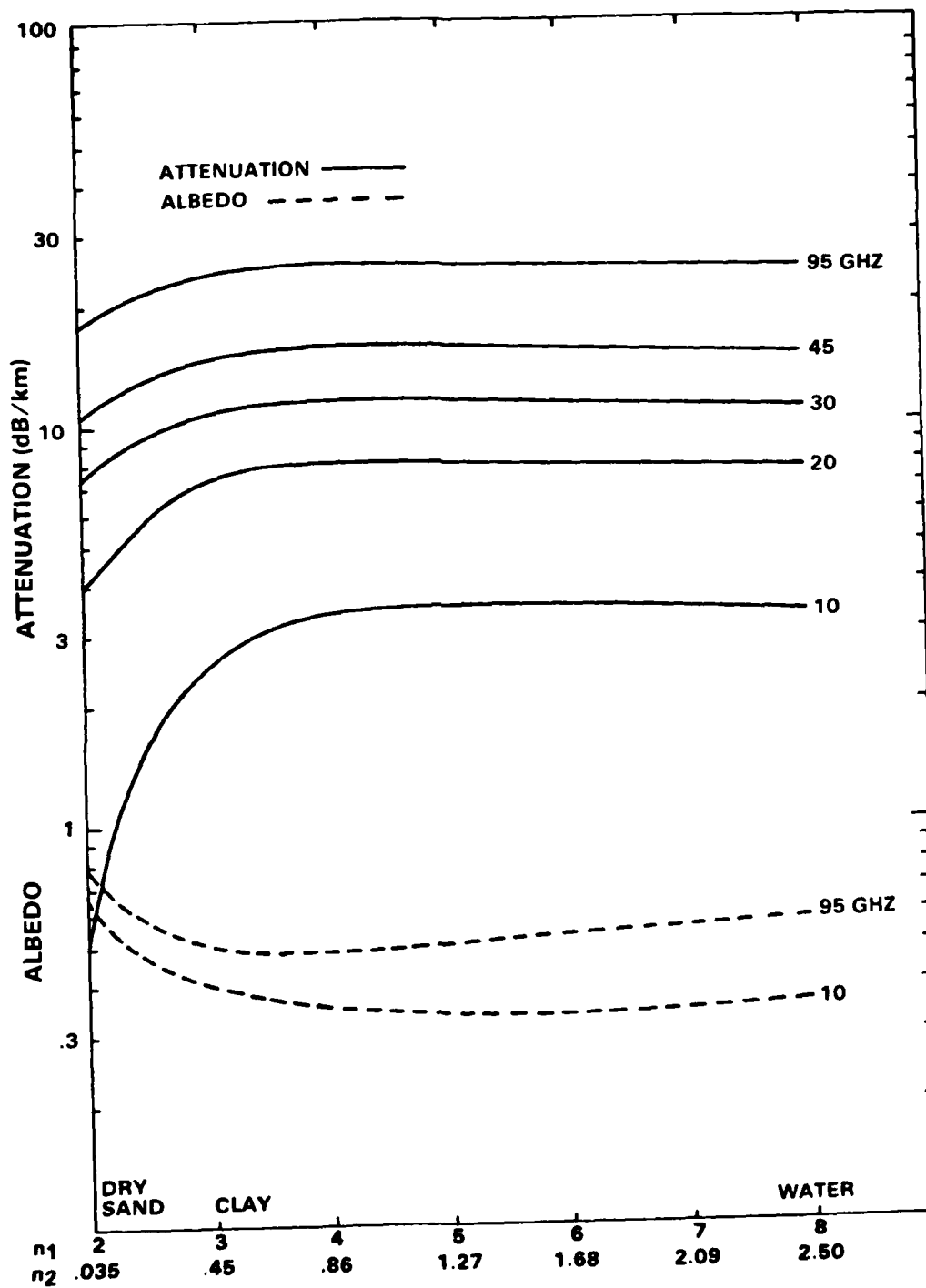


Fig. 5 Attenuation and albedo at millimeter wavelengths as a function of index of refraction.

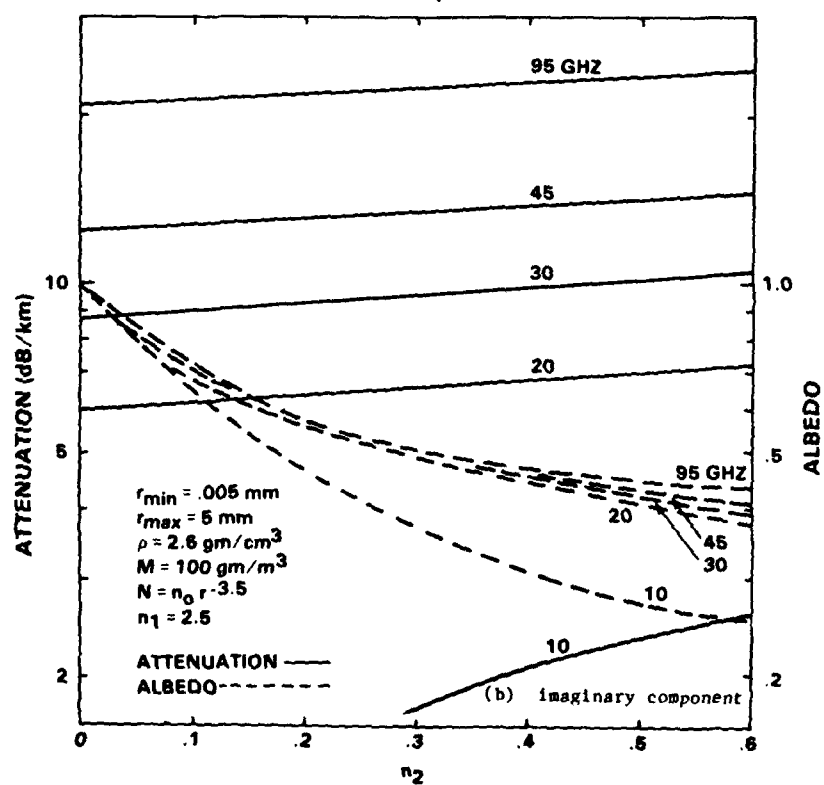
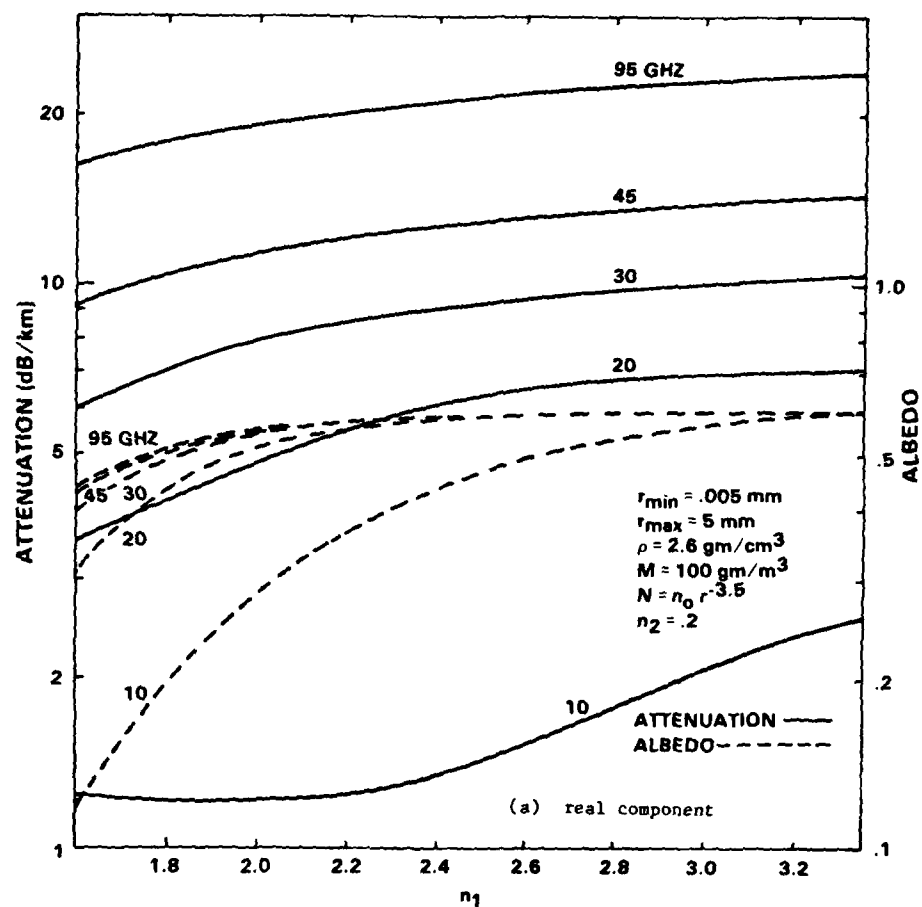


Fig. 6 Attenuation and albedo at millimeter wavelengths as a function of real and imaginary components of index of refraction.

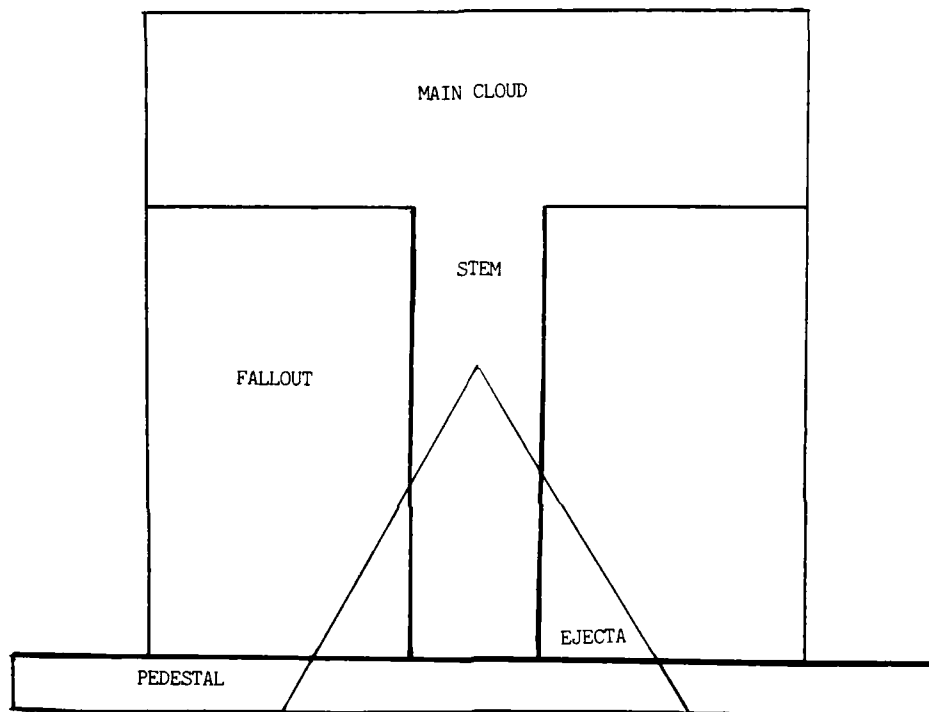
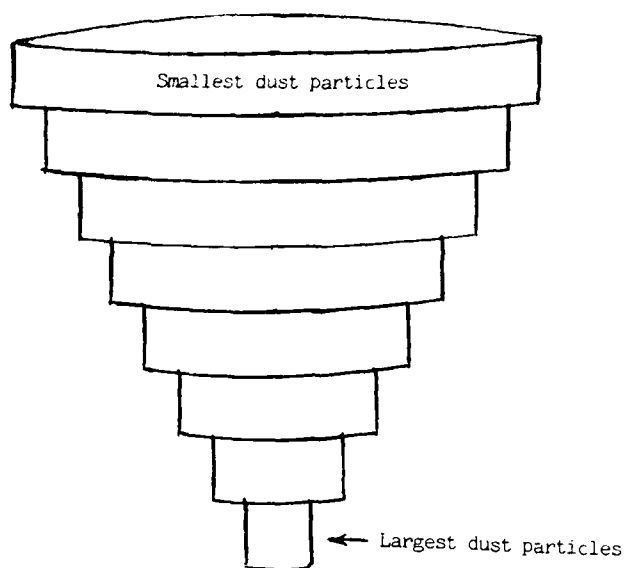
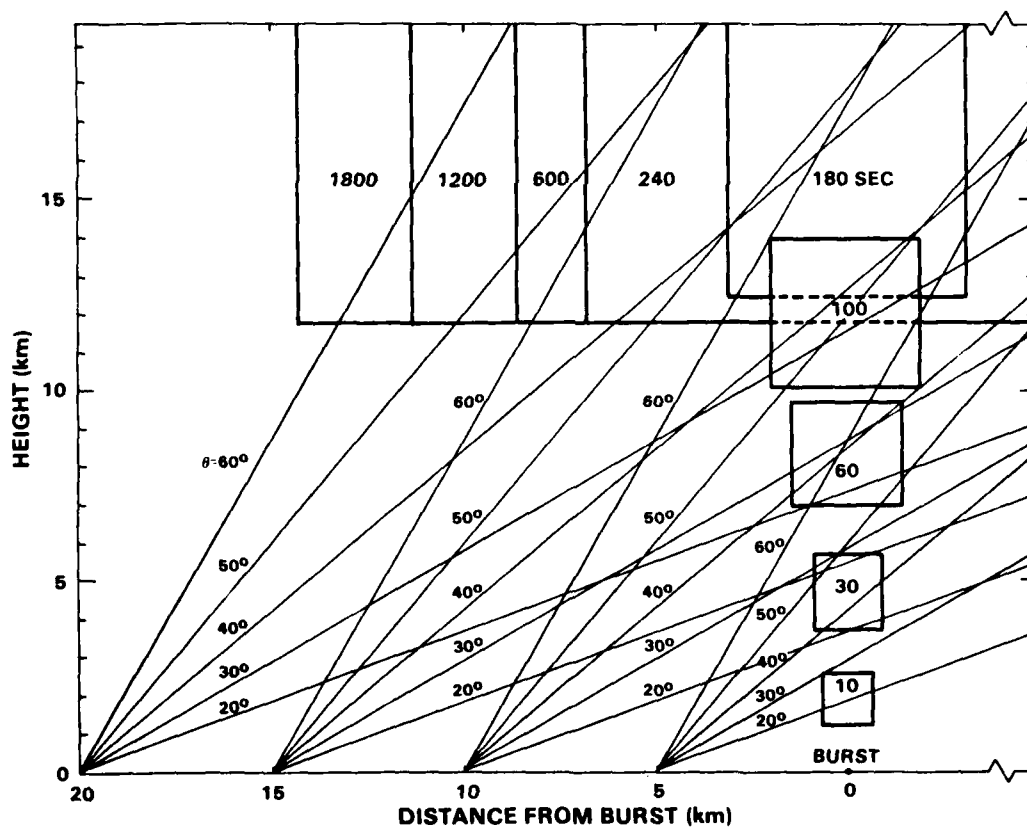


Fig. 7 Dust regions



(a) Disc-like regions within fireball



(b) Rising fireball as a function of time

Fig. 8 Dust model

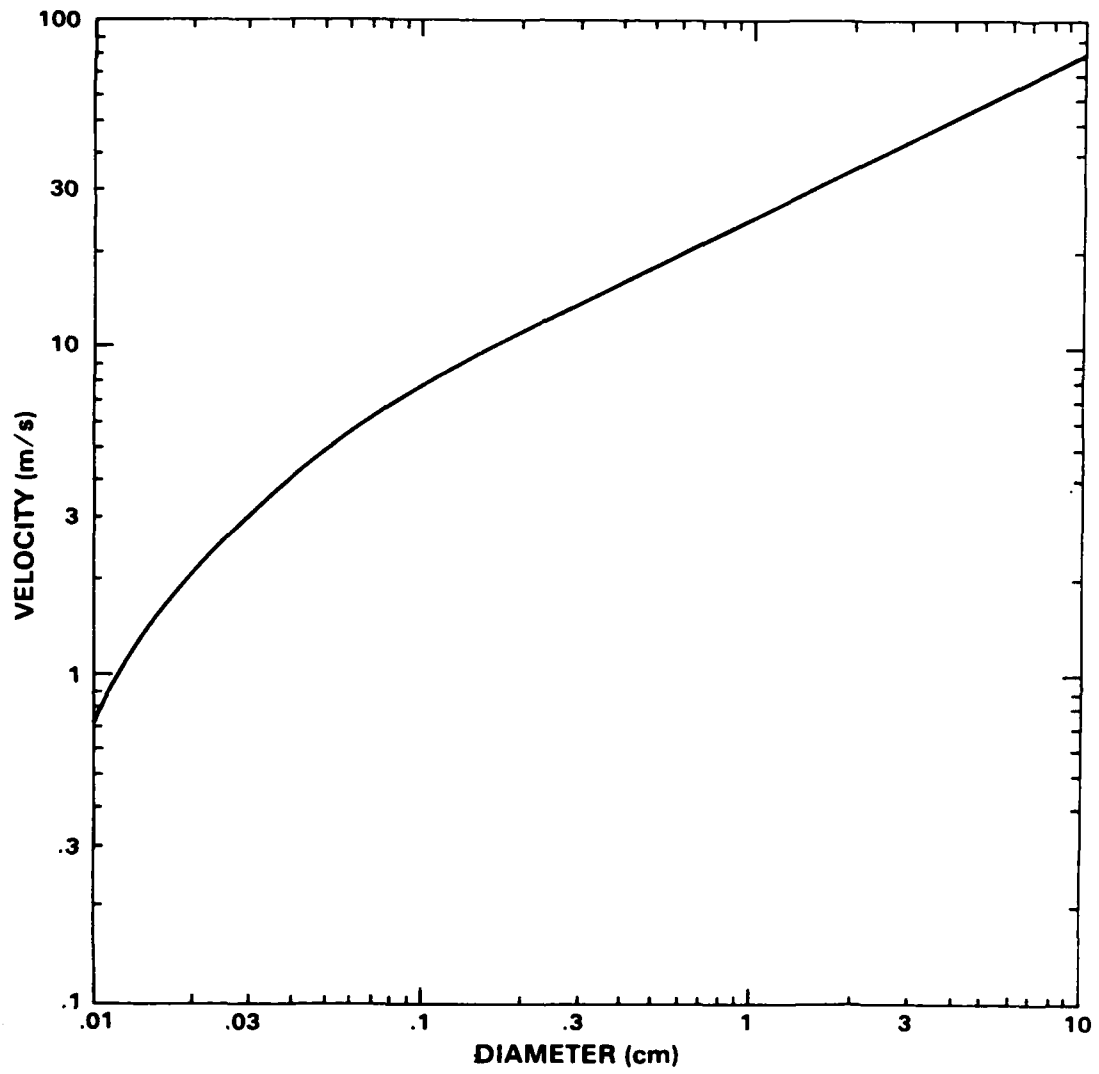


Fig. 9 Terminal velocity of dust as a function of particle radius.

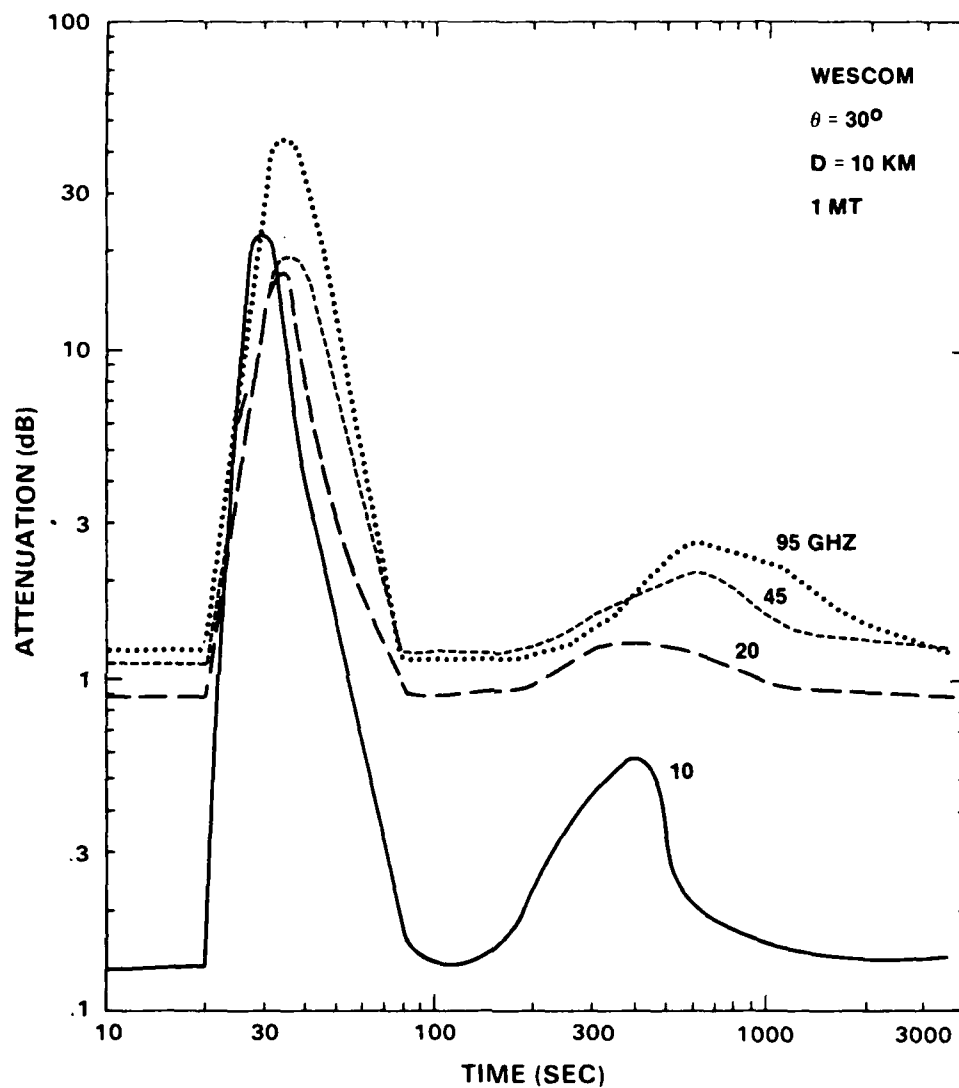


Fig. 10 Attenuation from 1 MT burst as a function of frequency.

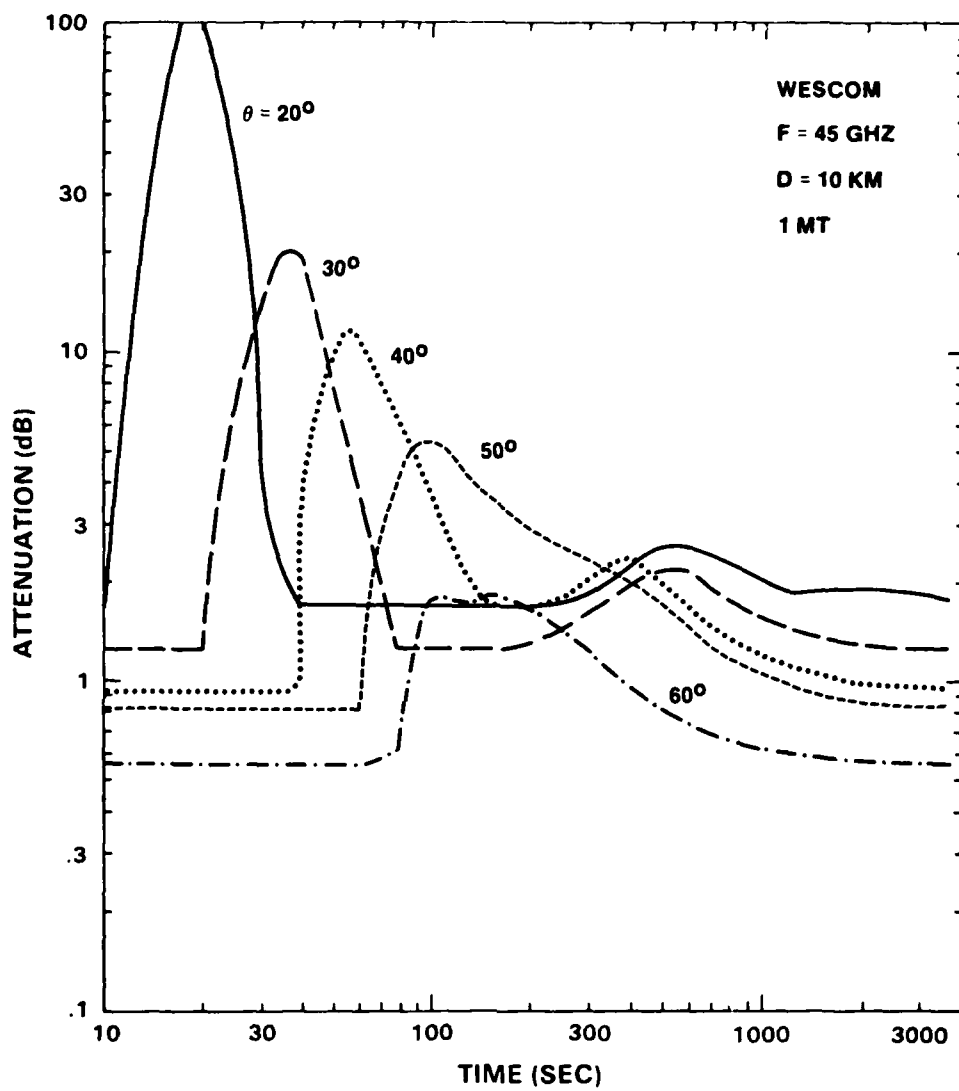


Fig. 11 Attenuation from 1 MT burst as a function of elevation angle.

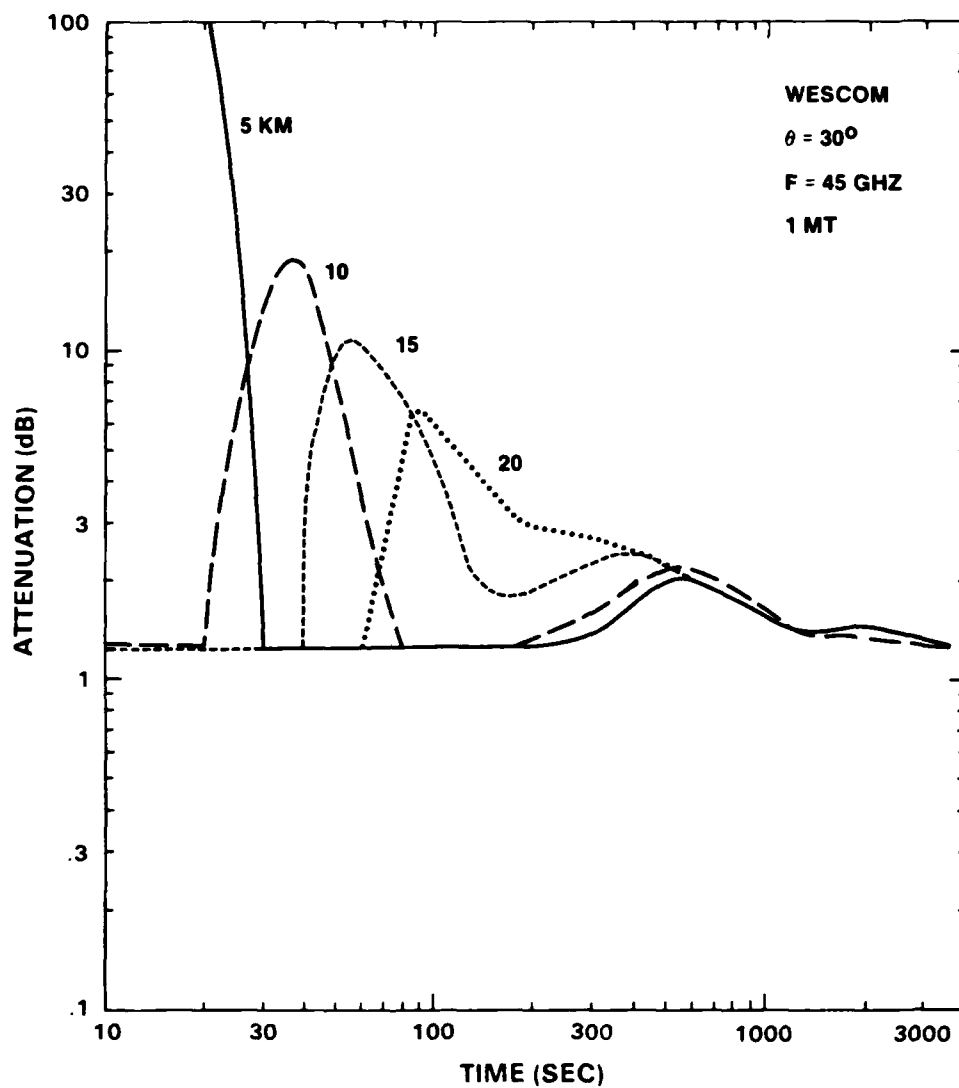


Fig. 12 Attenuation from 1 MT burst as a function of distance from burst.

## DISCUSSION

I. Anderson (U.K.): Since opportunities for propagation measurements through atmospheric nuclear explosions are limited, how do you substantiate the assumptions used in your theoretical model?

E. E. Altshuler (U.S.): Measurements made with conventional explosives have been extrapolated to nuclear levels. There is however a great deal of uncertainty in the nuclear dust model. Hopefully we shall never have to verify this model.

W.G. Burrows (U.K.): While you have considered the attenuation effects of dust from a nuclear explosion in your paper, have you also considered the distortion effects (and therefore attenuation) that the central "hot column" must have on the transmitted beam? There must be a very severe change of refractive index in the region of the hot column due to the change in the gas density. For example, the "hot gas" effluent from an aircraft jet engine will completely destroy a narrow beam at mm wavelengths.

E. E. Altshuler (U.S.): The distortion effects were considered. However, the attenuation effects produced by the fireball are so severe that distortion effects are believed to be of minor importance.

M.P.M. Hall (U.K.): In addition to military interest in your subject, there is civil interest in the effects of sand and dust storms. Figure 3 in your paper shows specific attenuation in dB/km for particles up to 100 mm radius and for an atmospheric particle density  $M$  of 100 gm/m<sup>3</sup>. When the radius of particles is below 0.3 mm in natural sand and dust storms, your Figure 3 indicates that specific attenuation becomes independent of maximum particle size and scales directly with  $M$ . Could you please comment on likely values of  $M$  in these storms?

E. E. Altshuler (U.S.): Although there is only limited data on the particle size distribution of naturally occurring dust, indications are that the maximum particle sizes would be less than a few mm. Thus the Rayleigh approximation is valid and dust attenuation is directly proportional to the mass density of dust. Attenuations for other mass densities can be estimated from Figure 3.



MEASUREMENTS OF ATMOSPHERIC EFFECTS ON SATELLITE  
LINKS AT VERY LOW ELEVATION ANGLE

by

Odd Gutteberg

Norwegian Telecommunications Administration  
Research Establishment  
2007 Kjeller  
Norway

SUMMARY

This paper describes experiments and results obtained from propagation measurements with the Orbital Test Satellite (OTS) at the Arctic islands of Spitzbergen (78°N). The elevation angle to the satellite was 3.2° and the frequency 11.8 GHz.

The experiments carried out included measurements of atmospheric scintillations, cross-polarisation discrimination and space diversity improvements. The measurements showed that the distributions of the received satellite beacon amplitude can be approximated by Rice-distributions. Large diversity gain was obtained by using horizontal spacing of 1 km. A wideband (TV) transmission experiment was also performed with good result.

1 INTRODUCTION

One of the prime parameters in geostationary satellite system design is the margin in signal level needed to take account of signal attenuation by the atmosphere. At present, attention is focussed on the knowledge of climatic variations and the influence of elevation angle on signal attenuation and crosspolarisation at frequencies above 10 GHz [CCIR, 1982].

A considerable amount of data has been collected on attenuation and crosspolarisation statistics, measured at mid-latitudes. However, relatively little is known on the characteristics of low-elevation paths to high-latitude stations, such as statistical properties of the fading, seasonal variations, crosspolarisation degradation and possible space diversity improvements.

To gain knowledge of these characteristics, propagation experiments at 11 GHz have been performed at Isfjord Radio, Spitzbergen (78°N, 13.6°E), figure 1, using the Orbital Test Satellite (OTS).

The different experiments were conducted during the period from April 1979 to August 1982. Some of the results have been presented earlier [Gutteberg, 1981].

2 DESCRIPTION OF EXPERIMENTS

The OTS-satellite is positioned at 5°E (until 14 April 1982 at 10°E), which means that the satellite is almost seen at the maximum elevation angle from Isfjord Radio. The geometric elevation angle is 3.2°, with an average ray bending of 0.2°. Assuming a tropospheric height of 8 km, the ray propagates through more than 120 km of the troposphere. One should therefore expect the received signal to be influenced by scattering and reflections due to turbulent air masses. At this very low elevation angle, temperature inversions could also cause duct transmissions.

The first experimental earth station was put into operation in April 1979, receiving both the co- and crosspolar components of the 11.8 GHz circularly polarised satellite beacon. The station was equipped with a 3 meter Cassegrain antenna and phase-locked receivers. The station characteristics are summarized in table 1 (station A).

During the spring 1982 two additional small earth stations for site diversity measurements were installed. The two equal small OTS terminals were receiving the linear polarised telemetry beacon at 11.6 GHz. The stations were equipped with 1 meter Cassegrain antennas and phase locked receivers. Other station characteristics are given in table 1 (station B).

Low angle space diversity measurements performed in Arctic Canada at 6 GHz [Strickland, 1978, 1980] showed poor diversity gain with horizontal spacing up to 500 meters. In our experiment it was therefore decided to use a spacing of more than 1 km.

For a further investigation of the scintillation phenomena, an acoustic sounder (SODAR) were used during the diversity experiment at Spitzbergen summer 1982. The SODAR was placed almost under the beam, 7 km away. Thus the radio and the acoustic beams intersected at an approximate height of 450 meter.

The beacon measurements at Spitzbergen in 1979 and 1980 showed large scintillations of the received signal. However, there existed little knowledge of the possible coherent bandwidth that could be received at such a low elevation angle. Therefore a wide band experiment was performed during July 1982. A frequency-modulated TV-signal with 27 MHz bandwidth was transmitted via OTS and received at Isfjord Radio. The receive earth station used in this experiment was a modified version of station A, table 1.

Table 1: Stations characteristics

Location	Isfjord Radio, Spitzbergen			
Coordinates	13,64°E/78,06°N			
Elevation angle (OTS, 10°E)	3,2°			
Azimuth angle (OTS, 10°E)	183,8°			
Station type:				
Station parameters	A	B	Units	
Beacon frequency	11,786	11,575	GHz	
Polarisation	Circular	Linear		
Antenna system				
Antenna type	Cassegrain	Cassegrain		
Diameter	3	1	meter	
Gain	49,5	39,6	dB	
Beamwidth	0,6	2,0	deg	
Crosspolarisation isolation	>35	-	dB	
Deicing power	8	none	kW	
Receiving system	Copol	Xpol		
Clear sky signal level at receiver input	~-104	~-139	~-123	dBm
G/T	20,5	24,7	11,6	dB
Noise temperature	800	300	630	°K
Level detector type	PLL	PLL	PLL	
Locking range	±200	±200	±40	kHz
Dynamic range	~20	~25	~15	dB
Post detection bandwidth	10	1	1	Hz
Data acquisition system				
Sampling rate	10	1	2	Hz
Tape recorder	Tandberg TDC-3000	Tandberg TDC-3000		
Strip chart recorder	Gould 816	hp 7130A		

### 3 EXPERIMENTAL RESULTS

#### 3.1 Atmospherique scintillations

Due to variations of the temperature and humidity within small volumes of the atmosphere, the refractive index profile will, at certain heights, depart from its normal exponential decay. This may cause bending, scattering and reflections of the ray. At very low elevation angle one should therefore expect the received signal to be heavily influenced by turbulent air masses.

Figure 2 shows an example of the recorded co-and crosspolar signals at Isfjord Radio. This is a typical plot of the signal variations (scintillations) during the Arctic summer months (July/August) with peak-to-peak variations around 5 dB. A compressed time plot of the received signal for an 87 hours period, is shown in figure 3.

In figure 4 and 5 are shown the cumulative amplitude distributions of the scintillations. As seen, there are large annual variations. During the Arctic winter (October-May), maximum fadings are only about 5 dB. This is also expected since the atmosphere is quite stable during the Arctic winter. However, in summer, deep fadings up to 20 dB are experienced. This may be due to high refraction index gradients.

The distribution for July/August 1979 is well above the distributions for the summer period 1980, probably due to the exceptional high mean temperature (7.6°C) during July 1979. The 30 year July average is 4.9°C.

It would have been of great help for the planning of earth stations in the Arctic, if one could find a correlation between the fading level and a simple meteorological parameter, e.g. the ground temperature.

In figure 6 is plotted the fading level at 99,99% availability versus the mean temperature for each month. It seems to exist a strong dependence between the scintillations, at a certain reliability level, and the monthly mean ground temperature (or  $N_0$ ). To a certain extent, we are therefore able to predict the fading level, knowing the mean ground temperature.

The received signal will consist of a direct one plus a scattered signal due to turbulence activity. If we assume that the scattered field consists of several components with random amplitude and phase, then the resulting signal distribution could be described by a Rice-distribution, i.e. a constant vector plus a Rayleigh distributed vector.

Rice-distributions with different values of  $K$ , where  $K$  is the ratio of power in the random component relative to the steady component, have been drawn in figure 7 together with the monthly and "worst day" distributions. It is seen that the "worst day" distributions fit quite well a Rice-distribution with  $K \approx 10$  dB. The monthly distributions, which is a sum of Rice-distributions with varying standard deviations, will generally not be a Rice-distribution. This is especially the case for large values of  $K$ , i.e. the summer months. If the scattered components, however, is small relative to the direct component, the distribution will be similar to a Normal-distribution. Therefore the distributions for the winter months will closely follow Rice-distributions with small values of  $K$ . This supports the assumption that the received signal consists of one direct component and several scattered components, and that the fadings are not due to beam bending effects.

Looking at the corresponding recordings from the OTS-receivers and the SODAR, one can see that the large peak-to-peak values of scintillations are clearly associated with the existence of temperature inversions at about 200 meters above sea level. During periods when no temperature inversions were detected, the scintillations were much smaller. Figure 8 shows an example of recordings from the SODAR, and the corresponding recording of the beacon signal. We can see two temperature layers above each other. When they disappear at approximately 1330 GMT, the signal variations drops from ca 6 dB peak-to-peak, down to less than 1 dB peak-to-peak. Another example is shown in figure 3, where a temperature inversion layer at 200 meters height existed from 0720-1220 on 27th July 82.

### 3.2 Crosspolarisation due to sleet and snow in the path

Crosspolarisation measurements were only systematically done during the summer months 1979 at Spitzbergen.

Figure 1 shows a recording of the co- and crosspolar signals on 25 July 1979 at Isfjord Radio. As seen, the scintillations of co- and crosspolar levels are equal. This is generally the case, and there is no degradation of the XPD. However, during overcast and sleet/snow in the path, the XPD becomes worse. In figure 9 is shown the cumulative distributions of the crosspolarisation discrimination. Also for the XPD's the summer months are the worst months.

The resulting distributions of attenuation and XPD for the period May-August 1979 have been calculated. Using these distributions, the XPD value corresponding to the co-polar value for the same probability level, has been plotted in figure 10. It is seen that there seems to exist a statistical relationship between the attenuation (ATT) and crosspolarisation discrimination (XPD) due to sleet/snow in the path, given by the equi-probability equation:

$$\text{XPD (dB)} = 27 - 8 \lg \text{ATT (dB)}$$

### 3.3 Space diversity

For investigation of the space diversity improvement, two "mini"-OTS terminals were installed at Isfjord Radio, summer 1982, receiving the linear polarised telemetry beacon from OTS. One terminal was located at the radio-station (OTS-I) and the other (OTS-II) with a horizontal separation of 1150 meters, see figure 11. The vertical separation was approximately zero. The measuring period was from 14 July-2 August 1982.

The acoustic sounder (SODAR) was put up under the beam of the OTS-II terminal, thus the acoustic radar and the earth station were "seeing" a common volume of the atmosphere.

Examples of the received satellite signals from the two stations are shown in figures 3, 8 and 12. In figure 12, where the paper speed is 4,5 cm/min, we can clearly see that the short time variations of the signals are uncorrelated. The signals were also recorded digitally on magnetic tapes, and cumulative distributions of the signal levels, both for each station and for the site diversity system were calculated. The 87-hour period shown in figure 3, is representative for the whole measuring period. The cumulative distributions for this period is shown in figure 13.

The single site distributions (OTS-I and II) are almost identical, as the scintillations are random by nature, whereas a substantial site diversity improvement is achieved. For example at a 3 dB fading level the single site reliability is 99%, and the site diversity reliability is 99,92%.

The distributions for the total measuring period (17 July-2 August 1982) is shown, together with the other distributions, in figure 5. Since the distributions for OTS-I and II are almost identical, only one single site distribution is plotted. Again it is seen that at a 3,2 dB fading level the availability improves from 99% to 99,9%, due to site diversity.

### 3.4 Wide band transmission

As previously mentioned, little knowledge exists of the characteristics of selective fading at very low elevation angle. Comprehensive measurements of selective fading could be done by using multi- or swept frequency techniques. However, due to the limited time for planning and performing such experiments, it was decided to perform an direct experiment, involving the reception of a wide-band signal (FM-modulated TV-signal) at Isfjord Radio. As previously shown, the most severe fading is confined to the Arctic summer months. Accordingly this experiment was conducted during July 1982.

The transmit station was Goonhilly Downs in England. A frequency modulated TV-signal (PAL) saturated one of the wide band transponder of OTS to give a receive frequency of 11.6 GHz. The frequency deviation used was 13.5 MHz/V and receive filter bandwidth was 27 MHz. The link budget is given in table 2.

Due to the signal scintillations, the received C/N-ratio had large fluctuations. At 20 July 1982 the following values were measured between 2110-2225 GMT:

$$\frac{C}{N}_{\max} = 12,3 \text{ dB}$$

$$\frac{C}{N}_{\min} = 8,7 \text{ dB}$$

The TV-transmissions took place from 13-23 July, approximately 3 hours per day, containing colour bars, pulse and bar and videofilm sequences. Two hours were recorded on video-tape. The picture quality was judged to be fair (Q=3), and from observations of the colour bar spectrum, there seemed to be no severe selective fading during the experimental period.

## 4 CONCLUSIONS

In polar areas with low elevation angle (<5°) the predominant type of fading is scintillation. The fading seems to be caused by a combinations of scattering and reflections from turbulent air masses. Deep fades are, however, associated with temperature inversions in the atmosphere. The monthly distributions of the scintillations can be approximated by Rice-distributions with average values of the power ratio of the random component to the steady component of -20 dB, -13 dB and -10 dB for the best month, worst month and worst day, respectively.

At very low elevation angle, large improvement by using space diversity can be obtained. With a horizontal separation of the two stations of approximately 1 km, the availability is increased from 99% to 99,9% at a 3 dB fading level.

In areas with little rain, as the polar areas, cross polarisation due to sleet and snow on the path may be the most dominant effect. In the measurements at Spitzbergen, a statistical relationship (equi-probability equation) between attenuation (ATT) and crosspolarisation (XPD) were found:

$$XPD(\text{dB}) = 27 - 8 \lg \text{ATT}(\text{dB})$$

Selective fading over 27 MHz bandwidth was not observed at Spitzbergen, and reception of frequency modulated satellite TV-signals down to elevation angles of at least 3° is possible with good quality.

Table 2: Link budget, OTS-Spitzbergen

Transmit station: Goonhilly Downs, England

Receive station: Isfjord Radio, Spitzbergen

Frequencies up/down: 14262,5/11600.0 MHz

Satellite: OTS, 5°E

Transponder: Channel 4 bar (saturated), gain step 7

Modulation: FM, frequency deviation 13,5 MHz/V, energy dispersal 1,2 MHz peak-peak

EIRP (sat)	47,5	dBW	(1)
Aspect angle loss	6,8	dB	(2)
Down path loss	206,1	dB	
Atmospheric absorption	1,0	dB	(3)
Earth station G/T	24,0	dB	(4)
Pointing loss	0,1	dB	
Up-link noise	0,2	dB	
<hr/>			
Total link C/T	-142,7	dBW/K	
Receiver BW (27 MHz)	74,3	dBHz	
C/N at receiver	11,6	dB	

## Notes:

- (1) Beam centre EIRP; OTS report on in-orbit measurements vol 1; p 255 and 219
- (2) With OTS at 5°E, re-orientated in pitch bias by 0.4°, ref Interim EUTELSAT, private correspondence
- (3) Calculated using equivalent height of oxygen 6 km and water vapour 1,5 km, ref CCIR report 719, Geneva 1982
- (4) Measured value, assuming an antenna noise temperature (clear sky) of 100°K and an antenna gain of 49 dB

## 5 ACKNOWLEDGEMENTS

The author expresses his sincere appreciation to M Osmundsen for valuable assistance with all parts of the experimental work; to the staffs at Isfjord Radio and Goonhilly Downs for excellent co-operation, and to the National Meteorological Institute for supplying the meteorological data. Thanks also to T Tjelta, N Atland and T Heggelund for assistance with analyzing the site diversity data.

Part of the work described was done under contract with European Space Agency, ESTEC Contract no 5032/82 NL/GM(SC), technical management by G Brussaard.

## 6 REFERENCES

- |                      |   |
|----------------------|---|
| CCIR, 1982           | Vol V, Propagation in non-ionized media, Report 564-2   |
| Gutteberg O, 1981    | "Measurements of tropospheric fading and crosspolarisation in the Arctic using Orbital Test Satellite"<br>IEE Conf Publ No 195 (Antennas and Propagation) Part 2, 71-75, 1981 |
| Strickland J I, 1978 | "Site-diversity measurements of low-angle fading", 19th General Assembly of URSI, Helsinki, Finland   |
| Strickland J I, 1980 | "Site-diversity measurements of low-angle fading and comparison with a theoretical model", URSI Commission F International Symposium, Lennoxville, Quebec                     |

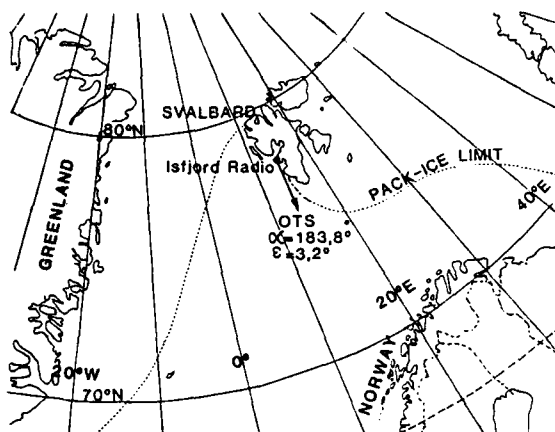


Figure 1 Location of the experimental site, Isfjord Radio, 78°N, 13.6°E. Elevation and azimuth angles are given for OTS positioned at 10°E.

# OTS, SVALBARD 25 JULY 1979

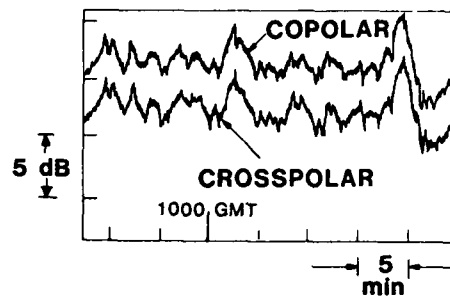


Figure 2 Plots of co- and crosspolar signals at Isfjord Radio, 25 July 1979. XPD  $\approx$  38 DB.

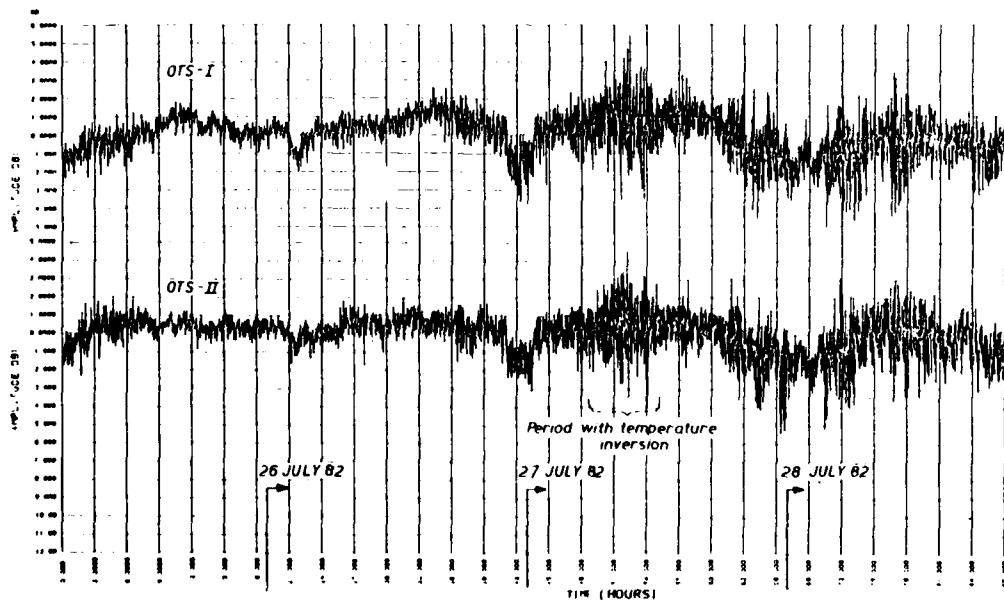


Figure 3 Time-plot for OTS-I and OTS-II  
Start: 25 July 82, 0500 GMT, Stop: 28 July 82, 2045 GMT,  
Recording time: 5265 min, Sampling: 2 samples/sec, Smoothing: 5 sec,  
Each: 100 points.

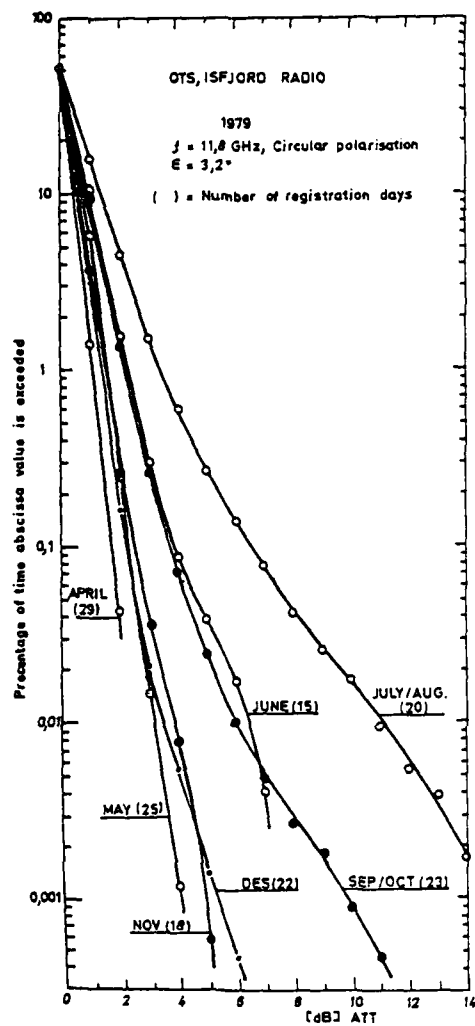


Figure 4 Cumulative distributions of scintillations (1979).

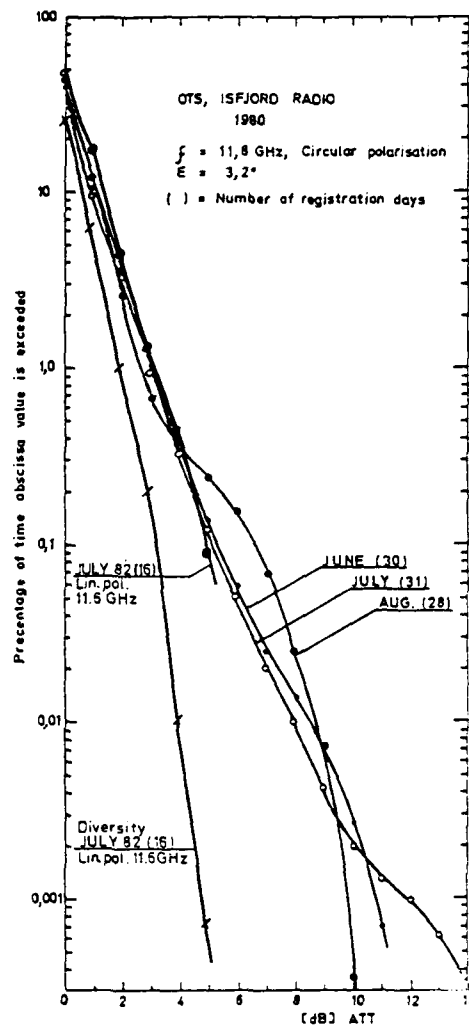


Figure 5 Cumulative distributions of scintillations (1980 and 82) and diversity (1982).

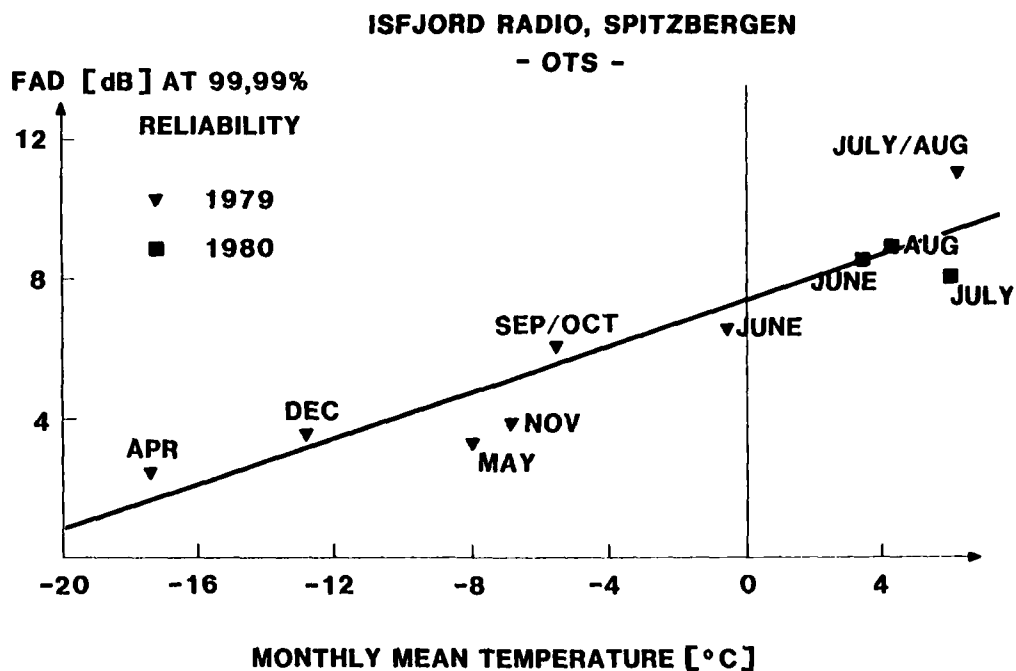


Figure 6 The fading level at 99,99% of time versus monthly mean ground temperature.

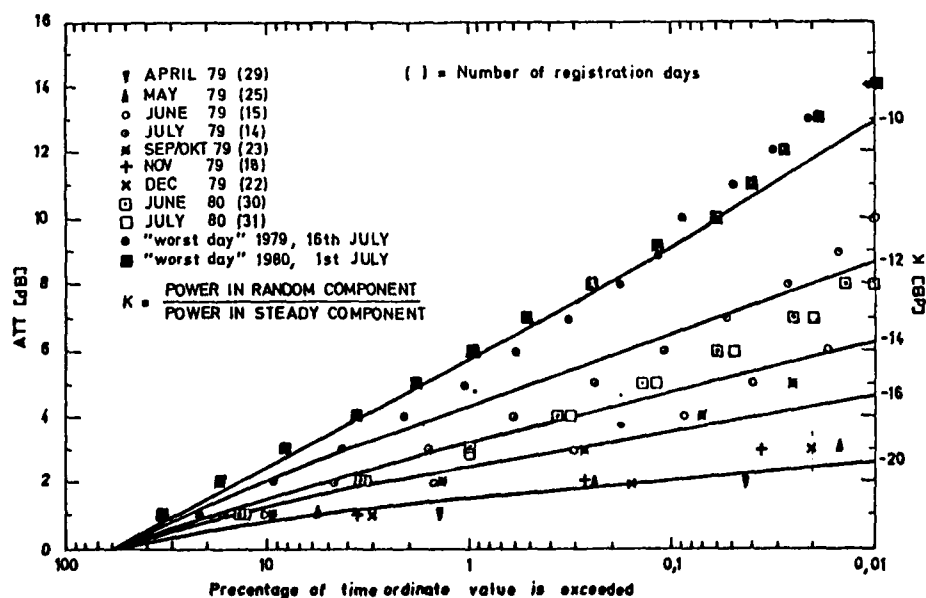


Figure 7 Rice-distributions for different values of K. Measured distributions are plotted.

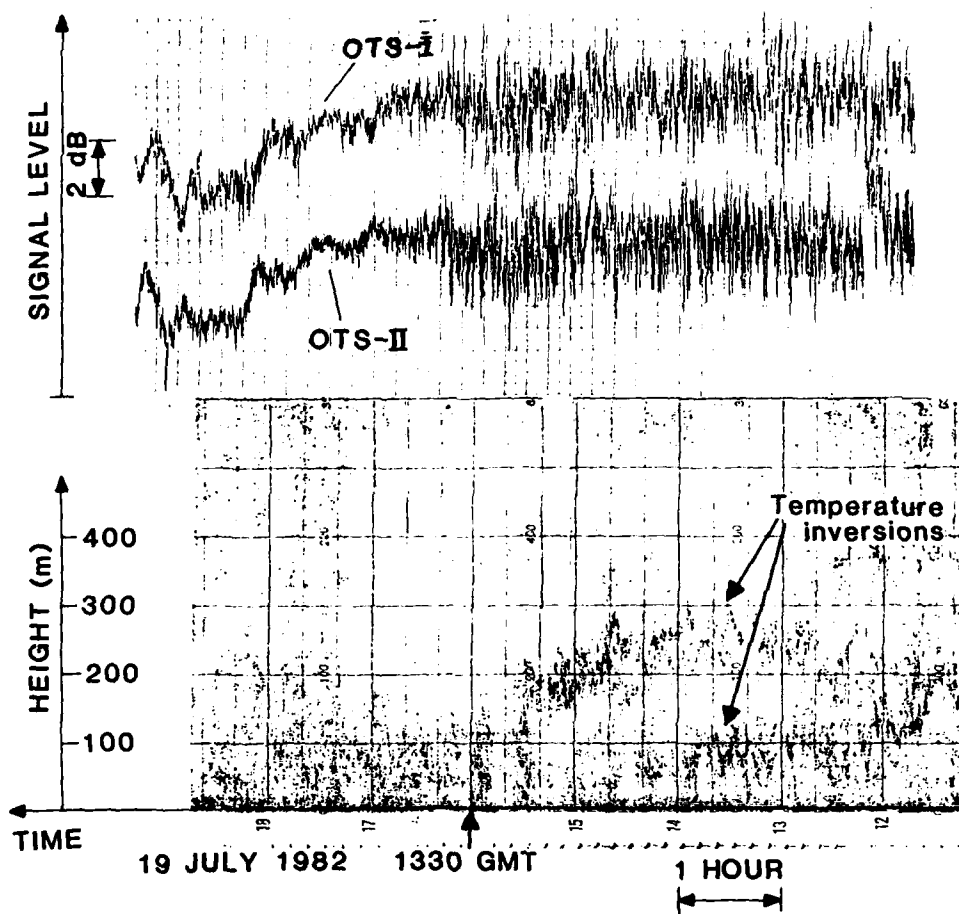


Figure 8 Recordings of the signal levels from OTS-I and OTS-II and corresponding SODAR registration. Isfjord Radio, 19 July 1982.

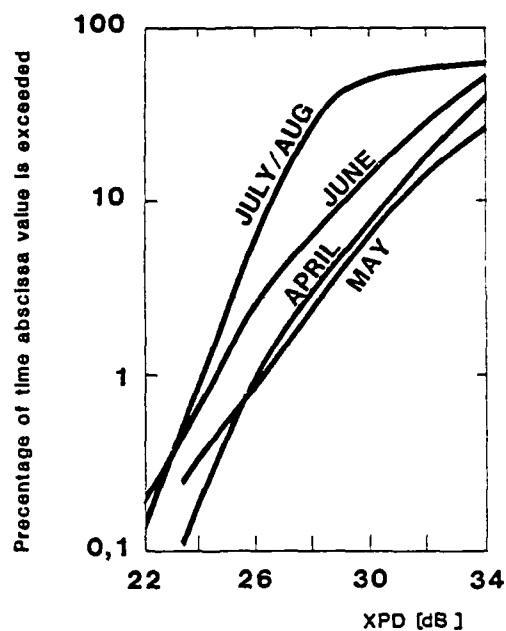


Figure 9 Cumulative distributions of cross-polarisation discrimination, 1979.

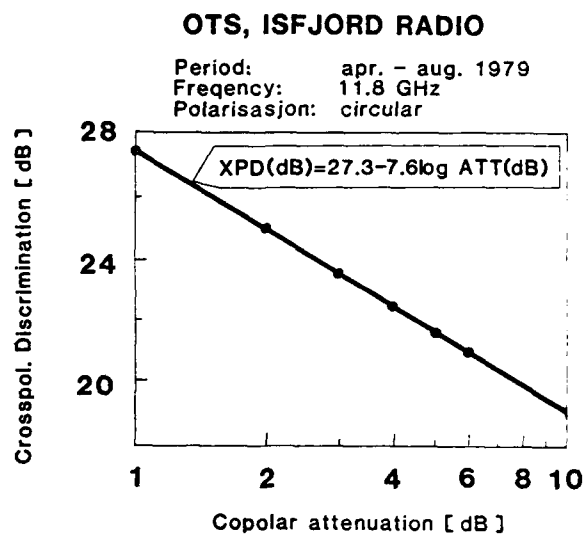


Figure 10 Statistical relationship between attenuation and crosspolar discrimination.

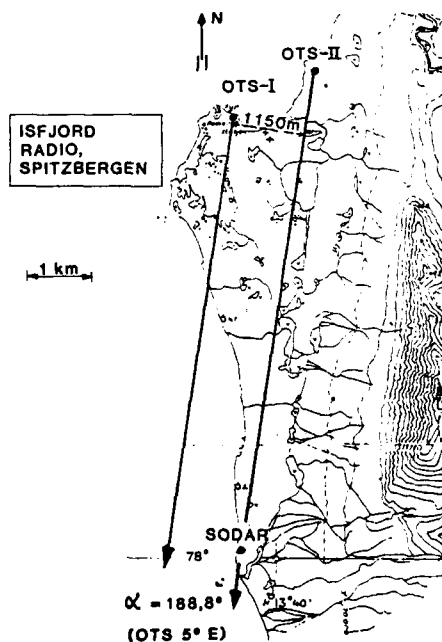


Figure 11 Geometry of the space diversity experiment at Isfjord Radio, 1982 (OTS  $5^\circ$  E). Both stations heights above sea level: 7 meters.

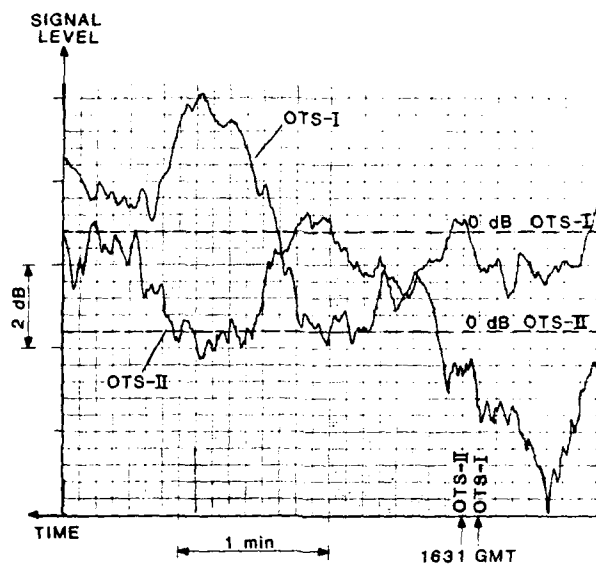


Figure 12 Registration of the linear polarised beacon from OTS. Space diversity experiment, Isfjord Radio 14 July 1982.

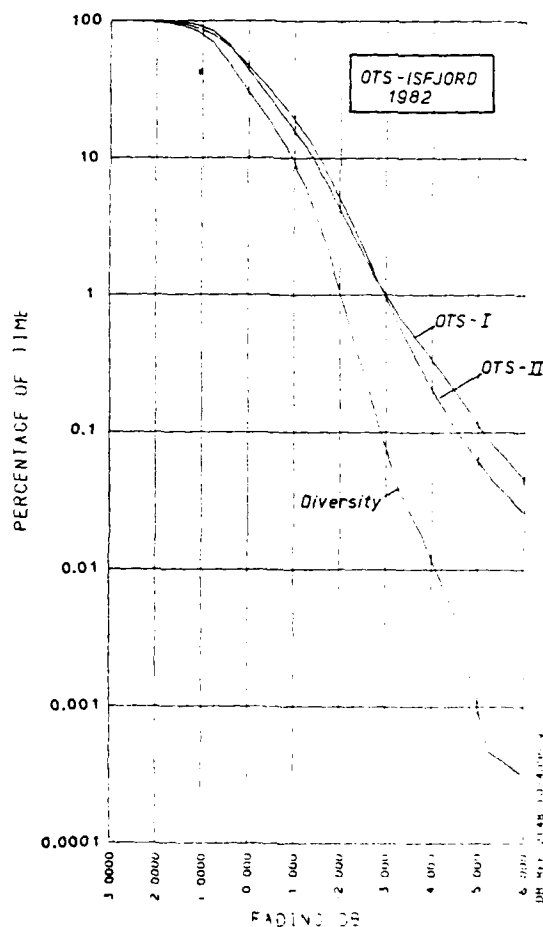


Figure 13 Cumulative distributions of scintillations for single sites (OTS-I and OTS-II) and the diversity system.

Period: 25-28 July 1982 (5265 min). Time-plot for the same period is shown in Figure 3.

## DISCUSSION

M.P.M. Hail (U.K.): 1) Your paper gives information which is all too scarce on low elevation angle paths. You include diversity spacing of 1.1 km. Could your observation of the time fading records and of the propagation phenomena allow you to speculate on whether diversity improvement would be similar for slightly lower spacing (e.g., a hundred meters or so), and how rapidly diversity improvement would increase with additional distance?

2) As well as the conventional 'worst month' data, you mentioned the 'worst day' and 'best month' data. Are you able to comment on the user requirement for such data?

O. Gutteberg (Norway): 1) The signal level variations are most probably due to scattering from the turbulent part of the atmosphere. I would therefore expect the diversity gain to be related to the size of the turbulent atmospheric structure. Since the size of turbulent air masses can be much smaller than 1.0 km, I would say that the diversity improvement would be similar for horizontal spacing slightly lower than 1.0 km. However, I would like to mention that low angle space diversity measurements performed in Arctic Canada showed poor diversity gain with horizontal spacing of 490 meters. The same diversity improvement was also obtained with vertical spacing of 20 meters.

2) I have given the 'worst month,' the 'worst day,' and the 'best month' distributions to indicate the range of fading levels (or the K-value) as shown in Figure 7. I have no comment for the user requirement for such data.

L. Boithias (France): Sur les abscisses des figures 4 et 5, où se situe le niveau d'espace libre?

O. Gutteberg (Norway): As we do not know neither the exact EIRP from the OTS towards Spitzbergen nor the variations in EIRP, is difficult to do an accurate calculation of the free space level. The received signal varies all of the time, c.f., Figures 2, 3, and 8. Accordingly, as a reference level (0 dB), we are using the average value of the signal level for the last recorded 18 hours. This corresponds to approximately the median value as seen from Figures 4, 5, and 13, and this is again close to the approximated value of the free space level.

E. Vilar (U.K.): 1) Have you carried out a spectral analysis?

2) This is only a comment. I suggest that your records show scintillation phenomena with a good symmetrical pattern superimposed on a variation of the mean value. The knowledge of the carrier frequency of the spectrum (likely to be in the range from 0.01 to 0.10 Hz) gives an indication of the natural periodicity of the process (i.e., the period is about 100 seconds), and that several times this value, such as 10 times (about 20 minutes) would give you a reliable mean value. This mean value varies according to gaseous absorption, which is significant at X-band for such long "effective" earth-space paths.

O. Gutteberg (Norway): 1) No.

T.J. Moulisley (U.K.): This is only a comment. With regard to your scintillation measurements there arises the problem of removing fluctuations in amplitude due to other causes (beacon level fluctuations, receiver system effects, etc). Observations of OTS at Portsmouth, United Kingdom, and at other sites have shown a diurnal pattern of level variations of the order of  $\pm 1$  dB with significant changes occurring over fairly short periods (such as one hour). This would suggest that the time constant of any high pass filtering should be shorter than one hour. The diurnal variations in mean level can be seen in Figure 3 of your paper.

O. Gutteberg (Norway): The diurnal variation of the circularly polarized beacon (B0) from OTS is of the order of 1.0 dB. Figure 3 shows, however, recordings of the linearly polarized telemetry beacon (TM) from OTS. The diurnal variation of this beacon is much less, approximately 0.2 dB.

The variations in mean level shown in Figure 3 is probably not due to diurnal effects in the satellite. This can also be seen from recordings longer than the 87 hour period shown in Figure 3.

S. Rotheram (U.K.): The paper refers to scintillation arising from tropospheric structures. Is ionospheric scintillation associated with auroral events a significant effect at these high latitudes?

O. Gutteberg (Norway): We have not observed any scintillations associated with auroral events.

## BLUE-GREEN PROPAGATION THROUGH CLOUDS

by

G.C.Mooradian  
Naval Ocean Systems Center  
San Diego, Ca 92152

### ABSTRACT

Optical communications in the atmosphere, space and underwater is being investigated for a variety of applications. The performance of a space to earth/underwater link through the adverse atmospheric propagation channel is of paramount importance. The presence of clouds along the propagation path scatter the blue-green radiation (selected for minimum cloud and sea-water absorption) and cause spatial, angular, and temporal spreading of the beam. This condition decreases the peak power at the receiver by both multipath time delays, and spatial spreading and also increases the apparent source size. Performance may be seriously degraded. This effect can be somewhat compensated for by adapting the receiver: for example, increasing the field-of-view of the receiver to accept the scattered radiation. Measurements of the temporal, spatial, and angular spreading of a blue-green pulse through clouds and fogs have been made as a function of optical thickness and receiver field-of-view. The fog data was collected between two ground sites at Point Loma, San Diego, separated by 1 km. The cloud data was obtained from a receiver on the ground (Kauai, Hawaii) looking upward to a large (6 km) spot on the cloud from a laser beam on an aircraft at 40,000 feet. Comparison of experiments with theory are made.

## THE EFFECTS OF METEOROLOGY ON MARINE AEROSOL AND OPTICAL AND IR PROPAGATION

Stuart G. Gathman  
Code 4117  
Naval Research Laboratory  
Washington, DC 20375

AD-P003 888

Optical and IR propagation can be strongly influenced by aerosol in the marine boundary layer. The effects are wavelength dependent and there is no "best" wavelength to use in all cases. There are sources and sinks of this aerosol in operation over the ocean which can be predicted from a full knowledge of the meteorological situation. Once airborne the spatial distribution of the aerosol is a function of the mixing processes, the micrometeorology of the marine boundary layer as well as the history of these processes to which the aerosol is exposed.

Much of the marine aerosol is hygroscopic which means that the size of individual particles depends on the ambient relative humidity to which they are exposed. Since the relative humidity in the marine boundary layer is high, the aerosol has the form of small spheres or droplets. The index of refraction of these droplets is also a function of the relative humidity being close to that of water for relative humidities close to 100 percent. The marine aerosol size distribution, which describes the concentration of droplets for each size class, can be modeled from standard meteorological parameters. Once this function is known, the resultant extinction and absorption can be calculated from the size distribution for wavelengths of from 0.2 to 40.0 micrometers using Mie theory.

In addition to the assessment of current optical and IR properties from the current meteorological measurements, the model allows the stored historical marine data bases to be used to produce climatologies of the optical and IR properties over the oceans because any standard set of meteorological measurements can be utilized for this purpose. In addition the art of meteorological forecasting can be employed to forecast the necessary model inputs from which desired future optical, and IR properties can be determined.

#### Introduction:

The reception of electromagnetic energy through the atmosphere is a basic form of human communication. I am speaking of course to both the reception of highly developed optical information with our eyes as well as the less developed sense of heat radiation from a hot object we can feel with our skins.

From our earliest memories, most of us can remember the obscurity of a distant object such as a mountain peak during hazy days or nearby objects during a misty fog event. The subject I will address today is an elaboration of these natural processes. As we have expanded and developed our sensors and transmitters in the optical and infrared wavelengths, we have become aware of the physical hinderances to good communication which our natural environment produces.

The coupling of science of meteorology to the understanding of optical and infrared communication has been the object of recent research. An important parameter in describing the degradation in the performance of point-to-point communication in the visible/IR frequency domain is the concept of the extinction coefficient. This is a parameter quantifying this process of removing energy from a beam by both scattering and absorption of the energy. Extinction is caused by both individual atmospheric molecules as well as large groups of molecules called aerosols.

Atmospheric air is a mixture of gases made up of both nonvarying and varying components. It is composed of dry air plus water in any of its three physical states and its airborne particulates. The optical/IR properties of the nonvarying gaseous component of atmospheric air once measured, can be easily accounted for. Problems come when a major portion of the extinction is done by the varying atmospheric constituents, both molecular and particulate. It is at this point that meteorological processes must be invoked in order to predict the extinction from the varying portion of the atmosphere.

The relationship of the processes of molecular extinction with the in-situ meteorological situation is beyond the scope of this presentation. Many have studied these processes and indeed these extinctions can be predicted with computer programs such as LOWTRAN and HITRAN. In the interest of the time available it is necessary to limit the scope of this discussion to the extinctions produced by atmospheric aerosol and in particular to that subclass of the aerosol known as the natural marine aerosol. Under certain conditions this is the dominant cause of extinction and it is important for the effectiveness of our fleets to know when and why such conditions will be present in the marine boundary layer.

An exact theory was developed in 1908 by Mie which relates the scattering and absorption of electromagnetic energy from a sphere of known index of refraction. Therefore, if we know the concentration of each size class of aerosol and their index of refraction we also can know about the passage of visible/IR energy through an atmosphere containing this aerosol. One can thus describe the physics of the production and lifetimes as well as characteristics of the whole population of this aerosol in terms of

Copy available to DTIC does not  
permit fully legible reproduction

Copy available to DTIC does not  
permit fully legible reproduction

the meteorological processes taking place and then calculate the optical/IR properties of the aerosol from Mie's theory.

#### Sources and Sinks of Aerosol.

What are aerosols, where do they come from, how do we measure them, what happens to them, are all questions which are of interest to us. A general definition of an aerosol found in a typical scientific glossary is that it is a gaseous suspension of ultrasmall particles in either the liquid or solid state. Smoke, dust, or sea spray are all extreme forms of the largest aerosol particles. Most of the atmospheric aerosol particles are not even visible under optical microscopes and special techniques must be used to measure and detect them.

When we determine the optical/IR effects produced by the aerosol, the size distribution of the aerosol population must be known. This is a function describing for each size the number of particles within a certain band of sizes divided by the width of the band. Given this function, the index of refraction of the material making up the aerosol and the assumption that these particles are spherical in shape, the optical/IR-characteristics of the aerosol population can be calculated.

There are a number of natural sources of aerosol. However in urban areas, the total concentration is at least an order of magnitude greater than in remote rural locations which in turn is an order of magnitude greater than is usually found over the ocean. Table I illustrates the origin and chemical composition in a general way of the broad classes of atmospheric aerosol sources. The size distribution resulting from each of these production processes is not the same. It is obvious that at different sites on the earth's surface, certain processes will be more important than others. In the marine environment, process number four is the important aerosol source and is the one which will be concentrated on in this paper.

Whenever there are sources of quantities, they must be balanced by sinks of the quantities in order to achieve a balance in time. The sinks of atmospheric aerosol are size dependent. Aerosol of certain size class are removed rapidly whereas in other size classes, the removal process is slower. This of course is reflected in the shape of aerosol size distribution function. Table II lists the important aerosol elimination processes.

Many techniques have been developed to determine the size distribution of the atmospheric aerosol. A listing of these instruments and the range of applicability is shown in Table III. Unfortunately, there is no technique yet developed which is broad enough in range to measure the entire aerosol size spectrum. These functions then are usually determined by patching together several sets of instruments in order to obtain an overall view of the whole size distribution.

Other instruments have been developed which give related parameters of an aerosol cloud such as particle counters which measure the net concentration of aerosol particles and nephelometers which give the total amount of scattering produced by the aerosol population.

#### Marine Aerosol.

The marine environment and the aerosol it contains has certain properties which simplify the characterization of the aerosol population within the marine boundary layer, allowing us to relate certain features of the aerosol size distribution to causal meteorological processes producing these features. Given this causal relationship between the marine meteorology and the marine aerosol size distribution, it can be extended into a relationship between marine meteorology and the optical and IR-propagation parameters.

The marine atmosphere has certain advantages with respect to continental atmospheres because of its uniformity. The chemistry and geometry of the sea itself does not change appreciably from point to point about the globe. This uniformity allows a simplification in the construction of marine boundary layer models.

The only large scale source of atmospheric aerosol operating within the marine boundary layer is that associated with white water phenomena and its dispersion of liquid droplets into the atmosphere. Of course if an air mass has recently left a continental land area, the processes of aerosol elimination has not yet been in operation long enough to completely eliminate this component of the aerosol population. We would expect the aerosol composition in the marine layer to be somewhat "continental" in its characteristics for air masses which have recently come to sea and have not been long exposed to the processes which are modifying the aerosol population into a truly marine air mass.

#### Physics of the Aerosol.

One characteristic of all marine originated aerosol as well as some natural continental aerosol is that they are hygroscopic in nature. That is they tend to attract water molecules and to grow in size in a moist environment. Of particular interest to our optical/IR propagation studies is the aerosol size distribution and how this size distribution will be changed by the growth or shrinkage of individual aerosol droplets as the ambient relative humidity changes. Another property which changes in

hygroscopic aerosols as a function of the relative humidity is the index of refraction. A dry aerosol will have the index of refraction of the dry material whereas in high relative humidity environments the complex index of refraction will be close to that of water. The process of growth of an aerosol droplet with respect to the relative humidity is accomplished by the soluble portion of the solid dry aerosol material going into solution with the water that is attracted to it. The chemical composition of the aerosol droplet at some relative humidity other than 100% is a function both of the material of the dry aerosol nucleus and the amount of water in solution with the soluble parts of the nucleus.

Theories have been developed which will predict the relationship between the ambient relative humidity and the ratio of the volume of the aerosol droplet will have at the ambient relative humidity with respect to its volume in a perfectly dry environment. One of the latest, most complete theories describes this behavior by a single parameter,  $R_0$ , the activation parameter, based on the chemistry of the dry particle (Fitzgerald and Hoppel (1982)). Figure-1 is a plot of the particle size as a function of relative humidity for a number of representative  $R_0$  values. It will be noticed that there is only a slight change in the functional form for different sizes of a dry aerosol with the same  $R_0$ .

The aerosol found over the ocean is obviously not perfectly homogeneous in its chemical makeup. Those produced by white water processes reflect however the universal chemical composition of sea water, whereas the continental population will have a more varied composition. Nevertheless the concept of an "average" marine aerosol can be used to describe the hygroscopic behavior of these aerosol particles. The behavior of such an "average" aerosol is shown in the figure as curve " $R_0 = 1.3$ ". Although the continental aerosol in an air mass (as it leaves the shore line) is of heterogeneous origin and is usually well mixed throughout the boundary layer, it decreases in importance with respect to the marine originated aerosol with the passage of time. The marine aerosol can be considered to be mainly produced by white water processes at the sea surface.

Aerosol production at the marine surface is associated with nonzero wind speeds in the marine boundary layer. Marine aerosol are produced both by the direct disruption of wave crests and indirectly by various bubble bursting mechanisms at the surface. Monahan et al (1983) has distinguished three wave mechanisms which produce bubbles in the sea. They include trough bubbles, and bubbles introduced into the sea water by the spilling wave and the plunging wave. Each of these processes is activated at different wind speeds. Blanchard (1963) observed that small jet drops are ejected into the atmosphere after the bursting of bubbles produced in the sea by the spilling and plunging of waves. The airborne jet droplets can be ejected tens of centimeters into the marine atmosphere and remain airborne for extended periods of time. Many droplets of even smaller size are also produced by the disintegration of the bubble film. These film droplets are not mechanically ejected into the atmosphere but under appropriate mixing conditions, they too can be a source of the marine aerosol.

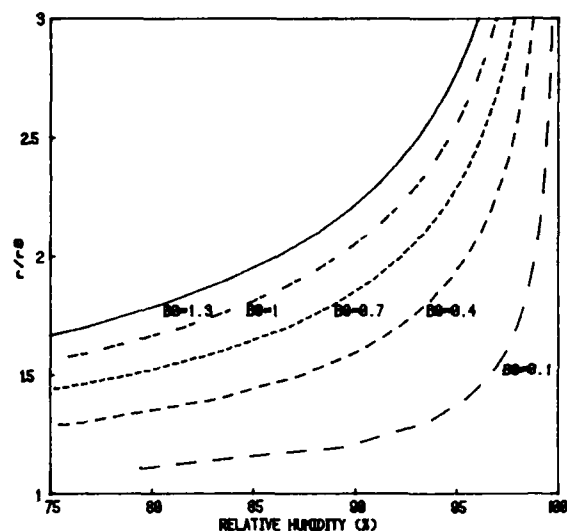
Two forms of sea water drops are put directly into the atmosphere by wave action. The chop-action of sea waves produce some large droplets even at low wind speeds. At high wind speeds, however, the spume drop becomes the dominant source of large aerosol.

Of importance to the modelers, is the flux of particles leaving the sea surface. Figure-2 shows the size spectra of this flux for various wind speeds according to an early sea surface aerosol generation model. This information coupled with the mixing qualities of the marine boundary layer allow us to construct a time dependent model which we can use to predict the evolution of the marine aerosol and its optical quantities. The relative humidity close to the sea water surface is 98% because of the salt. The droplets leaving the surface will of course reduce in size if they are mixed with drier air because they are hygroscopic and sensitive to the local relative humidity.

The relative humidity of the marine atmosphere at deck level is not usually 98%. Figure-3 shows a cumulative probability plot of relative humidity at 10 m altitude for the North Atlantic for both the summer and winter season. In comparing the data shown in this figure with the growth characteristics of marine particles Figure 1, it is seen that large change in the sizes of these droplets will take place during the mixing process. In addition, the relative humidity changes with respect to altitude differently for different meteorologic conditions therefore the relative humidity profile must be accounted for.

Relative humidity profile information can be either obtained by direct measurement or from models. Figure-4 shows the comparison of relative humidity model predictions obtained with an empirical model (Gathman, 1978b) from surface meteorological measurements with those obtained by direct measurement with a tethered balloon mounted instrument (Gathman, 1978a).

The description of the history of the concentration of any particular dry size class,  $N$ , in a volume of air moving over the ocean at a constant velocity can be described by "K" theory using the partial differential equation:



### AEROSOL FLUX SIZE DISTRIBUTION (and its response to wind speed)

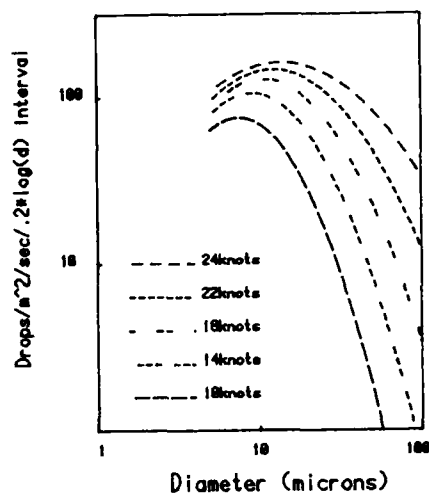


Fig. 1. Dependence of particle size on relative humidity.

Fig. 2. The aerosol flux size distribution plotted as a log normal for various wind speeds.

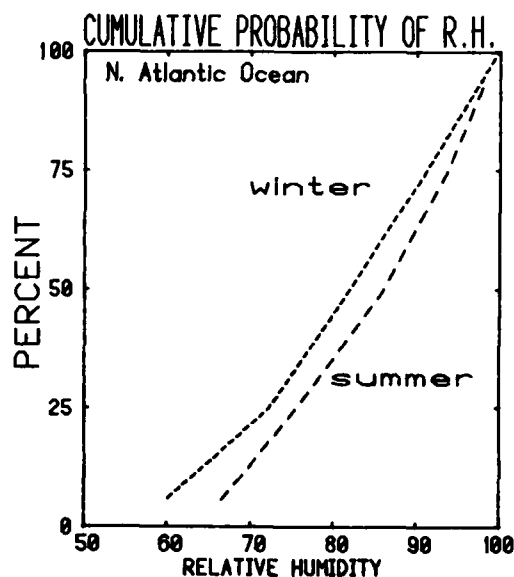


Fig. 3. The cumulative probability of relative humidity over the North Atlantic Ocean on a climatic scale for the summer and winter seasons.

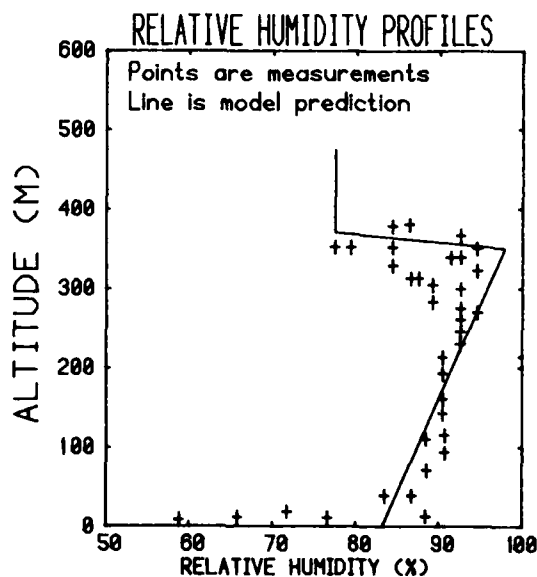


Fig. 4. Comparison of the model estimates of a relative humidity profile which predicted a dry upper air layer from surface measurements made at the time of flight and the kite-balloon measurements of relative humidity based on dry-bulb and wet-bulb temperatures (points) Pathman (1972).

$$\frac{dN_i}{dt} = \frac{\partial}{\partial z} K(z) \frac{\partial N_i}{\partial z} + V_i \frac{\partial N_i}{\partial z} \quad (1)$$

which describes the effects on the concentration,  $N_i$ , within the volume as it is acted on by eddy diffusion and gravitational fall. The generation rate at the sea surface is introduced into the problem by the lower boundary condition imposed during the solution of the equation. In this representation the mean micrometeorological state of the atmosphere is described by an altitude-dependent eddy diffusion coefficient represented by  $K(z)$ . The fall rate of the particles in class "i" is represented by  $V_i$  and will be a function of the ambient relative humidity as the size and weight of the droplets formed on the dry aerosol class i is a function of the relative humidity at whatever level in which it finds itself.

Gathman (1982) has constructed a time dependent aerosol profile model based on the numerical solution of equation (1). An example of the operation of this model can be seen for the hypothetical case where the wind speed, represented by a box car function, is suddenly increased for an hour and then returned to its initial level. The meteorological parameters for this case were set to be thermally stable and the relative humidity to be high throughout the boundary layer so as to simulate an encounter in a slightly subsaturated condition. The wind speed input was set to zero for the first hour, 15 m/s during the second hour, and again low for the remainder of the calculation. In this case of course, there is no input flux unless the wind speed is high. Likewise the eddy diffusion parameter is very low except for the mechanical mixing produced during the period of high wind speed. Four runs were made of this case for the sizes of 20, 10, 5, and 2.5 microns diameter with a relative humidity of 90%.

The results of the first 500 min of this run are plotted in Figure-5. These three dimensional plots show the surface defined by the altitude, concentration, and time of a certain dry sized aerosol computed by these runs. The vertical axis is altitude plotted linearly. The horizontal axis is the linear measure of aerosol concentration. The time axis goes back into the page at an angle. The altitude-time plane is a background concentration profile of  $N_i = 10^{-5}$  per cubic meter which is represented by the vertical lines describing constant  $N_i$  profiles every 10 min and the slanted lines depicting levels of constant altitude which show the variable grid levels used in the model. For comparison purposes, the scale of the concentration is not constant but is adjusted so that the maximum concentration distance of the whole surface is the same for each of the aerosol size classes. The absolute values of these concentrations vary by a considerable amount.

The interesting feature of these surfaces is the time responses of the atmosphere to each of the aerosol sizes. The largest aerosol size class mirrors the wind speed function and does not affect the atmosphere above 50m while the smallest size class appears to just stay in the atmosphere once introduced into it. It of course eventually falls out but at a much slower rate than the largest aerosol. This will be exhibited in a changing size distribution which will narrow and shift to smaller sizes as time goes on in the event there are no other generation processes.

This shifting of the size distribution can be seen in Figure-6 where the atmosphere was filled initially everywhere with the same log-normal distribution of aerosol shown by the solid line in the figure. The model was allowed to operate for 11 hours of model time under idealized conditions. These conditions included a constant relative humidity profile, and a wind speed such that no flux was introduced from the surface but yet there was enough eddy diffusion to keep the boundary layer stirred. The resulting size distribution is shown by the crosses in the figure. This calculation shows that indeed the size distribution does change with time as expected.

Aerosol size distribution measurements can be made with some difficulty at sea. Figure-7 illustrates typical size distributions in the coastal marine environment from aboard USNS HAYES as it sailed from the Chesapeake Bay to a station 130 nautical miles off the coast, Hoppel et. al. (1983). The data is presented here in log-log form because of the large differences in  $dN/dr$  and radius values encountered in the natural aerosol. At both the extremely large and small radii, the measurements show the aerosol concentration decreases while the function reaches maximum values at intermediate sizes. Such behavior can be represented mathematically by a set of log-normal functions.

When a large group of aerosol size distribution measurements are superimposed one upon another, a composite results such as is shown in Figure-8. The marine data for this plot came from many sources as shown in Table IV. The data on this plot contains all the variations in the size distribution from known cases such as the variation in ambient relative humidity and wind-speed measure. It is the objective of any predictive optical/IR model to account for the variations in these data which are of the obvious meteorological origin. Of particular interest is the amount of variation shown as a function of droplet radius. The variation in the  $dN/dr$  values of the small particles ( $r < .07$  microns) covers about four orders of magnitude. The variability in the larger sizes especially in the range of droplets with  $r > 2$  microns also shows a large amount of variation while the size range of radii between 0.07 microns and 0.5 microns is remarkably low. These variations are indicative of the variation in the production and dissipation mechanisms operating on the different size ranges of the aerosol population.

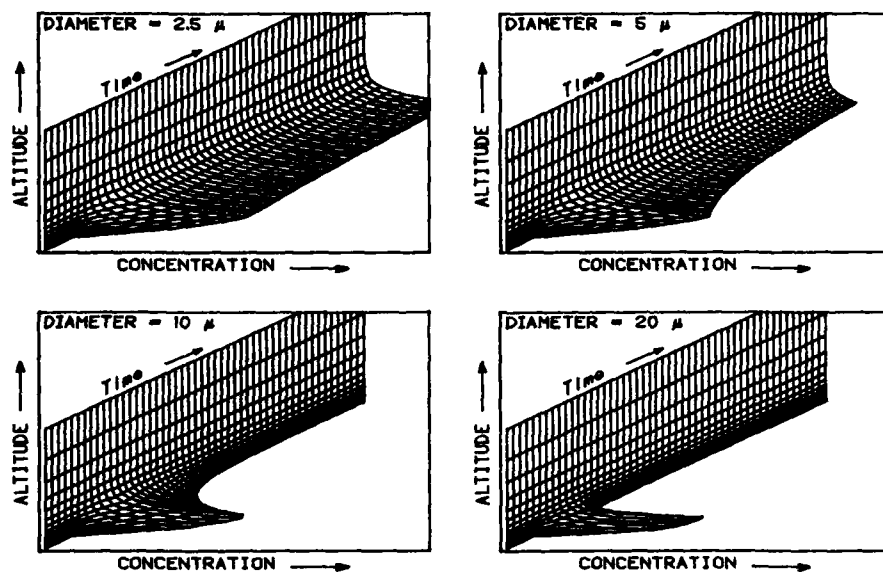


Fig. 5. Three-dimensional surfaces describing the time and space evolution of various size droplets.

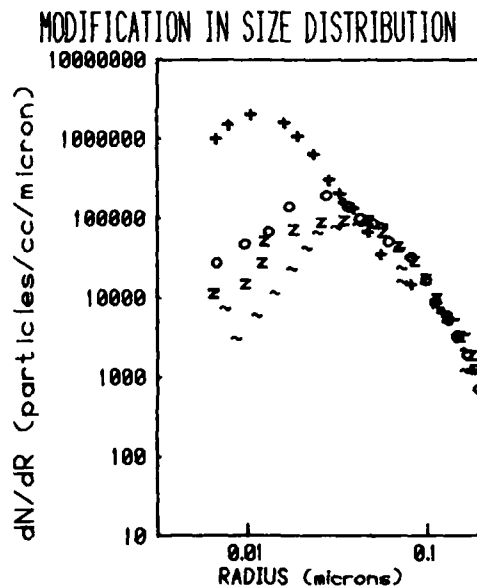
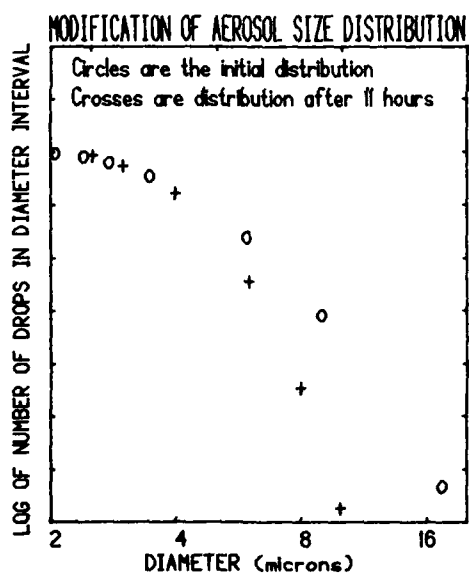


Fig. 6. The modification of an aerosol size distribution in nonequilibrium state. The curve is the initial size distribution throughout an atmospheric column. The crosses are the model calculations at an altitude of 2 m of the modified size distribution after a period of 11 h of mixing produced at a level just below the white cap threshold.

Fig. 7. Change in the size and area distributions as the ship left Chesapeake Bay and sailed into the Atlantic Ocean, Poppel et al (1973).

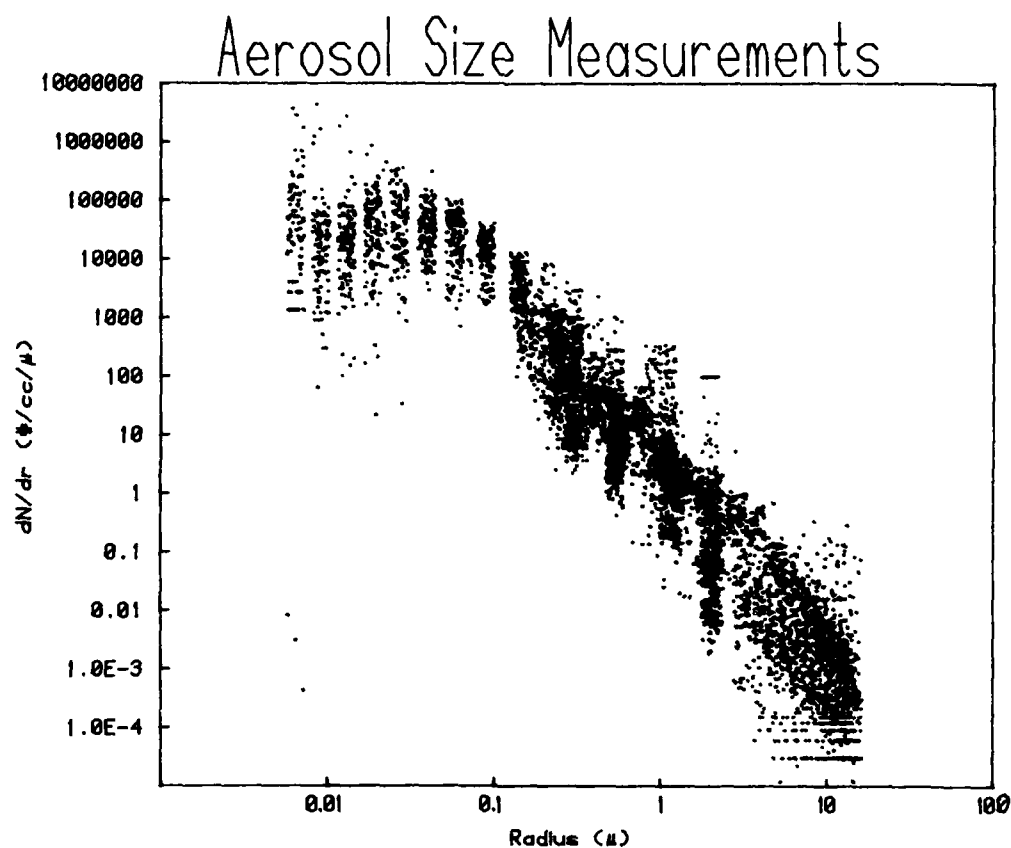


Fig. 8. All the marine aerosol size distribution data from the data sources in Table 4 plotted without correction for relative humidity or wind effects.

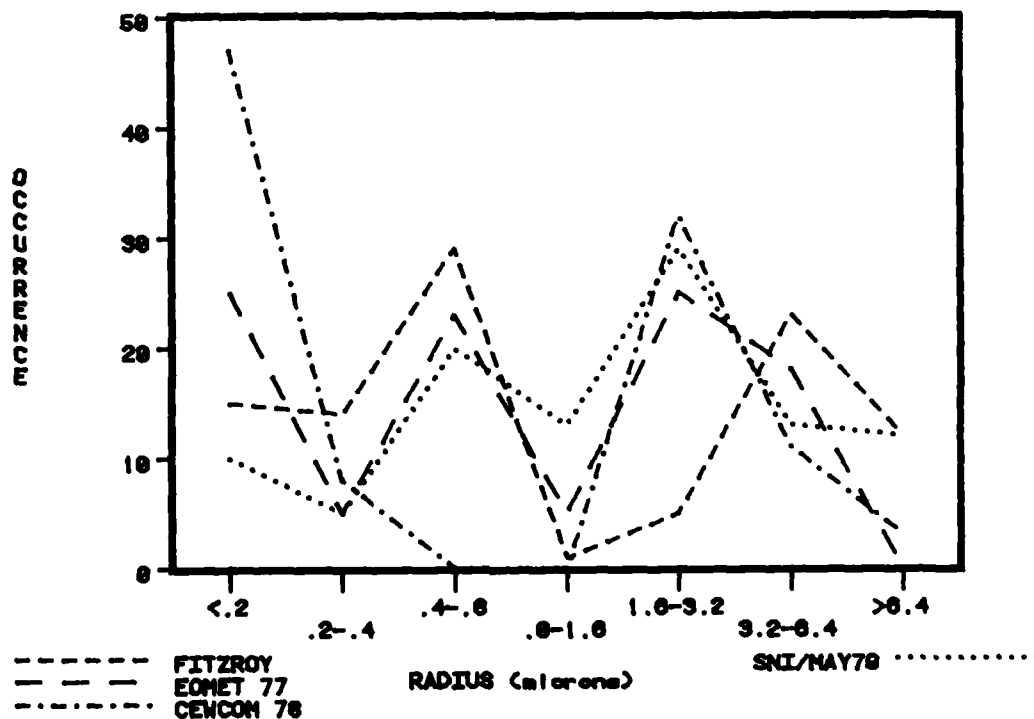


Fig. 9. A frequency distribution which describes the number of observations of inflection points which occur in smoother aerosol size distribution data plotted as a function of the radius bounds.

The variability in the size distribution caused by differences in the ambient relative humidities at the time of measurement can be theoretically accounted for by applying the functions of  $r/r_0$  shown in Figure-1. In the case of the following analysis all data was transformed to an equivalent standard 80% relative humidity size distribution.

The individual size distributions of this field data were first smoothed with cubic spline smoothing techniques. The maxima of the individual component populations of the aerosols are manifested in the total size distribution as inflections in the curve. Thus, by observing the behavior of the derivative of the cubic spline approximation, these inflection points are easily observed. Approximate locations of significant perturbations in the aerosol data were thus detected and these values are assumed to be near the maxima of certain subspecies of aerosol within the total aerosol population. The results of this analysis is shown in Figure-9 where the frequency of occurrence of the peaks is plotted as the y-coordinate and the approximate size classes in which these peaks occurred is plotted along the x-axis. It is of interest to note that the curves seem to hint that a maximum at a very small radius exists. Measurements with an electrostatic aerosol analyzer at sea by Hoppel et. al. (1983) confirms the idea that a component of aerosol peaking at mode radii below 0.1 microns exist very prominently at sea. Evidence of the component is also shown in Figure-9 where the envelope of the data points rolls off at the very small size range. All the curves indicate a bimodal distribution in the area between 0.2 microns and 6 microns. The plots of the data on this curve provide a strong reason which to base a three component aerosol model.

Thus the aerosol size distribution can be represented by a linear combination of three log-normal distributions; each of the functions are individually characterized by three independent parameters to give a total of 9 parameters describing the individual size distribution. This condition is illustrated in Figure-10 which shows in an idealized fashion this three-component model. One can obtain these parameters by using data-fitting techniques on a single size distribution measurement and assuming that the measurement contains at least nine different sizes. The various parameters describing these functions must then be related to the meteorological parameters.

In a log-normal function the parameters have visible and physical significance observable from plotted size distributions. The amplitude parameter, A is precisely the maximum value the function obtains. The mode radius,  $r_0$  describes where this maximum value occurs. Finally the sharpness parameter C describes the narrowness or broadness of the distribution. If C is large then the distribution is narrow and if C is a smaller number, then the distribution appears to be very broad.

After looking at hundreds of aerosol spectra, it was discovered that the width parameter of the log-normal distribution, C was not a noticeable function of wind speed. In fact, the widths of all three log-normal components could easily be kept at a value of  $C = -1$  with no loss in information. Hence 3 of 9 functional parameters have been specified. Of the remaining parameters, the values of  $r_0$  appears to be independent of the wind speed. Indeed, it was found that the  $r_0$  parameters of the log-normal functions could also be represented to the best of our present knowledge by three wind independent constants. Thus, the three amplitude parameters remain which seem to describe the size distribution through correlation with some form of wind representation.

Regression techniques can be employed to determine from the field data sets what the relationship between the A2 and A3 amplitude parameters and the 24-hour average wind and the instantaneous wind measurements. A model can now be made of the aerosol size distributions and is described completely as:

$$\begin{aligned} \frac{dN}{dr} = & k A1 \exp (-1(\ln(r/.03f))^2)/f \\ & + k A2 \exp (-1(\ln(r/.24f))^2)/f \\ & + k A3 \exp (-1(\ln(r/2f))^2)/f \end{aligned} \quad (2)$$

Where  $k = 1$  if no visibility measurement is available but can be adjusted to fit the measured visibility and "f" is the hygroscopic growth factor. Here the first amplitude is defined as:

$$A1 = 2000 (\text{Air mass parameter})^2 \quad (3)$$

where the air mass parameter is a number between 1 and 10 which is related to the length of time the air mass has been to sea. The second and third amplitudes are expressed as

$$A2 = 0.5 \text{ MAX } 5.865 (w_0 - 2.2) \quad (4)$$

$$A3 = .000014 \text{ MAX } .01527 (w_1 - 2.2) \quad (5)$$

where  $w_0$  is the 24-hour average wind and  $w_1$  is the current wind speed, all expressed in meters per second. The MAX function expresses the fact that the parameter is the largest of either of the two components. The units of A1, A2, and A3 are the number of particles per cubic centimeter per micron.

Figure-11 illustrates the aerosol size distribution predicted by the model for two widely differing sets of input conditions and shows that these plots roughly describe the envelope of the data shown in Figure-8. The lower curve is for an open ocean, very low wind speed case with a lower than normal relative humidity for an air mass which has experienced a low wind speed over the previous 24 hours. The upper curve is for a coastal region with a high current wind speed which has been high for the previous 24 hours.

#### Determination of the Optical/IR Properties

The second part of the problem is to express the atmospheric optical/IR properties in terms of the functional form of the aerosol number size distribution. This is accomplished by the application of Mie theory to a known size distribution of assumed spherical droplets suspended in the atmosphere. In order to proceed along this route, it is necessary to know the complex index of refraction of the droplets. It is known that the chemical composition of the droplets changes as a function of relative humidity. If a perfectly dry aerosol nucleus were studied, the complex index of refraction of the nucleus is necessary to describe the optical characteristics of the material. On the other hand, in a very high relative humidity environment, a hygroscopic aerosol will have changed size and taken on a considerable amount of water, the salt dissolving into the water. Hanel (1971) solves the problem by making a straight volume dependence between the complex index of refraction for the nucleus material and the complex index of refraction of water. This method is followed in our calculations. The wavelength dependence of the complex index of refraction for water used here are published in Paltridge and Platt (1976) and that for the nucleus which is assumed to be water soluble are those used by Voltz (1972).

The Mie efficiency coefficients,  $Q_{ext}$  and  $Q_{abs}$ , are calculated by the method of Dave (1968). By using these coefficients and the functional form of the aerosol size distribution, the volume extinction coefficient,  $\beta_{ext}$  and the volume absorption coefficient,  $\beta_{abs}$ , can be calculated for each wavelength of interest and for each relative humidity.

$$\beta_{ext} = \int Q_{ext} * n(r) * r^2 * dr \quad (6)$$

$$\beta_{abs} = \int Q_{abs} * n(r) * r^2 * dr \quad (7)$$

For this specific case the integration can be indicated as

$$\beta = \frac{\pi}{1000f} \int Q * \sum A_i * e^{-\ln^2(\frac{r}{f*r_{0i}})} r^2 dr \quad (8)$$

where the units of  $\beta$  are  $km^{-1}$ , and the units of A's and  $r_0$ 's are defined in Equations 2, 3, 4 and 5 above. One feature of this formulation is that now the time-consuming integration can be precalculated for various relative humidities as:

$$\beta = \frac{\pi}{1000f} \sum A_i * \int Q * e^{-\ln^2(\frac{r}{f*r_{0i}})} r^2 dr \quad (9)$$

The final form of the model now utilizes these precalculated integrals and stores a set of these values for various sets of relative humidities and wavelengths. In the practical application of this model, the solution is reduced to finding the value for a specific relative humidity and wavelength by interpolation between the stored values in a table.

Figure-12 is an illustration of the current wind-speed sensitivity of the model's predictions of aerosol extinction for a band of wavelengths from 0.2 microns to 40 microns. The meteorological conditions at this time are an air mass parameter of 1, indicating an oceanic air mass, an average wind speed over the previous 24 hours of 4.1 meters per second, and a relative humidity of 80%. This family of curves shows that under these conditions if the current wind speed suddenly increases from the value of 4.1 meters per second, the aerosol extinction at all wavelengths is roughly increased by the same amount. On the other hand, if the current wind speed should suddenly drop, the aerosol extinction in the far infrared bands will drop significantly more than does that of the visible and near visible bands. In contrast to this behavior, the conditions used to obtain Figure-13 shows a much different situation. The meteorological data for this plot is a very polluted coastal zone with a high relative humidity of 98%. The 24-hour average wind speed is in this case the same as that for the previous figure; however, in this case, the infrared bands exhibit a considerably lower extinction in respect to the visible wavelengths. If the current wind speed increases, the longer wave lengths increase their extinction due to aerosols whereas the visibility decreases by only a small amount. Likewise, if the current wind speed drops off, the infrared aerosol extinction drops even further whereas the extinction at the visible wavelengths does not vary much.

The sensitivity of the model's prediction of aerosol extinction to the relative humidity is shown in Figures-14 and 15. Figure-14 shows the case of an oceanic air mass where for the previous 24 hours, the wind speed was 4.1 meters per second and the

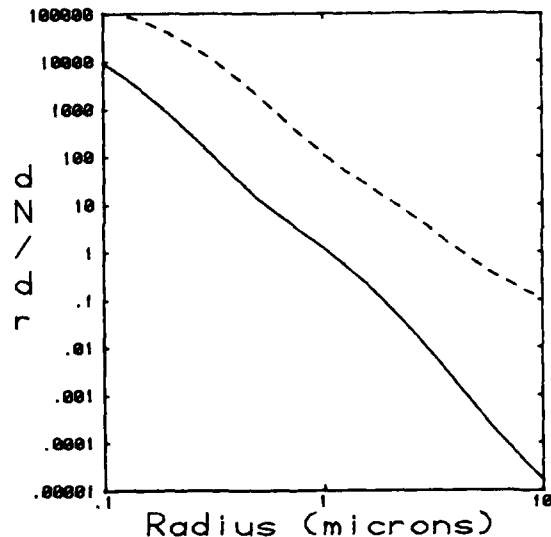
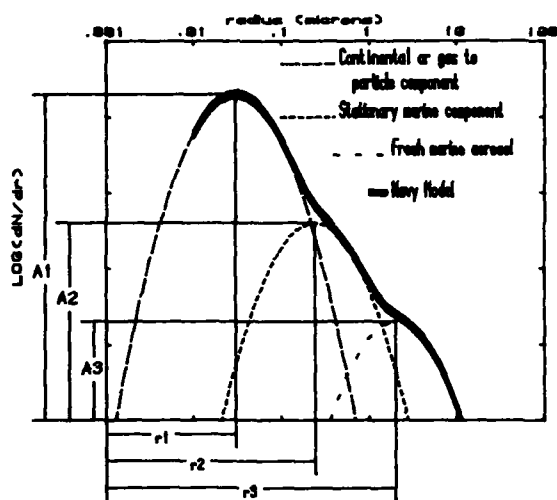


Fig. 10. An idealized three lognormal marine aerosol model.

Fig. 11. A plot of  $dN/dr$ , expressed in number/cc/microns, plotted as a function of radius for a range of aerosol sizes commonly measured in the field. The two lines represent extremes in input conditions in the model and illustrate the latitude of the  $dN/dr$  values that the model predicts.

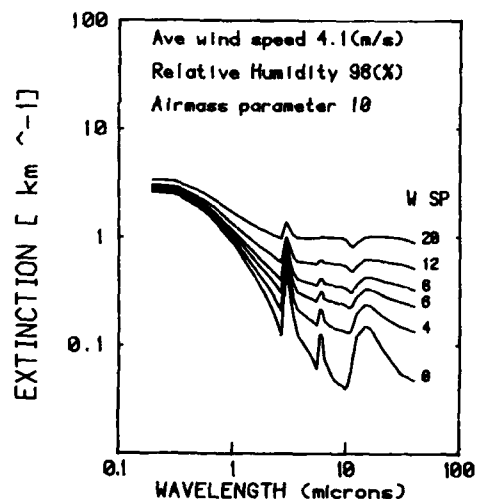
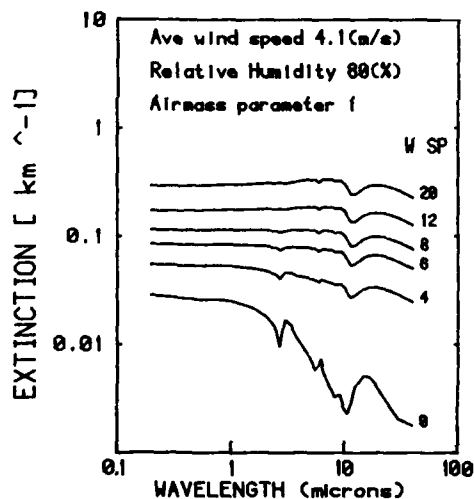
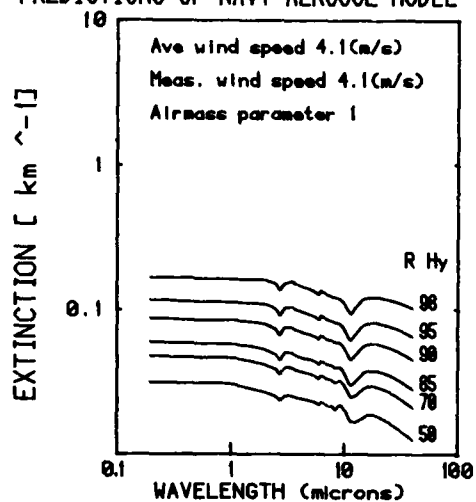


Fig. 12. A plot of extinction against wavelengths showing the model's sensitivity to changes in current wind speed in an open ocean environment.

Fig. 13. A plot of extinction against wavelength showing the model's sensitivity to changes in current wind speed in a high relative humidity, coastal environment.

## PREDICTIONS OF NAVY AEROSOL MODEL



## PREDICTIONS OF NAVY AEROSOL MODEL

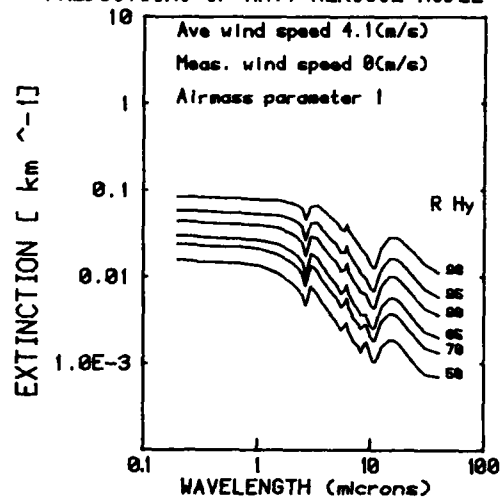


Fig. 14. A plot of extinction against wavelength showing the model's sensitivity to changes in relative humidity in a constant wind regime over the open ocean.

Fig. 15. A plot of extinction against wavelength showing the model's sensitivity to changes in the relative humidity as the current wind speed decreases over the open ocean.

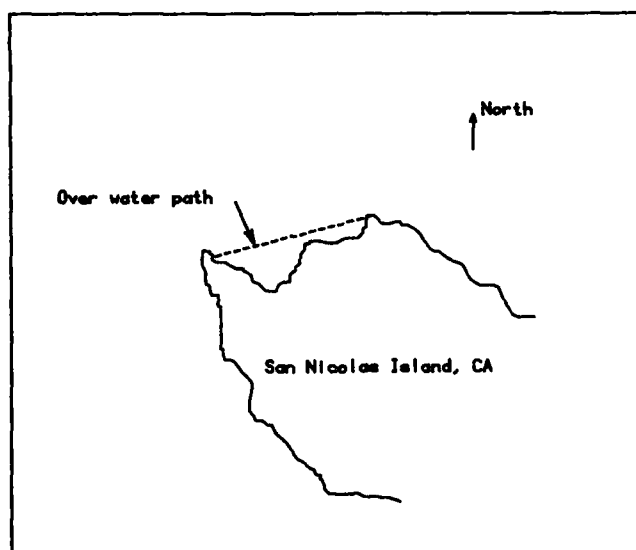


Fig. 16. San Nicolas Island, California.

current wind speed was the same. In this case the changes in the relative humidity essentially shifts the curve up or down independent of wavelength throughout the range of relative humidities of 50% to 98%. Figure-15 shows the results from the same set of meteorological conditions except that in this case the current wind speed has dropped. In this case, the range of relative humidities produce a larger range of aerosol extinction at the IR wavelengths than it does in the visible region.

The reliability of the predictions of this model can be obtained by the comparison of the model predictions with active IR transmissometer measurements. This is accomplished by comparing the calculations from the model using available meteorological measurements to the extinction measured in four bands of radiation made by visible and IR transmissometers at a test site in the marine environment. This comparison will give an outside limit on the accuracy of the model and provide a verification of the ability of this model to predict the optical parameters directly from the marine meteorological inputs.

The data for this comparison came from experiments which took place on San Nicolas Island, California during several extensive data taking periods in 1979 and 1980. Figure 16 illustrates the island and the location of the meteorological sites with respect to the transmissometer path. Instrumentation located at points A and C stand at the ends of two island projections located 4.07 km apart. Directly under this path is sea water which closely simulates the open ocean environment. It has been shown that the prevailing winds usually bring the sampled air from a pure marine origin and this condition can be ascertained by in-situ atmospheric radon measurements (Larson and Bressan, 1980).

The model calculates the extinction for a single wavelength and thus in order to match the calculations to measurements with these relatively broad band transmissometers, it is necessary to integrate the computed effects over all suitable wavelengths and to include the source, detector and any filter characteristics of the instruments used. This is accomplished by first finding the total atmospheric extinction for each wavelength using both the coefficient of extinction due to molecular influence and the coefficient of extinction due to aerosol influence. The LOWTRAN-4 Atmospheric Transmittance/Radiance computer program (Selby, et. al., 1978) was used to calculate the molecular coefficient of extinction at given wavelengths and the Navy Aerosol Model was used to calculate the coefficient of extinction due to aerosol influence at a given wavelength from the meteorological data. After the net transmittance is calculated the numerical integration is performed over the appropriate range of the wavelengths to simulate the total effective transmittance for the various instrumental arrangements. These values can then be compared with the measured value from the particular transmissometer.

All the transmissometer data selected came from the preliminary data reports. These reports were used to select the coefficients of extinction at four different wavelength bands centered around the wavelengths of 0.55, 1.06, 3.6, and 10.5 micrometers. As mentioned above the visibility data needed for the models were calculated directly from the 0.55 micrometer measured extinction.

For each sample for which both transmissometer and meteorological data were available, two determinations of the extinction coefficient were made and the difference between them calculated. Unfortunately this is not a question of making an absolute comparison between a precise standard and a sample value where the notion of error in the sample value is easily determined.

In this case, however, we have all sampled quantities which might contain error and might combine to cause a considerable difference between the two techniques we are trying to compare. At best we are determining an outside limit on the predictive ability of the model. Because of a host of possible instrumentation and sampling errors the actual quality of the model might be better than the results of any analysis would indicate. There is also the problem that the transmissometer data under question is of a preliminary nature and the relative error of these measurements is estimated to be a minimum of  $\pm 6\%$  in transmission. Thus for each time point we only have two determinations of extinction at any wavelength and can say nothing about the most probable extinction that exists at that time. Because of the nature of atmospheric measurements these experiments can never again be exactly repeated. It is therefore gratifying to see in Figures-17, 18 and 19 a scatter plot pattern which indicates a strong correlation between the extinction determinations by the two methods.

In Figure-17 is a scatter plot between the two extinction coefficients at a wavelength center of 1.06 micrometers with a 1% transmission bandwidth of .03 micrometers. This data at a wavelength relatively close to the visible shows a strong correlation between the model calculations and the transmissometer measurements. There is scatter in the points but they seem to be evenly distributed about the solid line which represents the perfect correlation between the two types of measurements. Measured visibility for the aerosol model was used as an input for this plot and the airmass parameter was set to 2.

Figures-18 and 19 show similar plots with the same input parameters but for the wavelengths of 3.6 and 10.5 micrometers. The 1% transmission bandwidth of these measurements are 0.375 and 0.724 micrometers respectively. Both show a strong correlation between two types of extinction coefficients indicating, on the average, a good predictive ability in the models to give reasonable extinction values from local

S.N.I. BARNES TRANSMISSOMETER VS. NAVY MODEL  
SCATTER PLOT

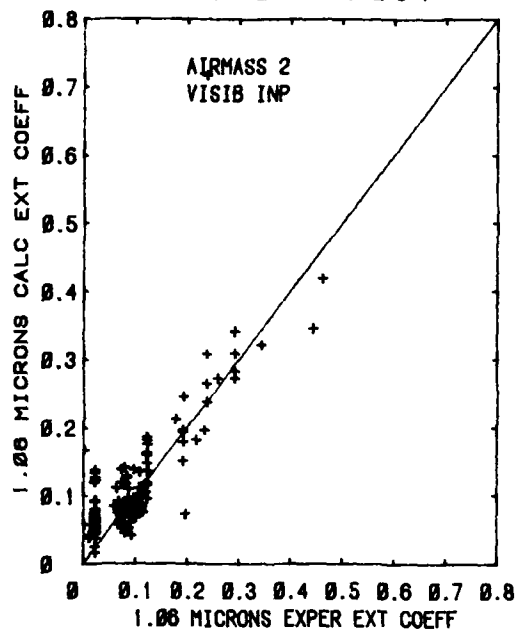


Fig. 17. Scatter plot of Barnes transmissometer data vs. Navy Model predictions at 1.06 microns.

S.N.I. BARNES TRANSMISSOMETER VS. NAVY MODEL  
SCATTER PLOT

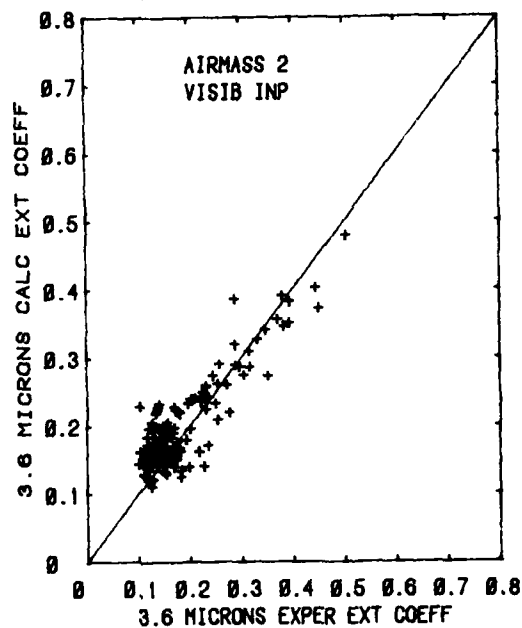


Fig. 18. Scatter plot of Barnes transmissometer data vs. Navy Model predictions at 3.6 microns.

S.N.I. BARNES TRANSMISSOMETER VS. NAVY MODEL  
SCATTER PLOT

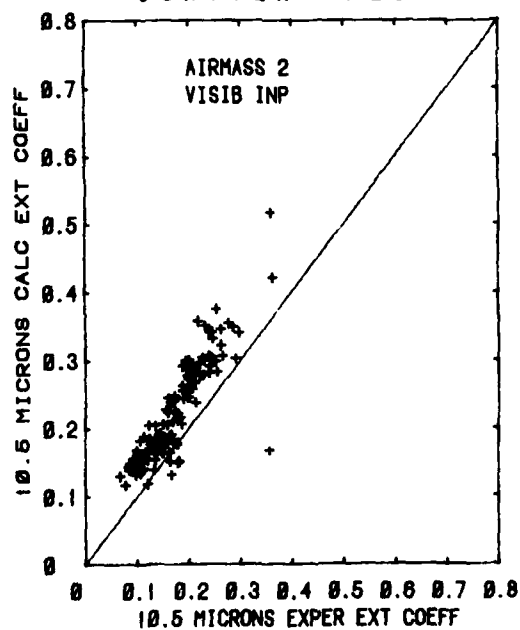


Fig. 19. Scatter plot of Barnes transmissometer data vs. Navy Model predictions at 10.5 microns.

meteorological data. The data in Figure-19 however, for the 10.5 micron data shows a slight deviation in the slope of the least squares line compared with that of the perfect fit line represented by the solid line in the graph.

#### CONCLUSIONS

With modeling tools described above, the extinction and absorption of optical and IR energy made by aerosols in the marine boundary layer can be predicted from a knowledge of the sea surface meteorology. These models can be used with the archived marine meteorological data base to obtain climatological characteristics of regions for optical/IR parameters. Meteorological forecasting techniques can be used as the basis for forecasting the optical/IR parameters.

While these models are not a substitute for actual optical/IR measurements they can provide a quick inexpensive estimate of their value from a knowledge of the meteorological situation.

Table I

Process	Aerosol Sources	Composition
1. Combustion	Natural and Industrial	Salts & Carbon
2. Gas to Particle Conversion	Gas Phase & Photo Chemical Reactions	Sulfates & Nitrates
3. Disp. of Solids	Chemical Reactions at Ground, Water Erosion, Wind Erosion	Silicates, Sodium Potassium & Calcium Salts
4. Disp. of Liquids	Sea Surface, White Water Processes	Sea Salt Water
5. Volcanoes		

Table II

Largest Aerosol.
Sedimentation
Impaction
Large Aerosol.
Cloud formation/precipitation
Scavenging by raindrops
Small Particles.
Attached to drops - eliminated by rainout
Brownian motion
Diffusiophoresis
Thermophoresis
Coagulation - to produce larger particles

Table III. SIZE MEASUREMENT GUIDE

Method	Diameter of Applicability, microns
Optical	
Light Imaging	0.5+
Electron Imaging	0.001-15
Light Scanning	1+
Electron Scanning	0.1+
Direct Photography	5+
Laser Holography	3+
Sieving	2+
Light Scattering	
Right Angle	0.5+
Forward	0.3-10
Polarization	0.3-3
With Condensation	0.01-0.1
Laser Scan	5+
Electric	
Current Alteration	0.5+
Ion Counting, Unit Charge	0.01-0.1
Ion Counting, Corona Charging	0.01-1.2
Mobility Analyzer	.012-1.0
Impactation	0.5+
Centrifugation	0.1+
Diffusion Battery	0.001-0.5
Acoustical	
Orifice Passage	15+
Sinusoidal Vibration	1+
Thermal	0.1-1
Spectrothermal Emission	0.1+

TABLE IV. DATA SOURCES

Description	Geographic Location	Investigator	Instrument	Reference
USNS HAYES (1977)	N. Atlantic Mediterranean	H. Katz E. Mack R. Jeck T. Cosden W. Hoppel	EAA ROYCO PMS-ASSP PMS-CSASP NRL-MSS	Gathman & Julian (1979)
USNS HAYES (1980)	N. Atlantic	W. Hoppel	NRL-MSS ROYCO	unpublished
Admiral Fitzroy (1978)	N. Atlantic	G. Trusty T. Cosden	PMS-ASASP PMS-CSASP	Trusty & Cosden (1981)
San Nicolas Island, CA (1979)	Pacific	D. Jensen R. Jeck G. Trusty G. Schacher	11 PMS Spectro- meters	Jensen et al. (1980)
San Nicolas Island, CA (May 1979)	Pacific	R. Jeck	PMS-ASSP	Blanc (1982)
FPN (1979)	North Sea	S. Gathman B. Julian	ROYCO	Gathman & Julian (1980)
R/V ACANIA (CEWCOM-78)	Pacific	E. Mack T. Niziol C. Rogers C. Akers	EAA ROYCO	Mack et al. (1979)
Aircraft (1976)	Baltic	B. Fitch T. Cress	ROYCO	Fitch & Cress (1981)
H. NL. MS. Tydeman (1980)	North Sea	J. Dielis	2 PMS sys w/6 probes	Dielis (1981)

## REFERENCES

1. Fitzgerald, J. W. and Hoppel, W. A. (1982), "Equilibrium size of atmospheric aerosol particles as a function of relative humidity calculations based on measured aerosol properties" in Proceedings of Workshop on Hygroscopic Aerosols in the Planetary Boundary Layer, A. Deepak and L. H. Ruhnke, editors, Spectrum Press, Hampton, VA, (in press).
2. Monahan, E. C., D. E. Spiel, and K. L. Davidson (1983), "Model of marine aerosol generation via whitecaps and wave disruption" in preprints of 9th Conference, Aerospace and Aeronautical Meteorology, June 6-9, 1983, Omaha, NE, A.M.S.
3. Blanchard, D. C. (1963), "Electrification of the atmosphere by particles from bubbles in the sea" in Prog. Oceanogr., Vol 1, p-71-202, M. Sears, editor.
4. Gathman, S. G. (1978a), "Real-Time meteorological profiles using the NRL marine boundary layer sonde", NRL Report #8271.
5. Gathman, S. G. (1978b), "Model for estimating meteorological profiles from shipboard observations", NRL Report #8279.
6. Gathman, S. G. (1982), "A time-dependent oceanic aerosol profile model", NRL Report #8536.
7. Hoppel, W. A. J. W. Fitzgerald, R. E. Larson (1983), "Measurements of atmospheric aerosols: Experimental methods and results of measurements off the east coast of the United States", NRL Report #8703.
8. HANEL, G. (1971), "New results concerning the dependence of visibility on relative humidity and their significance in a model for visibility forecast", Contrib. Atmos. Phys., Vol. 44, p-137-167.
9. Paltridge, A. W. and C. M. R. Platt (1976), Radiative Processes in Meteorology and Climatology, Elsevier Scientific Publishing Co., Amsterdam.
10. Volz, F. E. (1972), "Infrared refractive index of atmospheric aerosol substances", Appl. Opt., Vol. 11, p-755-759.
11. Dave, J. V. (1968), "Subroutines for computing the parameters of electromagnetic radiation scattered by a sphere", IBM Palo Alto Scientific Center Report #320-3237, 67 pp.
12. Larson, R. E. and R. J. Bressan (1980), "Air mass characteristics over coastal areas as determined by radon measurements", preprint vol, Second Conference on Coastal Meteorology, Jan 30-Feb 1, 1980, Los Angeles, CA, published by A.M.S., Boston, MA.
13. Selby, J. E. A., F. X. Kneizys, J. H. Chetwynd, Jr., and R. A. McClatchey (1978), "Atmospheric transmittance/radiance: Computer code LOWTRAN 4, Optical Physics Division, Project 7670, Air Force Geophysics Laboratory, Hanscom AFB, MA 01731.

## DISCUSSION

F. Kassner (Germany): Did you take water vapor absorption into account in your calculation?

S.G. Gathman (U.S.): Yes, the water vapor absorption was included in the LOWTRAN-4 (Atmospheric Transmission/Radiance) computer program used in my calculations.

## A SYSTEM TO MEASURE LOS ATMOSPHERIC TRANSMITTANCE AT 19 GHz

E. Vilar, T.J. Mouldsley, J. Austin, A. Hewitt  
Department of Electrical and Electronic Engineering  
Portsmouth Polytechnic  
Anglesea Road, Portsmouth, Hampshire, U.K.

J.R. Norbury, S.K. Barton  
Tropospheric Propagation Group  
Rutherford Appleton Laboratory  
Chilton, Didcot, Oxfordshire, U.K.

## SUMMARY

The paper is concerned with the principles and description of a wideband test system with the objective of measuring the complex transmittance of a line-of-sight (LOS) microwave radio link subject to fading and multipath. The technique which uses cross-correlation between pseudo-binary random sequences falls into the realm of spread spectrum techniques. The system described is designed to cover 1 GHz bandwidth at 19 GHz and has the objective of measuring both co-polar and cross-polar transmittance thus generating the complex transmittance matrix. Computer simulations and preliminary experimental results are presented together with a brief initial comparison with other systems.

Key words: multipath, wideband, transmittance, cross-polar, cross-correlation, impulse response, network analysis, spread spectrum, microwave.

## 1. BACKGROUND

Multipath propagation has been of interest to communications engineers for a very long time and this interest has increased in recent years with the growth of digital modulation methods. It is of significance in a variety of fields including mobile radio, troposcatter and microwave line-of-sight links, the last of which is the specific object of our attention. The time-variant frequency-selective fading which results from multipath, whether reflective or refractive, can cause significant performance degradation on digital links due to intersymbol interference and it is necessary to be able to characterise and predict these effects when designing a system. To this end, much work has been carried out on the measurement and modelling of multipath effects and also on means of reducing its impact to a tolerable level. A bibliographical survey is beyond the scope of this section, but journals of most relevance would include IEEE TRANS-AP, IEEE TRANS-COM, Bell Syst. Tech. Journal, Electronics Letters etc.

Over the years, a variety of techniques for measuring multipath channels have been used. Some involve measuring the channel transfer function, either coherently or non-coherently, others seek to evaluate the impulse response. Examples of the former are the frequency-comb technique [1] and the frequency sweep technique [e.g. 2,3]. Both of these may suffer from problems if wideband results are required: the comb method has conflicts of frequency resolution against equipment complexity and cost; the sweep method has problems of speed of measurement. Methods of compensating for this have been developed [3] but these involve significant computational effort.

In principle the simplest method of measuring the channel impulse response is to transmit RF pulses. However, for unambiguous wideband (high-resolution) results a large space/mark ratio is required which means that a conflict exists between peak power limitations and the need for adequate signal/noise ratios. The pseudo-random binary sequence (PRBS) method does not suffer this disadvantage because of its effective processing gain, but it does need more complex receiver techniques to extract the impulse response by correlation against a regenerated PRBS. This disadvantage is less serious than in times past since the PRBS method is equivalent to direct-sequence spread-spectrum modulation, in which extensive expertise is now available [4]. A PRBS approach is the one described in this paper and it offers in addition the possibility of simultaneous bit-error-rate (BER) measurements by treating the transmitted PRBS as a PSK signal.

As well as obtaining the impulse-response/transfer-function of a channel, it is of interest to gain data on its cross-polar behaviour during multipath. If a microwave link uses two orthogonal polarisations for distinct channels, then any effect which reduces cross-polar-discrimination (XPD) is of serious concern. Results on the probability of XPD-reduction are necessary for the system designer who needs to know if cross-polar cancellation is required to maintain a link at full capacity [e.g. 5]. The equipment under discussion is designed to provide cross-polar measurements over a wide band.

Modelling of a multipath channel is fundamental if one is interested in prediction and combating multipath effects rather than simply in description. The types of models used depend on the types of results obtained and the predictions required. Measurements over a narrow band tend to be unable to provide unambiguous data on ray delays/magnitudes [6] and thus non-physical models [1] or simplified models such as fixed-delay [7] are adopted. Wideband measurements enable the use of physically realistic models based on ray-optics providing data on the magnitudes and delays of the rays even when they vary during the period of measurement [3]. Also data on rates-of-change of the channel are very useful for prediction [8].

Having fitted a channel model to the data, one of the most important uses is to predict digital radio outages. One very useful technique is the 'signature' technique [9] which evaluates the effect a given channel model has on various digital modulation techniques, thus enabling a choice to be made on modulation methods, though there are always pros and cons. Another use of multipath models is the evaluation of various methods of combating multipath fading such as adaptive equalisation [10] and various forms of

diversity [1]. One special form of frequency diversity that is closely related to this project is the use of spread-spectrum modulation (e.g. [12]).

This paper is concerned with the description and preliminary results of a system which uses the PRBS technique. After introducing the basic concepts, the method used to cover a wide band (1 GHz as objective) by overlapping elementary transfer functions is outlined. A detailed description of the experimental system then follows (Sections 3 and 4) and computer simulations together with preliminary experimental results are presented (Section 5).

## 2. MEASUREMENT TECHNIQUE

### 2.1 Cross-Correlation

In principle, the transfer function of a linear system can be determined by observation of the system output generated by a known input signal. In practice, the power spectrum of the test signal should be matched to the frequency range of interest, and to avoid time delay ambiguity the repetition interval of the test signal should be greater than the greatest delay within the system.

Considering the measurement of the channel transmittance of a microwave link we can write:

$$Y(j\omega, t) = S_t(j\omega) H(j\omega, t) S_r(j\omega) X(j\omega) \quad \text{..... (1)}$$

where  $X$  is the input spectrum,  $S_t$  and  $S_r$  are the transmitter and receiver transfer functions respectively,  $H$  is the channel transfer function and  $Y$  is the output spectrum. All the terms in Equation (1) are complex functions of the frequency. Furthermore,  $H$ , and hence  $Y$ , are also time varying.

Assuming that a replica of the transmitted signal is available at the receiver, with a variable relative delay, then a cross-correlation function can be obtained. In general this correlation function is time varying in the same way as  $H(j\omega, t)$ , but provided the measurement time is short compared to the rate of change of the channel characteristics, it is given by:

$$R_{XY}(\tau, t) = F^{-1} [X * (j\omega), Y(j\omega, t)] \quad \text{..... (2)}$$

The channel transfer function can be calculated from the Fourier transform of  $R_{XY}$ :

$$H(j\omega, t) = \frac{F [R_{XY}(\tau, t)]}{|X(j\omega)|^2 S_r(j\omega) S_t(j\omega)} \quad \text{..... (3)}$$

The function  $|X(j\omega)|^2 S_r(j\omega) S_t(j\omega)$  can be found from back-to-back operation or under non-dispersive conditions. Experimental results of such a function obtained in the laboratory are presented in Section 5.3.

### 2.2 PRBS Technique

A pseudo-random binary sequence (PRBS) has time waveform, power spectrum and auto-correlation function which make it a useful channel test signal as described above. Such a signal can either be applied directly or used to modulate a carrier frequency. The PRBS technique has the following advantages:

- (i) With present technology, reliable high bit rate sequences ( $\sim 250$  M bits/s) can be generated to allow 'probing' of a wideband channel.
- (ii) Good frequency resolution can be obtained using a long sequence.
- (iii) Coherent detection and integration can be used to increase the measurement signal-to-noise ratio allowing low transmitter power.
- (iv) The technique is flexible in that the bit-rate or sequence length can be altered to suit the channel under investigation.
- (v) With sufficient signal-to-noise ratio bit error rates can be obtained directly.
- (vi) Rapid measurement of channel impulse response and hence of the transfer function is possible.

The main disadvantage of the technique is the relatively complex analogue and digital signal processing required.

### 2.3 Joining Transfer Functions

In the equipment described here the wideband test signal is generated by two-phase modulation of the microwave carrier by a PRBS. A similar signal is generated at the receiver for cross-correlation. This allows measurement of the channel transfer function over a bandwidth slightly greater than the PRBS clock frequency. However, there are practical limits on the bit-rate achievable with current technology to about 250 Mb/s. Wider measurement bandwidths can be achieved by switching the carrier frequency to cover adjacent frequency bands.

In principle the resulting transfer functions could simply be 'added together'. However, since the various local oscillators are not exactly phase locked there is a variable phase discontinuity which must be taken into account. This can be found from the mean phase error in the overlapping region of the spectrum

as illustrated in Figure 1. An algorithm for estimating this phase difference has been developed [13] which makes use of the properties of complex numbers to avoid frequent evaluation of trigonometrical functions. This algorithm also includes a windowing function to take into account the increasing errors in measurement away from the carrier frequency, and also to ensure a smooth transition region between the two transfer functions.

### 3. EXPERIMENTAL SYSTEM

#### 3.1 General

Because of the complexity of the system, this section outlines the principles and puts the following sections into perspective. Figure 2 shows the block diagram of the system to 'probe' the atmospheric channel transmittance. This system is currently near completion and Section 5.3 presents experimental results of back-to-back tests between transmitter and receiver units inclusive of the effects of a multi-path simulator. The system is scheduled to be tested during a Summer campaign in 1984. The channel will consist initially of a 33 km path near the RAL Chilbolton Observatory. The transmitter antenna will be mounted on a tower at about 30 metres, and the receiver antenna at about 10 metres. The antennas are 60 cm in diameter with a front feed system allowing simultaneous operation with vertical and horizontal polarisations. Within a 10 dB beamwidth the cross-polar isolation over the 1 GHz operation bandwidth 18-19 GHz is better than 26 dB. The  $1.9^\circ$  beamwidth should prevent 'spatial filtering' of indirect rays. Under the above conditions with an initial 10 dBm transmitter power, the free-space received S/N in 250 MHz can be estimated at about 18 dB. This means that the modulation is well above the receiver noise level even under rain-fading conditions and BER measurements could be carried out. Furthermore, as the correlator detection bandwidth is approximately 8 kHz (see below) this implies a post detection S/N of about 63 dB, that is a processing gain of  $63 - 18 = 45$  dB according to the definitions used in spread spectrum techniques.

The details of the system are given in the following sections. In brief the 18-19 GHz band is sensed by transmitting a 250 M bits/s PRBS which phase modulates four switched carriers. Clock, carrier and carrier switching sequence synchronisation are coherent with a 5 MHz master crystal oscillator. At the receiving end the correct polarisation being transmitted is selected, and this co-polar signal is sent to the correlator. The correlator cross-correlates the down-converted signal with the locally generated one. The complex impulse response is obtained by sliding (delaying or advancing) the locally generated PRBS in steps of 1 bit. Similar operation can be carried out with the cross-polar component so that a cross-polar transfer function is also obtained. The receiver operations are under control of a logic unit and this releases the burden of these repetitive operations from the computer (PDP 11/24). The computer task is the monitoring of the receiver under control of the logic unit, the sampling and storage of the complex cross-correlation data points, computation of the transfer function, up-dating of certain statistical data, storage on disk and later transfer to magnetic tape, and periodic house-keeping by monitoring and storing analogue voltages which reflect the receiver status.

#### 3.2 Transmitter

Figure 3 shows a simplified block diagram of the transmitter unit. A 750 MHz carrier is phase modulated by a 250 M bit/s pseudo-random binary sequence of length  $2^{10} - 1$  bits. After up-conversion by one of the four selected RF local oscillators followed by filtering and amplification, the resulting PRBS modulated carrier is sent to a microwave switch which allows the selection of vertical or horizontal polarisations. The use of 4 possible carriers leads to four bands with overlapping regions of 60 MHz so that after joining the four transfer functions as described in 2.3, an overall 1 GHz bandwidth can be studied. The final transmitted spectra and the overlapping regions are shown in Figure 4. Figure 5 shows the current strategy of transmission of frequencies and polarisations. Sixteen PRBS's are transmitted before another carrier is selected. Other strategies are possible, for example the dual polarisation can be omitted, or fewer carriers can be transmitted. As described in 3.4 during the full cycle of frequencies and polarisations the cross-correlator 'sits' at a particular lag and the various samples of the correlator corresponding to the various frequency bands and polarisations are later 'unscrambled' by the computer. Brief details of the logic control are given in 4.2.

The transmitter unit is composed of three sub-units mounted in a 19" rack. These units contain: (A) master oscillator and microwave oscillators, (B) the 750 MHz PRBS modulation unit, (C) the microwave up-converter/filter/amplifier and the control logic. A separate unit contains the power supplies and a system of thermal control which includes power supply cut-out in case of over-heating. Fans ensure appropriate air flow within the transmitter rack and temperature sensors together with power transistors and resistors fixed to the walls of the unit monitor and control the heating.

#### 3.3 Receiver

Figure 6 shows the block diagram of the receiver. This circuit delivers two IF's at 750 MHz with a bandwidth of 350 MHz at the nominal level of 0 dBm. The output 1 or channel 1, (reference polarisation) goes to the acquisition unit which acquires clock, carrier and the frequency/polarisation sequence (3.4). Channel 2 is connected to the correlator. A flat fading margin of some 20 dB over the band has been allowed in the design to account for excess attenuation due to rain fades or to longer links. On the assumption that the correct sequence of frequency and polarisations has been acquired (Section 3.4) the control logic (Section 4.2) operates the carrier switching of local oscillators SW1 and the switching matrix SW2. The operation is as follows: suppose that vertical polarisation is the reference one, then if cross-polar measurements are to be carried out, the switch SW2 ensures that only when V/F1 is present (65  $\mu$ s) channel 1 is connected to the acquisition units (Figure 6). For the remaining  $65 \times 7 = 455$   $\mu$ s, channel 1 is disconnected and the clock and carrier (local) oscillators 'fly-wheel' and remain in average phase until the next burst of 65  $\mu$ s of V/F1 appears. From the processing point of view, SW2 ensures that the measurement channel, Ch 2, is sequentially connected to the V, H, H and V front-end channels and therefore for the particular lag  $\tau_i$  being selected the cross-correlator produces samples of the cross-correlations corresponding to the vertical co-polar channel, horizontal co-polar, vertical cross-polar and horizontal cross-polar. The switching pattern of frequencies, polarisations and cross-correlation measurements is repeated for the next lag  $\tau_{i+1}$  (see Section 3.5). The switching matrix SW2 is composed of two 3 dB

couplers and 6 PIN diode switches arranged in such a way that the two receiver channels are terminated in  $50 \Omega$  at all times and thus well matched. Again as in the transmitter other switching patterns are possible for example to reduce the time between resynchronisation.

Finally Figure 6 shows also the arrangement for calibration. This is carried out by using the same local oscillators which are used to up-convert the 750 MHz PRBS output of the calibration unit. This unit is identical to that used in the transmitter.

### 3.4 Clock and Carrier Recovery Synchronisation

The reference polarisation output channel (Ch 1, Figure 6) is connected to the acquisition circuitry shown in Figure 7 via the switching matrix. The objectives of the unit are twofold. On the one hand it acquires clock, carrier and synchronises the switching of polarisations and frequencies, and on the other it supplies the cross-correlator with three outputs: the 250 MHz clock, the 750 MHz carrier and the sync pulse to indicate the beginning of the PRBS.

From the start the receiver logic ensures that only the local oscillator for F1 is applied to the RF mixer (Figure 6). When F1 is transmitted via the reference polarisation, the code lock loop can operate and the sampled phase error causes the VCXO to lock onto the arriving clock. If the frequency difference between the two before lock is, say,  $\Delta f$  Hz and N is the sequence length (1023), then, provided that  $\Delta f$  is within the acquisition range of the VCXO, it will take at most  $N/\Delta f$  seconds to acquire lock. If that range is 100 Hz, then the maximum time between lock is  $1023/100 = 10$  s. Note that the code lock loop error signal is sampled at about 2 kHz because  $V/F1$  appears every  $\sim 65 \times 8 \mu s$  (Figure 5).

Once the 250 MHz clock is available for carrier acquisition, that loop can operate provided that the microwave carriers are within the capture range. If required, a d.c. offset can be added to the control voltage of the 5 MHz reference. With the pulsed carrier recovered (750 MHz) and the clock available (now coherent with the carrier as at the transmitter), the synchronisation of polarisation and frequencies can operate. For this (Figure 7) when the VCO of  $\sim 250 \text{ kHz}/128 \sim 2 \text{ kHz}$  is synchronous with the rate of the arriving RF of 750 MHz, the phase reversals at the output of the first mixer are in the centre of the  $65 \mu s$  period so that areas 'A' and 'B' are equal and the mean voltage is zero. Any imbalance will be corrected by the loop. After locking, the logic states of the intermediate stages of the divider can be decoded and give a precise indication of transmitter frequency and polarisation state. It should now become apparent why the same polarisation must be applied to the acquisition unit for synchronisation of polarisations and frequencies.

### 3.5 Correlator

Figure 8 shows the block diagram of the cross-correlator which requires the three receiver outputs described in 3.4. Because the transmitted and received spectrum is truncated by filtering beyond  $\pm f_b$  (the clock frequency), complete information can be obtained by resolving the correlation function of each elementary channel, at lag intervals equal to  $1/2f_b$  or  $\frac{1}{2}$  the bit period (2 ns). For each relative advance or delay of the local PRBS sequence 'A' relative to the arriving sequence, the correlator delivers to the integrators and sampling and hold units (S/H) the real and imaginary parts of the cross-correlation at lags, say,  $\tau_n$  and  $\tau_n + \frac{1}{2}$  bit. Thus two values of the complex function are generated in parallel. Furthermore, as indicated before, in the present system a specific lag is present during the complete cycle (lasting up to  $2 \times 8 \times 65 \mu s$ ) of frequencies and polarisations, and the control logic commands the duration of the integration per band present to be the  $65 \mu s$ . This implies a post detection bandwidth of  $\frac{1}{2} 1/65 \mu s$  or about 8 kHz. As the baseband data transmitted is 250 MHz this implies a processing gain of  $250/8 \times 10^{-3}$  or 45 dB as quoted in 3.1. We note that because every  $65 \mu s$  four data samples are presented to the multiplexer of the computer controlled analogue-to-digital converter (during the subsequent  $65 \mu s$  while the next integration takes place), as a result the maximum ADC data rate is  $4 \times 16 \text{ k samples/s}$ . This data is unscrambled by the computer, transfer functions obtained, statistics up-dated and in case of 'no event' the data is not permanently stored (Sections 4.1, 4.3).

The operation of the correlator logic is as follows. Each of the PRBS generators (A,B) has three inputs: clock, data strobe, 10 bit word. At the start, the strobe input commands the load of the 10 bit data word into the PRBS (B). This word is one of the possible 1023 of the sequence and therefore represents a delay or an advance in relation to the 'all 1's' of the arriving sequence. The presence of a sync pulse loads the register of B onto A, so now both registers run with equal bit pattern at 250 M bits/s synchronously with the arriving pattern of the receiver except for the delay given by the start word. From then on the command 'advance' or 'delay' input to the PRBS (B) will shift the register by 1 bit. The pattern will only be passed onto the PRBS (A) when the sync pulse appears. Clearly if there is no change of advance/delay of PRBS (B) we keep loading the same word into (A) and therefore the lag remains the same. Under receiver logic control of the advance/delay and of the starting word we can explore a variety of lag ranges.

## 4. SYSTEM CONTROL AND DATA PROCESSING

### 4.1 Computer System

The computer system shown in Figure 9 which is self-explanatory carries out the following functions:

- (i) Control of receiver operation.
- (ii) Acquisition of correlation function data.
- (iii) Processing of correlation functions to give channel transfer function.
- (iv) Storage of raw transfer functions during propagation events.
- (v) Storage of channel propagation statistics (reduced data format).

The first two functions are performed in association with a hard-wired logic and control unit (Section 4.2). This relieves the processor of a considerable burden of repetitive timing operations. The remaining operations (Section 4.3) are carried out by the PDP 11/24 processor and MSP3X array processor. The latter is required to calculate the Fourier transform of the correlation function in 'real time'.

#### 4.2 Logic Unit and Computer Interaction

The logic unit is a set of TTL circuits whose purpose is to carry out the repetitive tasks of controlling the system. This has two consequences: as indicated above the computer is left free to carry out more important operations and also, it is possible to operate the receiver in a limited way even if the computer is unavailable for some reason such as failure. Consequently, the majority of controls originating from the computer have manual substitutes available on the front panel of the logic. Also, the interaction with the computer does not involve any handshaking arrangements, all lines in or out are treated as always being meaningful (whether 'active' or not).

The outputs of the logic fall into three categories. The first of these involves the overall settings of the system. This means telling the other units in the receiver whether they should be trying to acquire the received signal or tracking one already acquired. Similarly, switches are controlled which put the system into measuring mode rather than in calibration mode. These 'settings' do not change over long periods of time.

The second set of outputs can be called 'real time controls'. These are signals which are continuously changing during the period of a channel measurement, such as the current frequency and polarisation of the correlator input. Other signals control the correlator lag, the sample and holds in the correlator and the digitisation of the correlator analogue outputs by the computer. This last is carried out under DMA (direct memory access) so that, in a sense, the logic controls the computer.

The third category of outputs are those which keep the computer informed as to the current status of the receiver. These include indications of whether or not the various receiver loops are locked, the current frequency and polarisations and also whether the correlator is currently carrying out a measurement. As stated previously, all these are permanently 'meaningful', and the computer reads them when it needs to know.

The inputs which control the behaviour of the logic are also in three groups: timing synchronisation signals from other parts of the receiver, computer controls and manual front panel controls. The latter are mostly manual versions of the computer signals with two exceptions. The switch which determines whether the receiver is under computer or manual control has no equivalent from the computer, and neither do the switches which specify the kind of frequency/polarisation sequence expected to be sent by the transmitter.

The lines from the computer are, firstly, settings such as 'track/acquire', 'measure/calibrate', 'include cross-polar measurements' or the number of lags and scans (complete channel measurements). Secondly, there are strobes, i.e. signals whose leading edge is their only significant attribute. The primary one of these carries the meaning 'begin measurement'. When this is received (or its front panel substitute pressed) the logic unit enters a series of autonomous actions to carry out a set of channel measurements. The computer is left free to do other operations since all control of the receiver and even the storing of results in the computer memory is under the independent control of the logic.

#### 4.3 Data Acquisition and Processing

Figure 10 shows a simplified block diagram of the data processing scheme. Initially, the computer sets up the receiver in the appropriate mode of operation and supervises acquisition of the PRBS code and clock, the transmitted carrier and carrier switching synchronisation. This is achieved by receiving on only one frequency and one polarisation until all the loops involved are locked. Receiver carrier switching and sampling of the correlation functions are then enabled. For a full dual polarisation measurement with four carriers the data acquisition operation takes 32 ms. During this interval of time 2048 analogue samples are stored in the computer memory.

The next step is to Fourier transform the correlation function data, divide by the system transfer function and join the separate frequency bands to give the final transfer function measurement (or in the case of full co- and cross-polar measurements the channel transmittance). The processing software is written mainly in FORTRAN with MACRO-11 assembler routines for speed critical sections. The time interval between successive 'snapshots' of the channel characteristics limited by the processing time which is currently 0.1-10 seconds depending on the number of carriers and polarisations etc., and the processing required.

The channel transmittance is initially stored on disk, but it is apparent that the available 30 M bytes would soon be exhausted by continuous sampling at the above rates. Thus, only data obtained during propagation 'events' of interest are retained. The data selection criteria are programmable, with for example, multipath events being detectable by variations in the amplitude of the transfer function with frequency.

In parallel with the logging of event data, a statistical summary of the channel characteristics is calculated and stored periodically. This is effectively a greatly compressed version of the original data and will give information on the channel behaviour both between and during 'events'.

Finally, the data stored on disk will be transferred to 9-track magnetic tape for further off-line processing and analysis. It is anticipated that this will be carried out manually about once a week when the system is installed on the test link.

## 5. COMPUTER SIMULATIONS AND MEASUREMENTS

### 5.1 System Performance Simulations

The principles of the measurement technique and performance of the system have been extensively investigated using a computer model to test the effects of thermal and phase noise on the accuracy of the measurements. The algorithm for joining transfer functions has also been tested using computer simulation.

An example of the results obtained is shown in Figure 11. Here the r.m.s. phase error in the measured transfer function (of a non-dispersive channel) is plotted as a function of frequency. Gaussian phase errors with  $1^\circ$  r.m.s. amplitude were added at the correlator output. It can be seen that this has introduced about  $1^\circ$  phase error across the frequency band with an increase in the upper half due to inaccuracies introduced by the joining algorithm. The effective bandwidth for reliable measurement using two overlapping channel measurements is in this example about 500 MHz.

### 5.2 Channel Measurement Simulations

A variety of simulations have been carried out, in parallel with the development of the system, aimed at modelling the behaviour of the multipath channel which the system is designed to measure. The initial purpose of this activity was to provide an indication of the sort of behaviour the channel might display on the basis of a fairly simple physical model. Stemming from this, there grew an interest in using the simulations for assisting in the interpretation of any results obtained and in evaluating, in advance, a selection of techniques for analysing the data expected to be collected.

There are two types of simulations. The first of these is concerned with modelling the ray trajectories through the atmosphere. The behaviour of such models seems to depend on the model chosen for the refractive index profile along the path. A very common model is to describe the profile by a continuous piecewise linear function (e.g. [14]) and approximating the ray paths by arcs of circles. Other workers suggest that this model can suppress higher order delays, and propose smooth analytical models instead [15]. Our own work in this area is as yet inconclusive, but we are seeking a model that facilitates the deduction of an atmospheric structure from our channel measurements.

The second model type being developed simulates the transfer function of a multipath channel. The simplest form utilises just two rays: one direct and one refracted/reflected. This can provide substantial frequency-selective fading, but certain observed effects, such as sudden reversals of group delay polarity, cannot be explained. However, incorporating a third ray enables one to simulate such events (Figure 12) and careful examination of the parameter values involved tends to imply that sudden group-delay reversals are useful for implying the presence of extra rays, but they do not correspond to equally dramatic changes in the channel characteristics.

Having produced synthetic transfer functions due to known values of ray magnitudes and delays, a variety of analysis techniques can be applied to see how well they perform both on the clean spectrum and in the presence of controlled amounts of noise. The most obvious method for attempting to find the rays is to produce an 'impulse response' by Fourier transforming the spectrum using an appropriate window such as the Kaiser-Bessel [16]. This linear method is, in a sense, equivalent to fitting a model to the spectrum that assumes the spectrum is due to a large number of equally spaced 'rays' which then have to be examined by hand to select the 'real' rays.

A more satisfactory approach appears to be to fit a model with a few rays to the data by some best-fit technique. This has the disadvantage that it is inherently nonlinear and computationally complex [3] but it does seem at present to hold better hope for fully automated data analysis, which is likely to be necessary if any substantial database of fading results is obtained.

### 5.3 Preliminary Laboratory Results

The measurements presented here show the performance of the system in laboratory back-to-back tests.

Figure 13 shows the power spectrum of the 750 MHz carrier modulated by the 250 Mb/s. This signal is up-converted to 18 GHz, transmitted over the link (a coaxial cable) and down-converted to 750 MHz at the receiver resulting in the spectrum shown in Figure 14. A path loss of 70 dB was simulated using fixed attenuators. The irregularities in the spectrum are thought to be due to various reflections in the transmitter and receiver systems. The receiver front-end noise contribution can also be clearly seen.

Figure 15 shows the power spectrum with a simulated two ray multipath channel inserted at IF. The second path has a relative delay of about 11 ns.

Figure 16(a), (b), (c), (d) shows back-to-back IF system measurements after data acquisition and processing by the computer. The magnitude of the impulse response of the system is shown in Figure 16(a) and the corresponding power spectrum is shown in Figure 16(b). It can be seen that the system response within one channel is reasonably flat over the range of interest ( $\pm 150$  MHz).

The frequency response of a simulated flat channel after division by the system response is shown in Figure 16(c). It can be seen that the measurement accuracy decreases away from the carrier. This is due to thermal and phase noise (see Section 5.1). A similar spectrum for a simulated multipath channel is shown in Figure 16(d). The characteristic deep nulls can be compared with those in Figure 15.

## 6. DISCUSSION AND CONCLUSIONS

This paper has described the background and details of a cross-correlation measuring system with the objective of measuring the transfer function of a wideband channel which is linear and time variant. A multipath environment in the microwave region constitutes such a channel. The cross-correlation technique has long been known and has been used by the ITS/NBS of Boulder in their 'probe'. In it a continuous

slide-by technique is used and periodic fast 'snapshots' of the impulse response are generated [17]. The technique described in this paper is digital and the complex correlation function is evaluated at  $\frac{1}{2}$  bit lag intervals. Computer simulations have shown that with suitable filtering this sampling is sufficient in practice to reproduce the channel characteristics and that a higher sampling resolution is not necessary [13]. Additional techniques described in this paper include the use of overlapping bandwidth and summation of transfer functions in order to cover a much wider bandwidth than the one given by the spectrum of the PRBS sequence. In the case of 500 MHz or even 1 GHz it can be argued that, say, a 1 G bit/s PRBS generator/cross-correlator would simplify the technique. However the complexity of the fast digital technique is such that this approach is not yet feasible. The flexible arrangement of frequencies and polarisation switching will allow the measurement of the complete wideband transmittance matrix. To do this however in the present system, phase memory for the receiver carrier and clock oscillators is required during the transmission of frequencies and polarisations other than those selected as 'reference'. In between these periods the oscillators 'fly-wheel' and must keep phase memory before they are resynchronised and their memory refreshed.

Other features of the system described include its potential ability to measure BER. This is inherent to the PRBS and digital nature of the technique although it has not as yet been implemented in the present system. This digital aspect offers also the advantages of having soft-wired logic (PROM programmed) for the repetitive tasks of both transmitter and receiver, as well as a natural interaction with the computer (a PDP 11/24 in our system) via the peripherals. The availability of a fast array processor as one of the peripherals (2 ms for a complex FFT of 64 complex data points of the cross-correlation) speeds up computations and permits the use of the concept of data decimation and compression in the sense that raw data are usually not stored for later analysis. Instead we store only data which is meaningful in itself and this only when it is of some importance.

The main disadvantage of the present system, particularly in its present prototype phase, is the complexity. This complexity can be compared with the relative simplicity of other systems in use such as the sweeping technique of the French CNET of Lannion [8,16] which measures amplitude and group delay which are presented as analogue outputs. This technique as well as the NBS [17] permits a 'visual' assessment of the 'events' observed but the data has to be digitised for later analysis.

Finally the system which has been described can cover any VHF region using any carrier frequency greater than say, 1.5 GHz, quite apart from 750 MHz itself. One only requires to change the final local oscillators for the up-conversion and down-conversion at the transmitter and receiver respectively. The rest of the system operates at 750 MHz and this has the added advantage of allowing back-to-back tests in the laboratory and include a simulator and, if later desired, an adaptive equaliser, all under controlled laboratory conditions. A full 'system transfer function' must of course include the antennas and this implies the use of a short test range or path to test the full system in absence of multipath and of ground reflections.

#### 7. REFERENCES

- [1] Greenstein L.J. and Czekaj B.A.: 'Modelling Multipath Fading Responses using Multitone Probing Signals and Polynomial Approximation', Bell Syst. Tech. J., Vol. 60, No. 2, February 1981, pp 193-214.
- [2] Sylvain M. et al: 'The PACEM Experiment on Line-of-Sight Multipath Propagation', URSI Commission Symposium, Louvain (Belgium), June 1983.
- [3] Sandberg J.: 'Extraction of Multipath Parameters from Swept Measurements on a Line-of-Sight Path', IEEE Trans-AP, Vol. AP-28, No. 6, November 1980, pp 743-750.
- [4] Dixon R.C. (Ed): 'Spread Spectrum Techniques', IEEE Press, 1976.
- [5] Steinberger M.L.: 'Design of a Terrestrial Cross Pol Canceled', ICC '82, pp 2B.6.1 - 2B.6.5.
- [6] Rummier W.D.: 'Time and Frequency Domain Representation of Multipath Fading on Line-of-Sight Microwave Links', Bell Syst. Tech. J., Vol. 59, No. 5, May-June 1980, pp 763-796.
- [7] Rummier W.D.: 'More on the Multipath Fading Channel Model', IEEE Trans-COM, Vol. COM-29, No. 3, March 1981, pp 346-352.
- [8] Martin L.: 'Rates of Change of Propagation Medium Transfer Functions during Selective Fadings', URSI Commission Symposium, Louvain (Belgium), June 1983.
- [9] Emshwiller M.: 'Characterisation of the Performance of PSK Digital Radio Transmission in the Presence of Multipath Fading', ICC '78, pp 47.3.1 - 47.3.6.
- [10] Bello P.A.: 'Performance of Adaptive Equalisation for Staggered QPSK and QPR over Frequency-Selective LOS Microwave Channels', ICC '82, pp 3H.1.1 - 3H.1.6.
- [11] Haber F. and Noorhashm M.R.: 'Negatively Correlated Branches in Frequency Diversity Systems to Overcome Multipath Fading', IEEE Trans-COM, Vol. COM-22, No. 2, February 1974, pp 180-190.
- [12] Tou C.P.: 'On Combatting Multipath Effects using Spread-Spectrum Systems', AGARD Conference Proceedings, No. 332, pp 36.1 - 36.11.
- [13] Mouldsley T.J.: 'Computer Simulation of the Wideband Transmittance Measurement and Limitations Due to Additive Noise and Phase Jitter', Department of Electrical and Electronic Engineering, Portsmouth Polytechnic, Internal Report No. 83/2, January 1983.
- [14] Pickering L.W. and Derosa J.K.: 'Refractive Multipath Model for Line-of-Sight Microwave Relay Links', IEEE Trans-COM, Vol. COM-27, No. 8, August 1979, pp 1174-1182.

- [15] Webster A.R.: 'Raypath Parameters in Tropospheric Multipath Propagation', IEEE Trans-AP, Vol. AP-30, No. 4, July 1982, pp 796-800.
- [16] Martin L.: 'Relative Amplitudes and Delays of Rays during Multipath Fadings', Second International Conference on Antennas and Propagation, York U.K., 1981.
- [17] Linfield R.F., Hubbard R.W. and Pratt L.E.: 'Transmission Channel Characterisation by Impulse Response Measurements', ITS Boulder Co. U.S.A., Report OTR-76-96, 1976.

#### 8. ACKNOWLEDGEMENTS

This complex project is being financed under the auspices of the U.K. Departmental Users Committee. Acknowledgements for useful information and assistance during the feasibility study go to L.J. Greenstein, B.G. King, R. Hubbard, P. Bello, R. Freeman, P. Sargeant and R. Blake. Since the beginning of the project many colleagues directly or indirectly associated with the project have contributed in a variety of ways at the different stages; particular thanks go to M.P.M. Hall, J. Lewis, S.K. Cherry, J.K. Kazmierski, N. Whitehead, L. Martin, C.T. Mallet, H. Smith and W.P.A. Ditmar. Also much credit to the construction work goes to technical staff of the Polytechnic, in particular S. Hancock and K. West. Finally, the Portsmouth Polytechnic team acknowledges the special laboratory facilities provided by their institution and the encouragement of S.W.G. Reeves.

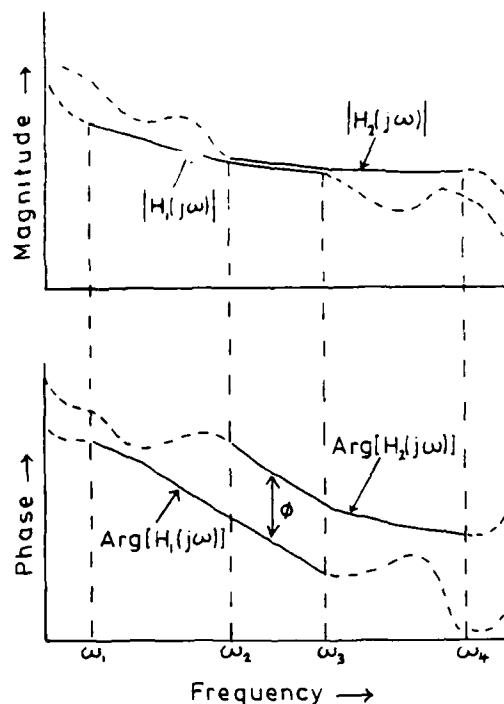


Figure 1: Joining transfer function estimates from adjacent frequency bands.

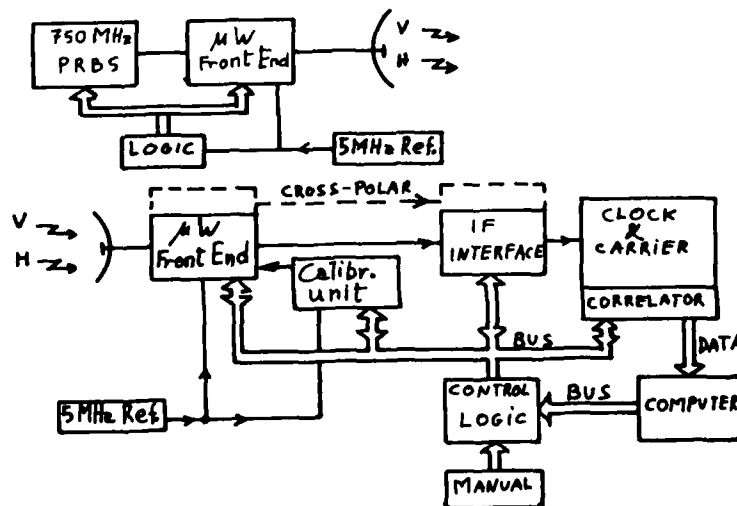


Figure 2: General configuration of transmitter and receiver units.

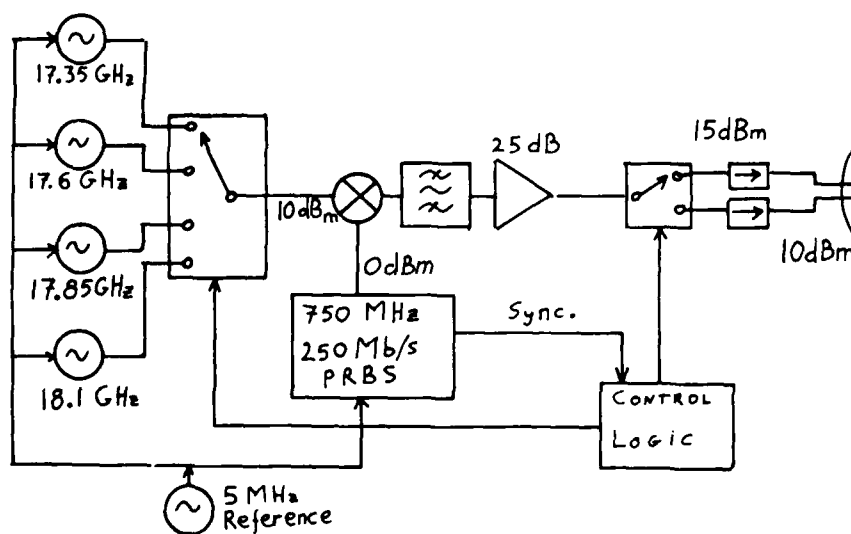


Figure 3: Block diagram of the transmitter.

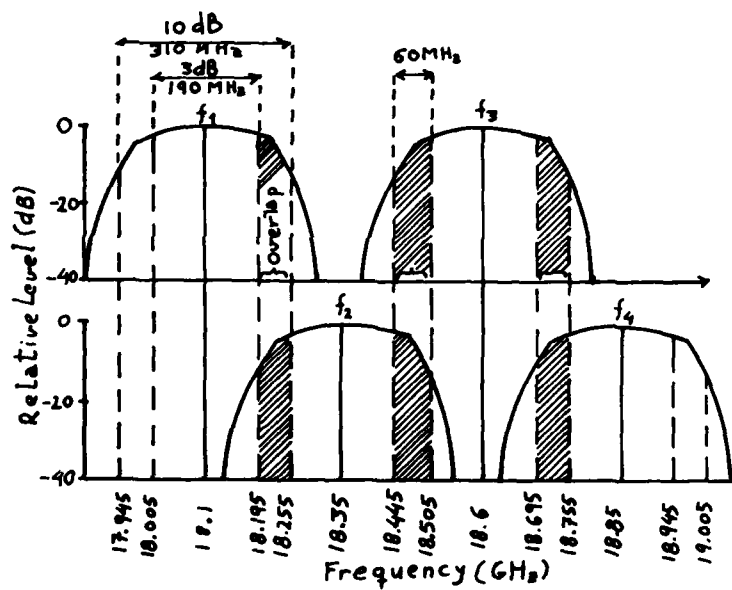


Figure 4: Strategy of overlapping RF spectral bands.

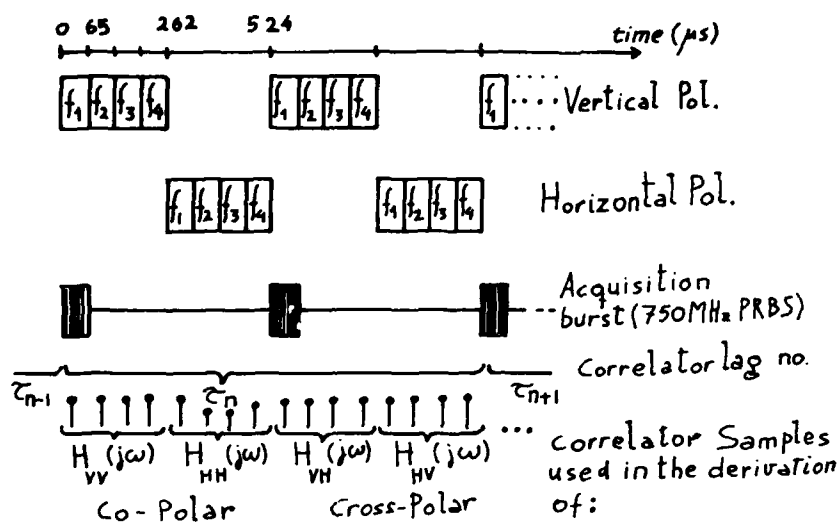


Figure 5: Strategy of transmitted frequencies and polarisations using a given lag.

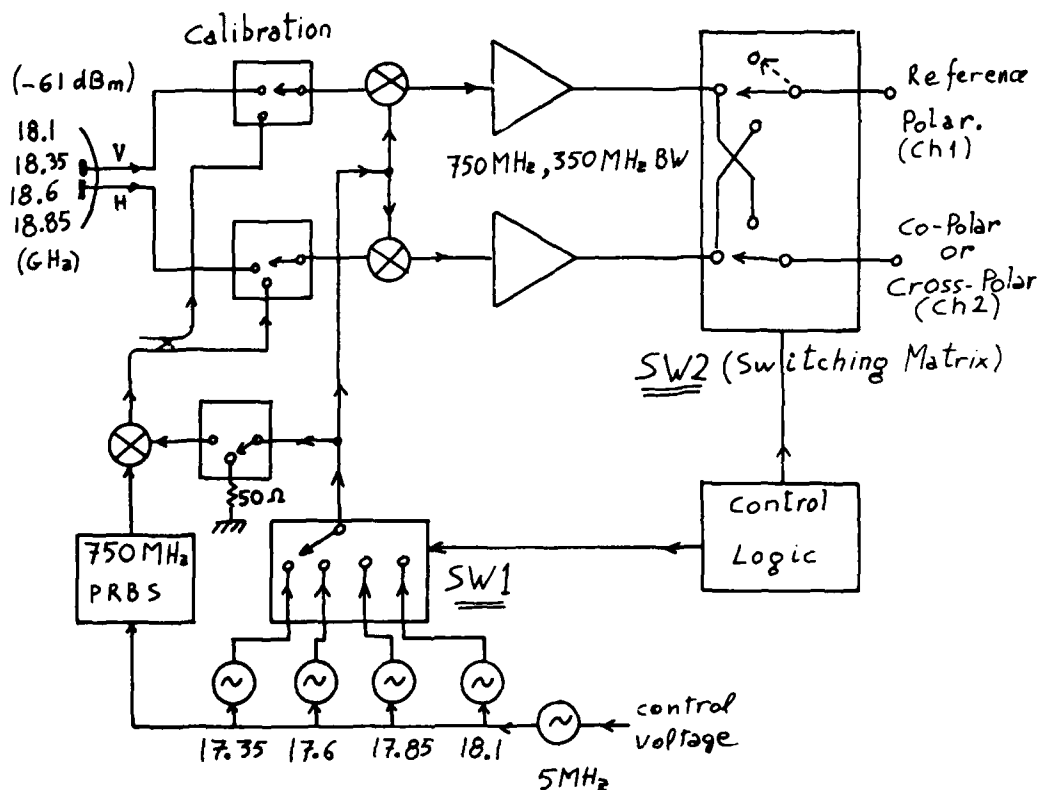


Figure 6: Block diagram of the receiver.

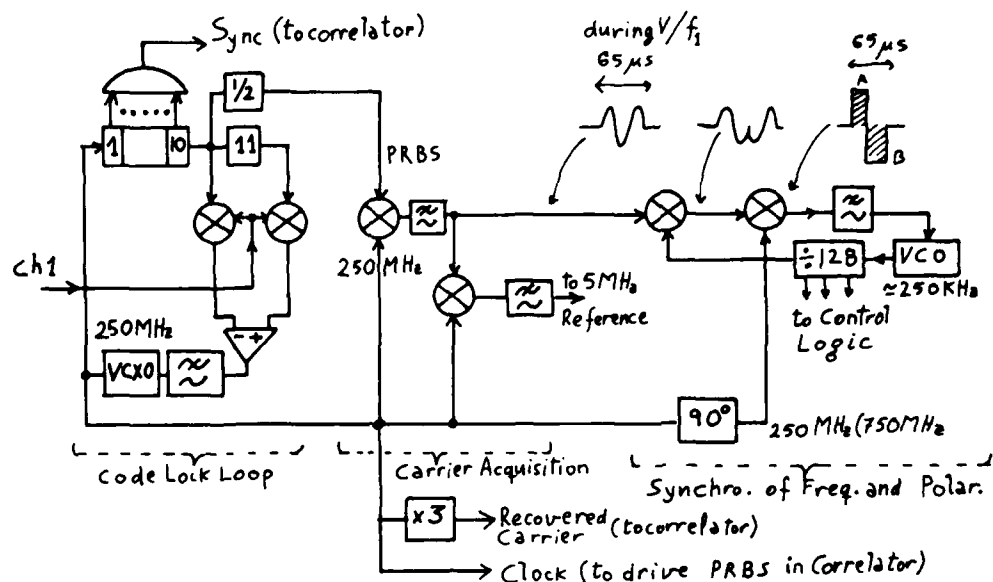


Figure 7: Synchronisation of clock, carrier and frequency/polarisation switching sequence.

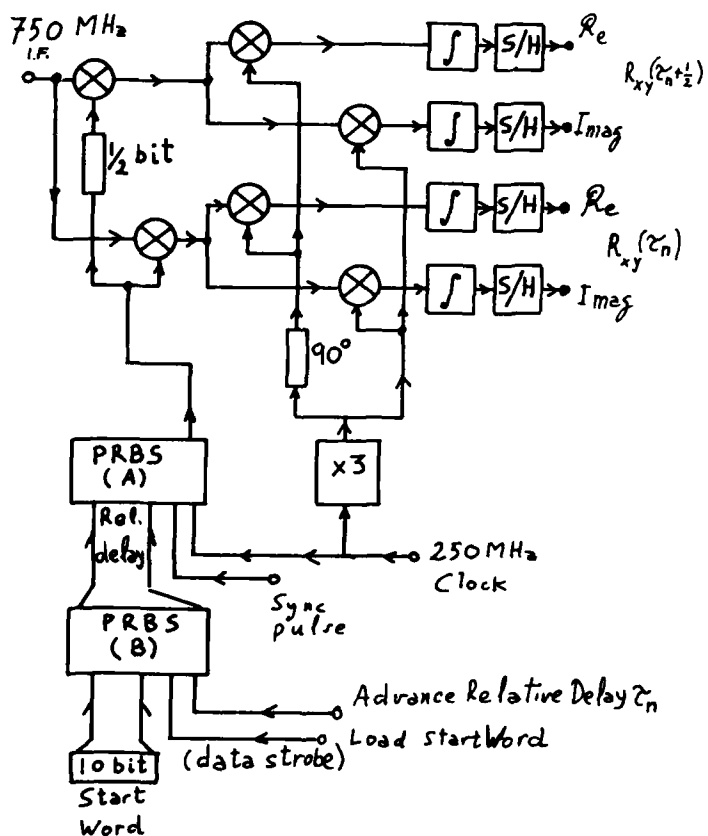


Figure 8: The cross-correlator.

Figure 9: Block diagram of the computer system.

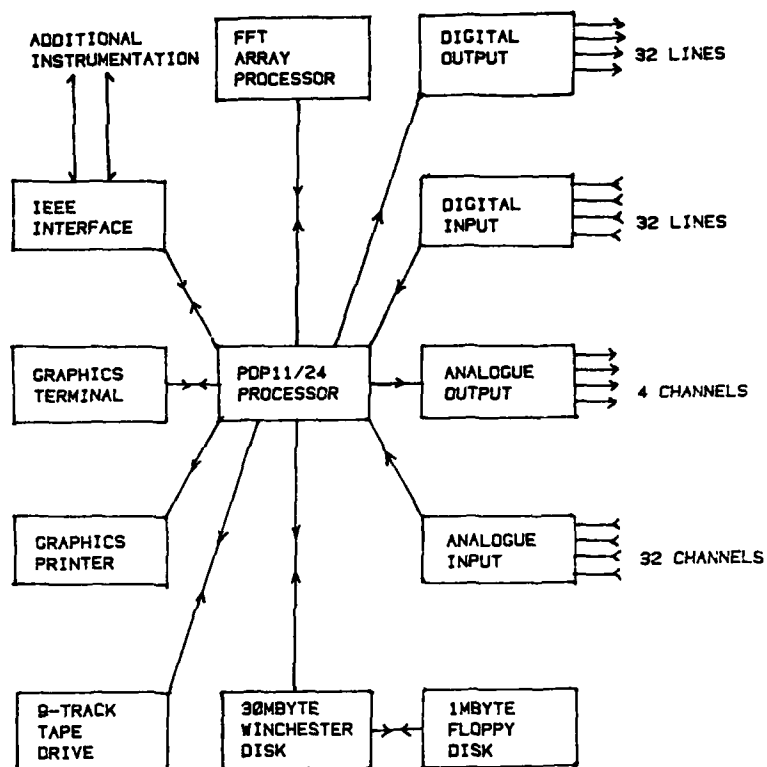
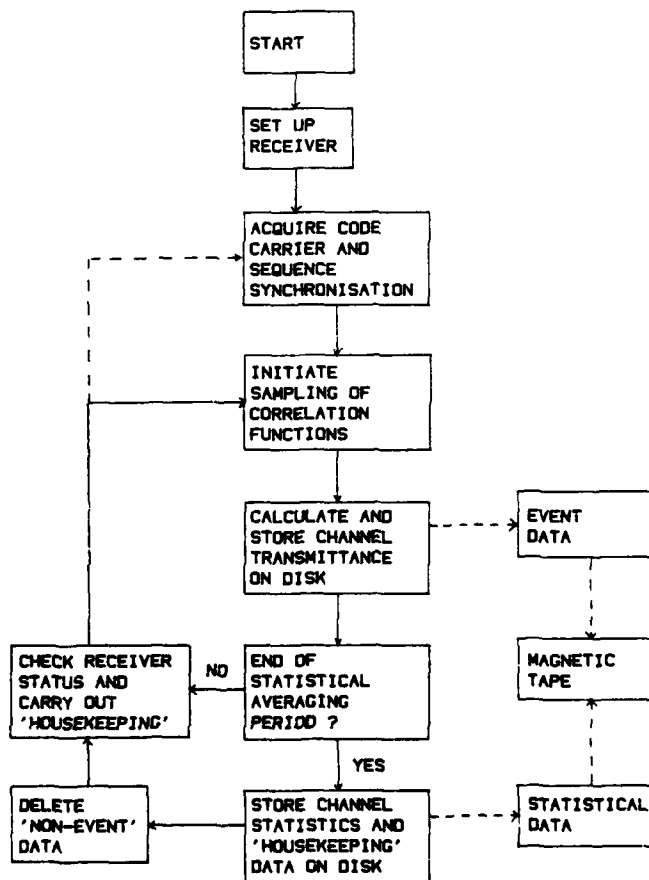


Figure 10: Block diagram showing the data processing.



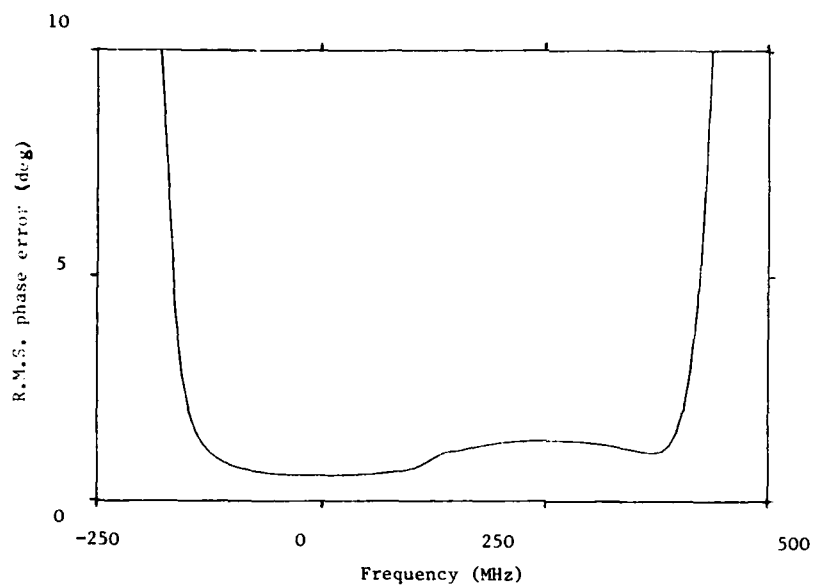


Figure 11: Resulting phase error in joined transfer functions due to  $1^{\circ}$  r.m.s. recovered carrier phase noise.

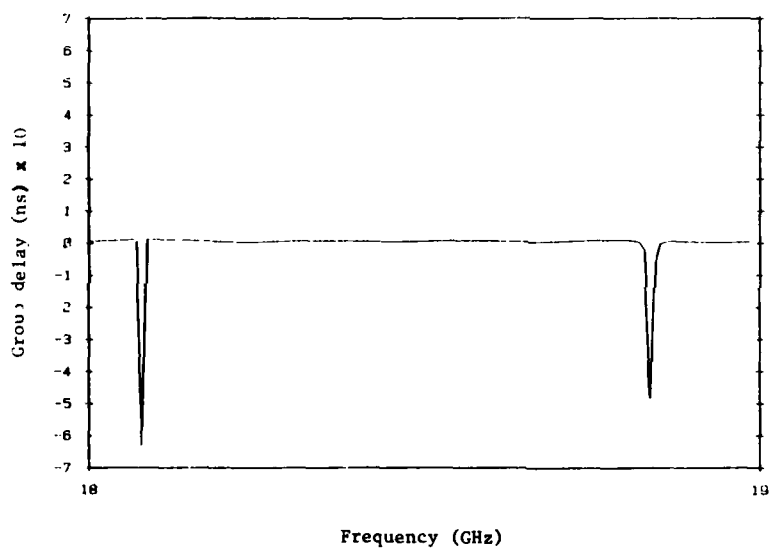


Figure 12(a): Group delay of a simulated three-ray fade.

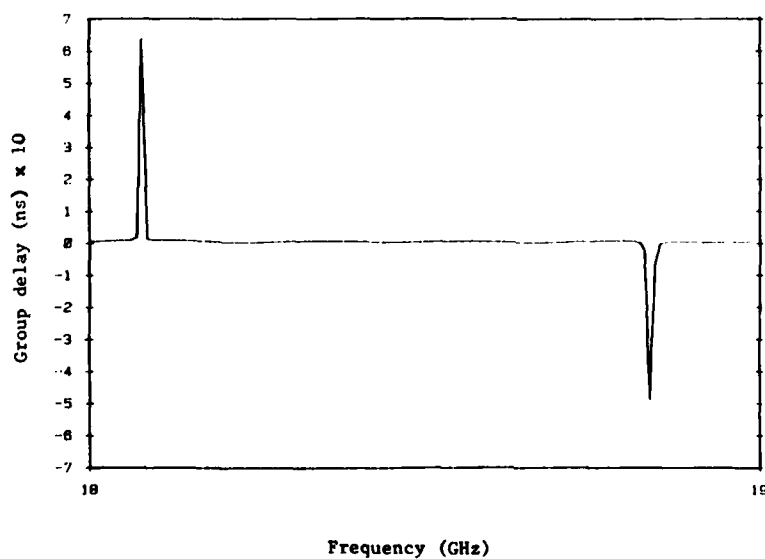


Figure 12(b): Group delay of a simulated three-ray fade with amplitude of third ray increased by 1%.

Figure 13: Power spectrum of the 750 MHz carrier modulated by 250 Mb/s PRBS.

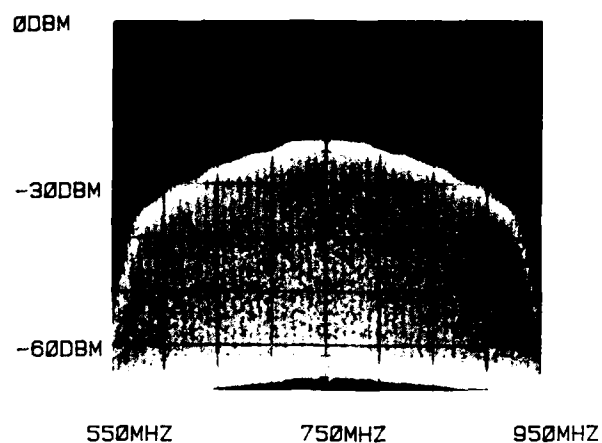


Figure 14: Power spectrum at the receiver after down-conversion and filtering.

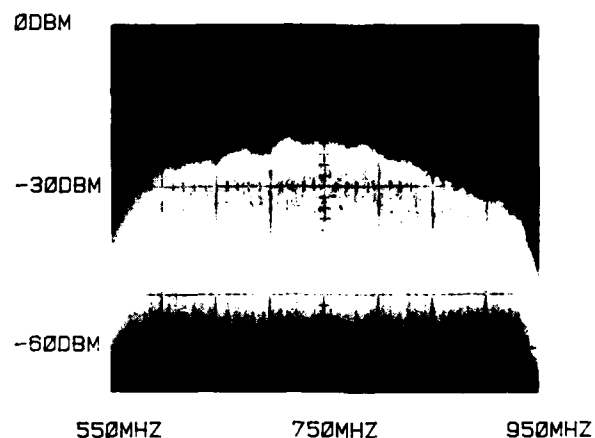
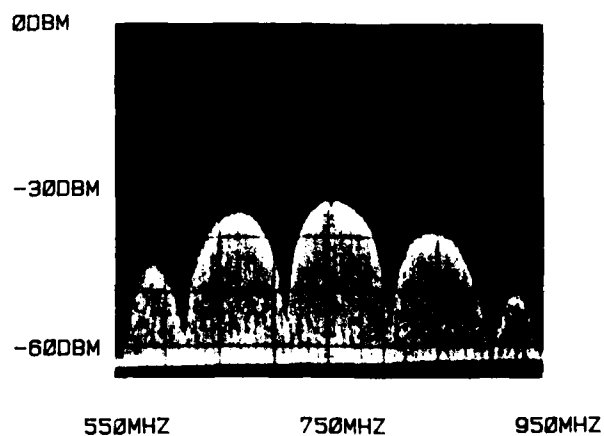


Figure 15: Power spectrum with simulated multipath event (second path delayed by 11 ns).



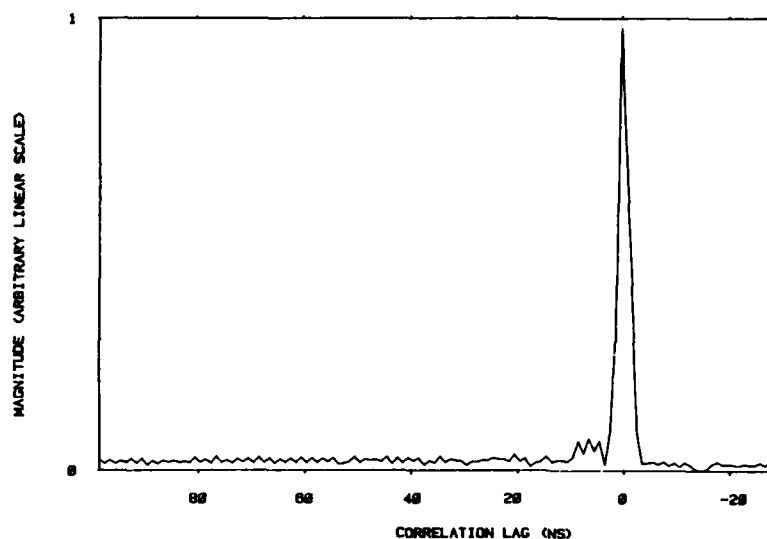
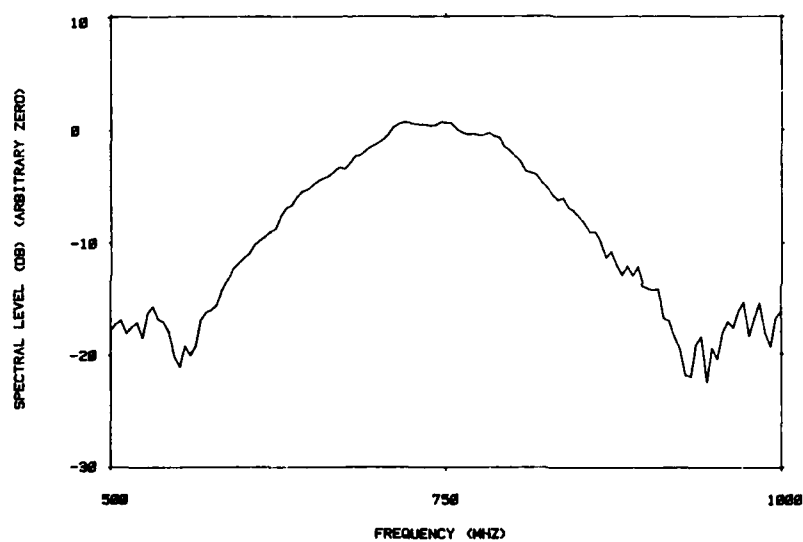
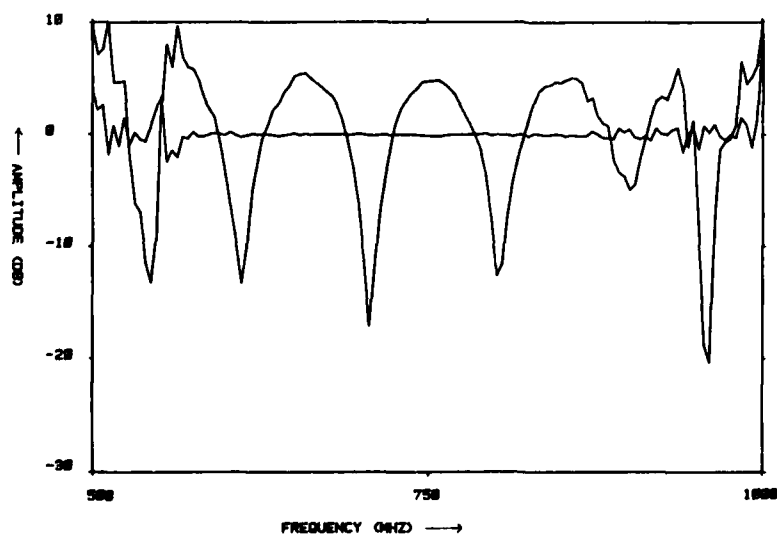


Figure 16: Results from back-to-back tests at 750 Mhz IF using a hardware multipath simulator.

(a) Magnitude of system impulse response.



(b) Power spectrum computed from system impulse response.



(c) Measured amplitude response of a simulated flat channel.

(d) Measured amplitude response of a simulated multipath channel.

## DISCUSSION

E.W. Lampert (Germany): What are the limitations of your system concerning propagation paths showing a multipath continuum, i.e., where no real main ray exists?

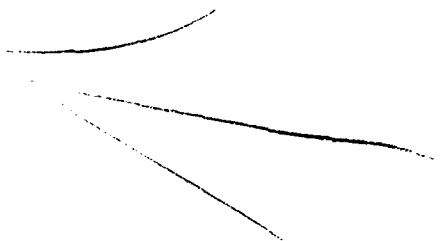
T.J. Mouldsley (U.K.): The behavior of the wide-band measurement system will, of course, depend on the precise nature of the multipath channel. The main requirement for successful operation is acquisition of the received code by the code-lock loop. A troposcatter link is a typical example of a path with a continuum of multipath components. On such a link the code-lock loop would touch the "centroid" of the correlation function of the received energy.

Reliable measurements would be obtained provided the channel could be considered "frozen" during the measurement interval. However, it is possible to imagine hypothetical characteristics which would prevent stable signal acquisition. An example is a channel with a small number of intermittent multipath components and no dominant "direct path" component. Our hardware multipath simulator could be used to simulate this hypothetical case and to assess the performance of the measuring system.

I. Anderson (U.K.): How sensitive is the accuracy of your system to code synchronization error caused, e.g., by the burst-time of the signal being too short compared with the acquisition time of the code-lock loop?

T.J. Mouldsley (U.K.): In the switched carrier mode of operation, the code-lock loop error signal is pulsed rather than continuous. This means that the code-lock loop is effectively a sampled system. When the loop bandwidth is sufficiently narrow and the carrier (and clock) phase noise is sufficiently small, the loop should function in much the same way as a continuous signal. Thus there should be little effect on measurement accuracy.

However, the question leads to an important point. The desirability of the code-lock loop "fly-wheeling" between signal bursts and the necessity of tracking carrier phase noise produce conflicting requirements on the loop bandwidth. The optimum loop parameters to meet these requirements are currently under investigation. It appears likely that the frequency and polarization switching strategy seen in Figure 5 of our paper will need to be modified to obtain reliable system operation.



A GaAs FET MICROWAVE REFRACTOMETER FOR TROPOSPHERIC STUDIES

U. M. Yilmaz, G. R. Kennedy and M.P.M. Hall  
Rutherford Appleton Laboratory  
Chilton, Oxfordshire, OX11 0QX, U.K.

## SUMMARY

The paper describes a microwave refractometer designed to be used in studies of multipath propagation on line-of-sight microwave links, and studies of transhorizon ducting. The application of a GaAs FET amplifier in a feedback loop containing the sampling cavity has produced a lightweight and simple refractometer which has been tested and used in a light aircraft with on-board data processing. These various aspects are discussed in some detail, together with the background requirements and specification.

## 1. INTRODUCTION

In the nineteen fifties and sixties much effort was put into making measurements with microwave refractometers. The interest was to resolve the part played by reflection from horizontally-layered discontinuities in refractive index and that by scatter from random variability in the medium. At that time, such refractometers were of a differential nature, giving the difference between the resonance frequency of a sampling cavity and that of a reference cavity. The differential system was less than ideal and emphasis on this type of work diminished as priorities changed.

More recently, with the ever-increasing problems of determining possible interference between signals from widely spaced transmitters on the same frequency, and a military interest in knowing the range to which signals may be ducted, there has been renewed interest in refractometers. The present paper describes a microwave refractometer designed to be used in studies of multipath propagation on line-of-sight microwave links, and studies of transhorizon ducting. Because microwave frequencies can now be measured directly, a differential device is no longer necessary. Furthermore, the application of an FET amplifier in a feedback loop containing the sampling cavity has produced a lightweight and simple refractometer which has been tested and used in a light aircraft with on-board data processing. The paper discusses these aspects in some detail, together with the background requirements and specification.

The principle of the microwave refractometer is to measure the frequency of a resonant cavity. Changes,  $\delta f$ , in the resonant frequency,  $f$ , of the cavity are related to changes,  $\delta n$ , in refractive index of the air,  $n$ , within the cavity by the relationship

$$\delta f/f = -\delta n/n \quad (1)$$

Since the radio refractive index of air is close to unity, it is usually expressed in parts per million above unity,  $N$ , and so changes,  $\delta N$ , are given by

$$\delta N = -10^6 \delta f/f \quad (2)$$

The cavity is designed to support a mode of oscillation which enables sufficient cavity wall to be removed for air to pass through freely (see ref. 1). These cavities are normally made of invar to minimise effects of thermal expansion.

Two types of microwave refractometers were described in 1950, one by Crain [2], the other by Birnbaum [3]. Both refractometers operated at X-band, and in each case resonance frequency of the sample cavity was compared to that of a reference cavity. The Crain refractometer used the cavities to control the frequencies of two oscillators, which when mixed produced a difference frequency linearly related to the difference between the values of refractive index of the air in the two cavities. The Birnbaum refractometer used a linear frequency sweep of a microwave source to determine the frequency difference between the two cavities. The two systems have been used extensively in aircraft.

Some work has also been carried out using balloon-borne refractometers. For instance, a lightweight Birnbaum-type battery-operated version was described by Steffen [4] which had a maximum error of about 5 N units, though the short-term error was put as low as 0.05 N units. Another battery-operated Birnbaum-type refractometer, a development of that described by Fowler, Champion and Tyler [5], was used with up to four sampling cavities (each referred to a reference cavity) to examine spatial variability of refractive index. The system had a short-term error of less than 0.1 N unit and enabled examination of spectral frequencies up to 30 Hz. Specialised radiosondes have also been developed for tropospheric studies [6].

The first specific requirement for the present refractometer is to examine changes of refractive index with height (and the way in which these change with distance) on a 33 km line-of-sight path on which multipath studies are being made at 19 GHz. Horizontally-stratified regions of particularly high refractive index lapse rate (i.e. large decrease with height) may cause not only the direct 'ray' to be received, but also an indirect 'ray' of different phase. In communication systems, where a finite bandwidth is necessary to carry a given information rate, the fading caused by this anomalous effect is quite serious, particularly as the fading pattern is frequency sensitive. Digital systems tend to suffer more seriously than FM systems, as the information content of a digital system tends to be carried at certain discrete frequencies related to the symbol rate.

A second requirement is to support studies of transhorizon interference. Layering at heights above those affecting line-of-sight links can cause interference over large distances. Layers typically between 1 and 2 km refract transmissions back towards the earth, thus overcoming the natural shielding due to the earth's curvature, which normally stops interference between geographically separated transmitters operating in the same frequency band.

The performance requirement for the refractometer depends to some extent on the way in which it is deployed. Before embarking on developing an aircraft-mounted refractometer, a study was made of deployment alternatives. Free-flight balloons with low-cost semi-expendable radiosondes would have been inadequately sensitive, and require excessive manpower for frequent soundings with time and distance. Tethered balloons would have been impractical for measuring variations with distance. A remotely piloted vehicle was considered to be more difficult to control than an aircraft, and more expensive, as well as being less acceptable to air traffic control or the public at large. Having decided on a suitable aircraft and assuming a maximum rate of climb or descent of about 3 m/s, a data sampling rate of 30/s was considered adequate. (The airspeed is about 40 m/s (80 kts) during measurements.) A sensitivity of about 0.1 N was sought (i.e. about that observed over 2.5 m height with 40 N/km lapse rate). It was expected that there would be a need to accept some zero drift (if only due to temperature changes in the sampling cavity), but to make periodic checks of absolute level (of N) using an aircraft psychrometer when in well mixed air conditions. (Accuracy of 0.1°C in both wet and dry bulb readings would give errors of 0.7 N from the wet bulb and 0.4 N from the dry [6]).

## 2. THE REFRACTOMETER

The refractometer is shown in block diagrammatic form in Figure 1, together with a diagram of the sampling cavity. The latter is of 41.5 mm internal diameter and similar length, with ends in the form of annular tubes. The cavity is made of invar, and gold plated to resist surface erosion by the atmosphere. Such cavities have been described earlier [5]. As in the earlier work, the present cavity resonates in the TE<sub>011</sub> mode at 9.45 GHz with a Q of 7000. Energy is coupled between waveguide stubs and the cavity by diametrically opposite holes in the cavity walls. The figure also shows the waveguide-to-coaxial transformers.

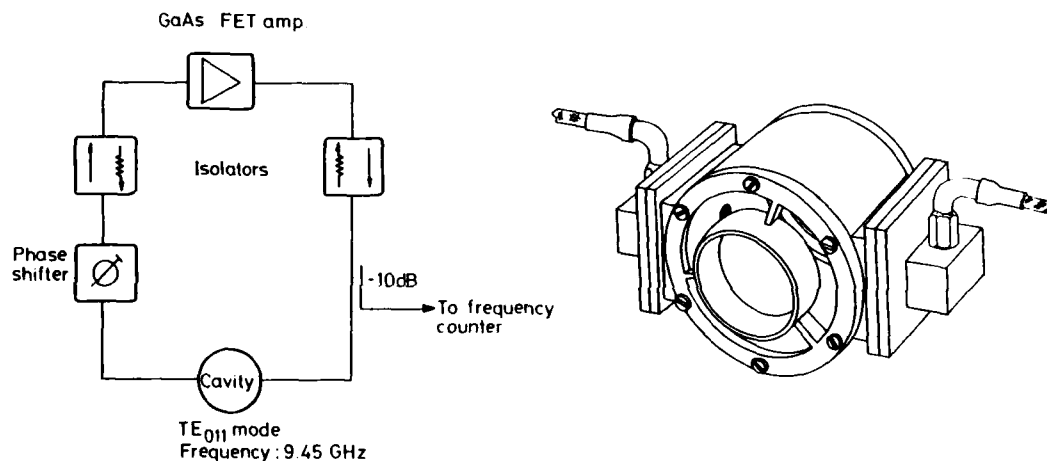


Figure 1. Refractometer block diagram and cavity. Inside diameter of cavity is 41.5 mm.

The annular-tube end plates are placed at what would be the ring of maximum current in a continuous wall plate, and the diameter of the tube is such that propagation within it is highly evanescent. By this means 92% of the cavity end plates have been removed. As is apparent from the high Q value, coupling through the end plates is minimal, and objects can be brought close to these plates without affecting the frequency of resonance, i.e. the sampling is of air within the cavity only.

The refractometer is based on a GaAs FET amplifier operating in a positive feedback loop at the resonant frequency of the sampling cavity. For the nominal cavity resonance frequency of 9.45 GHz, a change of 1 N unit is indicated by a change in frequency of 9.45 kHz. Consequently, to accommodate changes of 400 N units, the components must have a bandwidth of about 4 MHz. In normal operation the amplifier has a gain of 18 dB, but in the refractometer it is run near saturation with an output power of +16 dBm. Attenuation in the feedback loop is 10.5 dB. The sensitivity of the frequency counter is -30 dBm, and it is situated at the end of a cable having 20 dB loss. The isolators at the amplifier terminals attenuate any reflected power by 20 dB, thus minimising any mismatch introduced through the directional coupler and the phase shifter. Apart from the waveguide couplings to the cavity, all other connections are coaxial. The current requirement is 100 mA at a nominal 12 v. A voltage regulator in the FET amplifier package ensures that neither the frequency nor the power output of the refractometer is sensitive to supply voltage changes down to 8.5 v.

The two 230 mm long coaxial cables connecting the sampling cavity to the other refractometer components were chosen in preference to semi-rigid cable due to their phase stability with both temperature and flexing. Waveguides were rejected because of their bulk, vibrational problems and complexity of avoiding condensation. Noise on the refractometer output has proved no more during flight or ground movements than is encountered in the laboratory (i.e. less than 0.1 N unit).

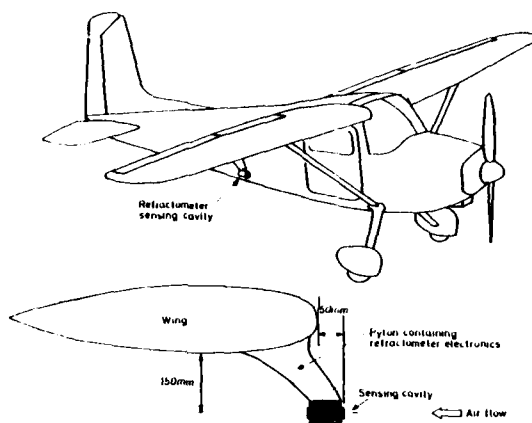
As the refractometer is sensitive to changes in humidity, temperature and atmospheric pressure initial tests were done with the whole instrument mounted in a tank of dry nitrogen for which the temperature and pressure could be varied. Under constant conditions, the stability (over several minutes) was found to be 1 part in  $10^8$ , i.e. 0.01 N unit. Changing the pressure of the nitrogen (at a constant temperature) confirmed (within experimental error) the linear 9.45 kHz/N unit relationship indicated from equations (1) and (2).

By varying the temperature (at a constant pressure) a temperature coefficient of 0.72 N unit/ $^{\circ}\text{C}$  was found after subtracting the effect of the refractive index of nitrogen. Consideration of the temperature coefficients of the feedback loop and of the cavity showed that 0.2 N units/ $^{\circ}\text{C}$  are due to the former, and 0.4 N units/ $^{\circ}\text{C}$  to the latter. In due course, it is intended to record the temperature of the sampling cavity and that of the other components in order to apply suitable corrections to the measured frequency. This will enable absolute refractive index to be obtained. In the meantime, useful relative refractive index measurements are made when the aircraft passes through atmospheric layers, since the temperature change of the sampling cavity and other elements is relatively slow.

### 3. AIRCRAFT USE

For the research objectives discussed in the Introduction, the refractometer has been mounted on a Cessna 175 aircraft in the manner indicated in Figure 2. It is 3.6 m from the centre of the 2.1 m diameter propeller. The front of the cavity leads the wing by 50 mm and its centre line is 150 mm below the wing. It is held rigidly by a stiff mounting plate and aligned to the air flow direction. The remainder of the refractometer components are mounted on this plate inside an aerodynamic pod which extends from the wing to within 30 mm of the sampling cavity. The waveguide-to-coaxial transformers present minimum air disturbance, indeed, the mounting is considered to give optimum sampling of undisturbed air. Including the other refractometer components inside the pod shields them from rapid temperature changes, wind pressure and precipitation. Ambient air temperature is not expected to change by more than some 3 to 5 $^{\circ}\text{C}$  within a 500 m height interval during a sequence of measurements.

Figure 2. Refractometer mounting on Cessna 175 aircraft.



A block diagram of the airborne data-processing equipment is shown in Figure 3. The system is based on an EXORset 33 microcomputer, which comprises a central processor, memory, input/output cards, power supplies, visual display unit, twin floppy-disk handlers and keyboard. The frequency counter enables data to be recorded at 24 readings per second with 100 Hz (0.01 N) resolution. The sensor interface allows air temperature to be recorded, and a further 15 channels are available for future sensors (e.g. thermometers on the sampling cavity and other refractometer components, and an airborne psychrometer). The encoding altimeter is an optically-encoded aneroid barometer, from which a binary code has been derived for recording. The instrument signals altitude increments every 30 m against the standard airways setting of 1013.2 mB. The power inverter can provide up to 500 W of 50 Hz power from the aircraft 14 V alternator. The power consumption of the computer and frequency counter amounts to some 300 W.

It is intended that additional navigational parameters be mounted in due course. On-board processing of data will be undertaken displaying to the operator the height at which distinct temperature and refractive index changes occur.

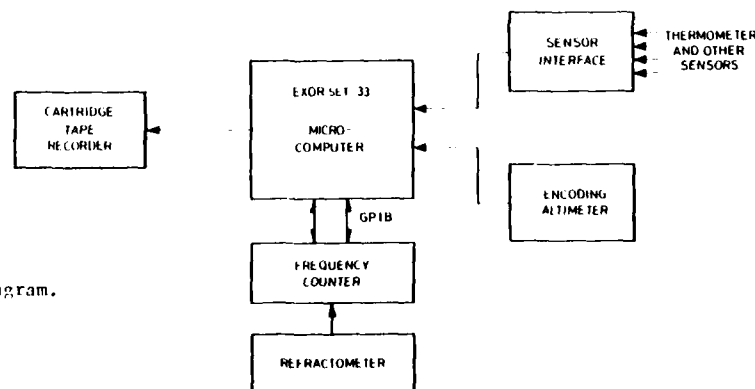


Figure 3. Equipment block diagram.

4. SAMPLE RESULTS

Figure 4 shows relative refractive index,  $N$  and temperature as a function of aircraft height during a descent at 110 m/min (curve 'a', 1609 to 1611 GMT) and an ascent at 150 m/min (curve 'b', 1612 to 1614 GMT) on 13th October 1982. The horizontal separation of the two data sets was about 8 km. Profiles of mean lapse rate for temperate regions (40 N/km) and dry adiabatic lapse rate of 10°C/km are shown for comparison. Curve 'a' shows a marked temperature inversion of 10°C/km (increase with height) between 880 m and 930 m whilst the rate of change of refractive index averages 212 N/km in this region. (It is considerably more than this within a narrow height interval.) Curve 'b' shows a refractive index lapse rate nearly as large as this but without a temperature inversion, in a height interval lower than that in 'a'.

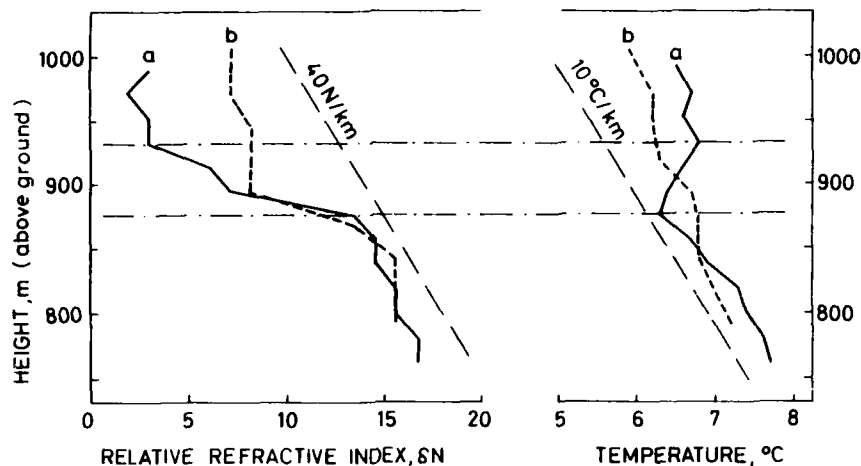


Figure 4. Descent (curve 'a') and ascent (curve 'b') on 13th October 1982.

Figure 5 shows an example of a layer observed with the full resolution of the data acquisition system (24 frequency readings per second), on 31st August 1983. The region of high refractive index lapse rate (6.1 N units over a 7 m height i.e. 871 N/km) occurs with regions of approximately 40 N/km above and below. At 1350 m, a change of about 3 N units occurs within 1 m height. Over very narrow height intervals much larger lapse rates (positive and negative) are observed but these may not have horizontal continuity. It is noteworthy that temperature (available only once per second) does not show any marked change with height. During these measurements the aircraft was descending at 150 m/min in clear air. On the rare occasion when it was necessary to fly through cloud, condensation in the cavity produced very large changes in apparent refractive index but these were easily discernable from clear air events. Experience has shown that it is easier to maintain a consistently uniform rate while descending and altimeter hysteresis is avoided by recording during descents only.

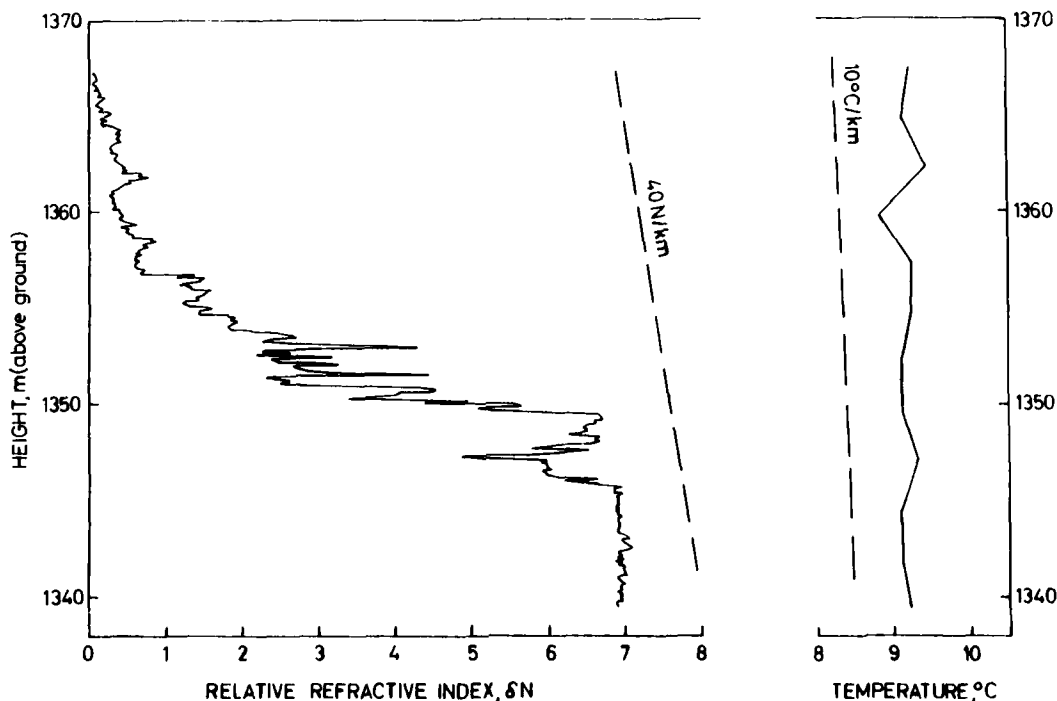


Figure 5. Microstructure of an atmospheric layer on 31st August 1983.

## 5. CONCLUSIONS

The use of a GaAs FET amplifier in a feedback loop containing a resonant cavity has produced a compact and lightweight refractometer operating at X-band. Recording is by way of a frequency counter, a microcomputer and floppy-disc. The system has been installed in a light aircraft and used to produce preliminary data. This has shown the microstructure of refractive index changes within atmospheric layers, although the full potential is yet to be realised. Future developments should give refractive index values in absolute units rather than relative to an arbitrary zero and an on-board display of the height at which distinct changes of air temperature or refractive index occur.

## ACKNOWLEDGEMENTS

The dry nitrogen constant temperature and pressure tests were undertaken by Mr. G.F.D. Levy. The authors are indebted to him, Mr. S. M. Cherry and several other colleagues for extremely helpful discussions and advice.

## REFERENCES

1. M. C. Thompson Jr., F. E. Freethy, D. M. Waters, "End plate modification of X-band TE<sub>011</sub> cavity resonators", *Trans. IEE, MTT*7, 1959, pp. 388-389.
2. C. M. Crain, "Apparatus for recording fluctuations in the refractive index of the atmosphere at 3.2 cm wavelength", *Rev. Sci. Ins.*, 21, 1950, p. 456.
3. G. Birnbaum, "A recording microwave refractometer", *Rev. Sci. Ins.*, 21, 1950, p. 169.
4. W. Steffen, "A battery operated small size microwave refractometer", *Hochfrequenztech u Elekt Akust*, 70, 2, 1961, p. 47.
5. C. S. Fowler, R.J.B. Champion, J. N. Tyler, "A three-cavity refractometer and associated telemetry equipment", *Rad. and Elec. Eng.*, 32, 1966, pp. 186-190.
6. M.P.M. Hall, "Radiosondes for radiometeorological research", NATO Advanced Study Institute Proceedings: 'Statistical methods and instrumentation in geophysics', Teknologisk Forlag, Oslo, Norway, 1971.

## DISCUSSION

K.D. Anderson (U.S.): On your Figure 5, you show a very large refractivity gradient, but the temperature profile does not indicate any inversion. Is there a reason for this?

M.P.M. Hall (U.K.): We too were a little surprised by the lack of temperature change. However, a large refractive index decrease can be caused by various meteorological mechanisms, and need not always be accompanied by a temperature inversion. Hall and Comer (Proceedings of the IEE, 116, pp 685-690, May 1969) examined 488 special soundings of temperature and humidity with measurements made each 75 m up to 1200 m. Taking the height interval of largest refractive index lapse rate (most negative gradient), the median contribution for temperature alone was 0 N/km (i.e., no temperature change with height as median condition), whilst that due to humidity was 53 N/km. For layers of lapse-rate greater than 120 N/km, the figures became 14 and 127 N/km respectively, but the temperature increased with height (positive contribution to refractive index lapse rate) for only about 85% of occasions.

S.G. Gathman (U.S.): What is the effect of hydrometeors on the performance of the device? Can these effects be distinguished from normal operation?

M.P.M. Hall (U.K.): Water on the cavity walls, either by condensation or by precipitation, causes a major shift in the resonant frequency of the sampling cavity, and is very clearly distinguished from changes in the refractive index of the air. Drying of the cavity surface is rapid on the airborne refractometer once one flies out of the source of water. Our measurements are of clear air events, and we normally avoid clouds.

W.G. Burrows (U.K.): I would like to enquire whether the refractometer head has been subjected to wind tunnel studies. The structure at the front of the cavity could conceivably give rise to inequalities in the air flows through the cavity at different air speeds, e.g., stagnation, pressure points, etc., and therefore errors in refractivity values.

M.P.M. Hall (U.K.): A study of an earlier refractometer by Bussey and Birnbaum (Journal Res. NBS, vol 51, 1953), using a cavity with only 30% of the end plates removed and placed in a wind tunnel with air speeds up to 270 km/hour, showed the experimental error due to air density change within the cavity to be less than 0.5 to 1.0 N unit. Land, Froome, and McConnell (Proc. IEE, vol 108B, p 398, 1961), with 60 to 70% of the cavity end plates removed, found that wind speeds up to 400 km/hour had negligible effect on measured refractive index. No measurement has been made on the present cavity, which has 92% of the end plates removed. Stagnation of the air within the cavity may be a problem with certain balloon-borne devices, but not for those mounted on an aircraft.

R. G. Blake (U.K.): Since many of the refractive index variations affecting LOS microwave links occur as the result of radiation night cooling and at lower altitudes than that appearing as an example in your paper, would not the airborne equipment have limited use in these situations?

For elevated daytime ducts causing trans-horizon propagation interference, then this instrument should be invaluable.

M.P.M. Hall (U.K.): Fortunately, the "low-level" events, described in the first part of your comment, persist until they are destroyed by solar heating about mid morning. We are not seeking refractive index data on a statistical basis, but for case studies, and will not fly our refractometer at night.

# PREDICTION OF MULTIPATH FADING ON TERRESTRIAL MICROWAVE LINKS AT FREQUENCIES OF 11 GHz AND GREATER

by  
Douglass D. Crombie  
National Telecommunications and Information Administration  
U.S. Department of Commerce  
Boulder, Colorado 80303  
United States of America

## SUMMARY

Published data on the probability of multipath fading on different paths with lengths up to 45 km, at frequencies up to 37 GHz, measured in different countries, have been analyzed. For the paths which have probabilities greater than  $\sim 10^{-3}$  for 20 dB fades, it is found that the fading probability increases with antenna beam width. In addition, it is found that increasing the clearance of the path above surrounding terrain reduces the fading probability. Inclusion of these two variables, in addition to frequency and path length, reduces the uncertainty in prediction of fading probability by a factor of 80.

## 1. INTRODUCTION

Traditionally, microwave communication links suffer from two major causes of signal loss leading to unreliable operation: attenuation caused by precipitation, and destructive interference between the direct ray and other rays originating from ground reflection or in the atmosphere. The latter, commonly called multipath fading, is the subject of this paper.

On narrow band links (those for which the bandwidth is much less than the reciprocal of the delay between multipath components) the effects of multipath fading is simply to cause reduction of signal strength or deterioration of signal-to-noise ratio. Such problems can, in principle, be overcome by increasing transmitter power, or by using space or frequency diversity. On wider bandwidth links the effects of multipath are more complicated. Destructive interference can occur in different parts of the signal spectrum, giving rise to selective fading. In systems using analog modulation [1,2], selective fading causes distortion which in turn causes intermodulation noise. With digital modulation [3,4] the multipath provides echoes of the wanted signal which in turn causes intersymbol interference. In neither case can selective fading be overcome by increasing transmitter power.

Barnett [5] and Rutherford [6] developed a widely used model for predicting the probability of multipath fading as a function of path length and frequency, modifications of which have been adopted by the CCIR [7].

In the CCIR model, for fades greater than 15 dB, the probability  $P(\frac{w}{w_0})$ , of a signal level less than  $w$  is given by

$$P(\frac{w}{w_0}) = KQ \frac{w}{w_0} d^B f^C \quad (1)$$

where  $d$  = path length (km)  
 $f$  = frequency (GHz)  
 $K$  = climate factor  
 $Q$  = terrain factor  
 $w$  = received signal power  
 $w_0$  = received power in non-fading conditions.

The formula may not be applicable for very small values of  $d$ .

Many values of  $B$ ,  $C$ ,  $K$  and  $Q$  have been proposed for application in various parts of the world [7]. These values have been determined from analysis of empirical data. For example, values of  $C$  range from 0.85 to 1.5; and of  $B$  from 2.0 to 3.5. Values of the product  $K.Q$  show greater variability, and different functional forms have been used. In some cases,  $K.Q$  is identified as being dependent on the standard deviation of the elevation of the terrain between antennas (measured at 1 km intervals). In other cases,  $K.Q$  is a function of the RMS value of the terrain slopes (in milli-radians) measured at 1 km intervals along the path. Additionally,  $K.Q$  has been expressed as a function of antenna heights. Finally, some workers use empirical numerical values of  $K.Q$  which depend on the nature of the terrain and climate alone.

Most of the empirical data used in defining  $B$ ,  $C$  and  $K.Q$  have been obtained at frequencies of 11 GHz or less. In the present work, the objective is to obtain a formula such as that shown in Eq.(1) which is applicable to frequencies of about 11 GHz or higher. In addition, because of the great variability of the values suggested for the coefficients  $K$  and  $Q$ , the possibility of eliminating them is examined. Specifically, the effects of antenna beamwidth and of physical clearance of the center of the path above the ground are investigated, in addition to the effects of path length and frequency.

Thus a formula analogous to Eq.(1) of the form

$$P(\frac{w}{w_0}) = A(\frac{w}{w_0}) d^B f^C \Theta^D h^E \quad (2)$$

is sought, where  $A$ ,  $D$ ,  $E$  are constants,  $\Theta$  is a measure of antenna beamwidths, and  $h$  is the estimated height above the intervening terrain at the center of the path. The other symbols have the same meaning as in Eq.(1).

## 2. DATA USED FOR ANALYSIS

Data used in this analysis have been obtained from several sources. The primary source is work of the British Post Office [8] which contains a very comprehensive set of long duration measurements at frequencies between ~11 GHz and 37 GHz over path lengths ranging from 4 km to 58 km. In addition, earlier data obtained by the British Post Office on 11 GHz on two other paths has been used [11]. Additional data obtained in the U.S.A. [5], Denmark [9], and Japan [10] have also been used. Criteria used in selection of the data for analysis are:

1. Frequency of 11 GHz or greater.
2. Antenna beamwidths known or obtainable.
3. A measurable probability ( $\sim 10^{-3}\%$ ) for the worst month of fades  $> 20$  dB.
4. Duration of measurements of at least one month.
5. No evidence that the terrain clearance would be less than 0.577 Fresnel Zones when the effective earth radius factor  $k$  was 2/3.
6. Availability of path profiles.

The limited available data believed to meet most of these criteria are listed in Table I. For some paths, all the criteria were not met. But, because of the need to maximize the data base for increasing the significance of the results, this data has been used for restricted models. (However, data for three paths [8,11] were omitted because the fading depth did not reach 20 dB during the measurements.) The columns of Table I contain the path number, path description, the % probability of fades of 20 dB or more,  $P(.01)$ , for the worst month; the path length,  $d$ (km); the nominal frequency,  $f$ , in GHz; the nominal beamwidths,  $\theta$ , in mR together with their geometric mean when not equal; the estimated path clearance,  $h$ (m), at the center of the path; the duration of the measurements (months); and, finally, reference to the source of the data.

Table I. Characteristics of Propagation Paths Used

Path Number	Path	$P(.01)$ % Probability of Fades $> 20$ dB	$d$ Path Length (km)	$f$ Nominal Frequency (GHz)	$\theta$ Nominal Beamwidths (mR)	$h$ Estimated Path Clearance (m)	Duration of Measurement (months)	Reference
1.	Crowfield-Mendlesham (UK)	0.04	7.5	10.95	58/58	30	37	(8)
2.	Crowfield-Mendlesham (UK)	0.035	7.5	19.65	32/32	30	50	(8)
3.	Crowfield-Mendlesham (UK)	0.011	7.5	36.3	17/17	30	43	(8)
4.	Somersham-Mendlesham (UK)	0.05	16.6	11.65	36/36	40	37	(8)
5.	Somersham-Mendlesham (UK)	0.10	16.6	20.3	16/16	40	37	(8)
6.	Somersham-Mendlesham (UK)	0.06	16.6	37.0	17/17	45	34	(8)
7.	Martlesham-Mendlesham (UK)	0.25	22.8	20.95	15/15	35	45	(8)
8.	Forder Battery-Caradon Hill (UK)	0.0008	26.4	10.92	8.7/8.7	160	41	(8)
9.	Dalton-Quernmore (UK)	0.005	31.7	10.84	8.7/8.7	130	33	(8)
10.	Tinshill-Stillingfleet (UK)	0.008	34.9	10.84	8.7/5.8 (7.1)	63	34	(8)
11.	Stillingfleet-Cavewold (UK)	0.04	36.2	11.37	5.8/8.7 (7.1)	80	34	(8)
12.	Copenhagen (Denmark)	0.5	44.7	14.25	21.8/21.8	32	12	(9)
13.	Pleasant Lake-West Unity (USA)	0.69	45.9	11	20.9/20.9	40	2.3	(4)
14.	Shiroyama-Kosuzumel (Japan)	0.008	35.6	11	8.4/8.4	?	~1	(10)
15.	Shiroyama-Kosuzumel (Japan)	0.033	35.6	18.0	9.4/9.4	?	~1	(10)
16.	Purdown-Pen Hill (UK)	0.01	27.8	10.92	13/13	?	31	(8)
17.	Sibleys-Kelvedon Hatch (UK)	0.10	31.0	11	6/6	30	12?	(11)
18.	Greenmore Hill-Dollis Hill (UK)	0.30	58.0	11	6/6	30	12?	(11)

## 3. ANALYSIS OF DATA

As discussed above, there is a wide range of possible values for the coefficient  $K, Q$  of Eq.(1), depending on geographic location. Because of this, and because the available data given in Table I covers a wide range of geographic locations, by choice, an attempt was made to fit a limited equation of the type shown in Eq.(1) to the data using linear regression. Equation 1 can be written as:

$$\log P\left(\frac{W}{W_0}\right) = \log A' + \log (w/w_0) + B \log d + C \log f,$$

where the logs are base 10. The multipath fading probabilities shown in Table I are for fades equal to or greater than 20 dB. Thus,  $\log (w/w_0)$  is a constant ( $= -2$ ), and  $A'$  is a constant representing the effective value of  $K, Q$  in (1) for all paths used. The terms in  $A$  and  $w/w_0$  can then be lumped together with:

$$\log A = \log A' + \log (w/w_0),$$

giving:

$$\log P(.01) = \log A + B \log d + C \log f. \quad (3)$$

The data shown in Table I have been analyzed in three groups. The first group contains all the data. Information about the physical path clearances are missing for paths 14-16. Thus, the analysis is confined to the effects of path length, frequency and beamwidth, and is discussed in Sect. 3.1. and 3.2. All the paths in this group, except two (i.e., 17 and 18) are believed to meet criterion number 2 of Sect. 2. As a result, a further analysis is made in Sect. 3.3. of the remaining 16 paths. Finally, analysis is made in Sect. 3.4. of the group of data (paths 1-13 together with 17 and 18) for which the physical clearance can be estimated. In that analysis the effects of path clearance are included.

### 3.1. Effects of Path Length and Frequency (All Paths)

Using the data shown in the first 3 numerical columns of Table I, the linear regression fit yields the following values for A, B, C.

Table II. Regression Results - All Paths, d, f (Model 1)

Coefficient	t	
$A_1 = -4.424$		$F_1 = 0.978$
$B_1 = 1.045$	1.31	$s_1 = 0.766$
$C_1 = 1.351$	1.11	$R_1^2 = 0.115$

where t and F are Student's t and the variance ratio statistics, respectively, and R is the multiple correlating coefficient. The fraction of the variation of  $\log P(.01)$ , which is due to regression, is equal to  $R^2$ . Because there are 2 independent variables and 15 degrees of freedom, the critical values of t and F for a 5% significance level are 2.13 and 3.68, respectively. Thus the regression is meaningless and the observed data cannot be represented by a model of the type shown in Eq.(1). A comparison between the predicted and measured fading probability is shown in Fig. 1a.

In addition to the use of the F statistic, a convenient means of visualizing the goodness of fit of the regression surface to the data is the standard error, s, given by:

$$s = \sqrt{\sum_i (P_i - M_i)^2 / (n - k - 1)} ,$$

where  $M_i$  and  $P_i$  are the measured values and the predicted values of  $\log P(w)$  for the  $i^{\text{th}}$  path, n is the number of paths and k is the number of independent variables. With a large sample in which the residuals,  $P_i - M_i$ , are normally distributed, about 95% of the residuals will lie within  $\pm 2s$  of the regression surface (measured in the P direction). Accordingly, the values of s are given for this and subsequent calculations, and are shown in the relevant figures.

### 3.2. Effects of Antenna Beamwidth

In view of the inadequacy of using only path length and frequency, the effects of including antenna beamwidth were investigated. The beamwidths of the antennas used on the various paths are listed in Table I for both antennas on each path. For analysis, the geometric mean of the two beamwidths was used for the  $\Theta$  term of the new regression equation

$$\log P\left(\frac{w}{w_0}\right) = \log A + B \log d + C \log f + D \log \Theta , \quad (4)$$

$$\text{where } \Theta = \sqrt{\Theta_T \cdot \Theta_R} .$$

The regression analysis yielded the results shown in Table III.

Table III. Regression Results - All Paths, d, f,  $\Theta$  (Model 2)

Coefficient	t	
$A_2 = -10.162$		$F_2 = 4.29$
$B_2 = 2.846$	3.32	$s_2 = 0.608$
$C_2 = 1.939$	1.97	$R_2^2 = 0.479$
$D_2 = 2.264$	3.12	

With 3 independent variables and 18 data sets, there are 14 degrees of freedom. Thus, at the 5% significance level, the critical value of t is 2.145 and of F, 3.34. Thus the overall regression is quite significant (because  $F_2 > 3.34$ ) even though the significance of the frequency coefficient is marginal.

### 3.3. Analysis for Paths with Adequate Fresnel Zone Clearance

The data analyzed in the previous Section contain two paths [11] for which the Fresnel Zone clearance (criterion No. 5 of Section 2) may not always be achieved, although the physical clearance is known. Deletion of these paths yields a model for predicting the fading probability of paths with adequate Fresnel Zone clearance. Analysis of the remaining data leads to the new set of coefficients shown in Table IV. The fit has been improved by deleting the data for the two inconsistent paths as can be seen from comparing Tables III and IV and Figures 1 and 2.

Table IV. Paths with Adequate Fresnel Zone Clearance - d, f,  $\Theta$  (Model 3)

Coefficients	t	
$A_3 = -12.230$		
$B_3 = 3.096$	4.88	$F_3 = 11.78$
$C_3 = 2.454$	3.42	$s_3 = 0.432$
$D_3 = 3.111$	5.53	$R_3^2 = 0.747$

In this case, there are now 3 independent variables and 12 degrees of freedom. At the 5% significance level, the critical values of t and F are 2.179 and 3.49. Clearly, as shown in Fig. 2b, the correlation is very marked, being significant at less than the 0.5% level. Without the beamwidth term, the regression analysis (Fig. 2a) gives results which are very similar to those obtained for the whole data set. That is, there is no statistically meaningful dependence of fading probability on the path length and frequency.

#### 3.4. Effect of Physical Path Clearance

In view of the apparent importance of Fresnel Zone clearance noted above, the use of physical path clearance in some geographical areas, and other indications [12], additional analysis using the path clearance term was done. In this case, the variable used, h, was simply the mean height of the line-of-sight (assuming a 4/3 earth radius) above the terrain at the center of the path. This data was not available for paths 14 and 15, and the available data for path 16 was uncertain. As a result, these three paths were omitted, leaving a total of 15 paths and 10 degrees of freedom.

The new regression equation is now of the form

$$\log P\left(\frac{W}{W_0}\right) = \log A + B \log d + C \log f + D \log \Theta + E \log h. \quad (5)$$

The results of the analysis are shown in Table V and in Fig. 3c

Table V. Paths with Known Clearance, d, f,  $\Theta$ , h (Model 4)

Coefficients	t	
$A_4 = -2.997$		
$B_4 = 2.487$	5.42	$F_4 = 20.18$
$C_4 = 0.840$	1.49	$s_4 = 0.298$
$D_4 = 1.190$	2.88	$R_4^2 = 0.889$
$E_4 = -2.440$	-5.89	

With four independent variables and 10 degrees of freedom, the critical value of F at the 0.5% level is 7.34. Because the value calculated above, 20.18, is much greater than this, the regression is even more significant. The statistical significance of each variable, except f, is also high.

Deletion of the fourth variable, h, gives the results shown in Table VI and Fig. 3b.

Table VI. Paths with Known Clearance, d, f,  $\Theta$  (Model 5)

Coefficients	t	
$A_5 = -9.988$		
$B_5 = 2.931$	3.21	$F_5 = 3.78$
$C_5 = 1.860$	1.72	$s_5 = 0.635$
$D_5 = 2.171$	2.84	$R_5^2 = 0.507$

In this case, we have 15 data sets and 3 independent variables giving 11 degrees of freedom. The critical value of F at the 5% level of significance is then 3.59 and the overall regression is thus significant at this level. The goodness of fit is, however, materially worse than that obtained when clearance is included. Removal of the third variable,  $\Theta$ , yields similar results to those obtained previously - absence of any significant correlation, as shown in Fig. 3a. Figure 3 also shows that inclusion of  $\Theta$  and h, in the regression equation, reduces the range of uncertainty in the predictions by a factor of  $\sim 80$ .

#### 4. COMPARISON WITH OTHER MEASUREMENTS

Because of the paucity of other data meeting the requirements, it is somewhat difficult to make adequate comparisons. Only two additional sources (13, 14) of data in the relevant frequency range have been identified. Although adequate Fresnel Zone clearance apparently occurs on these paths, detailed terrain profiles are not provided and the duration of observations is smaller than desired.

Measurements at  $\sim 11.5$  GHz on two paths (near Atlanta, GA) of lengths 42.5 km and 25.6 km are summarized by Lin [13]. Observations were made for a period of 6 1/2 months (280800 minutes) using antennas having beamwidths of  $\sim 13$  mR. Multipath fading of depth  $> 20$  dB occurred for 600 minutes (0.21%) and 30 minutes (0.11%), respectively on the two paths. Because these are total values for the observation period, the worst month value is presumably larger. Application of Eq.(4) with coefficients from Table IV gives  $P(.01) = 0.078\%$  for the 42.5 km path and 0.016% for the shorter path. Because the calculated values should refer to the "worst month", the agreement with the observed values is quite good. The results are plotted on Fig. 2b.

The second set of data is reported by Butler [14] for two sets of frequencies near 11 and 16.7 GHz in the vicinity of Ottawa, Canada. The path length was 16 km and the antenna beamwidths were 26.2 mR and 34.9 mR, respectively. Path profiles are not described, but adequate Fresnel Zone clearance was provided. Data covering a period of 153 days (May to September, 1979) were reported. Multipath fading of depth  $> 20$  dB occurred at 11 GHz for  $\sim 0.006\%$  of the time and at 16.7 GHz for  $\sim 0.002\%$  of the time. There was no apparent concentration of clear-air fading in any month, so that worst month statistics are not available. Application of Eq.(4), with coefficients from Table IV, give values of  $P(.01) = 0.029\%$  at 11 GHz and 0.2% at 16.7 GHz. Again, in view of the fact that the latter values represent worst month values, the agreement for 11 GHz is reasonably good, as can be seen in Fig. 2b. But, at 16.7 GHz, the agreement is very poor.

Butler also made simultaneous observations on a similar path oriented in a different direction, but with its receiver at the same location as the receiver of the previously discussed path. For this path, the fading probability was approximately an order of magnitude less than for the other.

Clearly, these paths appear to be behaving in a peculiar manner, perhaps because of the rather small data sampling period. Because the data on the two paths seems inconsistent, it may not be surprising that data for the two frequency pairs on the two paths are not closely related to each other or to the predictions of this paper.

## 5. DISCUSSION

Apart from some of Butler's [14] results, the available 20 dB multipath fading data seems to be reasonably well modelled by Eq.(4) or (5), with coefficients from Tables IV or V, respectively. Because of the wide variety of locations in which the data were obtained, it is significant that this modelling appears to be feasible without knowledge of climate or detailed knowledge of path terrain. However, particularly because of the discrepancies between some of Butler's data and the predictions of this paper, it is clear that there is room for improvement. Inclusion of climatic or detailed terrain information may be necessary to achieve this improvement.

Two new variables are used in this paper to aid the prediction of multipath fading probabilities. They are (1) antenna beamwidth, and (2) clearance between the ray path ( $4/3$  earth radius) and the average terrain in the vicinity of the center of the path. Because of the high statistical significance of these variables (e.g., as compared with that of frequency), it is of interest to speculate about their physical significance.

The role of antenna beamwidth might be explained, qualitatively at least, if it is assumed (as usual) that indirectly received signals scattered or reflected by atmospheric layers interfere with the direct signal to cause the interferences. If these scattered or reflected signals are received over a finite range of angles comparable with the antenna beamwidths, then the amplitude of the indirect component of the received signal will increase, on the average, with beamwidth. Thus the fraction of time for which the indirect signal is comparable in amplitude with the direct signal will also increase with beamwidth. Although Crawford and Sharpless [15] have observed multipath components (in the vertical plane) as far as 13 mR from the direct ray, a greater angular spread than this appears necessary to account for the results obtained here. However, ground reflections cannot be ruled out because increased antenna beamwidths increase the illuminated ground area under the path.

The role of path clearance is less obvious. Recently, however, Schiavone [16] has suggested that a good predictor of monthly clear air fading probability in one locality, at least (Palmetto, Georgia), is early morning surface wind speed. Increasing wind speeds reduce the probability of fading. It is probably reasonable to assume that this dependence is a result of the removal by the wind of the moisture and temperature irregularities causing reflections. Now, it is well known that wind speed often increases with height. Thus, if Schiavone's result is applicable in other geographic regions, the frequency of occurrence of atmospheric layers causing reflection should decrease with height. This very qualitative argument may explain the strong dependence of fading probability on path clearance exhibited by the data used in this paper.

## 6. CONCLUSIONS

The analysis in this paper suggests that multipath fading probability (on terrestrial paths at frequencies above  $\approx 11$  GHz) can be estimated without detailed knowledge of climate or terrain. Such estimates require knowledge of path clearance and/or antenna beamwidths, in addition to path length and operating frequency.

Without clearance and bandwidth information, as shown in Figs. 1a, 2a, and 3a, no meaningful correlation of fading probability with path length and frequency is found, using the data of Table I. These data cover a wide variety of operating frequencies and path lengths in several countries.

Inclusion of antenna beamwidths increases the predictability of fading probability as shown in the figures. Inclusion of path clearance shows (cf Figs. 3b and 3c) a further increase in predictability.

In these two cases, the percentage of time for which multipath fading,  $\geq 20$  dB, occurs in the worst month can be expressed in the following forms:

Model 5 (variables are  $d, f, \Theta$ ) :  $R = 0.71$

$$\log P(.01) = -9.99 + 2.93 \log d + 1.86 \log f + 2.17 \log \Theta$$

or

$$P(.01) = 10^{-10} \cdot d^{2.93} \cdot f^{1.86} \cdot \Theta^{2.17}$$

Model 4 (variables  $d, f, \Theta, h$ ) :  $R = 0.94$

$$\log P(.01) = -2.997 + 2.49 \log d + 0.84 \log f + 1.19 \log \Theta - 2.44 \log h$$

or

$$P(.01) = 10^{-3} \cdot d^{2.49} \cdot f^{0.84} \cdot \Theta^{1.19} \cdot h^{-2.44}$$

In each case, the logarithms are base 10,  $d$  is the path length in km,  $f$  the frequency in GHz,  $\Theta$  the geometric mean of the antenna beamwidths in mR, and  $h$  is the clearance in meters.

These formulas, and others developed above, represent the behavior of the paths described in Table I fairly well. Thus the formula should be applicable to other paths having similar characteristics to those used in Table I. As noted earlier, these paths cover a wide range of frequencies and path lengths in a number of countries. However, examination of two other independent sets of measurements (each of somewhat limited duration) in Section 4, shows that while predictions for one set match the observations quite well, the reverse is true for the other set. This difference needs further examination.

#### ACKNOWLEDGEMENTS

I would like to express my appreciation to my colleagues H. T. Dougherty, R. H. Ott, and W. F. Utlaut, for helpful discussions, and to the staff of the Post Office Research Centre (Martlesham Heath, UK) for providing information about the elevation profiles of the UK paths.

#### REFERENCES

1. W. R. Bennet, H. E. Curtis and S. O. Rice, "Interchannel Interferences in FM and PM Systems Under Noise Loading Conditions," Bell System Technical Journal, 34, 1977, pp. 645-674.
2. R. G. Medhurst and G. F. Small, "An Extended Analysis of Echo Distortion in the FM Distortion of Frequency Division Multiplex," Proc. IEE, 103B, 1956, pp. 191-198.
3. C. W. Anderson, S. Barber and R. Patel, "The Effect of Selective Fading on Digital Radio," Paper 33.5, ICC 78 Conference Record, Toronto, Canada: IEEE, June 1978.
4. W. T. Barnett, "Measured Performance of a High Capacity 6 GHz Digital Radio System," Paper 47.4, ICC 78 Conference Record, Toronto, Canada: IEEE, June 1978.
5. W. T. Barnett, "Multipath Propagation at 4, 6, and 11 GHz," Bell System Technical Journal, 56, No. 2, 1972, pp. 321-361.
6. C. L. Ruthroff, "Multiple-Path Fading on Line-of-Sight Microwave Systems as a Function of Path Length and Frequency," Bell System Technical Journal, 50, 1971, pp. 2375-2398.
7. CCIR, "Propagation Data Required for Line-of-Sight Radio Relay Systems," CCIR Report 338-4, XV Plenary Assembly, International Telecommunications Union, Geneva, 1982, Vol. V, pp. 279-314.
8. R. L. O. Tattersall and N. E. Cartwright, "Multipath Propagation Data Collected from Tests on Line-of-Sight Radio Paths at 11, 20, and 37 GHz During the Period 1972-1975," Post Office Communication, Research Dept. Report No. 594, 1977.
9. E. T. Stephansen and G. E. Mogensen, "Experimental Investigation of Some Effects of Multipath Propagation on a Line-of-Sight Path at 14 GHz," IEEE Transactions on Communications, Vol. COM 27, No. 3, March 1979, pp. 643-647.
10. U. Sasaki and T. Akiyama, "Characteristics of Fadeout and Fade Speed in Microwave Radio Links," Review of the Electrical Communication Laboratories, 25, No. 3-4, March-April 1977, pp. 315-323.
11. D. Turner, B. J. Easterbrook and J. E. Golding, "Experimental Investigation into Radio Propagation at 11.0-11.5 Gc/s," Proc. IEE, 113, September 1966, pp. 1477-1489.
12. M. S. Wheeler, "Microwave Relay Fading as a Function of a Terrain Clearance Factor," IEEE Trans. on Antennas and Propagation, Vol. AP-25, No. 2, March 1977, pp. 269-273.
13. S. H. Lin, "Impact of Microwave Depolarization During Multipath Fading on Digital Radio Performance," Bell System Technical Journal, 56, 1977, pp. 645-674.
14. R. S. Butler, "Cross-Polarization Discrimination at 11 and 17 GHz," Annales des Telecommunications, 36, No. 7-8, July-August 1981, pp. 466-467.
15. A. G. Crawford and W. M. Sharpless, "Further Observations of the Angle-of-Arrival of Microwaves," Proc. IRE, 34, No. 11, 1946, pp. 845-848.
16. J. A. Schiavone, "Microwave Radio Meteorology: Seasonal Fading Distributions," Radio Science, 18, No. 3, May-June 1983, pp. 369-380.

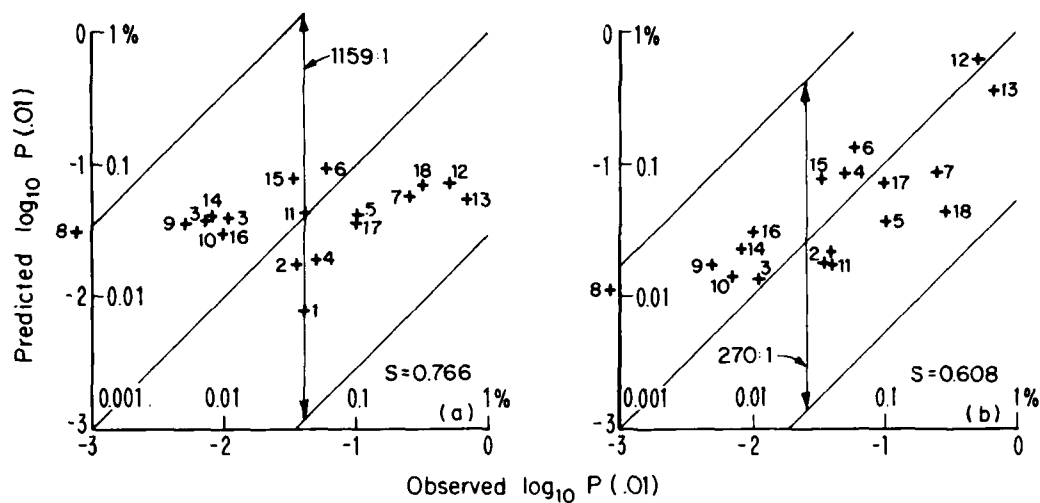


Figure 1. Comparison of observed and predicted probabilities of multipath fading  $> 20$  dB for all paths  
 a)  $d$  and  $f$  as independent variables (Eq.(3), Table II)  
 b)  $d$ ,  $f$ , and  $\Theta$  as independent variables (Eq.(4), Table III)

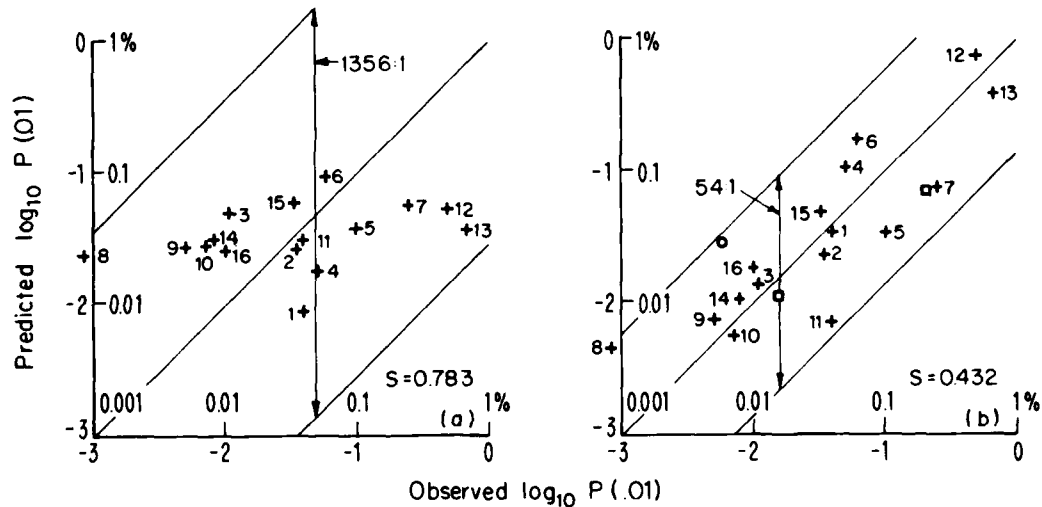


Figure 2. Comparison of observed and predicted probabilities of multipath fading  $> 20$  dB on paths with adequate Fresnel Zone clearance  
 a)  $d$  and  $f$  as independent variables (Eq.(3))  
 b)  $d$ ,  $f$ , and  $\Theta$  as independent variables (Eq.(4), Table IV)  
 + data from Table I  
 □ 11 GHz data from Lin [13]  
 ○ 11 GHz data from Butler [14]

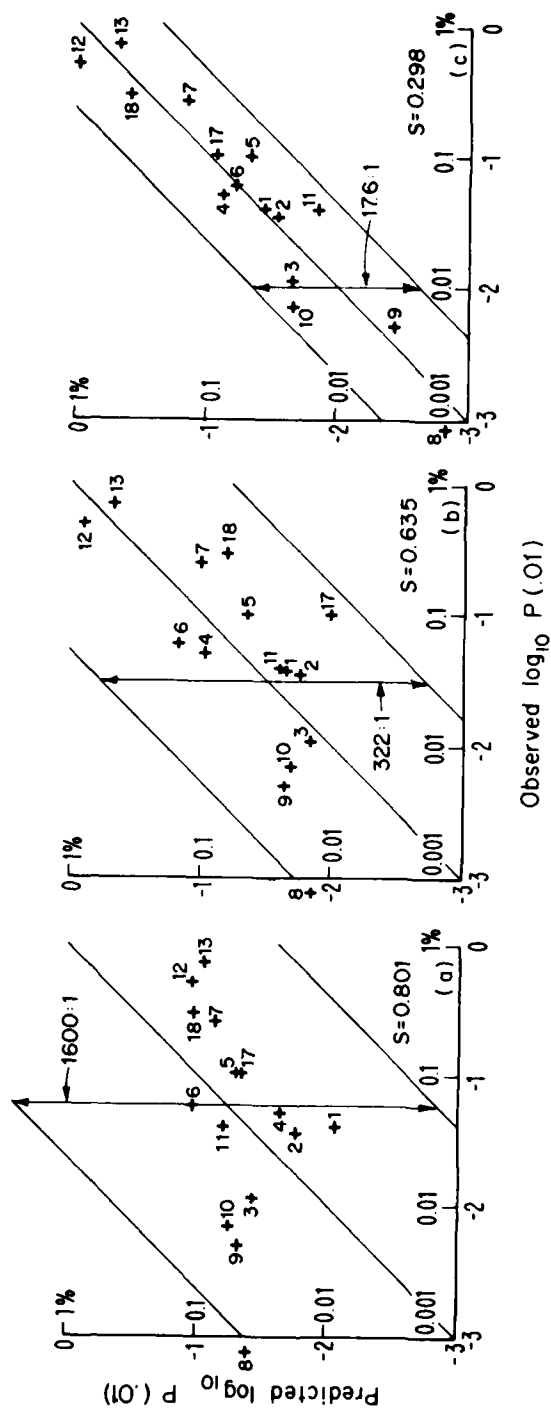


Figure 3. Comparison of observed and predicted probabilities of multipath fading  $\geq 20$  dB for paths with known physical clearance

a)  $d$  and  $f$  as independent variables (Eq.(3))  
 b)  $d$ ,  $f$ , and  $\theta$  as independent variables (Eq.(4), Table VI)  
 c)  $d$ ,  $f$ ,  $\theta$ , and  $h$  as independent variables (Eq.(5), Table V)

## DISCUSSION

J.E. Doble (U.K.): 1) You have suggested that the possibility of multipath fading can be estimated without knowledge of climate or terrain. Have you considered a term to take account of localized factors affecting multipath?

2) In the case of paths 1-7 in your paper, the proximity of the links to the North Sea gives rise to a ducting environment which gives enhanced probability of fading relative to that found in central parts of the United Kingdom.

D.D. Crombie (U.S.): 1) A further product term of the form  $J \cdot x_i$  could be added to Equation (2) in my paper to cover the situation mentioned. The new variable  $x_i$  and the coefficient  $J$  could be determined from the regression analysis of the data which now includes  $x_i$ . To be useful,  $x_i$  should be determined objectively and should not be correlated with the other variables. The analysis would also yield a measure of the significance of the new variable. As an example,  $x_i$  might be the distance of the center of each path from the coastline.

2) If the suggested situation is having an effect, it should be revealed by comparing the statistics for two groups of paths. For example, let us compare paths 1-7 (group A) with paths 8-13 and 17, 18 (group B). Using model 4 (page 10-6 in my paper) to normalize the data, the difference of mean residues for the two groups is approximately 0.069. The standard error of this difference (using Bessel's correction because of the small number of groups of samples in each group) is approximately 0.270. Since the standard error is four times as large as the difference of the means, the difference is statistically insignificant. Thus a difference is not established. Of course, one could use any other prediction model for normalization.

In terms of this paper an apparent difference in the un-normalized data for the two groups could result from the greater beamwidths of the group A paths when compared with those used in group B.

R.G. Blake (U.K.): 1) If the prediction model is concerned with atmospheric-multipath fading, then why should center path clearance have any effect on fading?

2) What happens in a valley?

D.D. Crombie (U.S.): 1) The first point is discussed in the last paragraph of Section 5 - DISCUSSION, of my paper.

2) In terms of my paper, propagation across a valley should result in lower fading probabilities than would be observed for a path, with the same length, antenna beamwidth, antenna heights, and frequency, located on flat land.

T.J. Mouldsley (U.K.): You state in your paper that the statistical significance of the coefficient of frequency ( $f$ ) is not high.

Could you comment further on this, and state whether it is necessary or desirable to include frequency dependence in your model?

D.D. Crombie (U.S.): In general, when the coefficient of a variable is statistically insignificant, it should be deleted unless the contribution of the variable is numerically important. Its deletion increases the number of degrees of freedom which is desirable when only small quantities of data are available, which is the case here. Deletion of  $f$  in this paper would require recalculation of the regression equation, because the deletion will require alteration of the constant term.

J. Battesti (France): J'estime qu'il est inutile d'avoir un dégagement aussi important que celui que semble recommander l'auteur. Un dégagement très important ne diminue pas la probabilité d'évanouissements dus aux trajets multiples dans l'atmosphère et augmente les risques de réflexion par le sol.



# EFFET DE LA LONGUEUR DU BOND SUR LA QUALITE DES LIAISONS NUMERIQUES A GRANDE CAPACITE

J. BATTESTI  
C.N.E.T. ISSY LES MOULINEAUX  
FRANCE

## SOMMAIRE

Compte tenu de la sélectivité en fréquence des évanouissements dus aux trajets multiples, ces évanouissements produisent une dégradation du signal plus importante que celle d'un évanouissement non sélectif de même profondeur. Tout se passe donc comme si la marge de l'équipement pour les évanouissements était réduite en présence de propagation par trajets multiples, ce qui amène à introduire la notion de marge nette par opposition à la marge brute mesurée dans le cas d'évanouissements non sélectifs.

On montre que pour un signal numérique de caractéristiques données (débit numérique, type de modulation), la marge nette est indépendante de la longueur du bond.

## 1. INTRODUCTION

Sur les liaisons en visibilité, la sélectivité des évanouissements dus aux trajets multiples a pour conséquence un rétrécissement de la bande passante de l'atmosphère. Ce rétrécissement se manifeste sur les liaisons à grande capacité, par un bruit d'intermodulation sur les liaisons analogiques à modulation de fréquence et par une augmentation du taux d'erreur sur les liaisons numériques.

Sur les liaisons analogiques, l'expérience montre que, même avec des capacités de 2 700 voies téléphoniques, le bruit d'intermodulation est négligeable vis-à-vis du bruit thermique provoqué par les baisses de niveau reçu, c'est-à-dire que la qualité est pratiquement la même que si les évanouissements n'étaient pas sélectifs. Si on connaît les caractéristiques des équipements et la loi de distribution des affaiblissements à fréquence fixe sur un bond, on peut calculer la loi de distribution du bruit sur ce bond, et, donc, la qualité de la liaison.

Sur les liaisons numériques, par contre, la sélectivité des équipements provoque une augmentation considérable du taux d'erreur, et la connaissance de la loi de distribution des affaiblissements à fréquence fixe ne permet pas de calculer la qualité d'une liaison.

Cette qualité étant limitée par l'existence d'évanouissements sélectifs, on commencera par donner quelques caractéristiques de ces évanouissements.

## 2. GRANDEURS CARACTERISANT LA SELECTIVITE DES EVANOUISSEMENTS ET LEUR VITESSE DE VARIATION

La variation de l'amplitude d'un évanouissement sélectif en fonction de la fréquence, dans une bande de quelques centaines de MHz, a généralement l'allure représentée fig. 1. Elle est caractérisée par les 3 grandeurs suivantes :

$A_m$  : affaiblissement maximal par rapport à l'espace libre  
 $f_m$  : fréquence pour laquelle l'affaiblissement est maximal (on peut trouver plusieurs valeurs de  $f$ )  
 $A_n$  : affaiblissement minimal par rapport à l'espace libre.

Il n'est pas question de donner ici des statistiques détaillées de ces 3 grandeurs, on signalera seulement que, généralement les fortes valeurs de  $A_m$  ne s'observent que pour des fortes valeurs de  $A_n$ , et que, d'autre part, la variation de ces grandeurs peut être extrêmement rapide. Des mesures effectuées en France sur une liaison de 50 km à 11,5 GHz [1] ont montré que la vitesse de variation de  $A_m$  pouvait dépasser 270 dB par seconde et la vitesse de variation de  $f_m$  2 000 MHz par seconde.

## 3. MARGE BRUTE ET MARGE NETTE

Pour une liaison numérique, on appelle marge brute de la liaison pour un taux d'erreur donné, la profondeur d'un évanouissement apériodique (tel qu'on peut le réaliser en laboratoire à l'aide d'un atténuateur) qui provoquerait ce taux d'erreur. Le taux d'erreur servant à définir la marge est généralement pris égal à  $10^{-3}$  car un taux d'erreur supérieur provoque pratiquement la coupure de la liaison.

On appelle marge nette, pour un équipement donné et pour le bond considéré, la valeur de l'affaiblissement sur fréquence fixe non dépassé durant un temps égal à celui où le taux d'erreur n'a pas dépassé  $10^{-3}$ . On appelle marge nette limite la marge nette qui ne peut être dépassée, quelle que soit la valeur de la marge brute. Pour les liaisons à grande capacité, la valeur de la marge nette limite n'est que peu supérieure à la marge nette obtenue pour une marge brute de 40 dB [2]. On supposera qu'on est dans ce cas, et par suite, on confondra marge nette et marge nette limite. Si on connaît, d'une part, la loi de distribution des affaiblissements à fréquence fixe, d'autre part, la marge nette, on peut calculer le temps de coupure de la liaison. La première peut être déterminée avec une assez bonne précision à l'aide de courbes ou de formules établies pour différents climats (voir rapport 338 du CCIR) ; malheureusement, on ne sait calculer la seconde que dans des cas particuliers, en se basant toujours sur des mesures de marge nette faites sur le bond où la liaison doit être installée, ou sur un bond semblable (même longueur, même rugosité du terrain, même climat) dans la même bande de fréquence. Le nombre de mesures sur la marge nette, effectuées dans le monde, étant extrêmement réduit d'une part, et d'autre part, les mesures ayant été faites dans des climats différents, avec des vitesses de modulation différentes, dans des bandes de fréquences différentes, il est pratiquement impossible de déterminer l'effet de la longueur du bond sur la valeur de la marge nette.

A défaut de mesures directes du taux d'erreur, on peut utiliser des mesures de sélectivité ou des considérations théoriques pour déterminer la loi de variation du temps durant lequel un certain taux d'erreur n'est pas dépassé, et, de là, déduire la valeur de la marge nette.

#### 4. INFLUENCE DE LA LONGUEUR DU BOND SUR LE TEMPS DURANT LEQUEL UN TAUX D'ERREUR DONNE N'EST PAS DÉPASSÉ

Aux U.S.A., une étude expérimentale [3] sur 5 trajets alignés de longueur comprise entre 23 et 57 km a consisté à mesurer le temps durant lequel une différence de valeur donnée en dB existe entre les niveaux reçus sur deux fréquences espacées de 20 MHz dans la bande des 6 GHz. Cette étude a montré que ce temps variait comme le cube de la distance.

Il en a été déduit que le taux d'erreur variait également comme le cube de la distance, car on ne peut estimer qu'à une différence donnée entre les niveaux reçus correspond un taux d'erreur déterminé. Comme dans la région où les mesures ont été faites, l'affaiblissement varie également comme le cube de la distance ; il en a donc été déduit que la valeur de la marge nette était indépendante de la distance.

On peut se demander si ces résultats obtenus aux U.S.A. sont valables dans les climats où les conditions de propagation sont différentes, comme le climat du nord-ouest de l'Europe. Ne disposant pas pour ce climat de résultats de mesures analogiques, nous avons appliqué la méthode suivante pour déterminer, en fonction de la longueur du bond, le temps durant lequel un taux d'erreur n'est pas dépassé ainsi que la valeur de la marge nette.

On a montré [4] que les amplitudes des évanouissements dus aux trajets multiples avaient une distribution qui pouvait se modéliser par une loi de RICE-NAKAGAMI dont les paramètres dépendent, d'une façon déterminée, de la longueur de la liaison.

Or, ce modèle permet non seulement de déterminer la loi de distribution des affaiblissements  $A$  à la fréquence fixe  $f_0$ , mais également celle des affaiblissements  $A_m$ , affaiblissements qui se produisent à des fréquences variables [5].

Pour des longueurs de bond allant de 20 à 80 km, on a tracé les lois de distribution de  $A$  et de  $A_m$  pour le mois le plus défavorable ; on en déduit le temps durant lequel la différence entre  $A$  et  $A_m$  ne dépassait pas une valeur fixée  $n$  dB et on a tracé la loi de variation de ce temps en fonction de la longueur du bond (fig. 2). On trouve la même loi de variation quelle que soit la valeur de  $n$ , pourvu qu'elle soit supérieure à 10 dB.

On peut estimer que cette loi de variation est celle de la durée pendant laquelle un taux d'erreur n'est pas dépassé car à toute valeur de  $n$  doit correspondre un taux d'erreur déterminé.

D'autre part, on a calculé pour les mêmes longueurs de bond que précédemment le temps durant lequel un certain affaiblissement  $A$  était dépassé durant le mois le plus défavorable et on a tracé la loi de variation de ce temps en fonction de la distance. On obtient la même loi de variation, quelle que soit la valeur de  $A$  dès que  $A$  est supérieur à environ 20 dB, c'est-à-dire que la loi de distribution ait la pente de Rayleigh.

Afin de comparer les deux lois de variation ainsi obtenues, on a multiplié les temps obtenus par des coefficients convenables pour que dans les deux cas le temps soit de 100 secondes à 50 km. On a choisi la valeur de 50 km car elle est située à un coude de la courbe représentant la variation de l'affaiblissement en fonction de la distance.

On voit, fig. 2, que les courbes sont à peu près confondues, d'où l'on peut déduire que la loi de variation du temps durant lequel un certain taux d'erreur n'est pas dépassé et celle du temps durant lequel un affaiblissement A n'est pas dépassé sont les mêmes et que, donc, la marge nette est indépendante de la distance.

Ce résultat permet de calculer le temps de coupure d'une liaison numérique quelle que soit la longueur du bond, si une mesure de marge nette a été effectuée dans la bande de fréquence prévue pour cette liaison. Considérons, par exemple, le problème suivant : on demande le temps de coupure d'une liaison à 11 GHz 90 Mbit/s, 8 états de phase sur un bond de 40 km dans la région de Paris. On sait, par ailleurs, que des mesures effectuées dans la même région sur un bond de 58 km ont montré que la marge nette d'une liaison à 11 GHz, 140 Mbit/s, 8 états de phase, était de 28 dB.

La différence entre les marges nettes à 90 et 140 Mbit/s étant de 4 dB, la marge nette de la liaison est donc de 32 dB.

Sur la loi de distribution des affaiblissements à 11 GHz pour un bond de 40 km, on voit qu'un affaiblissement de 32 dB n'est pas dépassé durant  $4,4 \cdot 10^{-5}$  du mois, soit 114 secondes. Ce sera la durée de coupure de la liaison.

#### BIBLIOGRAPHIE

- 1 L. MARTIN : Rates of change of propagation medium transfer functions during relative fadings - Colloque de la commission F de l'URSI - Louvain, 1983
- 2 M. ROORYCK : Dégradation de la qualité due aux trajets multiples dans un système à transmission numérique à quatre états de phase - Annales des Télécommunications 37, n° 11-12, 1977, pp. 541-545
- 3 A. VIGANTS : One year results on distance variation of two-tone amplitude dispersion - IEEE, 1982, communication conference, vol. 1 et 2
- 4 L. BOITHIAS : Distribution statistique des niveaux reçus en propagation par trajets multiples troposphériques - Annales des Télécommunications, tome 36, Mai-Juin 1981
- 5 L. BOITHIAS : Communication personnelle

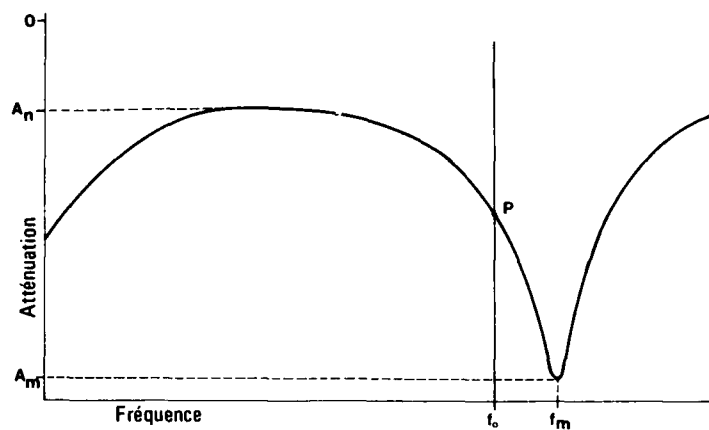


Fig.1 - Grandeurs caractéristiques d'un affaiblissement sélectif.

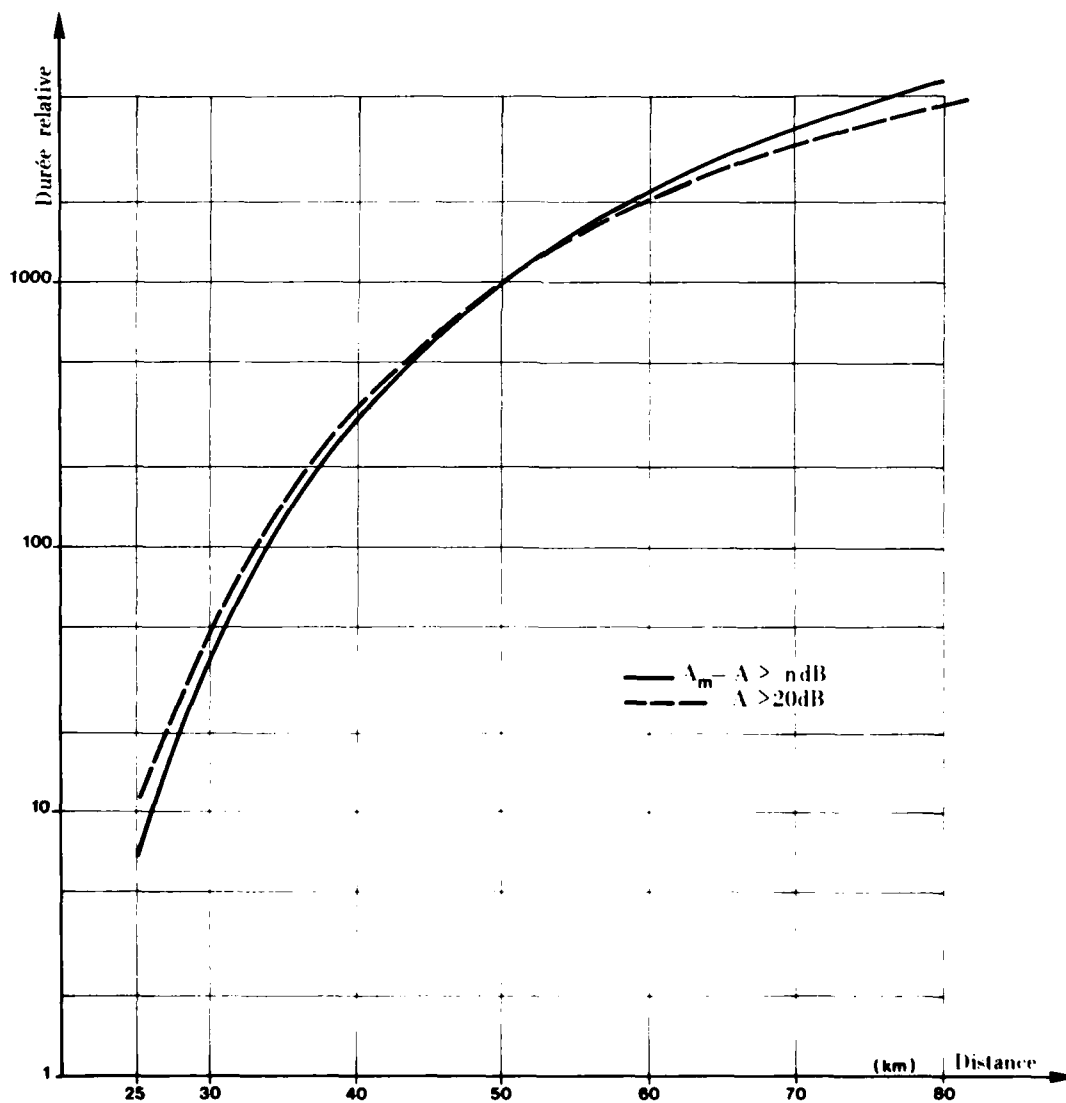


Fig.2 - Relation entre affaiblissement et sélectivité.

AD-P003 892

# MULTIPATH OUTAGE PERFORMANCE OF DIGITAL RADIO RECEIVERS USING FINITE-TAP ADAPTIVE EQUALIZERS

by

N. Amitay and L. J. Greenstein

Bell Telephone Laboratories  
Holmdel, NJ 07733  
U.S.A.

## ABSTRACT

Recent analysis/simulation studies have quantified the multi-path outage statistics of digital radio systems using ideal adaptive equalization. In this paper, we consider the use of finite-tap delay line equalizers, with the aim of determining how many taps are needed to approximate ideal performance. To this end, we assume an M-level QAM system using cosine rolloff spectral shaping and an adaptive equalizer with either fractionally-spaced or synchronously-spaced taps. We invoke a widely used statistical model for the fading channel and computer-simulate thousands of responses from its ensemble. For each trial, we compute a detection signal-to-distortion measure, suitably maximized with respect to the tap gains. We can thereby obtain probability distributions of this measure for specified combinations of system parameters. These distributions, in turn, can be interpreted as outage probabilities (or outage seconds) vs. the number of modulation levels.

A major finding of this study is that, for the assumed multipath fading model, very few taps (the order of five) are needed to approximate the performance of an ideal infinite-tap equalizer. We also find that a simple, suboptimal form of timing recovery is generally quite adequate; and that fractionally-spaced equalizers are more advantageous than synchronously-spaced equalizers with the same number of taps. This advantage is minor for rolloff factors of 0.5 and larger but increases dramatically as the rolloff factor approaches zero.

## 1. INTRODUCTION

Microwave digital radio systems subjected to multipath fading continue to be the focus of intense study. Many current efforts are addressing the use of space diversity and/or adaptive equalization to meet stringent outage objectives for high-level modulations.<sup>1-13</sup> One recent study<sup>14</sup> has combined analyses of such techniques with Monte Carlo simulations of the channel fading responses, using published statistical models of multipath fading.<sup>15,16</sup> We will do the same here, and thereby obtain probability distributions of key performance measures.

Most equalizer studies to date have assumed ideal structures (i.e., transversal filters with infinite taps and optimal tap gains) and optimal timing recovery. The results have served to quantify the limits of achievable performance. With this accomplished, various follow-on questions come to mind, such as: How many taps would suffice in an actual realization? How much does the answer depend on symbol rate and other system parameters? How critical are the method of timing recovery and the spacing between equalizer taps? The study reported here is addressed to these questions.

## 2. SYSTEM DESCRIPTION

The radio transmission is an M-level QAM signal whose baseband pulse has the Fourier transform  $T\sqrt{CR(f)}$ , where  $T$  is the symbol period and  $CR(f)$  is the cosine rolloff function.<sup>17</sup> The cosine rolloff factor  $\alpha$  can lie between 0 and 1 but, for microwave radio, would typically be 0.5 or smaller.

The receiver processing is depicted in Figure 1. The filtering is seen to consist of two stages, one fixed and one adaptive.<sup>†</sup> The fixed filter has the response  $\sqrt{CR(f)}$ , which provides matched filter reception in the absence of multipath fading. The adaptive filter, with response  $H_{eq}(f)$ , is assumed to be a tapped delay line (TDL) equalizer with  $N$  taps and spacings of either  $T$  (synchronous spacings) or  $T/2$  (fractional spacings). The tap gains are controlled adaptively, in gradient search fashion,<sup>17,18</sup> using the mean square error at the detector as the quantity to minimize.

The coherent demodulator stage uses a quadrature pair of local oscillator signals to bring the demodulator inputs to baseband. We make no assumptions about the phase accuracy of the local oscillators, as the action of the

<sup>†</sup> Because the receiver is linear, the order of the fixed and adaptive filters is immaterial for analysis purposes, as is the manner in which each is distributed among RF, IF, and baseband stages.

equalizer is such as to correct for any static phase error.

The demodulator output is a pair of baseband pulse streams (the in-phase and quadrature rails), each of which is sampled every  $T$  seconds in the detector. Data decisions are made by comparing these samples to optimally set decision thresholds. We assume the sampling phase (or *timing epoch*) to be either *optimal* (in the sense that it yields a minimum bit error rate) or *derived* via conventional timing recovery. The latter consists of square-law envelope detection, prior to the equalizer, followed by narrowband filtering of the spectral line at frequency  $1/T$ .

### 3. MULTIPATH FADING MODEL

The multipath fading model used here was derived from data collected on a 26.4-mile path in Georgia in the 6-GHz band. The details - data, methods and results - are well-documented in [15] and [16]. Here we will merely summarize the results, which form the basis of our simulations.

- (i) The expected number of fading seconds on a microwave hop in a "heavy-fading month" (June, July and August) is

$$T_o = 5400c(F/6)(D/25)^3 \quad (1)$$

where  $F$  is the frequency in GHz;  $D$  is the hop length in miles; and  $c$  is the terrain factor, varying between 0.25 and 4.

- (ii) During normal propagation, the relative channel response function is  $H_c = 1 + i0$ . During multipath fading, however, it can be approximated over the channel bandwidth,  $[-W/2, W/2]$ , by the following function:

$$H_c(f) = a[1 - b \exp(-i2\pi f\tau)]; |f| \leq W/2 \quad (2)$$

where  $f$  is referred - here and throughout the paper - to the center frequency of the radio channel;  $W = 40$  MHz, for the 11-GHz common carrier band;†  $\tau$  is a fixed parameter (6.3 nsec); and  $a$  (real) and  $b$  (complex) are parameters that vary slowly with time, but can be regarded as quasi-static. Also  $|b|$  lies between 0 and 1.‡

- (iii) We now define the following:

$$A \triangleq -20 \log_{10} a \quad (3a)$$

$$B \triangleq -20 \log_{10}(1 - |b|) \quad (3b)$$

$$\phi \triangleq \text{Arg}\{b\} \quad (3c)$$

The parameters  $B$  and  $\phi$  are mutually independent random variables across the ensemble of response functions. Their probability density functions (pdf's) are given by

$$p_B(B) = 3.8 \exp(-B/3.8); B \geq 0 \quad (4a)$$

$$p_\phi(\phi) = \begin{cases} 5/6\pi; & |\phi| < \pi/2 \\ 1/6\pi; & \pi/2 \leq |\phi| < \pi \end{cases} \quad (4b)$$

† Strictly speaking, the present model is based on measurements taken over a 25-MHz bandwidth. For convenience in this study, however, we assume a somewhat wider range of applicability.

‡ The issue of "minimum-phase" vs. "non-minimum-phase" is often raised in the multipath fading literature. With  $0 \leq |b| \leq 1$  and  $\tau$  positive,  $H_c(f)$  in (2) is minimum-phase; it would be non-minimum-phase, for the same  $|b|$ , if  $\tau$  were -6.3 nsec instead. The distinction is immaterial in the present study, however, because transversal equalizers respond equally well to both forms of  $H_c(f)$ . (See Sec. 4.4).

(iv) The parameter  $A$  is a gaussian random variable whose mean is a function of  $B$ , i.e.,

$$\bar{A} = 24.6 (500 + B^4) / (800 + B^4) \text{ dB}, \quad (5)$$

and whose standard deviation is  $\sigma_A = 5.0 \text{ dB}$ .

#### 4. PERTINENT PARAMETERS

To begin, we define the following:

$P_s \triangleq$  The squared signal sample (excluding intersymbol interference (ISI) and noise) in either baseband output when a data value of +1 or -1 is being detected;

$P_i, P_n \triangleq$  The mean square ISI and noise, respectively, associated with the periodic samples of either baseband signal;

and

$$\rho_D \triangleq P_s / (P_i + P_n). \quad (6)$$

The latter is the detection signal-to-distortion ratio and can be related to an upper bound on the bit error rate (BER) via<sup>14</sup>

$$BER \leq 2 \exp(-\rho_D/2). \quad (7)$$

This upper bound is particularly conservative when ISI dominates because it is generally peak-limited, in contrast to gaussian noise.

It can be shown that, in an M-QAM system,  $\rho_D$  has the general form

$$\rho_D = \left( \frac{3}{M-1} \right) \gamma; \quad M \geq 4 \quad (8)$$

where the factor  $\left( \frac{3}{M-1} \right)$  represents the influence of  $M$ ; and  $\gamma$  is an involved function of the symbol period ( $T$ ), cosine rolloff factor ( $\alpha$ ), unfaded carrier-to-noise ratio ( $CNR_0$ ), timing epoch ( $t_0$ ), channel response function ( $H_c(f)$ ) and equalizer tap gains. Now consider an N-tap equalizer whose complex gains  $\{C_n\}_N$  are adaptively adjusted, for any given  $t_0$ , so as to maximize  $\gamma$ . We define the following:

$$\gamma_N(t_0) \triangleq \max_{\{C_n\}_N} (\gamma) \quad (9)$$

and

$$\Gamma_N \triangleq \begin{cases} \max_t [\gamma_N(t_0)]; & \text{Optimal Timing} \\ \gamma_N(t_0 = t_d); & \text{Derived Timing} \end{cases} \quad (10)$$

where  $t_d$  is the timing epoch derived by using squared-envelope timing recovery.

The quantity  $\Gamma_N$  is the detection signal-to-distortion measure of interest in this study. It represents the (normalized) signal-to-distortion ratio for an optimally adjusted N-tap equalizer. We have used known analytical techniques to derive  $\gamma_N(t_d)$  and have then obtained  $\Gamma_N$  in each of the two ways indicated by (10). For the case of optimal timing, we found  $t_o$  via a numerical search; for the case of derived timing, we found  $t_d$  analytically.

Combining (7) and (8), and assuming the inequality in (7), we can find the  $\Gamma_N$  required in an M-level system to achieve a specified bit error rate. It is

$$\Gamma_{req} = \frac{M-1}{3} \left[ 2 \ell n \left( \frac{2}{BER} \right) \right] \quad (11)$$

If BER is the threshold bit error rate specified in the system design, then  $\Gamma_{req}$  is the smallest acceptable  $\Gamma_N$  for good detection performance.<sup>†</sup> This interpretation will be useful in evaluating the probability distributions for  $\Gamma_N$  obtained in our simulations. Decibel values of  $\Gamma_{req}$  corresponding to various combinations of M and BER are listed in Table I.

## 5. SIMULATION STUDY AND RESULTS

### 5.1 Parameters Studied

To get an estimate for the number of taps needed in the FFSTD L equalizer, we generated and analyzed a few "bad" fades. Figure 2 shows a channel response with a 36-dB fade at the band edge, i.e., at  $f = 1/2T$ . The computed measures  $\gamma_N(t_o)$  for this case, for  $N = 5, 15, 21, 31$  and  $\infty$ , are plotted against  $t_o$  in Fig. 3. As can be seen, sensitivity to  $t_o$  decreases with increasing N, as  $\gamma_N(t_o)$  rises to the asymptotic limit,  $\Gamma_{\infty}$ .

The system parameters studied were symbol rate, cosine rolloff factor, and number of taps. Symbol rate of 30 Mbd were considered, being typical values for channel bandwidth, of 40 MHz. We considered a "typical" cosine rolloff factor of 0.5 and also an extreme value of 0 ("brick wall" filter). In all cases, we used an unfaded carrier-to-noise ratio ( $CNR_o$ ) of 63 dB, and obtained results for  $N = \infty$  (MMSE equalizer), 5, 3, and 1<sup>‡</sup>. For synchronous equalizers with  $\alpha = 0$ , we also obtained results for  $N = 9$ .

For each combination of timing recovery method, type of equalizer, and system parameters,  $\Gamma_N$  was computed for 20,000 simulated responses, each response being obtained via Monte Carlo generation of A, B, and  $\phi$ , (3). The same set of 20,000 response functions was used for every case, to permit useful comparisons.

### 5.2 Results

#### 5.2.1 FFSTD L Equalizers

Figure 4 shows probability distributions for  $\alpha = 0$ . The abscissa is  $\Gamma$  expressed in dB; the ordinate  $Pr(\Gamma)$ , represents the fraction of fading time for which  $\Gamma_N$  for a given N would be smaller than  $\Gamma$ . Multiplying by  $T_o$ , as given in (1), we can convert  $Pr(\Gamma)$  into seconds per heavy-fading month, as shown on the right-side ordinate of the figure. In applying (1), we have assumed  $c=1$  (average terrain) and  $D=25$  miles.

In the figure, each solid curve is for a particular N and optimal timing, while each set of crosses is for a particular N and squared-envelope derived timing. Where crosses are omitted for a particular N, it is because the results are virtually identical for both kinds of timing.

On the abscissa three vertical markings indicate the minimum acceptable values of  $\Gamma$  for a threshold BER of  $10^{-4}$  and  $M=16, 64$ , and 256. (These values come from Table I.) Each curve can therefore be interpreted as giving the outage probability (or outage seconds) for a particular receiver approach (N and method of timing) and specified levels of performance (BER and M).

Having thus explained Fig. 4 we now cite Fig. 5 which gives the same results for  $\alpha = 0.5$ . From these two figures we can make the following observations:

- (i) For  $N = \infty$ , the probability curves in Figs. 4 and 5 are very similar, i.e., they hardly depend on  $\alpha$ .
- (ii) Dramatic improvements (one to almost two orders of magnitude) can be achieved relative to the unequalized ( $N = 1$ ) case using FFSTD L equalizers with as few as 5 taps, especially in the 20- to 25-dB range of  $\Gamma$ .
- (iii) The statistical performance of FFSTD L equalizers with 5 taps does not differ substantially from the corresponding MMSE equalizers at the various values of  $\alpha$ .
- (iv) For  $\alpha = 0$ , Fig. 4, the spread between the curves corresponding to  $N = 3$  and  $N = \infty$  is quite noticeable. For  $\alpha = 0.5$ , Fig. 5, this spread is not nearly as large.
- (v) For FFSTD L equalizers with  $N=1$  and  $N \geq 5$ , the differences in performance between the optimally timed equalizers and those with squared-envelope derived timing are minute.

<sup>†</sup> Since (7) is an upper bound on BER,  $\Gamma_{req}$  is actually an upper bound on the smallest acceptable  $\Gamma_N$ .

<sup>‡</sup> The case  $N = 1$  corresponds to no equalization, except for optimizing of the phase of the local carrier reference.

### 5.2.2 FSSTD L Equalizers

Early simulation runs of the performance of synchronously spaced equalizers indicated that, for all practical purposes, the squared-envelope derived timing is optimal. This applies for any  $N$  and  $\alpha$ . We therefore computed the performance statistics of FSSTD L equalizers for derived timing only. The results are shown in Figs. 6 and 7, which precisely parallel Figs. 4 and 5. As can be seen, there are dramatic differences in performance between equalizers with  $\alpha=0$  and  $\alpha=0.5$ . For  $\alpha=0$ , equalizers with  $N=9$  perform much more poorly than do ideal ( $N=\infty$ ) equalizers. For  $\alpha=0.5$ , the spread in performance between the ideal and  $N=5$  equalizers is much smaller.

### 6. CONCLUSION

The main conclusion of this study is that a practical fractionally-spaced TDL equalizer can provide digital radio outage performance close to that of an ideal infinite-tap equalizer. To make this point more concrete, consider a 64-QAM system ( $M = 64$ ) for which the threshold bit error rate is  $10^{-4}$ . Table 1 shows that  $\Gamma_{req}$  for this case is upperbounded by 26.2 dB. Figures 4 and 5 show that, in this neighborhood of  $\Gamma$ , there is a small difference in  $P_r(\Gamma)$  between  $N = 5$  and  $N = \infty$ . This is particularly true for typical cosine rolloff factors ( $\alpha$  near 0.5).

These findings are somewhat theoretical, ignoring such issues as the dynamic range of the optimized tap gains and the time dynamics of multipath fading. Further study is needed to address these topics properly.

Finally, our results show that, for the fading model assumed here, the outage performance of a fractionally-spaced equalizer exceeds that of a synchronously-spaced equalizer with the same number of taps. In addition, fractionally-spaced equalizers are far less sensitive to the timing epoch. Moreover, a simple timing recovery circuit preceding the adaptive equalizer can yield outage statistics which are very close to the theoretical optimum.

### REFERENCES

- [1] C. W. Anderson, S. G. Barber and R. N. Patel, "The Effect of Selective Fading on Digital Radio," IEEE Trans. on Commun., COM-27, No. 12 (December 1979), pp. 1870-1875.
- [2] S. Komaki, I. Horikawa, K. Morita and Y. Okamoto, "Characteristics of a High Capacity 16 QAM Digital Radio System in Multipath Fading," IEEE Trans. on Commun., COM-27, No. 12 (December 1979), pp. 1854-1861.
- [3] Y. Y. Wang, "Simulation and Measured Performance of a Space Diversity Combiner for 6 GHz Digital Radio," IEEE Trans. on Commun., COM-27, No. 12 (December 1979), pp. 1896-1907.
- [4] S. Komaki, Y. Okamoto and K. Tajima, "Performance of 16-QAM Digital Radio System Using New Space Diversity," Paper 52.2, Int. Conf. on Commun., June 8-12, 1980, Seattle, Washington.
- [5] T. Murase, K. Morita and S. Komaki, "200 Mb/s 16-QAM Digital Radio System with New Countermeasure Techniques for Multipath Fading," Paper 46.1, Int. Conf. on Commun., June 14-18, 1981, Denver, Colorado.
- [6] P. Hartmann and B. Bynum, "Design Consideration for an Extended Range Adaptive Equalizer," Paper 46.5, Int. Conf. on Commun., June 14-18, 1981, Denver, Colorado.
- [7] A. J. Giger and W. T. Barnett, "Effects of Multipath Propagation on Digital Radio," Paper 46.7, Int. Conf. on Commun., June 14-18, 1981, Denver, Colorado.
- [8] R. Iyer, S. Myrillas, J. C. Cartledge and A. Javed, "Effects of Space Diversity Reception on Multipath Induced Distortions in Terrestrial Microwave Channels," Paper 3.B.5, Intl. Conf. on Commun., June 13-17, 1982, Philadelphia, PA.
- [9] A. Ricagni and T. Testi, "IF Combining Techniques for Space Diversity in Analog and Digital Radio Systems," Paper 4.B.6, Intl. Conf. on Commun., June 13-17, 1982, Philadelphia, PA.
- [10] R. A. Nichols, "An IF Combiner for Digital and Analog Radio Systems," Paper 4.B.7, Intl. Conf. on Commun., June 13-17, 1982, Philadelphia, PA.
- [11] C. L. Chao and G. L. Lui, "A Comparative Performance Evaluation of Slope Equalizers and Decision-Directed Weight Control Equalizers," Paper F3.4, Globecom '82, Nov. 29 - Dec. 2, 1982, Miami, FL.
- [12] H. Sari, "A Comparison of Equalization Techniques on 16 QAM Digital Radio Systems During Selective Fading," Paper F3.5, Globecom '82, Nov. 29 - Dec. 2, 1982, Miami, FL.
- [13] P. D. Karabinis, "Maximum-Power and Amplitude-Equalizing Algorithms for Phase Control in Space Diversity Combining," BSTJ, Vol. 62, No. 1, Part 1, Jan. 1983; pp. 63-89.
- [14] G. J. Foschini and J. Salz, "Digital Communications Over Fading Radio Channels," BSTJ, Vol. 62, No. 2, Part 1, Feb. 1983; pp. 429-456.
- [15] W. D. Rummier, "A New Selective Fading Model: Application to Propagation Data," BSTJ, 58, No. 7 (May-June 1979), pp. 1037-1071.
- [16] W. D. Rummier, "More on the Multipath Fading Channel Model," IEEE Trans. on Commun., COM-29, No. 3 (March 1981), pp. 346-352.
- [17] R. W. Lucky, J. Salz and E. J. Weldon, Jr., *Principles of Data Communication*, McGraw Hill, 1968. [In particular, see pp. 50-51 for a description of the cosine rolloff pulse and its Fourier transform.]

- [18] R. D. Gittlin, H. C. Meadors and S. B. Weinstein, "The Tap-Leakage Algorithm: An Algorithm for the Stable Operation of a Digitally Implemented, Fractionally Spaced, Adaptive Equalizer," *BSTJ*, 61, No. 8 (October 1982), pp. 1817-1839.

TABLE I: VALUES OF  $\Gamma_{req}$  FOR VARIOUS

M AND THRESHOLD BER

M	16	64	256
BER			
$10^{-3}$	18.81 dB	25.04 dB	31.11 dB
$10^{-4}$	19.96 dB	26.19 dB	32.26 dB
$10^{-5}$	20.87 dB	27.10 dB	33.17 dB
$10^{-6}$	21.62 dB	27.85 dB	33.92 dB

Note: The Values Shown for  $\Gamma_{req}$  Are Upper Bounds.

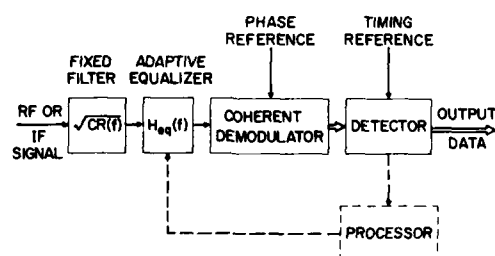


Fig. 1 Block diagram of the digital radio receiver assumed in the study.

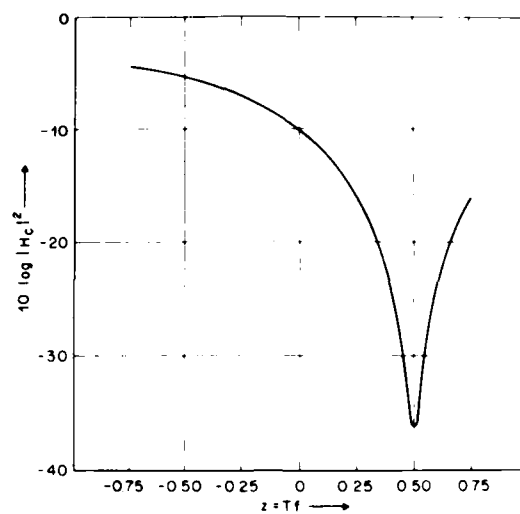


Fig. 2 Sample magnitude response, corresponding to a "bad" radio channel fade:  
 $H_c(z) = \sqrt{0.1} [1 - 0.95 \exp(i\pi(1-2z)/3)]$ .

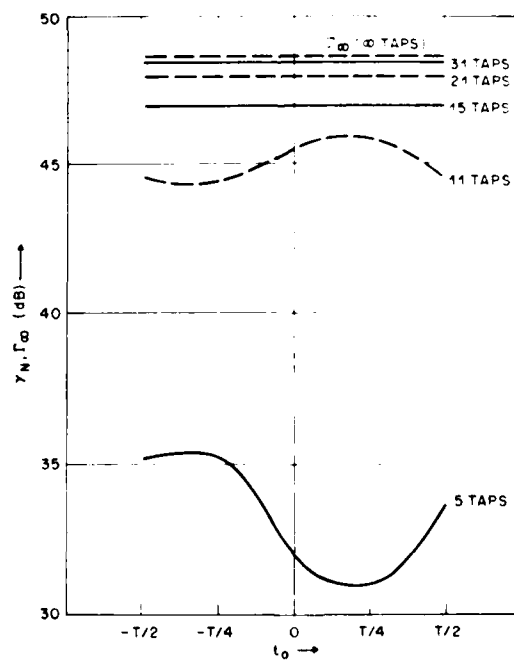


Fig. 3 Normalized maximum signal-to-distortion ratios,  $\gamma_N$  and  $\Gamma_\infty$ , vs. timing epoch,  $t_0$ . ( $\alpha = 0.5$  and  $H_c(z)$  of Fig. 2).

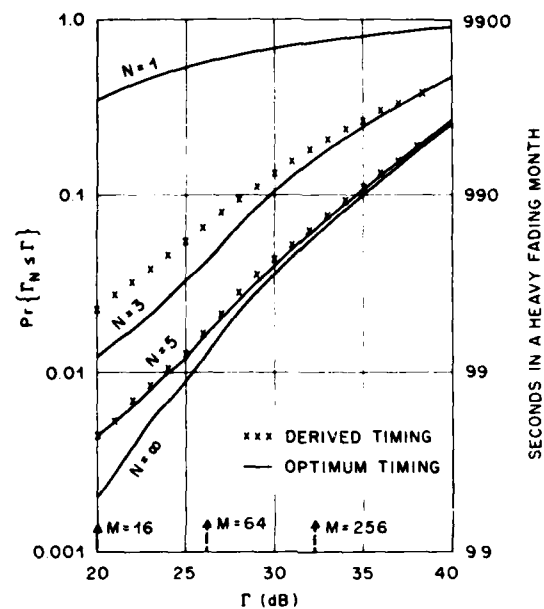


Fig. 4 Performance statistics for fractionally-spaced equalizers and  $\alpha = 0$ :  $Pr\{\Gamma_N \leq \Gamma\}$  vs.  $\Gamma$  for various  $N$ . Results are based on 20,000 simulation trials. Solid curves are for optimal timing, crosses are for derived timing. Vertical markings on abscissa identify  $\Gamma_{req}$ -values at  $BER = 10^{-4}$  for different  $M$  (16, 64, and 256). Symbol rate: 30 Mbd.

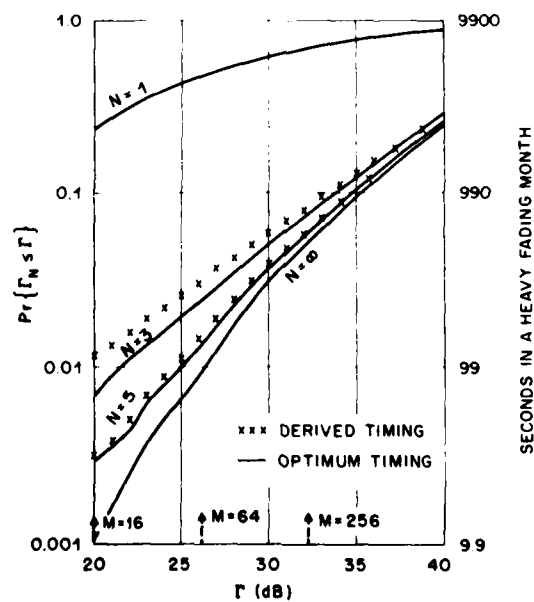


Fig. 5 Performance statistics for fractionally-spaced equalizers and  $\alpha = 0.5$ . All else the same as for Fig. 4.

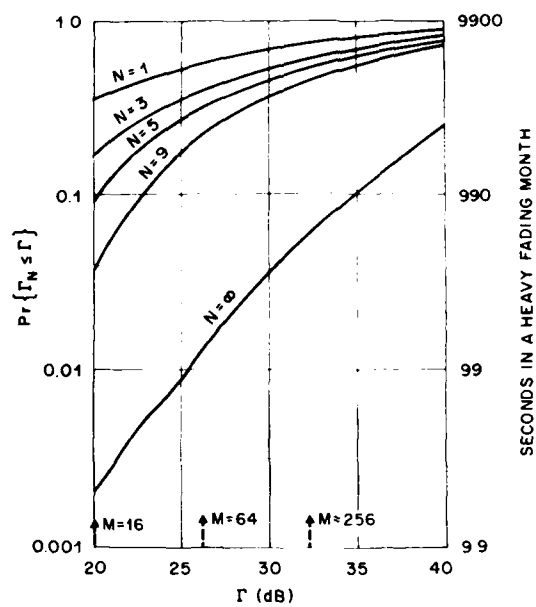


Fig. 6 Performance statistics for synchronously-spaced equalizers and  $\alpha = 0$ . Derived timing only. All else the same as for Fig. 4.

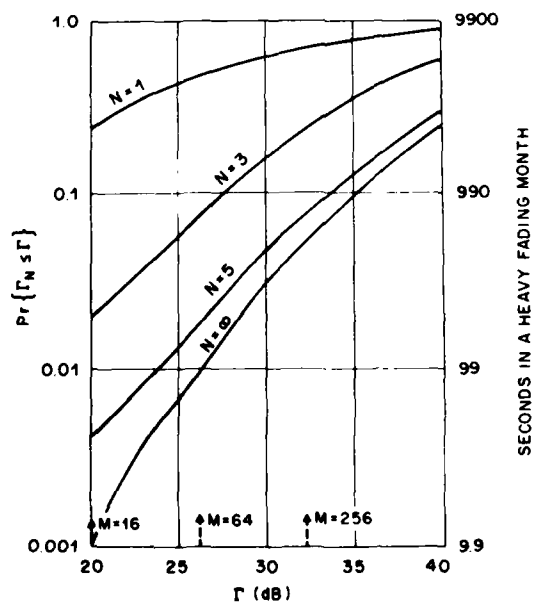


Fig. 7 Performance statistics for synchronously-spaced equalizers and  $\alpha = 0.5$ . Derived timing only. All else the same as for Fig. 4.

## DISCUSSION

T. J. Moulisley (U.K.): It may be useful to consider the tap spacing required for an equalizer in terms of the bandwidth (B) occupied by the signal spectrum, or its time-domain representation given by the auto correlation function. From the Nyquist criterion, the separation of samples in the time domain must be  $B/2$ . Thus in your system with cosine roll-off ( $\alpha = 0.5$ ), the bandwidth is about half of that for no roll-off ( $\alpha = 0$ ), and synchronously spaced taps could be used rather than fractional spacing.

Furthermore, it may be that the number of taps required for the adaptive filter realization depends upon the time delay spread of the auto correlation function of the required filter characteristic. Have you any comment on this way of looking at the above situation?

N. Amitay (U.S.): The bandwidth with  $\alpha = 0.5$  is not about half of that with  $\alpha = 0$  as stated above.

The tap spacing does not have to be considered in terms of the signal spectrum, because deletion would be less sensitive to the tuning recovery epoch. It is better to consider tap spacing in terms of the characteristics of the fading channel since this is what the equalizer is trying to correct.

We do not know a priori the required filter characteristics or its auto correlation function. The number of filter taps is obtained through complicated minimization of the mean square distortion, noise plus intersymbol interference (ISI), and search over timing epochs and number of taps. I cannot see at present any advantage of looking at the autocorrelation function. I think that more physical insight can be gained by looking at the tapped delay line equalizer as a weighted finite Fourier series for the construction of the filter which will minimize the mean square distortion.

## SPHERICAL PROPAGATION MODELS FOR MULTIPATH-PROPAGATION PREDICTIONS

by

L.P. Ligthart  
Delft University of Technology  
Dept. of Electrical Engineering  
Mekelweg 4  
2628 CD Delft

Summary

Multipath fading leads to a limitation in the availability and/or reliability of microwave links. To study the propagation mechanism under fading conditions propagation models, based on ray theory, above a spherical earth have been developed and compared to the well-known planar propagation model above a "flat-tened earth". The reasons for studying spherical propagation models are a) to avoid the limitation of small elevation angles in planar propagation models, b) to investigate the computed and measured path delay on the microwave line of sight links, and c) to set up an analytical approach for the spherical propagation model without numerical difficulties and computing-time intensive procedures.

In this paper computational results of the models are shown, including an accuracy analysis, and the use of spherical propagation models is illustrated for surface duct layers above water.

1. Introduction

Multipath propagation can cause large variations in the received signal level. To prevent multipath fading on terrestrial microwave radio links two diversity techniques are frequently used:

- frequency-diversity,
- height-diversity.

Another possibility for multipath fading reduction is derived from the angle of arrival dependency of incoming rays at the receiver antenna. This third diversity technique looks promising when use is made of electronically controlled limited scan antennas (Ref. 1). Hybrid reflector antennas for multipath fading reduction have determined the German and the Dutch contribution to the COST 204 project (European Co-Operation in the field of Scientific and Technical Research-Commission of the European Communities). The project is entitled "Phased Array Antennas and their Novel Applications" (Ref. 2).

In The Netherlands the Dr. Neher Laboratory of the Dutch PTT and the Microwave Laboratory of the Delft University of Technology have collaborated on a research program to investigate the possibilities of using limited scan antennas on digital microwave line of sight links. To come up with antenna specifications for fading reduction, group delay requirements in two ray propagation models have been considered. Firstly, the planar propagation model has been used. This model approximates small elevation angles and can be found by an "earth flattening" coordinate transformation to preserve relative curvature between rays and the earth. Because accurate time delay information is needed for specifying the wanted antenna characteristics spherical models have also been investigated.

In Section 2 some attention is paid to ray parameters in planar and spherical models, assuming a constant refractive index gradient over a given height segment.

In Section 3 results of time delay computations for both models and of the accuracy analysis for the spherical model are shown.

In Section 4 a modified logarithmic refractive index profile is assumed in order to study the propagation mechanism through surface ducts above water under different spherical model conditions.

2. Ray parameters for planar and spherical models

In the model with planar earth (Figure 1) the vertical refractive index profile  $n$  is assumed to be dependent on  $z$  only and is characterized by the transformation

$$\frac{dn(r)}{dr} \approx \frac{dn(z)}{dz} - \frac{1}{R_a} = B'' - \frac{1}{R_a}$$

where  $n$  = refractive index in the spherical model with earth radius  $R_a$  and with assumed radial dependency  $r$

$m$  = refractive index in the planar model

$B''$  = refractive index gradient per meter in the planar model

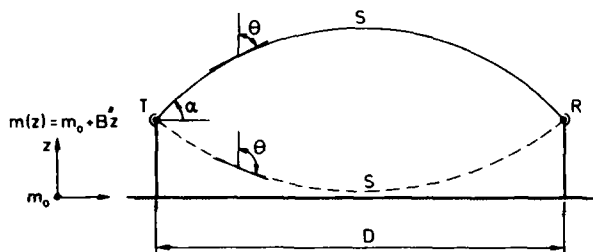


Figure 1. Planar propagation model

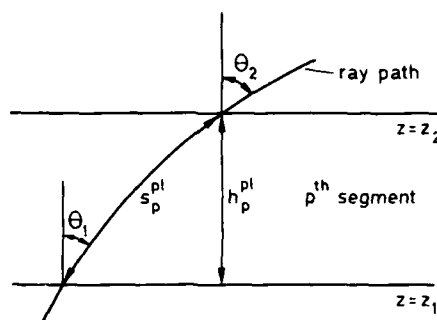


Figure 2. Ray parameters in planar propagation model

Segmentation is carried out in such a way that  $B'' = \text{constant}$  per segment  $p$  (Figure 2). The ray parameters are functions of the refractive index profile and  $\theta$ . In the planar model the ray parameters per segment become

- $h_p^{pl}$  = height difference of the ray = segment thickness
- $d_p^{pl}$  = horizontal distance of the ray along the earth surface
- $s_p^{pl}$  = path length of the ray
- $t_p^{pl}$  = path delay of the ray

If a ray reaches a maximum or minimum height within the segment an extra segment is introduced based on these heights. The whole radio path is described by summing the ray parameters. The appeal of the planar model is that analytical formulas of the of the ray parameters can be given.

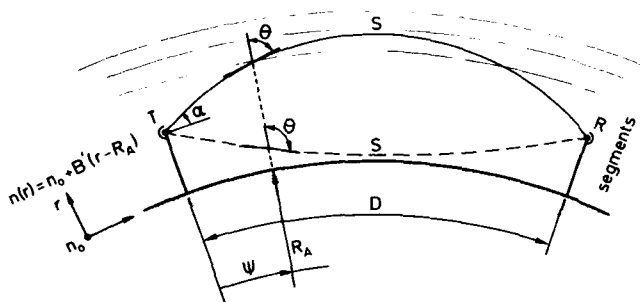


Figure 3. Spherical propagation model

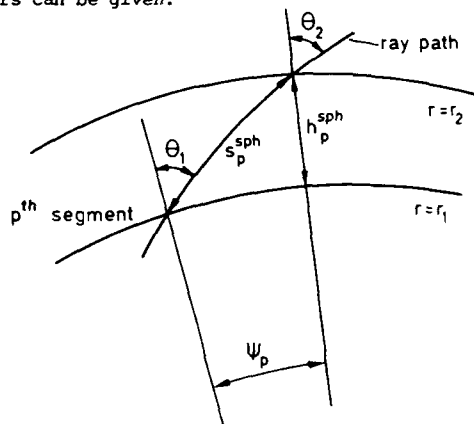


Figure 4. Ray parameters in spherical propagation model

In the model with spherical earth (Figure 3) the refractive index profile is characterized by the transformation

$$\frac{dn(r)}{dr} = \frac{dN(r_f)}{dr_f} - \frac{1}{R_A} + \frac{1}{R_f} = B' - \frac{1}{R_A} + \frac{1}{R_f}$$

where  $N$  = refractive index in the spherical model with arbitrary fictive radius  $R_f$   
 $B'$  = refractive index gradient per meter in the spherical model

Segmentation is illustrated in Figure 4 where  $B' = \text{constant}$  per segment  $p$ . The ray parameters in the spherical model become

- $h_p^{sph}$  = segment thickness
- $d_p^{sph} = R_f \cdot \psi_p$  = horizontal distance of the ray along the earth surface
- $s_p^{sph}$  = path length of the ray

-  $t_p^{\text{sph}}$  = path delay of the ray

Different analytical approximations for the ray parameters have been derived for  $B' > -N(r_f)/r_f$ ,  $B' < -N(r_f)/r_f$  and for the rays which reach maximum heights. Per segment analytical expressions can be obtained by making approximations in the ray theory, especially of the term

$$I = \sqrt{r_f^2 N^2(r_f) - C^2}$$

Using Snell's law for a spherical layered medium the ray path constant  $C$  becomes

$$C = N(r_f) \cdot r_f \cdot \sin\theta$$

For  $B' < -N(r_f)/r_f$  the term  $I$  yields

$$I \approx \sqrt{(r_m^2 - r_f^2) K_p}$$

$r_m$  is the maximum  $r_f$  value the ray would reach if the refractive index gradient  $B'_p = \text{constant}$  were extended to above. This means  $r_m \geq r_2$ . The factor  $K_p$  is chosen so that for  $r_m > r_2$

$$(r_m^2 - r_2^2) K_p = r_2^2 N^2(r_2) - C^2$$

and for  $r_m = r_2$

$$K_p = -N^2(r_1) - B'_p \cdot N(r_1) \cdot r_1$$

For  $B' > -N(r_f)/r_f$  the term  $I$  yields

$$I \approx \sqrt{K'_p(r_f^2 - r_1^2) + K''_p}$$

$K'_p$  and  $K''_p$  are chosen so that the approximation is optimal for  $r_f = r_1$ ;  $K'_p$  and  $K''_p$  become

$$K'_p = N^2(r_1) + B'_p \cdot N(r_1) \cdot r_1$$

$$K''_p = N^2(r_1) \cdot r_1^2 - C^2$$

### 3. Path delay computations and accuracy analysis

To make comparisons between planar and spherical models computer programs have been developed. The input parameters in the programs are

- link geometry (i.e. antenna heights, distance between antennas, earth radius)
- refractive index profiles linearized in a given number of segments
- elevation angles of transmitted rays

For an incoming ray at the aperture of the receiver antenna the results are

- path length and path delay  $\tau$
- angle of arrival  $\alpha$
- amplitude and phase

In case the elevation angles of transmitted and received rays are within 1 degree the main differences between the models are mostly found in path delay and amplitude computations. Therefore, in this section results of path delay computations are compared for the spherical model with  $R_f = R_a$  and the planar model. For simplicity a constant refractive index gradient  $B'$  and thus a constant  $B''$  has been assumed over the atmospheric height region of interest. For the spherical model this height region is subdivided into seg-

ments with a constant thickness of 10 meters. The antenna heights at transmitter and receiver equals 100 m above the earth. Three different  $B'$  (and  $B''$ ) values are considered:

- $B'_a = -5 \cdot 10^{-7} \text{ [m}^{-1}] \Rightarrow B''_a = -3.4 \cdot 10^{-7} \text{ [m}^{-1}]$
- $B'_b = -.78 \cdot 10^{-7} \text{ [m}^{-1}] \Rightarrow B''_b = .78 \cdot 10^{-7} \text{ [m}^{-1}]$
- $B'_c = 1 \cdot 10^{-7} \text{ [m}^{-1}] \Rightarrow B''_c = 2.6 \cdot 10^{-7} \text{ [m}^{-1}]$

In these three cases the angle of arrival  $\alpha$  dependency of the distance  $D$  is approximated by

- $D_a \approx 106 \cdot \alpha \text{ [km]}$        $\alpha$  in degrees
- $D_b \approx 420 \cdot \alpha \text{ [km]}$
- $D_c \approx -135 \cdot \alpha \text{ [km]}$

The path delay computations  $\Delta\tau = T_{\text{total}} - T_o$  for both models are shown in Figures 5-7 where:

- $T_{\text{total}}$  = total path delay time from transmitting to receiving antenna
- $T_o$  = delay time of a ray propagating at the earth's surface with a refractive index at earth  $n_o = 1.0002$  and  $B' \approx -1/R_a$

The figures give indication of larger  $\Delta\tau$  values in the spherical model. By way of

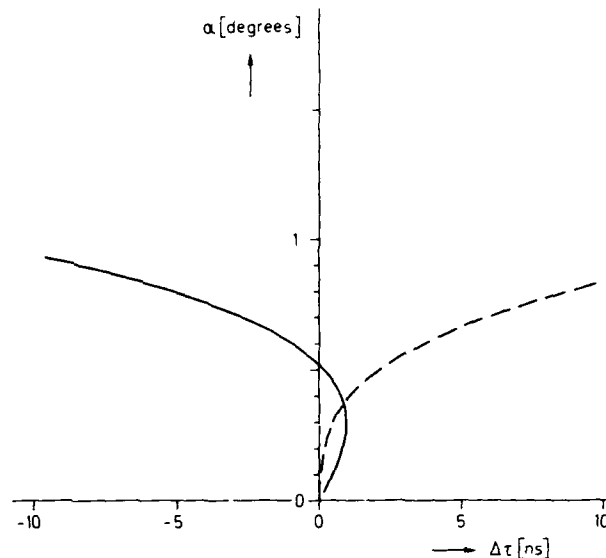


Figure 5. Path delay as function of  $\alpha$ , for

$B'_a = -5.0 \cdot 10^{-7} \text{ [m}^{-1}]$  (solid line), and  
 $B''_a = -3.4 \cdot 10^{-7} \text{ [m}^{-1}]$  (dotted line)

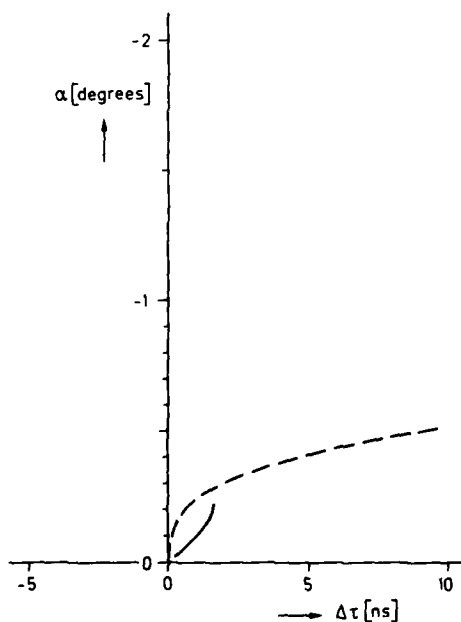


Figure 6. Path delay as function of  $\alpha$ , for

$B'_a = -.78 \cdot 10^{-7} \text{ [m}^{-1}]$  (solid line), and  
 $B''_a = .78 \cdot 10^{-7} \text{ [m}^{-1}]$  (dotted line)

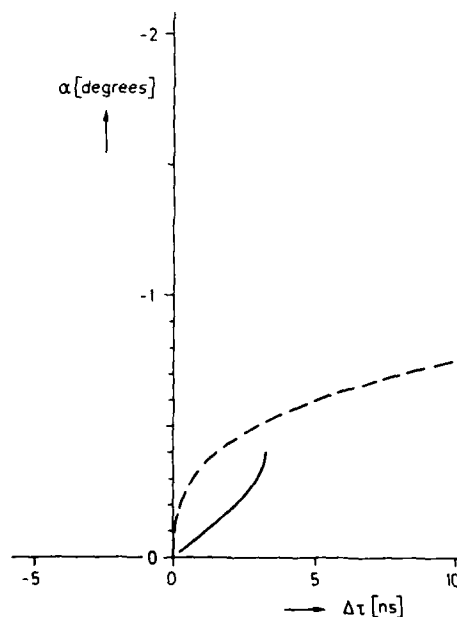


Figure 7. Path delay as function of  $\alpha$ , for

$B'_a = 1.0 \cdot 10^{-7} \text{ [m}^{-1}]$  (solid line), and  
 $B''_a = 2.6 \cdot 10^{-7} \text{ [m}^{-1}]$  (dotted line)

example, differences in  $\Delta\tau$  up to 2.5 ns are found for angles less than 0.3 degrees and distances less than 40 km.

To verify the convergence in the accuracy of the numerical computations for the spherical model  $\Delta t$  computations have been made for specific angles and the number of segments (segment thicknesses which have been chosen are 10, 5, 1, and 0.25 meters) has been increased. In Figures 8 and 9 the accuracies are given

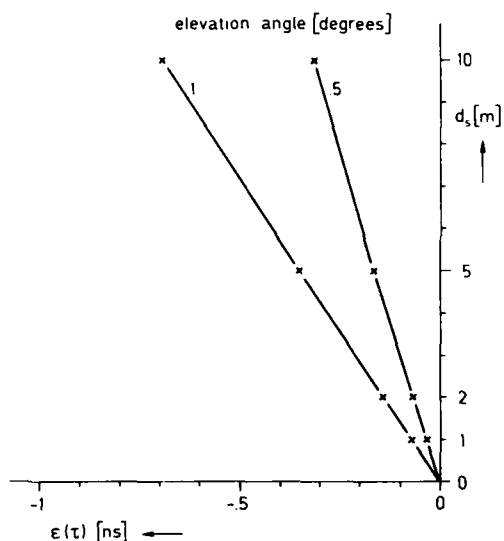


Figure 8. Error  $\epsilon(t)$  in  $\Delta t$  computations as function of segment thickness  $d_s$  for  $B' = -5.0 \cdot 10^{-7} \text{ [m}^{-1}\text{]}$

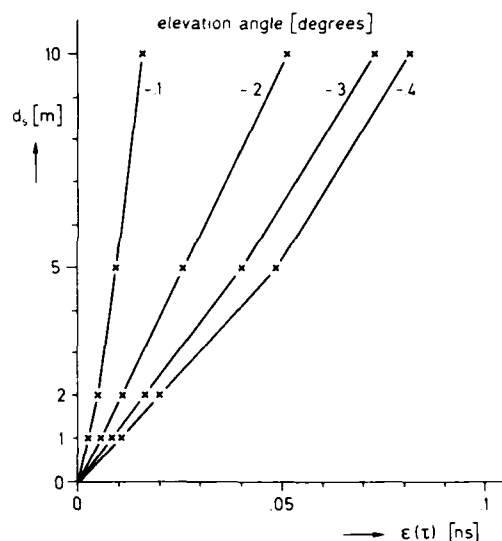


Figure 9. Error  $\epsilon(t)$  in  $\Delta t$  computations as function of segment thickness  $d_s$  for  $B' = 1.0 \cdot 10^{-7} \text{ [m}^{-1}\text{]}$

for  $B' = -5 \cdot 10^{-7} \text{ [m}^{-1}\text{]}$  and  $B' = 10^{-7} \text{ [m}^{-1}\text{]}$ . The point of convergence in the origin has been obtained by extrapolation of the curve for a segment thickness of 1 m and a thickness of 0.25 m. From these results it can be seen that for segment thicknesses less than 10 meters the accuracy lies within 1 ns, which is less than the differences between the spherical and the planar model.

#### 4. The modified logarithmic refractive index profile

An application of the theory is given for a refractive index profile characteristic of a duct above water. This model has been chosen because strong gradients and thus strong convergence or divergence of the rays can be expected just above the water surface. At the same time there is the possibility to investigate whether a simple relationship exists between the amplitude of incoming rays and their delay time.

For the microwave link the following is selected:

- distance between transmitter and receiver = 40 km
- antenna heights = 80 m

The modified logarithmic refractive index profile above a flattened earth is given by (Figure 10).

$$M(z) = C_2 \left[ z - z_1 - (d + z_0) \ln \left( \frac{z + z_0}{z_1 + z_0} \right) \right] + M_1$$

where

- $d$  = duct height (5 - 50 meters)
- $z_0$  = roughness parameter at the earth's surface ( $10^{-3} \text{ m}$ )
- $z_1$  = height where  $M(z_1) = M_1$
- and  $C_2$  characterizes  $dM/dz$  at high altitudes ( $z > 3d$ ).

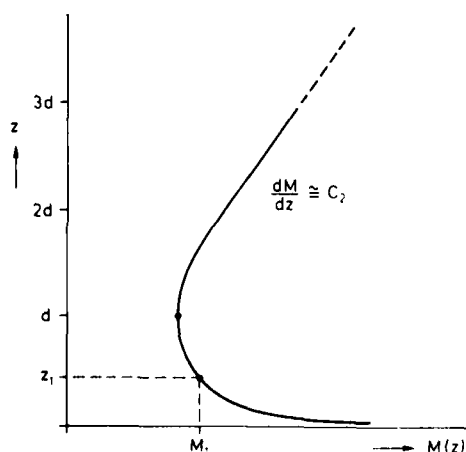


Figure 10. Modified logarithmic refractive index profile above a planar earth

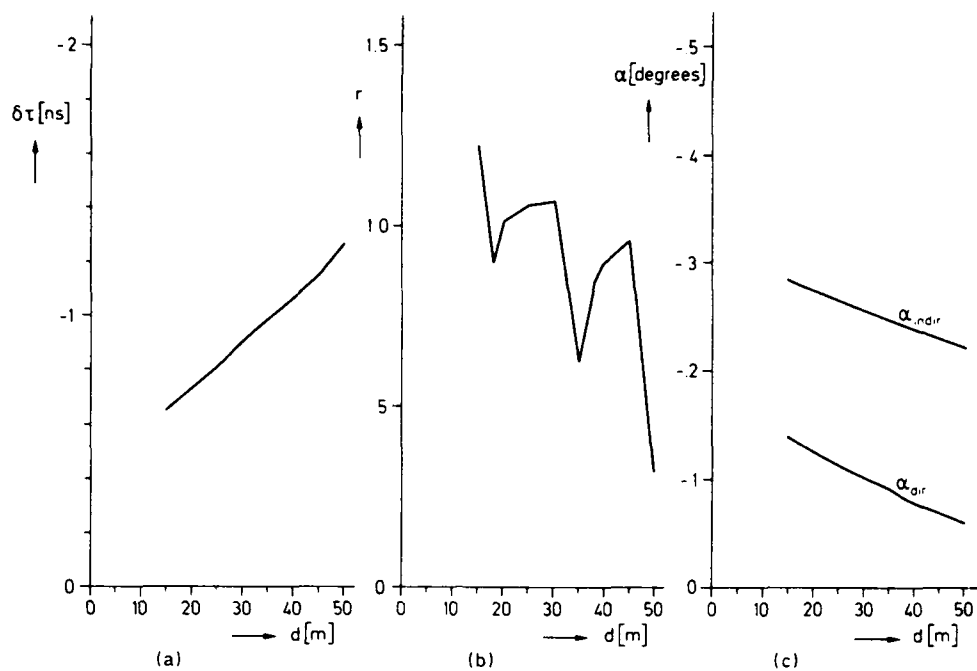


Figure 11. Computational results as function of duct height  $d$ .

Model 1:  $k = 1$ ,  $M_1 = 325$ ; a) time delay difference  $\delta\tau$ ; b) relative amplitude of the indirect ray; c) angles of arrival

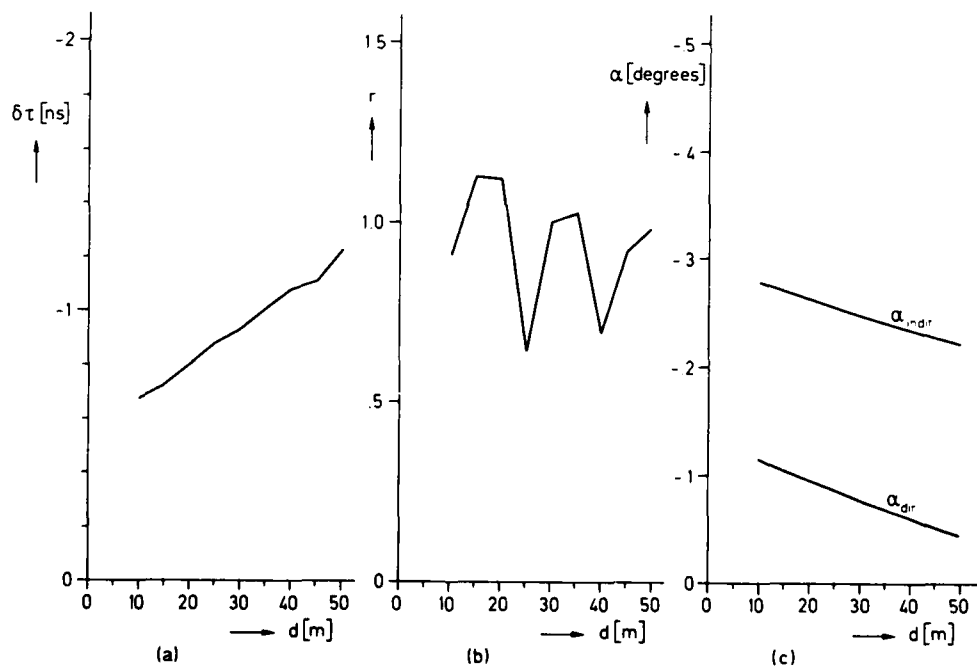


Figure 12. Computational results as function of duct height  $d$ .

Model 2:  $k = 4/3$ ,  $M_1 = 325$ ; a) time delay difference  $\delta\tau$ ; b) relative amplitude of the indirect ray; c) angles of arrival

The refractive index  $n$  above the spherical earth is determined by:

$$M(z) = (n - 1 + \frac{z}{R_a}) 10^6 \Rightarrow dM/dz = (dn/dz + 1/R_a) 10^6$$

where  $dn/dz$  = refractive index gradient above a spherical earth with earth radius  $R_a$ .

For a fictive earth radius  $R_f = kR_a$  it is found that:

$$R_f = \frac{1}{(dn/dz + 1/R_a)} \Rightarrow dM/dz = \frac{10^6}{kR_a} \approx C_2 \quad \text{for } z > 3d$$

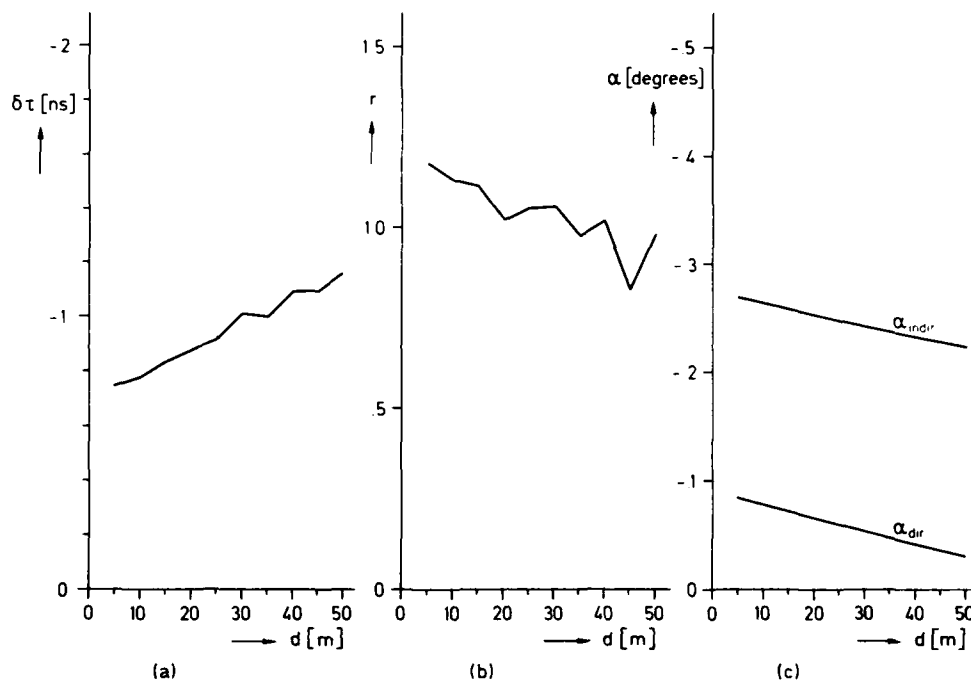


Figure 13. Computational results as function of duct height  $d$ ;

Model 3:  $k = 2$ ,  $M_1 = 325$ ; a) time delay difference  $\delta\tau$ ; b) relative amplitude of the indirect ray; c) angles of arrival

This means that  $k$  determines the model conditions for high altitudes. The computations with 1 meter segmentation and for  $k = 1$ ,  $4/3$  (standard atmosphere above the duct) and  $k = 2$ , are presented in Figures 11, 12 and 13. In these figures  $\delta\tau$  is the delay time difference and  $r$  is the relative amplitude factor of the two rays in this two-way propagation model.

A dominant  $k$ -dependency on  $\delta\tau$  and a clear correlation between  $\delta\tau$  and  $\alpha$  are found as a function of the duct height, while no simple relationship exists between  $\delta\tau$  and  $r$ . From Section 3 it is known that the appropriate spherical model has to be used for accurate  $\delta\tau$  computations.

### Conclusions

In this paper it is proposed that for path delay computations in multipath fading conditions spherical models be used. In the spherical model analytical formulas for the ray parameters have been used, assuming constant refractive index gradients per segment. By doing so the computing time can be reduced considerably relative to numerical solutions of the differential equations. The accuracy analysis shows strong convergence in path delay results by decreasing segment thicknesses. The example of a two-way spherical model based on surface duct layers above water indicates a strong relationship between time delay differences and angles of arrival combined with a dominant dependency of the model on the time delay computations.

### Acknowledgements

Many thanks are due to the Dutch PTT, Dr. Neher Laboratory, for having made this study possible.

### References

- (1) K.P. Dombek: "Minderung von Mehrwegeschwund durch adaptive Schwenkung der Antennecharakteristik", NTG-Fachtagung, "Richtfunk" München 1980, NTG-Fachberichte Band 70, VDE-Verlag, GmbH, Berlin, pp. 133-138
- (2) L.P. Ligthart, K.P. Dombek, G. Doro, V. Santomaa: "COST-204 review on limited scan arrays", paper presented at the joint ESA/COST 204 Phased-Array Antenna Workshop, held at ESTEC, Noordwijk, The Netherlands, 13 June 1983, ESA SP-204, pp. 15-21

### DISCUSSION

M.P.M. Hall (U.K.): Your Figures 1-4 show a rather simple case where both transmitter and receiver are situated at a height above which the refractive index decreases sharply with height, and below which it increases sharply with height. Could you please comment on how the main conclusions of your paper would be different for a more general ducting geometry in which the terminal height would not be at this region of refractive index change, and where the curvature of each ray would change significantly with height and even change direction along its path?

L.P. Ligthart (The Netherlands): In the spherical model, arbitrary refractive index profiles may be used and antenna heights may vary. Maximum time differences  $\Delta \tau$  occur in the case you mentioned and are shown in Figures 1-4. The main conclusion remains, as can be seen from Figures 11-13 in which a modified logarithmic refractive index profile has been taken.

U. Buse (Germany): At which frequency range are your models valid?

L.P. Ligthart (The Netherlands): At 4 and 6 GHz.

S. Rotheram (U.K.): The use of a flat earth with an earth flattening transformation and a modified refractive index should give the same answer as a spherical earth and the ordinary refractive index. In two dimensions (cylindrical geometry) the earth flattening transformation can be made exact.

L.P. Ligthart (The Netherlands): The earth flattening transformation yields a modified refractive index, which gives approximate results. In the limit of small elevation angles, exact results are obtained. In comparison between planar and spherical propagation models, differences have been found only in the path delay.

L. Boithias (France): Vous ne tenez pas compte des variations horizontales de l'indice de réfraction. Les erreurs introduites ainsi ne sont-elles pas supérieures à celles que vous envisagez de corriger?

L.P. Ligthart (The Netherlands): Horizontal variations in the refractive index can influence the numerical results. Therefore experimental verification of the models is needed.

T.A.Th. Spoelstra (The Netherlands): This is a comment. The necessity to use a planar or spherical earth approximation in the model depends on the accuracy one needs. In radio astronomy, correlation of signals from telescopes at distances of a few hundred meters make a spherical approximation mandatory. Furthermore it should be valid for all elevation angles.

N. Amitay (U.S.): Roughly, what improvement can you expect to obtain by using angular diversity?

L.P. Ligthart (The Netherlands): Deep fades can be reduced between 5 to 10 dB by using angular diversity. The effects on group delay depends on delay time differences.

# CORRECTING RADIO ASTRONOMY INTERFEROMETRY OBSERVATIONS FOR IONOSPHERIC REFRACTION

T.A.Th.Spoelstra

Netherlands Foundation for Radio Astronomy  
Postbus 2  
7990 AA Dwingeloo, The Netherlands

## SUMMARY

Radio astronomical observations with local interferometers and very long baseline interferometers (VLBI) are affected by atmospheric (i.e. tropospheric and ionospheric) refraction. A correction procedure for ionospheric refraction for radio astronomy interferometry is reviewed in the present paper. This correction is applied to observations made with the Westerbork Synthesis Radio Telescope (WSRT). The method used for WSRT observations can also be used to correct VLBI observations for ionospheric refraction. If networks of ionosonde and satellite observing stations operate during the astronomical VLBI observations, pathlength corrections ranging from several wavelengths to a fraction of a wavelength are possible, provided the geographical distribution of these stations is similar to the VLBI network. The possibilities of this procedure are compared with the results derived by e.g. dual frequency VLBI observations.

## LIST OF SYMBOLS

(b,h)	orientation of the interferometer baseline
c	speed of light (km/s)
d	total effective thickness of the ionosphere (km) ( $d = \frac{2}{3}(y_m + y'_m)$ )
D	pathlength (m)
f	fringe rate ( $f = \frac{dD}{dt}$ )
foF2(t)	critical frequency of the F2-layer at time t (MHz)
i <sub>0</sub>	zenith angle, angle between the ray and the local vertical
l <sub>1</sub>	L sin b
l <sub>2</sub>	L cos b
l <sub>2</sub> '	l <sub>2</sub> v/c
r	distance from Earth centre (km)
r <sub>b</sub>	radius of bottomside of F2-region (km)
r <sub>e</sub>	radius of the Earth (km)
r <sub>m</sub>	radius of surface of maximum electron density (km)
r <sub>t</sub>	radius of topside of F2-region (km)
t	time (hours)
y <sub>m</sub> , y' <sub>m</sub>	"semithickness" of regions above and below maximum density (a parabolic model for the electron density as a function of altitude was assumed)
α	right ascension (radians)
δ	declination (radians)
Δα	refraction angle in right ascension (radians)
Δδ	refraction angle in declination (radians)
Δf <sub>i</sub>	shift of f due to the ionosphere
Δt	clock error (msec)
Δτ <sub>i</sub>	shift of τ due to the ionosphere
Δδ <sub>p</sub>	error in the declination of the baseline pole (arcsec)
Δv	frequency error (kHz)
λ	longitude to the east of the observer (radians)
v	frequency of the wave (MHz)
φ	interferometer phase (degrees)
φ	geographic latitude (radians)
φ <sub>0</sub>	geographic latitude of the observer (radians)
φ <sub>a</sub>	latitude of the point at which the ray intersects the upper ionospheric boundary (radians)
τ	time delay
T	hour angle
Ω	angular velocity due to the Earth's rotation ( $\Omega = \frac{dh}{dt}$ )
ω(σ)	$\frac{3}{4\sigma} \left\{ \frac{(1+\sigma)}{2\sigma} \ln \left[ \frac{(1+\sigma)}{(1-\sigma)} \right] - 1 \right\}$
σ	$\frac{fo^2}{f^2} \sec^2 i_{om}$

## 1. INTRODUCTION

Radio interferometric observations are affected by tropospheric and ionospheric refraction. At radio frequencies tropospheric refraction is basically independent of frequency, while ionospheric refraction varies in inverse proportion to the observing frequency squared. The effects of refraction are visible as Faraday rotation of the plane of polarization of the incident wave and as errors in the interferometer phase which are to first approximation (as long as the ionosphere is 'coherent' over the interferometer baseline) linearly proportional to the baseline length in meters. The fundamental phenomenon is a delay error. It translates into fringe rate or phase errors. The "interferometer fringe phase" or the relative phase in radians of a signal received at each end of an interferometer baseline is the pathlength difference to these interferometer elements expressed in units of the observing wavelength. Owing to the earth's rotation, the relative signal phase is changing with a rate, known as the fringe rate, which is the time derivative of the phase. Ionospheric refraction is a significant effect for Connected Element Radio Interferometry (CERI) at frequencies up to about 2 GHz. Although in general the observing frequencies used in Very Long Baseline Interferometry (VLBI) are higher than 2 GHz, the long baselines involved imply that this technique is also sensitive to effects of ionospheric refraction.

These refraction effects cause very often serious changes in both angular position and polarization. These highly variable and unpredictable effects can be a source of degradation for radio astronomical observations. In this paper we will review a procedure to correct radio interferometric observations for ionospheric refraction on the basis of available ionospheric data. Results are shown for observations done with the Westerbork Synthesis Radio Telescope (WSRT) at 608.5 and 1412.0 MHz and a procedure for VLBI observations is outlined.

## 2. IONOSPHERIC REFRACTION

Refraction causes a shift of the apparent positions of extra-terrestrial objects on the celestial sphere. This shift depends on the geometry of the ionosphere and on the distribution of ionospheric electrons along the line of sight and perpendicular to it (i.e. gradients in this distribution) (Komesaroff, 1960; Hagfors, 1976; Spoelstra, 1983a). If the zenith angle for a particular object at the height of the maximum electron density,  $r_m$ , is denoted by  $i_{om}$ , the change of the apparent celestial coordinates by refraction due to the horizontal structure (in radians) can be expressed by the following relations:

for right ascension:

$$\Delta\alpha_H = \frac{d\omega(\sigma) \sec \delta \sec \phi_a \sec i_{om}}{2(r_b + \frac{3}{2}d) v^2} \frac{d(fo^2)}{d\lambda} \quad (1)$$

for declination:

$$\Delta\delta = -\frac{dfo^2}{2r_m v^2} \sec^2 i_{om} \tan i_{om} + \frac{d\omega(\sigma) \sec^2 i_{om}}{2(r_b + \frac{3}{2}d) v^2} \frac{d(fo^2)}{d\phi} \quad (2)$$

and for the refraction due to vertical gradients (in radians):

$$\Delta\alpha_V = \frac{1}{2v^2} \int_{r_e}^r \frac{r_e \sin i_{om}}{(r^2 - r_e^2 \sin^2 i_{om})^{1/2}} \frac{d(fo^2)}{dr} dr \quad (3)$$

(Spoelstra, 1983a and references therein; De Munck, 1982). The accuracy with which refraction errors can be corrected on the basis of this approach is typically 10-15%.

The procedure to correct for ionospheric refraction depends very much on the availability and accuracy of ionospheric data (i.e. the electron content). In our case we had only access to the ionosonde data collected by the Royal Netherlands Meteorological Institute (KNMI) at De Bilt (52°E, 52°N).

## 3. CORRECTION METHOD FOR THE WSRT

The Westerbork Synthesis Radio Telescope (WSRT) is a radio interferometer array described in detail elsewhere (Baars et al., 1973; Högbom and Brouw, 1974; Casse and Muller, 1974; Bos et al., 1981). The instrument is situated at 6°6' E, 52°7' N and consists of 14 steerable paraboloids with diameters of 25 m each, which are situated along an east-west baseline with a deviation of 1°2' ( $\pm 0'1$ ) from a perfect east-west baseline (Bregman, 1983; private communication). Ten occupy fixed positions at 144 m intervals, which are denoted 0, 1, 2, 3, ..., 9. Four additional paraboloids (i.e. A, B, C and D) serve as references with respect to which the phase of the radiation received by the antennas 0 to 9 is measured. To this end the latter are connected to the former to form a total of 40 correlation interferometers. The back end of each of these consists of a correlator system which measures the four complex correlations necessary to characterize the polarization state of the radiation. The main wavelength bands are 6, 21, 50 and 90 cm.

A source is observed by tracking it in its diurnal rotation from 6 hours before to 6 hours after meridian transit or over some fraction of this range. The array beam is continuously steered by proper phasing of the elements. This is done with very high precision: the positional accuracy in the sky is better than 0'1, corresponding with a phase accuracy better than 1 mm. This precision is reached by the application of a number of corrections, both for astrometric effects (Brouw, 1969; Högbom and Brouw, 1974; Spoelstra, 1983a) and for known instrumental errors (Brouw and Van Someren Gréve, 1973; Van Someren Gréve, 1974).

Point sources are observed quite frequently for checking and calibrating the instrument. For such sources, we know that the incident wavefront should be perfectly flat; any deviation must be the result of propagation effects (e.g. Hamaker, 1978; Spoelstra, 1983a). However, after application of the proper corrections many observations showed phase errors which are much larger than the internal accuracy of the system. These errors could have the character of a phase slope as a function of hour angle (Figure 1) and/or are wave-like variations as a function of hour angle (Figure 2). Since these effects are most severe at 608.5 MHz (327 MHz was not yet in operation during our tests) and linearly proportional with interferometer baseline (characteristic for a refraction problem) they are interpreted as being due to ionospheric refraction as the result of horizontal stratification in the ionosphere, electron density gradients and their variations. Since the WSRT is aligned along an east-west line the errors are mainly due to the east-west components of the ionospheric characteristics. Ionospheric refraction may then be described by Eqs.(1) and (3).

In Eq.(1) the gradients appear as  $d(fo^2)/d\lambda$ . Observations of the critical frequency of the F2-layer, foF2, are done at the KNMI at De Bilt by using an ionosonde (De Bilt is located about 140 km south-west of the WSRT). The foF2 information is available to us every hour. Since only one station provides us with ionospheric data, gradients are not measured directly. However, by taking into account the orientation of the WSRT array which is parallel to the direction of the rotation of the earth, Eq.(1) is approximated by assuming

$$\frac{d(fo^2)}{d\lambda} = \{ \frac{1}{2} (foF2(t+1) + foF2(t)) \}^2 - \{ \frac{1}{2} (foF2(t) + foF2(t-1)) \}^2 \quad (4)$$

where foF2(t) is the value of foF2 at time t (t in integer hours). By this means the data taken by the KNMI at De Bilt are sufficient to account for east-west gradients in the electron density. This approximation is valid because of the scale of the horizontal variations in the electron density which is several hundred kilometers.

Vertical gradients are calculated on the basis of a simple model for the vertical electron distribution which is scaled by the foF2 data. I.e. it is assumed that the vertical electron distribution is proportional to

$$fo^2 = A + Br + \frac{1}{2}Cr^2 \quad (5)$$

(De Munck, 1982; Spoelstra, 1981, 1983a).

The corrections are determined for the subionospheric point where the line of sight crosses the layer of maximum electron density.

#### 4. RESULTS

The effect of the application of the corrections for ionospheric refraction on interferometric observations is best visible in observations of point sources (since they have intrinsically the most simple phase behaviour).

During 15-19 December 1978 a series of short observations of several calibration sources were done with the WSRT at both 608.5 and 1412.0 MHz. For this purpose 608.5 MHz frontends have been installed at the odd fixed telescopes and telescopes C and D. 1412.0 MHz frontends have been installed at the even fixed telescopes and A and B. The radio sources 3C48, 3C147, 3C286, 3C309.1, 3C380 and 3C454.3 were observed alternately at both frequencies during 5 minutes. The total number of observations was 537, equally distributed over both frequencies. The resulting database contained amplitude and phase information as a function of hour angle and declination. The hour angle and declination coverage of the data made it possible to calculate residual baseline corrections: i.e. corrections for errors in the positions of the individual telescopes, for the observing frequency,  $\Delta v$ , for the declination of the baseline pole,  $\Delta \delta_p$ , and for the clock,  $\Delta t$ .  $\Delta v$  is a correction for the scale of the baseline and  $\Delta \delta_p$  and  $\Delta t$  are corrections for the orientation of the baseline. The influence of ionospheric refraction was not visible in the corrections found for the individual telescopes. The influence on the other baseline parameters is shown in Table 1.

Table 1  
Influence of ionospheric refraction  
on WSRT baseline parameters

$v$ (MHz)	ionospheric refraction correction	$\Delta v$ (kHz)	m.e. $\Delta v$ (kHz)	$\Delta t$ (ms)	m.e. $\Delta t$ (ms)	$\Delta \delta_p$ (")	m.e. $\Delta \delta_p$ (")
1412.0	no	0.5	0.3	28.0	3.0	0.68	0.06
1412.0	yes	2.8	0.3	29.0	3.0	0.48	0.06
608.5	no	-6.7	0.2	13.0	9.0	1.57	0.14
608.5	yes	-1.2	0.2	7.0	9.0	0.31	0.16

The corrections given in Table 1 are differential corrections with respect to those already applied to the data. We can conclude from these results that the ionosphere tends to make the baseline of the interferometer somewhat longer. At 1412.0 MHz this correction is 0.4 mm at a baseline of 1 km. At 608.5 MHz it is 4.4 mm at 1 km baseline. Furthermore, the orientation of the array changed. This is most clearly visible in  $\Delta \delta_p$  (especially at 608.5 MHz). Although only east-west effects of the ionosphere have been taken into account, the change of  $\Delta \delta_p$  suggests the influence of north-south gradients, but is an effect introduced by the observing technique (Spoelstra, 1983a).

After the application of all relevant corrections the phase residuals for point sources should be  $0^\circ$ . But in practice this is almost never the case. The influence of ionospheric refraction on the phase residuals (i.e. the deviations from  $0^\circ$ ) is given in Table 2. Again the database of the observations of December 1978 was used.

Table 2  
Phase residuals

$v$ (MHz)	corrected for ionospheric refraction	phase residuals ( $^\circ$ )
1412.0	no	$\pm 9$
1412.0	yes	$\pm 7$
608.5	no	$\pm 12$
608.5	yes	$\pm 7$

The improvement of the phase residuals due to the correction for ionospheric refraction is clear. Phase variations with time scales less than an hour could not be corrected. Therefore, the remaining residuals may be due to these effects since ionospheric information was only available for us per hour UT. Figure 1 shows the improvement by the present correction technique for a typical night observation. It turned out that the correction method failed for observations done during sunrise (Spoelstra, 1983a). Since the interferometer phase contains astrometric information these corrections may influence the apparent position as well as the observed structure of a radio source. Spoelstra (1983a) showed that the present correction method reduces the differences between the observed source position at e.g. 608.5 MHz and its catalogue position (determined at much higher frequency). He also showed an example of the change of structure in a field: see Figure 3. The shaded features in figure 3 show the source structure at 608.5 MHz. The contours in figure 3 show the difference map for processing without and with corrections for ionospheric refraction. The peak intensity of the difference map is about 3% of the peak intensity of the main source. Since averaged over the whole 12h observation the change of position due to the correction for ionospheric

refraction is only 0.6 ( $\pm 0.3$ ) the contours show changes of structure in the field. The elongation of the contours roughly parallel to the structure of the main radio source is an accidental effect caused by the asymmetry in hour angle of the ionospheric refraction. If refraction changes the observed structure of radio sources, the grating responses of these sources will change too. This is visible in figure 3.

##### 5. CORRECTIONS FOR VLBI

Ionospheric refraction is a significant effect for CERI at frequencies up to about 2 GHz. In general the observing frequencies used in VLBI are higher than 2 GHz, but the long baselines involved imply that this technique is also sensitive to effects of ionospheric refraction. In VLBI it is common use to translate phase errors into errors in time delay,  $\tau$ , and fringe rate,  $f$  ( $= v \, d\tau/dt$ ). In general we cannot determine the values of  $\tau$  and  $f$  at anyone instant exactly, due to several effects: e.g. the rotation of the earth; averaging over a finite integration time, and sampling the data at discrete time intervals rather than continuously; unknown offsets in time and frequency; effects due to the earth's atmosphere (e.g.: Cohen and Shaffer, 1971).

The observed time delay can be written as

$$\tau_o = \frac{l_1}{c} \sin \delta + \frac{l_2}{c} \cos \delta \cos (\alpha-h) + \Delta\tau_c + \Delta\tau_a \quad (6)$$

and the observed fringe frequency as

$$f_o = -\Omega \, l_2' \cos \delta \sin (\alpha-h) + \Delta f_c + \Delta f_a \quad (7)$$

where  $\Delta\tau_c$  and  $\Delta f_c$  denote the influences of clock errors, of the rotation of the earth, etc. Atmospheric errors are included in  $\Delta\tau_a$  and  $\Delta f_a$ .  $\Delta\tau_a$  and  $\Delta f_a$  can be divided into a component due to the troposphere ( $\Delta\tau_t$  and  $\Delta f_t$ , respectively) and the ionosphere ( $\Delta\tau_i$  and  $\Delta f_i$ , respectively).

One technique to correct VLBI observations for ionospheric influences is to compare the group delays of the signals observed at two widely separated frequencies simultaneously. This technique has been applied successfully by e.g. Robertson and Carter (1982) and Campbell (1982, private communication). They derive corrections for ionospheric refraction with typical accuracies of about  $4.0 \times 10^{-3}$  times the baseline used. This accuracy depends also on the resolution of the MkIII VLBI-processor. The analysis of dual frequency data make it mandatory to pass through all the data at least twice. The amount of data involved makes a cheaper solution attractive. Furthermore, the dual frequency option is not yet available on a standard basis for complete VLBI networks. An advantage of this method is that for calibration, correction and reduction of the data no additional information about the ionosphere is necessary.

As was discussed in sections 2 - 4 it is possible for CERI to represent ionospheric refraction as position errors which are used to correct interferometric parameters. In VLBI an important problem is that the line of sight for each element of the interferometer points through a part of the atmosphere whose physical state is not correlated with that of the other elements. We assume that the refraction error is the arithmetic mean of the contributions by the atmosphere above each of the interferometer elements. For each element the position error due to refraction can be calculated by Eqs. (1) and (3). The F2-layer of the ionosphere dominates ionospheric influences at the frequencies used. The columnar electron density,  $N$ , of the F2-layer can be derived from observations of the critical frequency of the F2-layer, foF2. The foF2 values can be derived from ionosonde observations. Since east-west gradients giving rises to  $\Delta\alpha$  are equivalent to gradients in time (Eq. (4)), continuous time series of foF2 observed at an ionosonde station close to an element of the interferometer (e.g. at distances less than 100 - 200 km) are needed to calculate  $\Delta\alpha$  for the line of sight of that element.

The refraction error in declination,  $\Delta\delta$ , can be determined on the basis of e.g. differential Doppler data measured from NNSS navigational satellites. These satellites travel in polar orbits with speeds which are high with respect to changes in the ionosphere. With these measurements the electron content of the ionosphere can be determined (De Mendonça, 1962, 1963). Differential Doppler data combined from two stations (at distances about 300 km apart) give reliable results for the horizontal structure in the ionosphere (Ebel et al., 1969; Leitinger et al., 1975). Thus differential Doppler measurements of signals from NNSS satellites made at one or more stations close to an element of the interferometer (within about 200 km distance) can provide information about  $N$  and its north-south gradients. From these values  $\Delta\delta$  can be derived.

The error in the time delay and fringe frequency due to ionospheric refraction can be interpreted as due to a position error. Then we can write (Spoelstra, 1983b):

$$\Delta\tau_i = -\frac{l_1}{c} \cos \delta_o \Delta\alpha + \frac{l_2}{c} \cos \delta_o \sin (\alpha_o-h) \Delta\alpha + \frac{l_2}{c} \sin \delta_o \sin (\alpha_o-h) \Delta\delta \quad (8)$$

and

$$\Delta f_i = \Omega \, l_2' \{ \cos \delta_o \cos (\alpha_o-h) \Delta\alpha - \Delta\delta \sin \delta_o \sin (\alpha_o-h) \} \quad (9)$$

where  $\alpha_o$  and  $\delta_o$  are the true  $\alpha$  and  $\delta$  for the source.

With the aid of these relations the influence of ionospheric refraction on VLBI observations can be calculated.

At e.g. 5 GHz the correction factors can be determined with a typical accuracy of about  $2.5 \times 10^{-4}$  times the baseline used (Spoelstra, 1983b).

This method may be cheaper than the dual-frequency technique. This with respect to (i) computing time - because the method is a simple algorithm with 'known' ionospheric parameters -, and (ii) the instrumentation used to monitor the ionosphere - e.g. the satellite receivers often designed for geodetic research are available off the shelf for about k\$35 or less (including peripherals) -. At VLBI stations no additional hardware is necessary for dual frequency observations.

## 6. DISCUSSION

With the procedure presented in this paper it is in principle possible to correct radio astronomical observations for ionospheric refraction. These corrections imply improvement of the baseline parameters of the radio interferometer and the astrometric accuracy of the observations made with it. In the case of VLBI the method can only be applied if a network of ionosonde and satellite tracking stations "co-located" with the VLBI stations is operational during the astronomical observations.

Since in the case of the WSRT only one station, the KNMI at De Bilt, gives us ionospheric information we are very sensitive to defects in these data. Furthermore, since ionospheric information is only available each integral hour we can not correct for phase variations at shorter time scales. The correction fails for observations done around sunrise. This is due to the fact that at this time the plasma in the ionosphere is heated and will move upward. A move which is also supported by changes in the winds in the ionosphere due to this heating. Since with an ionosonde only the bottomside of the F2-layer can be studied, we obtain inadequate information to estimate the total electron content along the line of sight around sunrise. It is expected that in the near future when we use information from satellites (e.g. differential Doppler observations of NNSS satellites) the quality of the results derived with the present method will increase. Since the schedule of the passages of the NNSS satellites may have occasional gaps of about 2 to 3 hours, measurements using these satellites have to be complemented by other means: i.e. additional ionosonde observations.

## ACKNOWLEDGEMENTS

The Westerbork Synthesis Radio Telescope is operated by the Netherlands Foundation for Radio Astronomy with financial support from the Netherlands Organization for the Advancement of Pure Research (Z.W.O.).

## REFERENCES

- Baars, J.W.M., Van der Brugge, J.F., Casse, J.L., Hamaker, J.P., Sondaar, L.H., Visser, J.J., Wellington, K.J., 1973, "The Synthesis Radio Telescope at Westerbork", *Proc. IEEE*, 61, 1258.
- Bos, A., Raimond, E., van Someren Gréve, H.W., 1981, "A Digital Spectrometer for the Westerbork Synthesis Radio Telescope", *Astron. Astrophys.*, 98, 251.
- Brouw, W.N., 1969, Netherlands Foundation for Radio Astronomy, Internal Technical Report 78.
- Brouw, W.N., Van Someren Gréve, H.W., 1973, Netherlands Foundation for Radio Astronomy, Internal Technical Report 112.
- Casse, J.L., Muller, C.A., 1974, "The Synthesis Radio Telescope at Westerbork. The 21 cm Continuum Receiver System", *Astron. Astrophys.*, 31, 333.
- Cohen, M.H., Shaffer, D.B., 1971, "Positions of Radio Sources from Long-baseline Interferometry", *Astron. J.*, 76, 91.
- De Mendonça, F., 1962, "Ionospheric Electron Content and Variations Measured by Doppler Shifts in Satellite Transmissions", *J. Geophys. Res.*, 67, 2315.
- De Mendonça, F., 1963, "Ionospheric studies with the differential Doppler technique", in "Radio Astronomical and Satellite Studies of the Atmosphere", J. Aarons editor, North-Holland Publ. Comp., Amsterdam, p. 289.
- De Munck, J.C., 1982, "Ionospheric correction for (pseudo) range measurements to satellites", *J. Geod. Soc. Japan*, Spec. Issue October 1982, p. 553-561.
- Ebel, A., Hartmann, G., Leitinger, R., Schmidt, G., Schodel, J.P., 1969, "Vergleichende Auswertung von Faraday-Effekt-Beobachtungen zweier Empfangstationen, Grundlagen und Ergebnisse", *Zeitschrift für Geophysik*, 35, 373.
- Hagfors, T., 1976, "The ionosphere", in: "Methods of Experimental Physics", Vol. 128, ed. M.L. Meeks, New York, 119.
- Högbom, J.A., Brouw, W.N., 1974, "The Synthesis Radio Telescope at Westerbork. Principles of Operation, Performance and Data Reduction", *Astron. Astrophys.*, 33, 289.
- Komesaroff, M.M., 1960, "Ionospheric refraction in radio astronomy", *Australian J. Phys.*, 13, 153.
- Leitinger, R., Schmidt, G., Tauriainen, A., 1975, "An Evaluation Method Combining the Differential Doppler Measurements from Two Stations that Enables the Calculation of the Electron Content of the Ionosphere", *J. Geophys.*, 41, 201.
- Robertson, D.S., Carter, W.E., 1982, "Earth rotation information derived from MERIT and POLARIS VLBI observations", in "High-precision Earth rotation and Earth-Moon dynamics", ed.: O. Calame, Reidel, Dordrecht, 97.
- Spoelstra, T.A.Th., 1981, Netherlands Foundation for Radio Astronomy, Internal Technical Report 162.
- Spoelstra, T.A.Th., 1983a, "The influence of ionospheric refraction on radio astronomy interferometry", *Astron. Astrophys.*, 120, 313.

Spoelstra, T.A.Th., 1983b, "Correcting VLBI-observations for ionospheric refraction, in: "Proceedings of the Symposium on 'Beacon Satellite Studies of the Earth's Environment', ed.: T.R. Tyagi (in press).

Van Someren Gréve, H.W., 1974, "The Data Handling of the Westerbork Synthesis Radio Telescope", Astron. Astrophys., 15, 343.

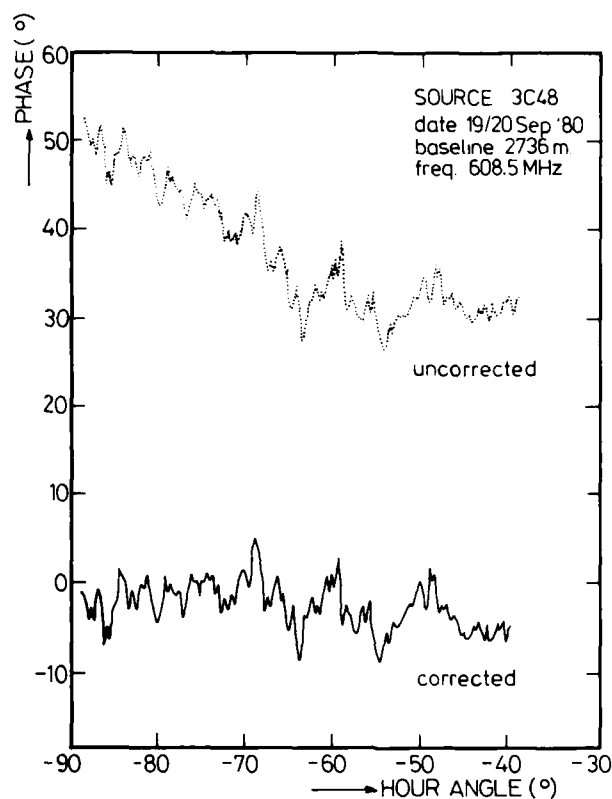


Figure 1: Phase variations as a function of hour angle for an observation of 3C48 as observed and as corrected (including corrections for ionospheric refraction). The baseline was 2736 m. The observation was done on 19 September 1980 between 19<sup>h</sup>20 and 22<sup>h</sup>40 UT (from Spoelstra, 1983a).

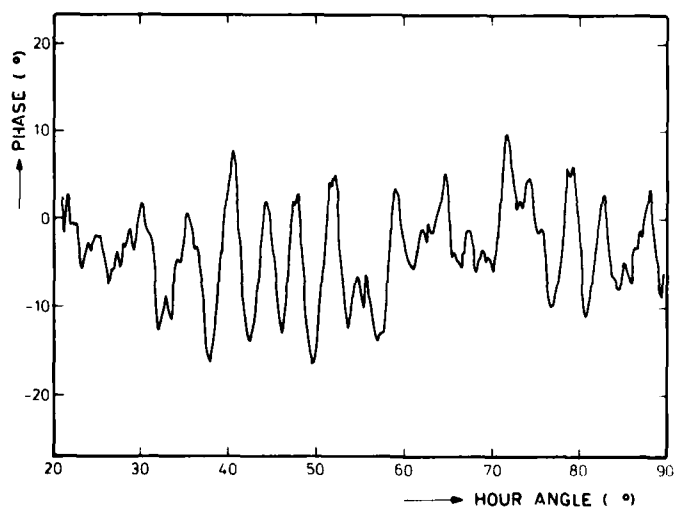


Figure 2: Phase variations as a function of hour angle for an observation of 3C147 as observed with the WSRT at 2736 m baseline. The observing time was 06<sup>h</sup>37 - 11<sup>h</sup>11 UT. The observing date was 21 September 1980. This observation has already been corrected for ionospheric refraction.

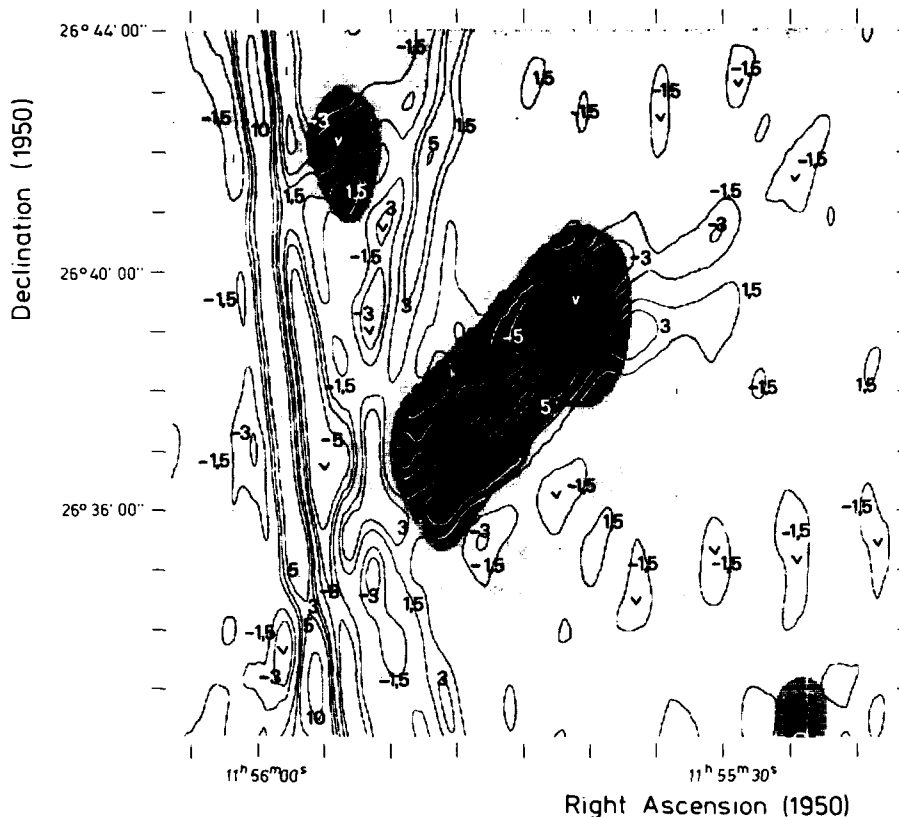


Figure 3: Map of the differences between the brightness distribution of radio source 1155+266 processed with and without corrections for ionospheric refraction (contour plot). This difference map is superimposed on a cleaned map of the radio source (grey scale representation). The observing frequency is 608.5 MHz. The contour values are given in mJy ( $1 \text{ mJy} = 10^{-29} \text{ W m}^{-2} \text{ Hz}^{-1} \text{ sterad}^{-1}$ ). Minima are indicated by "v" (from Spoelstra, 1983a).

#### DISCUSSION

E. E. Altshuler (U.S.): How do you obtain the tropospheric refraction correction?

T.A.Th. Spoelstra (The Netherlands): In the case of the Westerbork Synthesis Radio Telescope (WSRT) observations, we use a constant refractive index at present because the main factor is the spherical geometry of the earth and atmosphere. At very low elevation angles, less than  $4^\circ$ , we have still interferometric phase errors up to  $150^\circ$ . These can be reduced to include real time corrections based on ambient temperatures, humidities, and air pressures. Then we finally have errors of about  $5^\circ$  at a 6 cm wavelength. A method to use this approach will be operational in a few months.

H. Soicher (U.S.): This is only a comment. The relevant ionospheric parameter is the integrated electron density, which is available from a network of polarimeters (for Faraday rotation monitoring) or Doppler receivers.

In the future Global Positioning System (GPS), satellites may be used for determination of total electron content (TEC) by the differential group delay method.

THE ESTIMATION AND CORRECTION OF REFRACTIVE BENDING  
-----  
IN THE AR3-D TACTICAL RADAR SYSTEMS  
-----

by  
Frank Barker  
Head of Operational Research  
Plessey Radar Systems  
Oakcroft Road, Chessington  
Surrey, England KT9 1QZ

SUMMARY

----- This paper deals with the development of techniques for the estimation and correction of refractive bending, in the vertical plane, in the evolution of a family of radar systems. The systems are based on the AR3-D radar and are in service in several countries and climates. After a brief description of the AR3-D radar systems, we consider the Operational requirements; then the Engineering solutions; then some of the Human Factors which affect the design and implementation, and, finally, future possibilities. Appendix 1 describes a simple and exact approach to sensitivity analysis. Appendix 2 describes a fast algorithm for the on-line correction of radar plot elevation data. The thrust of the paper is the need for education on refractive effects and for understanding of the possibilities which exist for estimation and correction in 3-D radar systems.

1. Introduction  
-----

1.1 The main sensor for the systems being described, is the AR3-D radar (Refs 1,2) which provides ground based PSR and SSR coverage to about 300 n.m. range, with an altitude ceiling above 100 Kft. The radar scans mechanically in azimuth, usually at 6 rpm, with a prf of 250 Hz. The antenna is frequency sensitive in elevation and radiates a pencil beam which is scanned vertically by a 36 usec frequency swept pulse. The sweep is non-linear and, in conjunction with the appropriate receiver circuits, it provides :-

- .1 Control of the vertical energy distribution.
- .2 Compression of the received signal to 0.1 usec.
- .3 Measurement of elevation angle by the measurement of the frequency of the received signal.

1.2 The C-3 sub-systems into which these radars are connected, cover a wide spectrum of facilities and capabilities, from single reporting posts up to integrated networks with numerous radars and aircraft control stations.

### 1.3 The facilities which are provided include :-

- .1 Control of the radar sensors
- .2 Processing of radar plots, including computation of height on each plot, after correcting for the estimated refractive bending.
- .3 Automatic (and manual) initiation and tracking of aircraft on both PSR and SSR radar data.
- .4 Flight plan handling with automatic plan-track comparison.
- .4 Threat evaluation and reaction-suggestion, including collision warning where appropriate.
- .5 Self-adaptive interception and recovery calculations.

## 2. Operational Aspects

-----

2.1 In such systems, the errors and uncertainties in the estimation of aircraft height are important parameters, having major effects on the confidence which can be placed in the system (Ref 3). Therefore we have to answer the question :-

"How small must be the errors and uncertainties in the estimation and correction of refractive bending if they are to have no serious adverse effects on the confidence of the user in the ability of the system to perform its operational mission ?"

2.2 Given that the confidence of the operational user is a matter of considerable importance in such systems, we can avoid all those other aspects of this question which can so easily become both sensitive and contentious, and concentrate upon this one point. Because this is largely a matter of psychology, the answer cannot be numerically exact, but we can bracket an answer by considering particular cases.

2.3 Consider a civil supersonic transport flying at a height of perhaps 60 Kft and which may be detected at a range beyond 250 n.m. For the purpose of this analysis, we assume that this aircraft normally reports its height automatically and accurately by Mode-C responses on SSR. At the same time, it will be detected by PSR, and its height will be estimated from the PSR returns. Given this scene, we can ask the question :- "What are the effects of discrepancies between the SSR height and the PSR height ?"

2.4 Obviously, the effects of discrepancies depend upon their magnitudes and the frequencies with which they occur. For example, if the discrepancy is normally about a hundred feet, then if a discrepancy of several thousand feet occurs on a particular occasion, the surveillance operator will want to know whether it is a fault or a deliberate act.

2.5 Whatever the answer, the situation reveals a threat which requires a positive reaction. But, if the gap between SSR heights and PSR heights is often several thousands of feet, then the probability of the situation being perceived as a threat is greatly diminished, as is the probability of positive reaction. Alternatively, valuable resources may be wasted.

2.6 Given this scene, we can now bring in the fact that, an uncertainty of 0.04 deg. in the angle of elevation of an aircraft at a range of 250 n.m. corresponds with an uncertainty of 1,000 ft in height. Clearly, therefore, at low angles of elevation, the performance is very sensitive to errors and uncertainties in the estimation and correction of refractive bending. (Appendix 1).

### 3. Engineering solutions

-----

3.1 The oldest solution to the problem of refractive bending, which we used during the 1960's, was to take the effective radius of the earth to be  $4/3$  x the geometric value, (Refs 4,5). Limitations on this approximation are discussed in the literature, although they tend to concentrate on macroscopic effects and to ignore the effects of the micro-climate.

3.2 Continuing with the 'effective radius', the next idea was to measure the surface refractivity at the radar site and then to estimate the effective radius by assuming an 'exponential atmosphere', (Refs 4,5). This was tentatively adopted as a policy early in the 1970's, but was not implemented in AR3-D systems.

3.3 Continuing with the notion of an 'exponential atmosphere', we implemented a solution based upon a single measurement of refractivity at the surface. The value of this measurement then became the independent variable in a formula which generated the co-efficients of a polynomial which, in turn, generated an elevation correction as a function of the observed range and elevation of the plot. The formula which generated the co-efficients was derived by first tracing a set of rays through various exponential atmospheres and then performing a least-squares analysis. This method provided a more accurate correspondence with an exponential atmosphere than did the effective radius method, but it took no account of actual gradients.

3.4 The decision to use dynamic ray tracing was made when we realised that the ray tracing process can be a background computational task, running only when new meteorological data is received, and generating a table of range-and-elevation dependent corrections for use in the on-line correction of PSR plots. This method was implemented some years ago, using the aviation met-data which is generally available.

3.5 Later, it was perceived that instead of using the general aviation met-data for this purpose, one could obtain better performance by taking detailed soundings of the micro climate at the radar.

3.6 Although there are plenty of technical problems which we have to overcome for a full implementation of this solution, they are simplified by the fact that the overall process is a linear train, without the recursive loops which complicate so many matters in systems engineering.

3.7 The essential parts of the process are :-

- .1 A mechanically constrained sounding system which measures and transmits the raw data by wire.
- .2 A data recording facility.
- .3 A pre-processor for examination of the profile and for the extraction of the salient points.
- .4 A facility for transferring the extracted profile to the radar data processor.
- .5 An improved ray tracing process to handle the detailed profile data and to tabulate the elevation correction as a "fast function" of observed range and elevation.
- .6 A fast process for the on-line correction of plots.

3.8 While most of the parts described above are still under investigation, we can report an interesting success in finding a "fast function" for use in the on-line correction of plots. The problem is that the correction is a non-linear function of observed range and elevation. Thus, a simple tabulation entails a binary search for the on-line correction process, and this is slow, (about 600 usec has been quoted). However, we have found that, by forming specially structured tables at the output of the ray-tracer, the on-line correction can be turned into an essentially linear process with an average execution time of about 150 usec. (Appendix 2)

3.9 There are however cases where it may not be possible to take the desired soundings at the desired frequency. In such cases, we may model typical profiles, from which, by means of an off-line ray-tracing process, we can pre-compute sets of tables which are held on disc and can be individually selected either according to the user's perceptions of current conditions, or according to the time of year and the time of day.

3.10 Often, however, there are problems in obtaining enough data to construct basic models. Micro climates around the world seem to be, as yet, but little documented, and it is not a trivial matter to arrange the necessary data gathering activities on a global basis.

#### 4. Human Factors

-----

4.1 In all organisations which procure, supply, operate, and maintain radar systems, there are significant human factors which enter into the design and implementation of an acceptable solution to the problem of refractive bending.

4.2 The basic problem is that only fairly recently have we come to see the significance of the micro climate in the region of the radar, (Refs 6,7), and lay people are often surprised to realise how little we know about the detailed structure and dynamics of the micro climate around us.

4.3 Thus, there is still quite widespread belief that older systems had no problems in dealing with refraction. This belief is bolstered by the tradition that radar performance under non-standard tropospheric conditions is outside the specifiable performance envelope. The tradition may still be valid for the performance of the basic radar sensor, but its validity seems questionable in the wider systems context.

4.4 It may also be difficult to get people to accept responsibility for refraction correction on a regular basis. Traditionally, it is the job of nobody to take detailed low-level soundings at a radar site at frequent intervals, to extract salient points on the refractivity profile and to supply the data to the on-line system.

4.5 However, if we are generally right in our estimation of the significance of refractive bending, then the human problem can be clearly seen as needing a determined programme of education.

#### 5. The Future

-----

5.1 Looking to the future, some of the ways in which we expect our approach to develop are :-

- .1 Modelling of typical profile development patterns to permit forecasting and on-line interpolation between soundings.
- .2 The use of self-piloted sounding vehicles to give lateral extension of the data for a truly 3-D approach, (Ref 8).
- .3 The use of the radar system itself as a refraction sensor.

## References

-----

1. Milne, K: "The Combination of Pulse Compression with Frequency Scanning for Three-dimensional radars" : Radio and Electronics Engineer : August 1964.
2. Jane's Weapon Systems edn 1981-82, p490.
3. Buckley, T: "The Effects of Atmospheric Refraction on the Accuracy of Radar Height Measurements" : RRE Technical Note 734 : October 1967.
4. Hall, M.P.M: "Effects of the troposphere on radio communication" : Peregrinus : 1979.
5. Bean B.R. and Dutton E.J : "Radio Meteorology" : National Bureau of Standards, USA, March 1966.
6. Gossard E.E : "Clear weather meteorological effects on propagation at frequencies above 1 GHz" : Radio Science : September-October 1981.
7. Gossard E.E : "Formation of elevated refractive layers in the oceanic boundary layer by modification of land air flowing offshore" : Radio Science : March-April 1982.
8. Barton Ian J : "The importance of tilted layers in the tropospheric ducting of radio waves over the Timor Sea" : Radio Science : August-September 1973.

## Acknowledgements

-----

The support of the Directors of the Plessey Company plc in the preparation of this paper, and the work which it describes, is gratefully acknowledged. We are also grateful to Mr Martin Hall and his colleagues at the Rutherford-Appleton Laboratories for their kind help and encouragement, to our colleagues at Cowes and Chessington, and, especially to all our Customers for their constant desire that we should "Do it better".

## APPENDIX 1

Bending Sensitivity Analysis  
-----

A1.1 The initial aim of this work was simply to obtain figures for the sensitivity of bending to variations in the refractivity profile.

A1.2 The first approach was naive and over-complicated in that it used ray-tracing in conjunction with a variable profile. It gave lots of figures, but very little information, and it was seen that an approach was needed which would show the connections between bending and refractivity much more directly.

A1.3 The next approach was therefore based on an assumption of a linear profile over the first 50 feet. The slope was then varied with a view to finding a simple model which would give good insight and quick estimates of the bending.

A1.4 The difficulty with this approach is that the length of the ray through the bending layer is a function of the bending, which throws us back to ray-tracing.

A1.5 The difficulty can, however, be overcome if we define a height band of interest, through which the ray undergoes uniform bending, and we then postulate rays of various path-lengths being propagated through this layer. This is an inherently simple model by which we can examine the relationship between the refractivity slope and the bending.

A1.6 The following figures show:-  
(1) the geometry of an exact solution,  
(2) the outline algorithm for the exact solution,  
(3) the geometry of a simple approximate solution,  
(4) extracts from a program to evaluate the parameters

A1.7 As can be seen from the figures, it is much easier to get an exact solution if we define the ground-range rather than the path length. As the distances are nearly equal, especially when there is a lot of bending, our feel for the problem is not much affected.

A1.8 The tables which follow show the correspondence between the bending in a defined surface layer, the N-gradient in the layer, the difference in the value of N across the layer, and the effect of the bending on the apparent height of an aircraft at 200 n.m.





## Figure A1(3)

## Extracts from bending analysis program

```

c      Evaluate the bending formulae at the specified intervals
      DO 240 I=1,25
      C=L(I)/RE

C      Evaluate the approximate bending formula
      APPRX=(C/2)-(H/L(I))

C      Compute the exact value

      RH=RE+H
      B1=RH*SIN(C)
      B2=RH*COS(C)
      P1=0.5*B1
      P2=0.5*(B2+RE)
      F2=0.5*((RH**2)-RE**2)/(RH*COS(C)-RE)
      PB1=B1-P1
      PB2=B2-P2
      PBLENG=((PB1**2)+(PB2**2))**0.5
      BF1=-B1
      BF2=F2-B2
      BFLENG=((BF1**2)+(BF2**2))**0.5
      ST=PBLENG/BFLENG

      BETA=ASIN(ST)

c      Compute the profile slope
      DNDH=-2*(10**6)*BETA/L(I)

C      Compute the refractivity difference
      NDIFF=DNDH*H

C      Compute the height difference at 200 n.m.
      FEET=6080*200*BETA

c      Output the results

C      Increment the ground range
      L(I+1)=L(I)+DL

240    CONTINUE

```

Table A1(1)

Launch angle = 0.0 deg.

Height of layer = 13 metres.

LENGTH KM	APPROX DEG	BENDING DEG	DN/DH N/KM	N-DIFF AT H	FEET AT 200NM
20.0	0.0527	0.0526	-91.8	-1.193	1115.8
22.0	0.0651	0.0647	-102.6	-1.334	1372.7
24.0	0.0769	0.0766	-111.4	-1.448	1625.4
26.0	0.0883	0.0880	-118.1	-1.535	1866.6
28.0	0.0993	0.0989	-123.3	-1.603	2099.5
30.0	0.1101	0.1098	-127.7	-1.661	2329.8
32.0	0.1206	0.1203	-131.3	-1.707	2554.1
34.0	0.1310	0.1307	-134.2	-1.744	2773.7
36.0	0.1412	0.1409	-136.6	-1.776	2989.6
38.0	0.1513	0.1510	-138.7	-1.803	3204.4
40.0	0.1612	0.1610	-140.5	-1.826	3416.2
42.0	0.1711	0.1709	-142.0	-1.846	3627.1
44.0	0.1809	0.1807	-143.3	-1.863	3834.5
46.0	0.1907	0.1904	-144.5	-1.878	4041.3
48.0	0.2003	0.2001	-145.5	-1.892	4246.5
50.0	0.2099	0.2097	-146.4	-1.903	4451.1
52.0	0.2195	0.2193	-147.2	-1.914	4654.4
54.0	0.2290	0.2288	-147.9	-1.923	4856.7
56.0	0.2385	0.2383	-148.6	-1.931	5057.9
58.0	0.2480	0.2478	-149.1	-1.939	5258.8
60.0	0.2574	0.2572	-149.6	-1.945	5458.9
62.0	0.2668	0.2666	-150.1	-1.951	5658.3
64.0	0.2761	0.2760	-150.5	-1.957	5857.4
66.0	0.2855	0.2853	-150.9	-1.962	6055.6
68.0	0.2948	0.2947	-151.3	-1.966	6253.6

Table A1(2)

Launch angle = 0.0 deg

HEIGHT OF LAYER = 26 metres

LENGTH KM	APPROX DEG	BENDING DEG	DN/DH N/KM	N-DIFF AT H	FEET AT 200NM
20.0	0.0154	0.0165	-28.8	-0.749	350.4
22.0	0.0312	0.0316	-50.1	-1.302	669.8
24.0	0.0458	0.0462	-67.2	-1.748	981.3
26.0	0.0596	0.0599	-80.4	-2.090	1270.6
28.0	0.0727	0.0727	-90.7	-2.358	1543.7
30.0	0.0852	0.0854	-99.3	-2.583	1812.0
32.0	0.0973	0.0975	-106.3	-2.764	2068.4
34.0	0.1091	0.1091	-112.0	-2.912	2315.6
36.0	0.1205	0.1204	-116.8	-3.036	2555.7
38.0	0.1317	0.1316	-120.9	-3.144	2793.6
40.0	0.1426	0.1426	-124.4	-3.235	3025.8
42.0	0.1534	0.1534	-127.5	-3.315	3256.0
44.0	0.1640	0.1639	-130.1	-3.382	3479.4
46.0	0.1745	0.1744	-132.4	-3.441	3701.7
48.0	0.1848	0.1847	-134.3	-3.493	3920.8
50.0	0.1950	0.1950	-136.1	-3.540	4138.8
52.0	0.2052	0.2052	-137.7	-3.581	4354.2
54.0	0.2152	0.2152	-139.1	-3.617	4567.5
56.0	0.2252	0.2252	-140.4	-3.649	4778.8
58.0	0.2351	0.2351	-141.5	-3.679	4989.5
60.0	0.2450	0.2449	-142.5	-3.705	5198.6
62.0	0.2548	0.2547	-143.4	-3.729	5406.2
64.0	0.2645	0.2645	-144.3	-3.751	5613.4
66.0	0.2742	0.2742	-145.0	-3.770	5818.7
68.0	0.2839	0.2838	-145.7	-3.788	6023.6

Table A1(3)

Launch angle = 0.0 deg

HEIGHT OF LAYER = 13 metres

LENGTH KM	APPROX DEG	BENDING DEG	DN/DH N/KM	N-DIFF AT H	FEET AT 200NM
20.0	0.0527	0.0526	-91.8	-1.193	1115.8
25.0	0.0826	0.0821	-114.6	-1.490	1741.6
30.0	0.1101	0.1098	-127.7	-1.661	2329.8
35.0	0.1361	0.1358	-135.4	-1.761	2882.3
40.0	0.1612	0.1610	-140.5	-1.826	3416.2
45.0	0.1858	0.1856	-144.0	-1.871	3938.8
50.0	0.2099	0.2097	-146.4	-1.903	4451.1
55.0	0.2338	0.2336	-148.2	-1.927	4957.2
60.0	0.2574	0.2572	-149.6	-1.945	5458.9
65.0	0.2808	0.2807	-150.7	-1.959	5956.4
70.0	0.3041	0.3040	-151.6	-1.971	6451.4
75.0	0.3273	0.3272	-152.3	-1.980	6943.6
80.0	0.3504	0.3503	-152.8	-1.987	7434.3
85.0	0.3734	0.3733	-153.3	-1.993	7923.1
90.0	0.3964	0.3963	-153.7	-1.998	8410.8
95.0	0.4193	0.4192	-154.0	-2.002	8897.3
100.0	0.4422	0.4421	-154.3	-2.006	9383.0
105.0	0.4651	0.4649	-154.6	-2.009	9867.7
110.0	0.4879	0.4878	-154.8	-2.012	10351.8
115.0	0.5106	0.5105	-155.0	-2.015	10835.3
120.0	0.5334	0.5333	-155.1	-2.017	11318.3
125.0	0.5561	0.5560	-155.3	-2.019	11800.8
130.0	0.5788	0.5787	-155.4	-2.020	12282.9
135.0	0.6015	0.6014	-155.5	-2.022	12764.6
140.0	0.6242	0.6241	-155.6	-2.023	13246.1

Table A1(4)

Launch angle = 0.0 deg

HEIGHT OF LAYER = 26 metres

LENGTH KM	APPROX DEG	BENDING DEG	DN/DH N/KM	N-DIFF AT H	FEET AT 200NM
20.0	0.0154	0.0165	-28.8	-0.749	350.4
25.0	0.0528	0.0526	-73.5	-1.911	1117.3
30.0	0.0852	0.0854	-99.3	-2.583	1812.0
35.0	0.1148	0.1148	-114.5	-2.978	2437.0
40.0	0.1426	0.1426	-124.4	-3.235	3025.8
45.0	0.1692	0.1693	-131.3	-3.414	3592.3
50.0	0.1950	0.1950	-136.1	-3.540	4138.8
55.0	0.2202	0.2202	-139.7	-3.633	4672.9
60.0	0.2450	0.2449	-142.5	-3.705	5198.6
65.0	0.2694	0.2693	-144.6	-3.760	5715.9
70.0	0.2935	0.2935	-146.3	-3.805	6228.1
75.0	0.3174	0.3173	-147.7	-3.840	6735.1
80.0	0.3411	0.3411	-148.8	-3.869	7238.8
85.0	0.3647	0.3647	-149.7	-3.893	7739.1
90.0	0.3881	0.3881	-150.5	-3.914	8237.0
95.0	0.4115	0.4115	-151.2	-3.931	8732.5
100.0	0.4348	0.4347	-151.8	-3.946	9226.6
105.0	0.4580	0.4579	-152.2	-3.958	9718.7
110.0	0.4811	0.4811	-152.7	-3.969	10209.6
115.0	0.5042	0.5041	-153.0	-3.979	10699.2
120.0	0.5272	0.5272	-153.3	-3.987	11187.9
125.0	0.5502	0.5501	-153.6	-3.994	11675.6
130.0	0.5731	0.5731	-153.9	-4.001	12162.6
135.0	0.5960	0.5960	-154.1	-4.007	12648.7
140.0	0.6189	0.6189	-154.3	-4.012	13134.3

## APPENDIX 2

-----

Summary of report  
"Fast On-Line Refraction Correction Algorithms"

by Lesley Thexton and Helen Coslett

December 1981

## THE AIM

-----

A2.1 The aim was to devise a new on-line refraction correction procedure which would reduce the average run-time from 600usecs to under 100usecs and with a computational accuracy of  $\pm 0.005$  deg or better. The size of the elevation correction table was to be under 200 words. The processor is a PDP11/34.

## THE METHOD

-----

## Format of Tables

-----

A2.2 A temporary elevation correction table, CRKN, is set up by the Refraction Compiler with 42 elevations and 8 ranges. The first 7 ranges are evenly spaced; the eighth is the maximum range of the radar and is used purely for interpolation with the previous range.

A2.3 Two sets of smaller tables are then formed which, for each tabulated range in CKRN, give the corrections at 8 evenly spaced low elevations and 8 evenly spaced high elevations. (The spacing is usually wider for the higher elevations). In addition, there is a table of zero corrections at zero range, giving a total of 17 tables.

A2.4 For each tabulated range, a critical angle is tabulated, below which the lower table is used, and above which the upper table is used.

A2.5 Also, for each of the 17 tables, a shift value is tabulated which is used in the truncation of the plot elevation, as described below.

## Calculation of Corrected Elevation

-----

A2.6 To correct the elevation of a plot, the tabulated range immediately below the plot range is obtained by truncating the plot range to 3 bits.

A2.7 The plot elevation angle is then compared with the critical angle at the tabulated range to determine whether the upper table is to be used, or the lower table. If the upper table is used, the critical angle is subtracted from the plot angle to give the angle relative to the start of the table.

A2.8 The relative angle is then right-shifted by the number of places tabulated for the selected table. (Para A2.5 above). This gives an offset in the range 0-7, which is used as a pointer to the correction value at this range and angle. By this technique, high angles, at which corrections are generally smaller, are truncated more than low angles, thus giving approximately uniform accuracy of the angular correction over the operational range.

A2.9 The process is then repeated for the next higher tabulated range and a linear interpolation in range is performed on the two correction values thus obtained.

A2.10 The resultant correction value is added to the original elevation to give the corrected elevation.

#### THE RESULTS

A2.11 The worst computational error seems to be 0.015 deg. and results are generally more accurate than this.

A2.12 The main correction table uses 136 words. The table of critical elevations uses 9 words. The table of shift values uses 17 bytes.

A2.13 For negative elevations, we use the correction values at zero elevation.

A2.14 The run time is reduced from 600u secs to 140u secs.

## DISCUSSION

E. E. Altshuler (U.S.): Have you considered using "targets of opportunity" such as satellites or radio sources (the limb of the sun or other strong sources) for obtaining pointing corrections?

A. Morley (U.K.): We have not given serious consideration to your suggestion, since we believe it to be impractical in operational situations.

F. Thomsen (Denmark): 1) Errors in height measurements are mostly caused by ground based ducts originated from evaporation at the sea surface, while the upper atmosphere can be regarded as stable. Do you think it is possible to perform a correction based on surface data or data from the lower part of the atmosphere?

2) Do you think a measurement of the temperature profile, without finding the corresponding pressure and water vapor content, can be used to calculate approximately the refractivity profile?

3) In a tactical situation, the height measured by the aircraft pressure altimeter and transmitted in the IFF Mode C should be neglected. Do you think the height measurement errors due to refraction have any tactical impact as long as the intercepting aircraft and the target aircraft are tracked from the same radar?

A. Morley (U.K.): 1) In our situations, we generally do not have any ducting problems. It is important to have meteorological data at all altitudes, although having the data does not necessarily solve the problems, especially where ducts are present. It is difficult to make corrections in ducting situations. Even with very comprehensive meteorological information available, it is sometimes difficult to predict ducting situations.

2) You need both pressure and humidity profiles, as well as the temperature profile in order to calculate the refractivity profile  $N$  with

$$N = 77.6 P/T + 3.77 \times 10^5 H/T^2,$$

where  $P$ ,  $T$ , and  $H$  are pressure, temperature, and humidity, respectively.

3) In a tactical situation, one cannot necessarily trust the Mode C data transponded by an opponent. However, it is still important to apply refraction correction to primary elevation data because an interceptor still requires a commanded absolute height. One is not always involved in the relative height between two aircraft.

T. Almond (U.K.): 1) Mode C: have you considered the errors inherent in the  $d$ -factor?

2) Performance: it must be difficult to determine refractive corrections when the PSR height finding performance (in my experience) is only accusable to  $\pm 3000$  feet (or worse) at ranges in excess of 100 NM.

A. Morley (U.K.): 1) We store actual and ICAO standard pressures as a function of height in our systems in order to make  $d$ -factor corrections in both directions.

2) With sufficient meteorological data, it is not difficult to determine refraction correction. At ranges in excess of 100 nautical miles at low elevation angles, the refraction correction can be much greater than the measurement accuracy components (for example, exponential atmosphere, range is 500 km, elevation is  $0^\circ$ , correction is  $0.6^\circ$ , and error is  $0.1^\circ$ ).

K. Anderson (U.S.): 1) With respect to E. Altschuler's comments on targetting aircraft, we find it extremely difficult in any operational situation. It is practical in a strictly scientific environment.

2) We need to have the full refractivity profile. Our interest is more in ducting applications, which are the very severe problems. This requires either the refractometer or the balloon launched radiosonde, and we find that the latter is more than adequate for describing the environmental conditions. Gross features are the dominant characteristics, not the fine scale (10 or 1 meter samples), that influence radar performance. We looked at very low level observations of satellites to try to infer the refractivity profile (described by Ted Almond), but fine scale turbulent structures destroy the patterns. You might use satellites for transmissions through the atmosphere to infer the refractivity structure, but you will have no information on ducting effects. Your low level (1000 feet) duct will hurt you most, but it cannot be picked up because not enough of the path goes through it.

3) Again, I was not implying use of satellites for refractivity profiles, but just using them to determine the position of satellites and using that as a course correction for your angles is extremely difficult in the operational mode. Scientifically it can be done.

EFFECT OF MULTIPLE SCATTERING ON THE PROPAGATION  
OF LIGHT BEAMS IN DENSE NONHOMOGENEOUS MEDIA

P. Bruscaiglioni, A. Ismaelli, L. Lo Porto, G. Zaccanti

Istituto di Fisica Superiore, Università di Firenze  
Via Santa Marta, 3  
50139 Firenze, Italy

## SUMMARY

Calculations performed by means of a Monte Carlo method show that the contribution of forward single and multiple scattering to the received power in an optical transmission link through a turbid atmosphere increases when the scattering medium is more concentrated near the receiver. An experimental check of this result is also presented.

## LIST OF PRINCIPAL SYMBOLS

$\sigma$	scattering-extinction coefficient of the medium ( $m^{-1}$ )
$D$	link distance between transmitter and receiver
$\rho$	radius of the receiver's optical aperture
$\alpha$	receiver's F.O.V. semiangle
$\theta$	scattering angle
$L(\theta)$	scalar scattering function of the medium, normalized over the complete solid angle: $\int_{4\pi} L(\theta) d\Omega = 1$
$x$	axis of the laser beam
$\tau = \sigma D$	link optical depth in case of homogeneous medium
$\tau = \int_0^D \sigma(x) dx$	link optical depth for a nonhomogeneous medium.

## 1. INTRODUCTION

Deviation from the Lambert-Beer law for the transmission of light beams and pulses through a turbid atmosphere can be caused by forward single and multiple scattering. The contribution of singly forward scattered light to the received power can be evaluated by simple geometrical considerations as shown by Deepak and Box (1) (2), if the spatial and angular characteristics of link, beam, and receiver are given, and one assumes the scattering properties of the medium. Multiple scattering effects raise when the optical depth of the medium grows over some limit determined by the properties of the medium and the characteristics of the apparatus.

The theoretical problem of multiple scattering has been studied by solving the small angle approximation of the radiative transfer equation by Stotts, Deepak et al, Tam and Zardecki (3) (4) (5) (6). The case of a reflecting target present in the transmission link was also dealt with by Zardecki et al, by means of a numerical integration of the transfer equation (7). Monte Carlo methods were also used to study the propagation of light pulses through dense media (Bucher (8)). Experiments on the propagation of light pulses scattered and diffused by thick clouds showed that possible large temporal spread of the pulses shape can be caused by multiple scattering (Bucher and Lerner, Mooradian et al., Mooradian and Geller (9) (10) (11)).

The results of the above-mentioned studies show that, even in the simpler case of a homogeneous turbid medium, for which the numerical density of the diffusing particles, their size distribution and scattering properties do not vary along the whole transmission link, the contribution of the scattered radiation to the received power depends in a complicated way on the actual combination of the many parameters describing the particular link situation.

The possible presence of nonhomogeneities in the medium increases the number of practical situations to be investigated. In this paper we present the results of calculations aimed to study the effect of strong nonhomogeneities of the medium. For some simple configurations of the scattering-extinction coefficient profiles along the transmission path, a comparison is made between the calculated received power, and the power which would be received for a transmission link involving a homogeneous medium presenting the same optical depth. The calculations are made by means of a version of the Monte Carlo method, which was used for light propagation studies by Poole et al. (12), as well as by the present authors (13), with reference to the Lidar technique. Details on

the Monte Carlo (M.C.) method will be resumed in sect.2, where two scaling formulae, used to treat the variation of two parameters of the link, will be introduced.

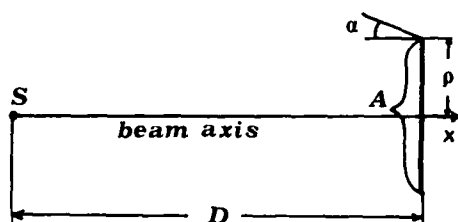


Fig.1 - Scheme of the transmission link.  
S: beam source, A: area of the receiver

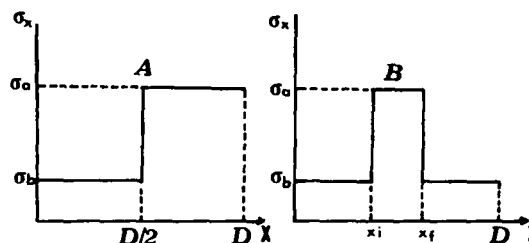


Fig.2 - Profiles of the extinction coefficient. A: Step, B: Bank.  $x_f - x_i = D/10$

The geometrical scheme of the problem is shown in Fig.1, where S is the source of a laser beam, A is the position of the receiver,  $\rho$  is the radius of the receiver's circular area,  $\alpha$  is the semiangular aperture of the receiver's field of view (F.O.V.). The x axis is the symmetry axis of the beam and of the source-receiver system. In this paper the single scattering albedo will be assumed equal to one, so that the scattering coefficient and the extinction coefficient will be assumed equal. The case of a plane stratified medium, where  $\sigma = \sigma(x)$ , is considered. A scalar scattering function has been commonly used in the theoretical problem of multiple scattering of light beams through fogs or clouds. This limitation can be accepted since the received power is often the interesting quantity, irrespective of the polarization characteristics of the radiation. The small scattering angle assumption concerning the direction of the scattered power with respect to the direction of the emitted beam, is consistent with the choice to neglect depolarization effects for a transmission link, when the scattering particles present in the medium can be assumed to be spherical, like in water fog or clouds. Depolarization effects are taken into account and have been measured in experiments concerning radiation back-scattered by dense media (Carswell and Pal (14) (15)).

For our calculations, the light beam emitted by the source will be modelled as a collimated cylindrical beam, whose power density presents a gaussian dependence on the distance y from the x axis of symmetry. The cross section of the cylindrical beam is assumed to be equal to the cross section presented at the receiver distance by a gaussian beam having a certain divergence angle  $\epsilon$ . This equivalence is justified when  $\epsilon$  is small, so that the scattering angles, evaluated by means of the M.C. method, differ by a very small amount for the two geometries. (This scheme was used for instance in Ref. (7)). Thus the power density  $p_e(y)$  of the emitted beam is given as:

$$(1) \quad p_e(y) = a \exp(-\delta^2 y^2) \text{ (W/m}^2\text{)} \quad a, \delta \text{ constants}$$

and is independent of x. The direction of power flow, in a vacuum, is the x direction over the whole cross section of the beam.

The results of the calculations will be presented in sect.4. As a common feature of the results, it will be shown that, when the scattering medium is concentrated nearer to the receiver, the contribution of multiple scattering to the received power increases with respect to the case of a homogeneous medium with the same optical depth. This effect will be found as very strong for some of the considered cases. An experimental confirmation of this effect has been obtained with laboratory measurements, where the diffusing medium was formed by heating water at the basis of a cubic box (1m size) and by cooling the vapors by means of circulating liquid nitrogen at the box top. Fog was obtained within the box through which a laser beam ( $\lambda = .63\mu$ ) was passed. The box was placed in different positions along the path of the beam. As will be shown in sect.5 the effect of multiple scattering resulted much stronger for the position of the box nearest to the receiver. A case of measurements for a homogeneous medium will also be reported.

## 2. MONTE CARLO METHOD - TWO SCALING FORMULAE

Fig.3 shows the scheme used for the M.C. calculations. The source S emits a thin beam of radiation in the x direction. (The case of a finite cross-section beam can be dealt with, by using the results of the case of an infinitely thin beam, as explained later in this section). Following the "semianalytical" M.C. procedure, as it was called by Poole (12), a random-number-generating-routine is used to determine the lengths and the directions of the parts composing the broken line representing a possible trajectory of a "photon", undergoing a scattering action at each bending point of the broken line

(points  $P_1, P_2, \dots$  of Fig.3). Let us first consider the case of a homogeneous medium, for which  $\sigma$  is independent of  $x$ . For each "emitted photon", the random procedure is employed to determine the positions of the point  $P_1, P_2, \dots, P_m, \dots$  where the first, second, ... mth... scattering events occur. For each of these points, for example for point  $P_k$ ,

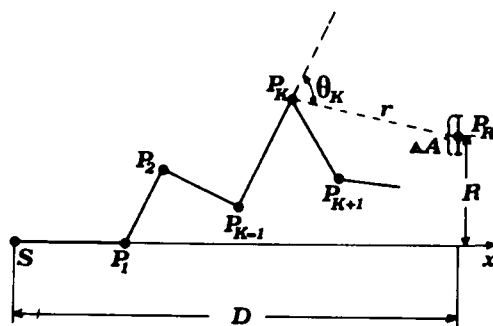


Fig.3 - Scheme for the Monte Carlo calculations.

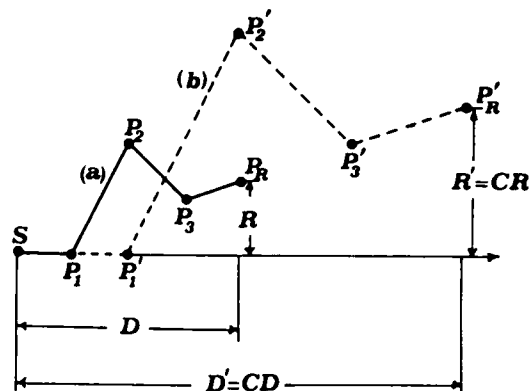


Fig.4 - Scheme used to deduce the scaling formula of eq.5.

one can evaluate the probability  $p_k$  that the "photon" will be received by an element of area  $\Delta A$  of a receiver placed at a point  $P_R$  having a distance  $R$  from the  $x$  axis, without encountering any further scattering action.

$$(2) \quad p_k = \frac{\Delta A}{r^2} L(\theta_k) e^{-\sigma r} \quad \hat{r} \times \hat{x} \leq 1$$

$$p_k = 0 \quad \hat{r} \times \hat{x} > 1$$

where  $r$  is the distance between  $P_k$  and  $P_R$ , and  $L(\theta_k)$  indicates the scattering function of the medium.  $\theta_k$  is the scattering angle as indicated in Fig.3 (in our calculations, scalar scattering functions have been used).

By following this procedure, each single "photon" path is used to study the effects of the different orders of scattering. After having determined the positions of the points  $P_k$ , up to a certain chosen order of scattering,  $p_k$  is readily evaluated. Thus, no large increase of time is necessary to repeat the calculation of  $p_k$  by varying  $R$  and  $D$ , and one can easily study the influence of the receiver's parameters. In our calculations, a very small  $\Delta A$  has been chosen, so that eq.(2) can be used even when  $P_k$  happens to be near the receiver. If the function  $S_k$  represents the contribution of the  $k$ th order of scattering to the received power per unit area at  $P_R$ , when a unit power is emitted, one has:

$$(3) \quad S_k = \frac{\sum p_k}{\Delta A N_T}$$

where the sum is made of the values of  $p_k$ , resulting from the complete set of "photons" emitted by the source, whose number is  $N_T$ . Given the scattering function of the medium,  $S_k$  is a function of  $\sigma, R, D, \alpha$ . An integration over the receiver area gives the received power. Simple modifications of the calculation program are necessary if one then assumes that  $\sigma$  has a simple dependence on  $x$ , like the one described in sect.3.

Given a scattering point one only has to take into account that the probability of being scattered for a photon depends on the position along the direction of motion, and that the probability function  $p_k$  of eq.2 contains the exponential factor  $\exp(-\int_0^L \sigma(e) de)$  where  $L$  is the rectilinear distance from the scattering point to  $\Delta A$ . M.C. methods offer the possibility of handling complicated situations. On the other hand a shortcoming of the methods comes from the possible long calculation time necessary for obtaining statistically reliable results.

For our problem, two possibilities of reducing the calculation time have been considered. First, the M.C. calculations have been performed by considering a very thin beam, coincident with the  $x$  axis of Fig.1, carrying unitary power. In order to use the results of these calculations to deal with the case of a finite cross section beam, one has to calculate the received power  $S_0$  per unit element of the receiver area, as a function of the radial distance  $R$  of the element from the  $x$  axis:  $S_0 = S_0(R)$ . The case of a cylindrical beam is then dealt with, by ideally dividing the beam into very thin parallel

sub-beams, each carrying the appropriate quantity of power. For each sub-beam the assumed circular area of the receiver is divided into (partial or complete) circular annuli of small width, centred on the intersection point of the subbeam with the receiver area. The contribution of the sub-beam to the power received through each circular annulus is obtained by using the calculated function  $S_0(R)$ . This calculation step, giving the results for a finite cross section beam by using the results valid for the case of a zero cross section, does not substantially increase the calculation time in comparison with the M.C. procedure. Further, in many cases, especially for high orders of scattering and for small  $\rho$  and large  $D$ ,  $S_0$  results as to almost independent of  $R$ , and the extension to the case of a finite cross section beam is straightforward. The assumption that the segments composing the broken line representing a photon path have a small inclination with respect to the beam axis (small angle approximation), allows one to perform M.C. calculations for a single value of  $\sigma$  and of  $D$ .

By first making reference to the case of a homogeneous medium, Fig.4 is used to show how the results obtained for one value of  $D$ , can be scaled to obtain the values of  $S_k$  for other values of  $D$ . Let us consider a broken path (a)  $S P_1 P_2 P_3 P_R$  arriving at point  $P_R$  of the receiver. The path (b)  $S P'_1 P'_2 P'_3 P'_R$  is obtained from the previous one by multiplying the distance for the same factor  $c$ , with the same scattering angles. (b) represents the path analogous to (a) when the distance  $D$  is multiplied by the factor  $c$ ;  $\sigma$  is considered equal in the two cases. Let us assume that the probability of obtaining the path (a) is  $p_a$ . The probability  $p_b$  of obtaining (b) is evaluated from  $p_a$ , by taking into account that the attenuation along the tract  $P P_{m+1}$ , equal to  $\exp(-r_{a,m+1}\sigma)$ , becomes equal to  $\exp(-r'_{m,m+1}\sigma)$ , for the tract  $P' P'_{m+1}$  where  $r'_{m,m+1}$  is the distance  $P' - P'_{m+1}$ . The total attenuation along the complete path changes from  $\exp(-\sigma L)$  to  $\exp(-\sigma Lc)$ , where  $L$  is the length of (a). The probability for the "photon" to be scattered within a tract  $\Delta S$  about the point  $P_m$ , equal to  $\sigma \Delta S$ , becomes equal to  $c\sigma \Delta S$ , for the path (b) and a tract  $c\Delta S$  about  $P'_m$ . The ratio between the two probabilities  $p_a$  and  $p_b$  results as

$$(4) \quad \frac{p_a}{p_b} = \frac{\exp(-(c-1)\sigma L)}{c^K}$$

where  $K$  is the number of scattering events along the path (a). The point  $P'_R$  is at a distance  $R' = cR$  from the  $x$  axis. In order to scale the results obtained for a receiver of area  $A$  at a distance  $D$  from the source, and obtain the results valid for a second receiver at a distance  $D' = cD$ , one has to consider this second receiver having an area  $A' = c^2 A$ . Thus the power per unit area calculated in the first case, is to be further divided by  $c^2$ . To obtain the scaling relation useful for our calculation, we have taken into account the results of the analysis of Stotts (3), Mooradian et al. (10) who showed that, with the exception of very large optical depths, the time spread of the power transmitted through a turbid atmosphere is very small, since forward multiple scattering is predominant over large angle scattering. Thus, one can put  $L \approx D$  and the following relation results:

$$(5) \quad S_k(R', D', \sigma, \alpha) = S_k(R, D, \sigma, \alpha) c^{K-2} \exp(-(c-1)\sigma D) \\ D' = cD \quad R' = cR$$

The position  $L \approx D$  corresponds to the assumption that only small scattering angles are important. A change of  $\sigma$ , when  $D$  is left unchanged, leads to the following scaling formula:

$$(6) \quad S_k(R, D, c\sigma, \alpha) = S_k(R, D, \sigma, \alpha) c^K \exp(-(c-1)\sigma D)$$

A simultaneous change of  $\sigma$  and  $D$  can be dealt with, by successively applying eq.s 5 and 6. The scaling formulae can be applied to the simple cases of nonhomogeneous media described in sect 3, when the small angle approximation is valid (see next section).

### 3. NONHOMOGENEOUS MEDIUM

The semianalytical M.C. method has been applied to the case of a nonhomogeneous medium. Since in a turbid atmosphere the scattering of visible or near i.r. light occurs prevalently in a nearly forward or in a nearly backward direction, the case of a plane stratified medium has been considered, with a scattering coefficient as a function of the  $x$  direction only. In our calculations the single scattering albedo is considered to be unitary, so that the extinction coefficient and the scattering coefficient, being equal, will be denoted as  $\sigma(x)$ . Fig.2 shows the considered dependence of  $\sigma$  on  $x$ , and the parameters describing this dependence.

Two simple types of profile for  $\sigma$  have been examined. They present one or two

strong discontinuities of  $\sigma(x)$ . For the case A of Fig.2, indicated as the "step" case,  $\sigma(x)$  takes the values  $\sigma_a, \sigma_b$ . In our calculations, whose results are presented in sect.4, the ratio  $\sigma_a/\sigma_b$  assumes the values: .05, .2, 1, 5, 20, 100. (The homogeneous case is included). For the case B of Fig.4, indicated as the "bank" case, the ratio  $\sigma_a/\sigma_b$  is equal to 20, and the width  $x_f - x_i$  of the bank is equal to  $D/10$ . The position  $x_i$  assumes the values: .1D, .3D, .5D, .7D, .9D. For all of the cases A and B the same average value of  $\sigma(x)$  is

assumed along the path and is indicated as  $\bar{\sigma} : \bar{\sigma} = \frac{1}{D} \int_0^D \sigma(x) dx$ . Thus a comparison will be

made of the results obtained for the homogeneous case (the 3<sup>rd</sup> one of case A) with the results for the other cases.

If the validity of the small scattering angle approximation is assumed, one sees that the scaling formulae presented in sect.2 can be applied to the case of the considered nonhomogeneous media. If  $D$  is changed by a factor  $c : D' = cD$ , one has to leave unchanged the relative extensions of the two (case A) or three (case B)  $x$  intervals where  $\sigma$  is uniform, so that the whole profile of  $\sigma$  is scaled along the  $x$  direction by the factor  $c$ . In particular the small angle approximation make the total extinction factor change from  $\exp(-\bar{\sigma}D)$  to  $\exp(-\bar{\sigma}cD)$ , as in the case of the homogeneous medium. The other factors in the scaling formulae are left unchanged, when the profile is scaled by the same factor as  $D$ .

#### 4. NUMERICAL RESULTS

Since for calculations and measurements pertaining to multiple scattering effects in turbid media, the results depend strongly on the choice of the particular situation examined, it is not reasonable to claim to be exhaustive by showing a limited number of example. We only show the results pertaining to the choice of 3 values for the link distance:  $D = 50m, 1000m, 3000m$ . The distance  $D = 50m$  corresponds to a typical case of a transmissometer used in meteorology to measure the medium extinction coefficient. The other two distances correspond to two possible cases of optical communication link through the atmosphere. For the case  $D = 50m$ , the radius  $\rho$  of the receiver has been taken equal to 5cm, while two values  $\rho = 5$  cm and  $\rho = 10$  cm have been assumed for the two longer distances. The values of  $\alpha$ , the semiangular aperture of the receiver's field of view, were taken as equal to 60, 80, 120, 160, 200 mrad, with possible extrapolation of the results to lower values of  $\alpha$ . The results also depend strongly on the choice of the scalar scattering function of the medium. The calculations were first performed for various combinations of the listed parameters, by using a scalar scattering function having a rather high value of the asymmetry parameter,  $g$ , (i.e. the average value of  $\cos \theta$ , where  $\theta$  is the argument of the scattering function). For these calculations the normalized Henyey-Greenstein function (H.G. function):

$$L(\theta) = \frac{1}{4\pi} \frac{1-g^2}{(1+g^2 - 2g\cos \theta)^{1.5}}$$

with  $g = .95$  has been used. Then a comparison of some results has been made with the ones pertaining to a scattering function presenting a lower average value of  $\cos \theta$ : some calculations were repeated by using a scattering function corresponding to the table given by Deirmendjian (16) for his C1 model and  $\lambda = .7\mu$ :

$$L(\theta) = \frac{1}{8\pi} [p_1(\theta) + p_2(\theta)]$$

where  $p_1(\theta)$  and  $p_2(\theta)$  are the two first diagonal elements of the scattering matrix taken in the form of Deirmendjian's book (eq. 76 of Ref. (16)). For this model of the scattering function the average value of  $\cos \theta$  is equal to .85. Both the considered scattering functions present a high forward peak and a high forward/backward scattering ratio. Before presenting the results pertaining to the examined cases of a finite beam cross section, we show an example of the intermediate results, directly coming from the application of the M.C. method to the case of an infinitely thin beam. These results are presented by means of the ratio  $S_k/S_0$ , where  $S_k$  is the quantity introduced in sect.2.  $S_k$  represents the contribution of  $k$ th order of scattering to the power received per unit area at a distance  $R$  from the  $x$  axis when a unitary power is emitted by the source, strictly in the  $x$  direction.  $S_0$  is the contribution to the received power due to the directly attenuated beam (in the case of an infinitely thin beam  $S_0$  is simply equal to

$\exp(-\int_0^D \sigma(x) dx)$ ). Fig.5 refers to a case of homogeneous medium and the chosen parameters

are:  $D = 500$  m.,  $\sigma = .005$  m<sup>-1</sup> uniformly along  $D$ ,  $R = .01$  m.  $S_k/S_0$  is plotted versus the order of scattering, and five values of the F.O.V. semiangle  $\alpha$  are considered. The H.G. scattering function with  $g = .95$  has been used. Fig.6 shows how the results of Fig.5 change when  $D$  changes to  $D = 3000$  m and  $R$  to  $R = .06$  m. The scaling formula of eq.5 has

been used to pass from Fig.5 to Fig.6. Fig.7 shows the ratio  $S_k/S_0$  evaluated for the "bank" cases of Fig.4, with the same average value of  $\sigma$  as Fig.5.  $S_k/S_0$  plotted versus  $K$  and the results for a fixed value of  $\alpha$  are shown. The different curves correspond to different values of  $x_1$ . The average  $\sigma$ , the scattering function and  $R$  are the same as for Fig.5. Figs 8,9,10 show the results of calculations made in order to check the validity of the scaling equation 5. In the figures, a comparison is made between the ratio  $S_k/S_0$  evaluated at  $D = 5$  m directly by means of the M.C. method, and the same function obtained by scaling the results obtained for  $D = 10$  m by means of eq.5. Figs 8 and 9, referring to the H.G.  $g = .95$ , and to the C1  $\lambda = .7\mu$  models respectively, show a good agreement between the calculated and scaled values of  $S_k$ . On the contrary, in order to show how the scaling formulae fail when the small scattering angle assumption is not valid, Fig.10 presents the large differences of the  $S_k$  values, obtained for the same value of  $D$  when the two procedures are followed, and a much flatter scattering function is used. For Fig.10 a fictitious scattering function has been used, which assumes the same behaviour between  $0^\circ$  and  $180^\circ$ , as the one of C1 model  $\lambda = .7\mu$  between  $0^\circ$  and  $3^\circ$ . The results obtained for the case of a finite cross section beam are shown in Figs 11 to 20. By referring to the case of a finite cross section beam, let us denote as  $P_t$  the received power when the orders of scattering up to the tenth are taken into account and a unitary power is emitted by the source. We write:

$$P_t = P_0 + P_1 + \dots + P_{10}$$

where  $P_0$  denotes the fraction of the received power due to direct attenuated beam if no forward scattering were effective, and  $P_k$ ,  $K \neq 0$ , indicates the fraction of the received power due to the  $K$ th order of scattering. In the figures the ratio  $R_1$  and  $R_{10}$  are presented. They are defined as:

$$R_1 = \frac{P_1}{P_0}$$

$$R_{10} = \frac{\sum_{k=1}^{10} P_k}{P_0}$$

Thus the quantity  $F$ :

$$F = 1 + R_{10}$$

would give the correction factor by which  $P_0$  should be multiplied to give the actual received power, when the orders of scattering higher than the tenth could be neglected. Table I gives the list of the parameters pertaining to the figures 11-20, and indicates the used scattering function.

Table I - Key to the Figs 11-20

Figure	Type of profile for $\sigma$ (Fig.4)	Distance $D$ (m)	Optical depth $\tau = \sigma D$	receiver's aperture radius $\rho$ (cm)	Scattering model
11	Step	50	6	5	H.G $g=.95$
12	"	"	10	"	" "
13	Bank	50	6	5	" "
14	"	"	10	"	" "
15	"	1000	6	5	" "
16	"	3000	6	5	" "
17	"	3000	6	10	" "
18	"	50	6	5	C1 $\lambda=.7\mu$
19	"	50	10	"	" "
20	"	1000	6	"	" "

Symbols used in Figs 11 to 20 :  $\square$ :R1,  $\alpha = 60$  mrad;  $\times$ :R1,  $\alpha = 200$  mrad;  $\Delta$ :R10,  $\alpha = 60$  mrad;  $+$ :R10,  $\alpha = 200$  mrad. For all of the cases the parameter,  $\delta$ , used in eq.1 is given as:  $\delta = 2.10^3/D$ . Figs 11,12 refer to the "step" case of Fig.4A. The ratios  $R_1$  and  $R_{10}$  are plotted versus the ratio  $\sigma_a/\sigma_b$  (see Fig.4A). The following Figs 13 to 20 refer to the "bank" case of Fig.4B, and the ratios  $R_1$  and  $R_{10}$  are plotted versus the position of the initial part of the bank (see Fig.4B, the ratio  $x_1/D$  is considered). For these case  $\sigma_a/\sigma_b = 20$ . The results for  $\alpha = 60$ , and  $200$  mrad are presented. In Figs 13-20 the results for the homogeneous medium presenting the same optical depth, are shown on the ordinate axis, for a comparison. In Figs 11,12 the homogeneous case corresponds to  $\sigma_a/\sigma_b = 1$ . As already mentioned, the effect of multiple scattering depends on the many factors defining the geometry of the link and the characteristics of the source and the receiver. Thus it is difficult to have a direct comparison with the results of other authors, who generally consider different situations. However, referring to recent results of Tam and Zardecki (T.Z.

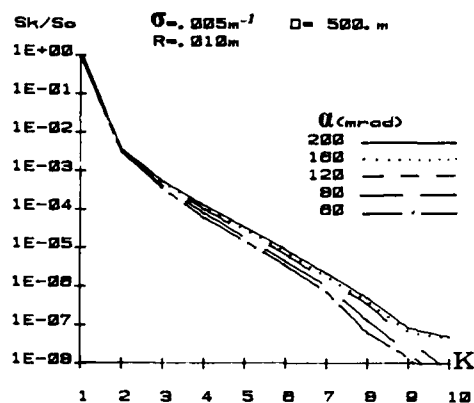


Fig. 5 -  $S_k/S_0$  versus order of scattering.  $D = 500 \text{ m}$ . Homogeneous case. H.G. model  $g = .95$ .

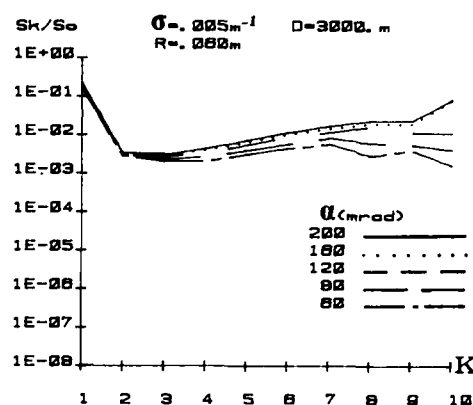


Fig. 6 -  $S_k/S_0$  versus  $K$ ,  $D = 3000 \text{ m}$ , deduced from the data of Fig. 5 by means of eq. 5

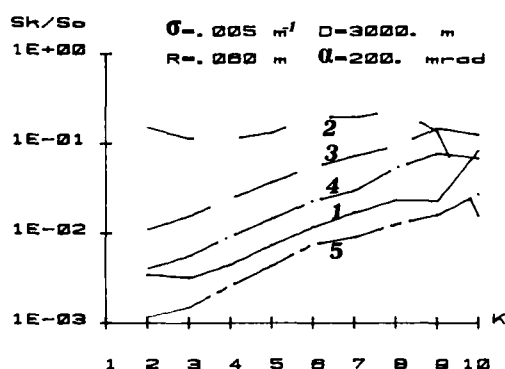


Fig. 7 -  $S_k/S_0$  versus  $K$ . "Bank" case. H.G. model,  $g = .95$ , for different values of  $x_1$ : 1: homogeneous case, 2:  $x_1 = 2700 \text{ m}$ , 3:  $x_1 = 2100 \text{ m}$ , 4:  $x_1 = 1500 \text{ m}$ , 5:  $x_1 = 300 \text{ m}$ .

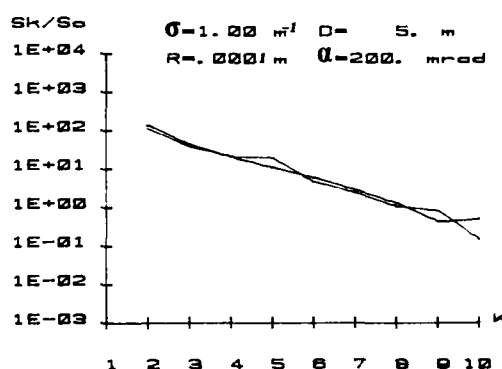


Fig. 8 - Comparison between the values of  $S_k/S_0$  obtained directly for  $D=5 \text{ m}$ , and the ones obtained by scaling the results for  $D=10 \text{ m}$ . Homogeneous case. H.G. model,  $g = .95$ .

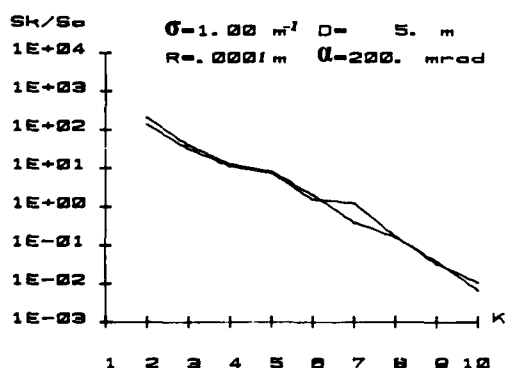


Fig. 9 - Same as Fig. 8. C1 model  $\lambda = .7 \mu$ .

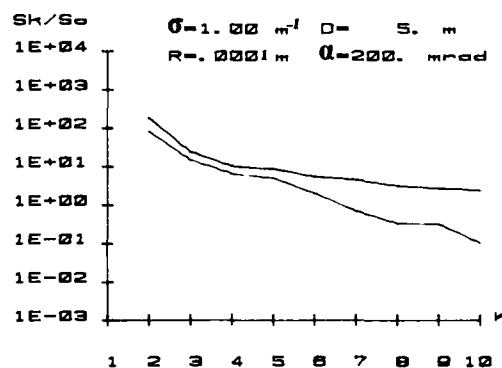


Fig. 10 - An example of inadequacy of the scaling eq. 5, when large scattering angles must be taken into account.

Ref. (5) and (6) concerning the case of homogeneous media, we have to notice some substantial differences between their results and ours. Let us take, for instance, Fig. 10 of Ref. (5). The figure shows the relative importances of different orders of scattering (considered in groups of three). One can see in the figure that the contribution of multiple scattering to the received power is of the same importance or larger than the contribution of the direct beam, even for optical depths of the order of a few units. A comparison with some of our results, for instance with what is shown in Fig. 11, case  $\sigma_a/\sigma_b = 1$ , optical depth 6, should take into account: (A) -The different values of  $\sigma$

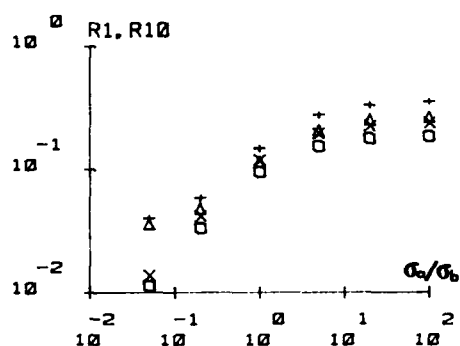


Fig. 11 - Ratios  $R_1, R_{10}$  (see table I). The significance of the marks is given at page 6 after table I.

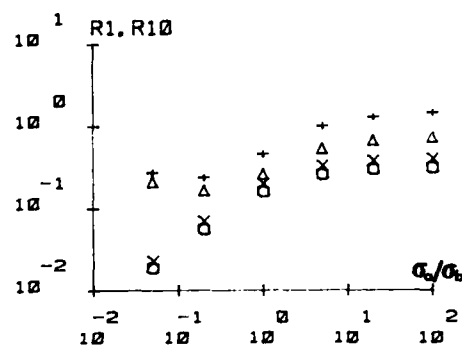


Fig. 12 - Ratios  $R_1, R_{10}$  (see text at page 6 and table I).

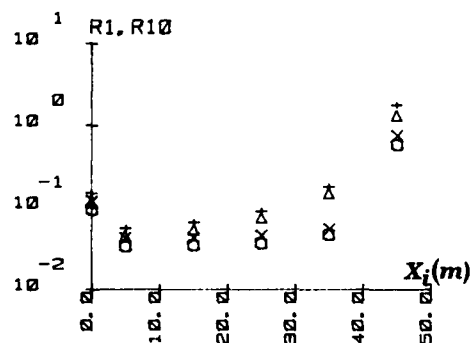


Fig. 13 - Ratios  $R_1, R_{10}$  (see text at page 6 and table I). For figures 13 to 20 the marks on the ordinate axis correspond to the homogeneous case.

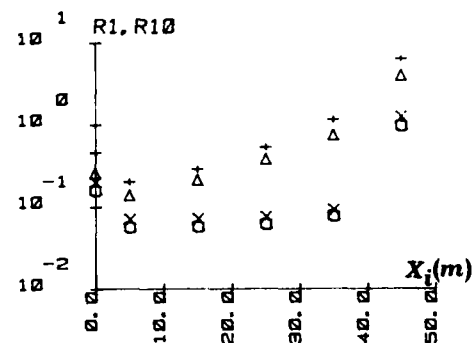


Fig. 14 - Ratios  $R_1, R_{10}$  (see text at page 6 and table I).

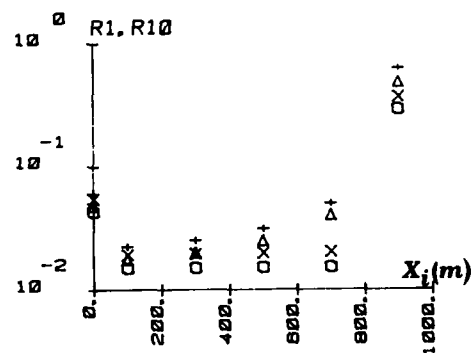


Fig. 15 - Ratios  $R_1, R_{10}$  (see text at page 6 and table I).

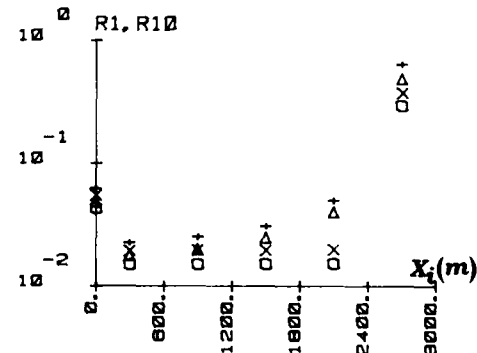


Fig. 16 - Ratios  $R_1, R_{10}$  (see text at page 6 and table I).

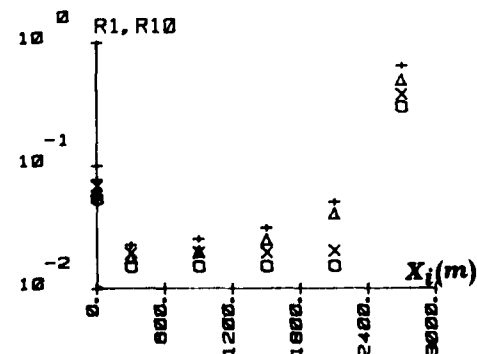


Fig. 17 - Ratios  $R_1, R_{10}$  (see text at page 6 and table I).

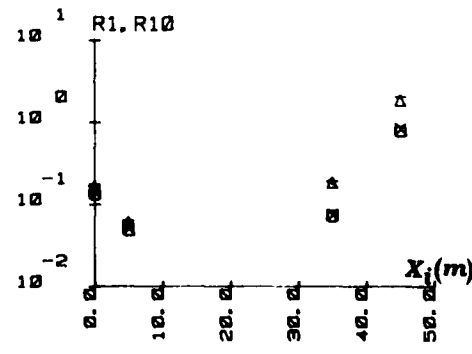


Fig. 18 - Ratios  $R_1, R_{10}$  (see text at page 6 and table I).

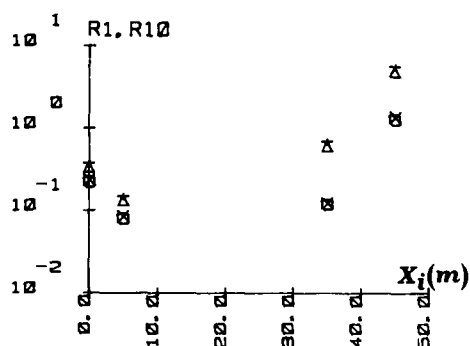


Fig. 19 - Ratios  $R_1, R_{10}$  (see text at page 6 and table I).

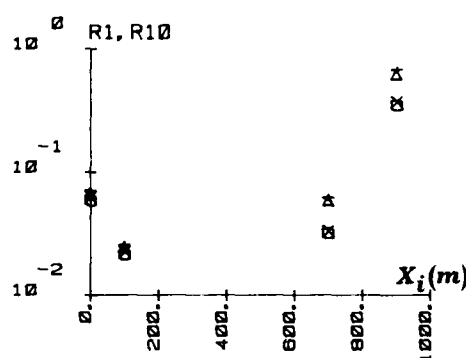


Fig. 20 - Ratios  $R_1, R_{10}$  (see text at page 6 and table I).

(.218  $\text{m}^{-1}$  for T.Z., .12  $\text{m}^{-1}$  for us). (B) The consequently different distances  $D$  at optical depth = 6 (36.7 m for T.Z., 50 m for Fig. 11). (C) The different scattering function. (D) The different area of the receiver and the characteristics of the beams.

A rough comparison may be anyway attempted. The effect of the changes in  $\sigma$  and  $D$  can be estimated by using the scaling formulas of pages 3 and 4. The different receiver's areas can also be taken into account: there is a strong effect on the received power due to the direct attenuated beam, (the different beam divergence and cross section have to be considered), as well as on the contribution of multiple scattering. There results a factor of about 5 between the contribution of orders of scattering higher than the first, as evaluated by T.Z. and reconduted to our situation, and our result for the same quantity. This difference cannot be ascribed to the different angles of F.O.V., as shown by T.Z. in Ref. (6). The different scattering functions cannot be responsible for the difference. The function used to deduce Fig. 11 of this paper presents a narrower forward peak than the one used by T.Z. We have again to remark that only a rough comparison procedure was possible.

A series of measurements of scattered radiation, in condition of fog with optical depth ranging from  $\sim 1$  to  $\sim 6$ , were made by using a variable F.O.V. transmissometer (17) with a link distance of 50 m. The results of the measurements showed that the contribution of scattered light to the received power depended on the receiver's F.O.V. angle, and reached the order of  $\sim 10\%$  when the semiangular F.O.V. was set to  $3^\circ$ . A new campaign of measurements, aimed to evaluate the effect of forward scattering in heavier fogs in our programs.

## 5. EXPERIMENTAL TESTS

Laboratory measurements have been made to make an experimental test of some features of the numerical results of Part I of this paper. As shown in Figs 11 to 20 the contribution of multiple scattering is higher when the diffusion medium is concentrated near the receiver aperture. The experimental set up used to check this result comprehended a HeNe laser source (10 mW), with a nominal divergence angle of .3 mrad (semiaperture) and a receiver apparatus presenting the possibility of varying its angular field of view. The variation of the F.O.V. semiangle  $\alpha$  was accomplished by placing a set of different circular diaphragms on the focal plane of the optical system. The angle  $\alpha$  could vary from  $.5^\circ$  to  $3^\circ$ , in steps of .5 degrees. The receiver radius,  $\rho$ , was 5 cm. The laser beam passed through a cubic box (size 1m), where the diffusion medium was obtained by heating water at the box base ( $t = 50^\circ\text{C}$  during the measurements), and by cooling the vapors at the top by means of circulating liquid nitrogen. Within the box a dense fog was formed, and outside practically no diffusion of the beam was present. During the measurements the box was held in three different positions along the path line transmitter-receiver.

Fig. 21 shows the geometry of the measurements. During the measurements the distance  $d$  was equal to 1 m, 3 m, or 6 m. Since the length of the box was 1 m, these positions correspond respectively: to the first case of the "bank" model of Fig. 24b ( $x_2 - x_1 = .1D, D = 10 \text{ m}, x_1 = .9D$ ), to the fourth case ( $x_1 = .7D$ ) and to a position intermediate between the second (for which  $x_1 = .3D$ ) and the third case (for which  $x_1 = .5D$ ).

Figs 22 a,b,c give an example of the measured attenuation of the beam, indicated as  $W_n/P_e$  plotted versus the index  $n$  of the F.O.V. angle,  $\alpha_n: \alpha_1 = .5^\circ, \dots, \alpha_6 = 3^\circ$ . ( $W_n$  = power received when  $\alpha = \alpha_n$ ,  $P_e$  power emitted by the source). In Fig. 22 a comparison is made

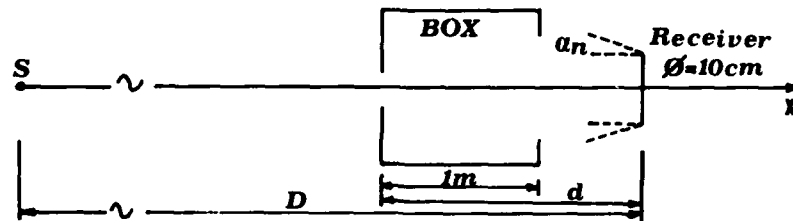
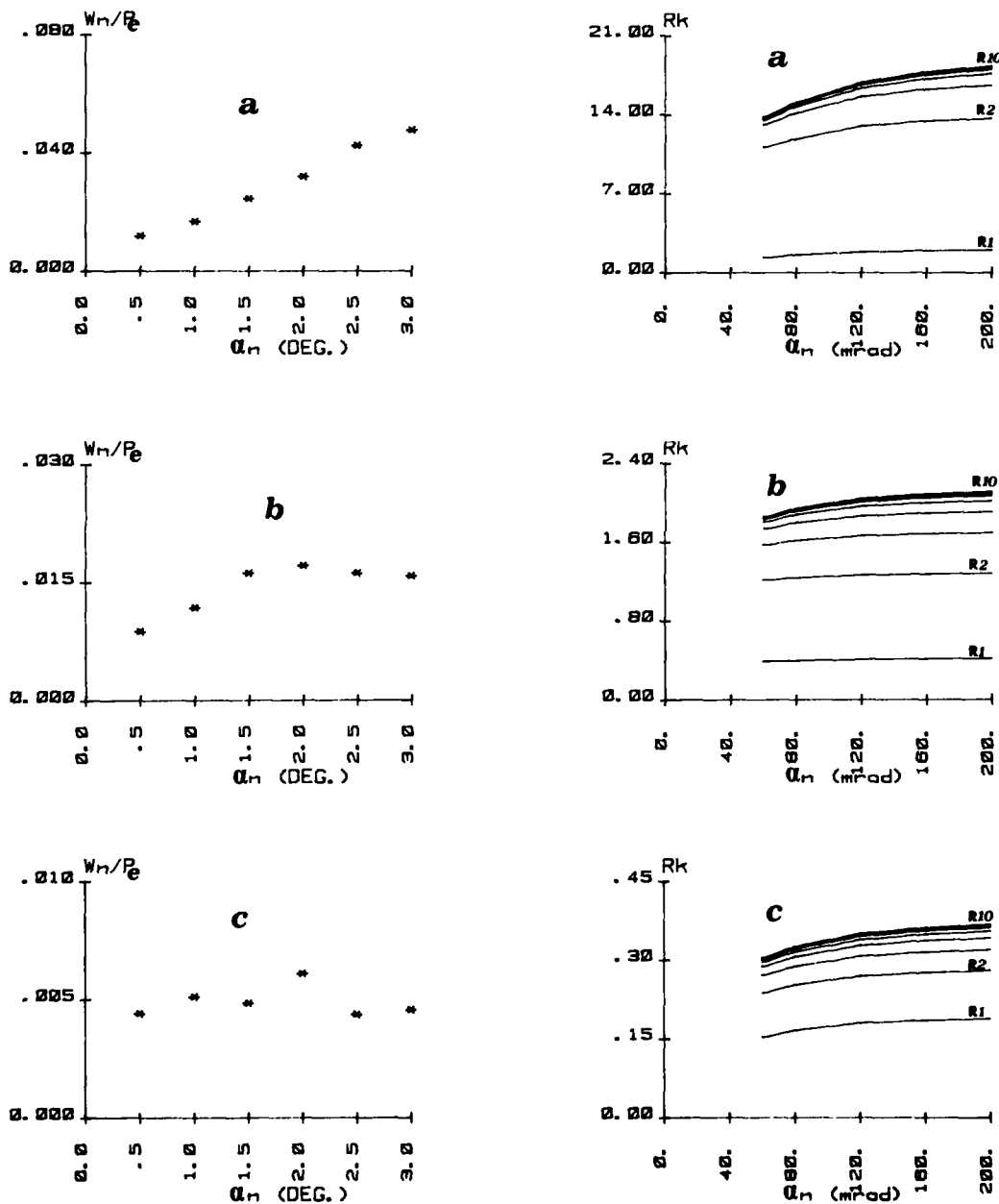


Fig. 21 - Scheme of the measurement set.

Fig. 22 - Measured attenuation versus  $\alpha_n$ .  $\tau = 5$ . With reference to Fig. 21: a)  $d = 1 \text{ m}$ , b)  $d = 3 \text{ m}$ , c)  $d = 6 \text{ m}$ .Fig. 23 - Calculated ratios  $R_k$  versus  $\alpha_n$ . Model H.G.,  $g = .95$ . Geometry of Fig. 21. a)  $d = 1 \text{ m}$ , b)  $d = 3 \text{ m}$ , c)  $d = 9 \text{ m}$ .

between the measured ratio  $W/P_e$  obtained with  $d = 1 \text{ m}$  ( $x_1 = .9D$ ),  $d = 3 \text{ m}$  ( $x_1 = .7D$ ) and  $d = 6 \text{ m}$  ( $x_1 = .4D$ ), in conditions of similar attenuation of the direct beam. This quan-

tity is defined as  $W_o/P_e$  when  $W_o$  indicates the power that would be received without any contribution of forward scattering.  $W_o$  can be obtained by means of an extrapolation to  $\alpha = 0$  of the points shown in Fig.22. For the three cases of Fig.22 the ratio  $W_o/P_e$  would correspond to  $\tau \approx 5$  ( $\tau$ : optical depth).

#### 6. COMPARISON WITH THE RESULTS OF CALCULATIONS

From Fig.22 one recognizes some typical features commonly shown by the results of the numerical computations, presented in the figures of sect.4 corresponding to the "bank" model. The ratio  $R_{10}$  plotted in those figures would correspond to the quantity  $W_o/W - 1$ , deduced from the measurements results, if orders of scattering higher than the tenth were not important in our measurement conditions. (Some check of this point will be made later). For the "bank" cases, the figures of sect. 4 showed that the calculated ratio  $R_{10}$  is largest for  $x_1 = .9D$  and decreases as  $x_1$  decreases. This feature is reproduced for our measurements ( $d = D - x_1$ ).

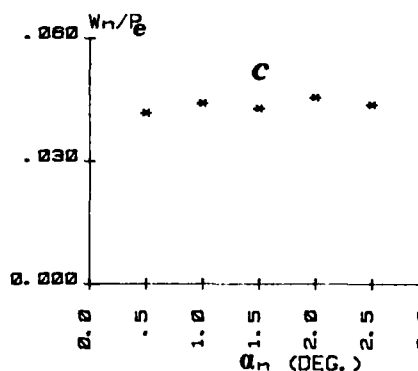
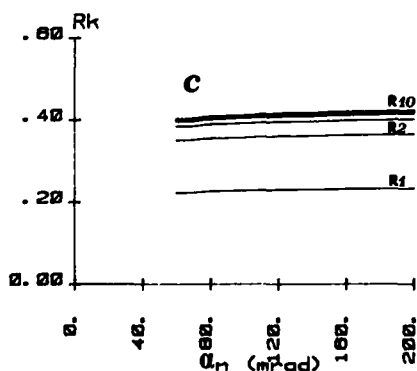
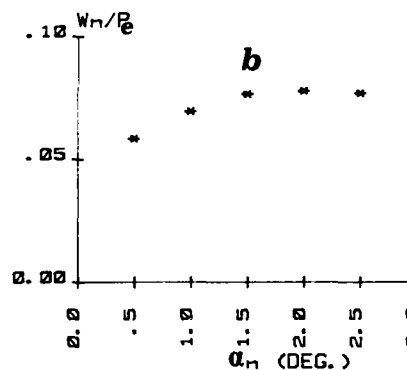
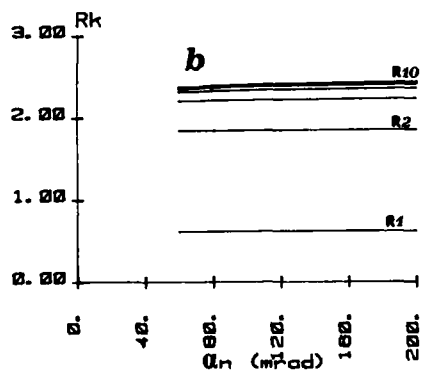
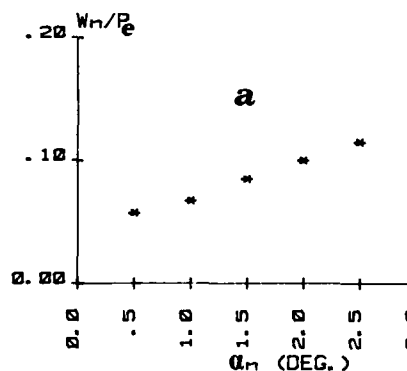
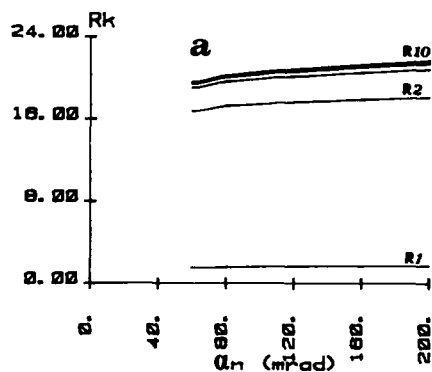


Fig.24 - Same as Fig.23. Model C1,  $\lambda = .7\mu$ . Fig.25 - Another case of measured attenuation versus  $\alpha_n$ .  $\tau \approx 3$ . a)  $d=1$  m, b)  $d=3$  m, c)  $d=6$  m.

The figures of sect.4 also showed that, for the considered range of  $\alpha$ ,  $R_{10}$  has a larger dependence on  $\alpha$ , for the case  $x_1 = .9D$  than for lower values of  $x_1$ . This is qualitatively confirmed by the measurements results, showing a fast saturation of  $W/P_e$  when  $\alpha$  grows over about  $2^\circ$ , for both cases  $d=3$  m and  $d=6$  m. A numerical comparison between the results of computations and of measurements, can be better made for the lowest value of  $\alpha$  considered for the computations, which is nearest to the largest  $\alpha$  of the measurements. (An extrapolation to  $\alpha = 60$  mrad has to be made of the measurements results). For the sake of comparison, we have repeated the calculations, by taking into account the geometry corresponding to the laboratory conditions. The calculations were made by using the two scattering functions of sect.4 of this paper, the H.G.  $g=.95$  function, and the one corresponding to Deirmendjian model C1 for  $\lambda = .7\mu$ . The numerical results are presented in Figs 23 and 24. Unlike the figures of sect.4, the ratios  $R_k$  are plotted versus the angle  $\alpha$ . Here the ratio  $R_k$  is equal to  $\sum_{j=1}^k P_j/P_0$ , where  $P_j$  denoted the contribution to the received power of the  $j$ th order of scattering, and  $P_0$  is the power that would be received if no forward scattering effect were present. The corresponding calculated ratios  $R_1$  and  $R_{10}$  were the quantities plotted in the figures of sect.4.

Fig.23 a,b,c shows the results for the H.G. scattering model, with  $\tau = 5$ . The bank case with  $D=10$  m,  $x_1 = .9D$ ,  $x_1 = .7D$ ,  $x_1 = .1D$  are shown. Fig.24 shows the analogous results for the C1 model,  $\lambda = .7\mu$ . A numerical comparison of the experimental and calculated results is made in Table II, presenting the obtained ratios  $R_{10}$  deduced from Figs 22,23 and 24. An extrapolation to  $\alpha = 60$  mrad has been made of the experimental results.

TABLE II ratio  $R_{10}$   $\tau = 5$

$x_1/D$	calculated		Measured
	H.G.	C1	
.1	.30	.40	-
.7	1.95	2.4	1.7
.9	13.8	19.5	11
homogeneous case	.7	.97	

As is seen from the table there is a qualitative agreement between measurements and calculations, with regard to the dependence of  $R_{10}$  on  $x_1/D$ . A quantitative agreement could be searched for, if one measured the actual scattering function of the medium in the box.

As already mentioned, and as is shown more clearly by Figs 22,23,24 the dependence of both measured and calculated ratios  $R_{10}$  on  $\alpha$  shows a fast saturation at small values of  $\alpha$ , for all of the case but the case  $x_1/D = .9$ . For this latter case there is an increase of  $R_{10}$  with  $\alpha$  even at the larger values of  $\alpha$ . Fig. 25 shows another case of measured ratio  $R_{10}$ , in a case of lower attenuation ( $\tau = 3$ ). In this case also,  $R_{10}$  is higher for the case  $x_1 = .9D$  than for the other cases. A similar saturation effect of  $R_{10}$  with  $\alpha$ .

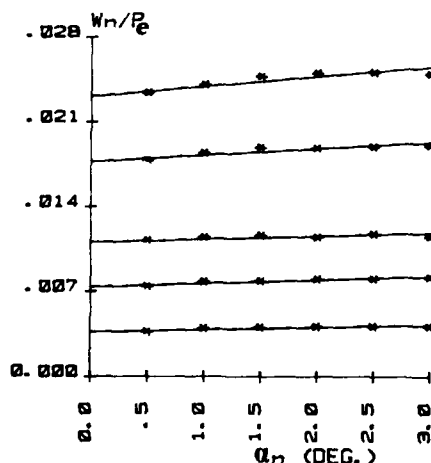


Fig.26 - Five examples of the received power attenuation measured at different values of  $\alpha_n$ . The set of 6 points corresponds to 5 different optical depths. The continuous lines connecting each set of points come from a best fit procedure by means of a quadratic dependence of  $W_n$  on  $\alpha_n$ . Homogeneous medium.

The figures of sect.4 also showed that, for the considered range of  $\alpha$ ,  $R_{10}$  has a larger dependence on  $\alpha$ , for the case  $x_i = .9D$  than for lower values of  $x_i$ . This is qualitatively confirmed by the measurements results, showing a fast saturation of  $W/P$  when  $\alpha$  grows over about  $2^\circ$ , for both cases  $d=3$  m and  $d=6$  m. A numerical comparison between the results of computations and of measurements, can be better made for the lowest value of  $\alpha$  considered for the computations, which is nearest to the largest  $\alpha_n$  of the measurements. (An extrapolation to  $\alpha = 60$  mrad has to be made of the measurements results). For the sake of comparison, we have repeated the calculations, by taking into account the geometry corresponding to the laboratory conditions. The calculations were made by using the two scattering functions of sect.4 of this paper, the H.G.  $g=.95$  function, and the one corresponding to Deirmendjian model C1 for  $\lambda = .7\mu$ . The numerical results are presented in Figs 23 and 24. Unlike the figures of sect.4, the ratios  $R_k$  are plotted versus the angle  $\alpha$ . Here the ratio  $R_k$  is equal to  $\sum_{j=1}^k P_j/P_0$ , where  $P_j$  denotes the contribution to the received power of the  $j$ th order of scattering, and  $P_0$  is the power that would be received if no forward scattering effect were present. The corresponding calculated ratios  $R_1$  and  $R_{10}$  were the quantities plotted in the figures of sect.4.

Fig.23 a,b,c shows the results for the H.G. scattering model, with  $\tau = 5$ . The bank case with  $D=10$  m,  $x_i = .9D$ ,  $x_i = .7D$ ,  $x_i = .1D$  are shown. Fig.24 shows the analogous results for the C1 model,  $\lambda = .7\mu$ . A numerical comparison of the experimental and calculated results is made in Table II, presenting the obtained ratios  $R_{10}$  deduced from Figs 22,23 and 24. An extrapolation to  $\alpha = 60$  mrad has been made of the experimental results.

TABLE II ratio  $R_{10}$   $\tau = 5$ 

$x_i/D$	calculated		Measured
	H.G.	C1	
.1	.30	.40	-
.7	1.95	2.4	1.7
.9	13.8	19.5	11
homogeneous case	.7	.97	

As is seen from the table there is a qualitative agreement between measurements and calculations, with regard to the dependence of  $R_{10}$  on  $x_i/D$ . A quantitative agreement could be searched for, if one measured the actual scattering function of the medium in the box.

As already mentioned, and as is shown more clearly by Figs 22,23,24 the dependence of both measured and calculated ratios  $R_{10}$  on  $\alpha$  shows a fast saturation at small values of  $\alpha$ , for all of the case but the case  $x_i/D = .9$ . For this latter case there is an increase of  $R_{10}$  with  $\alpha$  even at the larger values of  $\alpha$ . Fig. 25 shows another case of measured ratio  $R_{10}$ , in a case of lower attenuation ( $\tau = 3$ ). In this case also,  $R_{10}$  is higher for the case  $x_i = .9D$  than for the other cases. A similar saturation effect of  $R_{10}$  with  $\alpha$ .

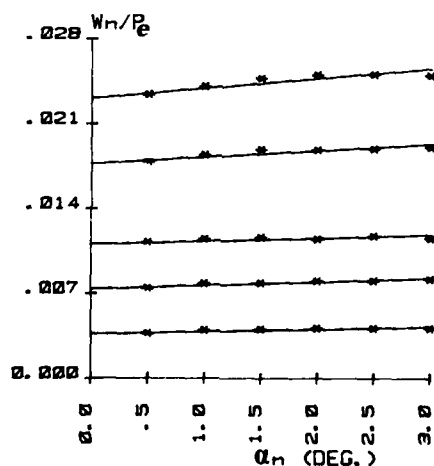


Fig.26 - Five examples of the received power attenuation measured at different values of  $\alpha_n$ . The set of 6 points corresponds to 5 different optical depths. The continuous lines connecting each set of points come from a best fit procedure by means of a quadratic dependence of  $W_n$  on  $\alpha_n$ . Homogeneous medium.

is shown as for Fig.22. Fig.26 shows the attenuation of the laser beam, which was measured in actual field conditions. The measurements were made in a dense fog, forming a homogeneous medium, at the C.N.R. base of San Pietro Capofiume (Bo). The source and the receiver were the ones used for the laboratory measurements. The measurement distance was 50 m. Results of calculations made with reference to this geometry and to a homogeneous medium are in agreement with the very small differences, which were found between the apparent attenuations measured at the 6 angles allowed for the receiver's F.O.V. As can be seen from Fig.26 the measured beam attenuation, presented as the ratio  $W/P_e$  plotted versus  $\alpha_n$ , depends very little on  $\alpha_n$ , even for optical depths as large as 6.

#### BIBLIOGRAPHY

- (1) A.Deepak, M.Box: Appl. Opt. 17, 2900 (1978)
- (2) A.Deepak, M.Box: Appl. Opt. 17, 3169 (1978)
- (3) L.B.Stotts: J.Opt.Soc.Am., 67, 815 (1977)
- (4) A.Deepak et al.: Appl.Opt. 21, 439 (1982)
- (5) W.G.Tam, A.Zardecki: Appl. Opt. 21, 2406 (1982)
- (6) A.Zardecki, W.G.Tam: Appl. Opt. 21, 2413 (1982)
- (7) A.Zardecki : Appl. Opt. 22, 1346 (1983)
- (8) E.A.Bucher: Appl. Opt. 12, 2391 (1973)
- (9) E.A.Bucher, R.M.Lerner: Appl. Opt. 12, 2401 (1973)
- (10) G.C.Mooradian et al. : Appl. Opt. 18, 429 (1979)
- (11) G.C.Mooradian, M.Geller : Appl. Opt. 21, 1572 (1982)
- (12) L.R.Poole et al.: Appl. Opt. 20, 3653 (1981)
- (13) P.Bruscaglioni et al.: Int.J. Remote Sensing, 4, 399 (1983)
- (14) A.I.Carswell, S.R.Pal : Appl.Opt. 19, 4123 (1980)
- (15) S.R.Pal, A.I.Carswell: Lidar Studies of Polarization Anisotropy in Multiple Back-scattering - paper presented at XI International Laser Radar Conference. Madison Wisconsin, June 21-25 (1982)
- (16) D.Deirmendjian: Electromagnetic Scattering on Spherical Polydispersions, Elsevier N.Y. 1969
- (17) P.Bruscaglioni et al.: A Variable Angular F.O.V. Transmissometer and its Use to Monitor Fog Conditions. - (to be published).

# ADAPTIVE COMPENSATION FOR ATMOSPHERIC TURBULENCE EFFECTS ON OPTICAL PROPAGATION

Darryl P. Greenwood  
M.I.T. Lincoln Laboratory  
P.O. Box 73, Lexington, Massachusetts 02173-0073  
USA

## SUMMARY

Optical wavefronts propagated in atmospheric turbulence suffer significant degradation manifested as beam spread, beam wander, and scintillation. We review, very generally, the state of progress of this field of research and discuss recent efforts to overcome the limiting effects of refractive turbulence. Adaptive optical systems are being developed to sense the phase distortion present on propagated beams and to compensate for these aberrations in real time. We present equations describing the magnitude of the turbulence effect and also describing the degree to which compensation may be achieved. Supporting data are presented as well.

## INTRODUCTION

Optical wavefronts propagated through the atmosphere suffer degradation due to refractive-index fluctuations. These fluctuations are due primarily to temperature "turbulence" which occurs on scales sizes ranging from millimeters to meters. There are, in addition, second-order effects due to humidity variations.<sup>1</sup> The phase of the electric field is related to the refractive index variation  $\delta n$  according to

$$\phi(x, y) = k \int_{\text{path}} \delta n(x, y, z) dz \quad (1)$$

(where  $k = 2\pi/\lambda$  is the wave number, and  $\lambda$  the wavelength) since the small-angle scattering approximation is valid in virtually all cases. Physically, the atmosphere may be thought of as consisting of an array of random lenses, the strength of which is changing as a function of time and space.<sup>2</sup> Although the strength of the lenses is small (with  $\delta n \leq 10^{-6}$ ), the wavelengths in the optical regime are also short, and often the path lengths are long. Hence, the integrated phase in Eq. (1) may amount to a few waves of deviation in the visible wavelengths over the aperture. This is certainly a substantial degradation.

Astronomers, as well as casual observers of stars, are well aware of the effects of atmospheric turbulence on star imaging. Integrated phase deviation through the upper atmosphere contributes to weak ray bending and thus scintillation. The relation between amplitude  $A$  and refractive index is

$$\ln A = -\int_{\text{path}} z \nabla^2 n(x, y, z) dz, \quad (2)$$

again assuming small angle scattering. Whereas expression (1) holds in virtually all cases, expression (2) is only valid in the regime of weak integrated turbulence. To put this limitation in perspective: Eq. (2) is valid for visible stars viewed near the zenith, but begins to break down for elevation angles below  $20^\circ$ .

Refractive turbulence is a major factor limiting optical systems operating in the atmosphere. The resolving power of large visible-wavelength telescopes is typically no better than that of a 5-cm diameter telescope because of the phase aberration denoted by Eq. (1). (Indeed, the light-collection ability of the larger telescope is clearly superior.) Infrared telescopes operating at 8-12  $\mu\text{m}$  wavelength have higher resolution limits, approximately 1.5-m diameter, but of course the inherent resolution of IR telescopes is poorer.

There has been considerable effort over the last 20 years to characterize the statistics of  $\phi$  and  $\ln A$  (with the latter given by  $\chi = \ln A$  usually). In Part I of this paper we review some highlights of this very large research area. The object of the discussion is to provide an appreciation for the state of knowledge: to include what theoretical derivations have been conducted, and what data exist to verify these results or not.

In a relatively new area of research, there are efforts to compensate for the phase aberrations, and thus increase these resolution limits -- conceptually to near the diffraction limit. Adaptive (or active) optics use a portion of the incoming light to sense wavefront deviations from the desired plane wave and compensate using a real-time correction system. In Part II of this paper we will describe the principles of such systems and will delineate the various error sources which must be minimized for such a system to work well. Astronomical applications represent one class of system -- passive imaging types -- however, it has been shown that the correction process is reciprocal.<sup>3</sup> If the measured wavefront is imposed in conjugate on an outgoing beam, then the resultant projected spot in the far field will be nearly diffraction limited as well. Throughout this paper we will refer to both imaging applications and projected laser beams.

## PART I PROPAGATION IN ATMOSPHERIC TURBULENCE

### A. General

When an image is formed by a lens observing a source through the atmosphere in the far field, or when a laser beam is propagated through the atmosphere, the spot in the focal plane is observed to broaden, wander, and scintillate. Since this behavior is a result of a random process -- the variation of atmospheric refractive index -- the descriptors are statistical averages.

The refractive index is characterized by its three-dimensional spatial-power spectrum  $\Phi_n(k)$  which has the power-law dependence derived by Kolmogorov to be  $k^{-11/3}$ , with a coefficient  $C_n^2$ . This power

law holds in the "inertial subrange," or cascade regime, which is between an outer-scale wavenumber  $2\pi/L_0$  denoting an input or generation regime and an inner-scale wavenumber  $2\pi/\ell_0$  denoting the onset of a dissipation regime. The outer scale is typically equal to height above ground, and the inner scale a few millimeters. Von Karman modified the spectral formula to include the inner scale, and Tatarskii provided a modification to include an outer scale. The result,<sup>4</sup> after making an additional assumption about isotropy, is

$$\Phi_n(K) = 0.033 C_n^2 (K^2 + L_0^{-2})^{-11/6} \exp(-K^2/K_m^2) \quad (3)$$

where  $K_m \approx 2\pi/\ell_0$ . Except in cases where a laser beam is propagated horizontally within a few meters of the ground, neither the  $L_0$  nor the  $\ell_0$  appear to have much effect on the behavior of the focused spot. Rather it is the coefficient  $C_n^2$ , termed the refractive-index structure parameter, which is the dominant descriptor. Although there is still considerable conjecture as to whether the  $K^{-11/3}$  dependence is valid above the refractive-turbulence boundary layer (which may only be within the first few hundred meters above ground level), it still appears to give an adequate representation of integrated path effects. Notice, however, the  $C_n^2$  only has meaning when the  $K^{-11/3}$  power law is valid.

In only a few cases can the  $C_n^2$  be considered constant along the path. Rather it varies, sometimes by orders of magnitude as a result of changes in altitude, terrain, or cloud cover. It is for this reason that controlled experiments are difficult to accomplish. Often it is not possible to provide sufficient instrumentation to adequately characterize the propagation medium. Representative plots of  $C_n^2$  versus height<sup>5</sup> are shown in Fig. 1. Near-ground behavior can be shown theoretically<sup>6</sup> to be  $z^{-4/3}$  during the daytime unstable conditions,  $z^{-2/3}$  during nighttime stable conditions, and  $z^0$  in the neutral zone periods of dawn and dusk. Also of importance is the diurnal variation. A plot of the average behavior of  $C_n^2$  versus time of day for a desert site is shown<sup>7</sup> in Fig. 2. Deviations about these mean values may be as much as an order of magnitude above to an order of magnitude below.

## B. Propagation Statistics

The most basic statistical descriptor of the wavefront deviation from the plane or spherical is the phase structure function, defined as

$$D_\phi(\bar{r}) = \langle (\phi(\bar{r}_1) - \phi(\bar{r}_1 + \bar{r}))^2 \rangle, \quad (4)$$

where the assumption (generally valid) of homogeneity has already been made. From derivations in Tatarskii,<sup>8</sup> extended by Fried,<sup>9</sup>  $D_\phi$  can be shown to be isotropic and has the form

$$D_\phi(r) = 6.88 (r/r_0)^{5/3} \cdot \begin{cases} 1, & r \gg \sqrt{\lambda L} \\ 1/2, & r \ll \sqrt{\lambda L} \end{cases} \quad (5)$$

where  $r_0$  is referred to as the coherence length and has the form

$$r_0^{-5/3} = 0.423 k^2 \int_0^L C_n^2(z) (z/L)^{5/6} dz \quad (6)$$

where  $z = 0$  represents the source of a spherical wave and  $z = L$  the receiver. The dependence on  $r^{5/3}$  in Eq. (5) has been verified by Clifford, et. al.<sup>10</sup> A plot of their data is repeated in Fig. 3. Also, representative plots of  $r_0$  versus time of day for propagation to zenith are shown in Fig. 4, from Walters.<sup>11</sup> We have recognized in Eq. (6) that plane waves are merely a special case of spherical in that a plane wave is simply a spherical wave with source removed to infinity. For beam waves, Eqs. (5) and (6) are approximately correct, provided the beam is not very narrow. (Most applications of interest have sufficiently large beams.) The wave formulas are generally valid so long as  $D \gg \sqrt{\lambda L}$ , where  $D$  = beam diameter. For small diameters, diffraction becomes important, and diffraction has been ignored in Eqs. (1) and (2).

The log-amplitude  $\chi$  likewise has a computed structure function, but often it is sufficient to know the log-amplitude variance  $\sigma_\chi^2$ . From Lawrence and Strohbehn,<sup>12</sup> we find

$$\sigma_\chi^2 = 0.564 k^{7/6} \int_0^L C_n^2(z) z^{5/6} (1 - z/L)^{5/6} dz. \quad (7)$$

which is valid so long as  $\sigma_\chi^2 < 0.3$ . Ultimately,  $\sigma_\chi^2$  saturates<sup>13</sup> to a constant (or nearly so) value of 0.5 with increasing integrated  $C_n^2$ . A plot of experimentally-determined  $\sigma_\chi$  versus theoretical  $\sigma_\chi$  is in Fig. 5. Burke<sup>14</sup> reports values of  $\sigma_\chi^2$  for astronomical applications to have an average of about 0.05 at zenith in the visible. Hence, saturation occurs only for long endo-atmospheric paths where the integrated turbulence strength is high.

The quality of an optical system is characterized by its MTF, or Modulation Transfer Function, which is the modulus of the OTF, or Optical Transfer Function. The OTF is in turn equivalent to the mutual coherence function of the wavefront. Hufnagel and Stanley<sup>15</sup> showed analytically that the long-term average MTF of the atmosphere-telescope system was decouplable and generally isotropic:

$$M_s(r) = M_T(r) \cdot M_A(r), \quad (8)$$

where the subscripts are for system, telescope, and atmosphere respectively. The independent variable in Eq. (8) is spatial rather than spatial frequency, reflecting the mutual coherence function formulation. Hufnagel and Stanley further showed that  $M_A$  could be written in terms of a wave structure function  $D_w(r)$ , where  $D_w(r)$  is the sum of the phase and log-amplitude structure functions. (The latter is defined by Eq. (4) substituting  $\chi$  for  $\phi$ .) Conveniently, the expression for  $D_w(r)$  is

$$D_w(r) = 6.88 (r/r_0)^{5/3}, \quad (9)$$

which is identical to Eq. (5) but with the final multiplier equal to unity. The relation between  $M_A$  and  $D_w$  is found<sup>15</sup> to be

$$M_A(r) = \exp\left[-\frac{1}{2} D_w(r)\right] \quad (10)$$

The coefficient 6.88 in Eq. (9) was defined in such a way that the  $r_0$  represents the effective coherence diameter on the aperture. Fried<sup>9</sup> has shown that it is unnecessary on the basis of resolution to construct apertures much larger than  $r_0$ . (There is no sharp break in the performance so there is some improvement in going to perhaps  $2r_0$ .) The relationship between  $r_0$  and the semiquantitative "seeing angle"  $\theta_{\text{see}}$  is

$$\theta_{\text{see}} = 1.22\lambda/r_0 \quad (11)$$

where we have simply replaced  $D$  by  $r_0$  in the Rayleigh resolution criterion. Seeing angles of 1 arcsec ( $\sim 5 \mu\text{rad}$ ) are considered to be "good seeing" by astronomers.

The broadening (and thus degradation) of the focal spot may be thought of as consisting of a short-term spread due to high-spatial-frequency refractive-index fluctuations and a centroid wander which arises from low spatial frequencies. Also, the centroid wander can be shown to be roughly equivalent to a wavefront tilt. The expressions for the MTF in Eqs. (8) and (9) include both low and high spatial frequency effects. Yura,<sup>16</sup> however, subtracted the wavefront tilt from the phase and came up with an approximate expression for a short-term MTF:

$$M_A^{\text{ST}}(r) = \exp\left[-\frac{1}{2} D_w(r) (1 - 0.62(r/D)^{1/3})\right] \quad (12)$$

where now the diameter of the aperture  $D$  must be involved in the expression, as it is the inverse of the diameter which marks the boundary between high and low spatial frequencies. Land<sup>17</sup> performed experiments to measure long-term and short-term MTF's, and his results are repeated as Fig. 6. We see excellent agreement between theory and experiments.

Beam broadening, or spread in the short-term case, is the spatial Fourier transform of the MTF. There are no simple expressions for the result because of the awkward 5/3 and 1/3 exponents in Eqs. (9) and (12), however the Fourier transform is easily solved on the computer. Having solved for the irradiance distribution  $I(r)$ , we find the average spot area, measured at the radius where  $I(r)$  is down to 1/e of the peak, is

$$A = \pi(0.65 \lambda L/D)^2 [1 + (D/r_0)^2] \quad (13)$$

for long-term average beam broadening. (Yura<sup>16</sup> also provides an expression for short-term spread.) The reduction in on-axis antenna gain, relative to diffraction-limited, is derived from Eq. (13) for large  $D/r_0$ :

$$S = (r_0/D)^2 \quad (14)$$

which is referred to in optics as the Strehl ratio.

The beam centroid wander which was removed to arrive at the short-term MTF and spread has a variance given by

$$\sigma_\alpha^2 = 0.184(D/r_0)^{5/3} (\lambda/D)^2 \quad (15)$$

In spite of initial appearance, there is no wavelength dependence in  $\sigma_\alpha^2$ , in that  $r_0^{5/3} \sim \lambda^2$  from Eq. (6). The absence of a wavelength dependence was demonstrated in the data of Dowling and Livingston.<sup>18</sup> We repeat their beam wander data in Fig. 7 but over plot the theoretical curve Eq. (15). The fit is seen to be good, however the spread of the data indicates the difficulty of making adequate turbulence measurements.

This part of the paper is intended to provide the basic formulations relating atmospheric turbulence properties to optical beam characteristics. Selected data and references were provided to give some appreciation for the advanced level of understanding to which this field of investigation has developed.

## PART II COMPENSATION FOR PHASE DISTORTION

### A. General Description

As indicated in the introduction, most of the degradation of the spot in the focal plane is a result of phase aberrations. These phase errors  $\phi(x, y; t)$  can be compensated by the use of adaptive optics which sense and correct in real time. The concept of adaptive optics was first proposed by Babcock<sup>19</sup> in 1955 but little was accomplished until the early 1970's where the impetus was to compensate for propagated laser beams. Examples of recent results using phase-compensating systems are in Muller and Buffington<sup>20</sup> from stellar sources, and in Pearson<sup>21</sup> for propagating beams. Also, the entire March 1977 issue of J. Opt. Soc. Am. is devoted to adaptive optics.

The "phase conjugate" approach to adaptive optics is diagrammed in Fig. 8 which shows a passive imaging-only type of system (Fig. 8a) and an outgoing-beam correction system (Fig. 8b). In both cases there is a reference wavefront which has sampled the medium. In the imaging case the reference wave is often identical with the source wave to be imaged; in the outgoing beam case the reference wave in the outgoing beam case, the reference wave is provided by a co-propagating wavefront generated either by emission or reflection from the target. The reference wavefront is sensed by a "phase sensor," an interferometer which determines an estimate of the phase,  $\phi_{\text{est}}(x, y; t)$ . The estimate is limited by

spatial resolution, time response and signal-to-noise performance of the sensor. The phase estimate is then fed to the corrector element, which has spatio-temporal bandwidth limits as well. Since in the configuration shown, the phase sensor views the wavefront after reflection from the corrector, the servo operates in a null-seeking mode, in that the sensor attempts to try to minimize the phase at its input aperture. This approach is especially advantageous, as opposed to driving a corrector mirror open loop, in that any hysteresis or drift in the corrector element is automatically adjusted out.

The next step (Fig. 8b) is to inject an outgoing laser beam which must fully share the aperture with the phase sensor. The aperture-sharing element is a beamsplitter, a dichroic or perhaps a chopper. Once the beam exits the aperture it may or may not progress along the same path as the reference wave. This may occur for a variety of reasons; such as mispointing of the laser, dispersive bending of the outgoing and reference beams if they are of different wavelength, and reference waves emanating from an extended source. In the situation of non-overlapping paths, the error in making an adequate phase determination is referred to as "anisoplanatism."

Even if a system could be built with infinite signal-to-noise, infinite spatio-temporal bandwidth, and no isoplanatic errors, the correction could not be perfect owing to electric field amplitude degradation which is uncorrectable in these phase-only systems. Later we will explore the magnitude of the effect, but suffice it to say the residual error is small, and results in a reduction of the Strehl ratio (relative on-axis antenna gain) by typically no more than 10%.

#### B. Components

Having introduced the overall concepts, we now turn to practical implementation for the phase-only system. The phase sensor may be viewed as an array of trackers, each operating in parallel at sample rates ten times the expected atmospheric rates (so as to have sufficient phase margin in the servo). These trackers are measuring phase gradients in the region between the drive points on the corrector mirror (see Fig. 9). This array of phase gradients (in the figure there are 60 in the x-direction and 60 in the y-direction) are fed to a reconstructor circuit which "solves" Laplace's equation in a discrete network.<sup>22</sup> The output of the solver (or reconstructor) is then fed to the corrector element. The servo loop is then closed through the optical leg. There are in fact two more servo loops of interest. The overall average phase (termed piston) is subtracted from the phase array, as is the overall tilt. The piston value is discarded as it is irrelevant to driving the corrector; while two tilt signals (one in azimuth and one in elevation) are fed to a separate two-axis tilt corrector. Both of these operations preserve the usually-limited stroke of the corrector element.

The corrector element is usually a deformable mirror with an array of discrete actuators mounted on its backside. The drive points correspond one-to-one spatially with the output of the reconstructor. This is referred to as the zonal approach. There is also a modal scheme, conceptually worthwhile when there are only a few drive points, which converts signals to well-known modes such as focus and astigmatism. Soon we will see that for turbulence compensation in the visible wavelengths, the number of drive points may be hundreds to thousands. Various designs for corrector mirrors are being pursued at present and are discussed at some length by Hardy<sup>23</sup>. One approach he discusses consists of a monolithic slab of piezo-electric material which has holes drilled for implanting of electrodes. Other mirrors employ thin face plates mounted on an array of actuators, where each actuator consists of a stack of piezoelectric slabs.

#### C. Error Sources

The five major error sources limiting the performance of adaptive optics systems are (1) finite temporal bandwidth, (2) finite spatial bandwidth, (3) anisoplanatism, (4) finite signal-to-noise ratio, and (5) amplitude. Because of these errors, the phase estimate deviates from the desired by some amount, as given by:

$$\sigma_{\phi}^2 = \langle (\phi(x, y; t) - \phi_{est}(x, y; t))^2 \rangle \quad (16)$$

In the situation where  $\sigma_{\phi}^2$  is reduced to a small value ( $\sigma_{\phi}^2 < 1 \text{ rad}^2$ ), the Strehl ratio is given approximately by

$$S \approx \exp(-\sigma_{\phi}^2) \quad (17)$$

To a close approximation,  $\sigma_{\phi}^2$  is the sum of the individual  $\sigma_{\phi_i}^2$  resulting from the aforementioned residual error sources. We now describe the  $\sigma_{\phi_i}^2$  individually. In what follows we will give sample numbers for a system which could be used to correct the visible images of stars on a 1-m diameter astronomical telescope. Equivalent performance would be observed on a beam corrected by this system as well, since as noted previously the process is reciprocal. For this example we will use  $r_0 = 5 \text{ cm}$ , noted in Part I to be an average value for visible propagation at zenith.

The residual error due to finite temporal frequency is given by Greenwood<sup>24</sup> to be

$$\sigma_{\phi_1}^2 = C(f_A/f_C)^{5/3} \quad (18)$$

where  $C = 1$  or  $5.2$  depending upon whether the closed-loop servo response has a sharp cut-off or is the more gradual RC filter. The quantities  $f_C$  and  $f_A$  are respectively the servo cut-off frequency and the characteristic atmospheric frequency, given by

$$f_A^{5/3} = 0.0196 \text{ k}^2 \int_0^L C_n^2(z) v^{5/3}(z) dz \quad (19)$$

where  $v(z)$  is the wind velocity along the path. Typically,  $f_A$  is 10-20 Hz for astronomical cases, but to achieve a small  $\sigma_{\phi_1}^2$ , the  $f_c$  should be 5-10 times larger. Thus, a servo bandwidth of 50-200 Hz is sufficient for astronomical objects. Satellites, however, move at higher slew rates, and this additional pseudo-wind must be added to the wind velocity  $v(z)$  in Eq. (19). The result indicates bandwidths of 500-1000 Hz.

Residual error due to having a finite number of actuators  $N_a$  is given by Greenwood<sup>25</sup> to be

$$\sigma_{\phi_2}^2 = 0.274 (D/r_0)^{5/3} N_a^{-5/6} \quad (20)$$

The coefficient in Eq. (20) is for a representative corrector element. The precise coefficient for continuous deformable mirrors must be calculated for the specific mirror, based upon a measured influence function, where the influence function is defined as the surface deformation achieved as a result of pushing (or pulling) a single actuator. The example of astronomical imaging would require at least  $N_a = 1400$  actuators to reduce the  $\sigma_{\phi_2}^2$  to  $0.10 \text{ rad}^2$  (or  $1/20$  wave) for an  $r_0 = 5 \text{ cm}$ . If instead, the system performance could tolerate a residual error of  $0.4 \text{ rad}^2$  (or  $1/10$  wave) and further would only operate in good atmospheric conditions, where  $r_0 = 10 \text{ cm}$ , then  $N_a = 69$ , representing a much more modest system. For one-tenth wave residual error, the rule of thumb is one actuator per  $r_0$ .

The isoplanatic error may be a result of various mechanisms which cause the outgoing beam and the reference wave to propagate along different paths. For purposes here, we will assume that the paths are straight, meet at the aperture, and are separated by an angle  $\theta$ . The residual error is found by Fried<sup>26</sup> to be

$$\sigma_{\phi_3}^2 = (\theta/\theta_0)^{5/3} \cdot F(D/r_0, \theta/\theta_0) \quad (21)$$

where  $\theta_0$  is the isoplanatic angle, given by

$$\theta_0^{-5/3} = 2.91 k^2 \int_0^L C_n^2(z) z^{5/3} dz \quad (22)$$

The function  $F(D/r_0, \theta/\theta_0)$  is a correction factor which approaches 1 for very large  $D/r_0$ . Fried provides curves for  $\sigma_{\phi_3}^2$  which includes the correction factor. Recently, we have determined a rough approximation for  $F$  as

$$F(D/r_0, \theta/\theta_0) = \exp[-1.4(\theta/\theta_0)^{5/3} (D/r_0)^{-0.362}] \quad (23)$$

Again pursuing the example of astronomical imaging, we find from Eq. (22) and average  $C_n^2$  profiles that  $\theta_0 = 5 \mu\text{rad}$ . The offset angle  $\theta$  between the two paths must be maintained to  $\theta < 2 \mu\text{rad}$  in order to reduce  $\sigma_{\phi_3}^2$  to  $0.196 \text{ rad}^2$  (or  $0.07$  waves rms). Thus, if a star pair or an extended object such as a planet were being imaged, the correction would begin to degrade for angular extents beyond only a few micro-radians.

Signal-to-noise limitations are very dependent upon system and atmospheric transmission, sensitivity of detectors, and efficiency of aperture sharing components. In addition, the phase sensor itself will operate above the photon-shot-noise level by some amount, as a result of electronic noise and crosstalk typically. As an approximate expression for the relation between  $\sigma_{\phi_4}^2$  and the signal to noise ratio  $S_n$ , we provide

$$\sigma_{\phi_4}^2 = C'/S_n^2 \quad (24)$$

where  $C'$  is on the order of unity and  $S_n$  is for a photon counting system equal to  $\sqrt{N}$ , where  $N$  is the number of photoelectron counts per system update time and per subaperture. Ideally,  $C'$  might be as low as 1.2; however, the appropriate value must be evaluated for the particular sensor. Since  $S_n$  is proportional to the diameter of the subaperture,  $\sigma_{\phi_4}^2$  is inversely proportional to the area of the subaperture. However,  $\sigma_{\phi_2}^2$  due to finite spatial bandwidth is directly proportional to subaperture area to the 5/6 power. Hence, there is a trade off to be evaluated between  $\sigma_{\phi_2}^2$  and  $\sigma_{\phi_4}^2$ .

To continue to pursue our example: we will fix the subaperture size and determine signal-to-noise error. Suppose optimistically that  $C' = 1.2$ , and the desired  $\sigma_{\phi_4}^2 = 0.1 \text{ rad}^2$ . Then the desired  $S_n = 3.5$  and  $N = 12$ . Suppose furthermore that the atmospheric transmission is 0.75, the optical transmission 0.20, and the detector quantum efficiency 0.25. Then we require 320 photons per subaperture per update time at the top of the atmosphere. Finally, suppose the subaperture diameter is equal to 5 cm (based upon our rule of thumb) and the update time is 0.5 msec (based upon a sampling rate of ten times the servo bandwidth, 200 Hz). Then the required source irradiance, referenced to the top of the atmosphere, is  $1.2 \times 10^{-14} \text{ W/cm}^2$ , which corresponds to a star of visual magnitude  $m_v = 4.8$ . There are some stars and planets at least this bright. In Freeman Dyson's paper<sup>27</sup> on the subject of photon noise dependence of active optical systems he suggests that for a 10 cm subaperture and update time of 10 msec, the limiting brightness would be  $m_v = 14$ . If we scale our conditions accordingly, we would predict  $m_v = 9.5$ . The remaining difference lies in our rather conservative assumptions about system and atmospheric transmission, quantum efficiency and desired residual wavefront error.

The fifth residual error of concern is the amplitude fluctuation present in the aperture plane resulting from phase distortion at some distance from the aperture. This relationship needs little comment:

$$\sigma_{\phi_5}^2 = \sigma_x^2 \quad (25)$$

where  $\sigma_X^2$  is given by Eq. (7). At zenith  $\sigma_X^2 = 0.05$ , thus  $\sigma_{\phi_5}^2 = 0.05$ . This and all other parameters would have to be scaled for different elevation angle by reevaluating the various  $C_n^2$  integrals.

Thus, we have designed at a conceptual level a system capable of compensating for turbulence aberrations in astronomical imaging. The "first class" system (designed for a 1-m telescope, and anticipating  $r_0 = 5$  cm) would have a corrector element and servo with 1400 channels operating at 200 Hz, a phase sensor with 0.5 msec update rate operating at near the photon-shot-noise limit, and an optical system with reasonably high transmission. Also, it would be limited to angular extents of a few  $\mu$ rad. The resultant phase error would thus be the sum of the five components, each of which we endeavored to keep at 0.1 rad<sup>2</sup> or below. As a result, the total  $\sigma_{\phi}^2 \approx 0.5$  rad<sup>2</sup> and the Strehl ratio  $S = \exp(-0.5) = 0.61$ . This should be compared with the uncorrected Strehl ratio of approximately  $(r_0/D)^2$ , which for this example would be 0.0025. The antenna gain and the sharpness of the image would thus be improved enormously.

#### CONCLUSIONS

In Part I of this paper we reviewed the highlights of the research in propagation of optical waves in atmospheric turbulence, and provided a number of equations, references, and data plots. The state of understanding in this field is in reasonably good shape. It is unlikely that characteristics of the propagated wave could be predicted to 10%, however factors of 2 are reasonable expectations, provided there are adequate measurements of the propagating medium.

In Part II we surveyed the adaptive optics field, a field which is still maturing. We are able to present statistical parameters which describe the limits on the performance of adaptive optics systems, but find that data to substantiate the various relationships are lacking. Adaptive optics has the promise of approaching diffraction-limited performance, however each of these limiting factors must be thoroughly understood.

#### REFERENCES

- <sup>1</sup>Hill, R. J., S. F. Clifford, and R. S. Lawrence, 1980, "Refractive-index and absorption fluctuations in the infrared caused by temperature, humidity, and pressure fluctuations," J. Opt. Soc. Am. 70, n. 10, 1192-1205.
- <sup>2</sup>Strohbehn, J. W., 1968, "Line-of-Sight Wave Propagation Through the Turbulent Atmosphere," Proc. IEEE. 56, n. 8, 1301-1318.
- <sup>3</sup>Fried, D. L. and H. T. Yura, 1972, "Telescope-Performance Reciprocity for Propagation in a Turbulent Medium," J. Opt. Soc. Am. 62, n. 4, 600-602.
- <sup>4</sup>Fante, R. L., 1975, "Electromagnetic Beam Propagation in Turbulent Media," Proc. IEEE 63, n. 12, 1669-1692.
- <sup>5</sup>Ochs, G. R., T. Wang, R. S. Lawrence, and S. F. Clifford, 1976, "Refractive-turbulence profiles measured by one-dimensional spatial filtering of scintillations," Appl. Opt. 15, n. 10, 2504-2510.
- <sup>6</sup>Wyngaard, J. C., Y. Izumi, and S. A. Collins, Jr., 1971, "Behavior of the Reflective-Index Structure Parameter Near the Ground," J. Opt. Soc. Am. 61, n. 12, 1646-1650.
- <sup>7</sup>Walters, D. L. and K. E. Kunkel, 1981, "Atmospheric modulation transfer function for desert and mountain locations: the atmospheric effects on  $r_0$ ," J. Opt. Soc. Am. 71, n. 4, 397-405.
- <sup>8</sup>Tatarskii, V. I., 1971, The Effects of the Turbulent Atmosphere on Wave Propagation, Translated by Israel Program for Scientific Translations, avail. from U.S. Dept. of Commerce, National Technical Information Service, Springfield, VA 22151.
- <sup>9</sup>Fried, D. L., 1966, "Limiting Resolution Looking Down Through the Atmosphere," J. Opt. Soc. Am. 56, n. 10, 1380-1384.
- <sup>10</sup>Clifford, S. F., G.M.B. Bouricius, G. R. Ochs, and M. H. Ackley, 1971, "Phase Variations in Atmospheric Optical Propagation," J. Opt. Soc. Am. 61, n. 10, 1279-1284.
- <sup>11</sup>Walters, D. L., 1981, "Atmospheric modulation transfer function for desert and mountain locations:  $r_0$  measurements," J. Opt. Soc. Am. 71, n. 4, 406-409.
- <sup>12</sup>Lawrence, R. S. and J. W. Strohbehn, 1970, "A Survey of Clear-Air Propagation Effects Relevant to Optical Communications," Proc. IEEE 58, n. 10, 1523-1545.
- <sup>13</sup>Gracheva, M. E. and A. S. Gurvich, 1965, "On Strong Fluctuations of the Intensity of Light when Propagating in the Lower Layer of the Atmosphere," Izv. VUZ Radiofiz. 8, n.4, 717-724.
- <sup>14</sup>Burke, J. J., 1970, "Observations of the Wavelength Dependence of Stellar Scintillation," J. Opt. Soc. Am. 60, n. 9, 1262-1264.
- <sup>15</sup>Hufnagel, R. E. and N. R. Stanley, 1964, "Modulation Transfer Function Associated with Image Transmission through Turbulent Media," J. Opt. Soc. Am. 54, n. 1, 52-61.
- <sup>16</sup>Yura, H. T., 1973, "Short-term average optical-beam spread in a turbulent medium," J. Opt. Soc. Am. 63, n. 5, 567-572.

- <sup>17</sup>Land, D. J., 1978, "Effects of Atmospheric Turbulence on Imaging-Theory and Experiments," Proc. SPIE 142, Optical Properties of the Atmosphere, 80-90.
- <sup>18</sup>Dowling, J. A. and P. M. Livingston, 1973, "Behavior of focused beams in atmospheric turbulence: Measurements and comments on the theory," J. Opt. Soc. Am. 63, n. 7, 846-858.
- <sup>19</sup>Babcock, H. W., 1953, "The Possibility of Compensating Astronomical Seeing," Pub. Astron. Society of the Pacific 65, n. 386, 229-236.
- <sup>20</sup>Muller, R. A. and A. Buffington, 1974,, "Real-time correction of atmospherically degraded telescope images through image sharpening," J. Opt. Soc. Am. 64, n. 9, 1200-1210.
- <sup>21</sup>Pearson, J. E., 1976,, "Atmospheric turbulence compensation using coherent optical adaptive techniques," Appl. Opt. 15, n. 3, 622-631.
- <sup>22</sup>Herrmann, J., 1980, "Least-squares wave front errors of minimum norm," J. Opt. Soc. Am. 70, n.1, 28-35.
- <sup>23</sup>Hardy, J., 1978, "Active Optics: A New Technology for the Control of Light," Proc. IEEE 66, n. 6, 651-697.
- <sup>24</sup>Greenwood, D. P., 1977, "Bandwidth specification for adaptive optics systems," J. Opt. Soc. Am. 67, n. 3, 390-393.
- <sup>25</sup>Greenwood, D. P., 1979, "Mutual coherence function of a wavefront corrected by zonal adaptive optics," J. Opt. Soc. Am. 69, n. 4, 549-553.
- <sup>26</sup>Fried, D. L., 1982, "Anisoplanatism in adaptive optics," J. Opt. Soc. Am. 72, n. 1, 52-61.
- <sup>27</sup>Dyson, F. J., 1975, "Photon noise and atmospheric noise in active optical systems," J. Opt. Soc. Am. 65, n. 5, 551-558.

This work is sponsored by the Defense Advanced Research Projects Agency, DARPA/DEO.

"The U.S. Government assumes no responsibility for the information presented."

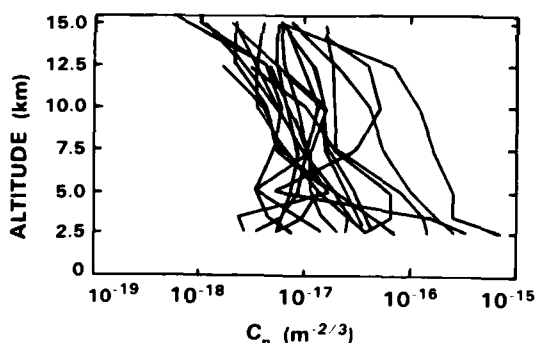


Figure 1. Representative measurements of  $C_n^2$  profiles made at Boulder, Colorado using a remote optical probe, from G. R. Ochs, et. al.<sup>5</sup>

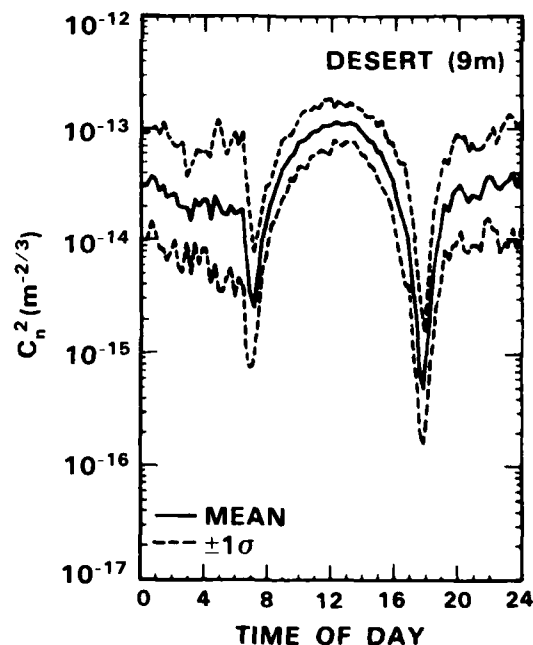


Figure 2. Seasonally averaged  $C_n^2$  at 9 m above the surface in the Tularosa basin, New Mexico, from Walters, et. al.

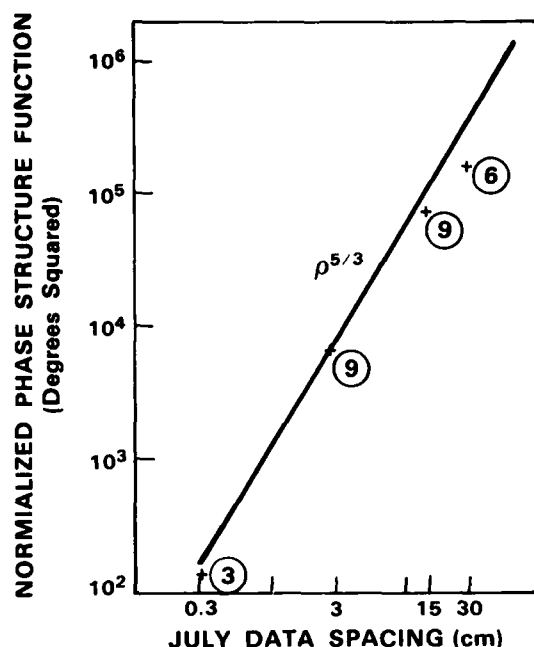


Figure 3. Phase Structure Function  $D_\phi(r)$ , measurements with  $C_\phi^2$  normalization, and theoretical  $r^{5/3}$  dependence, from Clifford, et. al.<sup>10</sup> Circles indicate number of data points averaged together.

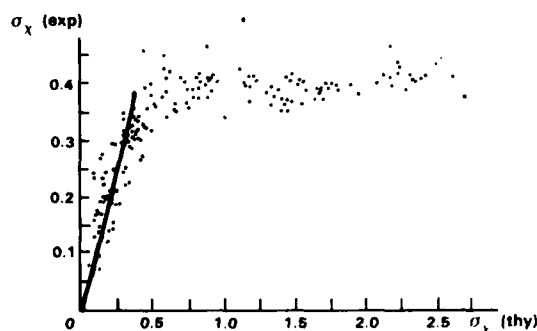


Figure 5. Plot of  $\sigma_X$  (experimental) versus  $\sigma_X$  (theoretical expectation) from Gracheva and Gurvich.<sup>13</sup> Strohbehn<sup>2</sup> believes that the originally reported values should be multiplied by 1/2, which we did. Although there have been numerous measurements of this sort since then, this represents the first to point out the failure of the theory for  $\sigma_X > 0.3$ .

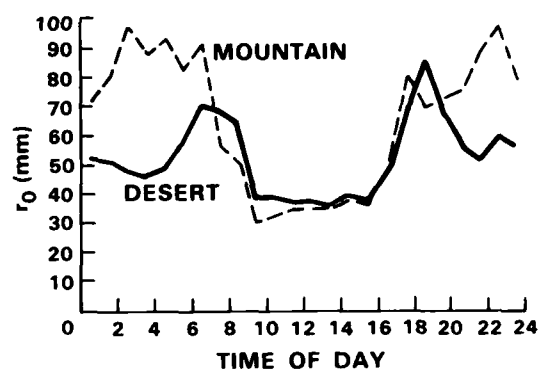


Figure 4. Coherence length  $r_0$  versus time of day for propagation at zenith from a 2-m desert site. Also shown are data from a 2-m (above local surface) mountain site. Plots borrowed from Walters.<sup>11</sup>

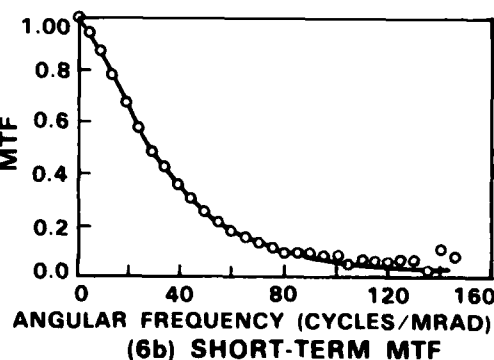
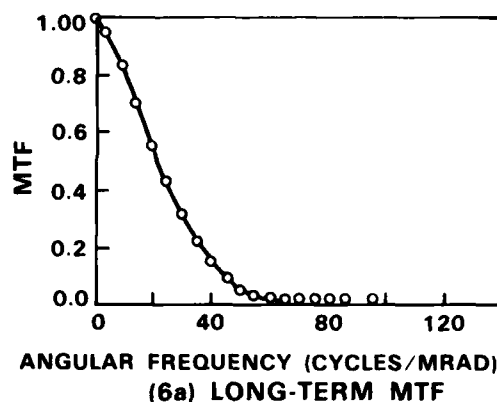


Figure 6. Long-term and short-term averaged MTF from Land's data plots,<sup>17</sup> and an overplot (solid lines) of Fried's theory.<sup>9</sup> (Curves directly from Land's paper.)

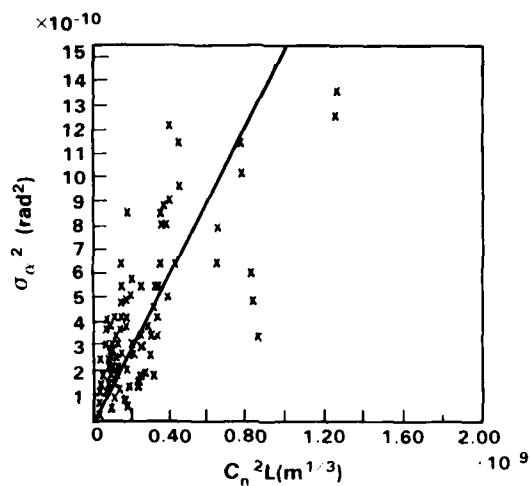


Figure 7. Beam wander variance -- data versus  $C_n^2 L$  dependence, repeated from Dowling and Livingston.<sup>18</sup> Theoretical Overplot is  $1.55 L C_n^2$ , given their  $D = 0.4$  m.

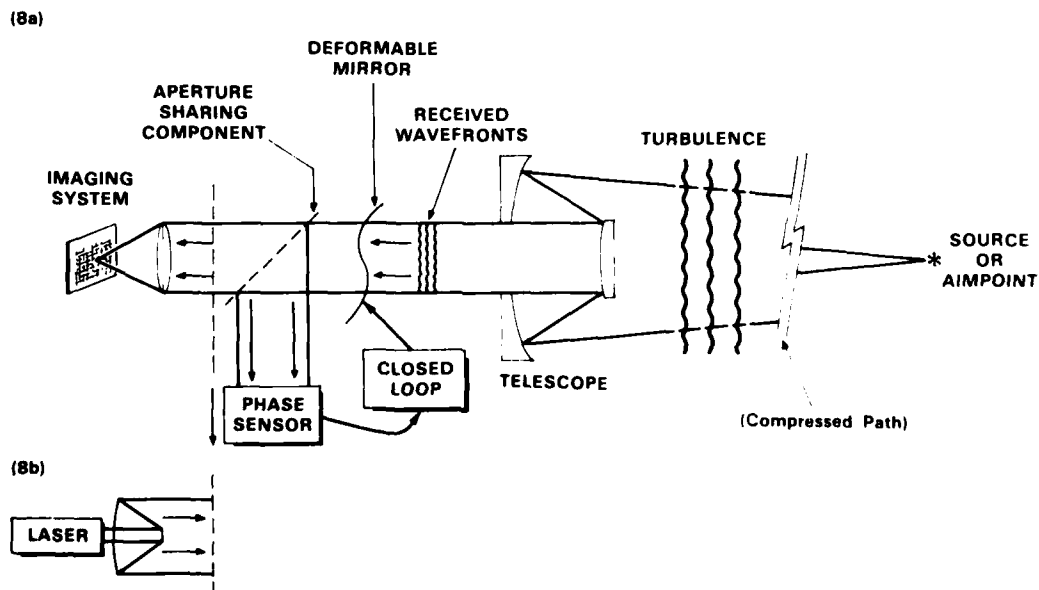


Figure 8a & b. Diagram of Adaptive Optics System implementation for Passive Imaging Application (8a), and the appropriate modification to allow injection of a laser beam at the indicated interface (8b).

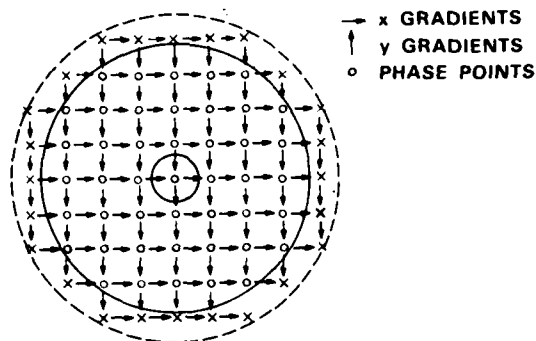


Figure 9. Example of a phase (circles) and phase gradient (arrows) arrays for a configuration with 120 gradients and 69 phase points.

#### DISCUSSION

S. Rotheram (U.K.): 1) When you measured phase gradients to reconstruct the phase, you had a two dimensional phase interrupting technique. You described an equivalent electrical circuit to achieve this. Can you tell us about the method used and an indication of the magnitudes of phases involved?

2) Do these adaptive optical methods work in the region of saturated irradiance fluctuation?

D. GREENWOOD (U.S.): (1) The phase reconstruction is an implementation of the solution to Laplace's equation. We use a resistor network, with phase gradients injected with current drivers.

(2) The phase variations are approximately  $\pm$  waves in the visible. Some margin should be allowed, however.

(3) The method should work in the saturated scintillation regime. Reciprocity is still valid, and we only compensate for phase effects.

## EFFECTS OF ATMOSPHERIC TURBULENCE ON OPTICAL PROPAGATION

Robert S. Lawrence  
D-Peck, Inc.  
5475 Western Avenue  
Boulder, Colorado 80301

## SUMMARY

The optical refractive index of the atmosphere depends on temperature, pressure, and humidity. Naturally occurring variations of these quantities, with scales of a few centimeters and associated with atmospheric turbulence, cause optical scintillation, image distortion, and laser beam broadening. I review the meteorological conditions that influence the occurrence of this optical turbulence, discuss the optical significance of turbulence at various heights in the atmosphere, and point out the differences between these optical effects and the corresponding phenomena at radio wavelengths.

While beam broadening increases indefinitely with the strength of optical turbulence, scintillation saturates and eventually decreases with increasing turbulence. I discuss this important effect and describe a phenomenological theory that explains it.

I conclude with estimates of the limitations imposed by atmospheric turbulence on various types of optical systems and mention the techniques that can be used to measure optical turbulence.

## 1. INTRODUCTION

Refractive-index variations in the clear atmosphere affect electromagnetic waves, both radio and optical, passing through them and, in most cases, degrade the performance of radio and optical systems. A notable exception, where the refractive-index variations are useful, occurs when radio-wave forward scatter is used for over-the-horizon communication. As we shall see, the sizes of the most important irregularities are near  $\sqrt{\lambda}L$ , where  $\lambda$  is the wavelength and  $L$  is the distance from the transmitter or receiver to the irregularity. Thus, while the irregularities that most affect radio systems have dimensions of meters, those that concern optical systems are only a few centimeters in size. We shall concentrate our attention on these small irregularities.

Besides their size, there is another important difference between the irregularities that affect optical systems and those that influence radio waves. The radio refractive index depends strongly on the water vapor in the air while, at optical wavelengths, the refractive index is principally affected by temperature variations.

I make no attempt to present mathematical details or a comprehensive bibliography. Those desiring such information are referred to review papers by LAWRENCE and STROHBEHN (1970) and by FANTE (1975), to a book edited by STROHBEHN (1978), and to a handbook chapter by HUFNAGEL (1978).

## 2. THE REFRACTIVE INDEX OF THE ATMOSPHERE

The refractivity of air at optical wavelengths is, to a good approximation, simply

$$N = 79 \frac{P}{T} \quad (1)$$

where  $P$  is the atmospheric pressure in mb and  $T$  is the temperature in K.  $N = (n-1) \cdot 10^6$  is the deviation of the refractive index from unity in parts per million, the familiar "N-units" used in radio work.  $N$  is roughly 290 at sea level. This approximation neglects the variation of air density caused by the presence of water vapor. The wavelength dependence of  $N$  is about 10 percent over the visible range of wavelengths; the humidity dependence is small but may occasionally be significant. These matters have been reviewed by OWENS (1967) and by FRIEHE et al. (1975). HILL et al. (1980) have discussed the refractive index in the infrared portion of the spectrum.

## 3. REFRACTIVE-INDEX TURBULENCE

Whenever I refer to "turbulence" I shall mean the refractive-index (or temperature) turbulence rather than the mechanical or velocity turbulence commonly measured with hot-wire probes. The distinction is important because, when the atmosphere is in neutral thermal stability, i.e., when the temperature lapse rate is adiabatic, strong mechanical turbulence may exist with little or no optical effect.

The most widely accepted description of the structure of mechanical turbulence appeared when KOLMOGOROV (1941) considered the structure function  $D$  between two components of velocity, call them  $\alpha, \beta$  where  $\alpha, \beta = x, y, z$ .

$$D_{\alpha, \beta}(r) = |V_{\alpha}(t) - V_{\beta}(t+r)|^2 \quad (2)$$

for a span  $r$  along coordinate  $\xi$ . Purely from dimensional analysis he found  $D_{\alpha, \beta}$  to be proportional to the two-thirds power of the separation, i.e.,

$$D_{\alpha\beta}(r) = C_{\alpha\beta}|r|^{2/3} \quad (3)$$

where  $C_{\alpha\beta}$  is a parameter depending on the components and the energy involved.

An advance of direct interest to optical propagation came when CORRSIN (1951) used a similar dimensional analysis to consider the temperature fluctuations in turbulence. The structure function of this scalar parameter turns out also to obey the two-thirds law, i.e.,

$$D_T(r) = C_T^2|r|^{2/3} \quad (4)$$

where  $C_T^2$ , the "temperature structure parameter", depends on the energy involved in the turbulence and on the temperature lapse rate of the atmosphere.

Pressure fluctuations in turbulent air are smoothed out with the speed of sound, and are negligible compared to temperature fluctuations. Differentiating the equation for refractivity and eliminating  $\delta P$ , we see that the refractive-index fluctuations are related to the temperature fluctuations by the formula

$$\delta N = -79 \frac{P}{T^2} \delta T \quad (5)$$

Accordingly, the refractive-index structure function,

$$D_N(r) = C_N^2|r|^{2/3} = \left[\frac{79P}{T}\right]^2 C_T^2|r|^{2/3} \quad (6)$$

where  $C_N^2 = C_T^2 \times 10^{12}$  and  $C_n^2$  is the refractive-index structure parameter.

#### 4. METEOROLOGICAL AND GEOGRAPHICAL INFLUENCES

The most important cause of optical turbulence is the convection generated when the air in contact with the sunlit ground is heated and rises. The turbulent temperature variations thus generated decrease rapidly with height and, up to the first temperature inversion which is typically about a kilometer above the ground,  $C_n^2$  is expected from theoretical considerations to decrease as the  $-4/3$  power of the height (WYNGAARD et al. (1971)). During cloudy weather and at night the decrease is less rapid. WALTERS and KUNKEL (1981) found an overall average decrease, over land, that varied as the  $-1.16$  power.

Above the first inversion, the variation of  $C_n^2$  with height has been modeled by HUFNAGEL (1978), using observations of stellar scintillation and the data from the few balloon-borne fast-response temperature probes that have been flown. In the Hufnagel model, the value of  $C_n^2$  depends slightly on wind speed. A typical  $C_n^2$  profile is shown by the dotted curve in Figure 1. Because there is so little water vapor at high altitudes even when the relative humidity is 100 percent, the radio and optical profiles of  $C_n^2$  must agree above a few kilometers. Observations of the radio profile have been reported by VANZANDT et al. (1978).

##### 4.1 Meteorological influences

The influence, over land, of meteorological conditions and time of day on the strength of optical turbulence has been discussed at length by WALTERS and KUNKEL (1981), using an extensive data set gathered at White Sands, New Mexico. There are three very different regimes, depending on atmospheric stability.

In the daytime, when the atmosphere is unstable because of solar heating of the ground, the average value of  $C_n^2$  decreases from  $10^{-12} \text{ m}^{-2/3}$  at a height of one meter to less than  $10^{-15} \text{ m}^{-2/3}$  at one kilometer. Near the ground, the value depends on the temperature difference between the air and the ground and, as seen in Figure 2, responds rapidly to the presence of cloud shadows. Optical turbulence is associated with the thermal plumes into which atmospheric convection is organized. These plumes have typical diameters of a hundred meters or so, and heights of 1 or 2 km; so the value of  $C_n^2$  observed near the ground varies dramatically and intermittently depending on the presence or absence of a plume at the observation point. This effect can be seen by using an acoustic sounder. Figure 3 shows the typical variation of atmospheric turbulence with height and time observed on a sunny day. In this figure, the dark area represents strong back-scattering of acoustic signals by the turbulent atmosphere.

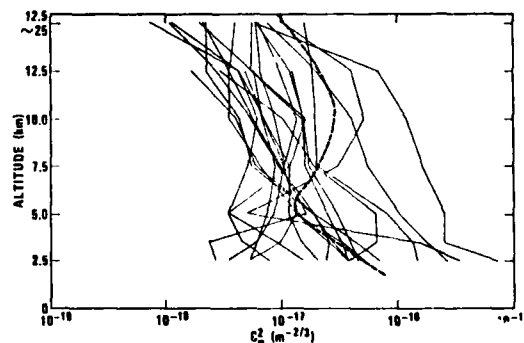


Fig. 1. Typical optically measured  $C_n^2$  profiles at Boulder, Colorado. Each curve is the average of the measurements of a single evening. The dashed line represents the statistical average profile of Hufnagel's model.

During these unstable conditions, the value of  $C_n^2$  is nearly independent of wind speed. Since it is associated with solar heating of the ground, the daytime turbulence cannot be avoided by climbing a mountain. The low-level turbulence, as organized into thermal plumes, is particularly annoying to solar astronomers who must, by definition, work on sunny days. Instructive discussions of solar "seeing" have been published by COULMAN (1969, 1974).

When the atmosphere is in neutral stability, i.e., when the temperature lapse rate is adiabatic, mechanical turbulence is not accompanied by optical effects. An interesting, though transitory, situation occurs near sunrise and sunset when, over land, the ground temperature and the air temperature are equal. Then, for a few moments,  $C_n^2$  assumes a minimum value. WALTERS and KUNKEL (1981) discuss these transition periods.

At night, the ground is cooler than the air and the atmosphere is generally stable. If the wind speed is low, there is little mixing of the air, and air of different temperatures settles into thin layers which, like the surface of the ocean, are subject to gravity waves. The temperature gradients can be very large in the stable atmosphere, and  $C_n^2$  can equal or exceed its daytime value. It varies greatly and intermittently. Figure 4 shows how these stable layers appear on an acoustic-sounder record. Incidentally, these same thin layers of contrasting refractive index can seriously distort or bend a horizontal laser beam and, in severe cases, may cause total internal reflection and produce discontinuous jumping of the beam, jumping that is difficult to track with a servo tracker.

Unlike the daytime case, a sharp mountain can elevate the observer above these troublesome stable layers. This explains the predilection of optical astronomers for mountaintops.

Over water, the diurnal effects are weaker than over land because the water temperature is nearly constant. Mild convection frequently occurs both day and night and the situation is complicated by the presence of water vapor. Few data exist for profiles in the marine atmosphere, though OCHS and LAWRENCE (1972) published some measurements.

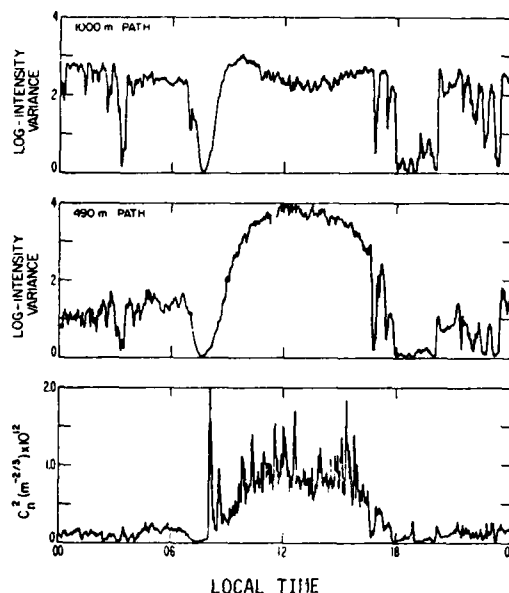


Fig. 2. Measurements of scintillation strength for a 24-hour period, made on horizontal paths 2 m above uniform terrain. The lowest curve shows  $C_n^2$  derived from measurements of temperature turbulence made simultaneously with a fine-wire temperature probe.

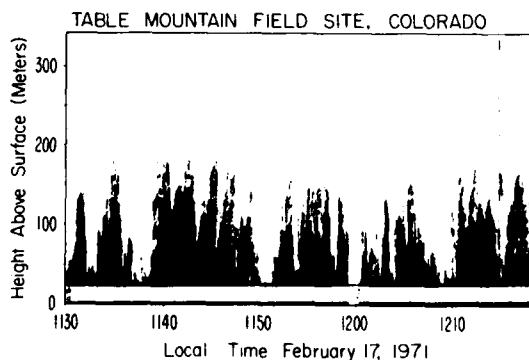


Fig. 3. A typical daytime acoustic sounding of the lower atmosphere showing, as dark areas, the turbulent thermal plumes caused by solar heating of the ground.

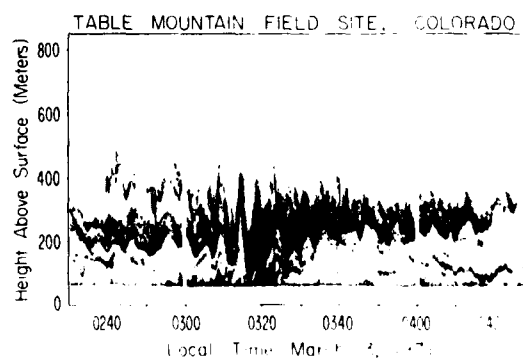


Fig. 4. A typical nighttime acoustic sounding of the lower atmosphere showing, as dark areas, the oscillating turbulent strata that are so common when the atmosphere is stable.

It is interesting to note that the addition of water vapor to the turbulent atmosphere will sometimes increase  $C_n^2$  but can also have the opposite effect. In the marine environment, all air is fully saturated and the warmer parcels, which already have a smaller refractive index than the others, contain more water vapor and that further decreases their refractive index. Thus, the refractivity contrast, and therefore  $C_n^2$  is increased. If hot, dry desert air passes over a lake, the parcels of air that pick up moisture are cooled by the process and the refractivity change caused by the cooling tends to cancel that caused by the increased water vapor. FRIEHE et al. (1975) discuss this matter at length.

#### 4.2 Geographical influence

Since optical turbulence is so strongly influenced by weather conditions, it follows that localities with different climates, may have very different amounts of optical turbulence. Surprisingly, little has been done to produce systematic surveys of  $C_n^2$  profiles. Astronomers, with their serious need to reduce atmospheric effects, have made surveys of the overall effect of the atmosphere and have concluded that the windward side of mountaintops in climates with high-pressure, stable atmospheric conditions are most favorable.  $C_n^2$  profile measurements have been made at some sites and reveal interesting trends. For example,  $C_n^2$  at Boulder, Colorado, downwind of more than 1000 km of mountainous terrain, averages about ten times greater than at Hawaii, at all altitudes.

Figure 5 shows a vertical section of the  $C_n^2$  structure over Mt. Haleakala in Hawaii. It is evident that the mountain increases  $C_n^2$  in its vicinity by a factor of 100.

#### 5. THE EFFECTS ON OPTICAL SYSTEMS

The small-scale variations in refractivity have three principal effects on optical systems:

##### 5.1 Scintillation

The turbulent irregularities in the atmosphere produce phase and amplitude distortions in optical waves. These are known as phase scintillations and intensity scintillations. The term "scintillation" is often used to mean intensity scintillations.

Referring to Figure 6, let us consider the behavior of a plane wave front A, such as might arrive from a star, as it travels through the turbulent atmosphere. Immediately after passing through a region of irregular refractive index, the wavefront B has been distorted. Since absorption and wide-angle scattering are negligible in the clear atmosphere, the energy density of the wavefront B is still uniform and equal to its freespace value. Thus an ordinary square-law detector placed at B would be unaffected by the wavefront distortions and incapable of measuring them. The distortions can, of course, be measured by a phase-sensitive detector such as an interferometer or a telescope.

As the wave progresses from B towards C, the various portions of the distorted wavefront travel in slightly different directions and eventually begin to interfere. The interference is equivalent to a redistribution of energy in the wave and causes intensity fluctuations, i.e., scintillations, that can be detected by a square-law detector. On the way from B to C the wave passes through additional refractive-index irregularities and so suffers additional phase perturbations. These new irregularities are, however, relatively ineffective in producing scintillations at C.

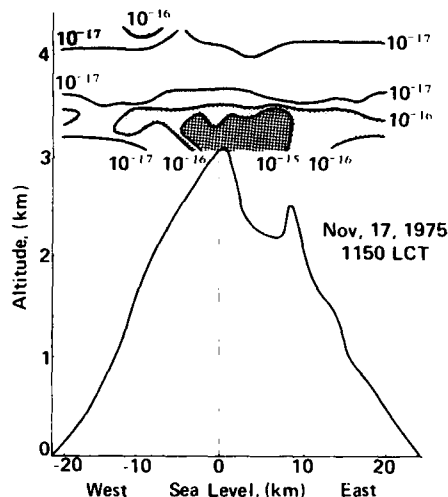


Fig. 5. Section of  $C_n^2$  derived from airborne high-speed temperature probe measurements over Mount Haleakala, Hawaii.

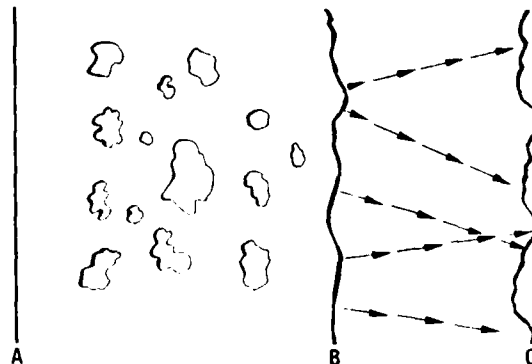


Fig. 6. A plane wavefront A, distorted by refractive-index irregularities between A and B, suffers only phase distortion at B, but then the wavefront interferes at C.

Let us examine the criteria that determine which of the turbulent irregularities along a line of sight are most effective in producing scintillations. In Figure 7, consider an irregularity of diameter  $\ell$  at an arbitrary point Z on the line of sight between the plane wave and the receiver at L. The irregularity can be fully effective in producing intensity variations only if the extreme ray paths AL and ZL differ in length by at least half a wavelength, i.e., the irregularity must be at least equal in size to the first zone of a Fresnel zone plate situated at Z. This minimum effective size is, in fact, the optimum size for the irregularity. Larger irregularities at the same point are ineffective because they do not diffract light through a large enough angle to reach the observer. While it is true that smaller irregularities produce intensity fluctuations at points closer than L and that these fluctuations persist in modified form until the wave reaches L, such smaller irregularities are relatively ineffective because of the steep increase in the Kolmogorov spectrum of atmospheric turbulence with irregularity size.

From the geometry of Figure 7, we see that the diameter of the most effective irregularity at height h is  $\ell = \sqrt{\lambda h}$ , where  $\lambda$  is the wavelength of the light. As a numerical example, for visible light of wavelength  $0.5 \mu\text{m}$  and for a height of 10 km,  $\ell = 7 \text{ cm}$ . When the same geometrical argument is applied to the spherical waves originating from a point source, we find that the same  $\sqrt{\lambda L}$  relationship holds where, in this case L is the distance between the source and the observer.

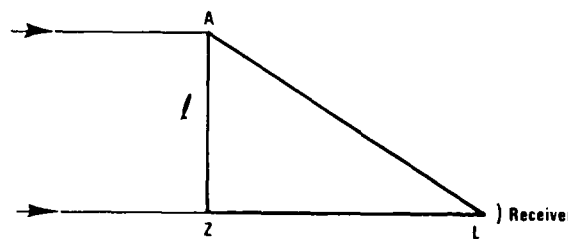


Fig. 7. The geometry involved in computing the size of the refractive-index irregularities that are most effective in producing scintillations.

We can get an idea of the probability distribution function of the irradiance (in radio terms, the power that would be received by a isotropic receiving antenna)

of a scintillating optical signal from very simple arguments. If, as in the case of ionospheric scintillation of radio stars, all the irregularities lie in a relatively thin, bounded region somewhere between the source and the receiver, the various irregularities that contribute to the observed scintillation do so additively and simultaneously. We know that the superposition of many scattered signals with random phases and the main, unscattered signal produce a Rice-Nakagami distribution (NORTON et al. (1955)) which, in the limit of strong scattering and no unscattered signal, becomes an exponential distribution (Rayleigh, in amplitude).

If, on the other hand, as in optical propagation through the atmosphere, the irregularities occur over many Fresnel distances along the path, the light repeatedly travels through irregularities and then proceeds far enough to develop additional scintillations. These repeated scintillations accumulate multiplicatively, that is, their logarithms add, so we can expect the irradiance distribution to be log-normal. In fact, observed scintillations are nearly, but not quite exactly, log-normal. This matter is discussed in detail by STROHBEHN (1978), pp. 97-104.

The temporal frequency spectrum of scintillations peaks near the frequency with which the predominant scintillation size,  $\sqrt{\lambda L}$ , is advected across the line of sight by the crosswind component of the mean wind. Thus, very few scintillations exceed 500 Hz in frequency, and a significant number are at frequencies below the 10 Hz cut-off of the human eye. GRACHEVA et al. (1978) show and discuss many observed frequency spectra.

The strength of scintillations, as measured by the variance of the logarithm of the amplitude, increases at first with the strength of the optical turbulence as measured by  $C_n^2$  and with the path length. However, when the integral of  $C_n^2$  along the path becomes large enough to produce a log-amplitude variance exceeding 0.4, the scintillations begin to increase more slowly and, with sufficient integrated  $C_n^2$ , actually decrease. This effect is known as "saturation" of scintillations and is well illustrated in the diurnal scintillation observations of Figure 2.

Saturation occurs because, once phase fluctuations have been imposed upon a wavefront, subsequent encounters with irregularities larger than those fluctuations are ineffective. After the wave has travelled through enough irregularities so that the phase correlation distance in the wavefront has been reduced to the Fresnel-zone size,  $\sqrt{\lambda L}$ , severe saturation ensues because all the irregularities that would have been most important in producing scintillations are rendered ineffective. A heuristic theory of saturation was first presented by CLIFFORD et al. (1974) and by CLIFFORD and YURA (1974). It has been made more exact by HILL and CLIFFORD (1981). The practical importance of saturation lies in the fact that, although the log-amplitude variance of scintillations is self-limiting, the scintillations become continuously smaller in size after saturation is reached. This means that the temporal frequencies of the scintillation become larger in the saturation region and that the resulting beam broadening increases indefinitely.

## 5.2 Beam broadening

When describing the origin of scintillations, we mentioned that various portions of the perturbed wavefront travel in different directions, each parallel to its local normal. This implies that any portion of the wavefront, a beam, must be broadened as a result of the refractive-index irregularities. The amount of broadening increases as  $(C_n^2)^{1/5}$  and is not limited by any saturation effect. In the absence of absorption, the total energy in the beam remains constant so the beam energy received by a given receiver must decrease with increasing turbulence, affecting the performance of lidar and optical communication systems. When the turbulence is not uniformly distributed along the beam,  $C_n^2$  at position  $z$  along a path  $L$  is weighted by a factor

$$\left(1 - \frac{z}{L}\right)^{5/3}$$

which simply states that turbulence near the transmitter is more destructive to the beam than is turbulence near the receiver. One practical implication of this fact is that, for optical communication between earth and space, downlinks work better than uplinks and, unlike uplinks, can benefit from space diversity.

It is not very useful to give an approximate formula for calculating beam broadening because, depending upon atmospheric conditions, turbulent beam broadening can be dominated by other effects. The beam wanders because of the turbulence, so the long-term average illumination of the observing plane occurs on a spot considerably larger than the instantaneous beam diameter. If the path is long or the turbulence strong, the spot is broken into isolated patches, each of which fluctuates and wanders. In addition, when the atmosphere is stable and gravity waves are present, a horizontal beam will wander, principally in the vertical direction, by amounts far exceeding the turbulent wander. In severe cases, this beam wander becomes discontinuous, with the spot disappearing at one location and re-appearing at a different location.

A succinct and authoritative treatment of beam broadening is given by HUFNAGEL (1978).

## 5.3 Loss of image resolution

In a manner analogous to the broadening of a beam, each point of an optical image is blurred by the atmosphere. Further, in analogy to the wandering of a beam, each point of the image moves relative to other points, further distorting the image. Thus, long and short exposures of images exhibit different amounts of image degradation. The blurring is described in terms of the "point spread function" or its Fourier transform, the "modulation transfer function". As with beam broadening, the effectiveness of the turbulence in destroying the image varies depending on its position. Turbulence near the object is much less effective than turbulence near the camera lens. Thus, it is possible to photograph the earth from a satellite and get resolution of only a few cm, while it is scarcely possible to resolve the major elements of a satellite photographed from the earth.

Two types of methods can be employed to improve the resolution of images made through the turbulent atmosphere.

First, interferometry can be used. Here, the phase of the fringes is discarded because the atmosphere primarily affects the phase. The amplitude, or "visibility", of the fringes is measured for various aperture separations, and the resulting visibility function is the Fourier transform of the autocorrelation function of the image. This is useful only for simple images, such as double stars, because only the spatial autocorrelation function is obtained, not the image itself. A variation is "speckle interferometry" where, for very simple objects, the mutual interference of various portions of the object can be used to derive the autocorrelation function of the image.

Second, it is possible to place a point source of light near the object to be imaged and, by actively distorting the optical system of the receiver so as to minimize the point spread function from that beacon, to partially correct for the atmospheric turbulence over a portion of the image near the image of the beacon. This method, called "adaptive optics", is very difficult because the distortion of the optical system must be accomplished in less than about a millisecond, and independently at many portions of the optical system. A special issue of the JOURNAL OF THE OPTICAL SOCIETY OF AMERICA (1977) was devoted to adaptive optics.

## 6. MEASUREMENT OF OPTICAL TURBULENCE

The most commonly used method of measuring optical turbulence in the atmosphere is an indirect one. Fine-wire probes measure the temperature fluctuations and  $C_n^2$  is derived using Eq.(6). The probes are not heated since the resistance of hot wires depends on the velocity of the passing air while the resistance of cold wires depends on the temperature of the air (LAWRENCE, OCHS, and CLIFFORD (1970)). This indirect measurement ignores the usually small effect of water vapor and is experimentally difficult because of breakage and contamination of the very fine wires. Larger, more durable wires can be used but this moves the spatial sizes of the observation away from the sizes of the optically important irregularities, requiring assumptions that the spectrum of turbulence agrees with some theoretical model.

Fine-wire probes have been used in a variety of situations near the ground and on towers, they have been carried aloft by high-altitude balloons, and they have been used on aircraft (OCHS and LAWRENCE (1972)). To a large extent, they are responsible for what we know of the morphology of  $C_n^2$ .

An optical method of measuring the integrated value of  $C_n^2$  along a path has been developed by WANG et al. (1978) and improved by OCHS and CARTWRIGHT (1981). When it was first proposed, this optical scintillometer was rightly criticized as being inaccurate because of the saturation effect, but this problem has been eliminated and, where experimental conditions permit its use, the method is more convenient and dependable than the use of probes.

The integrated amount of optical turbulence through the entire atmosphere can be measured by observing, at the ground, the size of a stellar image (WALTERS (1981)). Although such measurements are useful, it would be preferable to know the vertical profile of  $C_n^2$  so that the atmospheric effects on a variety of optical systems, with various vertical weighting functions, could be computed. OCHS et al. (1976) developed an optical stellar scintillometer to measure vertical profiles of  $C_n^2$ , and it has been used regularly at a limited number of sites. The problem is that the instrument is complex and expensive, and that the vertical resolution is poor. The instrument is, of course, limited to use only on clear nights. Figure 1 shows data from a stellar scintillometer.

The ideal way of studying the geographical distribution and climatology of  $C_n^2$  would be to find a method of predicting optical turbulence from conventional meteorological observations. If this could be done, the huge data banks of weather observations would become useful to the optical engineer. Several serious attempts to do this have been made, but the results have been disappointing, to say the least.

## 7. CONCLUSION

We understand, in a quantitative manner, the effects of atmospheric turbulence on optical propagation, and can use that understanding to predict the effects of given turbulence on a particular optical system. We know, in general terms, which parts of the atmosphere contain the most damaging turbulence. We can measure optical turbulence and we have theories for its causes, but we are unable to predict its detailed occurrence. Extensive surveys such as those that have been made at White Sands, New Mexico and at Maui, Hawaii tell us what to expect in several very different geographical situations, and suggest what the worldwide limiting values may be.

## 8. REFERENCES

- CLIFFORD, S. F., G. R. OCHS, and R. S. LAWRENCE 1974, "Saturation of optical scintillation by strong turbulence", *J. Opt. Soc. Am.*, **64**, 148-154.
- CLIFFORD, S. F. and H. T. YURA, 1974, "Equivalence of two theories of strong optical scintillation", *J. Opt. Soc. Am.*, **64**, 1641-1644.
- CORRSIN, S., 1951, "On the spectrum of isotropic temperature fluctuations in an isotropic isotropic turbulence", *J. Appl. Phys.*, **22**, 469-473.
- COULMAN, C. E., 1949, "A quantitative treatment of solar 'seeing', I." *Solar Physics*, **7**, 1, 122-143.
- COULMAN, C. E., 1974, "A quantitative treatment of solar 'seeing', II". *Solar Physics*, **34**, 491-506.
- FANTE, R. L., 1975, "Electromagnetic beam propagation in turbulent media", *Proc. IEEE*, **63**, 12, 1669-1692.
- FRIEHE, C. A., J. C. LARUE, F. H. CHAMPAGNE, C. H. GIBSON, and G. F. DREYER, 1975, "Effects of temperature and humidity fluctuations on the optical refractive index of the marine boundary layer", *J. Opt. Soc. Am.*, **65**, 1502-1511.
- GRACHEVA, M. E., A. S. GURVICH, S. S. KASHKAROV, and V. V. POKASOV, 1978, "Similarity relations and their experimental verification for strong intensity fluctuations of laser radiation", Chap. 4 of "Topics in Applied Physics -- Laser beam propagation in the atmosphere", ed. by J. W. Strohbehn. Springer-Verlag, New York.
- HILL, R. J., S. F. CLIFFORD, and R. S. LAWRENCE, 1980, "Refractive-index and absorption fluctuations in the infrared caused by temperature, humidity, and pressure fluctuations", *J. Opt. Soc. Am.*, **70**, 1192-1205.
- HILL, R. J. and S. F. CLIFFORD, 1981, "Theory of saturation of optical scintillation by strong turbulence for arbitrary refractive-index spectra", *J. Opt. Soc. Am.*, **71**, 675-686.
- HUFNAGEL, R. E., 1978, "Propagation through atmospheric turbulence", in "The infrared handbook", U. S. Gov't Printing Office, Washington, D. C., Chap. 6, pp. 6-1 - 6-56.
- KOLMOGOROV, A., 1941, "Turbulence, classic papers on statistical theory", S. K. Friedlander and L. Topper, eds., p. 151, Interscience, New York.

- LAWRENCE, R. S., G. R. OCHS, and S. F. CLIFFORD, 1970, "Measurements of atmospheric turbulence relevant to optical propagation", J. Opt. Soc. Am., 60, 826-830.
- LAWRENCE, R. S. and J. W. STROHBEHN, 1970, "A survey of clear-air propagation effects relevant to optical communications", Proc. IEEE, 58, 1523-1545.
- NORTON, K. A., L. E. VOGLER, W. V. MANSFIELD, and P. J. SHORT, 1955, "The probability distribution of the amplitude of a constant vector plus a Rayleigh-distributed vector" Proc. IRE, 43, 1354-1361.
- OCHS, G. R. and R. S. LAWRENCE, 1972, "Temperature and  $C_n^2$  profiles measured over land and ocean to 3 km above the surface", NOAA Tech. Rep't. ERL 251-WPL 22, Superintendent of Documents, U. S. Gov't Printing Office, Washington, D. C. 20402.
- OCHS, G. R., R. S. LAWRENCE, T-i WANG and P. ZIESKE, 1976, "Stellar-scintillation measurement of the vertical profile of refractive-index turbulence in the atmosphere", SPIE, 25 "Imaging Through the Atmosphere, Reston, Virginia, March 22-23, 1976, 48-54.
- OCHS, G. R. and W. C. CARTWRIGHT, 1981, "An optical device for path-averaged measurements of  $C_n^2$ ", SPIE, 277, "Atmospheric Transmission", 21-22 April 1981, Washington, D. C.
- OPTICAL SOCIETY OF AMERICA, Washington, D. C., 1977, "Journal of the Optical Society of America", 67, No. 3, (A special issue featuring adaptive optics.)
- OWENS, J. C., 1967, "Optical refractive index of air: dependence on pressure, temperature, and composition", Appl. Opt., 6, 51-59.
- STROHBEHN, J. W., 1978, "Modern theories in the propagation of optical waves in a turbulent medium", Chap. 3 of "Topics in Applied Physics -- Laser beam propagation in the atmosphere", ed. by J. W. Strohbehn. Springer-Verlag, New York.
- VanZANDT, T. E., et al., 1978, "Vertical profiles of refraction turbulence structure comparison of observations by the Sunset radar with a new theoretical model", Radio Sci., 13, 819-829.
- WALTERS, D. L. and K. E. KUNKEL, 1981, "Atmospheric modulation transfer function for desert and mountain locations: the atmospheric effects on  $r_0$ ", J. Opt. Soc. Am., 71, 397-405.
- WALTERS, D. L., 1981, "Atmospheric modulation transfer function for desert and mountain locations:  $r_0$  measurements", J. Opt. Soc. Am., 71, 406-409.
- WANG, T-i, G. R. OCHS, and S. F. CLIFFORD, 1978, "Saturation-resistant optical scintillometer to measure  $C_n^2$ ", J. Opt. Soc. Am., 68, 334-338.
- WYNGAARD, J. C., Y. IZUMI, and S. A. COLLINS, 1971, "Behavior of the refractive index structure parameter near the ground", J. Opt. Soc. Am., 61, 1646-1650.

#### DISCUSSION

D.P. Greenwood (U.S.): We find that in propagation from ground-to-space, the fading statistics are nearly Rayleigh. In your discussion you speak only of distributed turbulence where you have a log-normal distribution.

R.F. Lawrence (U.S.): Yes, thank you for pointing that out. If the turbulence is highly concentrated near one end of the path, the distribution is not log-normal.

E. Vilar (U.K.): You described the refractive index structure parameter  $C_n^2$ , brought about by turbulence and therefore by variability of temperature. Your extremes in the optical path of  $10^{-16}$  and  $10^{-17}$  compare with  $10^{-13}$  and  $10^{-14}$  in the radio path. One must use  $C_n^2$  carefully to sense layers in the microwave region.

R.S. Lawrence (U.S.): In a marine or a highly humid environment, water vapor is dominant in radio  $C_n^2$  than in optical  $C_n^2$  (so radio  $C_n^2$  is larger). In a desert, dry hot air passing over a lake picks up moisture and cools the air. Humidity reduces optical  $C_n^2$ , while temperature increases it, so that the best locales are in the center of a lake in the desert for optical  $C_n^2$ . Above the clouds or more than 3-4 km altitude, even with saturated water vapor, the optical  $C_n^2$  and radio  $C_n^2$  are similar.

## EVALUATION DE LA HAUTEUR DU CONDUIT TROPOSPHERIQUE D'EVAPORATION

B. STRAUSS

Météorologie SMM/ES

2 Avenue Rapp

75340 PARIS CEDEX 7 FRANCE

### RESUME :

On présente les premiers essais d'estimation de la hauteur du conduit d'évaporation à partir des sorties d'un modèle de prévision numérique utilisé en météorologie.

Le modèle utilisé est celui du CEPMMT. A partir des sorties en points de grille de vent à 10 mètres, température et  $T_d$  à 2 mètres, et température de surface de l'Océan, on calcule la hauteur du conduit d'évaporation.

On teste la méthode sur une partie de l'Atlantique Nord et sur une zone de l'Océan Indien, en comparant les estimations du modèle avec les observations des navires météorologiques.

### I - INTRODUCTION

Les seules informations actuellement disponibles sur la hauteur du conduit d'évaporation, tant du point de vue ponctuel (situation à un instant donné) que climatologique, viennent de mesures in-situ, soit de navires météo - rologiques, soit de conditions de propagation.

Or les progrès réalisés en modélisation des phénomènes météorologiques permettent, dans certaines applications, d'utiliser les sorties numériques quand les mesures font défaut. Il est donc intéressant d'examiner si le niveau actuel de sophistication des modèles météorologiques est suffisant dans le cas du conduit d'évaporation.

La démarche consiste à utiliser les champs en surface calculée par un modèle en exploitation, aussi performant que possible dans les très basses couches, pour calculer la hauteur du conduit (ainsi qu'un paramètre de stabilité, dans notre cas la longueur de Monin-Obukhov).

On compare le résultat avec les observations disponibles de navires météorologiques.

### II - DESCRIPTION DU MODELE METEOROLOGIQUE

Le modèle de prévision météorologique numérique utilisé est celui du Centre Européen pour les Prévisions Météorologiques à Moyen Terme (CEPMMT) situé à Reading (U.K.). Parmi les modèles actuellement exploités dans le monde, il est un de ceux qui traitent le mieux les basses couches, grâce à une résolution verticale de 4 niveaux entre 0 et 1500 m d'altitude.

Il est spectral, de troncature autorisant une définition de  $1.5^\circ$  environ, sur tout le globe. Il tourne une fois par jour à partir du réseau d'observation de 12 heures TU, et calcule des champs prévus sur tout le globe jusqu'à 10 jours d'échéance. Parmi ces champs se trouvent le vent à 10 m au dessus du sol, la température  $T$  et la température du point de rosée  $T_d$  à 2 m.

Le dernier champ dont nous avons besoin, qui est la température de surface de la mer  $T_s$ , n'évolue pas avec la prévision, mais reste identique au champ initial, qui est une analyse sur une grille de 5 degrés sur 5 degrés faite par le NMC (National Meteorological Center US).

Cela peut naturellement entraîner des erreurs importantes sur les échéances élevées. Pour le présent travail, nous avons utilisé les échéances 36, 48 et 72 heures, qui correspondent à des champs à 0h TU pour l'échéance 36, et 12 h TU pour 48 et 72. On aurait pu utiliser plutôt des champs analysés, mais leur qualité est a priori de même ordre que celle de champs prévus à échéance faible (l'information qui sert à les calculer étant essentiellement les champs prévus à partir des réseaux précédents). Il était donc plus intéressant de tester d'emblée des champs prévus.

La maille équivalente du modèle, qui vaut  $1.5^\circ$ , n'autorise pas une description fine des zones de transitions terre-mer. Ceci explique que les valeurs des champs de surface ( $T_d$  et  $T_s$  notamment) près des côtes ne sont pas représentatives des conditions maritimes réelles. Le calcul du conduit d'évaporation ne sera donc pas possible dans ce cas, ce qui exclut par exemple la Méditerranée.

### III CALCUL DE LA HAUTEUR DU CONDUIT

La méthode, la plus souvent appliquée, consiste à utiliser les grandeurs météorologiques "classiques" (vent, température, humidité) pour calculer les paramètres caractéristiques de la couche limite de surface. On en déduit une expression analytique des profils de température et humidité spécifique, et donc du profil de coindice de réfraction  $N$ , qui permet de déterminer la hauteur du conduit d'évaporation.

La formulation utilisée est celle de Paulson (1970), où l'on a ajouté deux relations pour l'humidité spécifique. On tient compte de la différence de hauteur entre le niveau de calcul du vent (10 m) et celui de T et Td (2 m) par le modèle du Centre Européen. La connaissance des valeurs de T à 0 et 2 m, de l'humidité spécifique à 0 et 2 m (en supposant l'atmosphère saturée au niveau 0 m), et de la force du vent à 10 m, est suffisante pour déterminer les flux turbulents de chaleur sensible et latente et de quantité de mouvement, et la longueur de Monin-Obukhov. La méthode n'est pas applicable dans toutes les conditions. Le cas le plus gênant est celui où le calcul donne des épaisseurs de conduit de plusieurs dizaines de mètres, ce qui met en contradiction avec une hypothèse de départ pour l'établissement des formules de Paulson, qui est que l'on se trouve dans une couche limite de surface, à flux constants sur la verticale.

Pour cette raison, dans la suite toutes les épaisseurs calculées supérieures à 40 mètres seront représentées par cette valeur de 40 m.

#### IV VALIDATION DES RESULTATS

La figure 1 donne des exemples de cartes d'épaisseur de conduit prévue. On a sélectionné deux zones très différentes, afin de pouvoir déceler d'éventuelles variations des performances en fonction de la localisation géographique (latitude notamment).

La validation (ou l'invalidation) des résultats est difficile du fait de la nature des données utilisables (observations météorologiques de navires sélectionnés, auxquelles on applique la méthode décrite en III).

En effet ces navires sont en petit nombre, comparativement à l'étendue du domaine de travail, et circulent sur des routes souvent près des côtes. A titre d'indication, le nombre moyen d'observations utilisables pour une situation donnée est d'environ 40 sur le domaine atlantique et 15 sur le domaine indien (voir la figure 1 pour la définition des domaines).

La période utilisée pour la validation va du 18/6/83 au 16/9/83, dans laquelle on dispose de 74 situations différentes.

##### 1°) NAVIRES STATIONNAIRES

On présente d'abord la comparaison avec les navires météorologiques stationnaires (points R, L et C, cf figure) car bien qu'ils soient un peu trop hauts en latitude pour bien illustrer le phénomène du conduit d'évaporation, ils ont l'avantage d'être toujours disponibles, et de présenter une très bonne garantie quant à la qualité des mesures.

La figure 2 montre le nuage de points obtenu en portant en abscisses l'épaisseur du conduit mesurée par les navires, et en ordonnées celle calculée par le modèle. Les valeurs supérieures à 20 m sont portées comme égales à 20 m.

En omettant les points de valeur 40 m ou plus (qui représentent moins de 3 % des cas, et pour lesquels on rappelle que la méthode de calcul de l'épaisseur est sujette à caution), on obtient une corrélation de 0.65. On observe un biais important, les valeurs calculées étant de l'ordre de 1.7 fois plus petites que les valeurs mesurées.

L'origine de ce biais réside dans la nature du modèle numérique, qui du fait de l'échantillonnage en 15 niveaux sur la verticale, filtre les variations importantes et donc atténue les gradients. On le vérifie sur l'humidité spécifique, en constatant que la différence (Tair-Td) à 2 m calculée par le modèle est inférieure à celle mesurée (après correction de la différence de hauteur) :

Valeur moyenne de (T-Td) mesurée pour une valeur calculée de :

0°	1.3°
1°	2.5°
2°	4.1°
3°	6.7°

L'assèchement a sur et à mesure que l'on s'élève est donc moins rapide pour le modèle qu'en réalité.

On peut calculer l'épaisseur du conduit en remplaçant Td sortie du modèle par Tair -  $\Delta$ ,  $\Delta$  étant la valeur de (T-Td) corrigée en fonction du tableau ci-dessus. On obtient alors le nuage de points de la figure 3, pour lequel la corrélation vaut 0.67, et le biais 1.1.

Il est intéressant de remarquer que la plupart des cas de sous-estimation importante par le modèle correspondent à des observations de jour (12h TU).

On peut penser que cela est dû à une représentation trop sommaire du cycle diurne par le modèle.

La cohérence des estimations par rapport aux phénomènes météorologiques est illustrée par la figure 4, qui représente l'évolution temporelle calculée et mesurée au point L du 21/6 au 26/6 et du 2/8 au 8/8/83. Les valeurs à 0 h TU sont celles prévues 36 h auparavant, et celles à 12 h TU 72 h auparavant, sauf dans les cas où seule l'échéance 48 était disponible.

Des passages successifs de perturbations sont signalés par les variations d'épaisseur de conduit, avec des déphasages entre modèle et mesure compatibles avec les performances attendues pour des échéances allant jusqu'à 72 heures.

On a représenté également des exemples de périodes perturbées et non perturbées, prises au point R.

## 2°) AUTRES NAVIRES

La figure 5 indique 3 zones pour lesquelles on a croisé toutes les observations ship disponibles dans la période avec la valeur au point de grille correspondant multipliée par le biais de 1,7 trouvé pour l'Atlantique Nord-Est. Les nuages de points obtenus sont portés figure 6, avec 71, 142 et 91 cas selon la zone. On a indiqué les limites de la plage dans laquelle la précision est meilleure que 30 %.

Dans les 3 zones, presque tous les cas de sous-estimation importante par le modèle ont lieu à 12 h TU (soit environ 16 h locales en Océan Indien, donc en période de convection développée), ce qui soulève le même problème que pour les navires stationnaires, et dégrade sensiblement les performances dans la zone Atlantique Equatoriale.

On constate d'autre part, que le biais de 1.7, déterminé pour 45° de latitude Nord et plus, s'applique bien dans les trois nouvelles zones.

Sur le plan climatologique, la représentativité des champs calculés semble être la même partout ; par contre l'absence de navire stationnaire dans les zones tropicales empêche d'examiner la représentativité de l'évolution temporelle vue par le modèle.

## V - DESCRIPTION CLIMATOLOGIQUE

La figure 7 montre les champs obtenus en moyennant tous les champs calculés sur la période où le modèle a tourné.

Sur l'Atlantique, l'information essentielle est la position de la limite entre faibles et fortes valeurs de l'épaisseur du conduit, aux alentours du 45° parallèle Nord (limite dont on suivait bien l'évolution au jour le jour, cf figure 3).

Sur l'Océan Indien, le trait dominant est l'organisation zonale.

On constate une quasi-similitude entre les champs obtenus par les échéances 36 h (soit 0 h TU) et 48 heures (soit 12 h TU), quelque soit la latitude, ce qui tend à confirmer que le cycle diurne est mal pris en compte par le modèle. Malgré cela, des estimations statistiques sont dès maintenant envisageables, temporelles (probabilité de dépassement de seuils,...) et spatiales (extensions géographiques, impossibles à déterminer à partir des ships).

## VI - CONCLUSION

La représentativité des estimations d'épaisseur de conduit d'évaporation à partir des sorties du modèle météorologique opérationnel au CEPMMT a été illustrée par divers aspects. Le niveau des performances est indiqué par la corrélation, de 0.67, trouvée avec les observations des navires météorologiques stationnaires. Les limitations ont été exposées : invalidité près des côtes, cycle diurne mal représenté, faiblesse relative de la résolution spatiale principalement.

Les limitations rappelées ci-dessus s'atténueront au fur et à mesure que les développements actuellement engagés sur les modèles météorologiques produiront des résultats. Notamment, la mise en service de modèles à maille très fine, de l'ordre de 30 km, permettra d'obtenir des estimations valables près des côtes, et d'étendre le calcul à des mers comme la Méditerranée. A terme, un suivi assez fin devrait être possible dans toutes les zones où cela sera utile.

## BIBLIOGRAPHIE

Newson R., C. Temperton and S. Tibaldi (1979) The ECMWF Forecasting system. ECMWF Lecture Note N° 11.

Paulson C. A. (1970) The Mathematical representation of wind speeds and temperature profiles in the unstable atmospheric surface layer. Journal of Applied Meteorology 9, p 857 - 861.

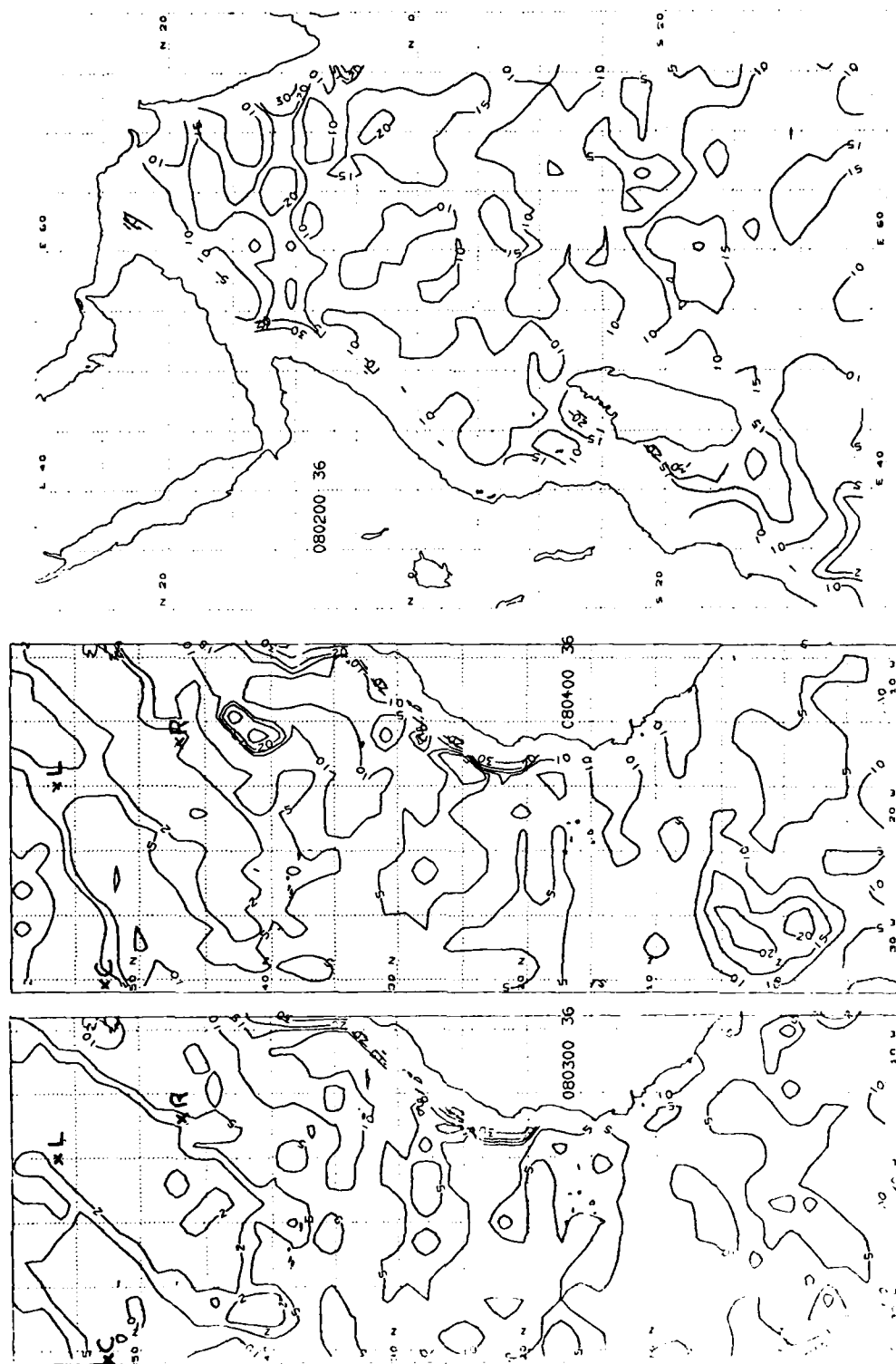


FIGURE 1: exemples de sorties: prévisions à échéance 36h, isolignes d'épaisseur de duct, en mètres.

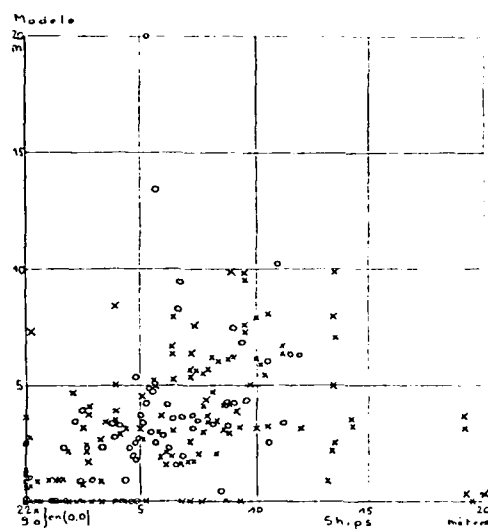


FIG. 2: épaisseurs du duct prévues (ordonnées) / épaisseurs mesurées (abscisses). Points R, L et C (cf fig. 1 pour la localisation).  
 o 0h TU  
 x 12h TU

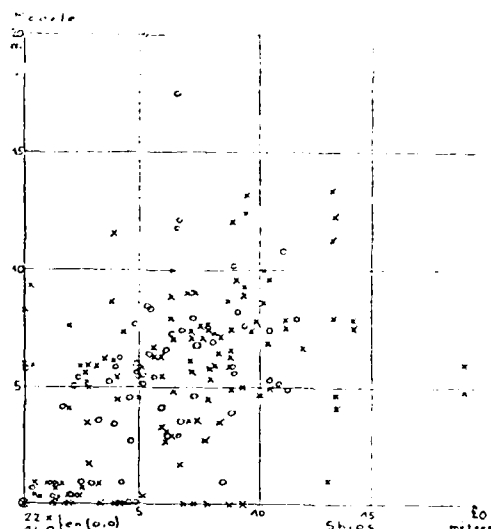


FIG. 3: comme la figure 2, mais après adaptation de la Td prévue.  
 Corrélation: 0.67.

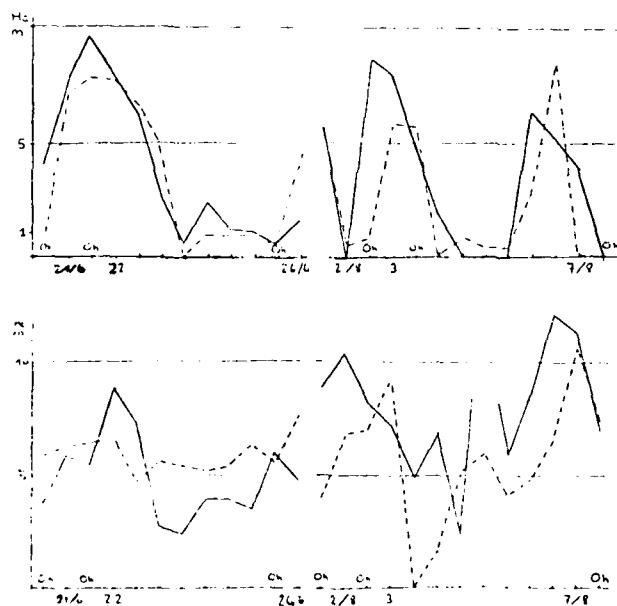


FIGURE 4: suivi temporel aux points L (en haut) et R (en bas).  
 Trait plein: mesures  
 Trait pointillé: prévisions.

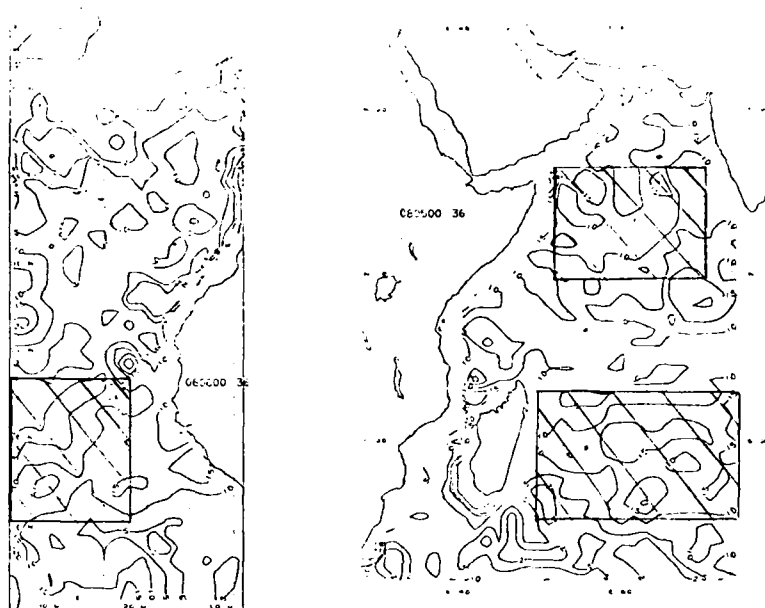


FIGURE 5: autres exemples de sorties, avec indication des zones test pour la validation.

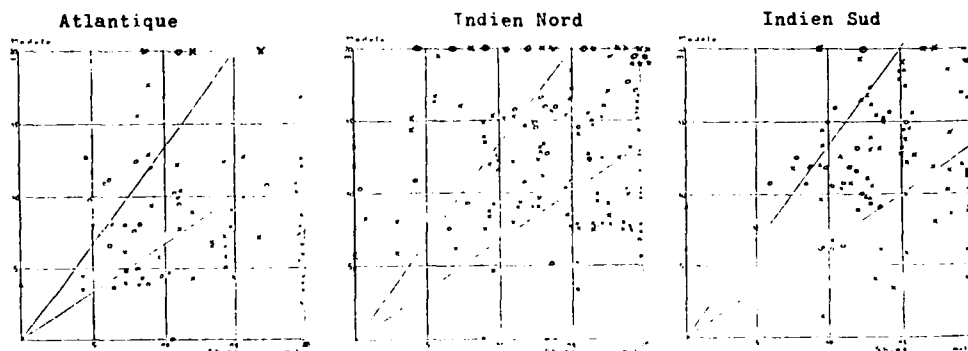
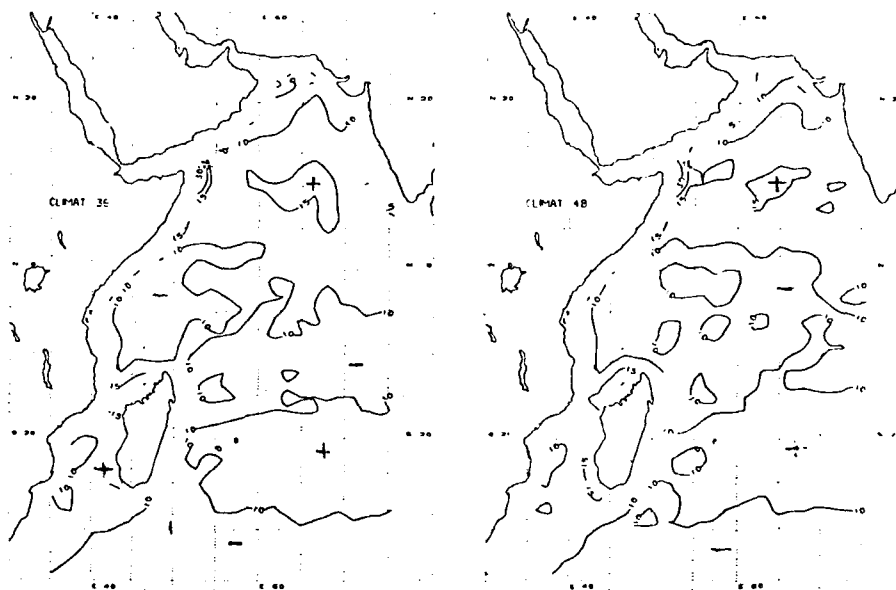
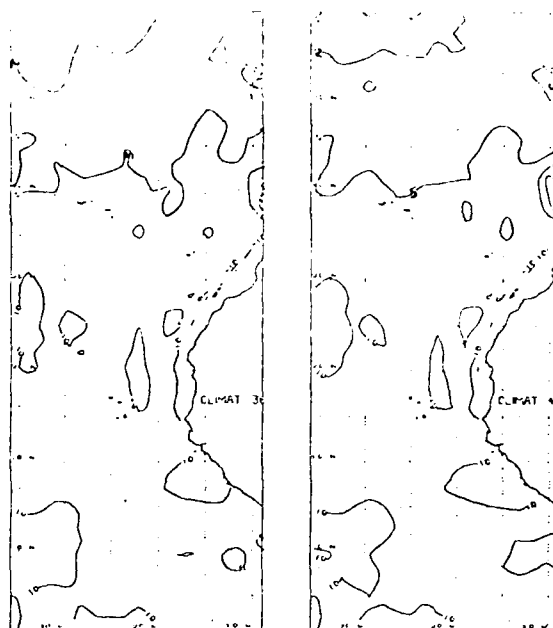


FIGURE 6: comme la figure 2, après correction du biais, pour les trois zones test de la fig. 5.



Echéances 36h (situations de OhTU)

Echéances 48h (12h TU)

FIGURE 7: cartes d'épaisseur de duct moyennée sur toute la période.  
Isolignes cotées en mètres.

## DISCUSSION

S. Rotheram (U.K.): We have investigated the possibility of using the United Kingdom Meteorological Office's 15 level model. With some minor software development, three-dimensional refractive index distributions would be the output. As the author points out, these could have some resolution for surface based ducts, but little resolution for elevated ducts. The model referred to by the author is the coarse mesh model on a 150 km (approx.) grid. The Meteorological Office recently introduced a fine mesh model on a 75 km grid covering most of the Northern hemisphere. In a few years time, a mesoscale model on a 10 km grid is to be introduced in the United Kingdom area.

B. Strauss (France): La météorologie Française développe également un modèle méso-échelle (30 km de maille), sur un domaine couvrant largement la France, ce qui devrait, en effet, permettre d'aborder les problèmes de conduits autres que les conduits d'évaporation.

## A RADIO INTERFERENCE MODEL FOR WESTERN EUROPE

by

S. Rotheram  
Marconi Research Centre,  
West Hanningfield Road,  
Great Baddow, Chelmsford, UK.

## SUMMARY

Field strength distributions for 106 land, sea and mixed paths of three terrain types are analysed for their dependence on scattering angle, probability, terrain type, frequency and terminal height. Good models are derived for the sea and low terrain land paths. The medium and high terrain land paths show greater variability. The frequency dependence is shown to be weak. The dependence on terminal heights is shown to be non-existent except for the effect on the scattering angle. Mixed paths are shown to be like land paths and are quite unlike sea paths.

## 1. INTRODUCTION

The planning of broadcasting and other services requires the ability to predict levels of interference between different services. The essence of such predictions is a knowledge of field strength variations with distance for small percentages of the time.

Within the radio horizon the dominant propagation mechanism is interference between direct and reflected waves. This gives signal levels close to free space in the vicinity of the horizon. Just beyond the radio horizon the dominant propagation mechanism is diffraction. At UHF and above this falls off very rapidly with distance and soon becomes negligible. Another transhorizon propagation mechanism is tropospheric scatter. It decays less rapidly than the diffracted field but from a lower base. It dominates the diffracted signal when this is more than about 50 dB below free space and is thus the dominant propagation mechanism well beyond the radio horizon.

For small time percentages other propagation mechanisms dominate the diffracted-scattered fields. These mechanisms have been reviewed recently by Crane [1]. The most important such mechanism is ducting by atmospheric layers. This dominates scatter for typically 1 to 10% of the time. Over the land ducting by elevated layers is the more important. These often occur at the boundaries of subsiding air masses in high pressure systems. These also occur over the sea but the statistics may be dominated, particularly in coastal waters, by surface ducts caused by advection and evaporation.

The object of this work is to describe a statistical model of the field strength variations with distance for a small percentage of the time when ducting is the dominant mechanism. The model applies to Western Europe. It includes sea land and mixed cases and the effects of terrain, frequency and terminal heights. Particular emphasis is given to mixed paths which are shown to be like land paths.

The data is for 106 paths given in references 2 and 3. This consists of field strength distributions. The degree of irregularity of terrain over a land path can be given by  $\Delta h$  which is the difference in height exceeded by 10% and 90% of the terrain. Land paths are designated L, M or H depending upon whether  $\Delta h$  is less than 50 m, is between 50 m and 100 m, or is greater than 100 m respectively. Sea paths are designated S. Mixed sea and land paths are designated either S+L, S+M or S+H depending upon the degree of irregularity of terrain over the land portion of the path.

## 2. SEA PATHS (S)

Data for 23 sea paths are shown in figures 1, 2, 3 and 4 for probabilities  $p = .01, .1, 1$  and 10% of the time with data points indicated by crosses. The figures show  $L(p) - 10 \log f$  plotted against  $\theta$ . Here  $L(p)$  is the path loss in dB above free space,  $f$  is the frequency in GHz and  $\theta$  is the scattering angle in milliradians. Over a smooth earth the scattering angle  $\theta$  is

$$\theta = \frac{D - D_h}{ka}, \quad D_h = (2ka)^{\frac{1}{2}} (h_T^{\frac{1}{2}} + h_R^{\frac{1}{2}}) \quad (1)$$

where  $a$  is the earth's radius,  $k$  is the effective earth's radius factor taken to be  $4/3$ ,  $D$  is range,  $D_h$  is the horizon distance, and  $h_T$  and  $h_R$  are the transmitter and receiver heights. Over a rough earth, rays are drawn from the transmitter and receiver to just clear the highest obstruction on the path using  $4/3$  earth geometry. The angle at which the two rays intersect is the scattering angle  $\theta$ .

The form of presentation in figures 1 to 4 is used in troposcatter prediction methods [4] though a different form is used in CCIR Report 569 [5] which is concerned with interference. Linear least mean square estimates of the data in figures 1 to 4 fit the general form

$$L(p) = 10 \log f + \alpha(p) + \beta(p) \theta + \sigma(p) \quad \text{dB} \quad (2)$$

The values of  $\alpha(p)$ ,  $\beta(p)$  and  $\sigma(p)$  found are shown in table 1. The regression lines (solid)  $\pm$  one standard deviation (dashed) are plotted in figures 1 to 4.

The regression lines for  $p = .01, .1, 1$  and 10% are shown together as the solid lines in figure 5. The dotted curves are taken from CCIR Report 569 [5] for  $p = .01, .1$  and 1% with  $f = 1$  GHz, and the term denoted  $A$  (additional diffraction loss) set to zero. These curves are for terminals on the ground so  $D_h = 0$  and we have made the correspondence  $D = ka \theta$  from eqn. (1). Although the functional forms are different, the two sets of curves are reasonably consistent.

Using the values in table 1, a plot of  $\log \beta$  against  $\log p$  lies close to a straight line showing that  $\beta$  depends upon  $p^{.4}$ . Figures 6 and 7 show  $\beta$  and  $\alpha$  plotted against  $p^{.4}$ . Evidently these are nearly straight lines with the least squares fit

$$\beta = .4 p^{.4}, \quad \alpha = -10.8 + 10.1 p^{.4} \quad (3)$$

Taking the average value  $\sigma = 7$  dB one has the complete model

$$L(p) = 10 \log f - 10.8 + p^{.4} (10.1 + 4 \theta) \pm 7 \text{ dB} \quad (4)$$

valid over the sea for  $p < 10\%$ . Eqn. (4) is plotted for  $p = .01, .1, 1$  and  $10\%$  as the dashed lines in figure 5. They differ from the solid lines based on eqn. (2) and table 1 by a negligible amount. This indicates that eqn. (4) may be quite a good formula. Note that eqn. (4) may be inverted to give  $p(L)$  explicitly as

$$p(L) = \left[ \frac{L - 10 \log f + 10.8 \pm 7}{10.1 + .4 \theta} \right]^{2.5} \quad (5)$$

For a given frequency and scattering angle this gives the probability (percent) that the path loss relative to free space will be less than  $L$ . Eqns. (4) and (5) also allow extrapolation to smaller values of  $p$ .

### 3. LAND PATHS - LOW TERRAIN (L)

Data from 10 land paths with low terrain irregularity ( $L$ ) are shown in figures 8, 9, 10 and 11 for  $p = .01, .1, 1$  and  $10\%$ . Linear least mean square estimates fit eqn. (2) with the values shown in table 2. The regression lines (solid) + one standard deviation (dashed) are also plotted in figures 8 to 11. The regression lines for  $p = .01, .1$  and  $1$  and  $10\%$  are shown together in figure 12 as the solid lines. The dotted curves are from CCIR Report 569 [5] as in section 2. There are significant differences with the CCIR method giving less loss at short distances and more loss at greater distances.

It is evident from figure 12 that the line for  $p = 10\%$  has a different character from the other lines in that its slope is less than one might expect from the other lines. It may be inferred from the few points in figure 11 that a steep line can be fitted to the points for small  $\theta$  and a shallow line can be fitted to the points for large  $\theta$ . This is because the points for small  $\theta$  are attributable to diffraction-ducting and those for large  $\theta$  to scatter. The two dotted lines in figure 11 are a guess at the variation of these two components. As this paper is trying to model the high signals due to ducting, one is justified in excluding the  $10\%$  data. This means that the models being given are valid for path losses up to about 60 dB above the free space loss.

Using the values in table 2, figure 13 shows a plot of  $\log \beta$  against  $\log p$ . The three points for  $p = .01, .1$  and  $1\%$  lie close to a straight line but the point for  $p = 10\%$  is quite distinct. This is further justification for neglecting this point in determining the ducting distribution. The other points fit the formula

$$\log \beta = -.096 + .294 \log p \text{ or } \beta = .8 p^{.294} \quad (6)$$

Figure 14 shows  $\alpha$  plotted against  $p^{.294}$ . The points lie close to the straight line

$$\alpha = -4 + 17 p^{.294} \quad (7)$$

Taking the average value  $\sigma = 7$  one has the complete model

$$L(p) = 10 \log f - 4 + p^{.294} (17 + .8 \theta) \pm 7 \text{ dB} \quad (8)$$

This can be inverted to give the probability distribution  $p(L)$ .

$$p(L) = \left[ \frac{L - 10 \log f + 4 \pm 7}{17 + .8 \theta} \right]^{3.4} \quad (9)$$

Because of their simplicity eqns. (4) and (8) for  $L(p)$ , or eqns. (5) and (9) for  $p(L)$ , are extremely useful formula for interference calculations.

### 4. LAND PATHS - MEDIUM TERRAIN (M)

Data from 18 paths with medium terrain irregularity ( $50\text{m} < \Delta h < 100\text{m}$ ) and designated M are shown in figures 15, 16 and 17 for  $p = .01, .1$  and  $1\%$ . Linear least mean square estimates fit eqn. (2) with the values shown in table 3. The regression lines (solid) + one standard deviation (dashed) are also plotted in figures 15, 16 and 17. The regression lines for  $p = .01, .1$  and  $1\%$  are shown together in figure 18. The data points for this case are much more scattered and a general formula such as eqns. (4) and (8) cannot be found.

### 5. LAND PATHS - HIGH TERRAIN (H)

Data from 26 paths with high terrain irregularity ( $\Delta h > 100\text{m}$ ) and designated H are shown in figures 19, 20 and 21 for  $p = .01, .1$  and  $1\%$ . Linear least mean square estimates fit eqn. (2) with the values shown in table 4. The regression lines (solid) + one standard deviation (dashed) are also plotted in figures 19, 20 and 21. The regression lines for  $p = .01, .1$  and  $1\%$  are shown together in figure 22. No general formula has been found.

## 6. MIXED SEA-LAND PATHS WITH LOW TERRAIN (S+L)

Data from 17 mixed sea-land paths with low terrain irregularity in the land segment ( $\Delta h < 50\text{m}$ ) and designated S+L are shown in figures 23, 24 and 25 for  $p = .01, .1$  and  $1\%$ . The data points are indicated by a number which is the percent of the path that is sea. Also shown are the regression lines for sea (S) and low terrain land (L). The object of this exercise is to determine whether S+L is like S or L, or is intermediate between S and L. Because of the wide differences in the amount of sea in the paths, no attempt has been made to fit curves to this data. What is obvious from the data is that S+L is very similar to L but is quite unlike S, irrespective of the amount of sea in the path. The physical reason for this is that high signal strengths on sea paths in coastal areas are largely caused by advection ducts. These end at the coast. High signals on land paths are largely caused by elevated subsidence inversions. Mixed paths do not benefit from the advection ducts as these only extend along part of the path and are not excited. However elevated subsidence inversions extend over large areas being relatively unaffected by coasts. The strong conclusion from this data is that for S+L paths one should use the L results. This is at variance with CCIR Report 569 which recommends using S and L in the proportion of the path that is sea and land.

## 7. MIXED SEA-LAND PATHS WITH MEDIUM (S+M) AND HIGH (S+H) TERRAIN

Data from 8 mixed sea-land paths with medium terrain (S+M) and 6 with high terrain (S+H) are shown in figures 26, 27 and 28 for  $p = .01, .1$  and  $1\%$ . The data points are indicated by a number which is the percentage of the path that is sea enclosed in a square for S+M paths and a circle for S+H paths. Also shown are the regression lines for sea (S), medium terrain land (M) and high terrain land (H). It is obvious that the mixed paths are like the land paths and are quite unlike the sea paths. The conclusion is that for S+M paths one should use the M results whilst for S+H paths one should use the H results.

## 8. FREQUENCY DEPENDENCE

Thus far it has been assumed that the frequency dependence of the data is contained in the term  $10 \log f$ . This assumption is tested here for  $p = 1\%$ . The path loss above free space is  $L(1)$ . The value predicted by the regression line in eqn. (2) with the values in tables 1 to 4 for  $p = 1\%$  will be denoted  $L_p(1)$ . The prediction error is then  $L(1) - L_p(1)$ . This is plotted in figure 29 against  $\log f$  to see if there is any systematic variation. The regression line is

$$L(1) - L_p(1) = .2 + 6 \log f \pm 9 \text{ dB} \quad (10)$$

indicating an overall frequency dependence of  $16 \log f$ . However the variation is relatively small compared with the spread of values and so the results are inconclusive. More data is required to resolve this question, particularly at the higher frequencies. The frequency dependence will also depend upon  $p$ .

## 9. HEIGHT DEPENDENCE

It is often assumed that the excitation of ducted modes of propagation depends upon the heights of the terminals. The heights of the terminals enters into the calculation of the scattering angle, but this is an additional effect. For a surface duct it is commonly assumed that terminals in the duct yield higher signal strengths than terminals above the duct. This proposition is tested here using the  $p = 1\%$  data from the sea paths (S). The terminal heights  $h_T$  and  $h_R$  above sea level are added to give  $H = h_T + h_R$ . Figure 30 shows the prediction error  $L(1) - L_p(1)$  plotted against  $H$ . If there was a significant excitation effect, the prediction error would be positive for small  $H$  and negative for large  $H$ . Evidently there is a large spread of values for small  $H$  whilst for large  $H$  the values are small and negative. It is clear that no systematic excitation effect can be discerned. Thus the conclusion is that the only effect of the height of the terminals is on the scattering angle. The reason for this can only be guessed. The excitation effect is often greatly exaggerated. Even for a deterministic surface duct, the effect is only of order 10 to 20 dB at the most due to leakage of energy through the duct. Real ducts have many other pathways whereby modes can be excited even for elevated ducts. These include rough surface scatter and irregularities in the duct structure such as turbulence and gravity waves.

## 10. CONCLUSIONS

The main results of this paper may be summarised as follows :-

- The regression formula in eqn. (2) with the values in tables 1 to 4 may be used for S, L, M and H paths.
- For S and L paths general formulae for  $L(p)$  are given by eqns. (4) and (8) and for  $p(L)$  by eqns. (5) and (9).
- For mixed paths one should use the land distributions.
- The frequency dependence is relatively weak compared to the spread in the data.
- No terminal height dependence is discerned other than the effect on the scattering angle.

## 11. REFERENCES

- [1] R.K. CRANE, A review of transhorizon propagation phenomena. Radio Science, Vol.16, No.5, pp.649-669, 1981.
- [2] P.J. BRICE, Propagation data at UHF and SHF for trans-horizon paths in Western Europe. Ministry of Posts and Telecommunications. RTD Technical Memorandum No. P41. 1973.
- [3] CCIR, Measured trans-horizon propagation data at microwave frequencies. UK Study Grp.5, CP.26, 1981.
- [4] P.L. RICE, A. LONGLY, K.A. NORTON, A.P. BARSIS, Transmission loss predictions for tropospheric communication circuits. NBS TN 101 Vols. 1 & 2, U.K. Dept. of Commerce, Washington, D.C. 1965.
- [5] CCIR, The evaluation of propagation factors in interference problems between stations on the surface of the earth at frequencies above about 0.5 GHz. Report 569-1 (Mod F). 1981.

p%	$\alpha$	$\beta$	$\sigma$
.01	- 8.7	.062	5.5
.1	- 7	.176	7.2
1	- 1	.4	6.3
10	14.8	.98	9.2

Table 1. Regression coefficients for sea paths (S).

p%	$\alpha$	$\beta$	$\sigma$
.01	.3	.207	5.9
.1	4.9	.407	6.8
1	13	.8	8.6
10	16.8	.743	9.7

Table 2. Regression coefficients for land paths with low terrain (L)

p%	$\alpha$	$\beta$	$\sigma$
.01	3.5	.715	11.4
.1	10	.768	9.5
1	22.7	.962	10.8

Table 3. Regression coefficients for land paths with medium terrain (M)

p%	$\alpha$	$\beta$	$\sigma$
.01	12.4	.727	9
.1	32.8	.395	10.7
1	40.3	.693	10.3

Table 4. Regression coefficients for land paths with high terrain (H).

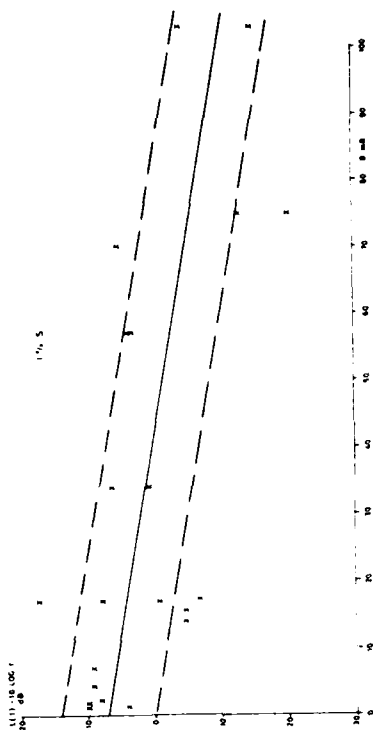


Figure 1. Path loss above free space  $L(0.01)$  for .01% over sea (S).

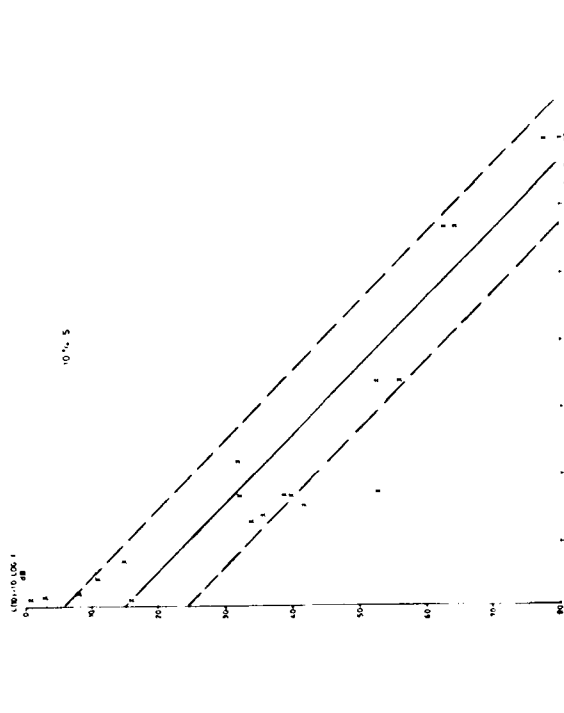


Figure 2. Path loss above free space  $L(0.1)$  for .1% over sea (S).

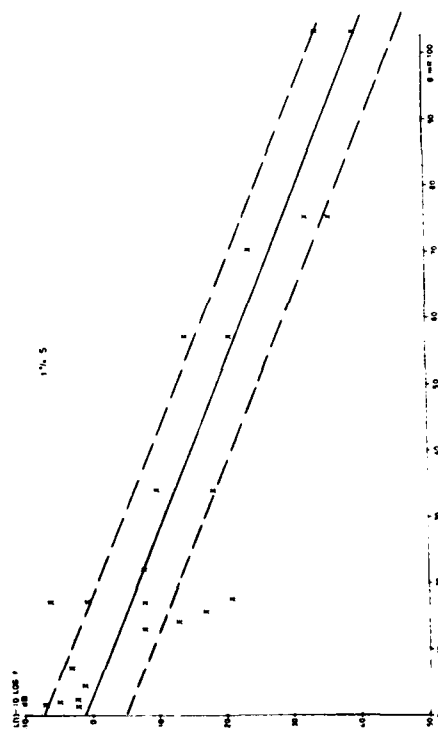
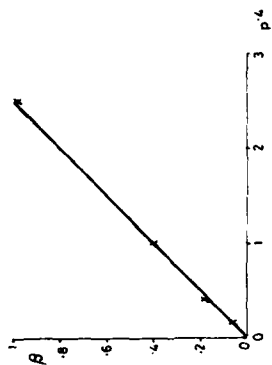
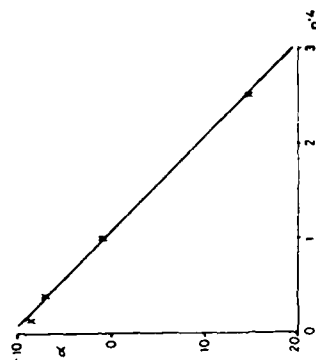
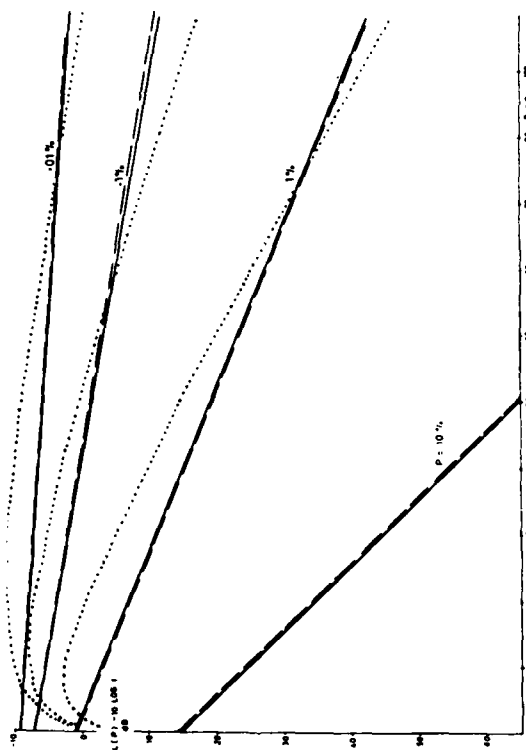


Figure 3. Path loss above free space  $L(1)$  for 1% over sea (S).

Figure 4. Path loss above free space  $L(10)$  for 10% over sea (S).

Figure 6. Plot of  $\beta$  against  $p^4$ Figure 7. Plot of  $\alpha$  against  $p^4$ Figure 5. Regression lines (solid lines) of path loss above free space  $L(p)$  for  $p\%$  over sea (S). Dashed lines are eqn. (4). Dotted lines are CCIR Report 569.

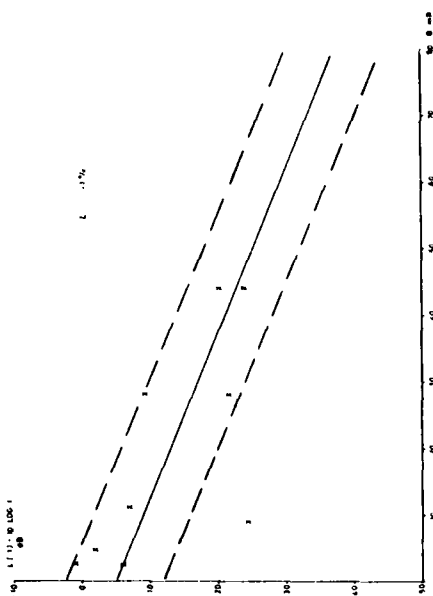


Figure 8. Path loss above free space  $L(.01)$  for .01% over land with low terrain (L).

Figure 9. Path loss above free space  $L(.1)$  for .1% over land with low terrain (L).

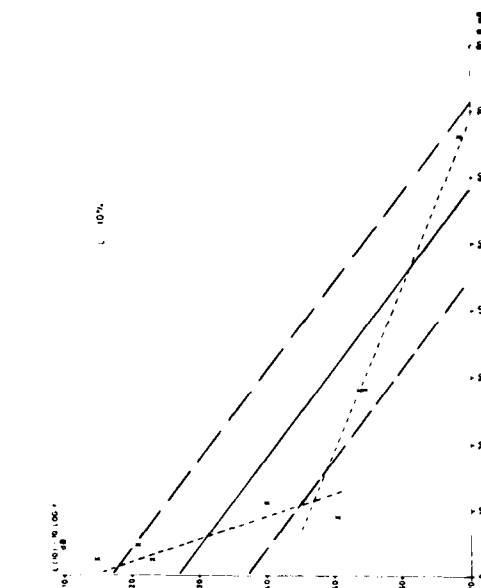


Figure 11. Path loss above free space  $L(10)$  for 10% over land with low terrain (L).

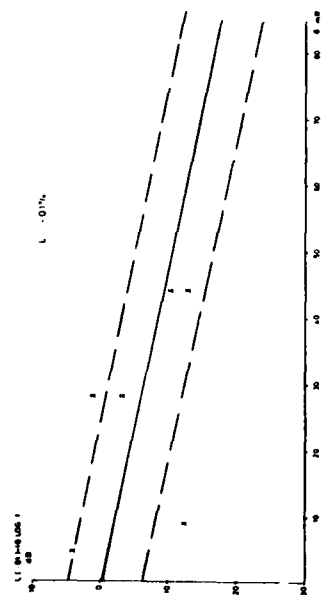
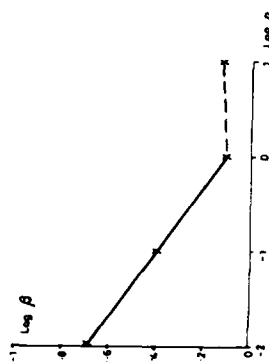
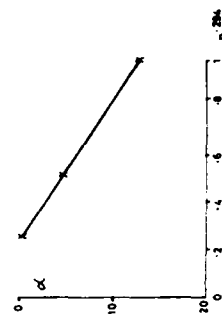
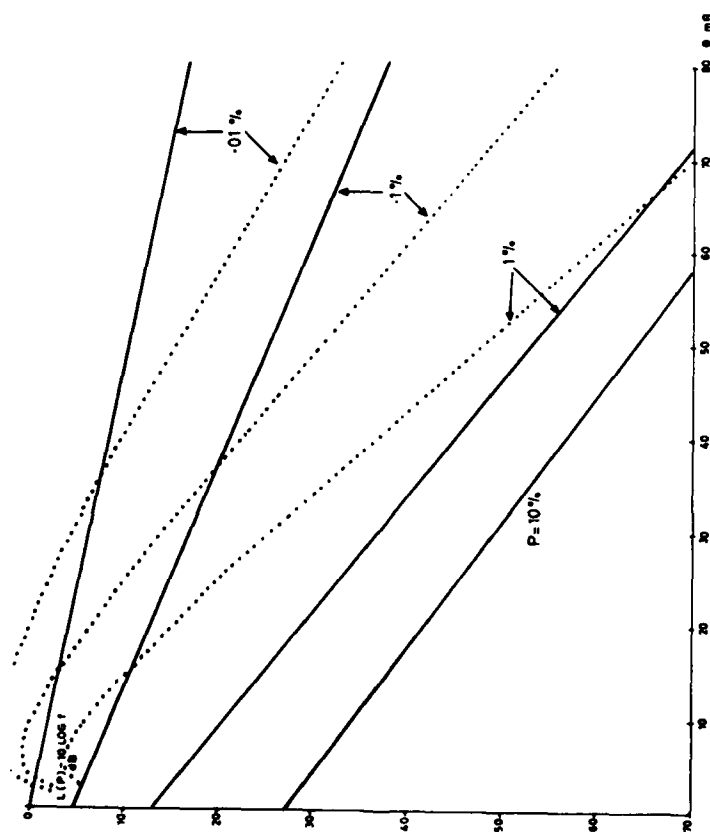


Figure 10. Path loss above free space  $L(1)$  for 1% over land with low terrain (L).

Figure 13. Plot of  $\log \beta$  against  $\log p$ .Figure 14. Plot of  $\alpha$  against  $p$ .<sup>294</sup>Figure 12. Regression lines (solid lines) of path loss above free space  $L(p)$  for  $p\%$  over land with low terrain ( $L$ ). Dotted lines are CCIR Report 569.

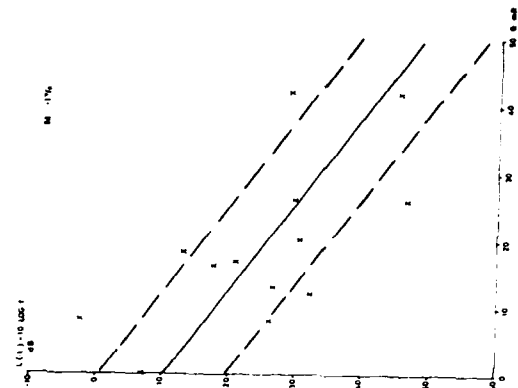


Figure 16. Path loss above free space  $L(1)$  for .1% over land with medium terrain (M).

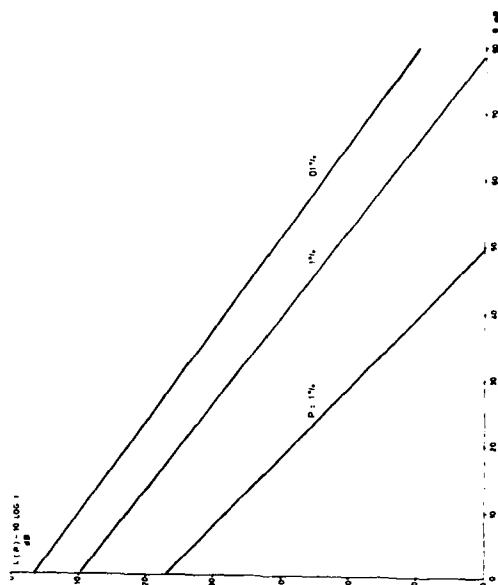


Figure 18. Regression lines of path loss above free space  $L(p)$  for  $p\%$  over land with medium terrain (M).

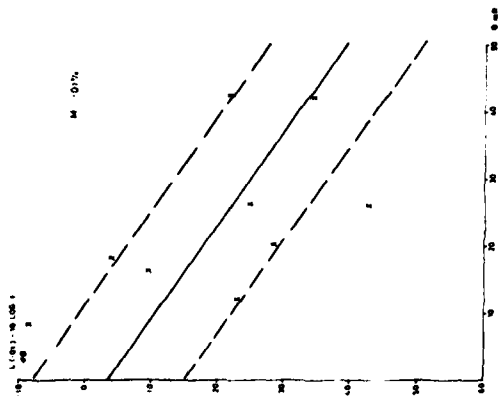


Figure 15. Path loss above free space  $L(.01)$  for .01% over land with medium terrain (M).

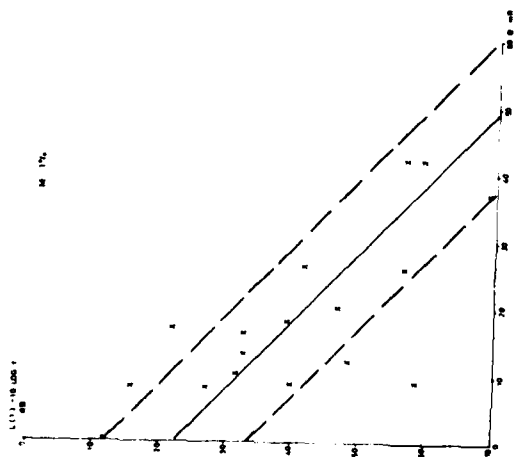


Figure 17. Path loss above free space  $L(1)$  for 1% over land with medium terrain (M).

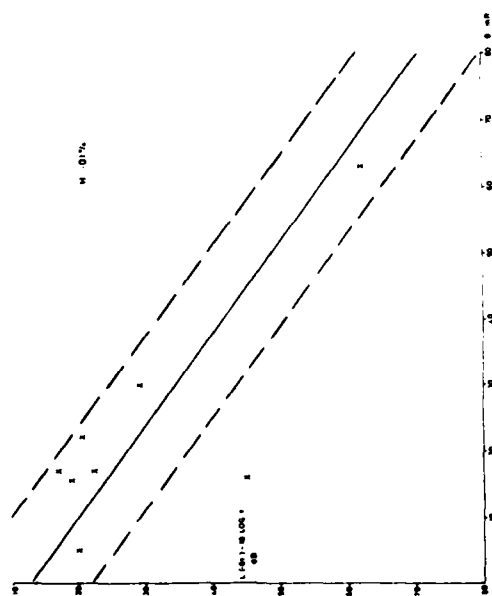


Figure 19. Path loss above free space  $L(0.01)$  for .01% over land with high terrain (H).



Figure 20. Path loss above free space  $L(0.1)$  for .1% over land with high terrain (H).

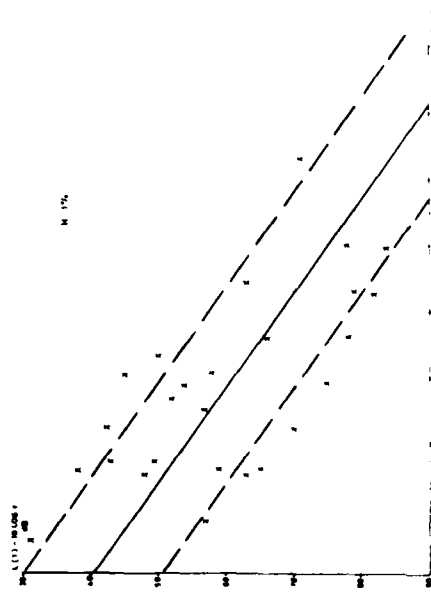


Figure 21. Path loss above free space  $L(1)$  for 1% over land with high terrain (H).

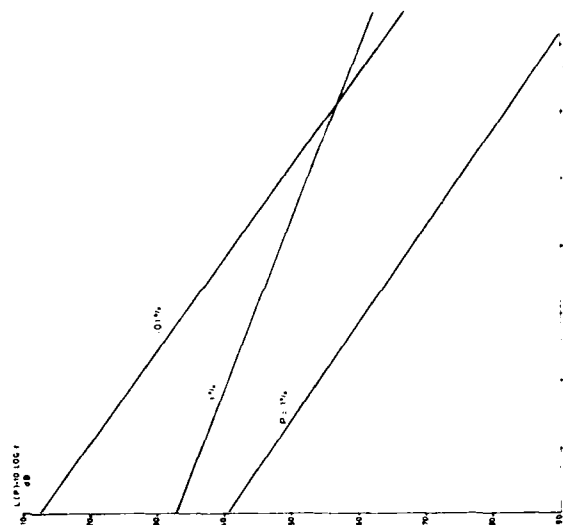


Figure 22. Regression lines of path loss above free space  $L(p)$  for  $p\%$  over land with high terrain (H).

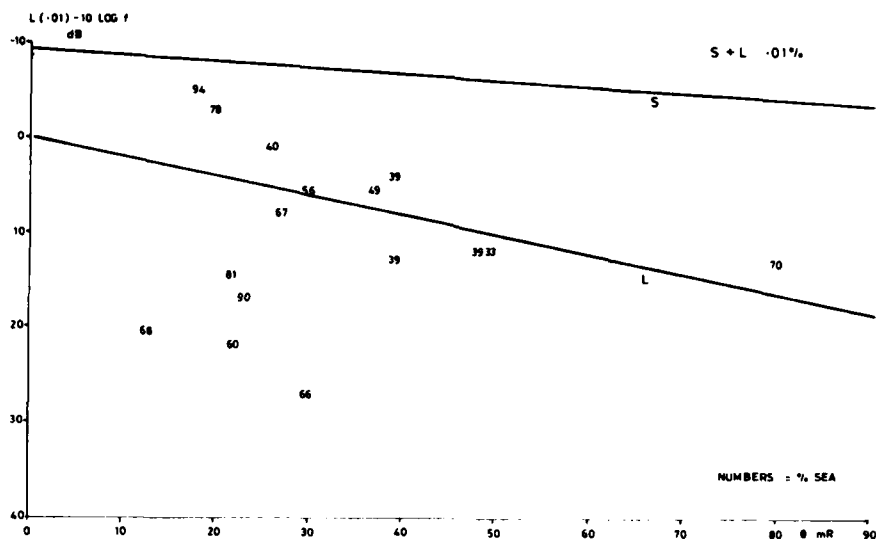


Figure 23. Path loss above free space  $L(.01)$  for .01% over mixed sea-land with low terrain (S+L).

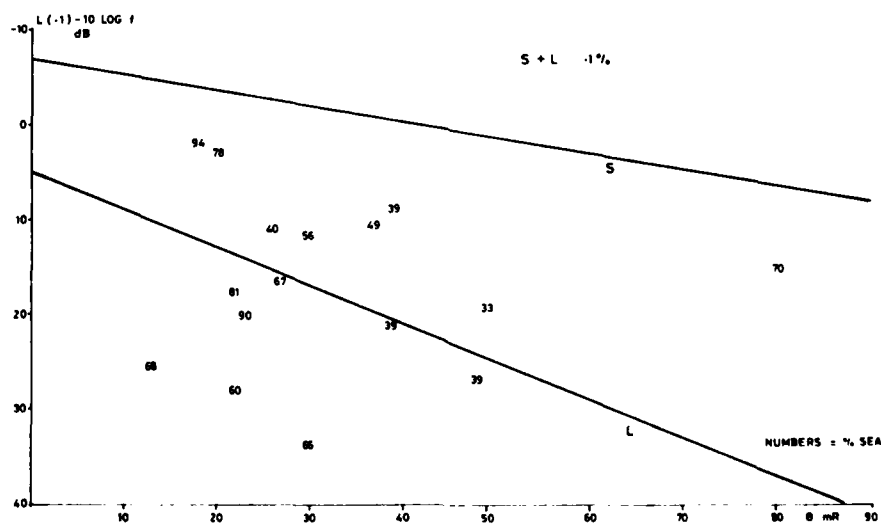


Figure 24. Path loss above free space  $L(.1)$  for .1% over mixed sea-land with low terrain (S+L).

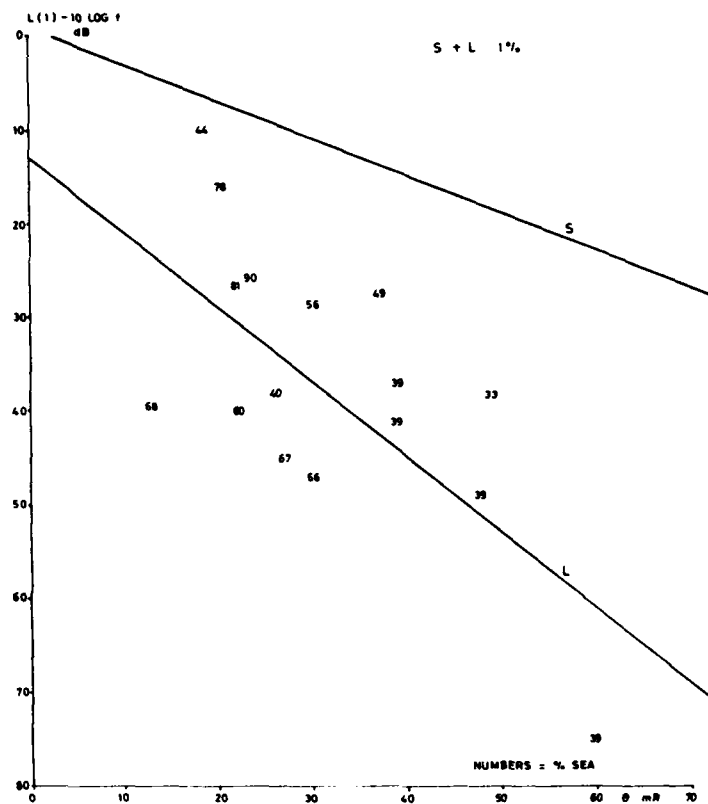


Figure 25. Path loss above free space  $L(1)$  for 1% over mixed sea-land with low terrain (S+L).

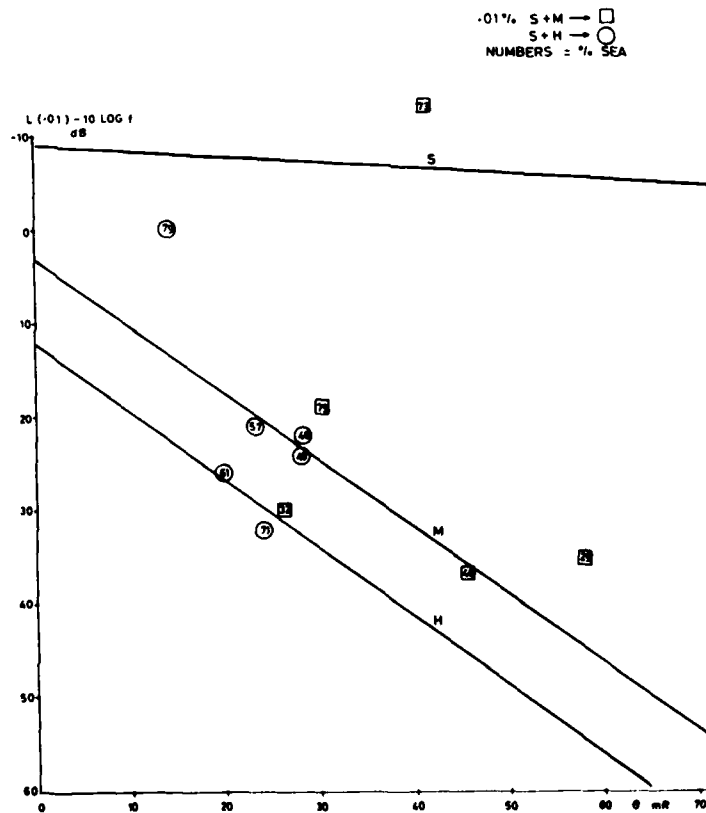


Figure 26. Path loss above free space  $L(.01)$  for .01% over mixed sea-land with medium (S+M) and high (S+H) terrain.

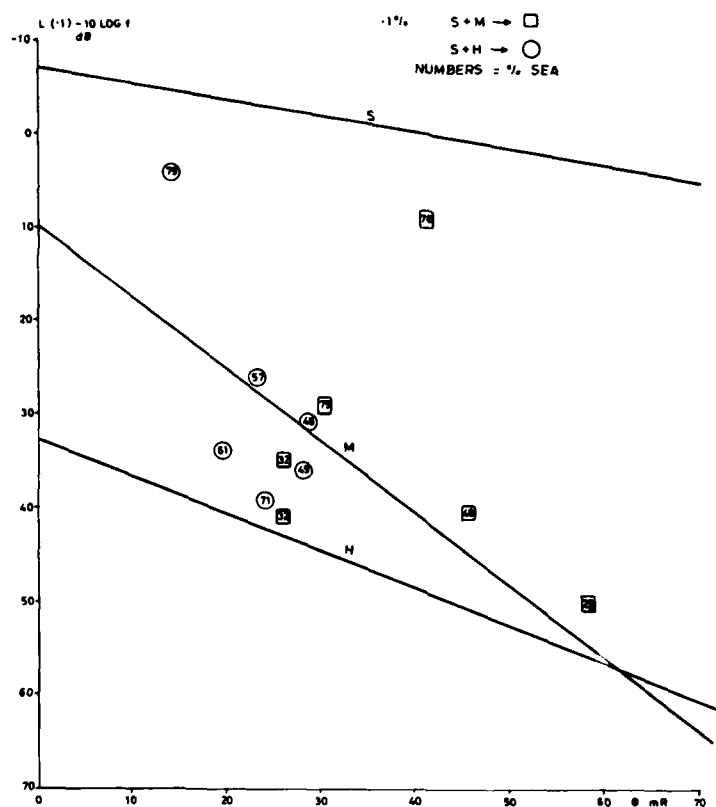


Figure 27. Path loss above free space  $L(1)$  for .1% over mixed sea land with medium (S+M) and high (S+H) terrain,

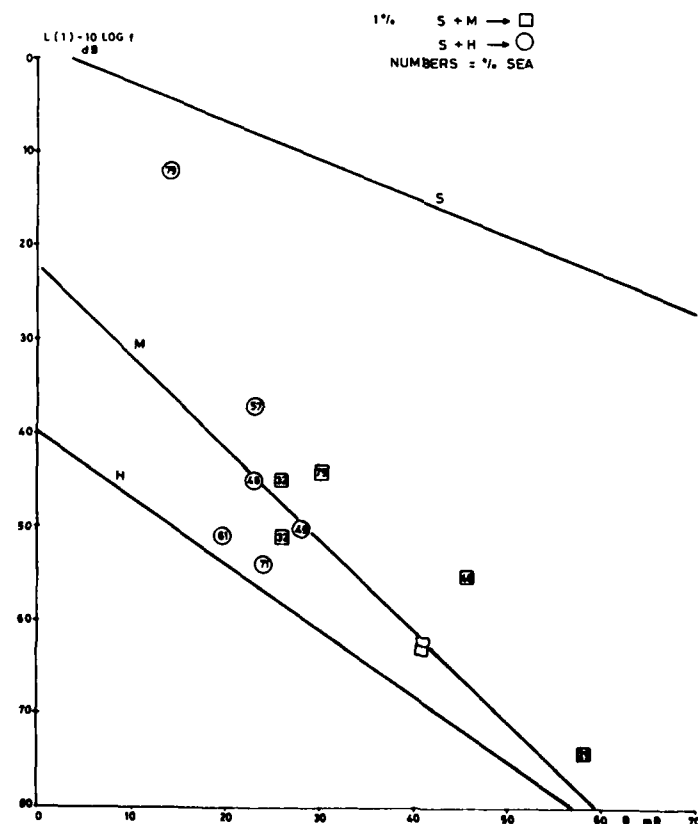


Figure 28. Path loss above free space  $L(1)$  for 1% over mixed sea land with medium (S+M) and high (S+H) terrain.

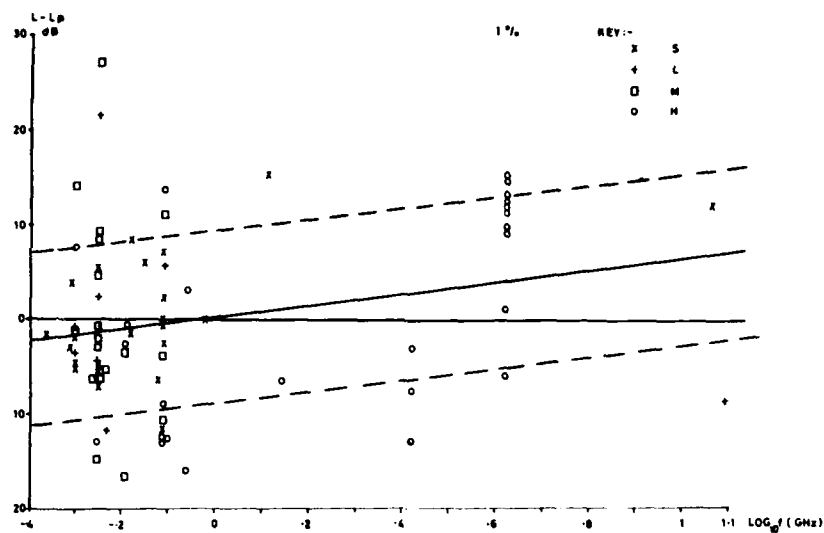


Figure 29. Frequency dependence of the prediction error.

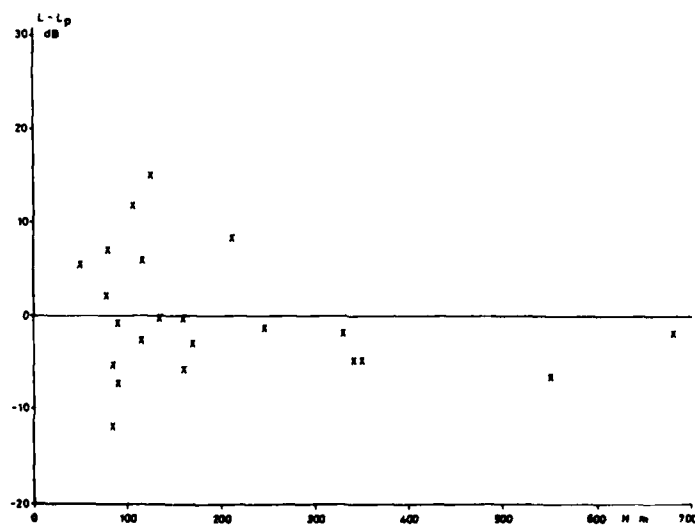


Figure 30. Height dependence of the prediction error over sea (S).

## DISCUSSION

L. Boithias (France): 1) Dans les rapports du CCIR, pour établir des méthodes de prévision, on utilise des données venant de diverses administrations et pas toujours compatibles entre elles. Il est donc difficile d'estimer à priori la précision de la méthode de prévisions. Pour cette raison le CCIR demande en général aux administrations de tester à posteriori les méthodes proposées afin de les améliorer.

2) Au dessus de la terre, on a parfois des conditions de forte superréfraction, mais on a beaucoup plus rarement des conditions de conduit avec réflexions successives sur le sol (contrairement aux trajets maritimes). Pour cette raison il est normal que l'atténuation sur un trajet mixte terre-mer, pour les niveaux de champ élevés, soit pratiquement déterminée par la partie du trajet située au dessus de la terre.

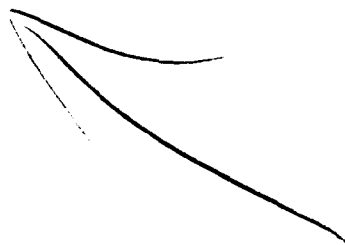
K.D. Anderson (U.S.): What are the typical path lengths?

S. Rotheram (U.K.): They are between 100 and 1000 km.

R.G. Blake (U.K.): It is difficult to conceive of a mixed path, which is 1000 km over sea and 50 km over land, being treated as 1050 km over land alone.

Our mixed path measurements over East Anglia clearly show signal strengths near to total sea path levels than to all land path levels, with a diurnal variation characteristic of advection ducts. Have you any comments?

S. Rotheram (U.K.): I accept the point being made. My study was a broad brush approach, lumping all of the mixed paths together. Particularly in flat areas such as East Anglia, the marine environment may extend some distance inland when the wind blows from sea to land. This may lead to "sea-like" ducting events over such mixed paths. CCIR Report 569 does include a 50 km transitional zone at the coast. Paper No. 25, at this Symposium, gives the physical mechanisms whereby ducts extend inland for sea-breeze conditions.



AD-P003 900

## TRANSHORIZON MICROWAVE PROPAGATION MEASUREMENTS RELATED TO SURFACE METEOROLOGICAL PARAMETERS

R. Ambrosini\*, M. Caporali\*\*, G. Tomassetti\*

\* Institute di Radioastronomy, CNR, Via Irnerio 46, Bologna, Italy

\*\*Department of Physics, University of Bologna, Italy

## SUMMARY

Experimental results of three months of continuous measurements at 3cm. wavelengths are given for the following aligned paths: the first, 100 Km. long, over flat land (Po Valley); the second, 140 Km. long, across the Adriatic sea; the third consisting of the sum of the previous ones. The stations are linked by radiowaves only during super standard atmospheric conditions. The period considered was in the autumn-winter season, from October to December, for 92 days of observations. Hourly efficiency histograms are drawn. They present a peculiar trend for the different paths: variable over land, with a strong maximum in the nocturnal hours; almost constant over sea, with a characteristic peak around noon for the combined path. Efficiencies up to 43% have been measured on flat land during the night, while lower values were found on the sea. An attempt to find a direct connection between radio signal reception in super standard conditions and surface meteorological parameters, has shown a strong correlation with water vapour pressure for the sea path: radio ducting sets up for a monotonic decaying of the water content of the air. Measurements over flat land show radio ducting to be almost nocturnal phenomenon. Radio propagation beyond the horizon detects temperature inversions caused by nocturnal cooling and therefore, there is not very clear evidence of correlation with ground meteorological data.

## INTRODUCTION

The connection between transhorizon microwave radio propagation at X band and some peculiar meteorological situations, suggested to the authors to attempt experimental observations in different conditions to understand their mutual relationship and in order to separate the meteorological responsible mechanisms. Microwave propagation measurements may be an inexpensive method to monitor the integrated values of meteorological quantities across areas extending several decades of kilometers of the low troposphere. This atmospheric region is also of principal importance in other applications like the transfer of pollutants and their ground deposition. The study of transhorizon propagation by itself is of great importance in forecasting radar coverages and possible interference levels between different terrestrial services for correct planning of the spatial re-use of the frequencies assigned to radio links.

According to well known theories (1) the path followed by a radio wave in the atmosphere depends on the gradient of the refractive index along the path (Snell's law). The horizontal component of the atmospheric refractive index is normally negligibly small; therefore only its vertical component must be considered. At radar frequencies the refractive index  $n$ , in the atmosphere, can be expressed:

$$(n - 1) 10^6 = 77.6 \frac{p}{T} + 4810 \frac{e}{T^2} \quad (1)$$

where  $p$  is air pressure,  $e$  is vapour pressure, both expressed in millibars;  $T$  is the absolute temperature in degrees Kelvin. The left hand term in (1) is called "refractivity" and placed equal to  $N$ . The first term on the right side represents the "dry term" and the second the "wet term". In a standard atmosphere  $p$  and  $e$  fall quickly in relation to the increase in height, while  $T$  generally decreases slowly. Consequently  $N$  diminishes with height. Due to this, radio waves are bent downwards and the radio horizon becomes greater than the geometrical one. If the temperature, instead of decreasing, increases with height (thermal inversion) and/or vapour pressure diminishes more quickly than usual, the refractivity gradient increases in absolute value and a duct is formed in which the microwave energy can be trapped. During these conditions radiowave bending is incremented so that radiowaves follow the curvature of the earth thus overcoming any defined horizon.

Nocturnal radiation and advection are the main processes responsible for the build up of thermal inversions and humidity lapses. In the first case the ground, which has been heated by the sun during the day, at night radiates heat back to the sky, thus getting cooler. In the second case a horizontal flow of warm and dry air flows over a cool surface (generally the sea). Local turbulent motion, caused by obstacles or by surface irregularities, tend to destroy the fairly calm atmospheric situation existing when radio ducts are present. So over seas and flat land areas are the most suitable sites for these phenomena to take place.

## EXPERIMENTAL OBSERVATIONS

A first set of measurements (8) have been done across different orographic paths to point out the main features of transhorizon propagation in the northern part of Italy (see Fig. 1). Two beacon stations have been installed, one in the town of Trieste and one in Milano; three receiving stations were installed at three different altitude and/or locations. The first in the town of Bologna (60 m.s.l.), the second at Monte Calvo (400 m.s.l.) and the third at P. Mocoguo (1300 m.s.l.)

The first result of our tests verified the feasibility of these microwave links with some efficiency, in spite of the small transmitted power (10 mW), the antenna diameter (1m.) and the moderate sensitivity of the receivers, both over sea and over flat land (Po Valley) across distances up to 285 Km. In particular the link between Trieste and P. Mocoguo shows that an optical path from a high mountain can enter into a sea duct when it is seen under a low angle of incidence (the Adriatic coast is near the optical horizon of P. Mocoguo). This conclusion seemed to be confirmed also from the observation that the strength and fading of the signals received at the three altitudes had different behaviours. When the stronger signal was received at the lower altitude station (town of Bologna) and eventually at the highest one (P. Mocoguo), the intermediate station was found to be less likely to receive signal coming from sites far beyond the horizon.

These first results suggested to the authors to implement a fixed measurement set-up to perform continuous observations to characterize the physics and climatology of radio ducts over land and over sea. For this purpose the previous mixed path between Bologna and Trieste was divided in two parts, one across the sea only and one across the land only. A microwave beacon generator was installed at Porto Tolle (see Fig. 1), in such a way that it radiates toward the two opposite receiving stations, one in Bologna and the second in Trieste, with two equal horn antennas. A transceiver station in Trieste records the data of the sea path while two receivers in Bologna record the total mixed path and the one over land only (3). The characteristics of the stations are reported in Tab. 1. To overcome the frequency drift, due to temperature variations, of all the free running Gunn Oscillators, one receiver in Bologna and the transceiver in Trieste, were continuously frequency swept across  $\pm 10$  MHz of bandwidth within a period of almost one minute.

The sea path Porto-Trieste, across the Northern Adriatic sea, is 140 Km. long; the flat land path Porto Tolle - Bologna, in the Po Valley, is 100 Km. long; the continued path Trieste-Bologna is the sum of the previous ones. The path geometry and the low radiated power allow signal reception only in the presence of radio ducts. Three months of continuous measurements in autumn-winter time from October to December have been analyzed.

#### RADIO PROPAGATION EXPERIMENTAL RESULTS

To overcome statistical uncertainty on the daytime evolution of the phenomenon, hourly efficiency histograms have been drawn for the three paths and are reported in Fig. 2. The hourly efficiency represents the total time  $N$  (in hours) over the 92 days of signal reception in the one hour intervals reported in the abscissa. These profiles present a peculiar trend in the different paths: strongly variable over land, almost constant over sea, with a characteristic peak around noon over the mixed path. Over land the curve slope is smoother in the phase of duct destruction (a.m.) and steeper in the phase of its building up (p.m.). The efficiency is 28% but increases up to 40% if one considers the nocturnal hours, the only ones characteristic of the phenomenon. The profile of the sea path has a maximum at almost 6 p.m. and two minima around 6 and 12 a.m., while efficiency is 15%. But other previous measurements by the authors in summer months had shown much higher efficiencies, suggesting a seasonal dependence for the sea path.

At last the histogram for the mixed path Trieste-Bologna shows a lower efficiency, 10%, and a characteristic peak around noon. To analyze this phenomenon the periods of reception have been divided in periods of coincidence and periods of anti-coincidence with the signal reception on the signal paths. When the microwave signal is received across the path Trieste-Bologna contemporarily to that across Porto Tolle-Trieste and/or Porto Tolle - Bologna, the hourly efficiency histogram (Fig. 3a) shows the same profile of the histograms reported in Fig. 2a and 2b. But when the signal from Trieste is received in Bologna and there is no link across the two single paths, the peak around noon-time is again evident; so it seems to be characteristic of a mixed path as a duct not referenced to ground but to some higher level (see Fig. 3b).

The difference between the total efficiencies of the three paths may be explained in terms of the different path lengths. From a statistical point of view, the probability that a favourable meteorological situation may extend over a longer distance is lower: any local disturbance can abruptly interrupt signal reception. During strong duct conditions the signal strength approaches the free space path loss, but the fading, particularly at the beginning and at the end of the phenomenon may be very steep.

#### METEOROLOGICAL CORRELATIONS

A comparison has been done separately for the path Porto Tolle-Trieste and Porto Tolle-Bologna between extra standard microwave signal reception and ground level meteorological data. The most meaningful data would have been taken in the middle of the path. Unfortunately, meteorological stations in these locations were not available, so we had only the chance to use the data of the Italian Air Force Station at Venezia Tessera (see Fig. 1) as the data characteristic of the sea path, and the data of Bologna Airport for the flat land path. The orography justifies our choices but, given the non-optimal positioning of the stations, the authors decided to limit the comparison between days with total absence of signal reception and days when the propagation conditions were at their maximum. Because only one month of meteorological data have been available, the correlation with radio propagation measurements is restricted to that period of time.

Clear evidence of connection between signal reception and high value of the refractivity at ground level has been found for the sea path, as can be seen in Fig. 4. Pressure and temperature counteract this effect, then the main contributor and the most sensitive parameter looks to be the water vapor pressure. During favourable days this last quantity rises up to the double of the value characteristic of unfavourable days. During favourable days, two cases of abrupt and short anti-correlation between vapour pressure and radio propagation have been found and investigated. It was verified that in the same periods strong wind gusts were recorded at the metostation, making its data not representative of the middle of the path, some 10 Km. away. The same kind of analysis applied to the flat ground path has not shown very clear evidence of correlation between extra standard propagation and meteorological quantities. This can be explained if one considers the mechanism that is more often responsible for duct formation over land: thermal inversions. In this case temperature is no longer a monotonic function with altitude and ground level data are no longer representative of the atmospheric thickness responsible of transhorizon radio propagation.

#### CONCLUSIONS

The actual mechanisms responsible for microwave propagation well beyond the standard horizon may be better understood by comparing measurements over different orographic paths. The different time evolution of hourly efficiency histograms may identify the characteristics of the meteorological responsible mechanisms. From the authors' measurements strong daily dependence is clear over flat land, where the nocturnal hours are the most favourable due to thermal inversions; the almost constant efficiency over the sea is explained in terms of its high thermal capacity, that smoothes the meteorological difference between day and night.

A deeper knowledge of these phenomena will require extended campaigns comparing different techniques of measurements to reduce statistical errors and to make correlations with more representative meteorological data. This work is now beyond the possibility of the authors who started this research to understand un-

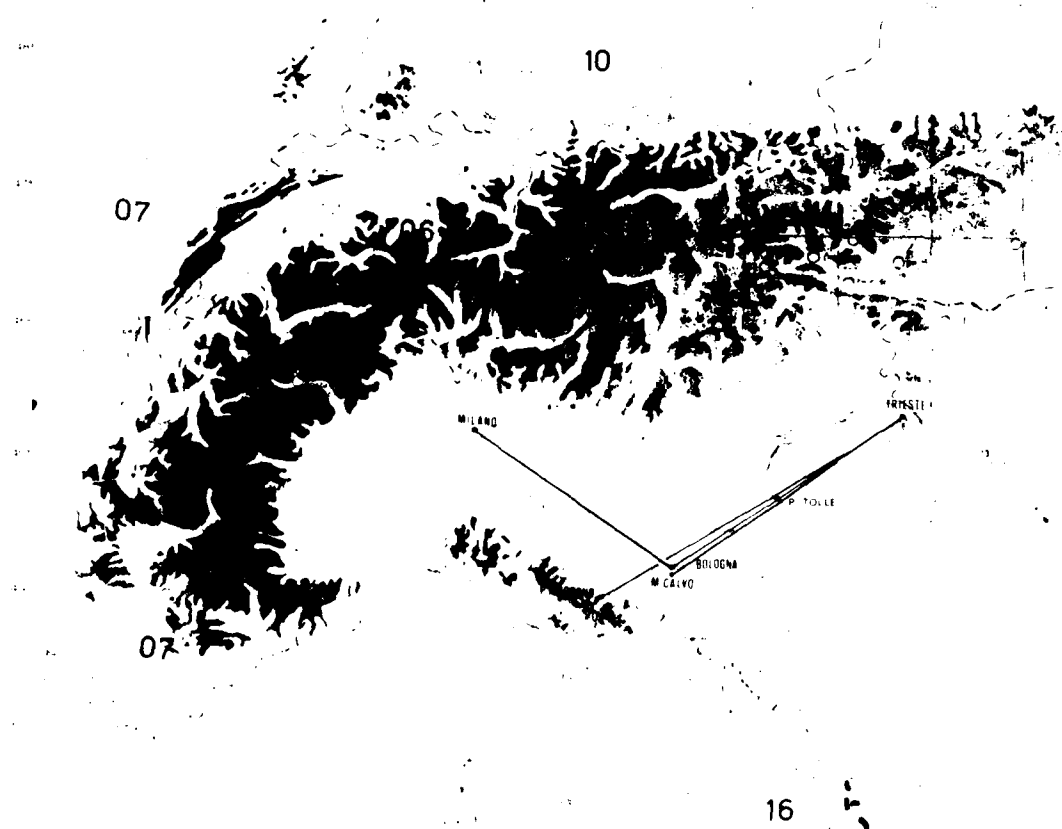
usual propagation conditions in radioastronomy work and as a possible method to monitor meteorological quantities. From this last point of view, transhorizon microwave propagation might be an inexpensive technique to identify and monitor thermal inversions.

#### BIBLIOGRAPHY

- 1) B.R. Beau and E.J. Dutton, "Radio Meteorology", Dover Publication, Inc. New York (1968)
- 2) G. Tomassetti, R. Ambrosini, M. Caporali, "Osservazioni sperimentali di propagazione anomale in banda X", *Elettronica e Telecomunicazioni*, Anno XXVII, N°1, 1979, pp. 19-22
- 3) G. Tomassetti, R. Ambrosini, M. Caporali, G. Steffè, "Misure di efficienza ed evoluzione temporale di propagazione anomale in banda X", *Anno XXI*, N°3, 1980, pp. 117-120.

Sites	Antenna	Transmitted Power (mW)	Noise Figure (dB)	Altitude (meters a.s.l.)
Porto Tolle	Two horns 25dB	10/each	-	35
Trieste	Ø 0.7m. dish	10	8	40
Bologna	Ø 1m. dish	-	<10 (channel 1) <10 (channel 2)	50

Tab. 1 The characteristics of the radio stations



Geographic arrangement of the observed paths.

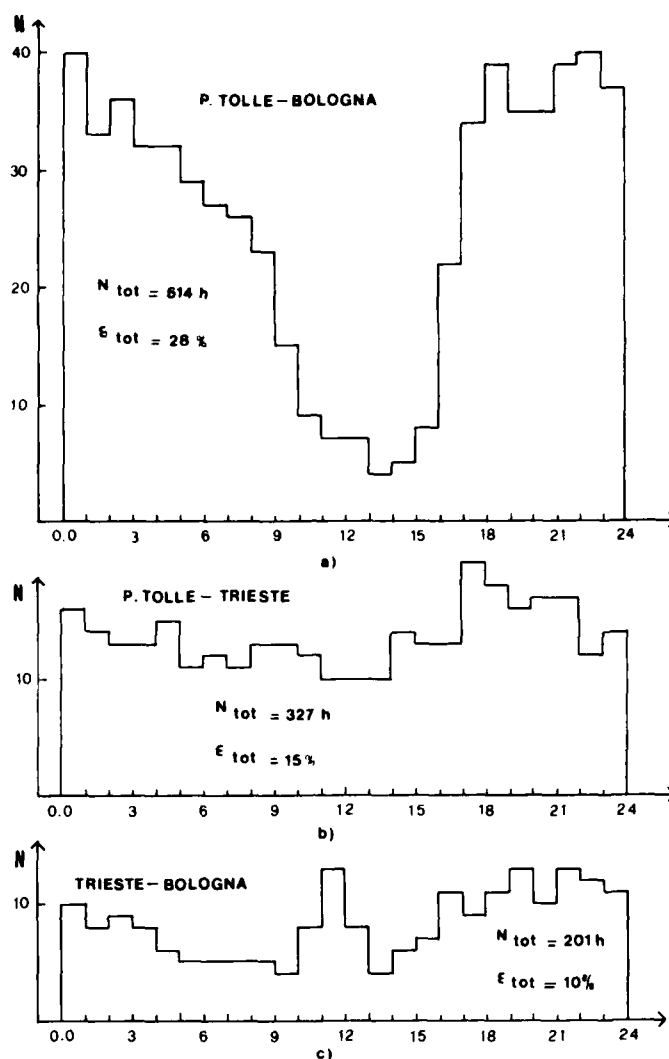


Fig. 2. Hourly efficiency histograms of extra-standard microwave propagation: a) flat land path, Porto Tolle-Bologna b) sea path, Porto Tolle-Trieste c) mixed path, Trieste-Bologna.

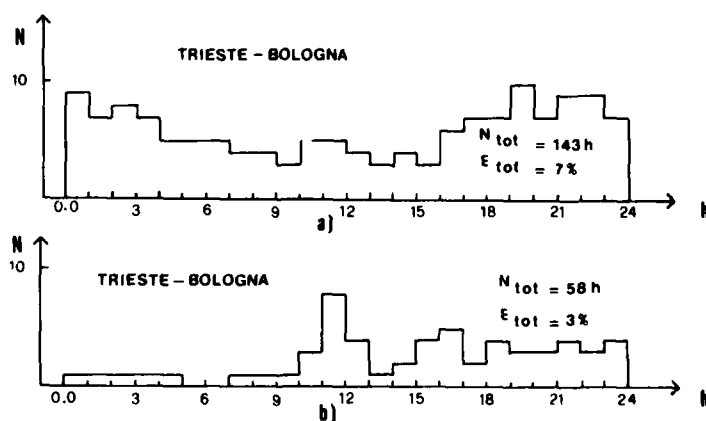


Fig. 3. Hourly efficiency histograms for the path Trieste-Bologna of: a) favourable events occurring contemporarily with signal reception across the path Porto Tolle-Trieste and/or Porto Tolle-Bologna; b) favourable events with unfavourable conditions across both the two single paths.

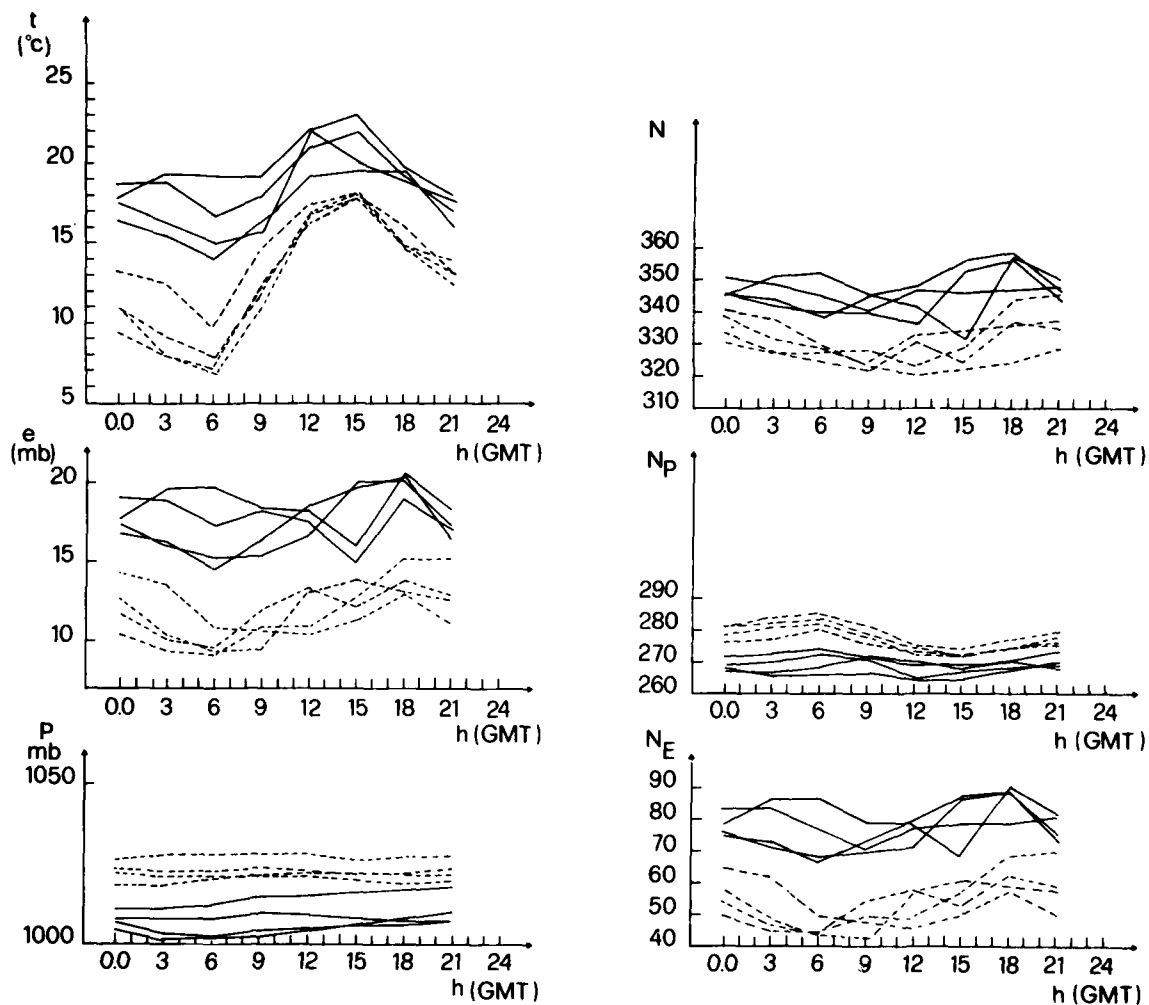


Fig. 4 Three hourly ground level meteorological data measured at Venezia-Tessera:  $t$ , ambient temperature and  $p$ , pressure, and the author's computed values of  $e$ , vapour pressure;  $N$ , total refractivity,  $N_p$ , dry term;  $N_e$ , wet term. Continuous lines refer to completely favourable days of radio propagation; dashed lines refer to days without any signal reception.

AD-P003 901

## TROPOSPHERIC PROPAGATION ASSESSMENT

by  
K. D. Anderson,  
J. H. Richter,  
and  
H. V. Hitney,

Ocean and Atmospheric Sciences Division  
Naval Ocean Systems Center  
San Diego, CA 92152

ABSTRACT

It is well known that microwave propagation in a marine environment frequently exhibits unexpected behavior. The deviation from 4/3 earth propagation calculations is due to the fact that the vertical refractivity distribution of the troposphere rarely follows the standard lapse rate of  $-39$  N/km. Instead, the troposphere is generally composed of horizontally stratified layers of differing refractivity gradients. The most striking propagation anomalies result when a layer gradient is less than  $-157$  N/km, forming a trapping layer. In the marine environment, there are two mechanisms which produce such layers. An elevated trapping layer is created by the advection of a warm, dry air mass over a cold, moist air mass producing either a surface-based or an elevated duct which may affect frequencies as low as 100 MHz. A very persistent surface trapping layer is due to water evaporation at the air-sea interface. This surface, or evaporation, duct is generally thin, on the order of 10 m in vertical extent, and is an effective trapping mechanism for frequencies greater than 3 GHz. With the introduction of the Integrated Refractive Effects Prediction System (IREPS) into the US Navy, fleet units now have the capability to evaluate accurately the performance of their EM systems when the refractive environment is known. However, these units may have to plan for operations thousands of miles away under different refractivity conditions. To assist in planning, a worldwide upper air and surface climatology has been developed for use through the IREPS programs. The IREPS concept is reviewed and a description of the tropospheric ducting data base is presented.

INTRODUCTION

Any system which relies on propagation of electromagnetic waves in the earth's environment is to some extent propagation limited. There are a number of examples. Solar disturbances affecting the ionosphere can result in complete disruption of the Navy's vital hf communications and surveillance network. Refractive layers in the lower atmosphere can cause "holes" in shipboard radar coverage. Oceanic ducting phenomena may be exploited for over-the-horizon detection capabilities. Aerosols (clouds) are often the limiting factors in electro-optical systems. Nuclear explosions in the atmosphere can cause blackout of hf communications, seriously degrade both vlf and satellite strategic communications systems, and, for critical minutes, make radar useless by absorption, noise, and clutter. In general, these propagation phenomena are understood qualitatively and most can be modeled quantitatively with varying degrees of accuracy. However, the quantitative modeling often involves complex physical processes and cumbersome mathematical solutions. It has been, therefore, difficult to provide real time performance assessment to the user of equipment that depends on the propagation environment. The advent of small, inexpensive digital processing equipment changed this. Mini- and microcomputers with appropriate peripherals can store the geophysical models for calculating propagation conditions, perform the mathematical processing and provide a systems performance assessment in a form that is understandable and practical to the user.

Consequently, several propagation assessment systems were developed in the past decade. One example is the PROPHET (for propagation forecasting terminal) system for hf communications assessment (Richter et al., 1977). It uses satellite sensed solar x-ray emissions and other solar and geophysical data to provide, in real time, propagation conditions. This system was so successful that its capabilities were expanded to include propagation effects on geolocation systems, signal exploitation, vulnerability assessments, and development of propagation dependent tactics.

Another highly successful propagation assessment system, IREPS (Integrated Refractive Effects Prediction System) (Hitney and Richter, 1976), addresses microwave propagation in the lower atmosphere. Its capabilities are described in the following.

IREPS

In many maritime regions of the world, there exist frequent abnormal vertical distributions of refractive index that create non-standard propagation effects such as trapping or ducting and radio or radar holes. These effects can lead to both greatly extended operating ranges for certain cases and to greatly reduced ranges for other cases. Since the U.S. Navy operates in areas where such anomalous propagation is frequent, there is a requirement for a capability to assess and exploit atmospheric refractive effects and the resultant enhancement or degradation to naval surveillance, communications, and electronic warfare (EW) equipment. The system that has emerged to fulfill this requirement is IREPS. The IREPS concept is based on a shipboard computing capability which generates displays of electromagnetic equipment performance from inputs of both environmental and equipment parameters. The environmental inputs required are pressure, temperature, and humidity from a radiosonde ascent, or refractivity and altitude obtained directly from an airborne microwave refractometer, and surface measurements of air temperature, humidity, and wind velocity plus sea-surface temperature. Alternately, there is a capability to access a climatology of refractive effects for much of the world's ocean areas which will display and provide typical environmental inputs for IREPS processing. This climatology will be discussed in detail later in this paper.

There are several products from IREPS, but most widely used is the coverage diagram, an example of which is shown in figure 1. The coverage diagram shows the vertical region in space on a spherical altitude-versus-range plot where a specified radar, communications, or EW system will achieve or exceed one or more predefined levels of performance. The example is for the case of an arbitrary 400 MHz air search radar where the three shaded regions represent the .9, .5, and .1 probability of detection of a 1 square meter target. The environmental conditions for the example were characterized by a strong surface-based duct that has resulted in extended ranges below about 500 m. The equipment parameters required for the coverage diagram are frequency, polarization, emitter antenna height, antenna pattern type, vertical beamwidth, antenna pointing angle, and one or more free-space ranges associated with desired levels of performance. Scale factors for the display must also be specified.

A second IREPS product that is quite valuable is the path loss display that shows one-way path loss in dB versus range. Figure 2 is an example of this product for an environmental case characterized by a standard atmosphere and for surface-to-air 300 MHz UHF communications equipment. The equipment parameters required for the path loss display are the same as those for the coverage diagram, plus a specification of receiver or target height. The horizontal dashed line threshold is based on the free-space range specified and establishes the maximum path loss that can be tolerated for the equipment to operate at or above the desired level of performance. In this example, the threshold is based on acceptable communications ability at 200 km in free space. As the example shows, this same level of performance for a receiver at 1000 m altitude will be achieved out to ranges of 120 km for the environmental conditions specified. The loss display can be used effectively to assess radar detection ranges and Electronic Support Measurement (ESM) intercept ranges as well as communication ranges.

Other major IREPS products that exist but for which no examples are presented here are tables of maximum ESM intercept ranges for predefined lists of emitters, and tables of expected maximum surface-search radar ranges for predefined lists of surface targets.

The models upon which all of the products are based are combinations of ray-optics, simplified full-wave solutions, semi-empirical formulations based on measured data, and interpolations to smooth transitions between the various models. In the optical region, standard ray-trace techniques are used along with calculations of the interference between direct and sea-reflected rays. Reflection coefficients for horizontal, vertical, or circular polarization, modified for ocean roughness, and the spherical-earth divergence factor are calculated as necessary. For ranges well beyond the horizon, there are models to account for standard diffraction, effects of the evaporation duct and surface-based ducts from elevated layers, and tropospheric scatter. The models for diffraction and the evaporation duct are based on simple-to-calculate functions that have been fit to the results of numerical full-wave solutions. The model for the surface-based duct is largely empirical in nature.

IREPS displays that are under development combine results from the various products already discussed to show composite effects of propagation on a formation of ships. Figure 3 shows an example for an aircraft carrier and three escort ships. The darker shaded regions on this display represent the composite areas of detection of a particular surface target by the ships' radars. The lighter shaded region represents the composite vulnerability of the ships' emissions to reception by an adversary's ESM capability. Such a display will allow a user to quickly evaluate the capabilities and trade-offs between detection and counter-detection in light of the current propagation environment.

All of the IREPS products require a description of the atmospheric refractivity conditions in which the EM system is expected to operate. Obviously, for the shipboard users, the most recent upper air sounding provides the best description of the environment. However, the need may arise for environmental data at an area far removed from the ships' present location. In response to this need, a climatology of worldwide maritime refractivity conditions has been compiled and made directly available to the IREPS users.

#### TROPOSPHERIC DUCT CLIMATOLOGY

The purpose of the climatology is to provide an estimation of the tropospheric ducting conditions for any maritime region. As with all statistical descriptions of the environment it is intended to aid in long range or long term planning. Since fleet units are highly mobile a description of the expected ducting environment at distant locations may aid in the formulation of tactics. Consider, for example, an air strike against a radar protected installation. The classical strike aircraft altitude is low to the surface to achieve maximum penetration before detection. That is, the strike aircraft attempt to fly in under the radar horizon. However, in some regions of the world, strong surface-based ducts are observed to occur 50% of the time or more. As a surface-based duct may greatly increase the radar detection range against low flying targets, the classical strike aircraft altitude would be the worst possible location for surprise. Without insitu measurements, which are always preferable to statistical descriptions, the climatology can supply needed data for making judicious decisions. In addition, the climatology provides the meteorological officer with a guide to determine the frequency or need for ship launched upper air soundings. In general, few soundings are required at northern latitudes to assess the local refractivity conditions whereas, in regions of persistent ducting, two or more soundings per day may be needed.

The climatology consists of data from two distinct sources. The first source is upper air radiosonde observations describing the vertical refractivity profile. These profiles are derived from an analysis by Ortenburger (1977) of all radiosonde stations reporting for five selected years. Pertinent profile statistics were extracted from this analysis for 399 coastal, island and weather ship stations. On figure 4, the dots mark the location of the radiosonde stations included in the climatology. Shipboard surface meteorological observations comprise the second source of data. The National Climatic Center, Asheville, NC, processed all shipboard surface observations taken during the years 1970 through 1979 to obtain histograms of evaporation duct height, wind speed and other parameters. Calculations of the evaporation duct height are based on the theory proposed by Jeske (1971) and are described in Witney (1975). These histograms were developed for ocean regions in grids of 10° latitude and 10° longitude known as Marsden Squares. A total of 213 such squares are included in the climatology and are shown as the shaded ocean areas in figure 4.

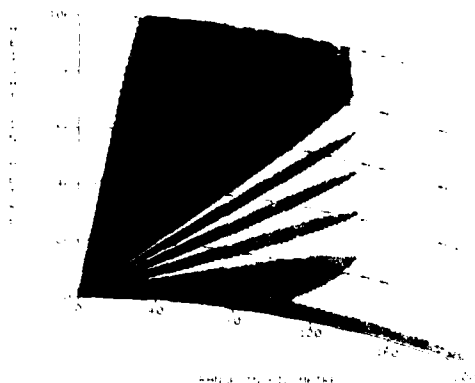


Figure 1. 400 MHz air search radar coverage diagram. The shaded regions represent the .9, .5, and .1 detection probabilities for a target of 1 square metre cross section.

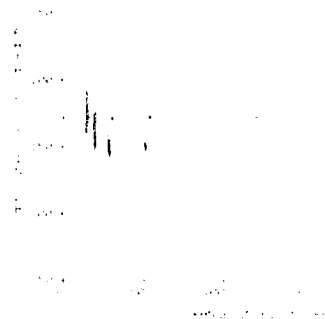


Figure 2. Path loss display for a 300 MHz surface-to-air communication system. Successful communication is shown for ranges where the predicted path loss (solid line) is less than the maximum path loss threshold (dashed line).

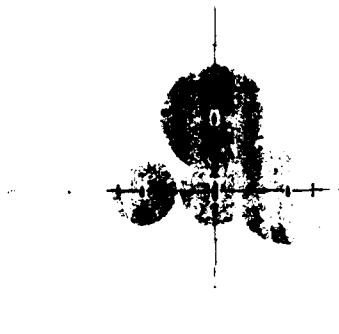


Figure 3. Display of detection and counter detection envelopes for a formation of ships. The darker shaded circular region centered on a ship shows that ships' detection capability against a particular surface target. The lighter shaded region represents the area where a specified ESM system is able to counter detect the ships' emissions.

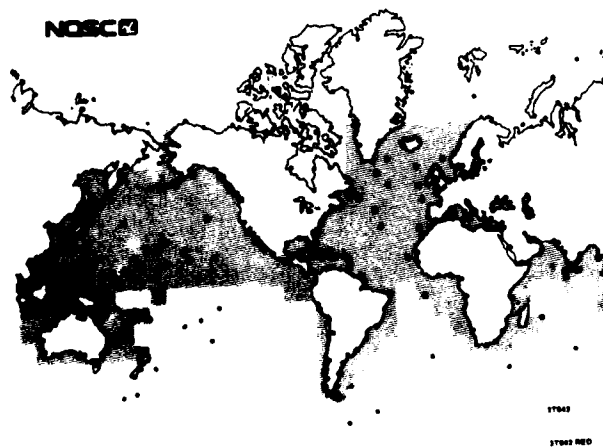


Figure 4. Geographic extent of the tropospheric ducting climatology. Shaded ocean regions indicate areas containing surface meteorological observations. Dots show the location of the radiosonde stations.

## PERCENT OCCURRENCE OF ENHANCED SURFACE-TO-SURFACE RADAR ESM COM RANGES:

FREQUENCY	YEARLY			JAN-MAR			APR-JUN			JUL-SEP			OCT-DEC		
	day	nit	dgn	day	nit	dgn	day	nit	dgn	day	nit	dgn	day	nit	dgn
100 MHz	0	0	0	0	0	0	0	0	0	0	1	0	0	0	0
1 GHz	6	3	4	1	1	1	8	4	6	12	6	9	2	1	1
3 GHz	7	3	5	2	1	1	9	5	7	14	7	10	2	1	1
6 GHz	13	8	11	3	1	2	14	8	11	27	17	22	9	5	7
10 GHz	37	30	34	19	15	17	31	22	26	57	48	52	43	35	38
20 GHz	60	53	57	46	40	43	50	42	46	75	69	72	69	62	65

## SURFACE BASED DUCT SUMMARY:

PARAMETER	YEARLY			JAN-MAR			APR-JUN			JUL-SEP			OCT-DEC		
	day	nit	dgn	day	nit	dgn	day	nit	dgn	day	nit	dgn	day	nit	dgn
Percent occurrence	1	2	1	0	0	0	1	2	2	2	4	3	0	0	0
AVG thickness kft			.31			.30			.25			.36			.31
AVG trap freq GHz			1.4			.45			1.7			1.0			2.5
AVG lwr grd -N kft			136			167			135			136			105

## ELEVATED DUCT SUMMARY:

PARAMETER	YEARLY			JAN-MAR			APR-JUN			JUL-SEP			OCT-DEC		
	day	nit	dgn	day	nit	dgn	day	nit	dgn	day	nit	dgn	day	nit	dgn
Percent occurrence	10	12	11	4	5	5	10	10	10	22	23	23	5	8	7
AVG top ht kft			3.4			3.5			2.8			3.9			3.5
AVG thickness kft			.29			.20			.28			.39			.29
AVG trap freq GHz			1.1			1.8			1.2			.56			.94
AVG lwr grd -N kft			54			54			52			54			56
AVG lwr base kft			3.2			3.3			2.6			3.5			3.3

## EVAPORATION DUCT HISTOGRAM IN PERCENT OCCURRENCE:

PERCENT OCCURRENCE	YEARLY			JAN-MAR			APR-JUN			JUL-SEP			OCT-DEC		
	day	nit	dgn	day	nit	dgn	day	nit	dgn	day	nit	dgn	day	nit	dgn
0 to 10 Feet	18	20	19	22	25	24	25	29	27	12	13	12	12	15	13
10 to 20 Feet	22	26	24	31	34	33	25	30	27	14	18	16	19	23	21
20 to 30 Feet	23	24	23	27	25	26	19	20	20	19	22	21	26	27	26
30 to 40 Feet	16	16	16	12	12	12	12	10	11	18	20	19	23	21	22
40 to 50 Feet	8	6	7	3	2	2	5	3	4	13	12	12	12	9	10
50 to 60 Feet	4	3	4	1	1	1	3	2	2	8	6	7	5	3	4
60 to 70 Feet	2	1	1	0	0	0	1	1	1	3	2	3	1	1	1
70 to 80 Feet	1	0	1	0	0	0	1	1	1	2	1	1	0	0	0
80 to 90 Feet	1	0	0	0	0	0	1	0	1	1	1	1	0	0	0
90 to 100 Feet	0	0	0	0	0	0	1	0	1	1	0	1	0	0	0
above 100 Feet	5	2	4	1	1	1	8	3	5	11	4	7	2	1	1
Mean height Feet	33	25	29	22	19	21	33	24	28	45	33	39	30	26	28

## GENERAL METEOROLOGY SUMMARY:

PARAMETER	YEARLY			JAN-MAR			APR-JUN			JUL-SEP			OCT-DEC		
	day	nit	dgn	day	nit	dgn	day	nit	dgn	day	nit	dgn	day	nit	dgn
% occur EL&SB dets			0			0			0			1			0
% occur 2+ EL dets			1			0			0			3			1
AVG station N			323			316			322			333			319
AVG station -N kft			13			12			12			14			12
AVG sfc wind Kts	16	16	16	18	18	18	14	13	14	14	14	14	20	20	20

Figure 5. IREPS Historical Propagation Conditions Summary for the North Sea region at 55° N latitude and 5° E longitude.

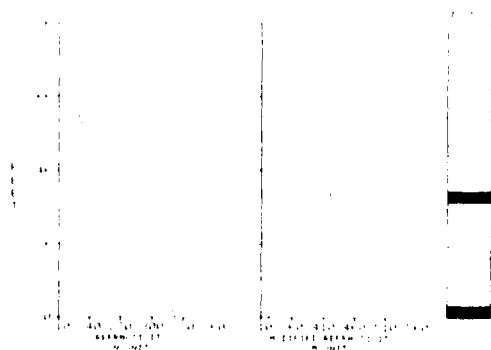


Figure 6. Profiles of the refractivity and modified refractivity versus height constructed from the yearly day and night statistics of Figure 5.

A sample of the IREPS Historical Propagation Conditions Summary is shown by figure 5. This product describes the ducting climatology for a specified location in the North Sea at 55° N latitude and 5° E longitude. The closest radiosonde station, in the great circle sense, contained in the climatology is Schleswig, Germany, located at 54°31' N, 9°33' E. The closest surface observation source is Marsden Square 216 which is centered at 55° N, 5° E. From these two data sources, the program constructs five tables for three month time periods and an overall yearly average. The five time period columns are further separated into day, night, and day and night combined columns for diurnal analysis.

The first table provides the percent of time that surface-to-surface communication ranges exceed the ranges expected under standard atmospheric conditions. For example, on a yearly basis a surface-to-surface communication system operating in this area using frequencies near 6 GHz is expected to experience enhanced ranges 13% of the time during the day and 8% of the time during night. A similar system using frequencies near 10 GHz is predicted to observe greater ranges 34% of the time.

The next two tables describe the percent occurrence and geometries of surface-based and elevated ducts. These data are derived directly or computed from Ortenburger's results. In his analysis, diurnal statistics of the duct geometries were not generated and this information is not available within the climatology.

The final two tables show the percent occurrence of evaporation duct heights in ten foot intervals, mean evaporation duct height, joint probability of an elevated duct with a surface-based duct, probability of two or more elevated ducts, station refractivity and surface wind speed.

Figure 6 illustrates the vertical refractivity and modified refractivity profiles constructed for the specified location. These profiles are generated from the yearly day and night statistics and include both the surface-based and elevated ducts. Optional profiles can be created for standard atmospheric conditions (no ducts), surface-based duct only, or elevated duct only for any of the time periods shown in figure 4. The mean evaporation duct height and the average surface wind speed for the time period selected accompany the profile data. These data become available for use by the IREPS propagation prediction programs.

#### REFERENCES

- Hitney, H. V., Propagation Modeling in the Evaporation Duct, Naval Electronics Laboratory Center Technical Report TR 1947, 1 April 1975.
- Hitney, H. V., and J. H. Richter, Integrated Refractive Effects Prediction System (IREPS), Naval Engineer's Journal, 88, 1976, pp. 257-262.
- Jeske, H., The State of Radar Range Prediction Over Sea, Tropospheric Radio Wave Propagation - Part II, NATO- AGARD Conference Proceedings, 70-71, February 1971, pp 50-1 - 50-10.
- Ortenburger, L. N., Radiosonde Data Analysis II, GTE/Sylvania Inc., Electronics Systems Group/Western Division, 29 July 1977.
- Richter, J. H., I. J. Rothmuller and R. B. Rose, "PROPHET Real Time Propagation Forecasting Terminal," Proc. 7th Technical Exchange Conf. (Published by ASL, USMR, NM 88002), 1977, pp. 77-81.

## DISCUSSION

S. Rotheram (U.K.): 1) Evaporation duct predictions such as those produced by IREPS and by our own methods indicate prediction errors for path loss of  $\pm 20$  dB. Could you comment on the operational significance of these errors?

2) Roger Helvey of PMTC has pointed out that temperature induced humidity errors systematically bias the lowest part of radiosonde ascents, producing spurious surface based ducts. This appears to invalidate much of the Sylvania data base mentioned in the paper.

K.D. Anderson (U.S.): 1) Statistically, the predictions are very good. We question the validity for operational purposes, but it is currently the best that can be done.

2) This is true for the surface layer, although the elevated trapping layers are probably very good observations. Roger is working on a possible solution for the surface layer problem.

T. Almond (U.K.): I think that it is important to ensure confidence in the IREPS model. It cannot be 100% efficient.

K.D. Anderson (U.S.): I agree with you. It is a difficult job, but one of the reasons for the success of IREPS has been the open and sometimes blunt communication between the laboratory and fleet users.

F. Thomsen (Denmark): Your coverage diagrams show a distinguished lobing effect caused by reflection of the transmitted energy by the sea surface. The exact position and depth of these nulls are very dependent on the sea surface state, i.e., surface roughness and slope distribution. Has this effect been considered?

K.D. Anderson (U.S.): Yes. We do include surface roughness effects in the models for the reflection coefficient. However, we do not account for clutter effects. The clutter is very difficult to model with any success.

T.J. Boulton (U.K.): 1) Data is available from the South Atlantic via the British Navy.

2) With regard to Vertical Coverage Diagrams, is the HP 9845 locally programmable to account for antenna characteristics?

K.D. Anderson (U.S.): All of the electromagnetic system parameters can locally be changed. These parameters include antenna heights, types ([sin x]/x, Omni, height finder, fan beam, etc.), power, sensitivity, and many more. We have tried to make the IREPS program as "user friendly" as possible.

E. Vilar (U.K.): I would like to comment on the subject of reliability of radiosonde measurements. We have found, in an experiment using a tethered balloon and scanning the height  $h$  between 800 and 1000 meters up and down at various speeds, that the wet bulb temperature  $T'$  features were smoothed out during the usual ascent and descent speeds of several meters per second. In order to see layers of 30 meters or less in thickness and to receive a good indication of the refractivity  $N(h)$  gradient within the layer, one needed ascent and descent speeds of about one meter per second. This was clearly unsatisfactory and inconvenient. The manufacturer later acknowledged that the time constant, defined in the usual manner, response/time, could be as high as 10 to 15 seconds. Could you comment on the possible impact of this on your data bank?

K.D. Anderson (U.S.): The large structures are most important. It is believed that these are adequately sensed by the beam.

DISTORTION OF A NARROW RADIO BEAM IN A CONVECTIVE MEDIUM

W.G. Burrows  
 Head of The Department of Radiocommunications and Radar  
 Brunel College, Bristol.

Summary

→ In considering the basic mechanism of heat exchange by convective circulation in the atmosphere it is apparent that the resultant thermal cell structure, as proposed by Bénard, may possess refractive index properties which will influence the cross-sectional shape of a narrow conical radio beam. A simplified classical toroidal cell is considered for the purpose of analysis to show that the core of such a cell in the atmosphere may act as a cylindrical concave lens. The resultant distortion of a narrow beam is then discussed. The concept is then developed further to show that trans-horizon propagation may result from an in-line array of thermal cells. ←

1. Introduction

In trans-horizon tropospheric radio systems it has become almost traditional to assume that the major propagation mechanism occurs within the constraints of the atmospheric volume which is common to both transmitter and receiver terminals. Using this concept a number of extremely elegant hypotheses have been presented to suggest the existence of a variety of 'scatter' processes which are assumed essential to this mode of propagation. Atmospheric ducting is another concept which contrasts with the common volume idea. However, experience in the planning and use of actual systems does not necessarily support either the 'duct' or 'scatter' concepts but relies to a very great extent on operational experience and empirical rules. The prediction of system performance is an extremely hazardous process by virtue of this lack of support for the 'scatter' mechanisms which are also extremely difficult to predict on the micro-meteorological scale. Even on a meso-meteorological scale, the complex structures of the atmosphere provide a considerable challenge to the meteorologist who might attempt to predict the future behaviour of such structures over just a few hours. In maritime regions such predictions are particularly difficult because of the severe and complex mixtures of land and water masses. Simple observations have shown that success rates in excess of 35 - 40% for basic weather predictions are extremely rare for at least the southern part of the British Isles.

Under these circumstances the hazards associated with predicting the future performance of a trans-horizon radio system are akin to those of a gamble, particularly in the absence of any prior experience. It also suggests that our knowledge of basic meteorology, and its impact on the radio wave is still extremely limited in spite of the many great improvements that have been made in the general fields of instrumentation and measurement which are applicable to the lower regions of the atmospheric medium. Much of the present day development, research activity and effort has however, moved to consider those meteorological parameters which may be of primary importance to the commercial and military use of transmission systems operating in the millimeter wave bands.

Whilst all of the parameters which can be defined for a commercial communication system, particularly those which are directly related to both development and operating costs, are of paramount importance it does not necessarily follow that all of the essential parameters are either known or quantifiable. Nor indeed does it follow that all of the parameters which are known are considered to be of significance. Whilst the historical issues which give rise to the original surge of interest in

tropospheric radio wave propagation are well known, together with some of the initial very elegant theoretical works which proposed the propagation mechanisms, the basic conceptual model of the common volume has been retained by the vast number of research workers who have been and are concerned with the parameters of the meteorological structure which are constrained within the boundaries of that volume. The 'radio duct' is of course, an exceptional case which at this point might be temporarily excluded from the discussion.

However, it would seem that in almost all instances where a common volume model is assumed, the meteorological structures which are constrained within that volume are considered to be either of turbulent 'blob' form or of an horizontal stratiform type. Curiously, any structure which is likely to give a vertical boundary is never, or very rarely, given any serious consideration. Vertical boundaries or interfaces have been given some consideration in a number of experimental investigations but in all cases they have been dismissed in favour of horizontal forms. Equally curious few, if any workers seem to have given any consideration to those regions of both the transmitter and receiver beams which are not contained within the common volume. Whilst it is obviously elementary to assume that there may be no disturbances to the beam shape or cross-section which are significant when a common volume is only considered, it is equally obvious that if changes or disturbances do occur in the beam shape or cross-sections then the validity of the common volume concept weakens very considerably. Indeed, in the presence of extreme disturbances at all points along a transmission path, it is conceivable that the common volume concept would be totally invalid. In previous reports the author has described<sup>1,2</sup> experimental work which has been conducted both on full scale systems operating in a maritime climate and on laboratory scale models of the same system in which all the fading characteristics obtainable on the full scale systems could be simulated. The modelling technique which was inspired by the work of Avsec,<sup>3</sup> and which was pioneered by the author for the principal purpose of conducting controlled experimental studies on the causes of fading has also been subsequently used to advantage for the performance prediction of a number of commercial and military systems. With, perhaps, the principal advantage of allowing controlled studies to be made of the fading resulting from simulated simple meteorological structures which are known to exist at all points in the whole path region between transmitter and receiver, the modelling technique has suggested a number of somewhat controversial conclusions. The most significant of these are:-

- 1) that for a given system, operating at a particular wavelength the region of the atmosphere which is most likely to produce the most significant effects on a narrow transmitter beam lies in the first few thousands of wavelengths of altitude from ground or sea level.
- 2) that the distortion effects on the cross-section of the beam which occur as a result of the equivalent of a standard temperature gradient in the same altitude regions all along the path are such that a common-volume would be totally undefinable and therefore invalid even as a concept.

The refractive index profiles which are obtainable for the lower regions of the 'model atmosphere' are of shapes which are very similar to those which are obtainable for the full-scale system, but with one very important difference. For the full scale system, by whatever method, the measurement of a refractive index profile requires a significant period of time and only applies to an extremely restricted region of the atmosphere. In contrast, the profiles obtained in the laboratory model are obtained by a photographic method where all values of the refractive index for all possible profiles in a very considerable portion of the propagation path are obtained at one and the same instant of time. A series of such profiles, taken over a period of time, has shown that considerable changes

can occur in the shape of the profile for a particular vertical region over a relatively short period of time. Studies of these profiles and the very simple 'atmospheric' activities which can be related to their shapes also suggest that the interpretations which are often given to explain the shapes of the refractive index profiles for the real atmosphere may, at least, be speculative and at worst, quite wrong. Although the model techniques has many shortcomings, and is obviously a very simplified representation of an extremely complex atmospheric medium, the various studies that it has supported have, at very least, directed attention towards the meteorological activities in the lower regions of the troposphere and away from the Common Volume concept as it is applied to the communication system. Indeed most of these studies have suggested that the activities in the lowest regions of the troposphere and over the whole of the length of a given path may be of altogether greater significance to a transmission system, line of sight or trans-horizon, than the so-called common volume. Since much of the meteorological activity in the lower region of the troposphere is directly associated with the exchange of heat in the immediate regions of the earth - atmosphere boundary then the various forms of convective turbulence, which are the principal agents, must be considered in greater detail and particularly in respect of their effects on a radio beam. In 1939 Avsec<sup>3</sup> used a laboratory model technique to demonstrate many of the properties of the larger thermal or Bénard cell which is known to prevail in arrays of infinite varieties of shapes and sizes in the lower atmosphere and adjacent to the earth's surface at all times. Glider pilots and some birds profit by such structures, airline pilots and passengers frequently suffer from the effects of thermals, and many forms of precipitate are formed by the thermal cell. In 1959 Belatini<sup>4</sup> suggested that the thermal cell might act as a concave lens and that an array of such cells may provide a propagation mechanism for trans-horizon tropospheric transmissions. The experimental work, using the laboratory model technique to which reference has already been made, gives significant support to the importance of the near surface thermal activity and its effects on a radio beam. It would seem, therefore, that the simple effects that a thermal convective cell may impose on a narrow radio beam might be investigated with advantage.

## 2.1 The Convective Medium

In any discussion which concerns the sources of energy that are manifest in the continually moving and changing air masses which form the Troposphere, solar irradiation of the planet would be considered the prime source. As a result of the energy which is absorbed at the earth's surface, and which experiences diurnal changes in the amounts at any one point, there is the heat exchange between the earth's surface and the lower atmosphere. In general terms, it is the outward flow of heat in this exchange that is deemed responsible for most of the activity which takes place in the Troposphere. The exchange of heat in any situation is normally achieved by one or both of two basic processes, conduction or convection. In the case of the land or sea atmospheric air interface, it might be argued that an 'outward' flow of heat to the upper regions of the troposphere by conduction is virtually impossible since the Thermal conductivity of air is several orders of magnitude smaller than that of either land or water. However, heat may be transferred from the land/water surface by a conduction/diffusion process to the immediately adjacent air and then transported elsewhere by convection.

Quite frequently, when a convection state is considered to exist in the 'free' atmosphere, the mechanism is described in terms of the eddy or turbulent convection. Although neither of the terms

'eddy' or 'turbulent' precisely describe any particular mechanism, their use in the statistical methods appropriate to the problems of wave propagation in the Troposphere is well known.

In contrast, and perhaps more crudely the Bénard or Thermal Convective cell is a structure which has been the subject of considerable study by aerodynamicists, botanists, meteorologists, mathematical physicists and ornithologists. Initially observed and studied by Bénard, the convective cell has been created in the laboratory for study by Avsec and therefore may be regarded as a structure which is capable of definition in terms of all or most of its physical properties. In the real atmosphere thermal convective cells or 'Thermals' have been recorded to exist with a very large range of physical dimensions and shapes. By assuming a classical toroidal shape as shown in the Fig. 1 the range of the dimensions  $a$  and  $R$  may both extend from a few metres to a number of kilometres. Furthermore, there is much evidence to suggest that thermals exist singly or in arrays in both the horizontal and vertical planes in the atmosphere and with varying intensities according to their sources and positions.

Simple investigations of the bibliography on thermals very readily yields the information that such cells, particularly in the classical toroidal form,<sup>5</sup> are mainly characterised by the particular distributions of pressure, temperature, velocities and densities of the air within the entire structure.

## 2.2. The single toroidal cell

By assuming a simple toroidal form of cell as shown in the Fig. 1 the appropriate geometry may be developed by using the construction shown in the Fig. 2.

However, whilst it is clear that a three dimensional structure should be considered, for reasons of simplicity it is convenient only to consider an 'elemental section' in the plane parallel to and through the principal axis of the cell.

The elementary volume  $dV$  is given by:-

$$dV = \Delta B \cdot \Delta C \quad \text{-----} \quad 1$$

where  $\Delta B$  = 'side' area of the element

$$= \frac{1}{2}(r_2^2 - r_1^2)$$

and since  $r_2 = r + \frac{1}{2} dr$  and  $r_1 = \frac{1}{2} dr$

$$\text{then } \Delta B = r \cdot dr \cdot d\alpha \quad \text{-----} \quad 2$$

and the thickness  $\Delta C$  is given:-

$$\Delta C = R_0 d\theta \text{ within the region of interest.}$$

However, since  $R_0 = R - r \cos \alpha$ , then :-

$$\begin{aligned} \Delta C &= (R - r \cos \alpha) \cdot d\theta \\ &= R \left(1 - \frac{r}{R} \cos \alpha\right) \cdot d\theta \quad \text{-----} \quad 3 \end{aligned}$$

If the radius  $a$  is normalised with respect to the radius  $R$  to give a radius coefficient  $A$ , and thus give a description to the core of the cell, where:-

$$A = \frac{a}{R} \quad \text{-----} \quad 4$$

Similarly the 'shell radius' may be normalised to give a radius  $r_n$  relative to the radius  $a$  where:-

$$r_n = \frac{r}{a} \quad \text{-----} \quad 5$$

Substituting the equ. 4 and 5 into equ. 3

thus gives:-

$$\Delta C = R (1 - r_n A \cos \alpha) d\theta \quad \text{-----} \quad 6$$

The elemental shell volume  $dV = \Delta B \cdot \Delta C$  may now be given :-

$$\begin{aligned} dV &= r dr \cdot d\alpha \cdot R (1 - r_n A \cos \alpha) d\theta \\ &= R \cdot r (1 - r_n A \cos \alpha) dr \cdot d\alpha \cdot d\theta \quad \text{-----} \quad 7 \end{aligned}$$

The total volume for the elementary shell of the toroid will therefore be:-

$$\begin{aligned} V &= \int_{r=r_1}^{r=r_2} \int_{\alpha=0}^{\alpha=2\pi} \int_{\theta=0}^{\theta=2\pi} R \cdot r (1 - r_n A \cos \alpha) dr \cdot d\alpha \cdot d\theta \\ &= 2\pi^2 R (r_2^2 - r_1^2) \\ &\text{and since } \frac{r_2 + r_1}{2} = r, \quad r_2 - r_1 = dr \\ &\text{then } V = 4\pi^2 R \cdot r \cdot dr \quad \text{-----} \quad 8 \end{aligned}$$

Similarly for the same toroidal shell, the cross-sectional area which is offered normal to the direction of any tangential flow may be derived from the elemental area  $dA_T$  where

$$dA_T = \Delta C \cdot dr \quad \text{-----} \quad 9$$

Substituting equ. 6 into equ. 9 gives

$$dA_T = R (1 - r_n A \cos \alpha) d\theta \cdot dr$$

The total cross-sectional area  $A_T$  will be given :-

$$\begin{aligned} A_T &= \int_{r=r_1}^{r=r_2} \int_{\alpha=0}^{\alpha=2\pi} R (1 - r_n A \cos \alpha) d\theta \cdot dr \\ &= \int_{r=r_1}^{r=r_2} 2\pi R (1 - r_n A \cos \alpha) \cdot dr \\ &= 2\pi R (1 - r_n A \cos \alpha) \cdot dr \quad \text{-----} \quad 10 \end{aligned}$$

It can be readily observed in the equ. 10 that the cross-sectional area

$A_T = f(\alpha)$  with a minimum value when  $\alpha = 0$  i.e. at the centre of the whole toroid.

Whilst the maximum value occurs when  $\alpha = \pm \pi$  at the outer periphery of the whole structure, a mean value where  $A_T = 2\pi R \cdot dr$  occurs when  $\alpha = \pm \pi/2$ .

Thus the core of the toroidal

cell, for the purpose of any idealised steady state air flow, may be regarded as a tube of varying cross-section area between the upper and lower extremities of the cell.

If it is then assumed that the rate of mass flow of a fluid through that tube is constant, there will be variations in the density, pressure and velocity distributions in the effective length of the tube.

With the simplified assumptions given by Cone<sub>5</sub>, that all streamlines within the boundary of a single stationary cell are closed and that all the fluid mass  $m$  circulates around the vortex (toroid) ring, then the rate of fluid flow  $F$  at any point in the cell may be given by the general expression:-

$$F = \frac{dm}{dt} = \rho q A \quad 11$$

where  $\rho$  = fluid density,  $q$  = velocity and  $A$  = cross-sectional area normal to the velocity.

Whilst the parameters  $\rho$ ,  $q$  and  $A$  in equ. 11 are variable the total product to give the flow rate  $F$  is constant.

For the closed toroidal ring shell the total fluid flow rate may also be given:-

$$F = \frac{m_T}{T} \quad 12$$

where  $m_T$  = total fluid mass in the shell and  $T$  = time for the fluid to flow round a circuit of any cross-sectional area once.

For a fluid of static density  $\rho_0$  and a total volume  $V$  of the ring shell equ. 12 gives:-

$$F = \frac{m_T}{T} = \frac{\rho_0 V}{T} \quad 13$$

From equ. 11, the fluid flow rate per unit area,  $I$ , is given

$$I = \frac{F}{A} = \rho q \quad 14$$

Similarly, from equ. 13

$$I = \frac{F}{A} = \frac{\rho_0 V}{T A} \quad 15$$

Combining equ. 14 and 15 gives

$$\rho q = \frac{\rho_0 V}{T A} \quad 16$$

Now from equ. 8 and 10, the ratio of the volume  $V$  of the shell to its cross-sectional area  $A_T$  may be given:

$$\frac{V}{A_T} = \frac{2\pi R r_n A}{1 - r_n A \cos \alpha} \quad 17$$

The equ. 16 thus becomes:-

$$I = \frac{2\pi R \rho_0}{T} \left( \frac{r_n A}{1 - r_n A \cos \alpha} \right) \quad 18$$

Also for a radial path of radius  $R$ , the tangential velocity  $q_0$  may be given:-

$$q_0 = \frac{2\pi R}{T} \quad 19$$

Thus for the full radius  $a$  of the vortex core, the average tangential velocity  $q_t$  will be:-

$$q_t = \frac{2\pi a}{T} \quad 20$$

From equ. 19 and 20.

$$q_0 = \frac{q_e R}{a} = \frac{q_e}{A} \quad \text{21}$$

Thus if  $I_0 = \rho_0 q_0$  a normalised mass flow rate/unit area  $\Gamma$  may be given from equ. 16 and 21:-

$$\Gamma = \frac{I}{I_0} = \frac{\rho q}{\rho_0 q_0} = \frac{r_n A}{(1 - r_n A \cos \alpha)} \quad \text{22}$$

The function  $\Gamma$  in equ. 22 is plotted for the variables  $r_n$  and  $\alpha$  for a given value of the aperture coefficient  $A$  as shown in the Fig. 3. In this form, the figure conveniently displays an effective vertical cross-section of one of the vortex cores of a single cell to give the distribution of the surfaces of the flow-density function  $\Gamma$ .

In obtaining this distribution for the whole of a single cell it can be clearly seen that for a given fixed cell geometry the maximum flow-density exists at the centre of the core of the Toroidal structure and is a minimum at the outer periphery.

In determining an array of equal-flow density surfaces for the simple thermal cell, where each surface is concave in shape, it can be assumed that the cell must therefore, possess quasi-optical properties as far as the narrow radio beam is concerned. The significant changes in the flow density of the air or fluid in the region of the core of the cell will give rise to equally significant values of the radio-refractive index of that region which will cause the cell to behave in a manner similar to that of cylindrical biconcave lens.

By simple inspection of the Fig. 3 it can be seen that the function  $\Gamma$ , which is a function of both local density and tangential velocity, has an absolute maximum value of  $A/1-A$  and a minimum value of  $A/1+A$  at the outer periphery. At the boundary where  $r = a$ , at both the top and the bottom of the cell,  $\Gamma = 1$  and at the axis of the vortex core  $\Gamma = 0$ .

Whilst the flow of a gas through tubes has been the subject of considerable specialised study, some reference to the more elementary laws that have resulted from these studies will allow valuable information to be determined in respect of the core of the thermal cell.

In his work on hydrodynamic flow in 'stream tubes', Lamb, develops a relationship between local velocities, the gas constant and the velocity of sound for the steady flow of a gas which is subject to the adiabatic laws.

With a velocity  $q_0$  and the velocity of sound  $C_0$  at some fixed point in a 'tube' of gas flow, where the gas constant or ratio of specific heats is  $\gamma$ , a condition of equilibrium is established for any other point when:-

$$q^2 + \left(\frac{2}{\gamma-1}\right) \cdot c^2 = q_0^2 + \left(\frac{2}{\gamma+1}\right) c_0^2 \quad \text{23}$$

Where  $c$  is the velocity of sound corresponding to the local value of the velocity  $q$ .

Also for a cross-sectional area  $\epsilon$  and an element of tube length  $ds$  there is the additional equilibrium condition where:-

$$\frac{1}{\epsilon} \frac{d\epsilon}{ds} = \frac{1}{q} \frac{dq}{ds} \left(1 - \frac{q^2}{c^2}\right) \quad \text{24}$$

For a converging tube the equ. 23 and 24 show that when the local velocity  $q$  increases there is a corresponding reduction in the relevant local velocity of sound. The relationship reverses for the case of the divergent tube. Both cases depend, of course, upon whether  $q$  is less or greater than  $c$ . If, however, in the limit, the local values of the velocities  $q$  and  $c$

may be assumed to approach one another and to a common value  $q_m$ ,

$$\text{i.e. when } q = c = q_m \quad \text{25}$$

Then the equ. 23 may be given thus:-

$$q_m^2 \left[ 1 + \left( \frac{2}{\gamma - 1} \right) \right] = q_0^2 + \left( \frac{2}{\gamma - 1} \right) c_0^2 \quad \text{26}$$

For the practical atmospheric case where  $q_0 \ll c_0$  the equ. 26 reduces to:-

$$q_m^2 \left[ 1 + \left( \frac{2}{\gamma - 1} \right) \right] = \left( \frac{2}{\gamma - 1} \right) c_0^2$$

$$\text{from which } q_m = \sqrt{\left( \frac{2}{\gamma + 1} \right)} \cdot c_0 \quad \text{27}$$

For the normal value of the velocity of sound in dry air where  $c_0 = 331.45$  m/sec, and assuming a value of the gas constant  $\gamma = 1.408$ , the value of  $q_m$  will be given:-

$$q_m = 302.07 \text{ m/sec.} \quad \text{28}$$

This value of  $q_m$  which is some 9% less than  $c_0$  will be the local tangential propagation velocity of sound at the very centre of the core of the toroidal cell and will be a maximum value. Since this local propagation velocity of sound is related to both density  $\rho_m$  and the Young's Modulus  $M$  in the form:-

$$q_m = \sqrt{\frac{M}{\rho_m}}, \quad \text{29}$$

if  $M = 1.4 \cdot 10^5 \text{ Kg/m}^2 \text{ sec}^2$  and  $q_m = 302.07 \text{ m/sec}$  then,

$$\rho_m = 1.534 \text{ Kg/m}^3, \quad \text{30}$$

and if for dry air  $\rho_0 = 1.22 \text{ Kg/m}^3$ , then

$$\rho_m = 1.257 \rho_0 \text{ Kg/m}^3 \quad \text{31}$$

The equ. 31 thus suggests that there is an effective density compression ratio of 1.26 at the centre of the cell using the assumption that the Modulus of Elasticity  $M$  remains constant. Any change that is likely to occur in the value of  $M$  can only increase the compression ratio. By using these values of  $q_m$  and  $\rho_m$  with the known value of  $\rho_0$  for dry air, it is now possible to determine similar information for most regions of the whole thermal cell by using the families of the function  $\Gamma$ , given in equ. 22, for various values of the aperture function  $A$ . By considering the equilibrium condition given in equ. 22 where:-

$$\rho q = \rho_0 q \frac{r_n - A}{1 - r_n} A \cos \alpha$$

for the maximum values, where  $\rho = \rho_m$  and  $q = q_m$  at the centre of the cell, which also satisfies the condition where  $r_n = 1$  (i.e.  $r = a$ ) and  $\alpha = 0$ , then

$$\rho_m q_m = \rho_0 \frac{A}{1 - A} \quad \text{32}$$

Putting  $\rho_0 = 1.22 \text{ Kg/m}^3$ ,  $q_m = 302.07 \text{ m/sec}$  from equ 28,  $\rho_m = 1.257 \rho_0$  from equ 31, and giving  $q_0$  the arbitrary value of 0.1 m/s. the conditions of equilibrium in equ. 32 gives:-

$$1.257 \rho_0 \cdot 302.07 = \rho_0 \cdot 0.1 \frac{A}{1 - A}$$

which is satisfied by a value of  $A$ , the aperture function, where

$$A = 0.9997 \quad \text{33}$$

It will be noted that this solution is also directly related to a velocity ratio, at the very centre of the cell, of

$$q_m / q_0 = 3020.7 \quad \text{34}$$

The resultant associated tangential velocities at the full radius  $a$  at the top and bottom of the cell will be given from equ. 21 as:-

$$q_t = Aq_0 \sin \alpha = 0.1 \text{ m/s} \quad 35$$

For these same regions there will be density compression ratios of unity.

At the lateral extremities of the cell, and at the radius surface where  $r = a$  and  $\alpha = \pi$ , the conditions of equilibrium in equ. 22 may be used to give the relationship:-

$$\rho_e q_e = \rho_0 q_0 \frac{A}{1 + A} \quad 36$$

to give

$$\rho_e q_e = 6.099 \times 10^{-2} \text{ kg/m}^2/\text{sec.} \quad 37$$

The product value given in the equ. 37 suggests that the ratio  $\rho_e q_e / \rho_0 q_0$  is slightly less than 0.5 and which is principally due to a significant reduction in the velocity  $q$  rather than a change in the density  $\rho$ . If, for the purpose of obtaining relevant values of both  $\rho$  and  $q$ , it is assumed that  $q_e = 0.55$ ,  $q_0 = 0.055 \text{ m/s}$  then a density of  $\rho_e = 1.11 \text{ Kg/m}^3$  completes the product of equ. 37.

The values of  $q$  and  $\rho$  that have been calculated from the equ. 28 to 37 show that where a fluid flows through a 'tube' of varying cross-section there are changes in both density and velocity, particularly where the fluid is air and compressible. In the case of atmospheric gas (air), where the density  $\rho$  is low and the Modulus of Elasticity  $M$  is high, it would be expected that the changes of velocity with 'tube' cross-section would be significantly large whereas the changes in density would be relatively low. For other fluids the exact opposite might be true.

### 2.3 The Radio Refractive Index of the Thermal Cell Core.

For the atmosphere medium, the well known formula used for the calculation of the radio refractive index is given thus:-

$$N = (n-1) \times 10^6 = \frac{77.6}{T} \left[ P + \frac{4710e}{T} \right] \quad 38$$

in the 'N unit' form where  $n$  = radio refractive index,  
 $P$  = atmospheric pressure,  $e$  = the partial water vapour pressure and  $T$  = the absolute temperature.

For dry air, the eqn. 38 may be reduced to the simple relationship:-

$$\frac{N}{T} = \frac{77.6P}{T} \quad 39$$

Also, for a unit mass of gas, the simple gas law may be given.

$$PV = RT \quad 40$$

where  $R$  = the gas constant and  $V$  = the specific volume.

Since the specific volume  $V = 1/\rho$  then the eqn. 40 becomes:-

$$\begin{aligned} \frac{P}{\rho} &= RT \\ \therefore \frac{P}{T} &= \rho R \quad 41 \end{aligned}$$

Substituting equ. 41 into the equ. 39 gives:-

$$N = 77.6 \rho R \quad 42$$

Applying the value of R, the gas constant for air gives:-

$$N = 223 \rho \quad \text{43}$$

where  $\rho$  = gas density in  $\text{Kg/m}^3$

In equ. 43 it has been established that the radio refractivity of a 'dry air' atmosphere may be considered a direct function of the gas density. It is therefore possible now to determine the refractivity N values for various regions of the cell core. From the equ. 38 it can be seen that the presence of water vapour will only enhance the N values determined for the 'dry air' core.

If the density of air at ground level is given the value where  $\rho_0 = 1.22 \text{ Kg/m}^3$ , then the refractivity N is given from equ. 43 thus:-

$$N = 223 \rho_0 = 223 \cdot 1.22 = 272.1 \quad \text{44}$$

From the velocity given in the equ. 35 and the corresponding density values it can be seen that the radio refractivity at both the top and bottom of the cell core will have values similar to that given in equ. 44.

Similarly at the very centre of the cell core where, from equ. 31,  $\rho_m = 1.257 \rho_0$  the radio refractivity values may be determined from the density component of the equ. 37 thus.

$$N = 223 \cdot 1.11 = 248 \quad \text{46}$$

Whilst all of these refractivity values are based on both the density of dry air and the velocity of sound given for ground level the corresponding values of N at different altitudes are not expected to be significantly different. Although both pressures and velocities may change with altitude, neither density, compression or velocity ratios are expected to experience significant change. Similarly the aperture function of the cell will remain substantially independent of altitude.

The values of radio refractivity N given in the equ. 44-46 of course relate to specific points on the surface of  $\Gamma = 1$  for values of  $A = 0.9997$  and  $r_n = 1$  and for all values of  $\theta$ . These values are also quite typical of those which are exhibited by the many radio-refractive index profiles which are obtained by radio refractometer measurement methods. Indeed, full profiles calculated for the thermal cell will yield values which agree with most measured values and also suggest 'reasonable - fits' with the vertical extensions of Thermal cells to the positions of adjacent discontinuities in the normal refractive index profile.

The concave surfaces of the function  $\Gamma$ , any one of which forms an effective core of the thermal cell with different refractive properties from that of the surrounding air, may thus establish the basic cylindrical biconcave lens of the types shown in the Figs. 4 and 5.

### 3.1 Beam Distortion due to a Thermal Cell

In establishing that the core of a Bénard or Thermal Cell may be regarded as a cylindrical lens, of overall physical shape as shown in the Fig. 4, it is clear that such a structure could give rise to considerable distortion to the shape of a narrow radio beam. Since the majority of tropospheric radio systems employ narrow beams in the interest of power conservation, the presence of "thermal lenses" on a given propagation path may give rise to either considerable additional path loss or gain depending upon the nature of the actual distortion.

The interaction of the 'thermal lens' structure with a narrow radio beam clearly presents an extremely complex problem with an equally complex array of solutions. In the strictest sense the

'thermal core', by virtue of the distribution of the refractivity surfaces within the core, should be regarded as a distributed lens structure. In addition, for the true narrow divergent radio beam, this lens structure will provide additional divergence to the beam in the horizontal and vertical planes normal to the direction of propagation. The extent of the divergence in both planes will, of course, be dependent upon the relative dimensions of the lens and the cross-section of the incident beam. The effective focal length of the 'lens' is also of considerable significance as is the possible convergence that could result in the horizontal plane from the effective convex lens properties of the centre of the cell.

In the interests of simplicity, it is convenient only to consider the simplest possible 'lumped' lens structure and to express any distortion effects that it might induce in terms of those parameters which are of some significance to the radio system.

### 3.2 Attenuation due to the thermal cell

In the case of a narrow radio beam which is directed towards a distant point beyond the radio horizon the only effects which are of prime interest to the system designer are those which might be associated with distortion in the vertical plane only. Such distortion in the shape of the cross-section of a beam will inevitably result in a change in the power density distribution across the beam which, in turn, will appear as an attenuation. For the purpose of obtaining an estimate of this attenuation, a single thin bi-concave lens of the approximate form given in the Fig. 5 might be considered. It is also convenient to consider the thickness or width  $W$  of the slice to be determined from a cell core of radius  $(R-a)$  where:-

$$W = 2 (R - a) \quad 47$$

From the surfaces given in the Fig. 3 when  $\Gamma = 1$  and  $r_n = 1$  the radius of the effective concave lens becomes approximately  $= 1.25a$ .

Expressing equ. 47 in terms of the vortex core radius  $a$  and the aperture function  $A$  gives:-

$$W = 2a \left( \frac{1-A}{A} \right) \quad 48$$

Applying an 'illumination factor'  $K$  to the width of the lens gives an active width:-

$$KW = 2Ka \left( \frac{1-A}{A} \right) \quad 49$$

The active area  $L$  of the lens presented to a beam will thus be:-

$$\begin{aligned} L &= 2a KW \\ &= 4a^2 K \left( \frac{1-A}{A} \right) \quad 50 \end{aligned}$$

In the somewhat ideal situation where there is a concentration of thermal cells, as considered by Avsec et. al. the total area presented by a single thermal cell may be given:-

$$\begin{aligned} L_T &= 2 (R + a) \cdot 2a. \\ &= 4a^2 \left[ \frac{(1+A)}{A} \right] \quad 51 \end{aligned}$$

By taking the ratio of the two areas given in equ. 50 and 51 an estimate of the attenuation due to the presence of a thermal cell may be given as:-

$$\begin{aligned} L_c &= 10 \log_{10} \left( \frac{L}{L_T} \right) \text{ dB} \\ &= 10 \log_{10} \left[ K \left( \frac{1-A}{1+A} \right) \right] \text{ dB} \quad 52 \end{aligned}$$

For a value of  $K = 0.7$  and  $A = 0.9997$  from equ. 33,

$$L_c = 40.2 \text{ db} \quad \text{53}$$

In making these calculations it has been assumed that the total cross-sectional area of the radio beam in the vicinity of the thermal cells being considered is very much larger than the area  $L_T$  presented by any one cell. In general this condition is satisfied at a significant distance from the transmitter source. In regions nearer the transmitter, where the area  $L_T$  becomes comparable with the beam area the attenuation of loss  $L_c$  reduces considerably. As the area  $L_T$  greatly exceeds the beam area the loss  $L_c$  reduces to a negligible value. Simple calculations of the path geometry of a typical system, together with the assumption that the average effective diameter of a thermal cell is approximately 400m will show that the loss  $L_c$  would only be of significance beyond the radio horizon.

### 3.3 The Divergence due to a Thermal Cell

For any double spherical lens, the Lensmaker's equation is given:-

$$\frac{1}{f} = (\mu - 1) \left( \frac{1}{R_{c_1}} + \frac{1}{R_{c_2}} \right) \quad \text{54}$$

where  $f$  = focal length (principal focus)

$R_{c_1}$  and  $R_{c_2}$  = radii of curvature of the two lens surfaces

$\mu$  = refractive index of the lens material.

Applying this equation to the thin slice of the cylindrical biconcave lens due to the core of the thermal cell provides the relationships

where:-

$$(\mu - 1) = \Delta N$$

$$R_{c_1} = R_{c_2} = R_c \text{ for the symmetrical lens.}$$

$$\frac{1}{f} = \frac{2 \Delta N}{R_c} \quad \text{55}$$

$$\text{and if } R_c = 1.25a$$

$$\frac{1}{f} = \frac{2 \Delta N}{1.25a} \quad \text{56}$$

For a parallel beam directed along the optical axis of a biconcave lens the emergent beam will be divergent with the angle of divergence  $\delta$  being determined from the position of the principal focus.

For a lens of diameter  $h$ , principal focus  $f$ , the angle of divergence  $\delta$  for a beam which appears to emanate from the point of focus:-

$$h = 2f \tan \delta$$

$$\text{or } \frac{1}{f} = \frac{2 \tan \delta}{h} \quad \text{57}$$

combining the equ. 55 and 57 gives:-

$$\frac{2 \Delta N}{R_c} = \frac{2 \tan \delta}{h}$$

$$\text{or } \delta = \tan^{-1} \frac{h \Delta N}{R_c}$$

which for small angles where  $\tan \delta \rightarrow \delta$  becomes

$$\delta = \frac{h \Delta N}{R_c} \quad \text{58}$$

Applying the equ. 58 to the core of the thermal cell where  $R_c = 1.25a$  and  $h = 2a$  for the case where the beam cross-section diameter is very much greater than  $2a$  then:-

$$\begin{aligned} \delta &= \frac{2a \Delta N}{1.25a} = 1.6 \Delta N. \\ &= 1.6 \cdot 10^{-6} \Delta N. \text{ rad} \end{aligned} \quad \text{59}$$

The equ. 58 gives the angle of divergence per thermal cell core where compression has been considered. The additional and minor divergence that will be obtained from the peripheral regions between adjacent cells has not been considered. However, it can be seen from equ. 58 that the angle of divergence does not appear to be dependent upon the size of the cell. For a single thermal cell at ground level with refractivity  $N$  values similar to those already considered, the equ. 58 gives a divergence per cell where

$$\delta \approx 60 \mu \text{ rads} \quad \text{60}$$

The approximate value of  $\delta$  given in the equ. 60 will, of course, reduce with altitude and as a direct function of the air density  $\rho_a$ . Also, it should be appreciated that for the physical dimensions and properties that have been considered in respect of the basic 'thermal lens', the principal focus may be at a distance of some 150 - 250 Km from the lens. However, it is clear that the narrow radio beam will experience distortion in the vertical plain as a result of the presence of a thermal cell along the propagation path and which, for the somewhat idealised core, has been expressed in the form of an attenuation and a divergence. It is equally clear that in the more realistic condition, where thermal cells are distributed over the entire length of a transmission path, the combined effects of successive divergence and attenuation due to an in-line array of cells would be considered equivalent to a significant degree of distortion in the cross-section of a narrow beam.

### 3.4 Distortion of a narrow beam in an array of thermal cells

Where an array of similar thermal cells is considered to exist equally distributed over the whole length of a transmission path it is obvious that, for the atmospheric parameters that have already been considered, both attenuation and divergence in a narrow beam will result. In the simplest possible terms the total vertical divergence may be estimated from the number and the intensities of the cells involved. In contrast, the attenuation will not be simple and additive since the progressive divergence will change the power density distribution in the beam cross-section as the propagation distance increases.

An estimate of this attenuation may be obtained by considering two biconcave lens as shown in the Fig. 6.

If a beam, of angle  $\eta$  and from a source (object) distance  $x_1$  from the lens, emerges from the divergent lens with a new beam angle  $\eta'$  where

$$\eta' = \eta + 2\delta \quad \text{61}$$

the new beam will appear to emanate from a source at the image distance  $x'_1$  from the lens.

The traditional lens formula may be applied to this condition to give:

$$-\frac{1}{f} = \frac{1}{x_1} - \frac{1}{x'_1} \quad \text{62}$$

Now if the real transmitter is assumed to radiate a power  $P_T$ , the attenuation or loss due to a single thermal cell core may be evaluated by considering the areas which are illuminated by both the real and virtual sources.

At the first lens, as shown in the Fig. 6, both real and virtual transmitters are assumed to illuminate the same area. Therefore, for the power  $P_{x_1}$  at the plane  $ab$  from the real transmitter  $P_T$  :-

$$P_{x_1} = K \frac{P_T}{(x_1)^2} \quad \text{63}$$

Similarly, in assuming that the divergence due to the core lens is equivalent to considering the transmitter moving to the position of the "virtual source"  $P'_T$ , then:-

$$P_{x_1} = K \frac{P'_T}{(x'_1)^2} \quad \text{64}$$

Since in the plane ab,  $P_{x_1} = P_{x'_1}$ , then from equ. 63 and 64:-

$$P'_T = P_T \left( \frac{x'_1}{x_1} \right)^2 \quad \text{65}$$

Also from equ. 62 :-

$$x'_1 = \frac{x_1 f}{f + x_1} \quad \text{66}$$

Substitution equ. 66 in equ. 65 gives:-

$$P'_T = P_T \left( \frac{f}{f + x_1} \right)^2 \quad \text{67}$$

In addition, there is a loss of power associated with the effective change in illumination areas in the plane fcd through the axis of a possible second core lens  $L_2$ .

By assuming the relevant areas to be defined by  $(cd)^2$  and  $(ef)^2$  respectively, then:-

$$\frac{P'_T}{P_T} = \left( \frac{cd}{ef} \right)^2 \quad \text{68}$$

$$\text{Now the dimension } cd = 2 (x_1 + d) \tan \frac{\eta}{2} \quad \text{69}$$

$$\text{and the dimension } ef = 2 (x'_1 + d) \tan \left( \frac{\eta + 2\delta}{2} \right) \quad \text{70}$$

Equ. 69 and 70 in equ. 68 thus gives:-

$$\frac{P'_T}{P_T} = \left[ \frac{(x_1 + d) \tan \frac{\eta}{2}}{(x'_1 + d) \tan \left( \frac{\eta + 2\delta}{2} \right)} \right]^2 \quad \text{71}$$

However, it has already been established that both  $\eta$  and  $\delta$  are normally very small and as a result the equ. 71 simplifies to:-

$$\frac{P'_T}{P_T} = \left[ \frac{(x_1 + d) \cdot \eta}{(x'_1 + d) (\eta + 2\delta)} \right]^2 \quad \text{72}$$

With equ. 67 in equ. 72, then

$$P'_T = P_T \left[ \frac{\eta (x_1 + d)}{(x'_1 + d) (\eta + 2\delta)} \cdot \frac{f}{(f + x_1)} \right]^2 \quad \text{73}$$

If a second core lens  $L_2$  at an increased distance  $d$  is to be considered to produce the equivalent effect of moving the original transmitter  $P_T$  to a second virtual source  $P''_T$  then the total power radiated  $P_{T_2}$  will be given:-

$$P_{T_2} = P_T \left( \frac{\eta}{\eta + 2\delta} \right)^2 \left[ \frac{(x_1 + d)}{(x'_1 + d)} \cdot \frac{(x_2 + d)}{(x'_2 + d)} \cdot \frac{f}{(f + x_1)} \cdot \frac{f}{(f + x_2)} \right]^2 \quad \text{74}$$

For the  $n$ th transmitter of an array of cells spaced distance  $d$  apart,

then:-

$$P_T = P_T \left( \frac{\eta}{\eta + 2\delta} \right)^{2n} \left[ \frac{(x_1 + d)}{(x'_1 + d)} \cdot \frac{f}{(f + x_1)} \cdot \frac{(x_n + d)}{(x'_n + d)} \cdot \frac{f}{(f + x_n)} \right]^2 \quad \text{75}$$

In the practical case it is likely that, for an equally spaced array of thermal cells, the terms  $(x_n + d) / (x'_n + d)$  are going to be somewhat less than or equal to unity and  $f \gg x_n$  to give the more practical version of equ. 75 thus:-

$$P'_{T_n} = P_T \left( \frac{\eta}{\eta + 2\delta} \right)^{2n}$$

$$\text{or } P'_{T_n} = P_T \left( \frac{1}{1 + \frac{2\delta}{\eta}} \right)^{2n} \quad \text{76}$$

Expressing the equ. 76 as a path loss  $L_p$

$$L_p = 10 \log_{10} \left( \frac{P_T}{P'_{T_n}} \right) \text{ dB}$$

$$= 10 \log_{10} \left[ \left( 1 + \frac{2\delta}{\eta} \right)^{2n} \right] \text{ dB}$$

$$= 20n \log_{10} \left( 1 + \frac{2\delta}{\eta} \right) \text{ dB} \quad \text{77}$$

If the array of  $n$  cells are assumed to be distributed, with equal spacing  $d$ , over the entire length of a transmission path of total distance  $D$  then  $D = nd$ . The total path loss due to the presence of the cells will thus be given:-

$$L_p = \frac{20D}{d} \log_{10} \left( 1 + \frac{2\delta}{\eta} \right) \text{ dB} \quad \text{78}$$

Where the angles  $\delta$  and  $\eta$  are such that  $2\delta/\eta \ll 1$  then equ. 78 becomes

$$L_p = \frac{40D\delta}{2.3 d \cdot \eta}$$

$$= \frac{17.39 D\delta}{d \cdot \eta} \text{ dB} \quad \text{79}$$

$$\text{or } L_p = \frac{17.39 \delta}{d \cdot \eta} \text{ dB/Unit distance (Km)} \quad \text{80}$$

If now values for  $d$ ,  $\eta$  and  $\delta$  are assumed for a particular system where:-

$d$ , the distance between adjacent cells = 400 to 600 m

$\eta$ , the beam angle of the transmitter =  $1^\circ$

$\delta$ , the beam divergence due to each thermal cell, from eqn 60, =  $60 \mu\text{ rad}$ .

then the loss per kilometre of path will be given, from equ 80, to be in the range

$$L_p = 0.0991 \text{ to } 0.149 \text{ dB/km.}$$

An average value of  $L_p$  may thus be given where

$$L_p = 0.124 \text{ dB/km} \quad \text{81}$$

which is a value typical of that encountered in practice.

Clearly the loss value of  $L_p$  given in the equ. 80 does not show any dependence upon parameters such as the wavelength of the transmission. Again, this is in agreement with most practical experience. Of course, this basic argument is limited to the assumed ideal properties of the 'thermal lens'. Any consideration which might be given to the equivalent chromatic properties of the lens will introduce parameters which will be sensitive to the transmission wavelength.

#### 4. Conclusions

By conducting that which is little more than a modest geometric exercise on the physical attributes of a basic circular or toroidal form of the Bénard cell, it has been possible to show that the radio refractive index distribution in such a structure might be readily identified in almost any radio refractive index profile. By considering the shape of the cell core, together with

its refractive index properties, it has also been possible to show that the Bénard cell may introduce the equivalent of a concave lens into a narrow radio beam. Whilst the principal effects of such a lens are well known in optics, similar effects have been assumed to occur for the radio beam. For the particular type of cylindrical concave lens considered, the resulting divergence in the vertical plane has been used to calculate estimated values of attenuation due to a single cell and the equivalent of an 'over-the-horizon' scatter loss due to an array of cells. The estimates of both of these parameters are of the same order as those which are encountered in practice. For the real atmosphere these values will, however, be subject to variation as both the shape, size and refractive properties of the cell core change with prevailing conditions and time. In addition, where there are arrays of thermal cells which are in continual movement as a result of external mechanical forces due to winds etc., the distortion to which a narrow beam may be subjected will be in continual change to cause fading.

In summary, the presence of arrays of thermal cells which exist in various forms over the whole of the surface of the planet must be considered significant to the mechanisms of propagation in the tropospheric medium. The recognition of the effects of such cells on a narrow beam also allows an appreciation of such parameters as antenna-medium coupling loss and suggests that there is an optimum value for the beam width of an antenna designed for a tropospheric radio system to operate in a given environment.

#### References

- 1) Burrows, W.G. 'A Study of the Effects of Tropospheric Air Mass Movements on the Fading Characteristics of U.H.F. Transmissions by the Use of a Laboratory Model.'  
Proc. A.G.A.R.D/N.A.T.O. (E.P.C). Symposium on Tropospheric Radio Wave Propagation.  
Dusseldorf, September 1970.
- 2) Burrows, W.G. 'Electro-Magnetic Wave Propagation in an Inhomogeneous Medium - a Laboratory Study'.  
Proc. A.G.A.R.D/N.A.T.O. (E.P.C). Symposium on 'Aspects of E.M. Scattering in Radio Communications' Cambridge. MASS. October 1977.
- 3) Avsec, D. 'Tourbillons Thermoconvectifs Dan L'Air Application a La Meteorologie'  
Publications Scientifiques et Techniques Du Ministere de L'Air. 1939. Report No. 155.
- 4) Belatini, P.C.M. 'Inadequacy of Scatter Mechanisms in Tropospheric Radio Propagation'.  
Nature. Vol. 184. P. 1558.
- 5) Cone (jr), C.D. 'The Theory of Soaring Flight in Vortex Shells Part I'.  
Soaring. 1961. Vol. 25. No. 4.
- 6) Hirth, W. 'Die Hohe Schule des Segelfluges'.  
Stuttgarter Vereinsbuchdruckerei. A.G. Stuttgart 1938.
- 7) Woodward, B. 'Flight Measurement of Isolated Thermals'.  
Report, Meteorology Dept. Imperial College, London. Aug. 1962.
- 8) Woodward, B. 'The motion In and Around Isolated Thermals'.  
Quart. Jour. Roy. Met. Soc. April 1959.
- 9) Lamb, H. 'Hydrodynamics'. P.20 - 26.  
Cambridge University Press 1952.

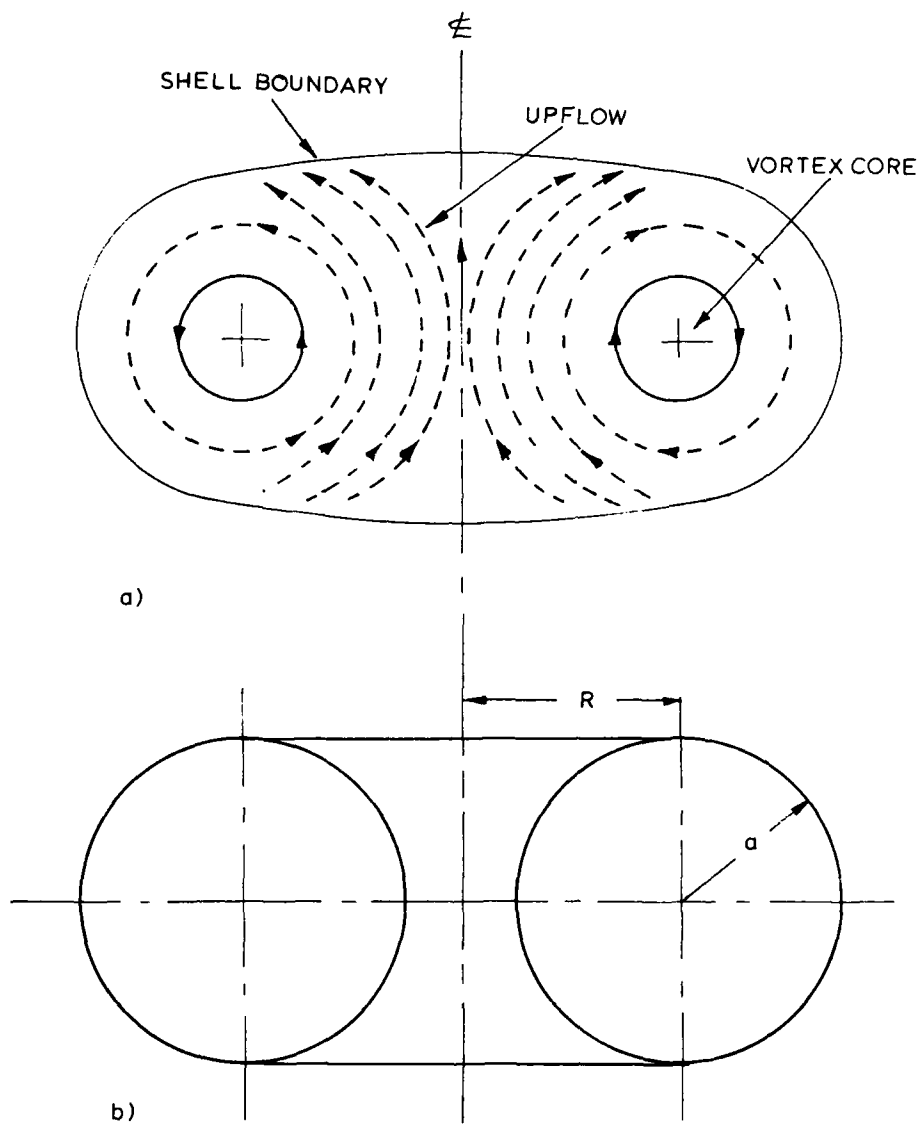


Fig.1.

The basic structure of a circular or toroidal form of the Bénard cell.

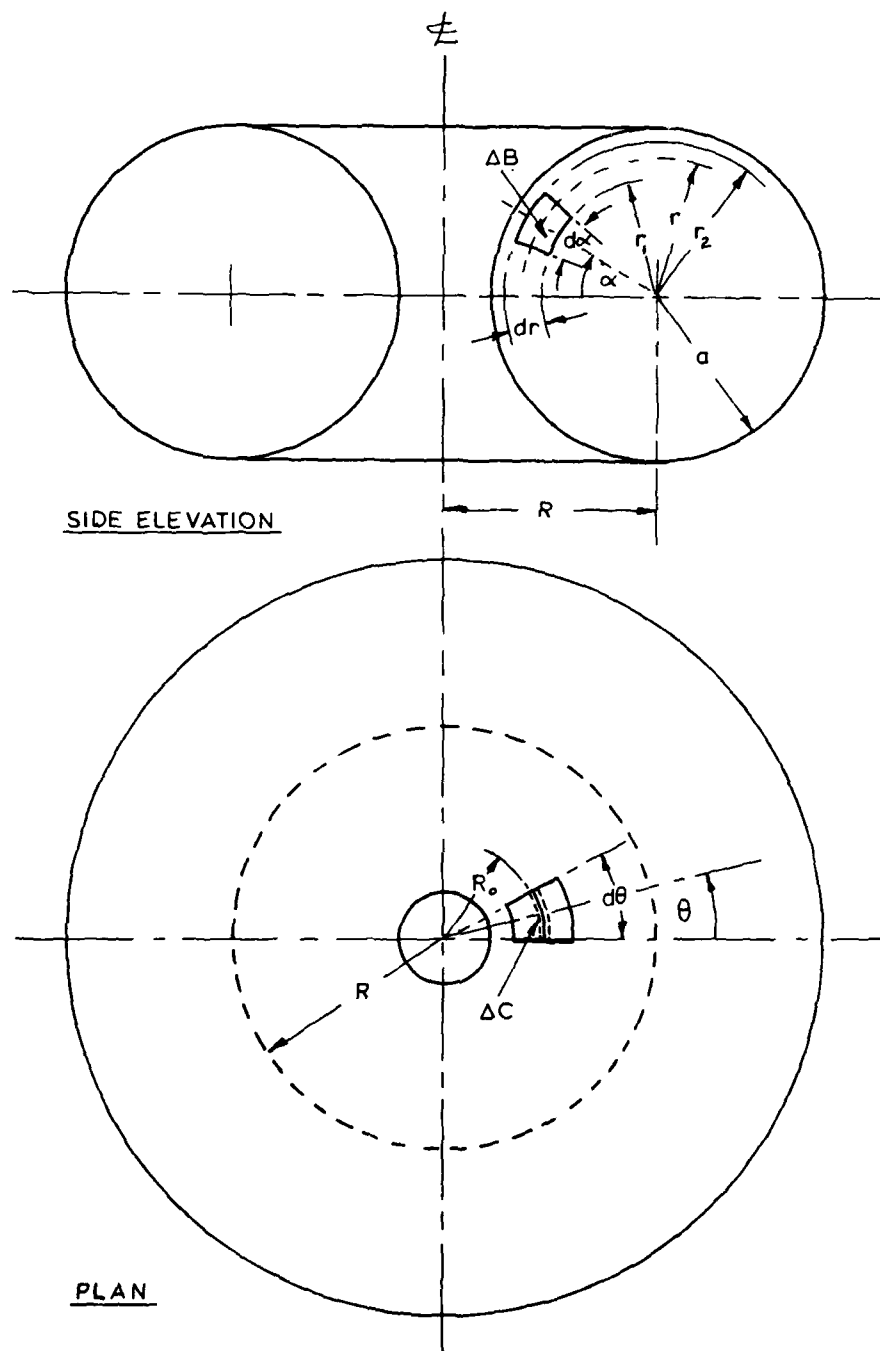
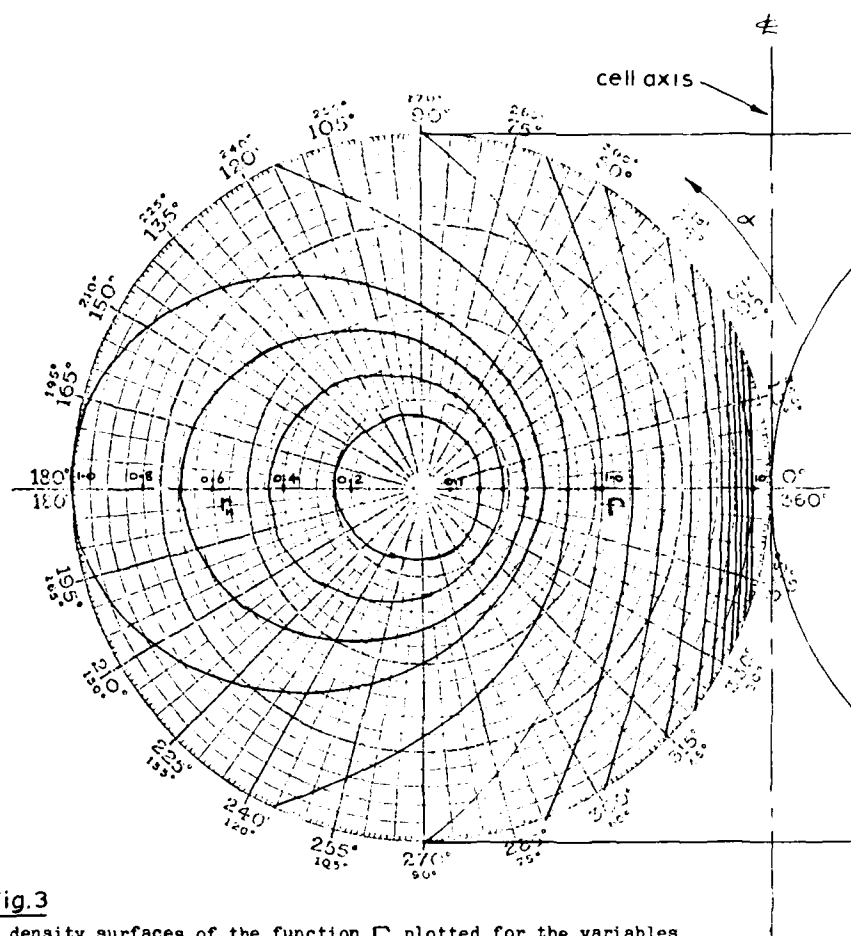
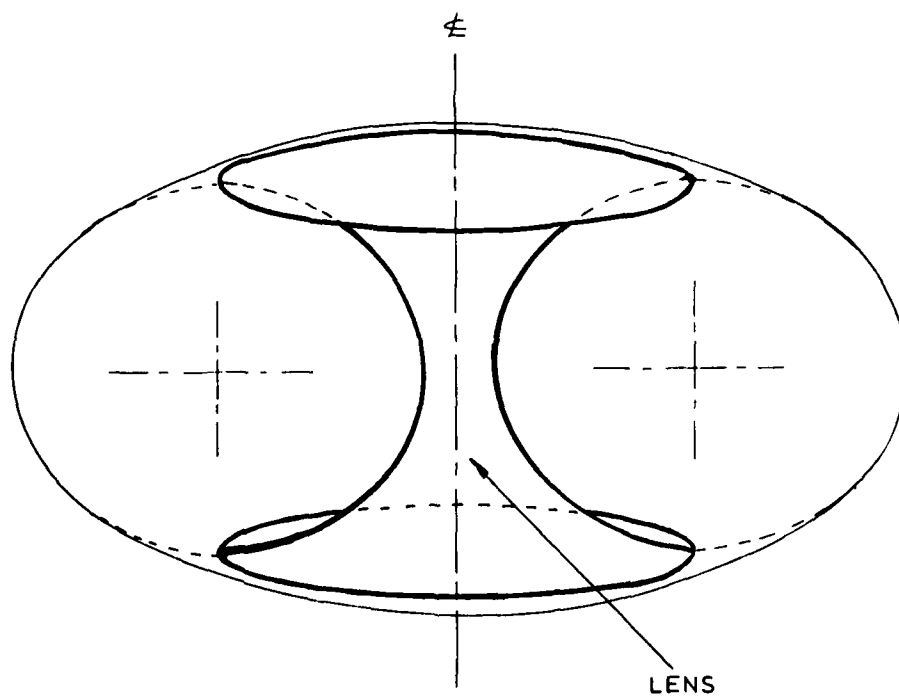


Fig. 2

Geometric details of the simple Bénard cell.



**Fig. 3**  
Flow density surfaces of the function  $\Gamma$  plotted for the variables  $r_n$  and  $\alpha$  for a value of the aperture coefficient  $A = 0.9997$ .



**Fig 4** A cylindrical biconcave lens at the core of a Hémond cell.

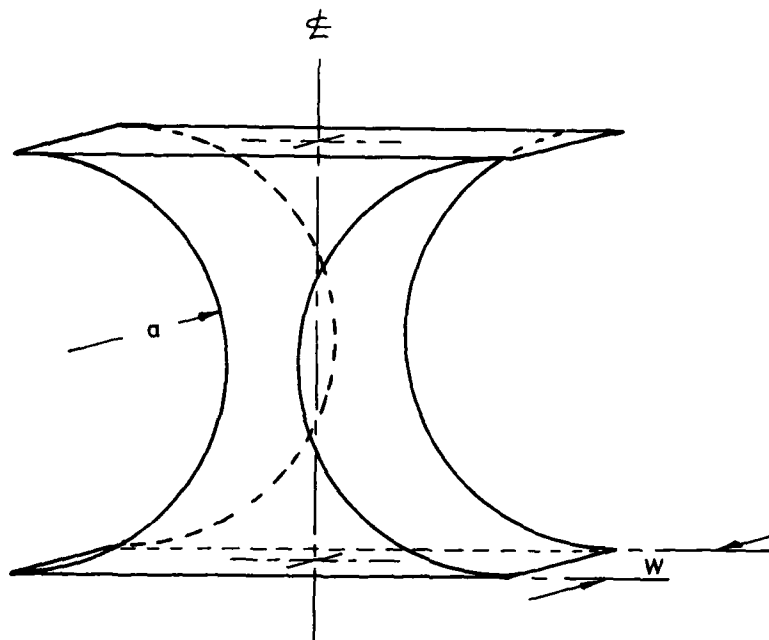


Fig 5

A thin biconcave lens form from the cell core.

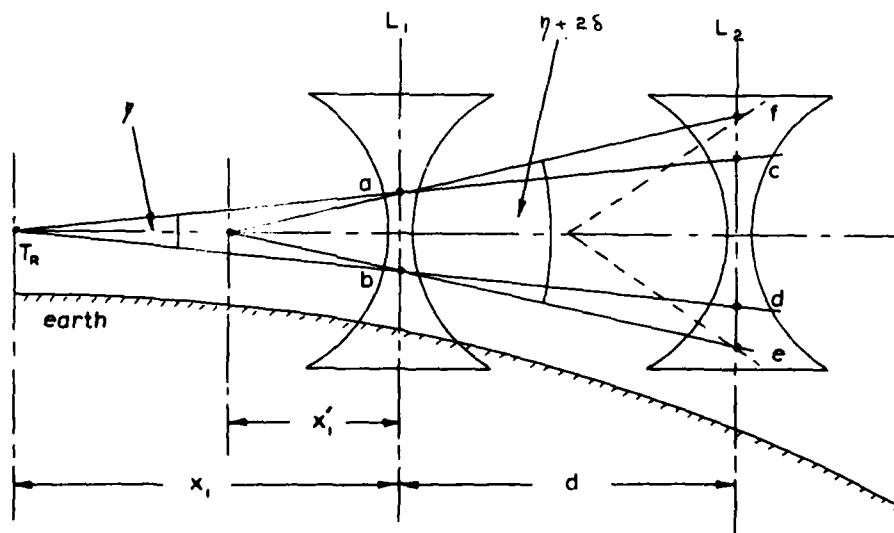


Fig 6

A simple in-line lens arrangement to show elementary divergence and the relevant geometric construction.

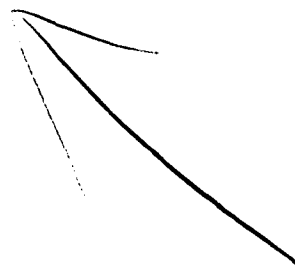
## DISCUSSION

K.D. Anderson (U.S.): This was an interesting paper. However, was the cell thickness about 400 meters?

W.G. Burrows (U.K.): I have used a cell of "average size" for the purpose of my paper. The "average size" is assumed to be about 400 meters, outside diameter, in the horizontal plane. It is about 200 meters high or deep. The full range of all cell sizes is, however, known to extend from a few meters to a few kilometers in diameter.

I. Anderson (U.K.): The antenna to medium coupling loss has always been a complex concept in conventional tropospheric theories. The simplest model is a sequence of lenses for a beam waveguide. The loss is a mismatch of the antenna beam and modes within the waveguide.

W.G. Burrows (U.K.): The cell structure is sensible if you launch a wave into an array or a beam structure. It corresponds to an array of cells along the surface, or also an upward array of cells formed with the wave motion of the heat transfer process.



# ANOMALOUS PROPAGATION AND RADAR COVERAGE THROUGH INHOMOGENEOUS ATMOSPHERES

H. W. Ko, J. W. Sari, M. E. Thomas, P. J. Herchenroeder  
Applied Physics Laboratory, Johns Hopkins University  
and  
P. J. Martone  
Electronics Systems Division, Hanscom AFB, MA 01731

## ABSTRACT

A method is outlined which enables radar coverage predictions to be made under anomalous propagation conditions. Spatial and temporal changes in the height and strength of refractive layers in the troposphere are known to compromise radar coverage. Refractive layers may create coverage voids by diverting rays and may introduce anomalous clutter and range height errors in radar systems. In this paper, elements of meteorology, atmospheric boundary layer physics, and electromagnetic wave propagation are combined to investigate the effect of inhomogeneous refractive layers on radar coverage.

A computer program called EMPE (Electromagnetic Parabolic Equation) has been developed to aid in these investigations. A special feature of EMPE is its ability to deal with inhomogeneous atmospheric changes in both the horizontal and vertical directions. Predictions for anomalous wave behavior have been made for frequencies from 100 MHz to 10 GHz. The results are relevant to a variety of microwave electromagnetic systems such as those used for communications, radar, and aircraft instrument landing.

Sponsored by the Electronic Systems Division, Hanscom AFB, MA  
under Contract No. N00024-83-C5301.

## INTRODUCTION

Severe compromises in radar coverage in coastal regions may occur because of the effect of refractive layers resulting from surface thermal and topographic influences on lower atmospheric circulation. Not to be confused with the well-known coastline effect, which is due to the change of surface impedance at the land-sea interface, these anomalous propagation problems are due to the establishment of an internal atmospheric boundary layer during the land-sea breeze cycle. Boundary layer creation leads to alterations in the strength and height of anomalous refractive layers, such as the maritime surface duct or elevated duct. In order to arrive at an understanding of the resultant radar problems, elements of meteorology, atmospheric boundary layer physics, and electromagnetic wave propagation in both horizontally and vertically inhomogeneous media need to be combined. This paper describes the results of simulations which have predicted spatial and temporal variations in the refractive index. These results are employed in calculations of electromagnetic propagation in inhomogeneous environments. Thus, a methodology is introduced to study radar coverage voids, range height errors and anomalous clutter in a maritime coastal environment.

## BOUNDARY LAYER ALTERATION OF ELEVATED DUCTS

In a coastal region, thermal and mechanical effects can influence the tropospheric circulation and distribution of moisture, thereby affecting the electromagnetic index of refraction. Important mesoscale meteorological flows of concern are the land and sea breezes. The land and sea breezes are phenomena generally experienced when the land is subjected to considerable heating, and a large temperature differential develops between land and water. The juxtaposition of contrasting thermal environments results in the development of horizontal pressure gradient forces that, if sufficient to overcome the retarding influence of friction, will cause air motion across the boundary between the surfaces. The driving force behind the land and sea breeze circulation system is the contrasting thermal response of land and water surfaces to the solar heating cycle.

The land-water temperature differences and their diurnal reversal (by day, land warmer than water; at night, land cooler than water) produce corresponding land-water air pressure differences. These differences in turn result in a system of breezes across the shoreline that reverses its direction between day and night. The daytime sea breeze circulation has a greater vertical and horizontal extent, and its wind speeds are higher than those in the nocturnal land breeze. During the sea breeze, the cooler and more humid sea air advects across the coast and wedges under the warmer land

air. The advancing sea breeze front produces uplift in what is already an unstable atmosphere over the land. The stable marine air is warmed over the land, producing a more unstable internal boundary layer that grows in depth with time and distance from the shore. The nature of uplifting of anomalous refractive layers can be visualized with the aid of Figure 1, which is a stylized representation of the daytime sea breeze condition. The curves illustrate the spatial change of the internal boundary layer whose height grows slowly with inland distance. The height of the boundary layer,  $H_B$ , can be calculated at each horizontal position,  $x$ , from the formula

$$H_B = z_2 [0.75 + 0.03 \ln(z_1/z_2)] (x/z_2)^{0.8} \quad (1)$$

where  $z_1$  and  $z_2$  are the upwind (water) and downwind (land) surface roughness lengths, respectively.<sup>1</sup> This is an empirical relationship that has been found to be in reasonable agreement with measurements at various locations worldwide. As air passes from one surface type to a new and meteorologically different surface, it must readjust itself to a new set of boundary conditions. Therefore, two boundary layers are shown in Figure 1: Layer A for the sea-land surface transition, and Layer B for the

sand-mountain surface transition. Boundary Layer A uses  $z_1 = 10^{-3}$  centimeters (water) and  $z_2 = 5 \times 10^{-2}$  centimeters (sand) and  $z_2 = 10$  centimeters (mountains).

The computed variations in the index of refraction caused by the atmospheric layers are illustrated in Figure 1 as vertical profiles of  $M$ . At Position 1, the presence of an elevated duct is indicated by the negative gradient of  $M$  and the local minimum  $M$  value at a height of about 700 meters. By the time the sea breeze penetrates 100 kilometers inland, the boundary layer uplifts the elevated duct to 1400 meters for Boundary Layer A, or to 1800 meters for Boundary Layer B. Precisely which boundary layer applies is open to question because of the stylized nature of this  $M$  data extrapolation. Figure 1 is used here only for illustrative purposes. Nevertheless, it is clear that electromagnetic wave propagation (e.g., from a site at 2000-meter elevation in the mountains [Position 4] looking out to sea) can be complicated by horizontal as well as vertical inhomogeneities in refractivity. A method to compute electromagnetic propagation in such an environment is described below.

#### THE PARABOLIC APPROXIMATION FOR INHOMOGENEOUS PROPAGATION

When inhomogeneities in the dielectric constant are considered as varying both in the vertical and horizontal directions, Maxwell's equations for propagation in the troposphere are generally non-separable and difficult to solve analytically. Cho and Wait<sup>2</sup> have approached this problem numerically via coupled mode analysis using a cylindrical earth model and an infinite line source; horizontal inhomogeneities are considered by assuming horizontally piecewise uniform media. Modal analysis tends to be difficult with computer cost limiting convergent answers to simple refractive changes.

A well-known approximation, the "parabolic approximation", was obtained by Leontovich and Fock in 1946<sup>3</sup> for propagation in a vertically inhomogeneous, horizontally homogeneous atmosphere over a spherical earth. An extension of this approach for a horizontally and vertically inhomogeneous atmosphere has been made<sup>4</sup>; this begins with the spherical earth geometry shown in Figure 2. The inhomogeneities in the atmospheric dielectric constant,  $\epsilon$ , are modeled in terms of variations in the radial and polar angle directions,  $\epsilon = \epsilon(r, \theta)$ . Azimuthal symmetry in  $\epsilon$  is assumed about the origin of the field situated at the pole. The consequence of assuming azimuthal symmetry is that the variations in the atmospheric dielectric constant are limited to two dimensions; in a practical sense this assumption greatly simplifies the mathematics. In the geometry shown in Figure 2, the source field is assumed to originate from a raised vertical electric dipole (VED) situated at the pole; this assumption also is for mathematical simplification. The resultant approximate equation governing propagation, however, will be the same if a vertical magnetic dipole (VMD) source were assumed; only the boundary conditions to be satisfied at the earth's surface will differ.

Because of the VED source and the assumed symmetries, only the vector field,  $\vec{E}_r$ ,  $\vec{E}_\theta$ , and  $\vec{H}_\phi$  exist. One a scalar equation for the magnetic field,  $H_\phi = H(r, \theta) \hat{e}_\phi$ , by combining Maxwell's equations to eliminate the electric fields:

$$-\nabla \times \nabla \times \vec{H} + \omega^2 \mu \epsilon \vec{H} = -\frac{\nabla \epsilon}{\epsilon} \times (\nabla \times \vec{H}). \quad (2)$$

The magnetic permeability,  $\mu$ , is constant, and the electric field can be obtained similarly. Generally, one is interested in examining variations in the fields which are relatively long compared to wavelength. One expects that along the earth's surface in the horizontal direction from the source, the fields will oscillate like  $e^{iks}$  (where  $k$ , the wavenumber, equals  $2\pi/\lambda$ ). A convenient substitution that factors out rapid oscillating behavior as well as large variations near the source (a linear trend in radius) is obtained in terms of an attenuation function  $U(r, \theta)$  defined by

$$H(r, \theta) = \frac{U(r, \theta)}{r} \sin \theta^{-1/2} \epsilon^{-1} e^{ik_0 a \theta}. \quad (3)$$

Here  $k_0^2 = \omega^2 \mu \epsilon(a, 0) = \omega^2 \mu \epsilon_0$  is the square of the electromagnetic wavenumber of the earth's surface,  $r = a$ .

A good deal of mathematics ensues as Equations (2) and (3) are combined into a propagation equation for  $U(r, \theta)$ , which is an elliptic differential equation in the horizontal and vertical directions. A first approximation to this equation may be obtained for typical variations of  $\epsilon$  in the troposphere, where gradient scale lengths are long compared to a wavelength. Then  $U(r, \theta)$  is found to a good approximation to be given by

$$\frac{\partial^2 U}{\partial h^2} + \frac{2ik_0}{a} \frac{\partial U}{\partial \theta} + k_0^2 \left[ \frac{\epsilon(h, \theta) - \epsilon_0}{\epsilon_0} + \frac{2h}{a} \right] U = 0. \quad (4)$$

This is a parabolic differential equation that is second order in the vertical direction and first order in the horizontal direction.

In obtaining Equation (4), the radial coordinate has been transformed into  $h = r - a$ , where  $h$  is the height above the earth's surface. The effect of the atmospheric inhomogeneities are contained in  $\epsilon(h, \theta)$ . If the horizontal direction along the earth's surface is defined as  $s = a\theta$ , Equation (4) can be thought of as representing propagation above a flat earth. The effect of a spherical earth is accounted for by an effective linear gradient in the index of refraction,  $2h/a$ ; this approximation, using a linear gradient, is good for tropospheric altitudes  $h \ll a$ . The treatment of a spherical earth by means of a linear gradient is conveniently handled by converting the refractivity index,  $N$ , into the modified refractivity index,  $M$ , defined as:

$$M = N + 0.157h, \text{ where } h \text{ is in feet.} \quad (5)$$

The conditions that must be satisfied so that the original elliptic equation may be approximated by the parabolic Equation (4) are summarized as follows:

$$\begin{aligned} (a) \quad & \frac{1}{\epsilon} \frac{\partial \epsilon}{\partial s} \leq 10^{-2} k_0, & (b) \quad & \theta > 10^2 (k_0 a)^{-1}, \\ (c) \quad & k_0 a \frac{\partial U}{\partial \theta} \gg \frac{\partial^2 U}{\partial \theta^2}, & (d) \quad & \frac{1}{\epsilon} \frac{\partial \epsilon}{\partial h} \ll \left[ \frac{2k_0^2}{a} \right]^{1/3}. \end{aligned}$$

If one associates  $\epsilon \left| \frac{\partial \epsilon}{\partial s} \right|$  and  $\epsilon \left| \frac{\partial \epsilon}{\partial h} \right|$  with the radii of curvature of rays resulting from horizontal and vertical variations in  $\epsilon$ , then Conditions (a) and (d) require that these radii be large compared with a wavelength. That is, the horizontal and vertical variation in  $\epsilon$  must be reasonably slow; for situations of interest in this article, this requirement holds. Condition (b) implies that reasonable values will be obtained for distances greater than 100 wavelengths from the source. Finally, Condition (c) requires that the propagation be relatively oblique; that is, that rays be launched with low grazing angles ( $\lesssim 20^\circ$ ).<sup>5</sup>

Solutions to the parabolic equation will be obtained if the initial source field is specified and the values of the field at the earth's boundary surface and ionosphere are properly defined. For simplicity, a nonreflecting or fully absorbing boundary is assumed at the ionosphere. For the surface boundary conditions, a smooth-conducting earth is assumed; further, it is reasonable to assume that the skin depth of radiation within the earth is small compared to the earth's radius of curvature. In that case, the earth's curvature can be ignored and Leontovich's impedance boundary condition<sup>6</sup> may be applied. If  $\eta_s$  is the complex dielectric constant of the earth, the boundary condition on  $U(r, \theta)$  will be satisfied for a VED if

$$\frac{\partial U}{\partial r} + \frac{ik\epsilon_s}{\sqrt{n_s}} U = 0, \text{ at } r = a. \quad (6)$$

For a VMD source, the boundary condition on  $U(r, \theta)$  will be

$$\frac{\partial U}{\partial r} + ik \sqrt{n_s} U = 0, \text{ at } r = a. \quad (7)$$

Practically speaking, vertical symmetric and antisymmetric solutions for  $U$  above the surface must be combined to satisfy either Equation (6) or Equation (7). However, if the earth's surface is approximated by a perfect conductor, Equations (6) and (7) reduce to the requirement that either  $\partial U / \partial r = 0$  (VED) or  $U = 0$  (VMD) at the surface. In those cases, one need obtain only symmetric (VED) or antisymmetric (VMD) vertical solutions about the surface, and these boundary conditions are automatically satisfied.

A number of numerical techniques exist for solving the parabolic equation. One technique that uses the computation speed of the Fast Fourier Transform is the split-step Fourier algorithm developed by Hardin and Tappert. The basis of the split-step algorithm is illustrated in Figure 3. A source field that satisfies the appropriate boundary condition is assumed to be known as a function of altitude,  $h$ , at an initial range step,  $s_0$ . An approximate solution to the parabolic equation for all altitudes,  $h$ , at a greater range,  $s_0 + \Delta s$  may be generated by first obtaining the Fourier transform,  $\psi(p, s)$ , of the source field distribution in the vertical direction,  $h$ , with the assumption that the effective propagation constant  $k$  is relatively constant over a small step size:

$$-p^2 \psi + 2ik_0 \frac{\partial \psi}{\partial s} + k^2 \psi = 0. \quad (8)$$

Equation (8) is first order in the horizontal direction and is exact if  $k$  is constant. For  $k$  varying, an updated, approximate solution to the field at  $s_0 + \Delta s$  is obtained by an inverse Fourier transform where the variation in the propagation constant is applied outside the inverse transform:

$$\psi(h, s_0 + \Delta s) = e^{ik\Delta s/2} \text{FT}^{-1} [e^{-i\Delta s p^2/2k_0} \psi(p, s_0)], \quad (9)$$

where  $p$  is the transform variable. This procedure is illustrated in Figure 3. The error in this approximate solution varies to some power of the step size, and stable solutions are obtained with stability generally depending on step size. The solution for the fields for arbitrary ranges are obtained in an identical manner for each step by using the field solution at each new range step as the initial condition for generating the solution at the subsequent range step. For this numerical solution, two Fast Fourier Transforms are required for each step.

A computer program called EMPE (Electromagnetic Parabolic Equation) has been developed based on these principles to allow propagation loss to be computed in horizontally and vertically inhomogeneous atmospheres. Predictions for anomalous wave behavior have been made for frequencies from 100 MHz to 10 GHz. Vertical profiles of refractivity are entered at any distance downrange from the antenna. Each refractivity profile may be of arbitrary complexity. Antenna parameters such as beam pattern, beamwidth, and elevation angle are stipulated as required. Various computer output plots and tables give the propagation loss.

#### ELEVATED DUCTING LAYERS

An example of this computation is given in Figure 4 which is a coverage diagram of transmission loss in dB relative to one meter, geometrically plotted in range-height coordinates. The legend for these types of diagrams is given as

dB	70	80	90	100	110	120
Symbol	●●●●	****	XXXX	++++	....	

and the 90-dB levels are outlined for the sake of comparison with other cases. An antenna at 7200 ft. height with zero degree elevation angle, two-degree vertical beamwidth, horizontal polarization, and  $\sin x/x$  pattern is used at 600 MHz to propagate into a standard atmosphere. The earth's surface is perfectly conducting. General

features which are clearly visible are the antenna pattern,  $r^{-2}$  loss away from the antenna, and constructive and destructive interference patterns caused by energy reflected off the earth's surface. Note the clearly visible regions outside the antenna beamwidth and the over-the-horizon shadow region.

Figure 5 gives the coverage diagram for a more complex situation. Here, the same antenna is now propagating into a situation closely mimicking the tropospheric conditions of Figure 1: a curving elevated duct. Initially, over the antenna position, the elevated duct is above the antenna at a height of 7400 ft., drops to a height of 2200 ft. at a range of 64 nm, and remains at 220 ft. to beyond 250 nm range. The initial M deficit for the elevated duct over the antenna position is 136 M units. Figure 5 shows that large continuous voids (120 dB), not formerly present in the standard atmosphere case, are located near the antenna just above the elevated duct, and at increasingly higher elevations away from the antenna, even above the normal line-of-sight. Thus, severe compromises in vertical coverage, not predicted by homogeneous propagation calculations, are revealed.

A comparison of EMPE calculations with elevated duct propagation measurements reported in Kerr is shown in Figures 6 and 7. The measurements were performed in 1944 by the Naval Electronics Laboratory at San Diego. Transmitters at 100 ft. were used at wavelengths of 4.8 m and 1.8 m, and 57 cm and 9 cm. The horizon is 10.6 nmi in this case. Vertical profiles from the surface to 500 ft altitude were taken out to distances of 124.3 nmi. Figures 6 and 7 show that the elevated M inversions taken on

two days of interest are horizontally inhomogeneous. In Figure 6, the inversion has the nature of an elevated duct near the transmitter but changes to a surface duct 70.4 nmi downrange. Linear interpolation of the M-profiles at ranges between these shown is used for the EMPE calculations. In Figure 6, the data clearly show trapped energy in the shadow region beyond the horizon. At 32.2 nmi, there is excellent agreement between the EMPE calculations and the measurements. Further interpretation is not warranted here because of the uncertainty in the antenna beamwidth, and the exact M-profile structure. In Figure 7, the elevated inversion retains an elevated duct structure downrange from the antenna. Given these above uncertainties, there is still a predicted concentration of energy about the duct elevation at 57 cm wavelength. Generally, however, there is less agreement between EMPE and the measurements in this case.

#### SURFACE DUCTING

An extensive series of propagation loss measurements in the surface duct environment were performed by the Naval Research Laboratory at Antigua, British West Indies in the Spring of 1945. Wavelengths of 3 and 9 cm were used with transmitters at 16 and 46 ft on a tower at water's edge.<sup>9,10</sup> If the reported M-profile with a duct height of about 50 ft is considered horizontally homogeneous, the resultant EMPE coverage diagram is displayed in Figure 8. Here the 3-cm energy is clearly trapped and ducted to great range. Note that a steady falloff rate with range is predicted for elevations near the surface, but that undulations are clearly seen at heights of about 40 ft and higher. An example of how the complexion of coverage can change with a horizontally inhomogeneous surface duct is shown in Figure 9. The original surface duct height is allowed to diminish at a rate of 0.49 ft/nm out to a range of 45 nm, when it is thereafter held constant at a height of 30 ft. The surface M value is reduced at a rate of 0.17 M/nm out to 150 nm in accordance with our boundary layer modeling procedures.<sup>11</sup> This progressively weaker duct allows energy to be trapped initially near the antenna, but duct leakage is seen away from the surface downrange. Note in comparison to Figure 8, that the 90-dB level extends to only 100 nmi near the surface, and that packets of 90 dB energy are found above the duct up to 100 ft altitude. In the duct beyond 100 nmi a faster falloff of energy is seen to exist in Figure 8 near the surface than in the homogeneous duct case. Also, at heights of about 100 ft., larger undulations in energy are seen. The difference in falloff rates between the homogeneous and inhomogeneous ducts can be seen with the aid of Figure 10 for the heights of 30 and 100 ft. Clearly, the falloff rate varies according to the type of duct environment present and the height chosen for examination.

EMPE results are compared with the measured Antigua data at the 3 cm wavelength in Figure 11. The data taken on 8 days from the 16 ft. transmitter to 14 ft. receiver are shown as dots in this figure. The difference in falloff rates computed by EMPE are shown for the standard atmosphere, homogeneous duct, and inhomogeneous duct cases. The free-space falloff rate is also shown. At ranges out to 50 nmi, both duct types seem to give EMPE results which are favorable with the data. However, beyond 50 nmi, the EMPE result for the inhomogeneous duct gives a distinctively better agreement than the homogeneous duct result. Data for the 9-cm wavelength measurements are shown in Figure 12 for the 46-ft transmitter and 94-ft receiver. Again, the EMPE result for the inhomogeneous duct model derived from the original M-profile gives the better agreement. Figures 11 and 12 demonstrate the importance of inhomogeneous duct modeling capabilities when analyzing actual ducting situations. They show the necessity for detailed meteorological measurements when scientific analysis is required for propagation loss investigations.

#### SUMMARY

Several important aspects of behavior in the anomalous environment are predicted and given in analyzable form by the EMPE approach:

- Specific values for propagation loss are given everywhere, particularly in surface or elevated ducts. Transmitters may be of any beamshape. The refractivity profiles may be range-dependent and of arbitrary complexity.
- Peculiar downrange behavior is allowed for horizontally inhomogeneous situations. For example, rays not initially trapped can be trapped downrange; energy can leak out of surface or elevated ducts; initially trapped rays can "burn" out of a duct.
- Excessive energy can be observed to be diverted away from normal coverage areas, resulting in coverage holes and/or and excessive clutter.
- Situations can be analyzed for antennas within or far away from anomalous refractive layers.
- The code allows computation to be usually accomplished in a few minutes giving the promise of a near-real-time analysis or predictive capability.

Presently, the EMPE approach is providing great insights for the behavior of electromagnetic systems under anomalous propagation conditions. The results are used to illustrate a variety of problems which impact technical design, tactical planning, and operational procedures. Future improvements to the EMPE code will allow a wider variety of analysis products to be made available, and an enhanced understanding of complex situations to be accomplished.

#### REFERENCES

1. Elliot, W. P., "The Growth of the Atmospheric Internal Boundary Layer," Trans. Amer. Geophys. Union 39, 1048, (1958).
2. Cho, S. H., and J. R. Wait, "Analysis of Microwave Ducting in an Inhomogeneous Troposphere," Pure Appl. Geophys., 116, 1118, (1978).
3. Leontovich, M. A., and V. A. Fock, "Solution of the Problem of Propagation of Electromagnetic Waves Along the Earth's Surface by the Method of Parabolic Equation," J. Phys. of U.S.S.R., 10, 13, (1946).
4. Sari, J. W. and R. I. Joseph, "Tropospheric Propagation of Radiation in an Inhomogeneous Stratified Atmosphere," National Radio Science Meeting, Boulder, Colo. (14 January 1982).
5. McDaniel, S. T. "Propagation of Normal Modes in the Parabolic Approximation," J. Acous. Soc. Am. 57, 307 (1975).
6. Leontovich, M. A. "On the Approximate Boundary Conditions for an Electromagnetic Field on the Surface of Well-Conducting Bodies," Investigations of Propagation of Radio Waves, B. A. Vedensky, ed. Academy of Science, Moscow, U.S.S.R (1948).
7. Hardin, R. H. and F. D. Tappert, "Application of the Split-Step Fourier Method to the Numerical Solution of Nonlinear and Variable Coefficient Wave Equations," SIAM Rev. 15, 423 (1973).
8. Kerr, D. E., ed. "Propagation of Short Radio Waves," McGraw Hill, New York, (1951) pp. 382-385.
9. Katzin, M., R. Bauchman, and W. Binnian "3 and 9 Centimeter Propagation in Low-Ocean Ducts," Proc. IRE, 35, 891 (1947).
10. Pekeris, C. L. "Wave Theoretical Interpretation of Propagation of 10-cm and 3-cm Waves in Low-Level Ocean Ducts," Proc IRE, 35, 453, (1947).
11. Burk, S. D., "Boundary Layer Response and Refractive Index Behavior Near Sea Surface Temperature Gradients" Second Conference on Coastal Meteorology, The American Meteorological Society, January 30th, February 1st 1980, Los Angeles, CA.

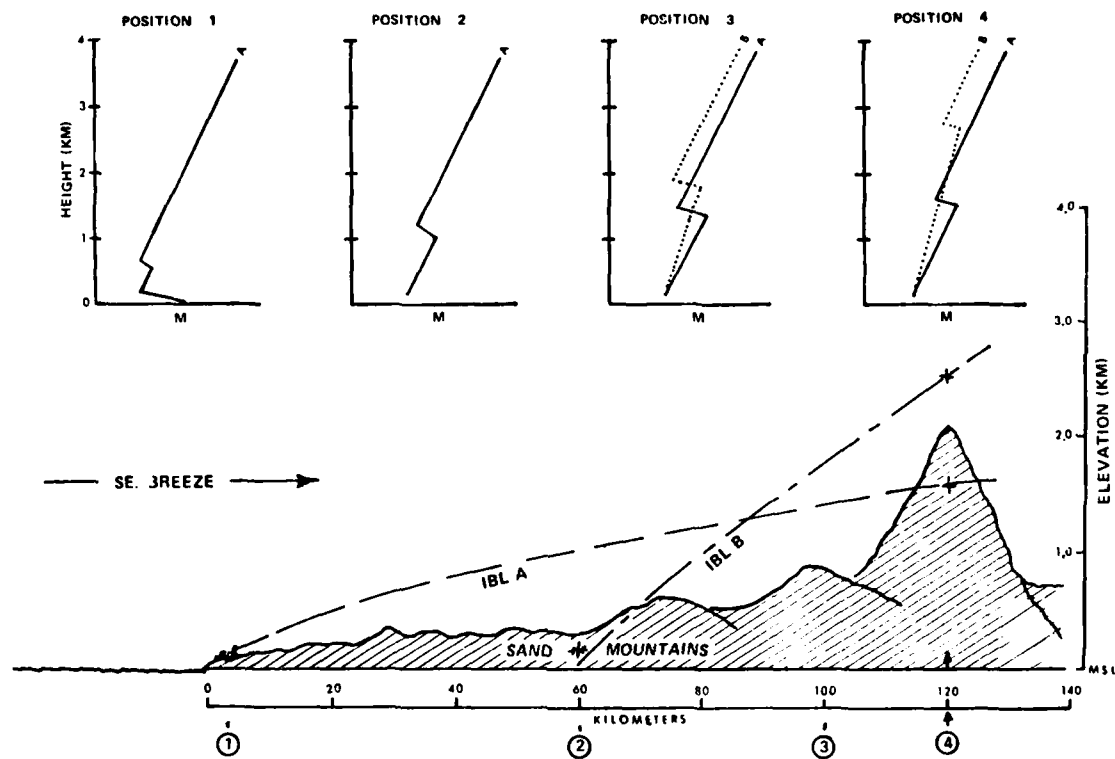
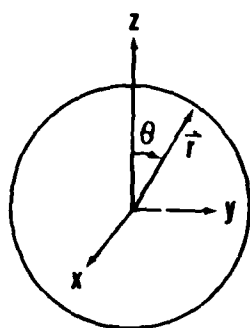


Figure 1  
Boundary Layer Alteration of Elevated Ducts

FIGURE 2

Coordinates for the EMPE Formulation

# SPHERICAL EARTH-VERTICAL ELECTRIC DIPOLE GEOMETRY

VED AT  $\theta = 0$ ,  $h' = r' - a$  $\epsilon = \epsilon(r, \theta)$ 

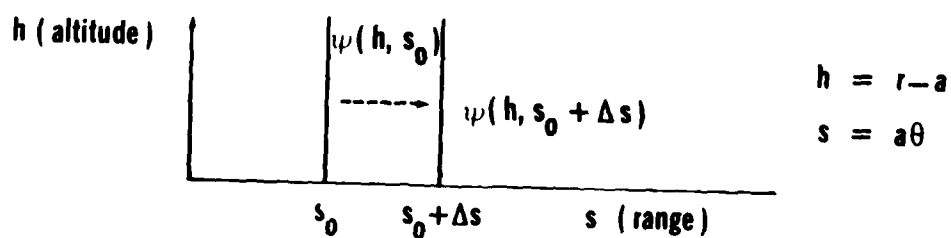
AZIMUTHAL SYMMETRY

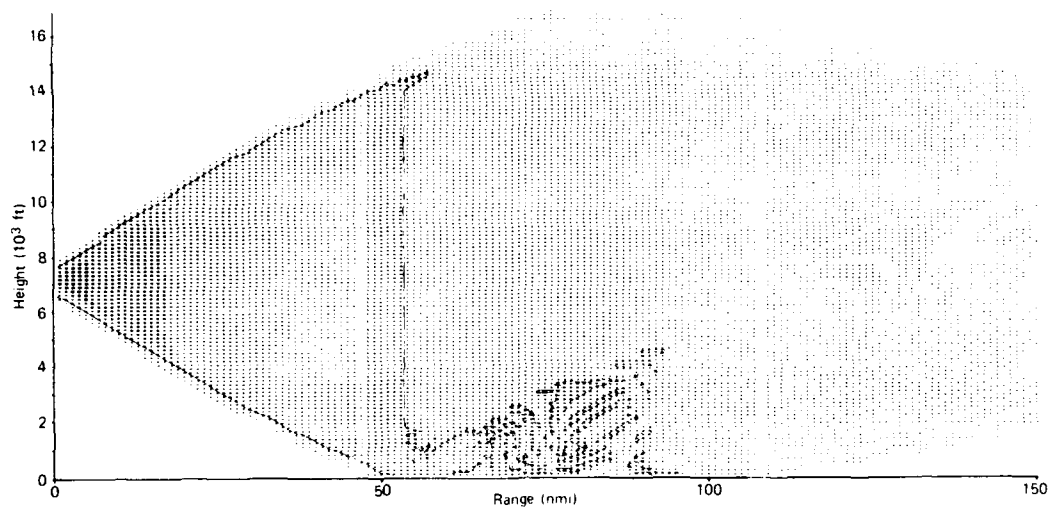
 $E_r, E_\theta, H_\phi$ 

Figure 3

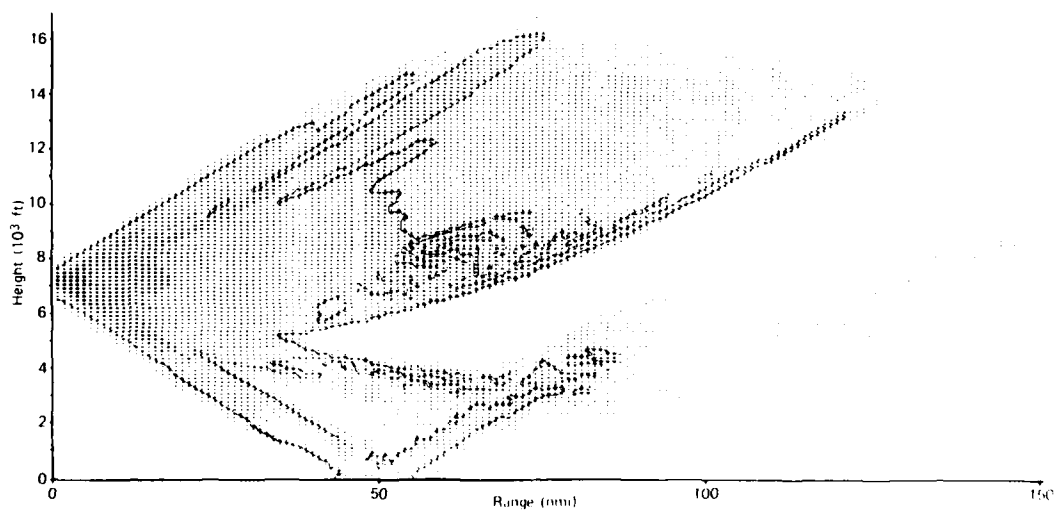
EMPE Split-Step Computation

# SPLIT STEP ALGORITHM





Coverage for Standard Atmosphere  
Figure 4



Coverage for Warped Elevated Duct  
Figure 5

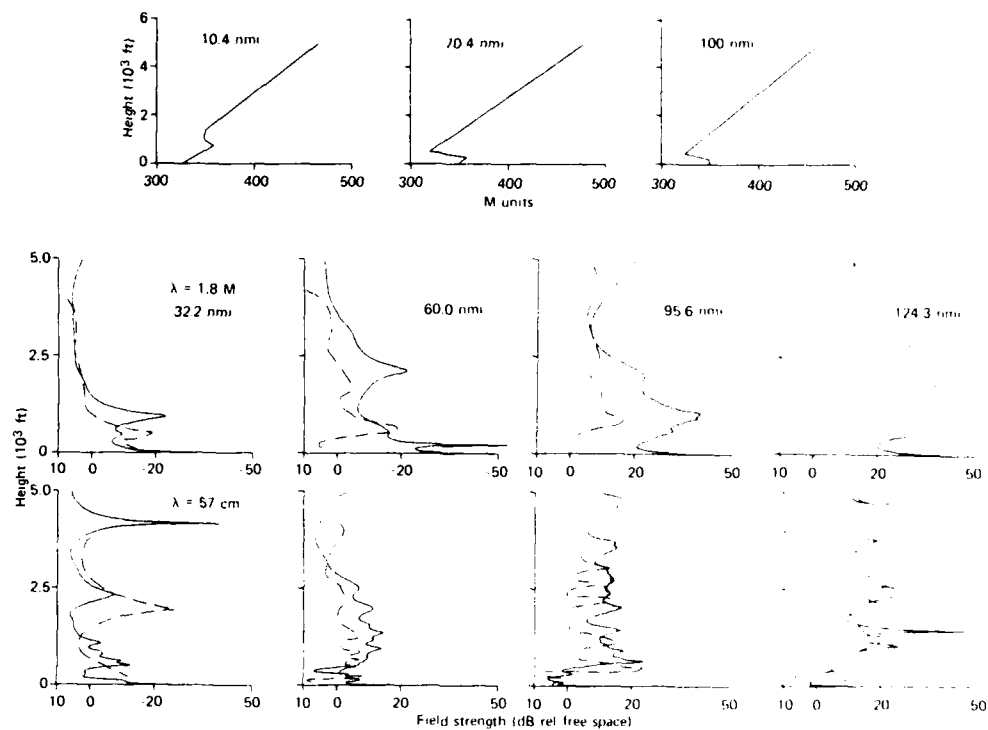


Figure 6  
EMPE Comparison to Elevated-Surface Duct Measurements

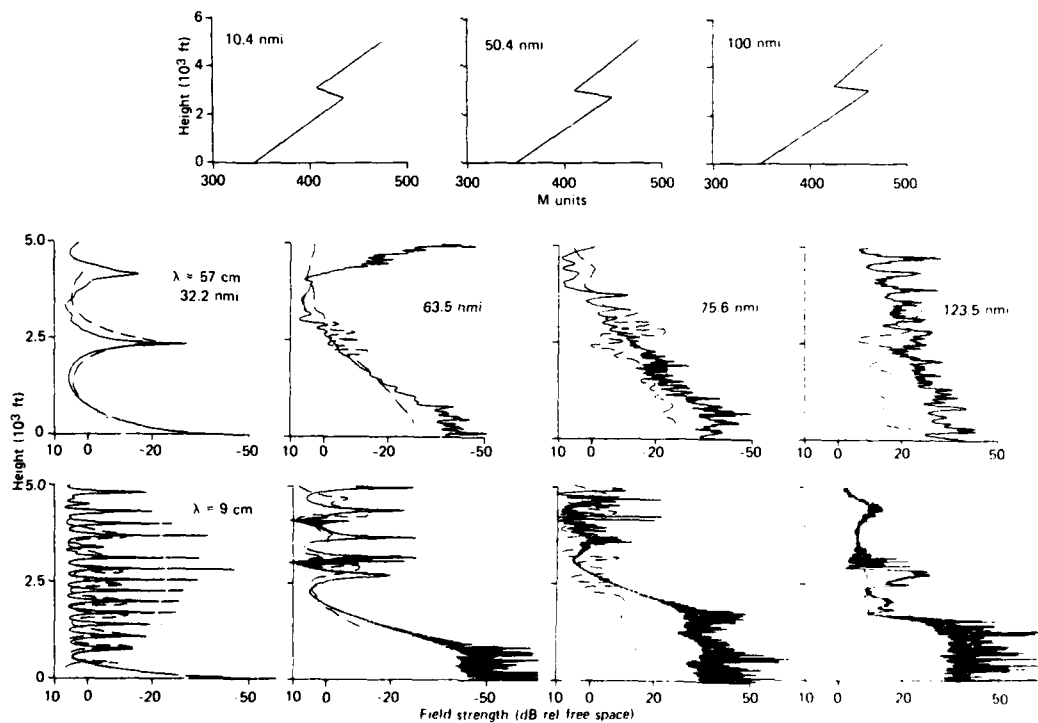
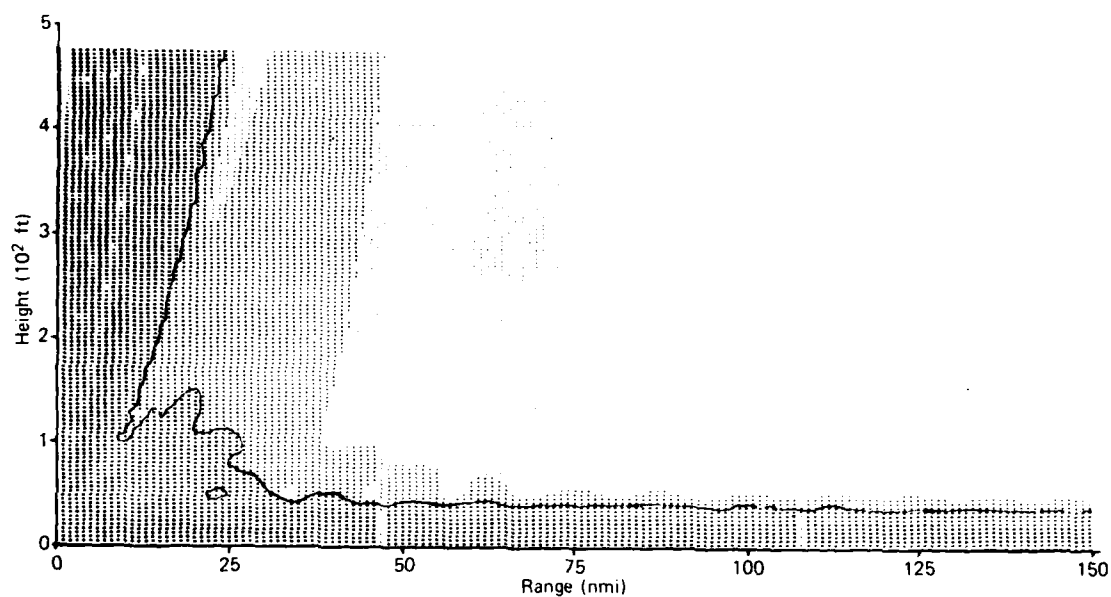
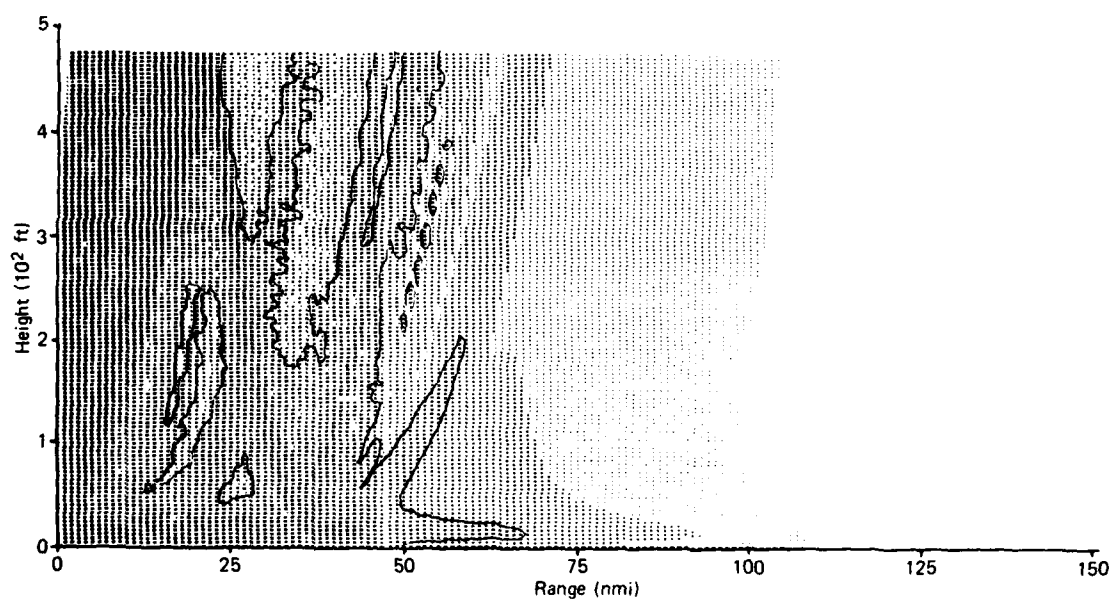


Figure 7  
EMPE Comparison to Elevated Duct Measurements



Coverage for Homogeneous Surface Duct  
Figure 8



Coverage for Inhomogeneous Surface Duct  
Figure 9

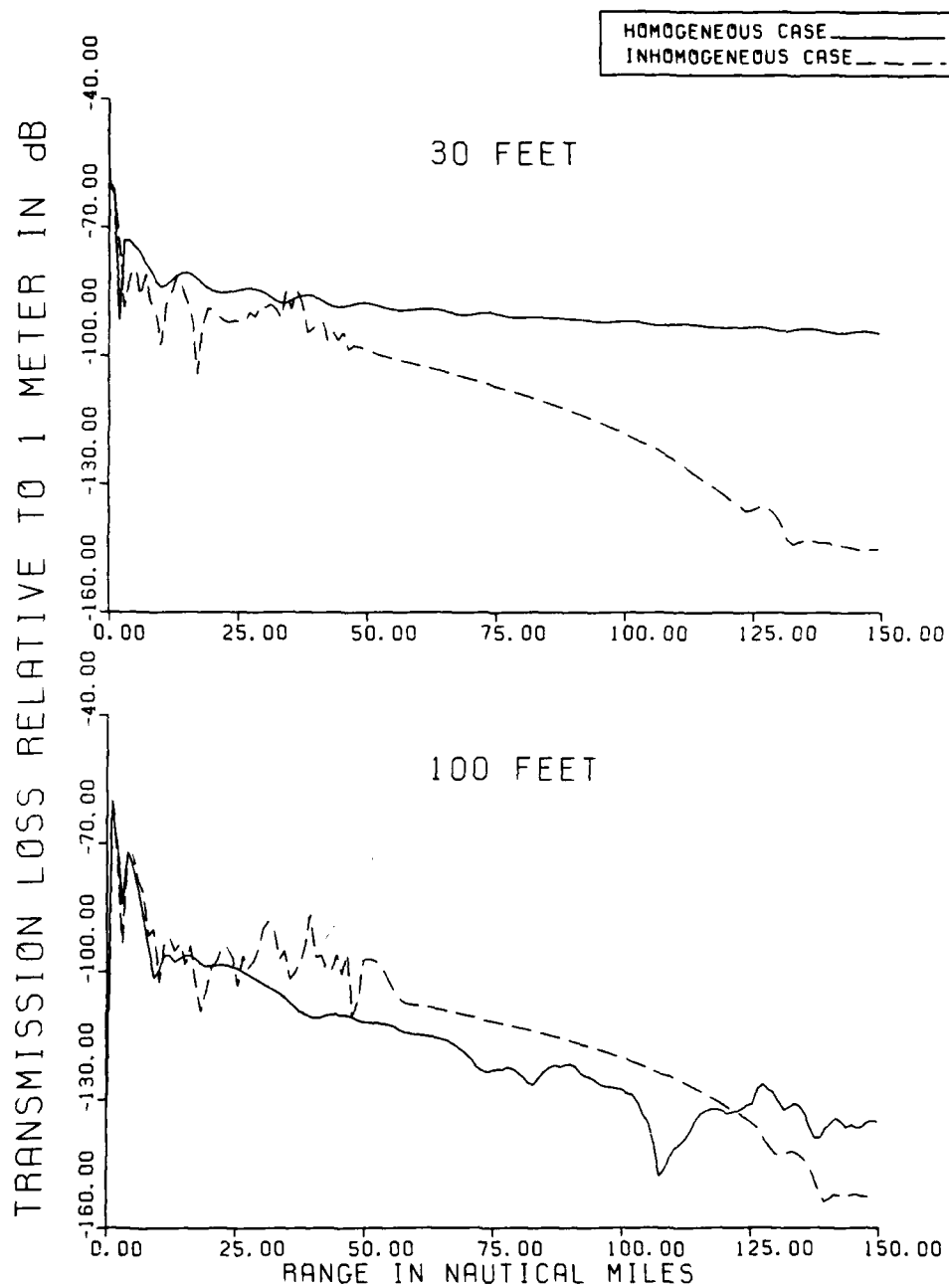
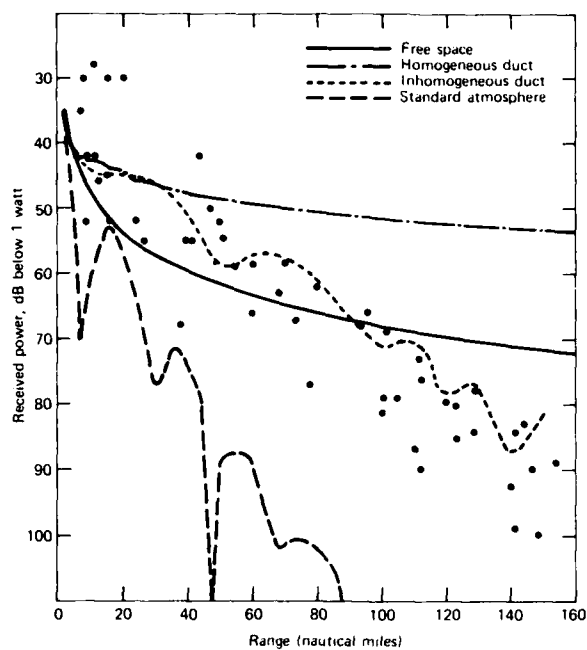
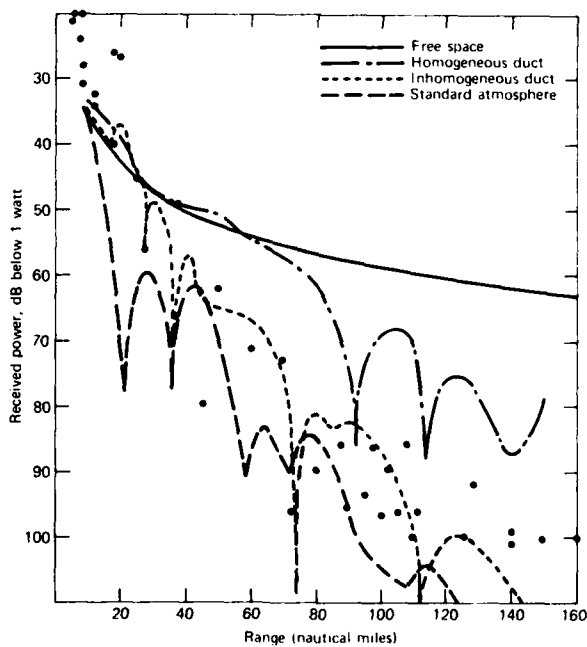


Figure 10  
Falloff Rates for Different Surface Duct Types



EMPE Comparison to X-Band Surface Duct Measurements  
Figure 11



EMPE Comparison to S-Band Surface Duct Measurements  
Figure 12

## DISCUSSION

S. Rotheram (U.K.): I have some queries about the algorithms used in this very interesting work. How does it relate to the parabolic equation methods used in underwater acoustic propagation over the last 15 years, e.g., Tappert's split step algorithm or the work of McDonald? How are the boundary conditions at the earth's surface handled? Can rough surface effects be included? How big is the computer code, and what are typical run times?

H.W. Ko (U.S.): This method is analogous to the acoustic parabolic methods. In fact, the parabolic equation acoustic code had its origins in work which described electromagnetic propagation through the ionosphere. At the present time, our boundary is perfectly conducting and smooth. We will shortly incorporate finitely conducting boundaries. Within one year we will also incorporate a rough surface.

K.D. Anderson (U.S.): 1) From the Antigua measurements, did you have any data to calculate the evaporation duct with respect to range, or did you model the structure?

2) The so-called "radar hole" does not seem to be observed in measurements. Do you have any comments?

H.W. Ko (U.S.): 1) Meteorological data were supplied from only one station near the transmitter. Therefore we used our modelling procedures to obtain different N profiles down-range.

2) At X-band, our results show a large hole for the homogeneous duct. However, when the inhomogeneous duct is used, the hole is filled. At S-band, virtually no hole was seen for either homogeneous or inhomogeneous ducts.

J.W. Sari (U.S.): This is only a comment. With regard to K.D. Anderson's comment that there seems to be a lack of very deep propagation loss above surface ducts, this lack may be the result of scattering from a rough sea surface. At the present time, our code does not include rough surface scattering. Presumably, our current predictions of large propagation losses will be modified when a rough surface is included.



THE PREDICTION OF FIELD STRENGTH IN THE FREQUENCY  
RANGE 30 - 1000 MHz

R.S. Sandell and D.W. Taplin  
British Broadcasting Corporation  
Research Department  
Kingswood Warren  
Tadworth  
Surrey KT20 6NP

SUMMARY

The BBC is reviewing the results of its past propagation experiments and survey measurements with the aim of refining its prediction methods, hence the data which formed a substantial contribution to Recommendation 370 of the CCIR are being re-examined. This paper reveals the problems facing the review. It refers to the background of the BBC's involvement in propagation measurement at VHF and UHF. Weaknesses in the original data are discussed with a view to improving specifications for future work. The accuracy of prediction is related to the accuracy of measurement as illustrated by an experiment dating to the development period of an interim BBC prediction method for UHF, and the accuracy of the current path loss prediction method is discussed. Possible directions of future development in prediction methods are indicated and the objectives of the BBC's research in this area are outlined.

1. INTRODUCTION

Efficient allocation of the radio spectrum for communication depends upon the accuracy of field strength prediction. Comprehensive measurements designed to investigate a particular propagation path must be the best evidence for planning, but for complete radio systems - such as a network of broadcasting stations - the amount of work needed to determine transmitter frequencies and operating characteristics prohibits such an approach. The service area of a broadcast station, which may have a range of up to 100 km, can be determined by measurement, but the effects of interference from distant stations, often involving the assessment of fading signals over long propagation paths, must be predicted. Internationally adopted techniques, such as those which form CCIR Recommendation 370 (CCIR, 1982) therefore provide an essential basis for planning. They are simple to use, a considerable asset in often complex international negotiations, and it is a tribute to this particular Recommendation that it has been in extensive use for planning purposes throughout the World for over 20 years.

There are, however, two reasons for questioning the continued use of Recommendation 370 in its present form - a series of propagation curves used in conjunction with various correction factors. Firstly, there is criticism about some of the corrections. Shortcomings in this regard are partly due to the fact that originally there was inadequate measurement evidence upon which to base a comprehensive prediction system, and as information has emerged over the years various ad hoc solutions have been adopted to fill the gaps. Secondly, the rapid development of computer systems over the past thirty years has provided the means whereby more intricate field strength calculations can be undertaken. Because such methods can take account of the unique features of each propagation path they offer much greater accuracy than can be achieved using statistical propagation curves. Of course, the full realisation of such techniques demands a great deal of data, and there are many barriers to be overcome before they could be adopted internationally. Nevertheless, the benefits are considerable, and they must be taken into account.

For many years the Research Department of the BBC has been active in propagation work, particularly concentrating on frequencies within the range 30 - 1000 MHz, which have been extensively developed for broadcast services since 1946. A great many field strength measurements have been made, some of them forming part of research studies designed to obtain propagation statistics, others made in the course of planning and operating the BBC's transmitter networks. In the case of the propagation studies, there was intensive activity in the period prior to the ITU Conference held in Stockholm in 1961, at which the European plans for broadcasting in the VHF and UHF bands were agreed (ITU, 1961). Evidence from the BBC propagation experiments and from other United Kingdom authorities (Jowett, Meadows, Rowden, 1963) formed a significant contribution to the technical data used at the Conference, and the propagation curves then produced subsequently formed the basis of CCIR Recommendation 370 (CCIR, 1961). It was clear, however, that these curves could only provide a first estimate of field strength values - adequate for the all-important international negotiations. More precise methods would be needed, and the BBC intensified its research into the subject. The importance of the project was emphasized in 1964 by the introduction of the UHF television service in the U.K. It looked as though this would need something like 1000 transmitting stations if national coverage was to be achieved, and each would be required to transmit four programmes. In view of the fact that the Stockholm Plan contained provision for only 64 U.K. high-power stations, it was apparent that the frequency planning problems were going to be severe. In due course a satisfactory computerised technique was developed, and it has now been in use for many years. As a result of its introduction the UHF network in the U.K. now covers more than 99% of the population, the total of stations so far being 660.

Throughout the decade following the Stockholm Conference propagation studies by the BBC were continued, and although these concentrated upon UHF work, with specific reference to mixed path calculations, several VHF tests were also conducted. In the case of the lower frequencies, there has been a growth of interest over the last five years or so, as attention has turned to developments in VHF/FM radio broadcasting and the growth of mobile radio systems. Some of the results obtained from this work have been fed back into Recommendation 370 through the appropriate CCIR study groups, but much analysis still remains to be done.

This paper discusses the accuracy of field strength prediction, with particular reference to the two distinct techniques - statistical curves and path loss calculations. It seems likely that for many years there will be a demand for both types, and the scope for improvement needs to be thoroughly explored. With this objective the paper surveys the contribution so far made by the BBC, and it reports on the development of the BBC prediction program. It outlines a programme of work which is now in progress intended both as a contribution to the improvement of Recommendation 370 and to allow further refinement of the computer prediction.

## 2. THE ACCURACY OF PREDICTION

The advantage of defining broadcasting coverage in terms of field strength is that it provides a quantitative basis for planning work. From subjective tests the minimum values needed to provide a satisfactory service can be defined, together with the protection ratios required to avoid interference from other stations. The relationship between field strength and the standard of service enjoyed by various proportions of the population can then be estimated (Sandell, 1969), but of course the actual situation is likely to be significantly different. Precise statements about field strength values which have been measured using a good receiving aerial mounted at 10 m a.g.l. may bear little relationship to what is actually obtained by a viewer or listener who has a less-than-efficient aerial indifferently mounted at some other height. For this reason detailed knowledge of the local variation of field strength is valuable, but this cannot be obtained with conventional measurement work carried out under normal circumstances. Even a very detailed measurement programme intended to survey coverage is unlikely to make more than 20 observations per square kilometre in a built-up area, an area which may ultimately contain several hundred domestic receiving aeriels. The situation is even more complex, of course, when mobile receivers need to be considered.

With what accuracy, therefore, can field strength at a point in space be estimated? Certainly, precise definition of the standing wave pattern is impracticable. This variation, which arises when the receiving aerial is moved through a small distance is caused by reflections from surrounding surfaces which contribute in-phase or out-of-phase components to the direct signal, which itself is fluctuating due to the effect of local obstacles in the propagation path. Measurements by several authorities have revealed the likely magnitude of these variations in the VHF/UHF bands, and it is not proposed to pursue this aspect here. In assessing the limitation of field strength prediction we assume the objective to be the estimation of the median value of the distribution which would be obtained if we recorded the results whilst moving the aerial through a small distance, say 10λ. It is assumed that this median value will be primarily decided by losses in the propagation path, and the accuracy of prediction is determined by the ability to forecast these.

One other important preliminary must be considered, and this is the accuracy of measurement itself, because such evidence is taken when judging the efficiency of a prediction technique. In an attempt to quantify this, the BBC some years ago conducted an experiment in which field strength measurements were made of various UHF transmissions at up to 200 receiving locations within the limits of a town, using a receiving aerial elevated to a height of 10 m a.g.l. (Lee, Causebrook, Sandell, 1970). At each of these locations measurements were made of up to five transmissions from stations within non-fading range. At each point and from each transmitter two distinct measurements were made, and the difference between first and second measurement was recorded. The distributions of these comparisons were then plotted, and the results for various conditions were as follows:-

- (i) Measurements repeated in the same location:  
In this case the first measurement of each pair was made, and the location of the receiving aerial was carefully recorded. On a subsequent visit the second measurement was made, care being taken to site the aerial in the same position. The distribution of the comparison between first and second measurement of many such pairs gave a standard deviation of 2 dB.
- (ii) Measurement repeated at a nearby receiving location:  
Here the second measurement was made within 20 m of the first. Comparison of the pairs produced a distribution with a standard deviation of 4.5 dB.

The distributions in both cases were Gaussian, so that 99% of the samples can be assumed to lie within 2.5σ of the median. Thus in the case of (i) it can be seen that the best that can be achieved by measurement is to define the field strength at a precise position in space within the limits of ± 5 dB. This result made an interesting comparison with experiments carried out separately by the U.K. Post Office in 1957 (Brice, Sandell, 1963), in which measurements at UHF within a metre cube of space produced field strength variations of ± 5 dB. Case (ii) above gives some indication of the effect on field strength of a lateral displacement of the receiving aerial of 20 m. Measurements at 20 m intervals relate to a measurement density of 2,500 to the square kilometre, and this can be compared with the 20 or so that is the limit used for present survey work. In the latter activities no attempt is made in practice to determine the precise field strength distribution; effort is concentrated on determining the limit of service contour. Having determined what could be achieved by measurement, the next phase of this particular experiment was to compare predictions with the measurements already made. At the time a comparatively simple technique was being used by the BBC, and a report on its performance is now irrelevant. However, a comment on the results obtained using the CCIR Recommendation 370 curves is appropriate. Application of these to the fine detail of the experimental measurements was difficult, because if maximum accuracy is to be obtained from the curves then correction must be made for receiving location, and this involves a subjective assessment of the percentage site factor. Substantial errors can arise, but after some preliminaries a prediction for each site measured was obtained and compared with the measurements. The distribution which resulted had a standard deviation of 15.6 dB.

One further result can be quoted from this experiment. To eliminate the difficulty created by the subjective assessment of the location variation factor the concept of site clearance angle was introduced. This took the form of a correction to the median location value given by the appropriate CCIR propagation curve, based on the angle subtended between the horizontal at the receiving site and a line drawn to the horizon within 16 km (Causebrook, Davis, Sandell, 1969). Comparison of these revised

predictions with measurements gave a distribution with a standard deviation of 10.6 dB - a significant improvement over the result described in the previous paragraph.

The performance of a more advanced prediction technique involving the assessment of path losses will be discussed later in this paper. It is appropriate now to consider the data which formed the basis of Recommendation 370 because this will illustrate the difficulties of achieving a satisfactory prediction technique using propagation curves.

### 3. MEASUREMENT DATA - INTERPRETATION AND APPLICATION

Because they formed a substantial proportion of the original CCIR evidence and because their history is known the BBC's contributions to Recommendation 370 have been looked at in some detail. Broadly, the measurements can be subdivided under two headings - short range and long range. The short range measurements are those made within the service ranges of broadcast transmitters, at distances up to 100 km from the high-power stations, and are median values representing groups of measurements made within confined areas. For path lengths exceeding 100 km fading becomes an increasingly important factor. The assessment of reception conditions requires long-term observation over a period of months or even years, ideally accompanied by research into tropospheric conditions along the propagation paths.

In 1961 when the basic CCIR propagation curves were agreed the BBC supplied data in the form of field strength measurements for both short and long paths. In the case of the former, many thousands of results obtained during routine site test and survey activities were analysed. Most of the early VHF work was carried out by making continuous field strength measurements in a vehicle fitted with a receiving aerial mounted 3 to 5 m a.g.l. These measurements were then corrected with a linear height gain to give results assumed to exist at 10 m a.g.l., the internationally-adopted standard for this work. Some error was inevitable with this adjustment, because the receiving aerial height gain certainly varies with local conditions, but for VHF the variation was assumed to be relatively small. By the late Fifties, when extensive UHF work started within the BBC, the practice of making spot measurements with the receiving aerial at 10 m a.g.l. had been adopted. All these measurements were concentrated in built-up areas, because at that time the primary objective was to ensure maximum population coverage of new services.

Measurements for the longer paths were derived from a number of special propagation experiments. In some cases measurements were made of broadcast service transmitters in normal operation, whereas in others special transmitters were set up. The signals were recorded at fixed receiving sites, and the probability distributions of field strength as a function of time were determined. Unfortunately there was little success in these early measurements in attempts to relate propagation to tropospheric conditions. Weather information was available, but there were little or no data concerning such factors of interest as lapse rates, which could have been used to determine the existence of ducting along paths under investigation. Nevertheless, a very considerable quantity of measured data was obtained, and the Appendix lists the early BBC experiments, together with those which were carried out after 1961. In all reception has been recorded over a total of 119 different paths, varying in length from less than 100 to nearly 1000 km. The experiments extended over a range of frequencies from 41.5 to 774 MHz, and many different types of terrain were included. Particular attention was devoted to propagation over the North Sea, with a transmitter in Holland and receiving sites along the East Coast of the U.K. The total measurement recording time available for analysis from all these experiments amounts to about 100 years.

The data emerging from the various BBC experiments formed a useful contribution to the work of the CCIR, and facilitated planning activities in Europe in the Fifties and Sixties. Indeed, insofar as the CCIR Recommendation remains substantially unchanged, the value of this early work continues. With hindsight, however, it is easy to identify weaknesses in the original evidence, and it is useful to analyse these if constructive comments are to be made with a view to improving future work.

Perhaps the most important discrepancy in the original data was the inconsistency which existed between the short-range and long-range measurements. As mentioned previously, the service area measurements came from work carried out in built-up areas and the median values are depressed by urban clutter. In contrast, the results for the longer ranges usually came from a relatively few receiving sites in open country. Site variation factors were determined which made allowance for terrain undulations in the vicinity of these sites, although in some instances realistic assessments were impracticable because the signals were only above noise levels for short periods. However, whilst there was some success in determining the influence of local terrain upon the median value, the long-range results are not comparable with the short-range, because the effects of urban clutter are missing. The published curves therefore tend to underestimate field strengths at the shorter ranges by comparison with those at greater distances. When used for planning, the net effect is to improve the chance of obtaining an interference-free service.

Another uncertainty in the original data which has been reflected in the Recommendation concerns the definition of location variability. The basic curves define median values, and corrections are provided to give results for different percentage locations. For the BBC's long-range measurements the site variation factor was determined by simultaneous observation within a radius of 0 km of the fixed site. At the shorter ranges the median values represented a distribution of measurements also often made over many square kilometres - dependent solely on the size of the built-up area which was being surveyed. In this case also the density of the measurements was dictated by the population distribution - a factor having only slight relationship with terrain characteristics. Both long and short range measurements therefore provided evidence of the distribution of the median values, but neither produced understandable parameters to permit correction for location variation.

Another parameter which has given rise to some concern is  $\Delta h$ . This defines the degree of terrain irregularity over the propagation path in the range 10 to 50 km from the transmitter, and is the difference in height exceeded by 10% and 90% of the terrain along that part of the path. The parameter was introduced into the CCIR curves in 1961 to improve medium range prediction for UHF overland paths.

although at that time the BBC's analyses had not considered this parameter, nor provided data to support the corrections for changes in effective aerial heights at beyond-horizon distances. These corrections were used to normalize results for a basic transmitting height of 300 m above mean terrain, and to provide the families of curves for different heights. Some attempt was made by the BBC to assess the effect of transmitting aerial height gain upon the measured results at short ranges, but the results could not support extrapolation to the longer distances.

However, it is important to remember that in 1961 there was considerable international pressure to produce basic propagation curves for the forthcoming Conference, and so the technical data were readily agreed. Had there been time and effort available during this period considerable improvements could have been realised then, because much evidence was available from many sources, it simply had not been fully analysed. Within the BBC for example, effects which had been studied but not reported included:-

- (i) the effect of altering the height of the receiving aerial,
- (ii) the influence of local clutter, e.g. buildings and trees,
- (iii) polarization,
- (iv) multipath, and
- (v) depression of signal at poor sites during abnormal propagation conditions.

Clearly, items such as this are interesting, especially in the development of a comprehensive prediction technique, but in 1961 they had to take second place to the main priority of devising a system which could be effectively used to progress the important work of international frequency negotiation.

Since 1961 much new evidence has become available, and some of it has been incorporated in Recommendation 370. Some of the more important gaps in the data have been filled, for example, separate curves for land and sea have been introduced for the band 40 to 250 MHz, and information covering the Mediterranean as well as the North Sea has been added. The use of the  $\Delta h$  parameter has been extended to the VHF bands, and in general the application of the recommendation has been clarified by the supporting Report 239 (CCIR, 1982). The terrain clearance angle correction, mentioned in the previous Section, has been introduced to improve the location distribution situation. Other investigations carried out by the BBC since 1961 have included the simultaneous recording of UHF transmissions over the North Sea paths. Data for propagation over mixed land and sea paths at UHF have been contributed, together with various proposals for mixed-path methods.

However, the development of Recommendation 370 over the past twenty years has been sporadic, and there is general concern that there is urgent need for further clarification and elaboration. Recent work by Interim Working Party 5/5 has included a critical analysis of the existing texts, and proposals have been made for certain modifications. Whilst welcoming the general objective, the BBC has reservations about further ad hoc adjustment of the method as it stands. Such an approach tends to create inconsistencies within the system, indeed there is past evidence of this, and this gives rise to the need for further modification. If measured evidence is not available to support such changes, then there is a risk that accuracy might suffer. A wide-ranging review of the whole Recommendation, taking account of all the reliable measured data, is clearly the best approach, and this is the optimum solution recommended by IWP 5/5. But it is conceded that a full re-appraisal will require a great deal of effort, and it is pertinent to query whether this should be undertaken, or whether the objective should be to concentrate upon the development of a path loss technique which would make full use of the computer facilities now available. The next Section considers what can be achieved with such a system.

#### 4. PATH LOSS PREDICTION USING A COMPUTER

The particular example considered here is the prediction program which has been developed by the BBC, with the full co-operation of the Independent Broadcasting Authority. It is readily acknowledged that other organizations throughout the world have developed similar techniques, but the details and performance of the BBC program will serve as a typical illustration.

The program, which has now been in use for some years within the BBC Research Department, was originally designed for planning work connected with the introduction of the UHF broadcast services (Causebrook, 1974, King, Causebrook, 1976). It has been designed to undertake not only the basic process of prediction, it also offers many other facilities of interest to the planning engineer. It has also now been extended to cover prediction work at VHF (Causebrook, Tait, 1978).

The prediction routine in the program is intended to calculate field strengths of transmitters at all ranges, although initially particular emphasis was placed on long-distance paths, where the effects of interference influence the choice of frequencies. There tends to be an inevitable relationship between the design of the prediction and the data available, and this case the existence of a terrain data bank of the U.K., in which heights were stored for elements of a 0.5 km grid, was influential. However, the method is capable of use with finer data, and then greater accuracy can be achieved, as will be described.

The sequence of prediction in the program starts with the acquisition of a ground profile for the selected path, either from the data bank, or directly from detailed maps giving height information. This profile is initially interpreted by the program in simplistic terms, and is classified as having a rounded or wedged shape. It is also separately interpreted as a series of knife edges, and predictions are made for both profiles. An empirical interpolation is then made between the two results to give the final answer. The effects of tropospheric inhomogeneity over the longer paths giving rise to various forms of fading are dealt with in the calculation by varying the effective earth's radius of each profile. To determine the extent of this adjustment and others used in the program a great deal of measurement data

has been used, and results are constantly monitored to ensure good agreement with such evidence. As occasion demands this empirical approach is used to make fine adjustment to the parameters of the prediction.

Using the comparison technique described in Section 2, the accuracy of the program can be checked against measurement. If the terrain data bank is used to provide the profile information, the comparison with measurements gives a standard deviation of the distribution of 7.3 dB for UHF work. If more detailed terrain data are used, and in this case height information can be made available at 0.1 km intervals along a profile, then the standard deviation approaches 5 dB, i.e., comparable with the accuracy of measurement. Results for frequencies in the range 90 to 230 MHz are slightly worse, and those for the lowest VHF channels are only marginally better than those obtained using Recommendation 370 with the horizon angle correction. It is likely that the reason for this is that no account is being taken of ground reflexion, and this is likely to be an important factor at the lower frequencies. This facility might be included in the program, but certainly the 0.5 km terrain data would be inadequate for this purpose.

It is evident that the accuracy of such a prediction technique is largely dependent on the terrain data. In the work so far the concentration has been upon the prediction of the field at 10 m a.g.l., and of course the standing wave pattern is ignored. The effect of obstacles close to the receiving aerial have only been dealt with superficially, and even if full data concerning these were available the program would have to be much more complicated to predict the additional attenuation created. But this is the very problem that affects the estimation of field strength at lower heights of receiving aerial, down to one metre a.g.l. This aspect interests both mobile radio users and the broadcasters, who are concerned with the quality of reception on car radios and portables. Until recently, such conditions have had to be inferred from measurements and predictions made for the 10 m a.g.l. condition, but increasing interest in the lower heights has led to a rapid increase in the amount of measured evidence, and much now exists which will help further prediction development.

## 5. FUTURE DEVELOPMENT

Although many countries have by now completed most of the planning work on their terrestrial broadcasting networks, the need for a reliable prediction method remains, and indeed becomes more pressing in some cases. There is a growing demand to share spectrum space between services, and in this respect the demand from new mobile interests is considerable. Then there is always the opportunity to improve existing networks - in the U.K. for example we are currently making substantial changes to our VHF/FM broadcasting system - a process likely to extend across Europe because next year will see the second stage of international discussions to agree the extension of the spectrum allocated to this service. Then, of course, it is recognized that even although satellite broadcasting is with us now, many countries throughout the world continue to develop terrestrial networks, and the need for an accurate technique on which to base their plans will exist far into the future. For these reasons broadcast engineers will want to improve prediction.

Given that further development is desirable, the objectives - as distinct from the reasons - must be identified. Is the primary intention to produce evidence which will allow a full revision of Recommendation 370 to be made, or is it to develop a computerised path loss prediction program which could be used internationally? The main obstacle to the latter must be the present scarcity of terrain data, even within Western Europe. Some countries have or are acquiring data banks, but the situation is uncertain and unco-ordinated, and seems likely to remain so for some years. This is regrettable, especially at a time when satellite mapping processes might offer a solution. It is certain therefore that the statistical curves will be in use for many years yet, although there will be a steady increase within various countries of more detailed techniques. It would seem desirable to look for international co-ordination in these developments.

The objectives of the BBC's research in this area may be stated as follows:-

- (i) to improve the present path loss method, so that reliable predictions can be obtained of the field strength at 10 m a.g.l. for all types of propagation path,
- (ii) to be able to predict the result of local movement of the receiving aerial - at any plane, and
- (iii) to forecast reception conditions on receivers used to obtain the various services.

The programme of work has started with a full re-investigation of the measurement data arising from the experiments listed in the Appendix, and contributions from other organizations are being added. In an attempt to give more meaning to the temporal variation parameter these data are being correlated with weather and tropospheric information, where this is available. Certainly at this time nothing can be done in respect of tropospheric data affecting measurements made 30 years ago, but even in this case it is hoped that certain basic weather information will show some correlation between abnormal propagation and stable weather conditions. The same long-distance data are also being used to re-examine the mixed-path prediction, and here several new results are available. New experiments are also being established to fill gaps in the evidence, and it is hoped that these will be comprehensively specified in order to provide much more data than was obtained from earlier work.

Particular emphasis is being placed upon the examination of field strength variation with receiving location. An enormous amount of measurement is available within the BBC, as an example the number of "spot" measurements made within service areas of VHF and UHF stations over the past twenty years is now well in excess of one million.

To this considerable library of results must be added a large range of specialized experiments designed to study particular aspects of the subject, such as the effects of polarization, receiving aerial height gain, multipath propagation, the effects of tidal fading, and many others. The main problems in

this project are those of selection and processing, although hopefully more advanced facilities will be available than were in use 20 years ago.

Although the work is intended to improve the accuracy and scope of the BBC's prediction program, the first priority is to assess the features of Recommendation 370, in the form that it is to be used for the forthcoming VHF/FM Conference. Even if serious discrepancies are felt to exist, it is now too late to influence the general application of this machinery for the Conference, because planning calculations have already started. However, it is hoped to report on any deficiencies, anomalies and uncertainties which are revealed between now and the middle of 1984. Even if solutions cannot be suggested within this time scale, it is felt that such evidence may be useful to those who will need to assess the international situation.

#### 6. ACKNOWLEDGEMENT

The authors wish to thank the Director of Engineering of the BBC for permission to publish this paper. Their thanks are also due to colleagues and former colleagues who installed and maintained the special transmitting and receiving equipment and who assisted in the analysis of recordings. Gratitude is also expressed to many organizations for providing receiving sites and facilities and to the Netherlands Postal and Telecommunications Services for many years of transmissions from the Scheveningen radio station.

#### 7. REFERENCES

- BRICE, P.J., SANDELL, R.S., 1963, "Field-strength Measurements of UHF Transmissions from Crystal Palace", IEE Paper No. 4158E, London.
- CAUSEBROOK, J.H., 1974, "Computer Prediction of UHF Broadcast Service Areas". BBC Research Department Report No. 1974/4.
- CAUSEBROOK, J.H., DAVIS, B., SANDELL, R.S., 1969, "The Prediction of Co-channel Interference to Television Broadcasting Services in the Frequency Range 470 to 960 MHz", BBC Research Department Report No. 1969/33.
- CAUSEBROOK, J.H., TAIT, B., 1978, "Computer Programs for VHF Interference Prediction using a Terrain Data Bank", BBC Research Department Report No. 1978/13.
- CCIR, 1961, "Report of the CCIR Meeting of Experts to Prepare for the European VHF and UHF Broadcasting Conference (Stockholm 1961)", Doc. 64-E, Cannes.
- CCIR, 1982, "Propagation Statistics Required for Broadcasting Services using the Frequency Range 30 to 1000 MHz", Report 239-5, Geneva.
- CCIR 1982, "VHF and UHF Propagation Curves for the Frequency Range from 30 to 1000 MHz", Recommendation 370-4, Geneva.
- ITU, 1961, "European Plans for Broadcasting in the VHF and UHF Bands", Stockholm 1961, Geneva.
- JOWETT, J.K.S., MEADOWS, R.W., ROWDEN, R.A., 1963, "VHF and UHF Propagation Data Assembled in the United Kingdom for the Planning of Television Broadcasting Services", IEE Paper No. 3951E, London.
- KING, R.W., CAUSEBROOK, J.H., 1976, "Computer Programs for UHF Co-channel Interference Prediction using a Terrain Data Bank", BBC Research Department Report No. 1976/6.
- LEE, R.W., CAUSEBROOK, J.H., SANDELL, R.S., 1970, "An Investigation into the Prediction of Field Strength: The Guildford Experiment", BBC Research Department Report No. 1970/26.
- SANDELL, R.S., 1969, "A Comparison of Standards Used to Plan UHF and VHF Networks", The Royal Television Society Journal, Vol. 12, No. 7, London.

## APPENDIX

BBC LONG-DISTANCE RECORDING EXPERIMENTS -  
ARRANGED IN ORDER OF FREQUENCY

Frequency MHz	Transmitter	Receiver	Path Length km	Period
41.5	Crystal Palace	Caversham	63	June 1961 - Dec. 1962
		Mursley	77	"
45.0	Alexandra Palace	Leeds	257	Sept 1946 - Oct. 1948
		Largoward	550	Sept 1949 - Mar. 1950
48.23	North Hessary Tor	Mursley	274	June 1961 - Dec. 1962
58.25	Sutton Coldfield	Caversham	138	"
		Mursley	100	"
		Largoward	422	Jan. 1951 - Mar. 1952
		Redmoss	505	"
		Portreath	356	Jan. 1951 - Oct. 1951
		Redruth	354	Nov. 1951 - Mar. 1952
63.27	Peterborough	Caversham	121	Jun. 1961 - Dec. 1962
63.25	Wenvoe	Caversham	161	"
		Mursley	180	"
88.1	North Hessary Tor	Mursley	274	"
88.3	Sutton Coldfield	Caversham	138	"
		Mursley	100	"
88.5	Rowridge	Mursley	146	"
88.95	Wenvoe	Caversham	161	"
89.1	Wrotham	Caversham	88	Jun. 1961 - Dec. 1962
89.95	Wenvoe	Mursley	180	"
90.1	Peterborough	Caversham	121	"
91.4 and 93.8	Wrotham	Dorset Head	220	Jan. 1951 - Sept 1952
		Pannal Ash	330	Apr. 1951 - Sept 1952
		Largoward	612	Jan. 1951 - Sept 1952
		Redmoss	680	"
		Portreath	412	Jan. 1951 - Oct. 1951
		Redruth	406	Nov. 1951 - Mar. 1952
		Heddon Laws	443	Apr. 1951 - Sept 1952
91.5	Moorside Edge	Wrexham	98	May 1949 - Mar. 1950
		Redruth	443	"
		Christchurch	321	"
		Kingswood	284	"
		Cambridge	207	"
		Great Bromley	278	"
		Start Point	398	Jun. 1947 - Oct. 1947
		Bartley	306	"
		Bagley Croft	217	"
93.1	Meldrum	Scousburgh	300	Sept 1956 - Oct. 1956
		Netherbutton	177	May 1957 - Jun. 1957
94.35	Scheveningen	Happisburgh	198	July 1954 - Sept 1955
		Flamborough Hd.	365	"
		Newton	543	"
		Bridge of Don	690	"
		Lerwick	950	"
180.4	Sutton Coldfield	Mursley	100	Nov. 1954 - Oct. 1956
		Kingswood	183	July 1954 - Nov. 1956
		Beddington	237	Oct. 1954 - Nov. 1956
180.4	Pontop Pike	Ottringham	172	Jan. 1957 - Feb. 1958
		Dorset Head	214	"
		Mursley	338	"
		Kingswood	420	"

Frequency MHz	Transmitter	Receiver	Path Length km	Period
180.4	Pontop Pike	Beddingham	473	Jan. 1957 - Feb. 1958
185.25	Lille	Kingswood	240	Nov. 1952 - Jun. 1953
187.0	Scheveningen	Happisburgh	198	Apr. 1957 - Dec. 1958
		Flamborough Hd.	365	"
		Newton	543	"
		Bridge of Don	690	"
		Lerwick	950	"
495	Sutton Coldfield	Mursley	100	Jul. 1955 - Jul. 1956
		Kingswood	183	Mar. 1955 - Jul. 1956
		Beddingham	237	Nov. 1955 - Jul. 1956
501.25	Rowridge	Alderney C.I.	120	Feb. 1967 - Sep. 1970
		Torteval C.I.	167	"
509.75	Caen	Christchurch	210	July 1968 - June 1970
		Kingswood	259	"
		Caversham	279	"
		Mursley	329	"
533.25	Caradon Hill	Torteval	174	July 1969 - July 1971
560.0	Holme Moss	Mursley	190	Jul. 1955 - Nov. 1956
		Kingswood	272	"
		Beddingham	326	Nov. 1955 - Nov. 1956
560.0	Pontop Pike	Ottringham	172	Jan. 1957 - Jun. 1958
		Dorset Head	214	"
		Mursley	338	"
		Kingswood	420	"
		Beddingham	473	"
560.0	Scheveningen	Happisburgh	198	Jun. 1959 - Jun. 1964
		Flamborough Hd.	365	Jun. 1959 - Jun. 1962
		Newton	543	"
		Bridge of Don	690	"
		Lerwick	950	"
		Tacolneston	217	Mar. 1963 - Jun. 1964
		Feltwell	258	"
		Peterborough	316	"
		Skeffington	356	"
573.25	Crystal Palace	Caversham	63	Mar. 1965 - Sept 1965
		Mursley	77	Mar. 1965 - Feb. 1967
		Manningtree	98	May 1965 - Mar. 1967
		Bawdsey	120	Aug. 1966 - Jul. 1967
		Peterborough	132	May 1965 - Jul. 1967
		Tacolneston	147	Nov. 1965 - Jul. 1967
629.25	Sutton Coldfield	Hatfield	144	Sept 1966 - Sept 1967
		Brookmans Park	149	"
653.75	Le Havre	Christchurch	195	July 1968 - Jun. 1970
		Kingswood	202	"
		Caversham	234	"
		Mursley	278	"
666.0	Portland	Alderney	95	Feb. 1970 - Nov. 1970
756.0	Stockland Hill	Alderney	137	Aug. 1970 - Nov. 1970
759.25	North Hessary Tor	Torteval	157	Dec. 1962 - Sept 1963
774.0	Pontop Pike	Dishforth	85	Jun. 1959 - Nov. 1960
		Moorside Edge	140	Jan. 1959 - Nov. 1960
		Dorset Head	214	"
		Mursley	338	"
		Kingswood	420	"
		Beddingham	473	"
774.0	Scheveningen	Happisburgh	198	Oct. 1961 - Dec. 1963
		Flamborough Hd.	365	"
		Newton	543	"
		Bridge of Don	690	"
		Lerwick	960	"

Frequency MHz	Transmitter	Receiver	Path Length km	Period
774.0	Scheveningen	Bawdsey	196	Apr. 1965 - Jul. 1967
		Manningtree	217	"
		Gt. Baddow	262	"
		Brookmans Park	307	Jun. 1966 - Jul. 1967
		Hatfield	311	Aug. 1965 - Sept 1966
		Kingswood	321	Apr. 1965 - Jul. 1966
		Caversham	365	Apr. 1965 - Sept 1965

The text of the paper does not require illustration in its published form. A number of figures were used to illustrate the oral presentation, however, and those which may be of general interest are reproduced here.

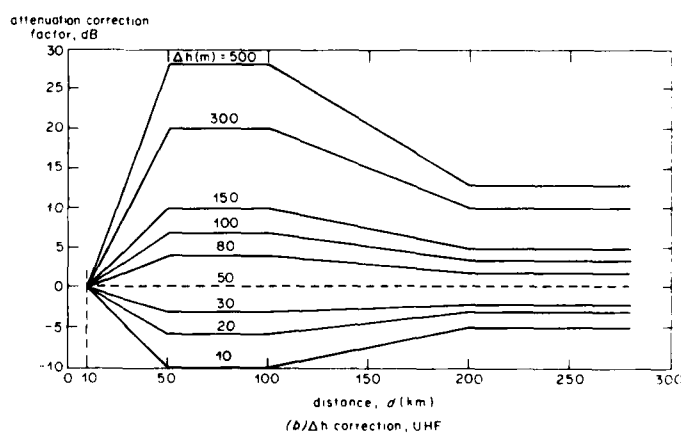
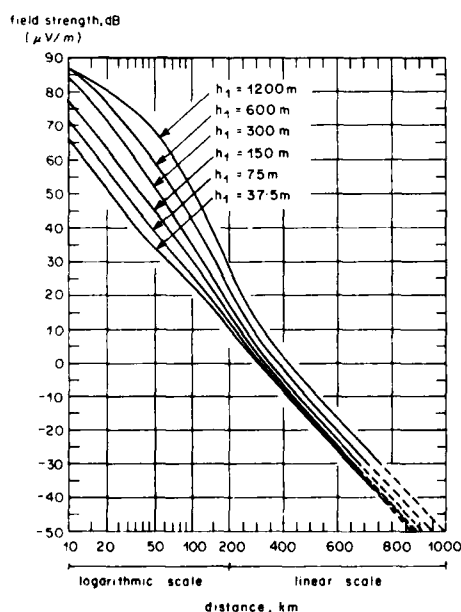
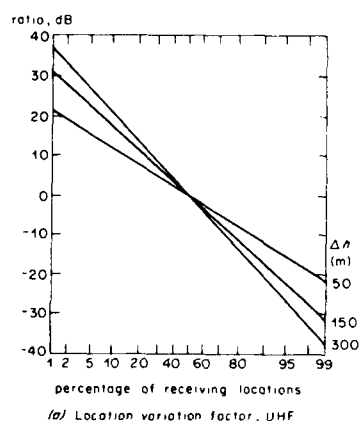
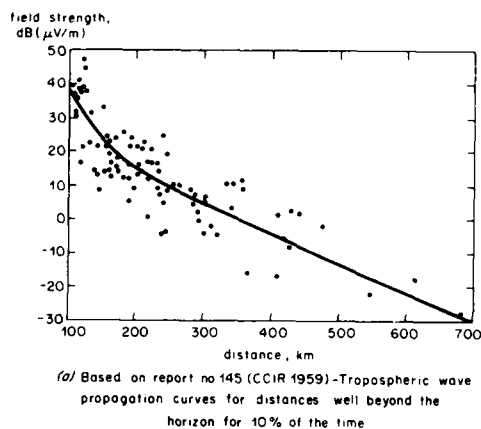


Fig 2 Correction factors from Recommendation 370-4 (CCIR 1962)

Fig 1 An example of the development of the CCIR propagation curves for VHF over the period of the Stockholm conference (1961)

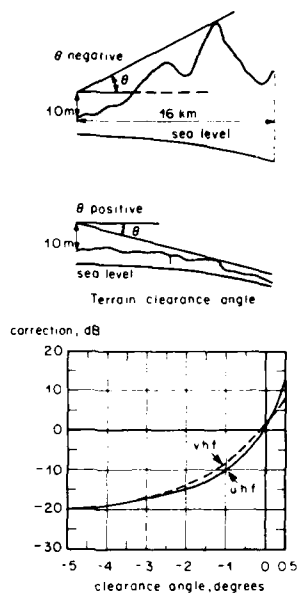
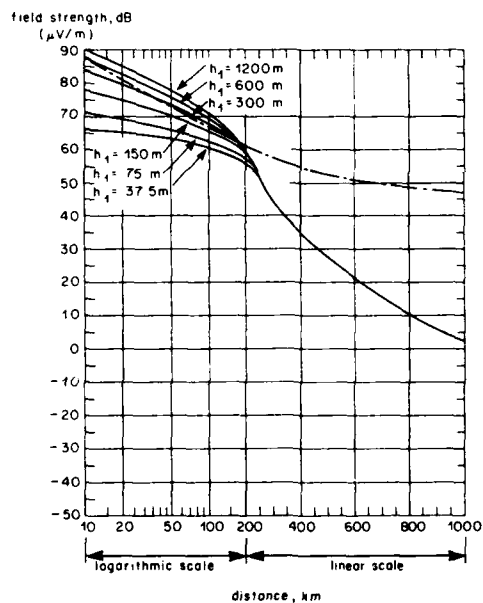
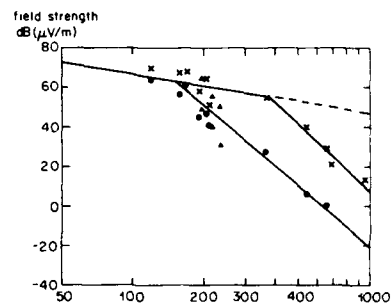


Fig 3 Receiver terrain clearance angle  
from Report 235-5 (CCIR 1982)



(a) Taken from Recommendation 370-4 propagation curves  
for 1% of the time

Note: The curves have a 7dB correction for coastal towns



\* data adjusted for receiver environmental losses  
Note: data for paths identified by \* are averages  
of separate 2 year experiments, one at  
560 MHz one at 774 MHz

b/ BBC prediction program-limiting curves  
for overseas paths  
Propagation data from open sites  
\* 1% time  
• 5% time

Fig 4 Propagation over the North Sea at UHF  
for low time percentages

## VHF AND UHF PROPAGATION IN THE CANADIAN HIGH ARCTIC

by  
R.S. Butler, J.I. Strickland, and C. Bilodeau  
Communications Research Centre  
P.O. Box 11490, Station "H"  
Ottawa, Ontario, K2H 8S2  
Canada

## SUMMARY

An experiment to study radio propagation in the Arctic maritime environment was undertaken in Canada in 1982. Five UHF radio paths between pairs of elevated points were selected along a 300 km east-west line which parallels a potentially important navigation route through the Arctic islands. Two VHF paths, each between an elevated site and a point near sea level were also chosen to simulate communications with a ship. Partial results from the summer-to-winter transition season show that propagation between the elevated points is highly reliable, but that propagation along the slanted paths appears to be strongly affected by radio-wave ducting.

## 1. INTRODUCTION

The portion of Canada north of the Arctic Circle includes an extensive group of islands, covering an area of about 2 million km<sup>2</sup> and extending to latitude 83°N. The Northwest Passage, the fabled northern sea route through the Americas from Europe to the Orient, passes through this archipelago near latitude 74°N between Baffin Bay on the east and the Beaufort Sea on the west.

Communications in this very sparsely populated region have traditionally used HF radio, supplemented by troposcatter systems farther south, and more recently by microwave links through geostationary satellites. However, the possibility of increased marine traffic because of natural resource development has led to the investigation of a VHF mobile radio system, and this has required a study of radio propagation in this unique Arctic region. The experimental VHF frequencies were chosen within the maritime mobile frequency band, 156 to 174 MHz, with a maximum link distance of 95 km between a simulated shipboard location and an elevated site. As well, UHF paths were investigated in the 450 to 470 MHz band, with lengths up to 100 km between elevated points. The purpose of the experiment at both VHF and UHF is to examine the range of path lengths needed to cover the whole Northwest Passage from longitude 80°W to 125°W.

The central islands of this region have an Arctic desert climate with only a few centimetres of annual precipitation, mostly as snow. Summer temperature maxima rarely exceed 5°C and winter minima can be lower than -50°C. The sea channels are ice-covered for nine to twelve months of the year and winter ice thicknesses are typically 2.5 to 3 m. The unbroken winter night at latitude 75°N lasts from November 3 to February 9, and the unbroken summer day from May 1 to August 13, while the length of the day changes from 0 to 24 hours, and back, around the spring and autumn equinoxes. The winter night-time atmosphere is characterized by a widespread thermal inversion as the earth and ice surface cool by radiation. The summer day-time atmosphere is stable and generally non-convective, with extensive fog and overcast below 200 m when the ice cover is discontinuous in late summer.

## 2. DESCRIPTION OF THE EXPERIMENT

The geographical location of the experimental area is shown in Figure 1. Figure 2 is a detailed map of the area, with the experimental links indicated. Near Cape Cockburn there are three independent sites, Cockburn Peak, Cockburn Lake, and Cockburn Flats, at different elevations along almost the same line, which are not differentiated on this map. Unofficial names and locations of all sites are given in Table 1, together with the approximate frequency of transmission from each site.

Table 1. Experimental Site Details

Site Name	Latitude	Longitude	Elevation (m)	Frequency (MHz)
Transfer Hill	75° 35.3'N	105° 35.1'W	140	451
Schomberg Peak	75° 33.7'	102° 40.8'	189	463
Cockburn Peak	75° 01.9'	100° 15.6'	151	453
Cockburn Lake	75° 01.5'	100° 10.0'	90	458
Cockburn Flats	75° 00.7'	100° 01.0'	15	164
Acland Acres	75° 00.0'	98° 51.0'	15	168
Lowther Peak	74° 31.8'	97° 27.2'	183	468
Martyr Peak	74° 41.2'	95° 02.9'	174	148

The signal level received from Transfer Hill was measured at Schomberg Peak. This level was then inserted as a serial digital data stream on the frequency-modulated transmission from Schomberg Peak and demodulated and recovered when the received level of that transmission was measured at Cockburn Peak. Both levels in turn were included in the FM serial digital data stream on the Cockburn Peak transmission, and the recovery and measurement process was repeated at the Lowther Peak receiver. The received levels of the transmissions from Cockburn Lake, Cockburn Flats, and Acland Acres were also measured at Lowther Peak. All six measurements were included on the Lowther Peak transmission, and the reception process was repeated at Martyr Peak. The transmission from Martyr Peak was a short range telemetry link to the recording equipment at Resolute.

At all sites the transmitting antennas had four vertically collinear half-wave folded dipole elements and a nominal gain of 8 dBi. All were vertically polarized and mounted on six-metre towers so that the radiation centres of the antennas were about 7 metres above ground level at UHF and 9 metres at VHF. All receiving antennas also had four vertically collinear half-wave dipole elements and were similarly mounted, except at Lowther Peak where a cylindrical paraboloid with a gain of 17 dB was mounted at a height of 5 metres and used for UHF reception. Path profiles of all the links with the line of sight above an effective earth radius of  $4R/3$ , and with the 0.6 Fresnel zone clearance indicated, are shown in Figure 3. Path clearances at UHF ranged from almost one full Fresnel zone on the link from Lowther Peak to Martyr Peak to zero on the link from Cockburn Lake to Lowther Peak. At VHF, the Acland Acres site was just on the horizon of Lowther Peak, while the Cockburn Flats site was obstructed, being about 25 km beyond the horizon. All paths were more than 90% over the sea and, except at Cockburn Flats, foreground blocking was negligible.

Because of the inaccessibility of the sites, all equipment was designed to operate unattended, unattended, and with minimal power consumption. Power was supplied by CIPEL primary cells chosen for their good performance at extremely low temperatures. The transmitters used frequency multiplication from stable crystal oscillators in the 50 MHz range, and had power outputs of 100 mW. The single-conversion receivers had simple mixer front-ends, and bandwidths of 12 kHz centred at 10.7 MHz IF. Quadrature detectors were used to demodulate the FM data stream of measured signal levels at each site.

All signal levels were recorded at Resolute by a data cartridge recorder at two-second intervals as 12-bit binary numbers, so that the resolution exceeded 0.1 dB at the middle of the approximately 60 dB dynamic range of the equipment. Data cartridges were forwarded to Ottawa weekly for analysis, but the system operation was monitored several times daily by real-time sampling of the data by telephone from Ottawa.

The two VHF paths from Cockburn Flats and Acland Acres and the UHF path from Lowther Peak came into operation on August 13, 1982. The remaining four UHF paths became operational on September 1, 1982. The experiment worked with only minor losses of data until early November 1982, when the data recording system became very noisy. Thus the results presented in this paper are confined to the period ending November 1, 1982. By chance this covers almost exactly the autumn transition period (August 13 to November 3) when the length of day decreases from 24 to 0 hours at these latitudes.

### 3. EXPERIMENTAL RESULTS

#### 3.1 UHF Results

The most striking characteristics of the signal levels measured on all the UHF paths is their stability. This is demonstrated by the cumulative distributions of relative signal strength over the period of measurement, as shown in Figure 4, where the two-letter abbreviations identify the paths by the names of the transmitter sites. The signal levels here are plotted relative to the median for each path, the medians are displaced by 5 dB intervals for clarity, and the abscissa scale is a normal probability scale. The slopes of the central portion of each curve are very nearly the same, and small, so that the spread between the 10% and 90% points is within  $\pm 3$  dB in all cases. It also appears from these curves that three propagation regimes may exist on these paths, i.e., the central portion already referred to, a regime of significant signal enhancement and a regime of moderate signal fading.

In the west-to-east progression of UHF transmitter sites from Transfer Hill to Cockburn Lake there is a matching progression of diminishing path clearance and this correlates strongly with the degree of signal enhancement observed. Thus at the 99% probability level the enhancements above the median are 4.7 dB, 6.9 dB, 10.6 dB and 18.3 dB, respectively, for the paths Transfer Hill-Schomberg Peak, Schomberg Peak-Cockburn Peak, Cockburn Peak-Lowther Peak, and Cockburn Lake-Lowther Peak. This presumably results when the gradient of the atmospheric refractive index becomes so negative as to make the earth appear almost flat to the radio waves which then propagate unobstructed. The degree of enhancement on the shortest and clearest path, Lowther Peak-Martyr Peak, does not follow this progression, being larger than expected for small percentages of time. The enhancements observed on this path occur in conjunction with deep fading events and are of short duration; they are probably caused by ducting or focussing of the radio waves and differ from the enhancements on the other UHF paths which last for hours or days. This behavior may reflect a real meteorological difference between the path from Lowther Peak to Martyr Peak and the other UHF paths at this season. The eastern end of the channel remains largely ice-free for much of the period, while ice cover is rarely broken at the western end. This undoubtedly influences the atmospheric temperature and humidity profiles along the paths.

The same data are presented with a logarithmic abscissa scale in Figure 5. The remaining conventions are the same as in Figure 4. This presentation emphasizes the third portion of the UHF signal distributions, where moderate fading occurs. Clearly this is significant only on the paths from Lowther Peak to Martyr Peak and, to a smaller extent, from Schomberg Peak to Cockburn Peak. In both cases the data can be well represented by a change of signal level of 8 dB per decade of time, with a very distinct break from higher signal levels at about 5% and 0.5% fractional occurrence, respectively. This factor of ten difference in percentage occurrence of signal fading on these paths and the almost total absence of

fading on the Transfer Hill-Schomberg Peak path may be additional evidence of meteorological differences between the eastern and western parts of the region. The stability of the longer paths from Cockburn Peak and Cockburn Lake to Lowther Peak is very striking and is presumably related to the small path clearances which may prevent multipath propagation from occurring. Inspection of the original fading data leads to the conclusion that all the deep fading is probably due to multipath propagation, but this is clearly a rare phenomenon, at least at this season.

There is no hint in the UHF signal levels of any diurnal variation even though this was the season where such effects would be most likely. The typical time scale of variation is several days, corresponding roughly to the movement of major air masses. On some occasions a progression of propagation effects was clearly noted, and is likely associated with weather fronts which were observed to move from west to east. It would seem that the almost total inhibition of convection by the nearly isothermal sea surface is the main factor in preventing signal variations on the diurnal scale.

### 3.2 VHF Results

The behaviour of the VHF paths was strikingly different from that of the UHF paths as shown in Figures 4 and 5, where AA refers to the VHF path between Acland Acres and Lowther Peak and CF to that between Cockburn Flats and Lowther Peak. The central portion of the data from Acland Acres are not approximately linear on the normal probability scale of Figure 4, as in the case of the UHF data. Inspection of the VHF records from Acland Acres reveals a tendency for the signals to cluster about two levels separated by 15 to 20 dB. This is reflected in Figure 4 where the cumulative time in the lower state is about 20 to 25% of the total, and the transition to the upper state begins at about 80% probability.

This behaviour could be attributed to an equipment malfunction, but is believed to be real largely because of the good agreement observed between the measurements of the signals from Acland Acres and Cockburn Flats, which were independent of each other. Only at the times of high signal level from Acland Acres did the signal from Cockburn Flat become measurable and at these times the correspondence of signal variations on the two paths was excellent but not exact. The median signal levels were depressed in both cases: the median from Acland Acres was about 16 dB lower than expected, and that from Cockburn Flats at least 20 dB lower than expected although some of this latter reduction may be the result of foreground terrain blocking. In addition the VHF signals tended to be strongest at times of enhancement of the UHF signals from Cockburn Peak and Cockburn Lake, which shows that both sets of signals respond to the same large-scale air mass variations. An example of this correlation of VHF and UHF signal strength is shown in Figure 6. The previously discussed close correspondence of the signals on the two VHF paths is also demonstrated in Figure 6, as the signal from Acland Acres abruptly drops to the lower state in correlation with the loss of the signal from Cockburn Flats.

This unusual behaviour on the VHF paths may be plausibly explained as the consequence of strong and stable stratification of the lowest 200 metres of the atmosphere, which produces pronounced ducting of the radio waves launched from near the sea surface. Normal propagation could occur only if the strata were displaced by intrusion of other air masses, and significant enhancements would require the duct thickness to increase to include the Lowther Peak receiver as well as the low elevation transmitters. The rarity of multipath propagation at UHF is compatible with this hypothesis, since propagation between elevated points would occur almost always above the sea-based duct. If the hypothesis is correct, then superior propagation reliability may be attained by lowering the elevated end of the path, so that both transmitter and receiver are within the same stratum. This will be the subject of further investigation.

As in the case of the UHF paths, no diurnal variation of received signal level was found in the VHF data. However, there is some indication that a seasonal dependence may exist, as the fraction of time for which the received VHF level was observed in the lower state increased steadily throughout the period of observation.

## 4. CONCLUSIONS

During the summer-to-winter transition season (mid-August to early November) UHF propagation on five paths between elevated points in the central Arctic islands of Canada was found to be highly reliable. Fading greater than 10 dB below median levels was observed on only the eastern-most path, which may indicate a longitude-dependent climatic variation of radio propagation conditions along the Northwest Passage. On two VHF paths, each between an elevated point and one near sea-level, median signal levels were at least 16 dB worse than expected, which is believed to be a consequence of strong ducting of the signal launched near the sea surface. No diurnal variations were found on either the VHF or UHF paths, but a seasonal effect may be present in the VHF data.

## 5. ACKNOWLEDGEMENTS

The assistance of Mr. Dick Galvin, Telecommunications Area Manager, Transport Canada, at Resolute was invaluable for the successful operation of this experiment. The logistical support of the Polar Continental Shelf Project of Energy, Mines and Resources Canada is also gratefully acknowledged.

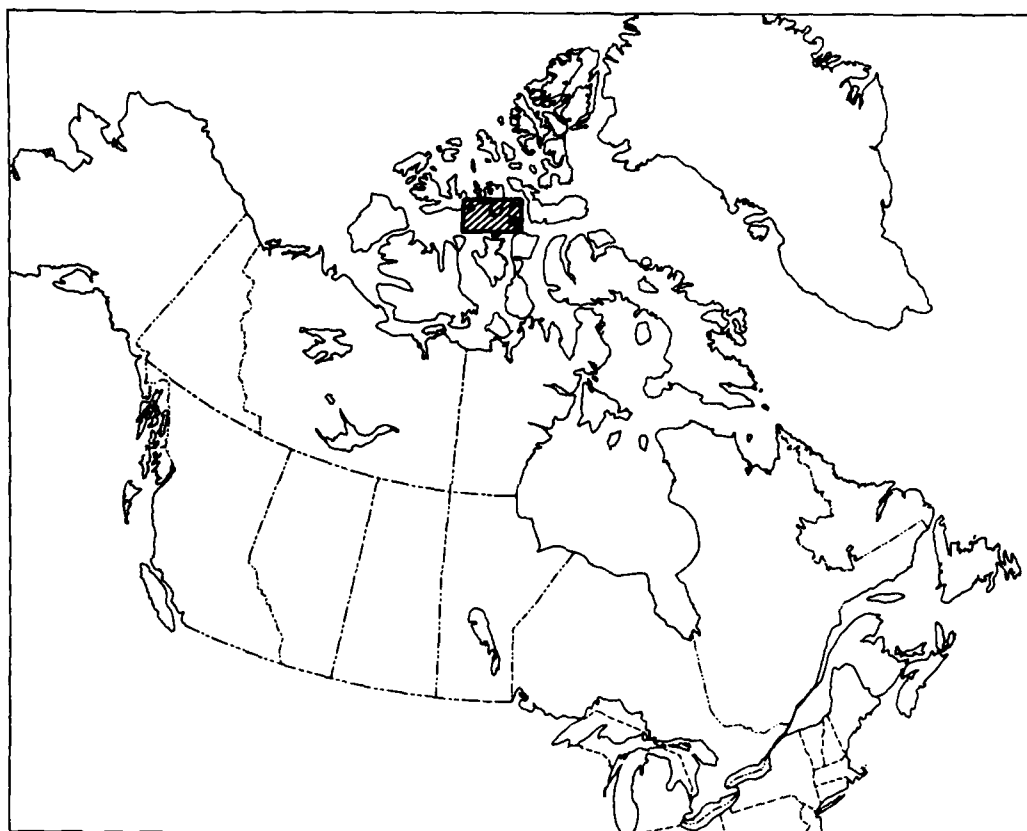


Figure 1. Canada, with the experimental region indicated in the central Arctic islands.

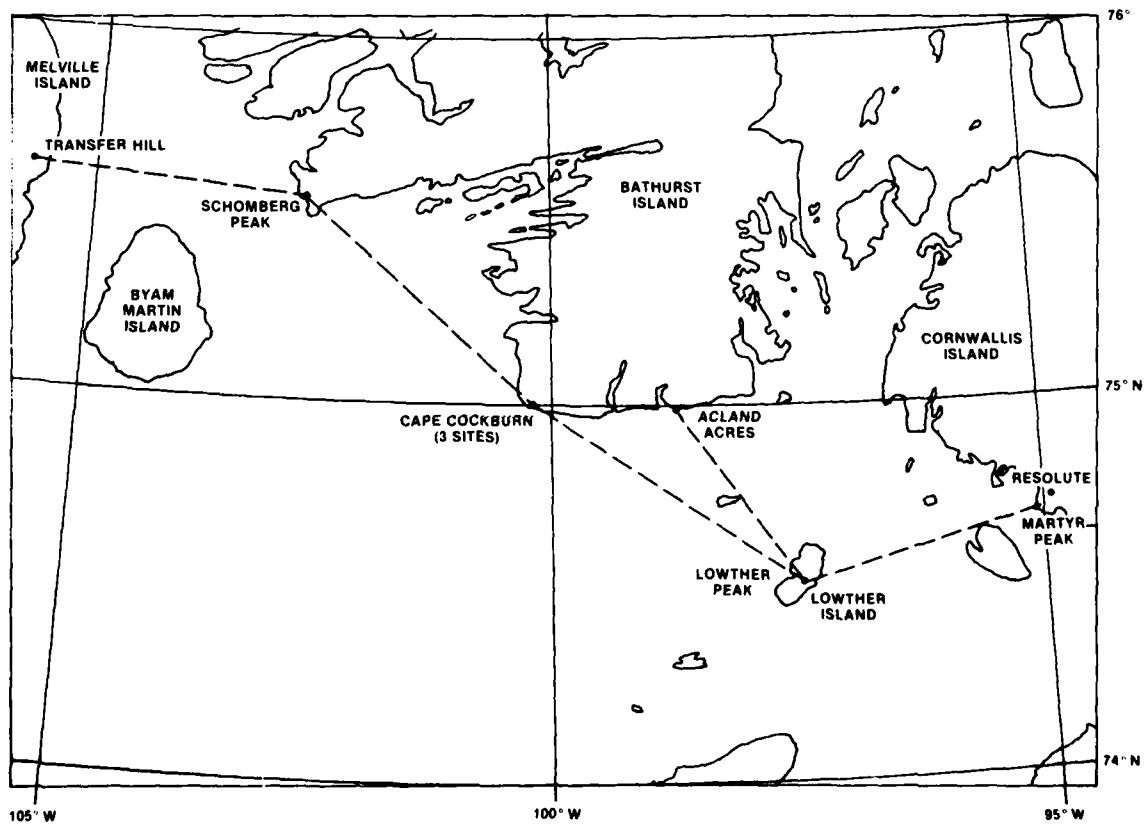


Figure 2. The experimental region, showing equipment locations and propagation paths.

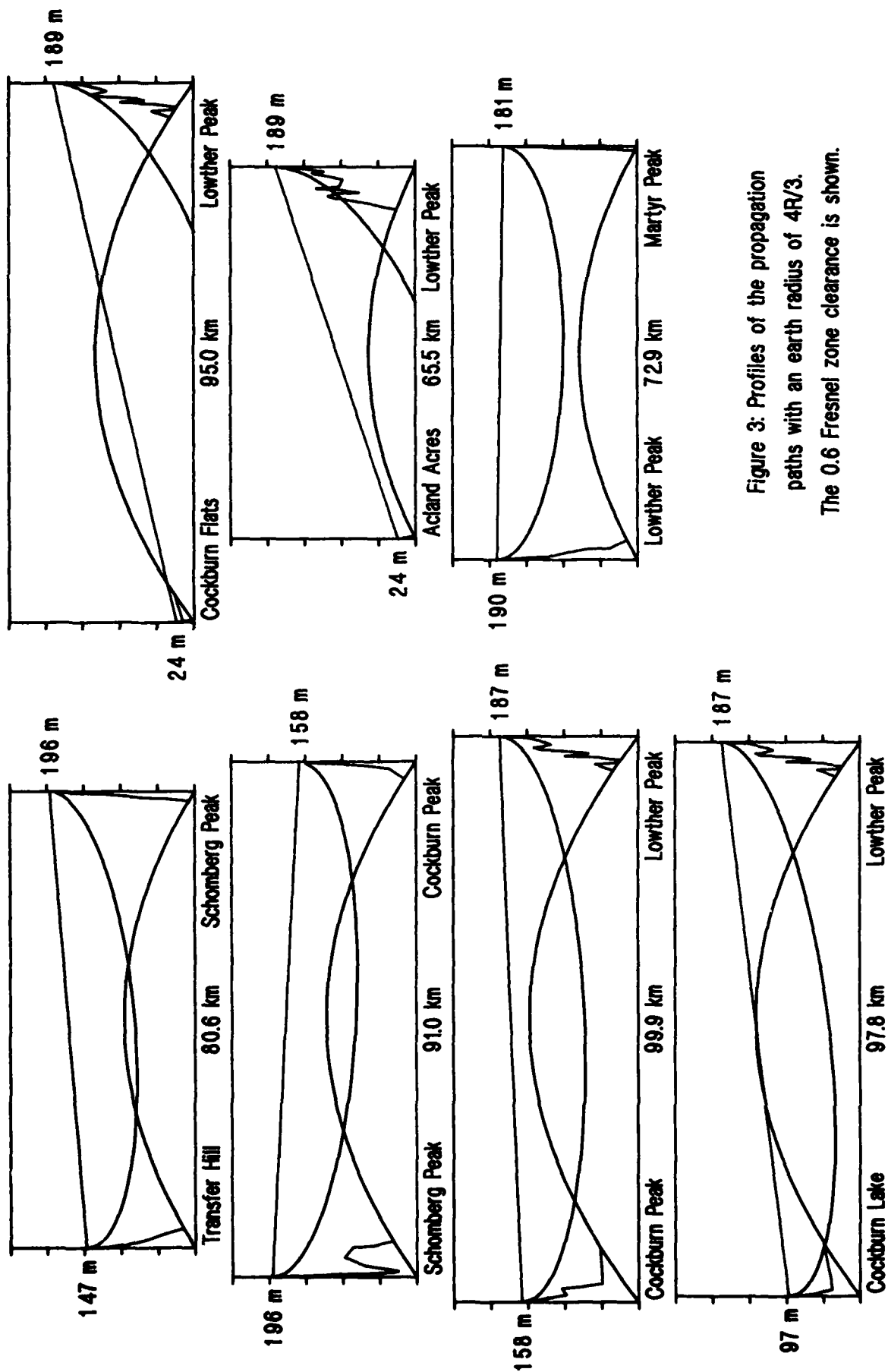


Figure 3: Profiles of the propagation paths with an earth radius of  $4R/3$ . The 0.6 Fresnel zone clearance is shown.

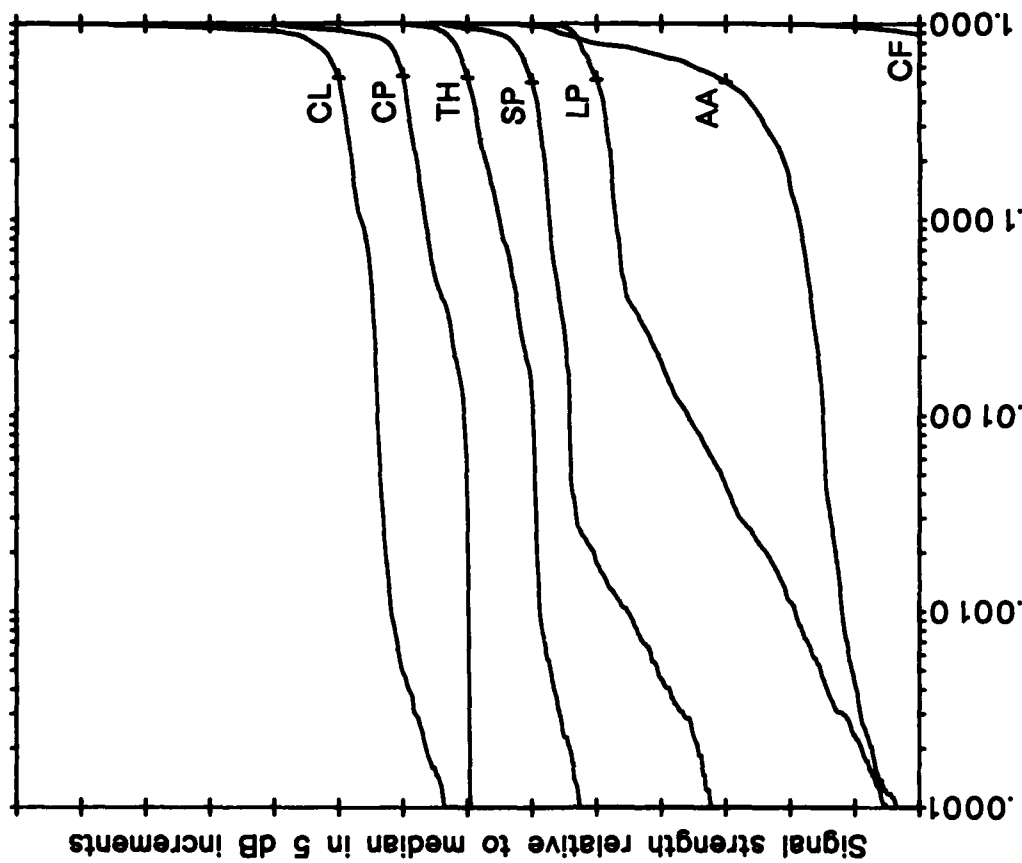


Figure 4: Probability (%) signal strength not exceeded.  
 CL=Cockburn Lake; CP=Cockburn Peak; TH=Transfer Hill;  
 SP=Schomberg Peak; LP=Lowther Peak; AA=Acland Acres;  
 CF=Cockburn Flats. Medians shown by crosses.

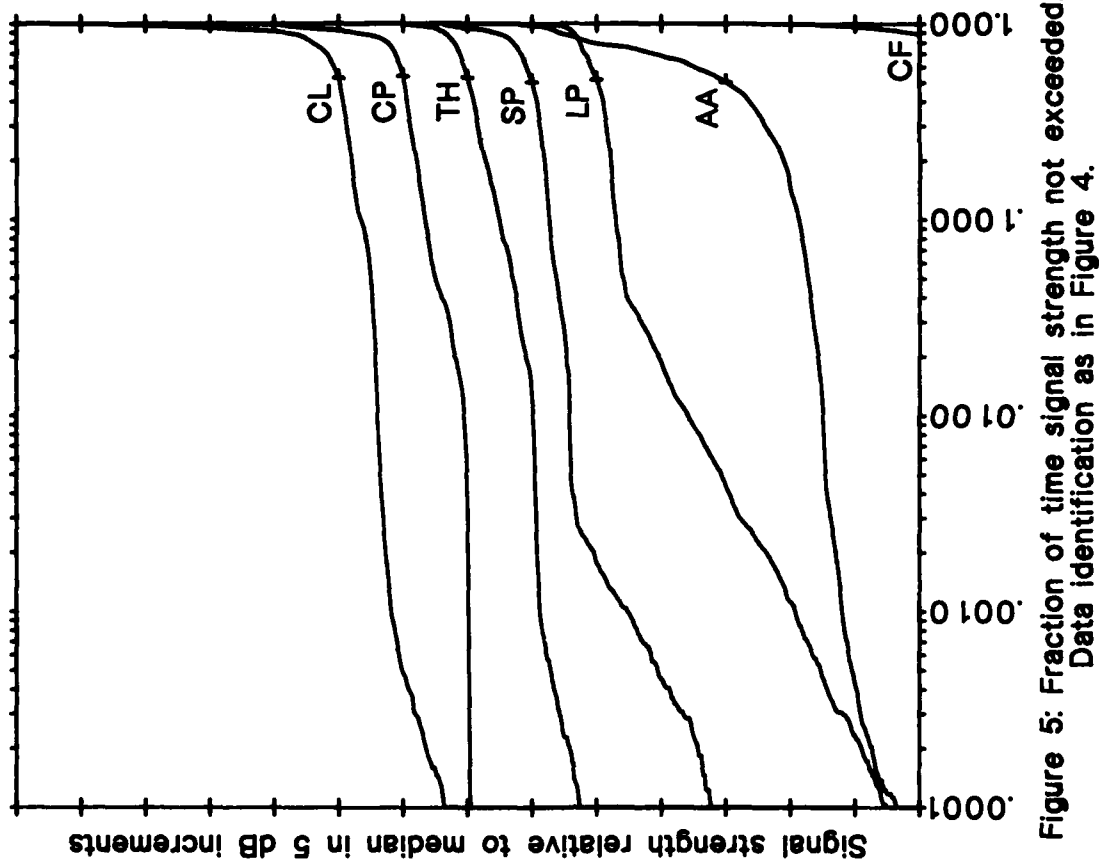


Figure 5: Fraction of time signal strength not exceeded.  
 Data identification as in Figure 4.

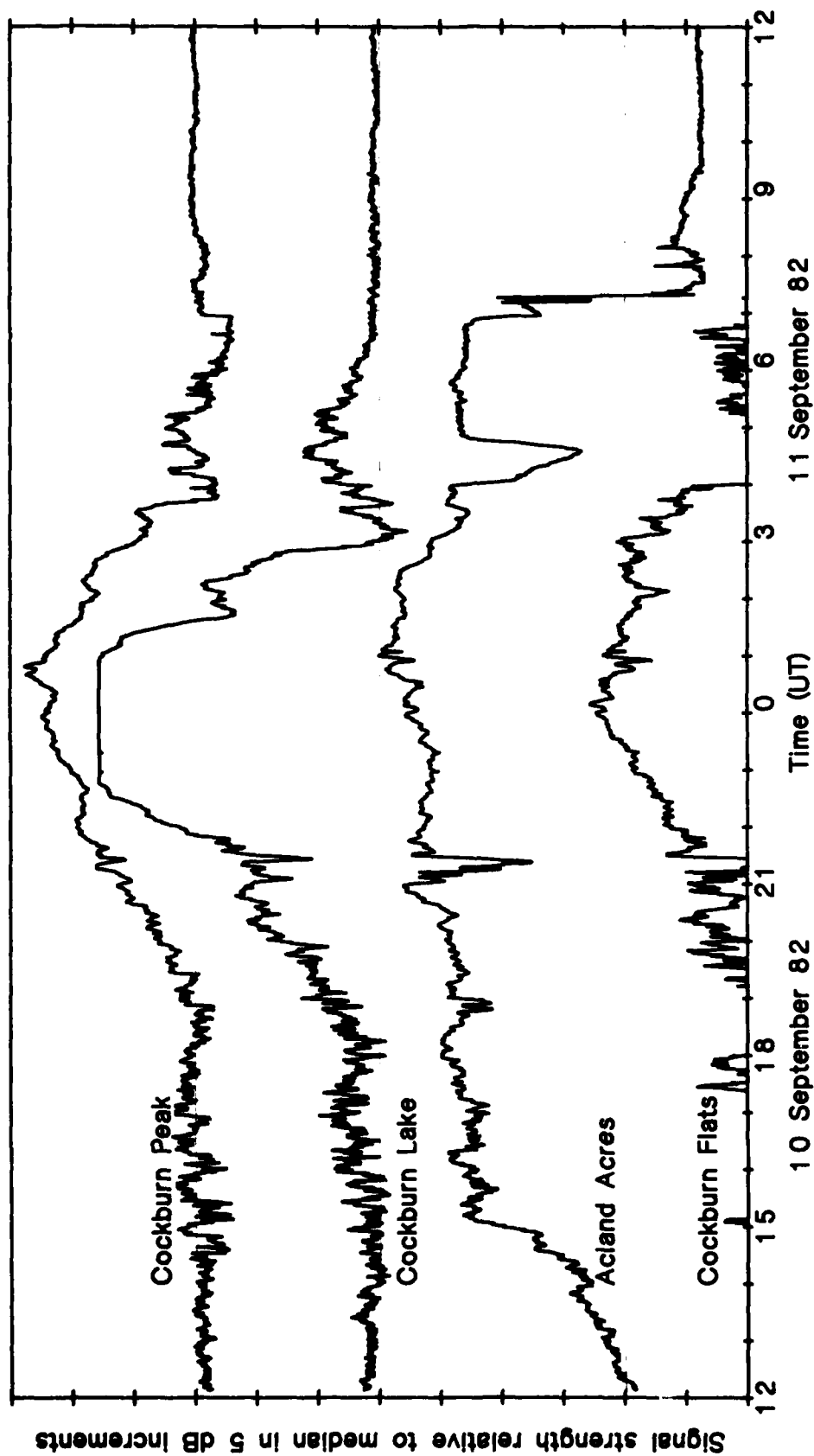
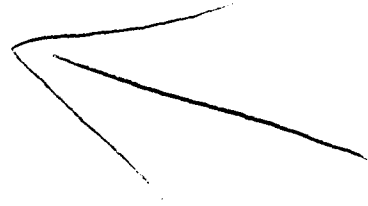


Figure 6: Signal record showing correlation of VHF and UHF signals. The median levels are also shown.

DISCUSSION

K.D. Anderson (U.S.): Do you have any supporting meteorological measurements?

S. McCormick (Canada): No supporting meteorological measurements have been made in this particular experiment. We are planning an expansion of the studies in 1984, and hope to use an acoustic sounder to give a qualitative assessment of atmospheric layers which also may be present.



AD-P003 906

# CONSIDERATIONS PERTINENT TO PROPAGATION PREDICTION METHODS APPLIED TO AIRBORNE MICROWAVE EQUIPMENTS

by  
T Almond  
Royal Signals and Radar Establishment  
St Andrews Road, Malvern, Worcs., WR14 3PS

## SUMMARY

Current coverage diagrams for certain airborne microwave equipments are of the greatest interest to their operators; these equipments include radars, navigation aids, communications, countermeasures sets and command links. A corresponding interest in current coverage resides with operators of similar surface equipments that deal with airborne targets. These coverage diagrams are affected, of course, by large-scale atmospheric refraction and super-refraction. Techniques of operational use for sounding the meteorological and radioelectrical characteristics of the troposphere are reviewed briefly together with coverage prediction methods. It is concluded that there is an unreasonable reliance on horizontal homogeneity in the current prediction techniques coupled with inadequate lateral spatial sampling of the tropospheric structure. It is argued that work should be directed towards devising sounding techniques of lower operating costs, though with sufficient accuracy, so that the spatial sampling is adequate. And, further, that computer prediction methods should be extended to accommodate multiple spatial samples and interpolate the tropospheric structure between sampling locations.

## 1. INTRODUCTION

"1976 was a year in which one of those rare events occurred in England, we were blessed with a summer. It was on 4 July 1976 that I found myself flying a surveillance aircraft over the North Sea and faced with a perplexing problem. My aircraft was at about 3500 feet and my radar equipment was serviceable. Why, then, did I have a totally blank radar screen? Moreover, I was finding it difficult to communicate with the ground agency, experiencing periods of total communications loss. The gods seemed to be against me that day. Intuitively I applied aircrew logic: 'if it doesn't work well here, let's see how well it doesn't work somewhere else!' I had the aircraft descend to 2000 feet. My action seemed to please the gods, the radar picture bloomed into life and the radio cracked into my ears as if it had stored its energy for the previous 2 hours".

If this opening paragraph reads like the introduction to an Air Forces fiction story, let me assure you that it is not. However, it does record my introduction to a phenomenon of which I had been informed but, like many aircrew, had chosen to ignore. I refer, of course, to Anomalous Propagation or Anaprop. What was of more interest to me, however, was not the phenomenon but the operational effect. For 2 hours, low level surveillance had been totally denied by Anaprop caused by a duct between 2800 and 3200 feet. A less fortunate aviator may well have returned to base recording an equipment failure. Had this layer presence and its effect been predicted it would have saved the loss of 2 hours operational flying time. Since that year I have taken an interest in the science of propagation from the point of view of a systems user. There have been some interesting discoveries and I have come to some specific conclusions. It is these discoveries and conclusions that are discussed in this paper.

The first section is a brief review of some of the systems available for use in trying to determine layer presence and assess their possible effects. The second section discusses the application of these equipments and highlights some of their operational limitations. The third section draws some conclusions and suggests some useful research effort could be channelled towards cheap simple sensors that might be distributed on such a scale as to improve lateral assessment of ducting layers.

## 2. ATMOSPHERIC MEASURING AND PROPAGATION MODELLING SYSTEMS

Here, a detailed exposition of the relationship between pressure temperature and humidity and their lapse rate variations that give rise to propagation anomalies will not be presented: Bean and Dutton<sup>(1)</sup> is a suitable treatise for reference. Tropospheric propagation anomalies affect electromagnetic waves of frequency 30 MHz and higher. Moreover, the shorter wavelengths are more prone to ducting than the longer wavelengths. Burrows and Attwood<sup>(2)</sup> conveniently summarize the effect

"At an interface between 2 media of different refractive indices there is partial reflection of radiation for any angle of incidence, but when the phenomenon (partial reflection and partial transmission) takes place in a layer of finite thickness, the reflected radiation is appreciable only at angles near grazing. Furthermore, the reflection coefficient increases with increasing wavelength. This feature distinguishes reflection by a layer from reflection within a layer (ducting) as the latter tends to become less pronounced for longer wavelengths. Reflection by a layer gives rise to additional field strengths near the ground for an emitter below the duct well beyond the optical horizon".

Partially transmitted waves are refracted or super refracted away from the norm. Moreover, it is evident that the ducting layer is not impervious, the layer acts prismatically until the angle of incidence between the ray and the layer is less than  $10^\circ$  in which case it acts as a reflector. The relative position of this reflection to an emitter depends on the vertical separation between the emitter and the layer. These facts have considerable tactical applications. A surveillance radar can achieve enhanced range detections by duct trapping or reflection. On the other hand, the trapping effect of a duct leaves gaps in the normal surveillance radar coverage which could allow intruding aircraft to approach without detection if the latter were aware of these "holes".

The crux of the matter is that in order to employ these tactics one has to be able to detect the presence of a layer, preferably in advance of deploying aircraft, and then determine the possible effect of the layer on the various systems employed. As this effect varies as a function of wavelength, determination can be complex. Equipments operating at 10-20 GHz are likely to suffer different anomalies than equipments operating at 500-1000 MHz. When one examines the range of systems available to a military user for communication and information gathering purposes, one begins to appreciate the problem. Examples are:

- Primary Radar
- Navigation Aids
- Secondary Surveillance Radar (SSR)
- Microwave Identification Systems (IFF)
- Radio Communication Equipments
- Telemetry
- Command Links
- Radiometers
- Countermeasures Emitters
- Electronic Warfare Support Measures

These equipments may be installed on either the airborne element or the terrestrial element. They cover a large and increasing portion of the spectrum and rely on the atmosphere as their medium for transmission. Thus, they are liable to disruption from propagation anomalies. If, however, foreknowledge of duct presence were available to a user action could be taken to avoid the problem or put the phenomenon to practical use. So what facilities are available to the user to accomplish this? As regards detection, a variety of sondes have been developed as well as refractometers and remote sensing devices. An outline of the instruments is now presented.

## 2.1 BALLOON RADIOSONDES

Balloon radiosondes are a familiar tool in radiometeorology. From selected ground stations, sondes are released at regular intervals, usually midday and midnight, and samples of atmospheric pressure, temperature and humidity are relayed to a ground receiver. In the United Kingdom, this is the mainstay of atmospheric condition measurement. The release stations are distributed as shown in fig 1. The inland stations are not shown, because for the purposes of this paper it is the coastal units that are of great interest. Examination of the distribution reveals the large horizontal separation between release stations. This is important as it points to the large uncertainty in atmospheric structure between the stations. A balloon sonde gives a useful indication of the atmospheric structure above the release point but no accurate indication on conditions even 1 km away. However, note the sonde information is also open to error. The sensitivity of the humidity element is poor once saturated because its recovery time is long. There are other problems: response time of the humidity and temperature sensors to temperature changes, thermal lag, hysteresis and contamination of the humidity sensor lead to inaccuracies. Additionally, the sampling rate allows the sonde to ascend through thin layers without detecting them. Hence, the balloon sonde can give an underestimation of duct presence. This is most pertinent in the first 200 m of an ascent.

## 2.2 MINI REFRACTIONSONDE

A recent development at the Naval Air Development Centre (NADC) in America has been the mini refractionsonde: it is primarily designed to overcome the difficulties of release at sea. Because it is single man portable/releasable and extremely light weight it is hoped that smaller military ships will make use of this sonde thereby obtaining more information (laterally) of the atmosphere surrounding, say, a Navy Task Force. The ascent rate is 3.6 m/s and sampling is every 400 ms allowing a complete data frame every 1.4 m. A Finnish company, Vaisala, have developed a similar equipment with compatible performance to that of the NADC sonde. The former is already commercially produced but is slightly heavier and has bulkier ground equipment than the latter. The accuracy of parameter measurement is compatible with that of the dropsonde discussed below.

## 2.3 DROPSONDES

One of the main difficulties of the radio sonde has been flexibility in terms of release points. The largest military ships can release sondes, but these are a slow transport medium and it requires 3-men to release the sonde. A radically different sonde application is the dropsonde deployed from aircraft. Because of the high aircraft speed several sondes can be deployed in areas of interest giving a high spatial sampling in a short period of time. The sondes can be released from high altitude (10 km) and descend to the surface under parachute retardation. Two examples of such a sonde are being used, one by the UK Met Office, one by NADC. Typical descent rates average at about 10 m/s and, because the sonde is of recent design, several sondes can be monitored at the same time giving a near real time indication of a 3-dimensional atmospheric structure within a specific area. Additionally, the sampling rates are higher than in the balloon-sonde leading to higher reliability of duct detection. Moreover, recovery times are better and furthermore, because the sonde has acclimatised by the time it reaches ground level, the readings in the sea-level to 200 m bracket are more accurate. However, thermal lag is still a significant problem. Typical accuracies are

- Temperature measurement to  $\pm 0.5^{\circ}\text{C}$  rms
- Pressure measurement to  $\pm 2\text{mbar}$  rms
- Humidity measurement to  $\pm 5\%$  rms

## 2.4 REFRACTOMETERS

We have noted that sondes are useful but have significant limitations. They can only give indications of atmospheric structures directly above or below release points, but lateral extent

indications requires extrapolation of the data. One equipment that can assist in horizontal structure determination is the refractometer. Airborne refractometers are not new equipments, Bean and Dutton discuss several. However, only recently has an Airborne Microwave Refractometer (AMR) been used consistently by a military unit. An externally mounted aircraft system employing a microwave cavity has been evaluated by the American Navy E-2C. Usually, however, the atmosphere is sampled during climbout and descent only, but could be used to confirm lateral extents of horizontal layers. However, employing aircraft to do this is very expensive in fuel and diverts it from its military task. Nevertheless, the quoted accuracy of measurement is to  $\pm 2N$  units (refractivity units) which satisfies determination criteria for layer presence.

## 2.5 GROUND BASED SENSORS

In the mid-60s radars were first used to examine the atmosphere in clear-air conditions. More recently sensitive doppler radars have been developed to obtain usable signals from all heights in the troposphere. Fixed single beam doppler systems have been used to obtain atmospheric profiles above the radar station. To cover a lateral area of 25 km x 25 km, pairs of scanning doppler systems have been used giving indications of air mass boundaries, wave structures, stable layers and convective thermals. Pk James<sup>(3)</sup> discusses these various techniques and shows interesting examples of the radar output where distinct layers and waves can be seen. James concludes that it may be economical to replace radiosonde ascents with remote sounders able to produce continuous profiles from an unattended station (see also Little 1982<sup>(4)</sup>).

## 2.6 SATELLITE OBSERVATIONS

Recently, interest has developed in the field of monitoring satellites to examine whether they can be used to determine propagation conditions over an extended area. Two such studies are worthy of mention. The first is Direct Inference Techniques (DIT). The technique is discussed by Anderson<sup>(5)</sup> and employs monitoring of satellite rf signals using methods developed by Hitney on Passive Refractive Index by Satellite Monitoring (PRISM). DIT utilize observed differences between the direct and sea reflected path lengths to deduce the true elevation angles at the ground station. By calculating the null locations for a number of assumed refractive profiles based on the known elevation angles from orbit parameters and comparing the modelled null locations with the observed over a period of time, a best fit is obtained thereby yielding a representation of the true refractive structure.

The geometry is shown in Fig. 2. Once the path length difference has been established the elevation angle of nulls for each of a number of assumed refractive profiles is calculated. The ground range to the satellite can then be obtained. Comparison of the computed and observed ranges gives the assumed profile which meets the best fit of the atmospheric profile. However, the results obtained were unreliable, predicting correctly on just over 50% of occasions. Anderson concluded that phase sensitive inversion processes were of doubtful use for extracting refractivity profiles for operational use. The second method is a proposal to use a convolution technique to determine refractive profiles by tracking satellites as they appear over the horizon. A paper by Fernandez and Chambers<sup>(6)</sup> describes the proposed technique.

## 2.7 PREDICTION SYSTEMS

There are, therefore, several methods available to detect the presence of ducts and discussion below assesses their practicalities. But, of more interest to the user is not whether a duct is present, but what effect this duct will have on his operational system. Thus a prediction system is needed. Ray tracing techniques have been available for many years but advances in computer techniques have allowed them to be implemented into a software program for use in real time prediction systems. The basic technique is to feed into a computer model the radar or communication parameters of interest, combine these with the atmospheric conditions of the day and produce a prediction of expected radar or radio coverage. A prominent computer model today is IREPS (Integrated Refractive Effects Prediction System) which has been described by Hitney<sup>(7)</sup>. The radar/communication data can either be input manually or called from store. The atmospheric data can be read from the E-2C AMR, a dropsonde or a conventional radiosonde. The printout of IREPS gives an indication of the height of a layer in the form of  $\Delta M$  or  $\Delta N$  graphs, a signal path loss diagram and a system coverage diagram. An example of the coverage diagram for a 1 GHz radar at 3500 is shown in Fig 3, the shaded area indicates coverage of a 150 m system. A user can obtain predicted propagation ranges for radar, communication and passive detection systems. A system designed at a later date in the United Kingdom produces similar outputs and is referred to as the Indicator of Microwave Propagation<sup>(8)</sup> (IMP). One interesting point about both these systems is that they use the input of a single atmospheric vertical profile and assume horizontal homogeneity.

## 3. DISCUSSION

It has emerged that a fundamental assumption underlying the use of these equipments is that of horizontal homogeneity. The larger lateral separation between UK sonde release stations has been mentioned. Dropsondes can have a reasonable lateral separation, and this can be varied as required. Aircraft mounted refractometers only make one assessment during an ascent. Thus any prediction from a layer presence determination must assume some level of horizontal homogeneity. How valid are such assumptions? Glevy<sup>(9)</sup> stated that the assumption of horizontal homogeneity could be expected to be correct for a majority of time. However, his work was carried out in relation to the Pacific Ocean in areas of stable anti-cyclonic air masses. Results of refractometer assessment suggested that horizontal homogeneity assumptions were reasonable provided that no major landmass was within 80 km if the aircraft was flying to leeward and further that homogeneity could not be expected to hold true across a significant air mass boundary such as a weather front. These E-2C findings highlight the problem of warm air overland disrupting the low level structure of the atmosphere. For example hilly terrain and cities would alter the levels and temperatures of any horizontal layers above them. At a weather front, an

incoming low pressure area would destroy any stable anti-cyclonic airmass layers thereby defeating the homogeneity assumption. This latter assessment was carried out in the Mediterranean, another area of consistent anti-cyclonic air masses. Additionally, in both these areas, only over-sea paths were monitored.

What of areas like the North Sea? As indicated in my opening paragraph anaprop can be operationally significant. Furthermore a study by GTE Sylvania<sup>(10)</sup> suggested that ducting occurs for up to 16% of occasions in the summer months. Unfortunately, consistent anti-cyclonic air masses are a rarity but air patterns tend to change from high to low pressure over relatively short periods. Nevertheless anaprop still leads to problems. Analysis is made more complex by the proximity of coastal regions, the lack of sounding apparatus in the North Sea, the disperse spread of sonde release stations around the North Sea coasts and the impact of local hot spots such as oil fields and coastal locations. On a majority of occasions, assuming horizontal homogeneity for oversea paths in the Mediterranean may be acceptable. For areas such as the North Sea it is less likely to be so.

If then, the user cannot assume horizontal homogeneity what can he do? He could try to improve the lateral extent of his sounding coverage. Currently, in the UK, no dropsondes or refractometers are in widespread use. The expense of using these systems for dedicated purposes could be prohibitive, but they could be used as supplementary capabilities to existing aircraft. However at present the user has to rely on the radiosonde releases. They are so dispersed as to be incapable of providing reliable horizontal indications of atmospheric structure. Moreover, their release times of mid-day and midnight are currently impractical for a user who requires as near real-time data as possible. Furthermore, the coastal locations of these release stations makes them prone to on and off shore airmasses giving rise to local coastal ducts (witness coastal sea fog). Thus, to give the user a reasonable level of confidence in propagation prediction a more extensive lateral system of sounding needs to be employed to cover the horizontal variations in ducting layers as shown in Fig 4.

What might be reasonably done? Deploying many more sonde stations would be expensive, likewise the provision of a network of ground based doppler sensors. Satellite techniques are only embryonic at the moment and again would require extensive signal processing to make them suitable for a user and inference techniques seem to be of little use. Additionally, there is the problem of over sea operation as well as overland. What is needed is a simple, cheap, effective technique for detecting ducting layers in as near real time as possible so that data can be fed into a computer which will accept multi profile inputs thereby giving predictions of coverage for different areas. This may not be as complex as it sounds.

Already, signal strength measurements are carried out between ground based receivers and emitters. Accurate indications of ducting presence can be obtained by assessing the variation in signal strengths. For example the British Telecom measurements between East Anglia and Holland do exactly this for paths over the North Sea. An extension of these techniques, although initially expensive, over the UK and between the UK and other European coastal countries could go some way to solving lateral problems. Additionally a system of weather radars with quite a large lateral coverage in the Southern UK and Southern North Sea (see Fig 5) use techniques to combat anaprop as the latter manifests on the display as rainfall. Inverting these techniques may well allow other users to put the information to tactical advantage.

I quote these two methods as examples of cheap, simple but effective techniques. Certainly in the long term they are cheap because they already exist for other uses. Their effectiveness in propagation determination is yet to be proven completely, but the results of British Telecom Research, Martlesham, have proved very reliable in determining duct presence over the southern North Sea. Simple is of course relative, but it does not rely on dedicated systems such as radars or sondes but on interpreting data already in existence. Moreover, they deal with layers on three dimensions rather than just the one or two dimensional measurements currently in existence. Obviously, feeding this information to user interested parties would involve some form of central communicating body. However, this would have the advantage of pooling information such as radiosonde information, weather forecast, signal strength measurements from various parts of the country and possibly radar detection of anaprop. The advent of digital data links over telephone lines makes this a viable proposition. Moreover, computer prediction could take place on board of large aircraft or at the squadron headquarters of smaller short flight fighter aircraft. This brings me to my second point. Multi-lateral sensor inputs would require a modification to the single input computer prediction programs. This seems only sensible as to cope with varying horizontal structures requires a more flexible prediction approach. However, developing such a model I agree may be difficult and expensive. On the other hand, it may be that with the improvement in mass-produced, cheap high technology a technique to fulfil horizontal extent measurement could be developed. Either way, I feel there is a need to put some effort into research into filling this gap in anaprop detection and prediction techniques and hope that the concern of a user may prompt such research. There is a quandary. Because of the UK weather patterns, lateral measurement attempts may prove fruitless. This is the whole point. Until practical lateral measurements are taken on a large scale, we will never know.

#### 4. CONCLUSIONS

Current sounding techniques are limited in their ability to give an indication of the lateral extent of ducts. Thus for prediction purposes horizontal homogeneity has to be assumed. However, this assumption is valid only in areas of consistent anti-cyclonic airmasses such as the Pacific Ocean. The assumption is not valid in areas of constantly changing airmasses such as the UK and North Sea. The latter areas are also prone to local variations caused by coastal regions, cities and topography. The sounding methods employed in this area (typical of most world regions) are incapable of dealing with these variations. For a user to be able to avoid the problems caused by anaprop or to put it to his advantage he must be aware of its presence and what effect it may have on his operational system. Thus, a near real time detection and prediction method is called for which positively addresses the problem of horizontal extent. Without, this form of technique it seems unlikely that users will be able to exploit anaprop with any degree of confidence.

## 5. REFERENCES

1. Bean B R, Dutton E J, "Radio Meteorology", Dover Publication, New York, 1968.
2. Burrow C R, Attwood S S, "Radio Wave Propagation", Academic Press Incorporated, New York, 1949.
3. James P K, "A review of Radar Observations of the Troposphere in Clear Air Conditions", Radio Science, Vol 15, No 2, Mar-Apr 80, p151-174.
4. Little C G, "Ground Based Remote Sensing for Meteorological Nowcasting", Nowcasting Ed. Browning K A, Academic Press, London.
5. Anderson K D, "Inference of Refractivity Profiles by Satellite-to-Ground RF Measurements", Radio Science, Vol 17, No 3, May-Jun 82, p653-663.
6. Fernandez L J, Chambers B, "On the possibility of Inverting Satellite Tracking Data by means of Convolution Techniques", Proceedings of 3rd International Conference on Antennas and Propagation Part II pp.4-8, Apr 83 (Norwich UK).
7. Hitney H V, "Integrated Refractive Effects Prediction System (IREPS) and Environmental/Weapons Effects Prediction System (E/WEPS)", Conference Proceedings on Atmospheric Refractive Effects Assessment 15 Jan 79, Naval Ocean Systems Centre USA.
8. Wright R E, Burton P J, Lambert C, Barr, J S, "The Tactical Application of Microwave Propagation Prediction" AGARD Proceedings No 331, Conference on Propagation Effects of ECM Resistant Systems in Communication and Navigation, Copenhagen, Denmark 24-28 May 82, pp.17.1 to 17.13.
9. Glevy D F, "Assessment of Radio Propagation Affected by Horizontal Changes in Refractivity", Nav Electronics Laboratory Centre, Private Communication, 3 May 76.
10. Ortenburger L N, "Radiosonde Data Analysis II", GTE Sylvania, Vol 2, Vol 6 and final Report 1977.



FIG.1 DISTRIBUTION OF RADIOSONDE STATIONS IN NORTH SEA REGION

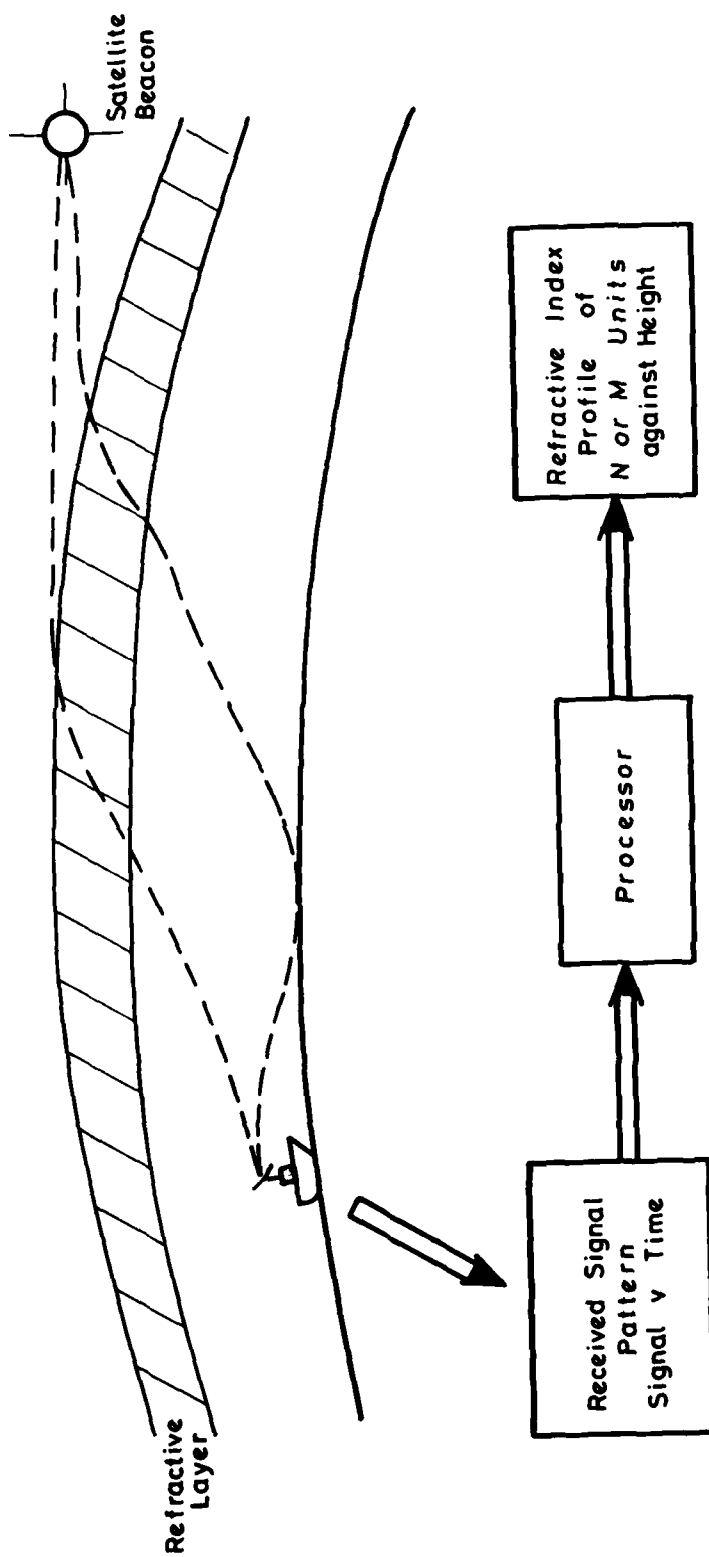


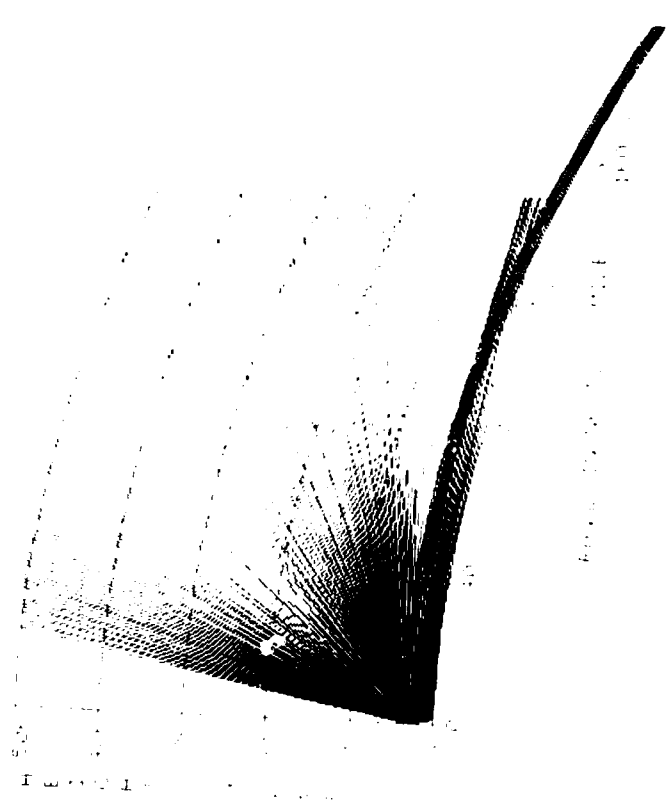
FIG. 2 DIT CONCEPT

\*\*\*\*\* COVER PAGE \*\*\*\*\*

FIG 3

FIG 3 IREPS COVERAGE DIAGRAM

LOCATIONS: EL DORT, DFT  
DATE TIME: EL DORT, DFT



EL DORT, DFT

LOCATIONS: EL DORT, DFT  
DATE TIME: EL DORT, DFT

LOCATIONS: EL DORT, DFT  
DATE TIME: EL DORT, DFT

FIG 3

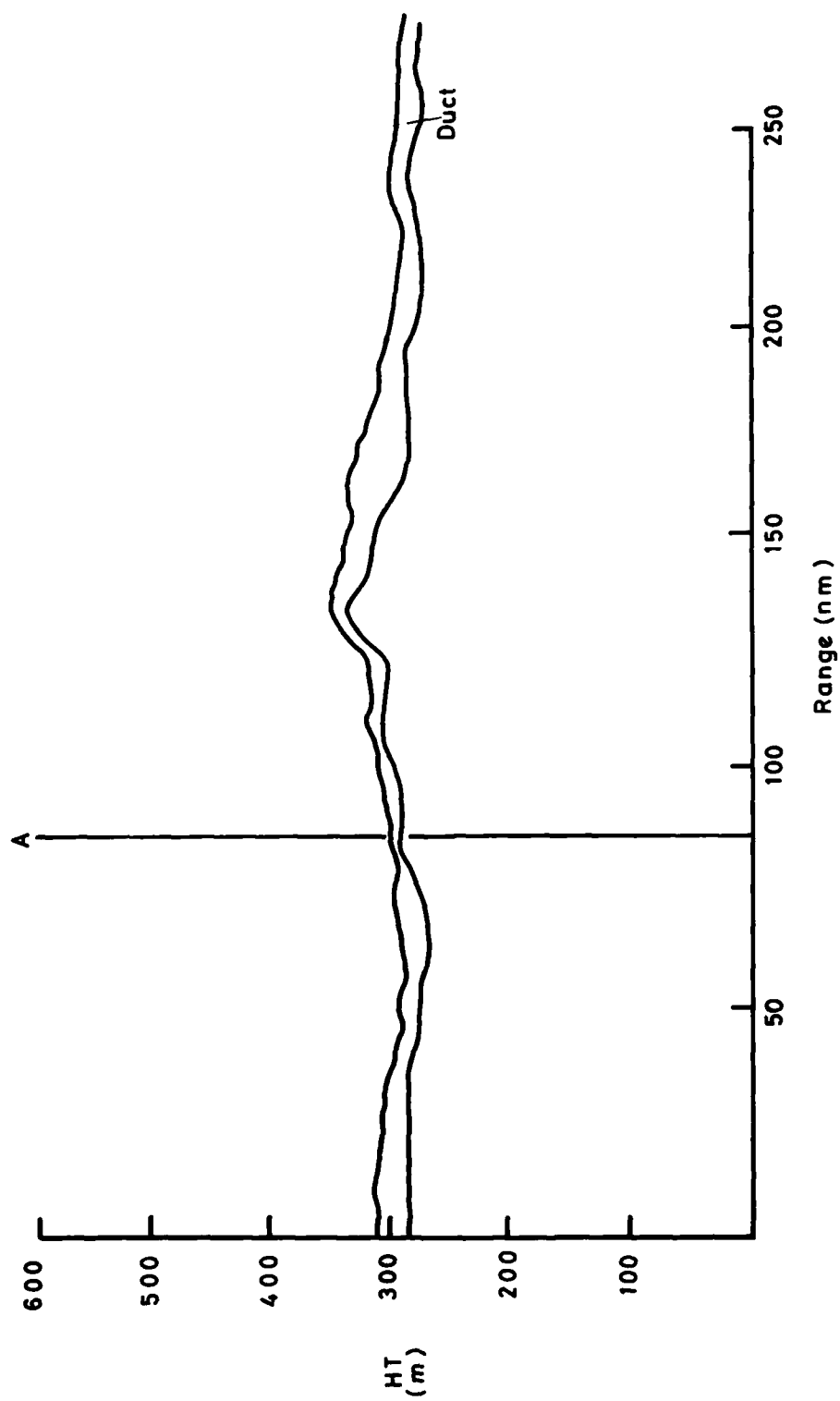


FIG. 4 SINGLE SONDE MEASUREMENT AT PTA DOES NOT REFLECT OVERALL LAYOUT OF DUCT

Existing and presently  
planned radar coverage

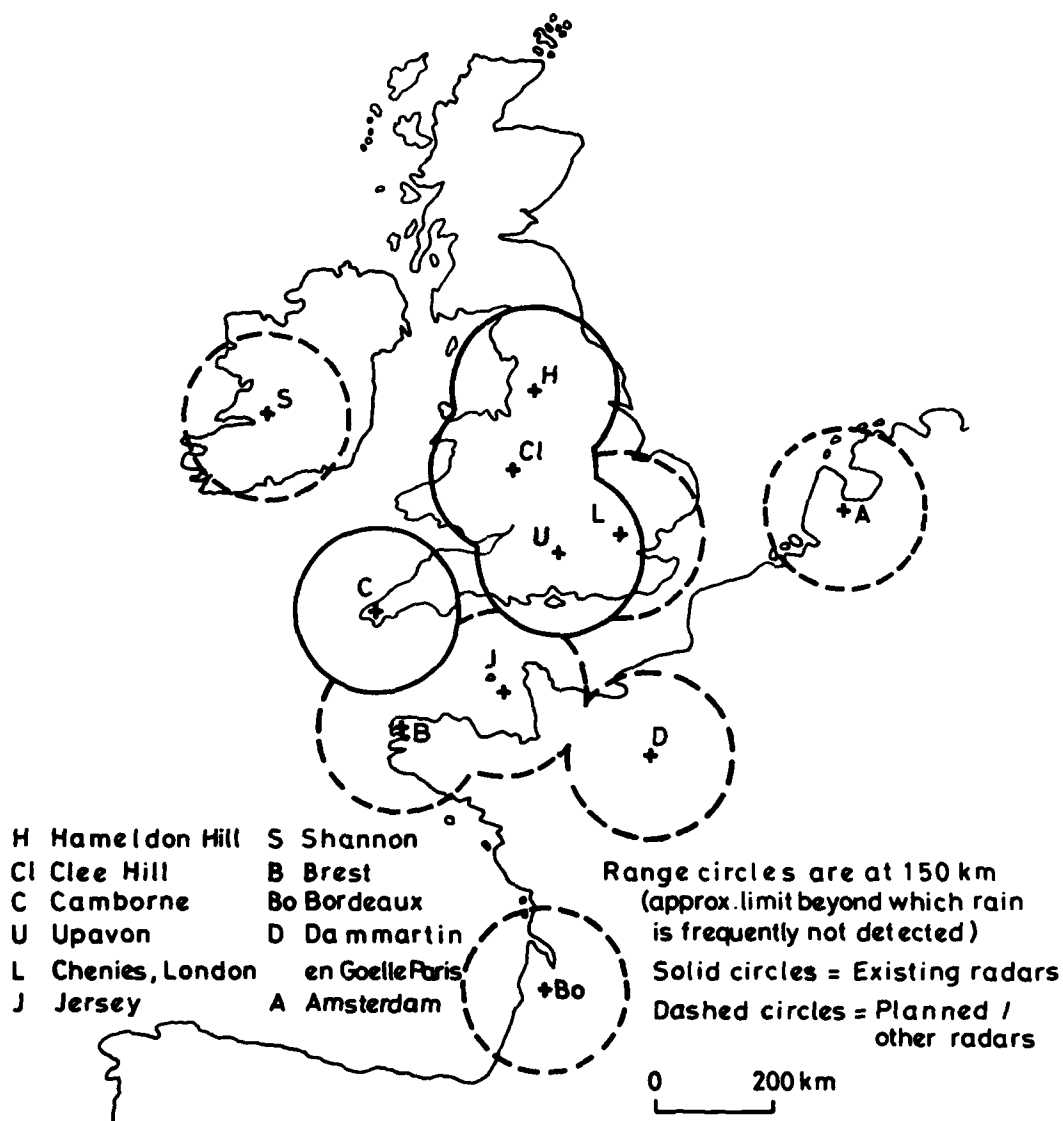


FIG.5 WEATHER RADAR LOCATIONS AND POTENTIAL COVERAGE

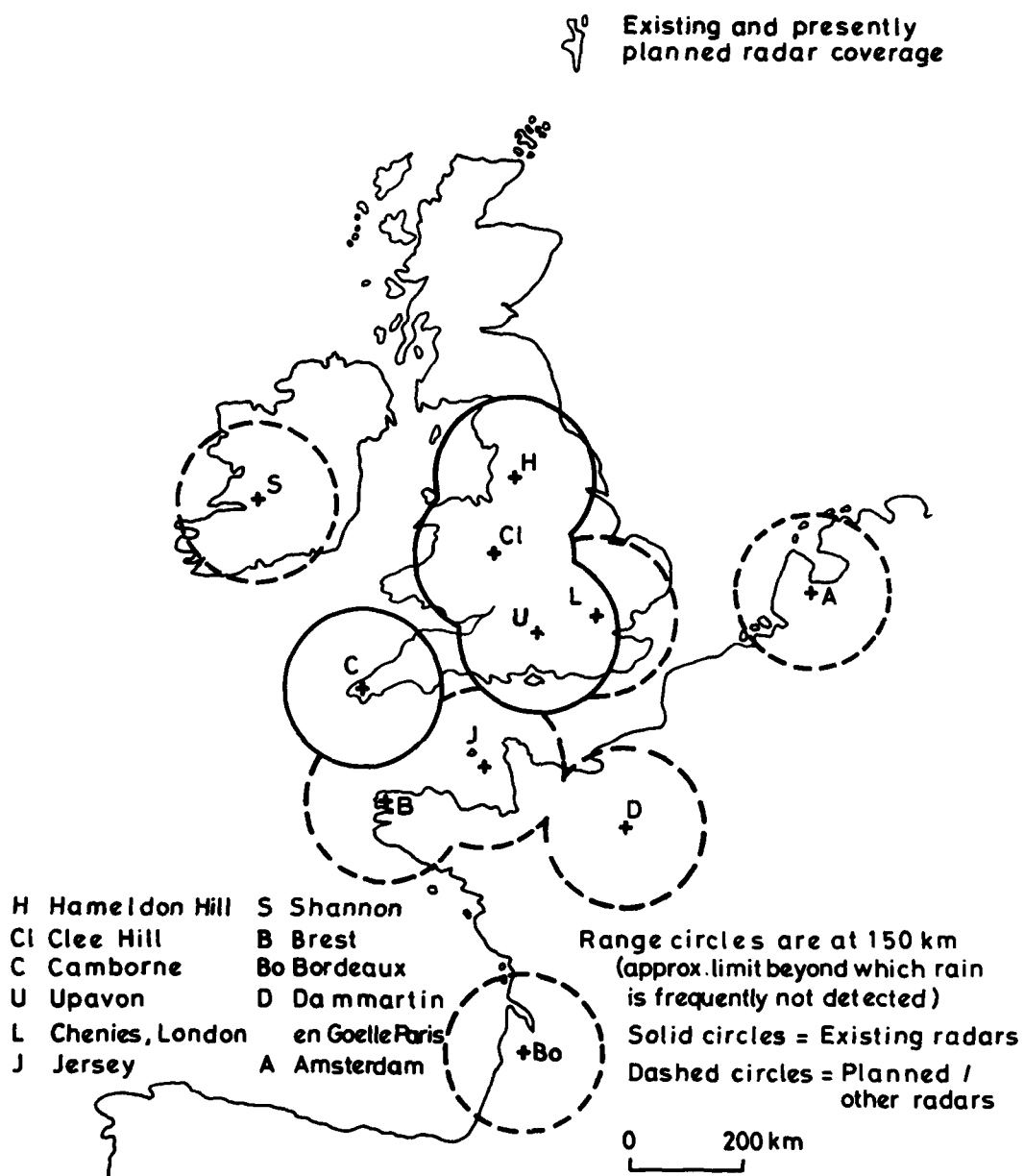


FIG.5 WEATHER RADAR LOCATIONS AND POTENTIAL COVERAGE

## DISCUSSION

H. Soicher (U.S.): Have you considered using remotely powered vehicles for your refractometers?

T. Almond (U.K.): It is very expensive. Suppose that you have an operational squadron that wants to attack a target. The atmosphere of interest is one within 50 km of the target. One argument proposed is that you could mount a refractometer on a remotely piloted vehicle, send it in, and data-link the information back. If it was shot down, you do not lose a pilot, but you do lose the tactical surprise. I am not saying that it is not an option. It is just one that I did not consider seriously.

K.D. Anderson (U.S.): 1) I believe that horizontal homogeneity in the North Sea region is still valid provided you have synoptic information.

2) Radars are generally good for detecting layers. However, it is very difficult to reconstruct the refractivity profile from these observations.

3) The ideas of using remotely sensing stations to monitor field strength, in order to estimate propagation, is being examined.

T. Almond (U.S.): 1) I agree, but the problem is accentuated by the coastal soundings trying to extrapolate for over sea regions.

2) I agree.

T.J. Boulton (U.K.): 1) Is the information presented by the Meteorological Office radars easily assimilated, differentiated, and understood by the users in the sky?

2) Can the computer-produced picture or print-out be up-linked to aircraft?

T. Almond (U.K.): 1) yes. 2) No.

H.W. Ko (U.S.): I concur with your comment on the need to have our two communities communicate more with each other. The stipulation of performance criteria, which could help direct decisions such as the worthiness of horizontal homogeneity assumptions, is missing. A third community, the systems people, could help both of us to organize our thoughts, list our requirements, and systematically attack each issue with technical expedience.

T. Almond (U.S.): I agree entirely.

M.P.M. Hall (U.K.): Earlier in the meeting, you discouraged us in terms of what we could get from satellite elevation to deduce refractive index structure in three dimensions. How can you expect to get information about refractive index, as functions of height and horizontal distance, from just a series of error angles (which are functions of satellite observed angles)?

T. Almond (U.K.): Ken Anderson is the best qualified person to answer your question.

K.D. Anderson (U.S.): We are presently looking at the interference pattern from a beacon satellite at low elevation angles, monitoring the location of the nulls with respect to position, and trying to reconstruct the atmospheric profiles from this information. We are looking for very large structures because it is almost impossible to find fine structures. Even our techniques are only 50% valid, and thus are operationally insignificant.

T. Almond (U.K.): This slide fits Ken's description. His information was really only accurate in 40% of the cases, and therefore was not useful for operational aspects. Sheffield University people want to track a satellite as it comes over the horizon, and compare known measured and apparent positions. The problems were considerable. The only way you can really get a three dimensional idea of the atmospheric or tropospheric structure is with several tracking stations at calculated locations.

K.D. Anderson (U.S.): Small scale turbulence is the limiting factor in using low angle satellites for profile inversion.

E. Vilar (U.K.): This is only a comment. We are using several techniques for remote sensing, with the goal of locating the turbulent layers and some indication of the intensity of the structure content of these layers. Our result will end with the product of  $C^2$  times the layer position, and hopefully another value such as the layer thickness. It involves a combination of spectral analysis of the fluctuation of the signal intensity, direction of arrival, and an extension of work described by Professor Biggs in Paper No. 29 (URSI-Commission F Meeting) from one antenna to a dual antenna.

R.G. Blake (U.K.): This is only a comment. Another source of indications of duct extent could be the monitoring of enhancements on long distance tropospheric scatter links.



## SOME OF THE PAPERS PRESENTED AT THE 1983 IEEE INTERNATIONAL SYMPOSIUM ON ANTENNAS AND

## PROPAGATION AND USNC/URSI MEETING

Albert W. Biggs  
Remote Sensing Laboratory  
Center for Research, Inc.  
The University of Kansas  
Lawrence, Kansas 66045, USA

## SUMMARY

The 1983 IEEE International Symposium on Antennas and Propagation, held jointly with the USNC/URSI Spring Meeting, was at the University of Houston, Houston, Texas, USA, from May 23 to May 26, 1983. This paper reviews some of the papers presented there. The papers reviewed are in the areas of propagation and scattering from randomly distributed particles. Selection was made to correspond with similar papers in the Electromagnetic Wave Propagation Panel (EWPP) Symposium of the Advisory Group on Aerospace Research and Development.

## 1. INTRODUCTION

The papers reviewed are not published in any collected format. Requests for them should be addressed to the authors who may have published them on their own initiative.

## 2. PAPERS ON SCATTERING FROM RAIN AND OTHER RANDOMLY DISTRIBUTED PARTICLES

## 2.1 Results from 19 and 29 GHz Beacon Signal Measurements with COMSTAR Satellites at Clarkson, Maryland

This paper was written by Prabha N. Kumar, Propagation Studies Department, COMSAT Laboratories, 22300 Comsat Drive, Clarksburg, MD 20871, USA. It described rain attenuations for given fade depths. Results are used for determination of switching interval in diversity operations and the transmitter response time for power control operations in satellite communications. Another parameter affecting performance of earth-satellite links is the time interval distribution between fading from rain attenuation. This parameter is useful for communication systems which repeats a message if a fading prevented earlier transmissions. Data was summarized for four years of beacon signals from COMSTAR satellites on fade duration statistics and intervals between fades statistics. For fade depths between 3 and 25 dB, the mean fade duration was between 11 to 3.5 minutes at 19 GHz, and from 16 to 7 minutes at 29 GHz. Seasonal and annual variations of these fades and elevation angle dependence was also described.

## 2.2 Radiative Transfer Theory for Randomly Distributed Nonspherical Particles

This paper was written by Akira Ishimaru, Electrical Engineering Department, University of Washington, Seattle, WA 98195, and Carvour Yeh, Electrical Engineering Department, UCLA, Los Angeles, CA 90024, USA.

Although the scalar radiative transfer theory is adequate for natural light when polarization effects can be neglected, the vector radiative transfer theory has been more appropriate with multiple scattering effects in randomly distributed nonspherical particles. Although studies on vector radiative transfer theory for spherical particles have been made, the general formulations of the vector radiative transfer theory for nonspherical particles have not been fully described. This paper presents a systematic and general formulation for nonspherical particles with Stokes' vectors with the inclusion of all polarization effects. The complete vector equation of transfer was given including the extinction matrix resulting from the nonspherical shapes. The coherent intensity vector was then found for the cross polarization effects. The formulation for the incoherent intensity vector involved Fourier decomposition of the equation of transfer and because of the nonspherical shape, each Fourier component was coupled to each other. Incident waves were polarized and obliquely incident on a slab medium of nonspherical particles, and the transmission and backscattering were considered. Also included were special cases of small particles and the first order scattering solutions for nonspherical particles.

## 2.3 Convergence of the "Spectral-IterativeTechnique" for the Case of Dielectric Scatterers

This paper was written by Raj Mittra and M. Sultan, Electrical Engineering Department, University of Illinois, Urbana, IL, USA. The recent Spectral Iterative Technique (SIT) was recently successfully applied to problems including perfectly conducting scatterers, dielectric scatterers, and combinations of both. This paper gave necessary and sufficient conditions for convergence of SIT for dielectric scatterers. It was found that the spatial current vector at the  $n^{th}$  iteration was

$$\vec{J}_n = \vec{J}_{ex} + \vec{M}^n (\vec{J}_0 - \vec{J}_{ex}), \quad (1)$$

where the vectors  $\vec{J}$  and  $\vec{J}_0$  are the exact and the initial guess for the currents, respectively, and the  $\vec{M}$  matrix is a function of the dielectric properties of the scatterer and the spacing between the sampling points.

In (1),  $\vec{J}_n \rightarrow \vec{J}_{ex}$  with  $n \rightarrow \infty$  provided  $\vec{M}^n \rightarrow \vec{0}$  with  $n \rightarrow \infty$  where  $\vec{0}$  is the null matrix. This latter condition is met when

$$||\vec{M}|| \equiv \max_k |\lambda_k| < 1, \quad (2)$$

where  $||\vec{M}||$  denotes the spectral radius of  $\vec{M}$ , and  $\lambda_k$  are the eigenvalues of the matrix. It is found that  $||\vec{M}||$  depends on the dielectric properties of the scatterer and on the spacing between the sampling points.

For a particular scatterer with fixed dielectric properties, the spacing between the sampling points may be chosen so that (2) is satisfied. The convergence of the iterative procedure does not depend on the initial guess of the current.

#### 2.4 Multiple Scattering Theory for Waves in Discrete Random Media and Comparison with Experiments

This paper was written by V.K. and V.V. Varadan, Ohio State University, Department of Engineering Mechanics, Columbus, Ohio 43210, USA., and V.N. Brongi, Department of Electrical Engineering, Colorado State University, Ft. Collins, CO 80523, USA, and A. Ishimaru, University of Washington, Seattle, WA 98195, USA. It described acoustic and electromagnetic wave attenuation due to multiple scattering in a discrete two-phase media. A self consistent multiple scattering theory with the T matrix of a single scatterer and a suitable averaging technique was used. Ensemble averaging accounted for the statistical position of scatterers. This created a series of equations relating different orders of correlations between scatterers. Lax's quasi-crystalline approximation is used to truncate the series of equations to allow passage to a continuum whose bulk propagation characteristics, phase velocity and coherent wave attenuation, could be studied. The pair-correlation function between scatterers with the Self Consistent Approach was superior to Percus Yevick Approximation when the volume fraction of scatterers was significant. In addition to low frequency analytical results for coherent wave speed and attenuation, the dispersion equation was solved numerically for higher frequencies. The numerical results in this study were in excellent agreement with experimental values.

#### 2.5 Scattering of Electromagnetic Waves from a Half Space of Densely Distributed Dielectric Scatterers

This paper was written by L. Tsang, Electrical Engineering Department, Texas A & M, College Station, TX 77843, USA, and J.A. Kong, Electrical Engineering Department, MIT, Cambridge, MA 02139, USA. Interest in scattering from dense distributions of scatterers continues to grow. An example is dry snow, which is a mixture of ice (10 to 40% in volume) and air. An essential feature of a medium with an appreciable volume of scatterer is that independent scattering is no longer true and that the radiative transfer theory with independent phase function is not valid. Foldy's approximation, which has been successful in scattering effects in tenuous media, is not applicable.

This paper considered the scattering of a plane wave obliquely incident on a half space of densely distributed dielectric scatterers. The quasi-crystalline approximation is used to truncate the hierarchy of multiple scattering equations, and the Percus Yevick Approximation is then used to represent the pair distribution function. The coherent reflected wave was studied with these two approximations. The incoherent scattered wave was calculated with the distorted Born approximation. In the low frequency limit, closed form expressions were obtained for the effective propagation constants, the coherent reflected wave and the bistatic scattering coefficients. Results for higher frequencies were calculated numerically. The advantages of the approach in this paper was that, in the low frequency limit, the effects of specular reflection, Brewster angle, and the Claussius Mossoti relation were obtained. In addition, bistatic scattering coefficients were also found. The theory here has been successfully applied to backscattering data from snow at microwave frequencies.

### 3. PAPERS ON RADAR CROSS SECTIONS OF SCATTERERS

#### 3.1 Radar Cross Section by the Physical Theory of Diffraction

This paper was written by H.B. Tran and T.J. Kim, Northrop Corporation, Hawthorne, CA 90250, CA, USA. It presented a method which utilized the equivalent current concept, developed at Ohio State University, and Ufimtsev's fringing wave current to calculate the monostatic and bistatic radar cross sections (RCS) of a circular or elliptical cylinder, a polygonal cylinder, or a combination of them. The method assumed that the scattered field from a target may be approximated by the sum of the scattered fields from each part of the target.

The equivalent current technique was first applied to the geometrical theory of diffraction (GTD) and to the physical theory of diffraction (PTD) in two dimensions. An arbitrarily oriented wedge of finite length was then studied. The physical optics formulation, which is useful for PTD cases, was also described. Results of monostatic and bistatic RCS of several shapes were shown, and these were compared with GTD results.

#### 3.2 Basic Theory of Radar Polarimetry

This paper was presented by Wolfgang M. Boerner, Electrical Engineering Department, University of Illinois-Chicago, P.O. Box 4348, Chicago, IL 60680, USA. This paper surveyed basic theories of polarization utilization in radar reconstruction, scatter polarization transformation matrices and its invariants of the associated optimal matrix polarizations, and the scatterer descriptive operators.

It then showed how the five independent matrix parameters for the relative phase monostatic scattering matrix describing an isolated, yet regionally distributed target in a reciprocal propagation medium can be recovered from (i) amplitude only, (ii) mixed amplitude plus partial phase, and (iii) complete two step amplitude and phase measurements. Basic properties of the radar target scattering matrix for linear and circular polarization basis were described in terms of geometrical target features as functions of the specular point surface coordinate parameters, known as Gaussian principal, main and related curvature functions. The theoretical part of the paper concluded with introduction of a transport equation formulation for precipitation clutter-wave interaction phenomena in the m to sub mm wave region, utilizing the properties of the partial theory of coherence.

#### 3.3 Polarization Dependence of Residues in the Radar Target Resonance Description

This paper was written by V.K.S. Mirmira and Wolfgang M. Boerner, University of Illinois. This paper described the singularity expansion method (SEM) to study the properties, estimates on material properties and shapes, of the scatterer. It reviewed areas where SEM was used to study defects in solids with acoustics, interaction of elementary particles with Regge pole theory, and radar target identification in electromagnetic scattering. It concluded with an analysis of the polarization dependence on SEM in the form of a Gaussian pulse incident upon a thin wire, and finding the polarization sensitivity of the residues associated with the eigenresonances.

#### 3.4 A Vector Inverse Algorithm for Electromagnetic Scattering

This paper was written by Brett Borden, Naval Weapons Center, China Lake, CA 93553, USA. It was a study of an inverse scattering technique that uses the polarization characteristics of the radar echo, along with a small amount of Doppler processing, to form an image of the convex parts of the scatterer. The depolarization of a radar signal  $\vec{H} = H_x \hat{i} + H_y \hat{j}$  by a scattering surface is related to the local principal curvatures  $K_x$  by the leading edge of the impulse response,

$$RH_{pol} = \frac{1}{2\pi} \left[ \frac{K_x - K_y}{2} \right] \frac{\partial S}{\partial t} [H_x \hat{i} - H_y \hat{j}] \quad , \quad (1)$$

where  $S$  is the illuminated surface area and  $R$  is the range. This equation provided a means by which the local curvature properties of the surface were determined from radar echo polarization. Also, a differential equation from Christoffel-Hurwitz dealt with reconstruction of such a surface from knowledge of this type of information,

$$r^2 \nabla^2 M(\theta, \phi) + 2M(\theta, \phi) = -\left[\frac{1}{K_x} + \frac{1}{K_y}\right] \quad , \quad (2)$$

where  $M$  is the spherical image of the convex scatterer. Since the exact solution required too much input data, the corresponding variational problem was solved,

$$\delta \int \left[ \left( \frac{\partial M}{\partial \theta} \right)^2 + \frac{1}{\sin^2 \theta} \left( \frac{\partial M}{\partial \phi} \right)^2 - 2M^2 - 2\left(\frac{1}{K_x} + \frac{1}{K_y}\right) \right] \sin \theta \, d\theta \, d\phi = 0 \quad , \quad (3)$$

and allow for a solution on a finite data set.

A Fortran program with this finite element inversion algorithm was formed and tested on synthetic data. The effect of perturbed data on the algorithm was investigated, as well as the extent to which the data set could be limited. The technique demonstrated an ability to reconstruct smooth convex bodies from a fairly sparse data set.

# REVIEW OF SOME PAPERS PRESENTED AT THE 1983 URSI COMMISSION F SYMPOSIUM

Albert W. Biggs  
Remote Sensing Laboratory  
Center for Research, Inc.  
The University of Kansas  
Lawrence, Kansas 66045, USA

## SUMMARY

The 1983 URSI Commission F Symposium, "Wave Propagation and Remote Sensing," was the third Commission F International Symposium. It was held at the Université Catholique de Louvain, in Louvain-la-Neuve, Belgium, from June 9 to June 15, 1983. Papers reviewed appear in three sections. The first section is on the influence of rain, dust, aerosols, and other particles on radio wave propagation. The second section is on refraction, turbulence, and multipath effects on line of sight paths. The third section is on long range propagation, ducting, and coverage or prediction problems.

## 1. INTRODUCTION

This paper is a review of some of the papers presented at the 1983 URSI Commission F Symposium held at the Université Catholique de Louvain in Louvain-la-Neuve, Belgium, from June 9 to June 15, 1983. It was the third Commission F International Symposium, following very successful symposia held at La Balle, France, in May, 1977, and at Lennoxville, Canada, in May, 1980. As was the case in La Balle, it was intended to cover the whole field of Commission F, namely wave propagation in non-ionized media, from two points of view: one was the limitations on the performance of telecommunications systems due to propagation effects in the lower atmosphere, and the second was the methods of using such effects for the remote sensing of the lower atmosphere, the surface, and the subsurface of the earth.

The topics at the symposium were relevant to the following aspects:

- clear air refractivity and turbulence,
- rain and dust characteristics,
- attenuation and radiometer measurements,
- surface and volume scattering,
- multipath effects,
- applications to remote sensing,
- inversion methods.

Only the papers in the three sections described in the above summary are reviewed so that there is a correlation with similar sections in the Electromagnetic Wave Propagation Panel (EWPP) Symposium, "Characteristics of the Lower Atmosphere Influencing Radio Wave Propagation," at which this review will be presented.

## 2. PAPERS ON THE INFLUENCE OF RAIN, DUST, AND OTHER PARTICLES ON RADIO WAVE PROPAGATION

### 2.1 Wave Propagation through Precipitations

This paper was an invited review paper and was written, and presented, by P. Delogne, Laboratoire de Télécommunications, Université Catholique de Louvain, Batiment Maxwell, B-1348 Louvain-la-Neuve, Belgium. It discussed (a) the propagation medium, (b) plane wave scattering by an isolated particle, (c) homogeneous plane waves and scattering, (d) scattering by a polydispersion, and (5) thermal radiation of a polydispersion and radiometry.

The major part of this paper described a unified model for interaction of electromagnetic waves with the precipitation medium. Since atmospheric precipitation structures of precipitation media are basically the same all over the world, with variations due to latitude and geographical environment, the model would provide prediction methods worldwide. The development of the model began with scattering of a plane wave by an isolated precipitation particle such as a raindrop or a hailstone. If an incident wave with arbitrary amplitude and polarization is given by

$$\vec{E}_i(\vec{r}) = \vec{E}_{i0} e^{-jk\vec{u}_i \cdot \vec{r}}, \quad (1)$$

then the scattered field is given by

$$\vec{E}_s(R\vec{u}_s) = \vec{G} \cdot \vec{E}_{i0} e^{-jkR/R}, \quad (2)$$

where unit vectors  $\vec{u}_i$  and  $\vec{u}_s$  relate to the incident and scattered fields and the scattering tensor  $\vec{G}$  is

$$\vec{G} = \vec{G}(\vec{u}_s, \vec{u}_i) = \sum_{l,m=1}^2 \vec{e}_{sl} G_{lm} \vec{e}_{im}, \quad (3)$$

with  $\vec{e}_{sl}$  and  $\vec{e}_{im}$  representing orthogonal components of  $\vec{u}_s$  and  $\vec{u}_i$ . Several methods for calculation of the scattering tensor have been reviewed by T. Oguchi (Radio Science, vol. 16, pp. 691-730, 1981).

Since a plane wave expansion of an arbitrary monochromatic field with a triple Fourier transform yields non homogeneous as well as homogeneous plane waves, the model for scattering of a homogeneous plane wave by an isolated particle must be expanded to non homogeneous plane waves. This requires some statistical properties of polydispersions. A macroscopic homogeneous particle dispersion is a three dimensional Poisson process. The mean density of class C particles per unit volume is  $\bar{n}_C$ , and the average distance of the nearest particle of class C,  $\langle R_1 \rangle$ , is  $0.609 \bar{n}_C^{-1/3}$ . Distances  $R_{1,p}$  describe a  $p$  percent chance to find

the nearest particle of class C,

$$R_{1,10} = 0.481 \langle R_1 \rangle, R_{1,90} = 1.345 \langle R_1 \rangle, R_{1,99} = 1.695 \langle R_1 \rangle. \quad (4)$$

The far field conditions for the scattered field require (a)  $R \gg D$ , (b)  $R \gg \lambda/2\pi$ , and (c)  $R > 2 D^2/\lambda$ , where  $D$  is the raindrop diameter, while at the same time a Laws-Parsons (L-P) rain relates rain rates, drop size, and radar reflectivity. For instance, with  $R = 200$  mm/h, 90% of radar reflectivity is from drops with  $D > 0.27$  cm. The average distance of 10 cm is violated by condition (b) for a low GHz radar. Although the author feels that this condition has not been sufficiently studied, it is met with X-band and higher frequencies.

If the above far field conditions are satisfied, homogeneous plane wave expansions can be found with Maxwell's equations, where the current density is  $[\epsilon(r) - \epsilon_0] \vec{E}(r)$ , with  $\epsilon(r)$  relating to the medium. Since a current density  $\vec{J}$  in a volume  $dV$  at  $\vec{r}_0$  is equivalent to a Hertz dipole moment  $d\vec{s} = \vec{J} dV$ , the fields at a point  $\vec{r}$  in air are found by contributions from all Hertz dipoles in the form

$$\vec{E}(\vec{r}) = \int_{4\pi} \vec{F}_E(\vec{r}, \vec{u}) e^{-jk\vec{u} \cdot \vec{r}} d\Omega(\vec{u}), \quad (5)$$

where  $\vec{F}_E$  is given by

$$\vec{F}_E(\vec{r}, \vec{u}) = -\frac{j\omega\mu_0}{4\pi} \int_0^\infty (\vec{r} - \vec{u}R) \cdot \vec{J}(\vec{r}_0) e^{jk\vec{r}_0 \cdot \vec{u}} dR, \quad (6)$$

when  $\vec{r} - \vec{r}_0 = \vec{u}R$  and  $d\Omega$  is a solid angle increment in any direction  $\vec{u}$ . Equation (5) is an expansion of plane waves propagating in all directions  $\vec{u}$  with angular amplitudes  $\vec{F}_E$  per steradian.

Random quasi-monochromatic plane waves are next introduced. The instantaneous field is composed of the coherent field, formed by the first order moment, and the incoherent field  $\xi_n(t)$ ,

$$\xi_n(t) = \xi(t) - \xi_c(t), \quad (7)$$

where  $\xi(t)$  and  $\xi_c(t)$  are instantaneous and coherent fields. Applied to (5), random fields have angular amplitudes which also are random, with the coherent field,

$$\vec{E}_c(\vec{r}) = \int_{4\pi} \vec{F}_c(\vec{r}, \vec{u}) e^{-jk\vec{u} \cdot \vec{r}} d\Omega(\vec{u}), \quad (8)$$

where  $\vec{F}$  is the statistical average of  $\vec{F}_E$ . When (8) is subtracted from (5), the incoherent field  $\vec{E}_n$  is obtained. With second order moments,

$$\langle \vec{E}_n(\vec{r}_1) \vec{E}_n^*(\vec{r}_2) \rangle = \iint_{4\pi \times 4\pi} \langle \vec{F}_n(\vec{r}_1, \vec{u}_1) \vec{F}_n^*(\vec{r}_2, \vec{u}_2) \rangle e^{-jk(\vec{u}_1 \cdot \vec{r}_1 - \vec{u}_2 \cdot \vec{r}_2)} d\Omega(\vec{u}_1) d\Omega(\vec{u}_2). \quad (9)$$

If  $\vec{r}_1 = \vec{r}_2$  and because there is no correlation between plane waves coming from different angular directions, we have

$$\langle \vec{F}_n(\vec{r}, \vec{u}_1) \vec{F}_n^*(\vec{r}, \vec{u}_2) \rangle = \vec{T}_n(\vec{r}, \vec{u}_1) \delta(\vec{u} - \vec{u}_1), \quad (10)$$

$$\langle \vec{E}_n(\vec{r}) \vec{E}_n^*(\vec{r}) \rangle = \int_{4\pi} \vec{T}_n(\vec{r}, \vec{u}) d\Omega(\vec{u}), \quad (11)$$

where the tensor  $\vec{T}$  is the intensity of the incoherent field.

The model is completed with the scattering of an incident electric field by a polydispersion of particles. The coherent field is found with the method of Van de Hulst ("Light Scattering by Small Particles," J. Wiley, 1957), while the incoherent field is from Chandrasekhar's ("Radiative Transfer," Dover, 1960) equation.

## 2.2 Experimental Study of Propagation Characteristics in Millimeter Wave Region

This paper was written by Y. Furukama, T. Manabe, T. Ihara, the presenter, K. Tohma, K. Kitamura, and Y. Imai, Radio Research Laboratories, Ministry of Posts and Communications, Tokyo, Japan. It described a propagation experiment at 50.4, 81.8, 140.7, and 245.5 GHz along a horizontal path of 810 m since October, 1982. With a heavy rainfall rate greater than 10 mm/h, there was no distinctive difference among attenuations at 81.8, 140.7, and 245.5 GHz. Attenuation at 245.5 GHz is slightly smaller than that at 140.7 GHz at the peak of the rainfall. Theoretical attenuations computed by assuming drop size distributions of Laws and Parsons (L-P), and Marshall and Palmer (M-P), and the three year statistical data of multi-frequency rain attenuations of the Radio Research Laboratories (RRL, to be published by Ihara, Furukama, and Manabe in 1983), were plotted against rain attenuation at 245.5 GHz. The drop size distribution was closest to L-P, where the density of drop sizes less than 1.0 mm diameter was less than M-P and RRL. Up to this time there were almost no similar multifrequency experiments.

Attenuations due to fog and water vapor were also measured. Fog has very small water droplets, less than a few ten micrometers, floating in the air. The Rayleigh approximation is suitable for the mm wave scatter of small particles. Attenuation is proportional to floating liquid water content at all four frequencies. Water vapor attenuation at 81.8 and 245.5 GHz increased linearly with the water vapor density. There was not much available data for comparison of the water vapor and fog attenuations. There is an

excess attenuation which cannot be explained by the water vapor absorptions at the frequencies of the radio frequency windows.

### 2.3 Measurements and Analysis of Raindrop Size Distributions in Southwestern Nigeria

This paper was written by G.O. Ajayi and R.L. Olsen, Department of Electrical Engineering, University of Ife, Ile-Ife, Nigeria, and Department of Communications, Communications Research Centre, Ottawa, Canada, respectively, and presented by John Strickland, Communications Research Centre. New Data on the drop size distribution of tropical rain at Ile-Ife, Nigeria (7.5° North, 4.5° East), using an impact-type distrometer, shows some of the differences between raindrop size distributions in this tropical station and in the temperate regions of the world. There are less raindrops in the low diameter drops in tropical regions than for the same rainfall rates in temperate regions. This result has an influence on rain attenuation calculations at higher frequencies, where small raindrops have greater effects. There could be a large error in estimation of attenuation due to tropical rain, especially at mm wavelengths, if the M-P law is used with the estimation.

The modified gamma distribution, using the method of moments regression, has been applied to model tropical raindrop size distribution. This method is based on the assumption of power law relationship between the moments of the measured drop size distribution and the rain rate. It is used to find parameters for modified gamma distributions. The drop size distribution  $N(D)$  is represented as

$$N(D) = A_1 D^p e^{-A_2 D^q}, \quad (1)$$

where  $A_2 = \alpha R^{-\beta}$ . The terms  $\alpha, \beta, A_1, p$ , and  $q$  are found from experimental data of drops size distribution. Good agreement with experimental data was found.

### 2.4 Theoretical and Experimental Study of Propagation by Equatorial and Tropical Rain

This paper was written by F. Moupfouma and J. Tiffon, CNET, 92131 Issy-les-Moulineaux, France, and was jointly presented by both authors. Raindrop size distributions were calculated for the equatorial and tropical climates from data collected for 16 months in the Congo. Predicted line of sight (LOS) attenuation was calculated from these distributions. This was compared with data collected in the Ivory Coast.

### 2.5 Radiometeorological Data for the Prediction of Rain Attenuation on Slant Paths

This paper was written by A. Mawira, presenter, and J. Neesen, Dr. Neher Laboratory, Leidschendam, The Netherlands. It describes the use of radiometeorological data in predicting rain attenuation. Assumptions are that contributions above a rain height  $H$  are negligible, that rain intensity is homogeneous in the vertical direction, and that attenuation  $A_s$  on a slant path can be derived from the attenuation  $A_g$  on the projected horizontal path. These assumptions lead to

$$A_s = A_g / \cos \theta \quad \text{dB}, \quad (1)$$

where

$$A_g = a \int_0^L R(x)^b dx = a R_0^b L_{\text{eff}} \quad \text{dB}, \quad (2)$$

with  $L = H / \tan \theta$ ,  $\theta$  is the elevation angle,  $R(x)$  is the point rain rate at a horizontal distance  $x$  from the earth station in mm/h, and  $L_{\text{eff}} = rL$  in km. The term  $r$  is the reduction coefficient which accounts for the horizontal structure of rain and depends on  $R_0$ , the point rain rate, the horizontal path length  $L$ , and the frequency dependent term  $b$ . A simple form for  $r$  is

$$r(R_0, L; 1) = \frac{240}{M_0} \ln \left[ 1 + \frac{M_0}{240} \right], \quad (3)$$

where  $M_0 = R_0 L$ , with  $R_0$  in mm/h and  $L$  in km.

The vertical structure of rain on the long term rain attenuation statistics is expressed by a single height  $H$ , its mean value instead of rain height statistics. The mean value of rain height equals the average value of the zero degree isotherm plus 0.6 km. The horizontal and vertical structure of rain may be different for different locations, so these must be determined for each location.

### 2.6 Statistics on the Fine Scale Structure of Rain in Stockholm 1977-79

This paper was written and presented by Lars Falk, National Defense Research Institute, Linköping, Sweden. Data on rain rates were collected in a region south of Stockholm for three years, 1977-79. There were 24 rain gauges at Farsta, which is at the southern edge of Stockholm. More rain fell at Farsta than at the gauges in the countryside. The gauges were operated between April and November, but the only yearly statistics affected are for rain rates below 10 mm/h. Statistics from several pairs of rain gauges were introduced over the 10 km path. Curves of correlated probability that a certain rainfall rate is exceeded at two rain gauges simultaneously as a function of distance show both the presence of rain cells and an extended rain structure. Cumulative distributions of the path averaged rain rate were also calculated for 7-10 km distances.

### 2.7 100 GHz Open-Resonator Measurements of Artificial Precipitation and Fog Propagation Parameters

This paper was written by D.J. Harris, presenter, and S. Pickard, Institute of Science and Technology, University of Wales, Cardiff, United Kingdom. An open-resonator cavity is used to measure the scattering cross sections of water drops and fog attenuation. The resonator consisted of two optical mirrors, inner surfaces aluminized with diameters of 23 cm and radii of curvature of 2.44 m, and with centrally placed

apertures 4 mm in diameter. A family of TEM modes are induced by introduction of energy through an aperture in one mirror, and the cavity energy is sampled through a similar aperture in the other mirror. The empty cavity has a value  $Q_0$ . The media loss introduces a Q-factor  $Q_m$ . A scattering object introduces an effective value  $Q_{sc}$ . The total measured Q-factor  $Q_T$  is

$$\frac{1}{Q_T} = \frac{1}{Q_0} + \frac{1}{Q_m} + \frac{1}{Q_{sc}} \quad (1)$$

Measurements may be affected by standing waves between mirrors, so that loss depends on axial position of the scatterer. This is eliminated by two measurements a quarter wavelength apart.

The frequency is 100 GHz, produced by an Impatt oscillator with a frequency sweep exceeding 100 MHz. The empty resonator Q-factor is about 500,000. Stationary scattering objects are suspended with nylon thread, while water drops with diameters 2.8-5.8 mm are produced by a water container with various diameter nozzles. The nozzles may be raised to allow a 6.5 m falling distance, enough for drops to reach near-terminal velocities. Artificial fog is created by placing a plastic box between the mirrors, cooling the upper surface of the box with solid carbon dioxide, and blowing moist air into the box.

The scattering cross sections of falling waterdrops were measured at 100 GHz, with experimental values being close to predicted values from Mie theory and the Ray model (Optics, vol. 11, pp. 1836-1844, 1972) for the complex refractive index of water. The ratio of attenuations of heavy artificial fogs at 0.63  $\mu$ m wavelengths was about 500.

## 2.8 Uncertainties in Estimating Worst Month Statistics for Earth-Space Links Influenced by Rain

This paper was written by P. Misme and P. Waldteufel, CNET, 92131 Issy-les-Moulineaux, France, and was presented by Misme. A recent paper by Misme et al (Ann. Télécom., vol. 37, pp. 325-333, 1981) studied attenuation statistics for several decades and showed that a ten year average cannot be considered as stable. The concept of 'worst month' ceases to apply readily to rain attenuation. Attenuation occurring a few percentages of the year are due most of the time to rain falling on antennas and radomes, and sometimes to clouds, bright band effects, or precipitating zones which do not yield any rain.

Attenuation distributions for Paris, at 12 GHz, were presented for the periods 1940-50, 1950-60, 1969-79, and 1965-79. The last three periods were almost identical. Another set of annual distributions for the 1965-79 period, including extremal curves, showed considerable scatter. One may consider excluding the 'worst year' in a ten year period for CCIR predictions.

## 2.9 An Analytical and Numerical Comparison Between Two Rain Attenuation Prediction Methods for Earth-Satellite Paths

This paper was written and presented by Emanuel Costa, CETUC-PUC/RJ, 22453 Rio de Janeiro RJ, Brazil. It shows that the Misme-Waldteufel integral for prediction of rain attenuation on an earth-satellite link can be analytically transformed. The most important term agrees with the Assis-Einloft method for the same prediction. Attenuations calculated by each method, assuming many combinations of input parameters (frequency, elevation angle, and rainfall rates), were compared with each other and with experimental data.

The Assis-Einloft and the Misme-Fimbel methods yielded almost equivalent results. The rms errors between experimental data and those predicted by each method are approximately equal. Since the Assis-Einloft method is much simpler than the complex Misme-Fimbel method, it should be chosen for predictions of rain attenuation on earth-satellite paths.

## 2.10 Prediction of Rain Attenuation Based on Point Rain Rate Statistics for Alexandria, Egypt

This paper was presented and written by Hassan N. Kheirallah, Electrical Engineering Department, Alexandria University, Alexandria, Egypt. Rain rate data, collected for 28 years in Alexandria, was described. Large variations of total accumulated rain from year to year were encountered. The rain rate models do not provide accurate rain attenuation predictions for regions with climates similar to Alexandria, Egypt, where rainfall is limited to a very few months of the year. Worst month statistics should be considered. When operating above 10 GHz in this area, rain attenuation is more severe than that provided by conventional prediction methods.

## 2.11 Attenuation by Rain on Earth-Space Paths at 13 GHz

Although this paper was written by R.V. Webber, J.I. Strickland, and J.J. Schlesak, Communications Research Centre, Ottawa, Canada, it was actually presented by Strickland. It described rain attenuation measurements at 13 GHz for seven locations across Canada to provide a sampling of different types of areas. Analyses of data from six locations, Mill Village for Atlantic maritime, Ottawa, Allan Park, Thunder Bay, and Melville for continental, and Lake Cowichan for Pacific maritime climates were made. Unfortunately, good data was not obtained from the Fort Smith (60° North) location. The worst monthly distributions were limited to four months beginning in May for Melville and delayed two months later for Allan Park. Ottawa was not sufficiently observed. Lake Cowichan experienced its worst month in the winter months. At Mill Village, any month is a worst month except for March to May.

Although Lake Cowichan has the highest rainfall accumulation, it is least likely to experience precipitation attenuations above 2 dB. Mill Village has the second highest rainfall accumulation and the second lowest thunderstorm days, and it has the highest rain attenuations and longest fading durations. The statistics of precipitation attenuation have a strong dependence on climate. Like Seattle, the rainfall in Lake Cowichan is almost a continuous light misty drizzle.

## 2.12 X-Band Measurements of the Dielectric Constant of Dust

This paper was written by S.M. Sharif and S.I. Ghobrial, Electrical Engineering Department, University of

Khartoum, Khartoum, Sudan. It was presented by N.J. McEwan, University of Bradford, United Kingdom. Descriptions of dielectric constants of dust were made. Effects of humidity, chemical composition, and frequency on the dielectric constant of dust were investigated with these measurements. Small, less than 5%, percentages of moisture create large increases in the real and imaginary parts of the dielectric constant.

Silicon dioxide has the major influence on the real part of the dielectric constant. Aluminum oxide has the greatest effect on the imaginary part of the dielectric constant. Frequency has little significance in the 8.2 to 9.0 GHz.

### 2.13 Effects of Dust/Sandstorms on Some Aspects of Microwave Propagation

Sofa Haddad presented this paper and was a co-author with M.J.H. Salman and R.K. Jha, Electrical Engineering Department, University of Technology, Baghdad, Iraq. Dust and sandstorms were expected to have behavior similar to that of rain, snow, hail, fog, and clouds in scattering microwave energy. Size distributions of duststorm particles are exponential. Dielectric constants at 9.35 GHz varied with moisture content.

Refractive indices and loss tangents increase with particle density and moisture contents of the dust and sandstorms. In severe local dust and sandstorms, terrestrial microwave links are likely to be out of action when they are near large water basins in the summer.

### 2.14 Scattering and Absorption by Atmospheric Aerosol Models

This paper was presented by P.E. Geller, who was a co-author with P.W. Barber, Electrician & Computer Engineering Department, Clarkson College, Potsdam, New York, USA. It used the T-matrix method to calculate scattering by prolate spheroids. It may also be applied to oblate spheroids.

The size and refractive index of the spheroids may be chosen to model atmospheric particulates at wavelengths of interest. The Mueller matrix relates the Stokes parameters I, Q, U, and V of the incident light for spheres and cigar-shaped spheroids.

### 2.15 Backscattering and Differential Backscattering Characteristics of the Melting Layer

This paper was written by A.W. Dissanayake, European Space Agency and Technology Center (ESTEC), Noordwijk, The Netherlands, and M. Chandra and P.A. Watson, University of Bradford, Bradford, United Kingdom. This paper presented an improved model for the radar bright band to characterize the anisotropy observed by dual polarized radars.

When atmospheric ice particles fall through the 0°C level, they begin to melt. The partially melted particles have a high reflectivity for microwaves. This part of the microwave spectrum is known as the "bright band." Although the micro-physics of the melting layer is not well understood, much work related to this layer has been done with radar systems. The modelling of the melting layer starts with the successful prediction of its radar characteristics.

Melting layers, indicated by radar bright bands, are present in stratiform clouds in temperate climates and in anvil clouds found with convective systems in tropical climates. Previous models assumed isotropic particles, and did not predict results predicted by dual polarized radars. The change in this model was to consider non-spherical particles to create anisotropy. Like the previous model, the particles were assumed to be a two layer structure formed by a layer of water on a solid ice particle.

Microwave scattering properties of the non-spherical model were evaluated with the Waterman T-matrix technique (Physical Review, D 10, pp. 2670-2684, 1974). A fairly good agreement for absolute reflectivity is in evidence. The forward scattering properties of these particles may be similarly evaluated, and such calculations can be used in predicting microwave attenuation and depolarization through the melting layer.

### 2.16 Propagation Characteristics at 35 and 78 GHz for Spaceborne Altimeters

This paper was written and presented by D. Tarducci, Centro Studi e Laboratori Telecomunicazioni, 274-10148 Torino, Italy. It described a comprehensive comparison of the propagation characteristics of the 35 and 78 GHz bands for spaceborne radar altimeters, and also for the currently used 13.5 GHz band for radar altimetry. Considerable impairment in rain attenuation was found as frequency increased from 13.5 to 35 GHz, but lesser impairment was found in going from 35 to 78 GHz, especially with rain rates above 30 mm/h. No bandwidth limitations were found at 35 or 78 GHz from in-band amplitude or phase shift behavior.

Although rain backscatter was less at the lowest 13.5 GHz frequency for rain rates above 30 mm/h, the interesting result was less at 78 than at 35 GHz for this rain rate level. This makes the 78 GHz band more suitable, along with advantages of higher resolution, smaller and lighter antennas, and subsequent lower satellite weight.

### 2.17 Site Diversity in Earth to Satellite Links: Radar Measurements and Theoretical Predictions

This paper was written by C. Caproni and J.P.V.P. Baptista, Politecnico di Milano, Spaziali of CNR, Milano, Italy, and E. Matriccioni, Politecnico di Milano, Milano, Italy, and was presented by J.P.V.P. Baptista. A Statistical performance of a site diversity system at 11.6 GHz for earth to satellite links with rain attenuation was described.

Simulation of site diversity links performed with radar data in the Po River Valley for earth satellite paths spaced 1.0 km apart, represented site diversity. Pairs of stations, 1.0 to 20 km apart, were evaluated in terms of rain attenuation and diversity gain. A theoretical model for prediction of single and site diversity attenuation provides excellent results when compared with experimental data.

## 2.18 Attenuation of Radio Waves by Atmospheric Wet Ice and Mixed Phase Hydrometers

The paper was presented by Y.M.M. Antar, who was a co-author with A. Hendry, National Research Council of Canada, Ottawa, Canada K1A 0R8. Observations of radio wave attenuation by wet ice and mixed phase hydrometeors along a slant path at  $36.6^\circ$  elevation angle were described. The attenuation at 28.56 GHz was noticeable larger than that due to rain along the path because of the melting layer constituents, mostly wet snow. When the medium was dry snow, negligible attenuation at microwave frequencies was detected. Only a differential phase shift was observed. An unusual snowstorm was encountered on 19 November 1976, when wet snow was seen on the ground. Although the local meteorological office report showed that 0.5 mm of rain and 1.5 cm of snow fell, no melting layer was detected from radar data.

Estimates of hail attenuation can be made only when the hail storm intersects the propagation path if the rain attenuation is accurately identified. If a heavy rain occurs, this cannot be done. On 22 July 1980, however, severe attenuation was caused by hail while the rain attenuation was relatively low. Hail produces appreciable attenuation, particularly when the hailstone has a coating of water.

### 3. PAPERS ON REFRACTION, TURBULENCE, AND MULTIPATH EFFECTS ON LINE OF SIGHT PATHS

#### 3.1 Wave Propagation: Turbulence in Clear Air

This paper, an invited review paper, was written and presented by Ralph Bolgiano, Junior, Electrical Engineering School, Cornell University, Ithaca, New York, USA. Fluid and thermodynamic processes responsible for the fine-scale structure of the atmospheric refractive index are identified and examined in this paper. The refractive index  $n(\vec{x}, t)$  is affected by both temporal and spatial variants,

$$n(\vec{x}, t) \equiv 1 + N(\vec{x}, t) \times 10^{-6}, \quad (1)$$

where the excess refractivity  $N$  is a function of density  $\rho(\vec{x}, t)$ , or pressure  $p(\vec{x}, t)$  and inverse temperature  $1/T(\vec{x}, t)$ , and of the composition, or specific humidity  $q(\vec{x}, t)$ .

$N(\vec{x}, t)$  consists of an average component  $\bar{N}$  and a fluctuation component  $N'(\vec{x}, t)$ , induced by atmospheric dynamics and resulting variations of pressure, temperature, and composition. At low Mach number  $M$  for atmospheric flow, pressure fluctuations  $p'(\vec{x}, t)$  are negligibly small, but fluctuations in temperature  $T'(\vec{x}, t)$  and specific humidity  $q'(\vec{x}, t)$  are significant for  $N'$ . The process of fluctuations in  $T'$  and  $q'$  is analyzed by (i) mixing process kinematics, and (ii) fluid motion dynamics. Assumptions are that the Reynolds Number  $R$ , the Peclet Number  $P$ , the Rossby Number  $R_0$ , and the ratio of characteristic period for a flow component to the gas molecular relaxation time are much greater than 1.0, and  $M$  is much less than 1.0. These assumptions make the atmosphere act as a perfect gas, and that we have isentropic flow.

Assuming a dynamically incompressible atmosphere, and a passive scalar contaminant  $\psi(\vec{x}, t)$ , that satisfies the conservation equation, the velocity  $\vec{u}(\vec{x}, t)$  and the contaminant  $\psi(\vec{x}, t)$  are resolved into mean and fluctuation components. The mixing process is elucidated by resolving the fluctuation terms into their Fourier components with a velocity fluctuation spectrum  $\vec{U}(\vec{k}, \omega)$  and a contaminant fluctuation spectrum  $\Psi(\vec{k}, \omega)$ . In Fourier space, the desired  $\psi$ -fluctuation component is

$$\Psi(\vec{k}, \omega) = -\frac{i}{\omega} \nabla \cdot \vec{U}(\vec{k}, \omega) + \int \frac{\vec{k}}{\omega} \cdot \vec{U}(\vec{k} - \vec{k}', \omega - \omega') \Psi(\vec{k}', \omega') d\vec{k}' d\omega' \quad (2)$$

$\vec{k}-\omega$  space

The first term is the production term, created by components produced by interaction with the sparse velocity spectrum with the mean gradient,  $\nabla \cdot \vec{U}$ . The second term, a convolution of the velocity spectrum with the contaminant spectrum, shows that a  $\psi$  component arises from a wide range of velocity components with the other  $\psi$  components. This assumes adequate richness in velocity components. If no richness were present, no internal mixing process would be present. A wealth of evidence indicates that internal mixing, represented by the convolution integral, is present. This indicates a broad and rich velocity spectrum.

Small scale motions in the atmosphere are discussed by relating fluctuation components of density, pressure, and velocity. When the medium is incompressible and stratified, subject to the force of gravity, the fluctuation quantities satisfy the associated equations with solutions identified as internal gravity waves. But for high Froude Numbers  $F$  much greater than 1.0, gravity effects are negligible and equilibrium flow is turbulent. The resulting refractive index spectrum exhibits a  $k^{-5/3}$  form.

#### 3.2 Analysis of Multipath Fading Observations on Certain Microwave Paths in British Columbia

This paper was written by N. Owen, British Columbia Telephone Company, Canada, and by E. Lee and M. Kharadly, University of British Columbia, Canada. It was also presented by J.J. Strickland, who did an excellent job of presentation. Results were given for measurements for 12 microwave links in British Columbia, Canada.

Microwave links are using extensive digital modulation during the past few years. Since the Bit Error Rate (BER) is of interest, designs keep the BER with Signal-to-Noise Ratios (SNR's) of about 25 dB. The BER's are high during shallow multipath fading. The probabilities of fading in these instances will be included in system design. The three regions evaluated are the Coastal Mountains and Islands, the Interior Plateau, and the Columbia Mountains and the Southern Rockies.

The first region has heavy precipitation in autumn and winter, mild winters and cool summers. The second is drier with warm summers and cold winters. The third has semi-arid valleys with most precipitation in the winter.

The Morita parameters of the CCIR formula for multipath fading are most appropriate for these links. Most active multipath fading occurs during July to October. Peaks of diurnal multipath fading for links over or along water is from afternoon to sunset. On plateaus or flat terrain, fadings occur at sunrise. The multipath mechanisms are (a) sea breeze, (b) radiation inversion for plateau links, and (c) trapped radiation fog in valleys associated with clear upper air for mountain links.

#### 3.3 The PACEM Experiment on Line of Sight Multipath Propagation

This paper was written by M. Sylvain et al at CNET/PAB/RPE, Issy-les-Moulineaux, France, and was presented by M. Sylvain. It describes a two month experiment on a 37 km path over land from Marcheville to Viabon, France. The purpose of the Propagation en Air Claire Et Météorologie (PACEM) was to gain physical insight into multipath propagation mechanisms on line of sight paths.

The transmitting antenna at Marcheville was 58 m above the ground, sweeping from 10.7 to 11.7 GHz with FM, and the receiving antenna at Viabon was 95 m above the ground. They were both 2 m diameter paraboloid antennas with a combined 44 dB gain. Meteorological instruments at Viabon were a permanently instrumented tower, a tethered balloon, two acoustic sounders, and a lidar for humidity profiles. The tower had sensors to record temperature, wind direction and velocity at seven levels and relative humidity at five levels. The balloon sensors measured the parameters and pressure. The sodar, or acoustic sounders, measured

vertical parameters to 680 m.

Multipath events were observed on 18 nights, about 34 hours. A typical fade lasted more than four hours one night. The refractive index profile obtained during an ascent and descent of the balloon indicated the presence of ducts. Sodar acoustic soundings indicated the presence of a layer of very intense reflectivity in the first few tens of meters during intense fading in a typical case. A second facsimile print of the mini sodar showed an echo layer below 60 m in greater detail than that of of sodar.

### 3.4 Microwave Multipath from Sea Reflections - The Bay of Fundy

This paper was written by A.R. Webster, presenter, and W.L. Lam, Centre for Radio Science, University of Western Ontario, London, Canada. It describes the amplitude distribution of direct and sea reflected rays on two separate links across the Bay of Fundy. The first measurements in 1980 were made between Aylesford, Nova Scotia (NS), and Otter Lake, New Brunswick (NB), Canada, a path of 80.025 km. The second measurement in 1981 was between Otter Lake and Nictaux South, NS, a path of 80.35 km. A transmitted signal is frequency swept from 9.5 to 10.5 GHz in 64 linear steps.

Much heavy fading during the summer months may be attributed to the formation of layers above the Bay. Layers, rather than general gradient changes, explain simultaneous variations in properties of directed and reflected rays. The layers have a large negative refractivity gradient, more or less level with the enclosing land on either side of the Bay. These layers are formed below the line of sight path.

### 3.5 Rates of Change of Propagation Medium Transfer Functions During Selective Fadings

This paper was written and presented by L. Martin, CNET Lannion, 22301 Lannion, France. It described several selective fadings on a 50 km path in a 400 MHz band, centered at 11.45 GHz. The amplitude distortion curves were recorded with maximum relative level  $A$  and its associated frequency  $F_x$ , and the minimum relative level  $A_x$  and its associated frequency  $F_x$ . The selectivity of many curves was due to the ray giving most distortion. The delay of this ray was

$$T = \frac{1}{2[F_x - F_n]} = \frac{2k + 1}{2F_x}, \quad (1)$$

where  $k$  is an integer.

The rates of change of  $A_x$  were fast because it depended on phase shift variations between components of received signal multipath fadings. Rates of change of  $A$  were low. It was assumed that rates of change of refractive index profile curvatures were low. Values of rates of change of  $T$  seem to be of the same order as layer height variations in multipath fading conditions. Seasonal selective fading was observed. Rates of change of selective fading parameters were lower in July 1979 than in January 1980. This phenomena was probably due to layer thicknesses, which are thick in the summer and thin in the winter.

### 3.6 Distortion in FM Car Radios Caused by Multipath Reception and Their Reduction by Means of Antenna Diversity

This paper was written by H.K. Lindenmeier, E.J. Manner, and L.M. Reiter, presenter, University of the Bundeswehr Munich, Werner-Heisenberg-Weg 39, D-8014 Munich, Federal Republic of Germany. It describes reception interruptions in the form of temporary noise increases or of distortion of AF-frequencies, especially in areas of poor signal levels. These distortions come from the spatial dependent carrier amplitude, and are caused by statistical interference of a multitude of waves with randomly distributed amplitudes and phases. Usually, the antenna reception  $\vec{V}_R(f)$  is

$$\vec{V}_R(f) = \vec{S}(f) \cdot \vec{V}_T(f), \quad (1)$$

where  $\vec{V}_T$  is the original spectrum at the transmitter, and  $\vec{S}$  is

$$\vec{S}(f) = \vec{A}_0 + \sum_{i=1}^n \vec{A}_i e^{-j\omega\tau_i}, \quad (2)$$

with  $\vec{A}_0$  being the direct wave and  $\vec{A}_i$ ,  $i=1, \dots, n$  being the reflected waves with time delays  $\tau_1, \dots, \tau_n$ .

Since multipath reception is always correlated with FM-AM conversion, the AM modulation can detect multipath reception. An RF-amplitude demodulator was used as a distortion detector to distinguish between an AM signal being caused by the movement of the car in a Rayleigh field (signal strength in multipath reception has a Rayleigh distribution) and an AM signal caused by multipath reception.

Four antennas were installed in the car, connected to the car radio with an electronic switch. Tests were made in city and in mountain areas. Permanent distortion was found in mountain areas, and this made the receiving improvement factor reduce to a value from 2 to 10 by application of antenna diversity compared with 5 to 20 (20 in many cases) in city areas.

### 3.7 Experimental and Analytical Aspects of Atmospheric EHF Refractivity

This paper was written by Hans J. Liebe, presenter, and Donald H. Layton, NTIA, Institute for Telecommunication Sciences, Boulder, Colorado 80303, USA. It discussed laboratory measurements of absolute attenuation rates and refractivities due to water vapor and moist nitrogen. Measurements were made at 138.2 GHz because this frequency falls into an Extremely High Frequency (EHF) window where little attenuation was caused by local lines. Nitrogen simulated dry air, and high relative humidity (RH) varied from 80% to 100%. Temperatures were chosen to be 282°K and 300°K. The continuum spectrum consisted of a self broadening term,  $e^y$ , and a foreign gas broadening term,  $ep$ ,

$$\alpha_c = (k_0 e^2 + k_f ep) \theta^y \text{ dB/km}, \quad (1)$$

where  $e$  is the partial vapor pressure in kPa,  $\theta = 300/T$  is a relative inverse temperature indicator, and  $p$  is the total air pressure in kPa. Line shape theory predicts the coefficients

$$k_0 = 3.80, \quad k_f = 1.38 f^2 \sum_i (b_i b_3 / v_o^3), \quad \gamma = 2.40. \quad (2)$$

A fit of data to (1) produced the results

$$\alpha_c = [39.2 e^2 + 1.44 ep] 10^{-14} \text{ dB/km}. \quad (3)$$

Except for the strong self broadening component proportional to  $e^2$ , no additional anomalous behavior was observed, contrary to findings of A. Deepak et al, "Atmospheric Water Vapor," Academic Press, 1980, and of D.T. Llewellyn-Jones et al, Nature, vol. 274, pp. 876-878, 1978, not even at saturation with RH = 100%. Anomalous absorption behavior, such as high rates, extreme temperature dependences, hystereses in pressure and temperature cycles, were identified as instrumental in the form of condensation effects on the spectrometer. Implications of the new, but preliminary EHF water vapor continuum, is not serious. Up to RH = 60%, the widely used empirical Gaut-Reifenstein (GR) continuum is confirmed. At higher RH, increases over the GR continuum are about 1.5 at RH = 100% and a nonlinear dependence on absolute humidity are predicted.

### 3.8 Propagation Anomalies in a 4, 7, and 11 GHz Line of Sight Path

J.P. Mon presented this paper, and was a co-author with G. Roux, CNET/RPE/ETP, Issy-les-Moulineaux, France. Results described deal with a propagation experiment which was carried out from August 3 to September 21, 1979, over a 48 km LOS path in France. Frequencies were 4.095, 7.184, and 11.603 GHz, with transmitting antenna heights 73, 59, and 61 m, receiving antenna heights 55, 61, and 63 m, antenna gains 41, 34, and 36 dB, antenna beam widths  $10^\circ$ ,  $19^\circ$ , and  $3^\circ$ , and transmit power equal to 30, 26, and 25 dBm, respectively. All antennas were horizontally polarized. An acoustic sounder (sodar) was at midpath. The sodar operated at 2 kHz, 100 ms pulse width, pulse period 4 sec, and 680 m maximum range. Temperature, wet bulb temperature, pressure and RH were recorded at 21.7, 49.3, 77.0, and 104.6 m on a tower near the sodar. A tethered balloon made the same measurements twice a day up to a height of 250 m. Refractivity  $N$  and related parameters  $M$ ,  $K$ , and their gradients were computed from this data.

Intense fades occurred almost every night. The number of fades from Barnett (BSTJ, vol. 51(2), pp. 321-361, 1972) follow

$$N = 1000 f M^{1/2}, \quad (1)$$

where  $f$  is frequency in GHz and  $M = W/W_0$ , the ratio of received power to free space power. The measured results were much less. For example, at 11 GHz, measured fades were  $1288 M^{-1/2}$ , while Barnett's number was  $12,300 M^{-1/2}$ .

A typical fading event during the night of August 13-14 started about 2100 with small amplitude oscillations. These deepened to 20 dB until 0100, then had intense narrow peaks to 45 dB until 0700. From 2100 to 2300, late evening, the upper layer height slowly disappeared as the lower layer height increases. From 0100 to 0300, night, only a single layer was seen (by sodar, as in the other layer observations) during the deep fades. From 0500 to 0700, morning, a new double layer appeared, with the upper layer more intense than the old lower layer. The evolution of the refractivity profiles, derived from the four tower level measurements, showed a negative rate of increase of the refractivity between 21 and 77 m in three profiles from 1802 to 0222. The slope of the refractivity changes from negative to positive between 50 and 104 m from 0234 to 0438.

Statistical properties of the carrier waves were in good agreement with previous experiments. The 11.6 GHz carrier behaved better than expected. Simultaneous recording with a sodar indicated (i) daytime convective activity did not affect microwave signal level, (ii) atmospheric layering, which always occurred at night, created intense multipath fades, (iii) the layer height, which caused fading, was between 40 and 100 m above local ground levels, and (iiii) sodar voltage profiles reflected the different behaviors of signal fades. If used properly, acoustic sounding is a very valuable predictor of microwave impairments on LOS paths.

### 3.9 A Comparison of Radio-Wave and In-Situ Observations of Tropospheric Turbulence and Wind Velocity

This paper was presented by M.H.A.J. Herben, Eindhoven University of Technology, Eindhoven, and co-authored by W. Kolsiek, Royal Netherlands Meteorological Institute, De Bilt, Netherlands. It described amplitude, phase-difference measurements, phase measurements of scintillation at 30 GHz on an 8.2 LOS path. Temperature, humidity fluctuations, and wind speed were measured midway along the path.

The 30 GHz signal from Mierlo was received and mixed in Eindhoven with 29.56 GHz from a voltage controlled oscillator (VCO), phase locked to the incoming signal with a 50 MHz crystal-controlled reference source. The 440 MHz from the mixer is then in turn mixed with 500 MHz (generated with a 10 x multiplier of the 50 MHz reference crystal source), and the 60 MHz is then mixed with the 50 MHz reference to form a 10 MHz signal, which is a measure of the received 30 MHz signal from Mierlo. The 29.56 GHz at Eindhoven is now retransmitted to Mierlo, where the 440 MHz phase locked loop bandwidth is sufficient to assure that the 29.56 GHz signal still has the phase fluctuations of the original 30 GHz signal from Mierlo. After mixing, the 29.56 GHz signal sent from Eindhoven is mixed with 30 GHz to form a 440 MHz reference. The 440 MHz reference is transmitted to Eindhoven, where it is downconverted in two steps with the 50 MHz reference and the 10 x multiplier. The phase of the 10 MHz signals are added, and will equal twice the phase fluctuations of the 30 GHz signal, or the sum of the 30 GHz and 29.56 GHz signal fluctuations.

The theory used in analyzing the data was the weak scattering theory with the application of the Kolmogoroff refractive index spectrum. The phase difference spectrum falls below the corresponding single aperture spectrum for low frequencies, but is twice as large for higher frequencies. This agrees with Taylor's frozen turbulence hypothesis used in weak scattering theory.

Wind velocities from the measured amplitude scintillation spectra agree rather well with the in-situ measured ones. The refractive index structure parameter  $C_n^2$  were about one third of those obtained from those obtained from the 30 GHz amplitude scintillations. Height scaling of  $-4/3$  may not be applicable to these measurements.

Turbulence grows during the mornings of sunny days. At 30 GHz, the contributions to  $C_n^2$  of the humidity structure parameter  $C_h^2$  and the structure parameter of temperature-humidity  $C_{TQ}^2$  were dominant, neglecting the temperature structure parameter  $C_T^2$ .

### 3.10 Amplitude Scintillations in Propagation Paths Above 10 GHz

This paper was written by P. Basili et al and was presented by D. Solimini, Istituto di Elettronica, Università di Roma, Italy. A theoretical form obtained from a spectral approach, combined with experimental data for a 35 GHz LOS link in urban Rome and for the 11 and 17 GHz earth-space path of the SIRIO experiment, were reported here.

Since the electromagnetic field in the atmosphere with a randomly varying refractivity is also random in both space and time, a spectral representation of the log-amplitude amplitude fluctuations are obtained with the Fourier transform of the corresponding temporal covariance function. With weak fluctuations, the Rytov approximation for a scalar field yields spectral densities for the plane and spherical wave cases. For a Kolmogorov spectrum of turbulence, the asymptotic forms as  $\omega \rightarrow 0$  are

$$W_{PW}(\omega) \equiv 2.77 \sigma_{PW}^2 / \omega_t, \quad W_{SW}(\omega) \equiv 1.52 \sigma_{SW}^2 / \omega_t, \quad (1)$$

where  $W_{PW}$  and  $W_{SW}$  are plane and spherical wave spectral densities,  $\sigma^2$  are the variances of the log-amplitude fluctuations, and  $\omega_t$  is related to the wind velocity  $V_t$  transverse to the direction of wave propagation by  $\omega_t = V_t(k_0/L)^{1/2}$ . When  $\omega \rightarrow \infty$ ,

$$\begin{aligned} W_{PW}(\omega) &\equiv 7.14 (\sigma_{PW}^2 / \omega_t) (\omega / \omega_t)^{-8/3}, \\ W_{SW}(\omega) &\equiv 17.67 (\sigma_{SW}^2 / \omega_t) (\omega / \omega_t)^{-8/3} \equiv W_{PW}(\omega). \end{aligned} \quad (2)$$

The breakpoint frequency, where spectral components asymptotically cross each other, is

$$\omega_{CPW} \equiv 1.43 \omega_t, \quad \omega_{CSW} \equiv 2.5 \omega_t, \quad (3)$$

leading to a direct retrieval method for finding  $V_t$ .

Experimental results for the 35 GHz LOS path near Rome show  $V_t$  to be 0.5 and 0.63 m/s at 0840 and 1125 CEMT, respectively. Corresponding values measured near the path center were 0.9 and 1.4 m/s. Field amplitude scintillations at 11 and 17 GHz for the SIRIO earth-space path are given for three different events of the 1979 summer. The spectra of the field fluctuations appear to exhibit common peculiar patterns, although the data refer to events with different average attenuations. At 2200 on July 29, 1979, the average attenuation was moderate. On 2246 on July 29, it was high because of rain on the path. At 0900 on August 4, no average attenuation was observed. The spectral density of sky brightness was linear with a slope slightly less than  $-8/3$ .

Meteorological parameters can be easily monitored for short LOS paths, but earth-space paths have fluctuations created by the entire atmosphere. Clouds, rain, and related forms or precipitation add more difficulties.

### 3.11 An Offsetting Technique to Study Scintillations in Direction of Arrival in Earth-Space Paths

This paper was presented by E. Vilar, and co-authored by P. Lo, G. Weaver, and H. Smith, Electrical Engineering Department, Portsmouth Polytechnic Institute, Anglesea Road, Portsmouth, PO1 3DJ, United Kingdom. It is an investigation of fluctuations in direction of arrival in an earth-space path. The instrumentation is a high gain ground based antenna, which can be offset by  $\pm 7^\circ$  both in elevation and in the horizontal plane. When the antenna is offset from the direction from which the satellite signal is received, the gain must be increased in the receiver amplifier to compensate for loss of antenna gain and the noise floor of the system also increases. The front-fed linearly polarized antenna, with a diameter of 2.4 m, receives beacon signals from the Orbital Test Satellite (OTS 2) at an elevation angle of 31 degrees and a frequency of 12 GHz.

The objectives of studies were short and long term statistics of scintillations on the turbulent slant path. The offset and non-offset configurations are compared to subtract contributions from amplitude scintillations. Values of wind speed and structure constant have been obtained together with numerical values for the angle of arrival spectral density.

#### 4. LONG RANGE PROPAGATION, DUCTING, AND COVERAGE OR PREDICTION PROBLEMS

##### 4.1 Results Obtained from Attenuation Measurements of the Deutsche Bundespost OTS - Propagation Experiment

This paper was presented and written by F. Dintelmann, Forschungsinstitut der Deutschen Bundespost, Darmstadt, Fed. Rep. of Germany. It covers four complete years of 11.6 GHz attenuation data at an elevation angle of 30°. One year, 1975, was obtained from radiometer measurements, while the other three years, 1979-81, were from Orbital Test Satellite (OTS) telemetry beacon recordings. Since a four-year average is less than the five-year average usually selected for long-term averages, computations of various combinations of three-year periods were made and compared with each other. It was concluded that the four-year average represented the average year.

From the data, attenuation distributions were calculated for five fixed time percentages, .05, .03, .01, .005, and .003, by which thresholds were exceeded during three-hour periods of a day. Increased attenuation in the afternoon and evening relative to the annual average will lead to higher system outages if a system designer relied only on annual attenuation data.

Traditional satellites, operating in the 4 to 6 GHz and in the 11 to 14 GHz bands, are usually designed to meet objectives of the Telecommunications Administration for "any month". The concept of "worst month" prompted compilation of annual "worst month" attenuation. This was compared with "worst three-hour period" and the average year cumulative distributions. For example, with 0.02%, the worst month exceeds the worst 3-hours by 5 dB, while the worst 3-hours exceeds the average year by 3 dB. Fade duration data did not follow the log-normal data of other European OTS stations.

##### 4.2 First Global Results of the European Space Agency OTS Propagation Campaign

A. LaLoux, presenter, M. Van Schingen, and P. Sobieski, Laboratoire de Telecommunications, Universite Catholique de Louvain, Belgium, and G. Brussard, ESTEC, Noordwijk, Netherlands, were authors of this paper, which described the first global results of the processing of data from the OTS propagation measurement campaign. This was done with the on-board beacons of OTS, the telemetry carrier TM and the beacon B0/B1.

The European Space Agency (ESA) has been making propagation measurements at fluxmeter stations in Milo (Italy), Stockholm, Dublin and Villafranca (Spain). A radiometer at each station was available. Attenuation was measured with the OTS beacons and calculated with radiometric data. The Fucino (Italy) SCTS collected sky noise temperature, and TM and B0/B1 co- and crosspolar levels. The Noordwijk (Netherlands) station recorded sky noise temperature, B0/B1 co- and crosspolar levels, and TM copolar level.

Cumulative distribution of B1 copolar attenuation for the first year at Fucino was repeated for the other three sites on monthly, yearly, and total bases and for each beacon. Processing of data accounted for variability in copolar beacon level (CPA), crosspolar discrimination level (XPD), diurnal variations, drifts of clear sky level, ranging operation, and losses of lock on receivers. The data base also produced fade duration statistics and diurnal distribution of fades.

Equal probability curves of medium versus sky noise temperatures, TM beacon versus B1 beacon attenuations, and B12 versus B1 attenuations were also plotted. The mean slope of TM versus B1 was about 1.1 for the first year, while it was about 0.85 for the second year. With B12 versus B1, the slope was 1.44.

##### 4.3 Radiometric Sensing of the Atmospheric Boundary Layer

P. Ciotti, A. Silbermann, D. Solimini, Università di Roma, Rome, Italy, and E.R. Westwater, NOAA/Wave Propagation Laboratory, Boulder, Colorado, USA, were authors. D. Solimini presented this paper, which described an experiment at the NOAA Boulder Atmospheric Observatory, where a 300 m instrumental tower provided adequate atmospheric truth. The output of an infrared radiometer, at the base of the tower, was recorded on several days with different meteorological conditions. The temporal data series indicated correlation between radiometer output and the structure of the atmospheric boundary layer.

The radiometric fluctuations were measured with an upward-viewing, highly sensitive radiometer, while simultaneous direct observations of temperature, moisture or humidity, and wind were taken at eight levels by fast response sensors mounted on the 300 m meteorological tower. The measurements were made in August and September 1981.

Fifteen temperature and profiles, averaged over 20 minutes at hourly intervals, from the evening of September 11 to the morning of September 12, 1981, showed the buildup of the nocturnal inversion about one hour after sunset, 1800 MST. At this time, the measured variables were changing at a relatively slow rate, and the radiometer output was decreasing steadily. However, at 1928 and again at 1941, sudden changes in the radiometer occurred, accompanied by rapid drops in the low-level temperature which substantially modified the temperature profile below 100 m. This decrease in temperature was due to the drainage flow from the Rocky Mountains nearby, indicated by wind recordings. A wedge of cold air descending from the mountains had passed the tower, undercutting the warmer air of the lower plains.

A very significant event occurred during the night from 0500 to 0540 with clear sky conditions, slight surface wind, and ground-based temperature inversion. Oscillations occurred in the boundary layer, and wavelike structures were found at various levels in the vertical wind velocities.

The morning of September 12, 1981, was clear and calm, with sunrise at 0545. The boundary layer was quite complex, with multiple layering and wavelike structures in vertical wind velocity at several levels. After 0645, solar heating of the ground began to erode the nocturnal inversion and the depth of the warm layer increased with time. The radiometer also increased its output with triangular patterns characteristic of convective or thermal plumes.

#### 4.4 Capability of Surface-Based Clear-Air Doppler Radar for Monitoring Meteorological Properties in Elevated Layers

This paper was written by Earl E. Gossard, University of Colorado/NOAA, Russell B. Chadwick, Thomas Detman and John Gaynor, NOAA/Wave Propagation Laboratory, Boulder, Colorado. The 300 m tower in this paper was the same tower described in the previous paper. Results were similar to those in the previous paper with the exception of some FM-CW radar measurements instead of radiometric measurements.

The tower was instrumented at levels 10, 22, 50, 100, 150, 250 and 300 m above the ground, with fast response platinum wire thermometers, sonic anemometers, and a Lyman  $\alpha$  humidometer, and slow response quartz thermometers, prop-vane anemometers, and dew-point sensors. The radar refractive index was calculated from temperature and the humidity "mixing ratio".

On February 10, 1982, a rare event occurred. A relatively strong layer was recorded by the radar as it traversed the tower. The radar was operating unmanned, pointing vertically, and it cycled automatically between the Doppler mode (15 seconds) and the backscatter-power-vs-range mode (45 seconds) every minute. It recorded the ascending temperature inversion. Height profiles of  $C_T^2$  were deduced from temperatures at different tower locations. Other temperature inversion data was also obtained, but the correlation of tower-measured and radar-measured turbulence dissipation rate were in good agreement in one case, but there were other cases where the two measurements showed very little correlation.

#### 4.5 Comparison of Two Methods for Estimating the Water Vapor Correction to Altimeter Readings from Radiometric Measurements

This paper was written and presented by Albert Guissard, Laboratoire de Telecommunications, Universite Catholique de Louvain, Belgium. It described two methods for finding the wet path correction to altimeter's range measurements from a two-frequency radiometer. One is a modification of Grody's method for determination of water vapor and liquid from space. The other is an extension of Wu's method for ground determination of the wet path length. Nadir observation is assumed.

Range errors are found from water vapor, clouds, and rain. An approximate form for water vapor range errors is

$$\Delta R = \frac{172}{T_m} V \quad \text{cm}, \quad (1)$$

where  $V$ , in  $\text{kg/m}^2$ , is the integrated water vapor content, and  $T_m$  is  $0.96 \times$  ground level temperature in K. With  $RH = 100\%$  at  $20^\circ \text{C}$ ,  $p_v(0) = 17.5 \text{ g/m}^3$  and  $h_v = 2.6 \text{ km}$ . The range error is 31 cm. The maximum value was found to be about 40 cm at Wake Island, Pago Pago, and Samoa. With clouds, the Rayleigh approximation results in  $\Delta R$  to be 1.5 cm for a very heavy and quite unlikely cloud. The M-P distribution for rain has a range error of only 3 cm at 14 GHz for a 5 km rain height. Thus, cloud and rain contributions to path error are negligible.

The upwelling brightness temperature comes from (i) power emitted by the sea surface, (ii) power emitted down from the atmosphere and scattered by the sea, and (iii) power emitted up from the atmosphere. The radiative transfer equation is

$$T_B = T_U + \tau(0, H) [e T_S + (1-e) T_d] \quad (2)$$

where  $T_B$  is the brightness temperature measured by a pencil beam antenna,  $T_U$  and  $T_d$  are up and down atmospheric contributions,  $T_S$  is the sea surface temperature,  $e$  is effective emissivity, and  $\tau(0, H)$  is the vertical transmittance between the surface and height of observation  $H$ .

Grody's method is a change of (2) into a simple form

$$2[nAV + BL + C] = -\ln[T_a - T_B] + \ln[(1-e)T_b], \quad (3)$$

where  $nAV$  is the total water vapor attenuation,  $BL$  is the total cloud attenuation, and  $C$  is the total oxygen attenuation from ground level to above the atmosphere. The new terms  $T_a$  and  $T_b$  are

$$T_a = T(0) + e \tau [T_S - T(0)], \quad T_b = T(0) - T_C. \quad (4)$$

Measurements at two frequencies yield  $V$  and  $L$  so that (1) yields the range error.

The second method had poorer results than the first method when 1080 cases were analyzed. The first method is also simpler to implement.

## FINAL ROUND TABLE DISCUSSION

To promote free and open discussion it was agreed that the Final Round Table Discussion that appeared in the Conference Proceedings would be written in a non-attribution format. The following paragraphs are a synopsis.

After the Program Chairman explained that there was no agenda and that the success of the Round Table Discussion would depend on the initiative of all participants, discussions began.

It was pointed out that though the Symposium participants were experts there was much more to learn about the propagation medium. Participants who would perhaps like to make a contribution feel somewhat overwhelmed by the immense task of dealing with very sophisticated systems. It is easy when a problem can be confined to a laboratory bench. But when dealing with the earth's atmosphere, how can we deal with the problem of obtaining reliable information so that the atmosphere can be better modelled to find, for example, refractivity profiles. It is remote sensing with a very tight grid with a lot of sensors at each point of that grid. This is impossible for researchers with limited means. Is it possible for this symposium to provide general guidelines that would tell us where our efforts should be directed and, therefore, optimized from the point of view of results?

A response indicated that we can never take all of the data that we would like to take. It is appropriate to try to initiate models which are more specific to smaller areas than models which would pertain to larger, almost global areas. These models would be used as the framework for the planning of tests to validate these models. The variability of the medium against the performance criteria of each system would be tested. There is no sponsor with enough money to saturate an area with meteorological measurement and no one with the capacity to handle that volume of data. However, it would only take a rather small effort from first principles to model certain site specific areas.

It was added that the word "model" is very broad and very vague. There are several ways to model a phenomena. There are complex models and simple models. The complex model is not always the best one. It all depends on the use intended for the model. A simple model dedicated for one type of use might prove unsuitable for a different application. It cannot be said there is one model for a given phenomenon. There are several models more or less adapted to what is needed. When the word "model" is used it means to simplify. This means that some features are dropped depending on the application. Some features can be completely neglected for a given application, while they are basic and fundamental for another application.

The final comment concerning models was that there are empirical models based only on long term statistics, and there are physical models which depend on knowing the physical processes that occur in a given medium. There are many cases where the empirical modelling has reached its ultimate condition. The only way in which it is possible to improve modelling is to study and understand the physical processes, and thereby arrive at a physical model.

Related to the use of models is the question of statistics. The point of view of civilians and military personnel regarding statistics in telecommunications are quite different. In civilian telecommunications, they must guarantee a certain level of standard of performance for the whole time. However, there might be an interruption of propagation between a given Wednesday evening and Thursday morning of a certain month. They cannot guarantee this performance, but only indicate a certain level of performance on the "worst month". In military telecommunications, the situation is different. They have a specific mission on a given day at a given time, and obviously they do not want to be shut down because there has been anomalous propagation on that particular day and at that particular time. Thus, in their case the user's statistics are entirely different. Care must be taken when dealing with statistics to avoid trying to go beyond the laws of nature and the limits of mathematical expectations. Then statistics are almost treated as deterministic laws, and of course they are not. Given a sufficient number of months or years, chances for a given percentage of time allow us to predict what happens in those periods. If we go beyond that, we are going to fail. When you look at statistics of the process, spectra, etc., they show a tremendous amount of variability. However, if you do have a sufficient number of events, then you can say, "In the long run I can now, or will not, exceed something 90% of the time". Therefore, for so many minutes this year, things will behave. But time averages do not make deterministic laws.

This led into a discussion of the modelling philosophies used by CCIR Commission 5 and URSI. One point of view was that there was a division between CCIR Commission 5 and URSI because their interests in one and the same phenomenon are different. URSI and some of the papers presented at this Symposium concentrate on measuring the refractive index profiles and such like. They try to meet the needs of people who want to know what a particular phenomenon is doing at a particular time. As for finding out whether the phenomenon takes place every 30 years or every other week, this may be of very little interest to them.

On the other hand CCIR Commission 5 uses long term statistics. Predictions are made on whether the phenomenon will take place frequently or whether it will be so infrequent that it is possible to neglect. The purpose is not only to understand the phenomenon, but to also find out whether it will be of importance for the communication link, whether it will occur very often or very seldom, and whether it will occur in one area rather than another. Sometimes the phenomenon can not be expressed very well scientifically, but the prediction of the occurrence of such phenomenon can be made with great accuracy. Those who follow the philosophy of CCIR Commission 5 as compared to those that follow URSI may not want to know in detail, if at all, the refractive index. They predict for example, that a particular system goes out for 0.001% of the time per year. Some of the papers presented at this Symposium followed the philosophy of CCIR Commission 5.

Not all participants agreed that there was a great division between CCIR Commission 5 and URSI. It was pointed out that many CCIR documents are based on results obtained at URSI meetings and published in the open literature by people who are concerned with pure science. Also mentioned was that those concerned with CCIR modelling can only do this if they understand the physical processes with which they are working. Some people engaged in URSI activities are involved with both physical processes and statistical modelling.

Noting that both CCIR and URSI dealt with propagation problems though from different aspects the Program Chairman asked for comments concerning how the Electromagnetic Wave Propagation Panel as an AGARD Panel serving the NATO community should address propagation problems. The Panel Chairman and others responded. During the past several years funds for propagation research have been scarce and our administrations have directed work more in the area of applied research. It has been usual for the Electromagnetic Wave Propagation Panel to have sessions on applications following sessions on particular propagation areas that address propagation limitations on systems. It is hoped that the interplay between propagation scientists and systems engineers which might produce a result that is more useful for systems people. However, there are occasions when the Panel decides that an overview on the propagation medium where physics is stressed is needed. Because the Panel covers the frequency spectrum some symposia cover radiowave propagation, some optical wave propagation, and some cover radiowave and optical wave propagation at the same time.

A lively debate between propagation experts and systems engineers ensued. Systems engineers were criticized for not informing theoretical scientists about the problems that needed to be solved and the propagation experts were criticized for not responding in a timely manner to the problems of the systems engineers. One example used was multipath fading for FM microwave links. A comment was made that these microwave links have been in existence since 1949 and attempts are still being made to predict multipath fading effects without models or full scientific explanation. Systems are still being built using empirical data and intuition. A counter argument was that when these systems were first installed they were lightly loaded and degraded gracefully. As requirements for communications channels increased with a corresponding demand for more capacity along with digital links, problems that arise do not allow the system to degrade gracefully. In many areas technology is advancing faster than fundamental physics problems can be resolved. Another counter argument was that propagation studies have followed a cyclic pattern with step-by-step evolution. Following World War II there were a great number of line of sight propagation studies. After a number of years these studies were reduced because, at the time of applications for analog relay systems with voice channel capabilities of a few hundred to a few thousand, it was felt that sufficient knowledge of the propagation medium was available. As digital techniques advanced, new problems such as cross-polarization and frequency selectivity appeared. A new range of line of sight propagation studies were reactivated at a higher level of detail. The issue of the debate was summarized when a comment was made that it was only two years ago that the major emphasis of theoretical scientists on the problems of rain on terrestrial links and earth-space links was reduced in favor of multipath studies. This is in comparison with systems engineers saying that they had to put in digital systems some time ago, and it is a pity they did not have the information needed about multipath. The general conclusion was that some mechanism for identifying the major emerging propagation problems should be established.

The research scientist, the system designer, and the system user are all able to identify propagation problems that need to be resolved. From the whole universe of propagation problems, a means to prioritize the most relevant problems should be established. Some governments have recently established formal procedures for setting priorities. There were several comments indicating that AGARD meetings enabled theoretical scientists, systems designers, and systems users of similar interests to meet and interchange ideas. Those individuals normally not involved in military work can become familiar with military requirements. The topics covered at this meeting were of timely interest. There was an URSI meeting a few months previous to this meeting and a CCIR meeting a few months after this meeting that have and will cover similar topics. The Panel perspective concerning propagation problems is different from that of CCIR and URSI, but it was generally agreed that the innovation at this meeting to highlight the topics presented at other recent symposia and conferences with similar themes was beneficial.

The Program Chairman thanked the participants for their contributions to the Round Table Discussion.

## LIST OF PARTICIPANTS

ALMOND, T. Flt. Lt.†	R.S.R.E., Malvern, Worcs., United Kingdom
ALTSHULER, E. Dr†	RADC/EEP, Hanscom AFB, MA 01731, United States
AMBROSINI, R. Dr†	Institute of Radioastronomy CNR, Via Irnerio 46, 40126 Bologna, Italy
AMITAY, N. Dr†	Bell Laboratories, Room 4G-616, Crawford Corner Road, Holmdel, N.J.07733, United States
ANDERSON, K.A. Mr†	Naval Ocean Systems Center (Code 532), San Diego, CA 92152, United States
ANDERSON, I. Dr	M42A, G.C.H.Q. Benhall, Cheltenham, Glos. GL51, United Kingdom
BATTESTI, J. Mr†	CNET, 38, rue du General Leclerc, 92131 Issy-les-Moulineaux, France
BELROSE, J.S. Dr*	C.R.C., Communications Research Center, Station H, P.O.Box 11490, Canada
(Panel Chairman)	
BESSERUDHAGEN, K. Mr	N.D.R.E., P.O.Box 25, 2007 Kjeller, Norway
BIGGS, A.W. Dr†	Remote Sensing Lab., The University of Kansas, 2291 Irving Hill Drive, Campus West, Lawrence, Kansas 66045, United States
BLAKE, R.G. Dr	R 6.2 British Telecom Research Labs., Martlesham Heath, Ipswich, IPS 7RE, United Kingdom
BLYTHE, J.H. Dr*	Communications Research Lab., Marconi Research Centre, West Hanningfield Road, Gt. Baddow, Chelmsford, Essex, CM2 8HN, United Kingdom
BOITHIAS, L. Mr†	CNET, 38, rue du General Leclerc, 92131 Issy-les-Moulineaux, France
BOSTIAN, C.W. Pr.†	Electrical Engineering Department, Virginia Polytechnic Institute & State University, Blacksburg, VA 24061, United States
BOULTON, T.J. Lt. Cdr.	OEG, HMS Warrior, Northwood, Middlesex, HA6 3HP, United Kingdom
BURROWS, W.G. Dr†	Head of Dept. Radiocommunication & Radar, Brunel Technical College, Ashley Down, Bristol BS7 9BU, United Kingdom
BUSE, U. Mr	ANT Nachrichtentechnik GmbH, RF/V61 Gerberstr.33, D 7150 Backnang, Federal Republic of Germany
CAPORALONI, M. Dr	Department of Physics, Physical Institute, Irnerio 46, 401265 Bologna, Italy
CASSOLA, R. Ing.	AERITALIA, S.A.I.p.a., Gruppo Sistemi Avionici ed Equip., 10072 Caselle T.S.E. Italy
COYNE, V.J. Mr *	Ast. Chief, Strategic Surveillance Br., Surveillance Division, Rome Air Development Center/OCS, Griffiss AFB, N.Y. 13441, United States
CROMBIE, D.D. Mr†	Chief Scientist, ITS.D8, US Department Commerce NTIA, 325 Broadway, Boulder, CO 80303, United States
DELOURMEL, F. Mr	Centre d'Electronique de l'Armement, 35170 BRUZ, France
DOBLE, J.E. Mr	R 634 British Telecom Research Labs., Martlesham Heath, Ipswich, IPS 7RE, United Kingdom
ERSDAL, P. Mr	SKAR, Oslo 8, Norway
FURNES, N. Mr	Norwegian Telecom. Adm., Kirkegt 14, Oslo 1, Norway
GATHMAN, S.G. Dr†	Naval Research Laboratory, 4555 Overlook Avenue, S.W., Washington D.C. 20375, United States
GOUTELARD, C.S. Prof.*	LETTI, Universite de Paris, 9, Avenue de la Division Leclerc, 94230 Cachan, France
GREENWOOD, D. Dr†	MIT, Lincoln Laboratory, P.O. Box 73, Lexington, MA 02173, United States
GUTTEBERG, A.O. Mr†	Norwegian Telecom. ADM, Research Establishment, P.O. Box 83, N-2007 Kjeller, Norway

\* Member of Electromagnetic Wave Propagation Panel

† Author of paper presented at the meeting.

HALL, M.P.M. Mr†	Rutherford Appleton Lab., Chilton Didcot, Oxon, OX11 0QX, United Kingdom
HJELMSTAD, J. Mr	P.O. Box 25, N-2007 Kjeller, Norway
HODARA, H. Dr *	Vice President, Tetra Tech. Inc., 630 North Rosemead Bld., Pasadena, CA 99107, United States
ISMAELLI, A. Mr†	Universita di Firenze, Via S. Marta 3, 50139 Firenze, Italy
JOHANSEN, H.K. Mr	Superintendent N.D.R.E., Division for Electronics, P.O. Box 25, N-2007 Kjeller, Norway
JUILLERAT, R. Mr*	ONERA, B.P. 72, 92322 Chatillon Cedex, France
KASSNER, F. Mr*	Amt fur Wehrgeophysik, Mont Royal, D-5580 Traben Trarbach, Federal Republic of Germany
KO, H. Dr†	Project Engineer, Applied Physics Lab., The Johns Hopkins University, Johns Hopkins Rd, Laurel, MD 2070, United States
LAMBERT, C. Mr	Ferranti Computer Systems Ltd., Western Road, Bracknell, Berks., United Kingdom
LAMPERT, E.W. Dr Ing. *	Postfach 700060, Siemens AG, 8000 Munchen 80, Federal Republic of Germany
LARSEN, J.R. Mr	Radio Communications Office, Noerrebrogade 10, DK 2200 Copenhagen, Denmark
LAWRENCE, R. Dr†	D-PEEK, INC., 5475 Western Avenue, Boulder, CO 80301, United States
LIGTHART, L.P. Mr†	Delft University of Technology, Department of Electrical Engineering, Mekelweg 11, P.O. Box 5031, 2600 B.A. Delft, Netherlands
LUND-HANSEN, T. Mr	N.D.R.E., P.O. Box 25, 2007 Kjeller, Norway
MARTONE, P. Mr†	ESD/FASE, Hanscom AFB, MA 01731, United States
McCORMICK, K.S. Dr	Communications Research Center, Station H, B.P. 490, Ottawa, K2H 8S2, Canada
MEUCCI, G.G. Associate Prof.	Rome University, Dept. Sc. Tec. Com., Via Eudossiana, 18, Roma, Italy
MORLEY, A. Dr†	Plessey Radar, 9 Oakcroft Road, Chessington, Surrey, KT9 1QZ, United Kingdom
MOULSLEY, T.J. Dr	Electrical and Electronic Eng., Portsmouth Polytechnic, Anglesea Rd, Portsmouth, Hants., United Kingdom
NAGTGLAS, B.C. Mr	Koninklijk Instituut v.d. Marine, Het Nieuwe Diep 8, 1781 AC Den Helder, Netherlands
NEESSEN, J.T.A. Ir*	Dr Neher Laboratories PTT, St. Paulusstraat 4, P.O. Box 421, 2260 Ak Leidschendam, Netherlands
NG, Kuen-Wai Mr	Cable & Wireless PLC, Mercury House, Theobalds Road, London WC1X 8RX, United Kingdom
NORDBOTTEN, A. Mr	N.D.R.E., P.O. Box 25, 2007 Kjeller, Norway
PIRWITZ, K.P. Mr	Flotten Kommando, Abt. Geophysik, Postfach 65, 2392 Glucksburg, Federal Republic of Germany
RANALLETTA, L. Lt. Colonel	Comando Coarpo Teccv Esercito, Via A. Scarpa 18, 00161 Roma, Italy
RÉMY, C. Mr*	DRET, Division Telecommunications, 26 Bld. Victor, 75996 Paris Armees, France
ROTHERAM, S. Dr†	Marconi Research Center, West Hanningfield Road, Great Baddow, Chelmsford, Essex, United Kingdom
SARI, J.W. Dr†	Johns Hopkins Un./Applied Physics La., John Hopkins Rd., Laurel, Md. 20707, United States
SKAUG, R. Dr*	N.D.R.E., P.O. Box 25, N-2007 Kjeller, Norway
SOICHER, H. Dr*	DRSEL-COM-RN-1, Fort Monmouth, N.J. 07703, United States
SPOELSTRA, T.A.TH. Dr†	Netherlands Foundation for Radio Ast., Postbus 2, 7990 AA Dwingeloo, Netherlands

\* Member of Electromagnetic Wave Propagation Panel

† Author of paper presented at the meeting.

SPRENKELS, C. Ir. Colonel d'Aviation*	Etat Major de la Force Aerienne, Section Communications & Electronique, (VDM), Quartier Reine Elisabeth, Rue d'Evere, B-1140 Bruxelles, Belgium
STOKKE, K. Mr	Norwegian Telecom Adm., Kirkegt 15, Oslo 1, Norway
STRAUSS, B. Mr†	Meteorologie, 2, Avenue Rapp, 75340 Paris Cedex 7, France
SWAIN, R.S. Mr	R 6.3 British Telecom Research Labs., Martlesham Heath, Ipswich, IPS 7RE, United Kingdom
TAAGHOLT, J. Mr*	Danish Scientific Liaison Officer for Greenland, Technical Univ. of Denmark, DK 2800 Lyngby, Denmark
TANEM, Mr	Norwegian Telecom Adm., Kirkegt 15, Oslo 1, Norway
TAPLIN, D.W. Mr†	BBC Research Department, Kingswood Warren, Tadworth, Surrey KT20 6NP, United Kingdom
THOMSEN, F. Mr	Flyvemateriel Kommandoen, Post Box 130, DK 3500 Varloese, Denmark
TJELTA, T. Mr	Norwegian Telecom. Adm., Research Est., P.O. Box 83, 2007 Kjeller, Norway
TORGERSE, B.P. Mr	Elektrisk Bureau, Division EF, 1360 Nesbru, Norway
UTLAUT, W.F. Dr*	Dir. Inst. for Telecommunication Sc., Natl. Telecom & Info. Admin., Depart- ment of Commerce, Boulder, CO 80303, United States
VILAR, E. Dr†	Departm. of Electrical & Electronic Engineering, Portsmouth Polytechnic, Anglesea Road, Portsmouth, United Kingdom
WANG, G. Mr*	Division for Electronics, N.D.R.E., P.O. Box 25, N-2007 Kjeller, Norway
ZACCANTI, G. Dr	Istituto Fisica Superiore, Universita di Firenze, V. Santa Marta 3, Firenze, Italy

---

\* Member of Electromagnetic Wave Propagation Panel

† Author of paper presented at the meeting

# REPORT DOCUMENTATION PAGE

1. Recipient's Reference	2. Originator's Reference AGARD-CP-346	3. Further Reference ISBN 92-835-0347-3	4. Security Classification of Document UNCLASSIFIED								
5. Originator	Advisory Group for Aerospace Research and Development North Atlantic Treaty Organization 7 rue Ancelle, 92200 Neuilly sur Seine, France										
6. Title	CHARACTERISTICS OF THE LOWER ATMOSPHERE INFLUENCING RADIO WAVE PROPAGATION										
7. Presented at	the 33rd Symposium of the Electromagnetic Wave Propagation Panel held in Spåtind, Norway 4-7 October 1983.										
8. Author(s)/Editor(s) Various	9. Date February 1984										
10. Author's/Editor's Address Various	11. Pages 320										
12. Distribution Statement	This document is distributed in accordance with AGARD policies and regulations, which are outlined on the Outside Back Covers of all AGARD publications.										
13. Keywords/Descriptors	<table border="0"> <tr> <td>Electromagnetic wave propagation</td> <td>Propagation models</td> </tr> <tr> <td>Telecommunication</td> <td>Optical propagation</td> </tr> <tr> <td>Ducting</td> <td>Electromagnetic refraction</td> </tr> <tr> <td>Propagation coverage</td> <td>Precipitation attenuation</td> </tr> </table>			Electromagnetic wave propagation	Propagation models	Telecommunication	Optical propagation	Ducting	Electromagnetic refraction	Propagation coverage	Precipitation attenuation
Electromagnetic wave propagation	Propagation models										
Telecommunication	Optical propagation										
Ducting	Electromagnetic refraction										
Propagation coverage	Precipitation attenuation										
14. Abstract  <p>These Proceedings for the 33rd Symposium/Meeting of the AGARD Electromagnetic Wave Propagation Panel held at the Spåtind Mountain Hotel, Norway, 4-7 October 1983 contain a Technical Evaluation Report, the papers presented, discussions following the presentations of papers and the final Round Table Discussion. There were seven presentations covering the influence of rain and other particles, eleven presentations covering refraction effects including multipath and LOS path, and nine presentations covering long range propagation, including ducting and coverage problems. Reviews of papers presented at the 1983 IEEE International Symposium on Antennas and Propagation and the USNC/URSI Spring Meeting and the URSI Commission F Symposium are also included.</p> <p>The objectives of the Symposium were:</p> <ul style="list-style-type: none"> <li>(a) To discuss the present knowledge of the meteorological and radio-meteorological parameters which may have an influence on terrestrial or earth-space radio links.</li> <li>(b) To discuss the various models and the various methods of predicting the effects of these parameters on radio waves.</li> <li>(c) To discuss the effects of turbulence and particle scattering on optical propagation.</li> <li>(d) To investigate possible methods to overcome the perturbations due to these propagation effects.</li> </ul>											

<p>AGARD Conference Proceedings No.346 Advisory Group for Aerospace Research and Development, NATO CHARACTERISTICS OF THE LOWER ATMOSPHERE INFLUENCING RADIO WAVE PROPAGATION Published February 1984 320 pages</p> <p>These Proceedings for the 33rd Symposium/Meeting of the AGARD Electromagnetic Wave Propagation Panel held at the Spåtind Mountain Hotel, Norway, 4-7 October 1983 contain a Technical Evaluation Report, the papers presented, discussions following the presentations of papers and the final Round Table Discussion. There were seven presentations covering the influence of rain and other particles, eleven presentations covering</p> <p>P.T.O.</p>	<p>AGARD-CP-346</p> <p>Electromagnetic wave propagation Telecommunication Ducting Propagation coverage Propagation models Optical propagation Electromagnetic refraction Precipitation attenuation</p>	<p>AGARD Conference Proceedings No.346 Advisory Group for Aerospace Research and Development, NATO CHARACTERISTICS OF THE LOWER ATMOSPHERE INFLUENCING RADIO WAVE PROPAGATION Published February 1984 320 pages</p> <p>These Proceedings for the 33rd Symposium/Meeting of the AGARD Electromagnetic Wave Propagation Panel held at the Spåtind Mountain Hotel, Norway, 4-7 October 1983 contain a Technical Evaluation Report, the papers presented, discussions following the presentations of papers and the final Round Table Discussion. There were seven presentations covering the influence of rain and other particles, eleven presentations covering</p> <p>P.T.O.</p>	<p>AGARD-CP-346</p> <p>Electromagnetic wave propagation Telecommunication Ducting Propagation coverage Propagation models Optical propagation Electromagnetic refraction Precipitation attenuation</p>
<p>AGARD Conference Proceedings No.346 Advisory Group for Aerospace Research and Development, NATO CHARACTERISTICS OF THE LOWER ATMOSPHERE INFLUENCING RADIO WAVE PROPAGATION Published February 1984 320 pages</p> <p>These Proceedings for the 33rd Symposium/Meeting of the AGARD Electromagnetic Wave Propagation Panel held at the Spåtind Mountain Hotel, Norway, 4-7 October 1983 contain a Technical Evaluation Report, the papers presented, discussions following the presentations of papers and the final Round Table Discussion. There were seven presentations covering the influence of rain and other particles, eleven presentations covering</p> <p>P.T.O.</p>	<p>AGARD-CP-346</p> <p>Electromagnetic wave propagation Telecommunication Ducting Propagation coverage Propagation models Optical propagation Electromagnetic refraction Precipitation attenuation</p>	<p>AGARD Conference Proceedings No.346 Advisory Group for Aerospace Research and Development, NATO CHARACTERISTICS OF THE LOWER ATMOSPHERE INFLUENCING RADIO WAVE PROPAGATION Published February 1984 320 pages</p> <p>These Proceedings for the 33rd Symposium/Meeting of the AGARD Electromagnetic Wave Propagation Panel held at the Spåtind Mountain Hotel, Norway, 4-7 October 1983 contain a Technical Evaluation Report, the papers presented, discussions following the presentations of papers and the final Round Table Discussion. There were seven presentations covering the influence of rain and other particles, eleven presentations covering</p> <p>P.T.O.</p>	<p>AGARD-CP-346</p> <p>Electromagnetic wave propagation Telecommunication Ducting Propagation coverage Propagation models Optical propagation Electromagnetic refraction Precipitation attenuation</p>

<p>refraction effects including multipath and LOS path, and nine presentations covering long range propagation including ducting and coverage problems. Reviews of papers presented at the 1983 IEEE International Symposium on Antennas and Propagation and the USNC/URSI Spring Meeting and the URSI Commission F Symposium are also included.</p> <p>The objectives of the Symposium were:</p> <ul style="list-style-type: none"> <li>(a) To discuss the present knowledge of the meteorological and radio-meteorological parameters which may have an influence on terrestrial or earth-space radio links.</li> <li>(b) To discuss the various models and the various methods of predicting the effects of these parameters on radio waves.</li> <li>(c) To discuss the effects of turbulence and particle scattering on optical propagation.</li> <li>(d) To investigate possible methods to overcome the perturbations due to these propagation effects.</li> </ul> <p>ISBN 92-835-0347-3</p>	<p>refraction effects including multipath and LOS path, and nine presentations covering long range propagation including ducting and coverage problems. Reviews of papers presented at the 1983 IEEE International Symposium on Antennas and Propagation and the USNC/URSI Spring Meeting and the URSI Commission F Symposium are also included.</p> <p>The objectives of the Symposium were:</p> <ul style="list-style-type: none"> <li>(a) To discuss the present knowledge of the meteorological and radio-meteorological parameters which may have an influence on terrestrial or earth-space radio links.</li> <li>(b) To discuss the various models and the various methods of predicting the effects of these parameters on radio waves.</li> <li>(c) To discuss the effects of turbulence and particle scattering on optical propagation.</li> <li>(d) To investigate possible methods to overcome the perturbations due to these propagation effects.</li> </ul> <p>ISBN 92-835-0347-3</p>
<p>refraction effects including multipath and LOS path, and nine presentations covering long range propagation including ducting and coverage problems. Reviews of papers presented at the 1983 IEEE International Symposium on Antennas and Propagation and the USNC/URSI Spring Meeting and the URSI Commission F Symposium are also included.</p> <p>The objectives of the Symposium were:</p> <ul style="list-style-type: none"> <li>(a) To discuss the present knowledge of the meteorological and radio-meteorological parameters which may have an influence on terrestrial or earth-space radio links.</li> <li>(b) To discuss the various models and the various methods of predicting the effects of these parameters on radio waves.</li> <li>(c) To discuss the effects of turbulence and particle scattering on optical propagation.</li> <li>(d) To investigate possible methods to overcome the perturbations due to these propagation effects.</li> </ul> <p>ISBN 92-835-0347-3</p>	<p>refraction effects including multipath and LOS path, and nine presentations covering long range propagation including ducting and coverage problems. Reviews of papers presented at the 1983 IEEE International Symposium on Antennas and Propagation and the USNC/URSI Spring Meeting and the URSI Commission F Symposium are also included.</p> <p>The objectives of the Symposium were:</p> <ul style="list-style-type: none"> <li>(a) To discuss the present knowledge of the meteorological and radio-meteorological parameters which may have an influence on terrestrial or earth-space radio links.</li> <li>(b) To discuss the various models and the various methods of predicting the effects of these parameters on radio waves.</li> <li>(c) To discuss the effects of turbulence and particle scattering on optical propagation.</li> <li>(d) To investigate possible methods to overcome the perturbations due to these propagation effects.</li> </ul> <p>ISBN 92-835-0347-3</p>